ASME
SETTING THE STANDARD

Transactions of the ASME, Journal of Turbomachinery (ISSN 0889-504X) is published quarterly (Jan., Apr., July, Oct.) by The American Society of Mechanical Engineers, Three Park Avenue, New York, NY 10016. Periodicals postage paid at New York, NY and additional mailing offices.
POSTMASTER: Send address changes to Transactions of the ASME, Journal of Turbomachinery, c/o THE AMERICAN SOCIETY OF MECHANICAL ENGINEERS, 22 Law Drive, Box 2300, Fairfield, NJ 07007-2300.
CHANGES OF ADDRESS must be received at Society headquarters seven weeks before they are to be effective. Please send old label and new address.
STATEMENT from By-Laws. The Society shall not be responsible for statements or opinions advanced in papers or ... printed in its publications (B7.1, Par. 3).

Journal of Turbomachinery

Published Quarterly by ASME

VOLUME 130 • NUMBER 2 • APRIL 2008

RESEARCH PAPERS

(Contents continued on inside back cover)

This journal is printed on acid-free paper, which exceeds the ANSI Z39.48-1992 specification for permanence of paper and library materials. ♾™
♻ 85% recycled content, including 10% post-consumer fibers.

(**Contents continued**)

Journal of Turbomachinery **Volume 130, Number 2** **APRIL 2008**

The ASME Journal of Turbomachinery is abstracted and indexed in the following:

Aluminum Industry Abstracts, Aquatic Science and Fisheries Abstracts, Ceramics Abstracts, Chemical Abstracts, Civil Engineering Abstracts, Compendex (The electronic equivalent of Engineering Index), Corrosion Abstracts, Current Contents, Ei EncompassLit, Electronics & Communications Abstracts, Energy Information Abstracts, Engineered Materials Abstracts, Engineering Index, Environmental Science and Pollution Management, Excerpta Medica, Fluidex, Fuel and Energy Abstracts, INSPEC, Index to Scientific Reviews, Materials Science Citation Index, Mechanical & Transportation Engineering Abstracts, Mechanical Engineering Abstracts, METADEX (The electronic equivalent of Metals Abstracts and Alloys Index), Metals Abstracts, Oceanic Abstracts, Pollution Abstracts, Referativnyi Zhurnal, Shock & Vibration Digest, Steels Alert

Analytical Modeling of Turbine Cascade Leading Edge Heat Transfer Using Skin Friction and Pressure Measurements

Brian M. Holley
e-mail: bmholley@engr.uconn.edu

Lee S. Langston
e-mail: langston@engr.uconn.edu

Department of Mechanical Engineering,
University of Connecticut,
191 Auditorium Road,
Storrs, CT 06269-3139

The flow near the leading edge stagnation line of a plane turbine cascade airfoil is analyzed using measurements, analytical modeling, and computational fluid dynamics modeling. New measurements of skin friction and pressure are used to show that the aerodynamics of the leading edge, within what we call the stagnation region, are well described by an exact analytical solution for laminar stagnation-point or Hiemenz flow. The skin friction measurements indicate the extent of the stagnation region. The same parameters that characterize Hiemenz flow also characterize stagnation-point potential flow. The thermal resistance of the laminar momentum boundary layer in Hiemenz flow is absent in the inviscid solution. Consequently, the heat transfer in stagnation-point potential flow is greater than the heat transfer in Hiemenz flow. Based on measurements from an earlier study, the highest heat transfer levels in the cascade occur along the leading edge stagnation line. Stagnation-point potential flow provides a close, upper bound for the measured heat transfer at this small but critical location within the stagnation region. This paper describes how to apply the analytical model for predicting cascade stagnation-line heat transfer using only surface pressure calculations.
[DOI: 10.1115/1.2812328]

Introduction

In a gas turbine, the leading edge of a turbine vane or blade withstands the highest gas path pressures and temperatures of any part of the airfoil surface. Detailed knowledge of the aerodynamics and heat transfer sustained by a turbine airfoil leading edge can help engineers develop designs that facilitate higher gas temperatures and reduced cooling air loads, which leads to enhanced efficiency, durability, and power density.

For example, consider the turbine designer's task in specifying leading edge film cooling hole location and cooling air flow rates, necessary to protect a turbine airfoil immersed in gas path flows whose temperatures exceed the airfoil's superalloy melting point. An error in hole location or in the cooling air pressure ratio in relation to the leading edge gas path stagnation line might cause airfoil gas path inhalation rather than film cooling exhalation, inducing airfoil expiration. Avoiding that situation requires excess cooling air, the use of which can be reduced only through improved design based on a more thorough knowledge of leading edge boundary layers and distributions of pressure and temperature.

It is difficult to get accurate and detailed flow field measurements around a turbine airfoil leading edge because of the thinness of the surface shear layers and the large gradients of velocity and pressure. In this paper, we present detailed nonobtrusive measurements of leading edge skin friction on a large-scale (ten times engine scale) turbine cascade, shown in Fig. 1. Oil film interferometry (OFI) measurements, described by Holley and Langston [1] and in the next section, were taken at 175 locations on the airfoil leading edge. The leading edge of the turbine airfoil is shown in detail in Fig. 2, with arclength s defined from the measured stagnation line and nondimensionalized by axial chord, b_x. A circular cylindrical leading edge with radius $r=0.053$ (1.49 cm/b_x) extends from $s=-0.098$ to $s=+0.048$ on the pressure side. Testing was carried out at engine Reynolds numbers (5.9×10^5) but at low Mach numbers, which approximated incompressible flow and duplicated conditions from earlier studies [1–3] carried out with the same cascade.

Under these test conditions and using OFI skin friction and static pressure measurements, it will be shown that Hiemenz flow [4] accurately models the airfoil leading edge flow field. We call this area of applicability the "stagnation region." This region amounts to 70% of the span and 55% of the circular cylinder leading edge (see Fig. 2), and we surmise that external turbulent motion in the stagnation region has been dissipated. This stagnation region, over which the Hiemenz exact solution to the Navier–Stokes equations applies, surrounds the leading edge spanwise stagnation line (i.e., attachment line in flow field topology). The stagnation line is formed by the loci of points where freestream stagnation streamlines (Fig. 2) impinge along the airfoil leading edge.

Experimental studies [1,3] have illustrated the complicated relationship between skin friction and heat transfer on the surfaces of a turbine cascade. Generally, high skin friction coincides with high heat transfer. For such locations, Reynolds analogy has been used by designers to infer heat transfer from skin friction. A testament to its utility is a recent study by Bons [5] that extends the understanding and applicability of Reynolds analogy. There are, however, locations in a cascade where high heat transfer coincides with little to no skin friction. The leading edge stagnation line is one such location, and it is the region of the highest heat transfer levels as measured by Graziani et al. [3] in the cascade first studied by Langston et al. [2].

Hiemenz flow and its inviscid counterpart, plane stagnation-point potential flow, have locations of zero skin friction, and the analytical models for these flows can be used to evaluate cascade stagnation-line heat transfer. A single parameter a characterizes Hiemenz flow [4]. We have found that the measured skin friction and surface pressure in the stagnation region are predicted by

Contributed by the International Gas Turbine Institute of ASME for publication in the JOURNAL OF TURBOMACHINERY. Manuscript received May 30, 2007; final manuscript received June 26, 2007; published online February 12, 2008. Review conducted by David Wisler. Paper presented at the ASME Turbo Expo 2007: Land, Sea and Air (GT2007), Montreal, Quebec, Canada, May 14–17, 2007.

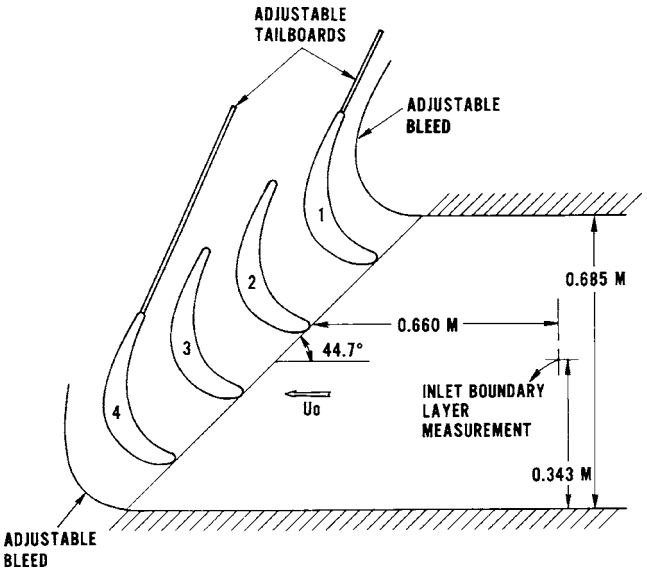

Fig. 1 Schematic of the large-scale airfoil cascade used for measurements of skin friction, static pressure, and heat transfer. The inlet boundary layer measurement location also serves as a reference location for total and static pressures.

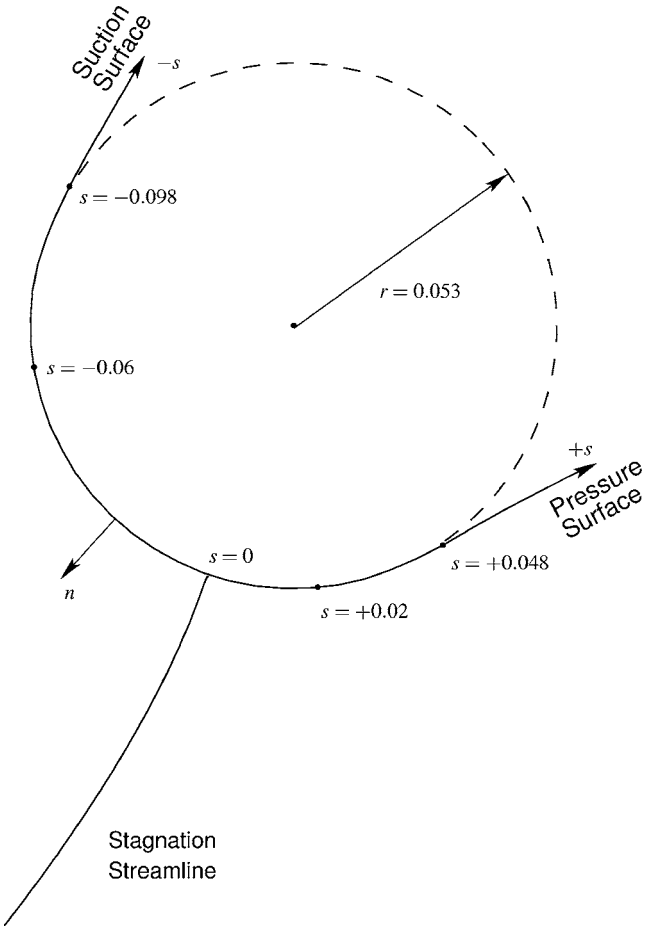

Fig. 2 Arclength and normal coordinate definitions for airfoil leading edge, with arclength and leading edge radius scaled by axial chord. The extent of the stagnation region is about $-0.06 < s < 0.02$.

Hiemenz flow when an appropriate value is chosen for the parameter a. We have also found that the stagnation-line heat transfer measurements from other studies lie between values obtained from Hiemenz flow and plane stagnation-point potential flow (both characterized by the same a). One implication is that turbulence in the freestream flow causes momentum and thermal boundary layers that are thinner than in Hiemenz flow, in a small portion of the stagnation region very close to the stagnation line.

Furthermore, the measurements and analytical analysis are complemented by computational fluid dynamics (CFD) analysis to determine how the leading edge aerodynamics and heat transfer might be predicted for other airfoil geometries. The best consistency among CFD, analytical, and measured values was with respect to surface pressure, which can be used to evaluate the parameter a. The analytical model characterized by a can then be used to evaluate the stagnation-region boundary layer displacement thickness and stagnation-line heat transfer.

Description of Experiment

The skin friction, static pressure, and Stanton number measurements discussed in this study were taken in a plane turbine cascade, represented in Fig. 1 and described briefly as follows. The cascade contains four Pratt and Whitney JT9D first stage turbine blades scaled to approximately ten times engine size, to an axial chord of 0.281 m. The measurements were taken in different studies (Ref. [3] and the current study), and they were taken with a similar geometrical configuration, Reynolds number of 5.9×10^5, boundary layer thickness, and incidence angle of 44.7 deg. This point was emphasized so sets of different measurement quantities could be compared, as is done in this study. More details of the cascade are given in the table that follows and in the original publication that details the experiment [2].

Axial chord	b_x=0.281 m
Pitch/axial chord	0.9555
Span/axial chord	0.9888
Mean camber line angles	43.99 deg, 25.98 deg
Boundary layer thickness	3.30 cm
Displacement thickness	0.376 cm
Momentum thickness	0.279 cm
Shape factor	1.35
Turbulence intensity [3]	1 % ± 0.1%

The coordinate system used in this study is described using axial, transverse, and arclength dimensions. All lengths are scaled by axial chord. Axial and transverse coordinates are x and y, respectively, as in Fig. 3. The leading edge begins at $x=0$ and the trailing edge ends at $x=1$; the center of the trailing edge radius defines $y=0$. This study pertains to a particular region of the cascade near the leading edge, as described in Fig. 2. The arclength dimension has its origin at the measured midspan leading edge attachment line, and is positive on the pressure side and negative along the suction side.

Skin friction was measured using OFI, and the measurements described in this study extend the sets of OFI measurements reported in previous studies [1,6] using the same cascade. The OFI technique provides simultaneous measurements of skin friction and limiting streamline direction, time averaged over a wind tunnel run. The technique varies with each investigator, and in this study, it is carried out by adhering a thin nickel foil strip to the cascade surface at the measurement location. A set of silicone oil droplets are applied to the foil, and the wind tunnel is run. During the wind tunnel run, the droplets flow downstream, leaving behind a trace amount of oil in the form of a film, the thickness of which is on the order of a quarter micrometer (half wavelength of reflected light) and is measured interferometrically at the conclusion of the wind tunnel run. Higher skin friction coincides with a more gradually increasing oil film thickness, with interference patterns that are more stretched. Lower skin friction, near the stagnation

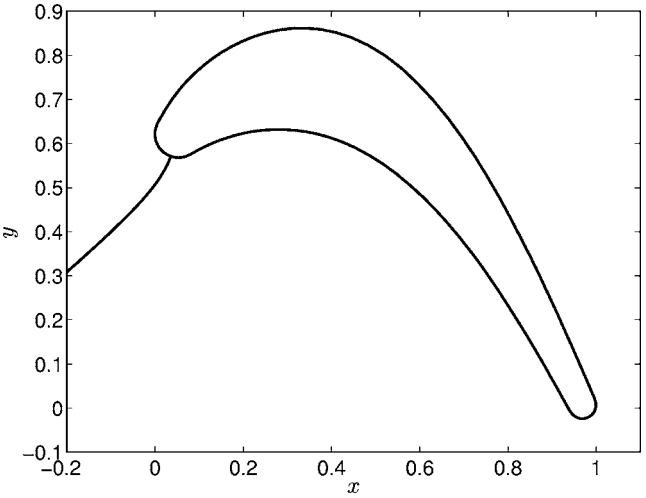

Fig. 3 Cascade coordinate system with stagnation streamline and lengths scaled by axial chord. Stagnation line measured at x=0.036, y=0.571, where s=0 is prescribed.

line, coincides with a more sharply increasing oil film thickness, characterized by smaller interference fringe spacing. The skin friction value at the location where each droplet was originally applied is related to the spatial variation in oil film thickness and wind tunnel run history of temperature, total pressure, and static pressure. Figure 4 is an interferogram, with fringes visible in many of the oil film traces. Dust renders some fringes useless for measurements, particularly those fringes close to the attachment or stagnation line. With repeated wind tunnel runs, dust filters, various wind tunnel run times, and various oil viscosities, the skin friction distribution was resolved. The error in the skin friction measurements was evaluated as being within $\pm 5\%$. More details of the OFI technique are given in previous studies [1,7], by Driver [8] and by Naughton and Sheplak [9].

This study was initiated by a measurement repeatability problem with the OFI technique. It was found that the *streamwise*

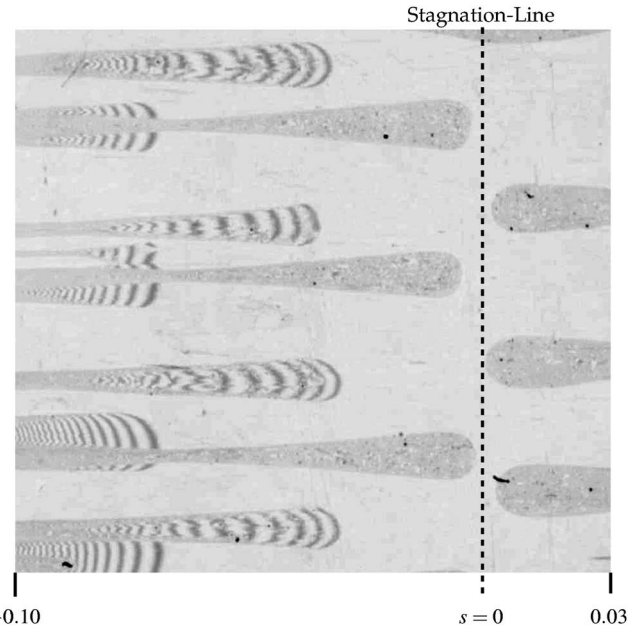

Fig. 4 This interferogram is from OFI applied to a 50 μm thick nickel foil substrate wrapped around the leading edge of a plane turbine cascade airfoil at midspan

edges of the nickel foil on the airfoil surface were causing the formation of wakes that propagated spanwise, interfering with measurements far downstream of the leading edge. As pointed out by Panton [10], the displacement thickness near the stagnation point of various shapes can be estimated from the Hiemenz flow solution, giving indication of the size of a surface feature that might cause a wake formation. Noting the defect introduced by the nickel foil, using wider nickel strips, and avoiding the wakes, the problem with the technique was resolved.

More detail of the wake problem is as follows. When using the nickel foil strip for OFI measurements, a good practice is to use multiple measurements to check repeatability with respect to placement of the nickel foil on the surface. Typically, the concern was that the upstream edge of the nickel foil strip might interfere with the measurement. Multiple measurements in the same location on the cascade surface can be used to establish the invariance of the measurement with respect to distance between the measurement location and the protuberance introduced with the nickel foil. When repeatability was not observed on the suction side, longer nickel foil strips were used, and eventually the foil strips were wrapped completely around the leading edge of the airfoil so that there was no upstream protuberance introduced with measurement. Measurements, however, were still not repeatable, and an explanation was posed that the flow was transitional and susceptible to wide fluctuations in skin friction. Then, it was observed that when wider foil strips were used, high values of skin friction were consistently measured toward the streamwise edges of the nickel foil strip. Further experiments indicated wake formation along the streamwise protuberance of the foil, and the same behavior was observed using a 50 μm diameter wire wrapped streamwise around the airfoil leading edge. The wakes formed near the leading edge, and grew in the spanwise direction as they flowed over the suction side of the airfoil, to where they detached from the surface at a separation bubble. The problem of wake formation was resolved by using nickel foil strips that were sufficiently wide so that the wakes did not affect the measurements toward the center of the strips. Measurements were repeated with the strip at different spanwise locations to check invariance with respect to placement of the strip. The indication of this problem and its solution is that the boundary layer thickness near the leading edge is on the order of the nickel foil thickness, which is 50 μm.

Static pressure measurements were taken at midspan locations of Airfoils 2 and 3 (see Fig. 1). The measurements are used to evaluate cascade periodicity, which is a criterion for reproducing cascade conditions for the skin friction, static pressure, and heat transfer measurements. The static pressure measurements are plotted in Fig. 5, showing comparison with a potential flow solution. The tailboards and bleeds in Fig. 1 are adjusted with the aim of matching the measurements between airfoils and with the potential flow solution for an infinite cascade. The largest deviation occurs approaching the suction side trailing edge, where the influence of the end walls in this low aspect ratio cascade causes decreased loading. The error in static pressure coefficient was evaluated as being within $\pm(0.02+1.4\%)$.

Heat transfer measurements were taken on Airfoils 2 and 3 and on the end wall between those airfoils in a study by Graziani et al. [3]. An electrically resistive surface provided constant heat flux, and thermocouples were used to measure surface temperature. That information, along with the reference temperature and pressures, were used to evaluate the Stanton number. The measurements were carried out with a thin and thick inlet boundary layer; the thick boundary layer is consistent with the original [2] and the current study.

Analytical Evaluation of Skin Friction, Static Pressure, and Heat Transfer in Hiemenz Flow

The relations used in this study to assess the airfoil leading edge measurements and calculations of skin friction, static pres-

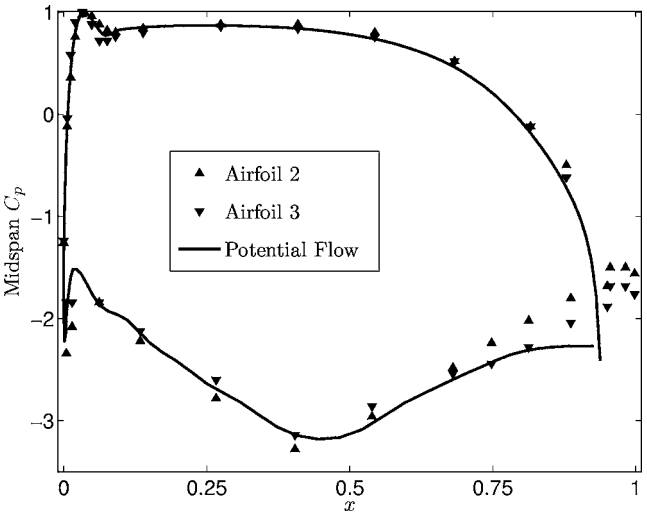

Fig. 5 Midspan static pressure measurements for Airfoils 2 and 3, and potential flow solution

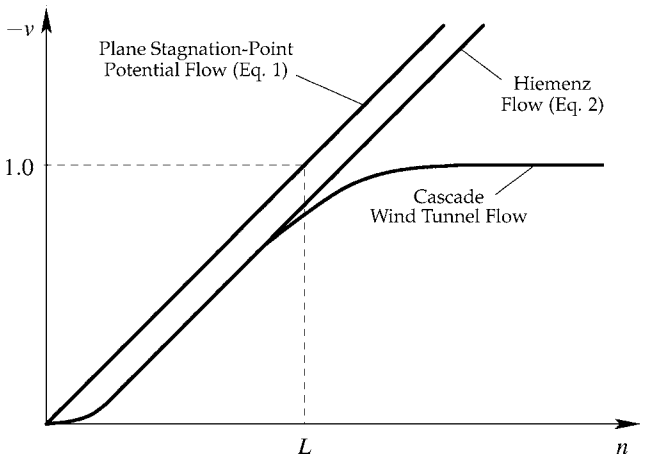

Fig. 7 Qualitative representation of velocity scaled by U_o and length scaled by b_x along a stagnation streamline for plane stagnation-point potential flow, Hiemenz flow, and cascade wind tunnel flow

sure, and heat transfer are based on Hiemenz flow. As shown in Fig. 6, Hiemenz flow is the description of a two-dimensional laminar incompressible viscous flow impinging on a surface, and is one of the few exact analytical solutions to the Navier–Stokes equations. Far from the surface, Hiemenz flow is described by a plane stagnation-point potential flow, where

$$u = \frac{s}{L} \quad v = -\frac{n}{L} \tag{1}$$

The parameter $a = U_o/Lb_x$ is typically used to describe the velocity gradient along the attachment streamline at the stagnation point, and a is represented implicitly in Eq. (1) with the length and velocity scales. We choose to represent the gradient in terms of the cascade reference velocity (nominally $U_o = 34$ m/s) and a distance L along the stagnation streamline from the airfoil leading edge or surface in Hiemenz flow, as shown in Fig. 7. In the potential flow solution for the cascade, the velocity along the inlet stagnation streamline is bounded by U_o, and the velocity gradient converges to a value of a near the stagnation point. The choice of U_o for the velocity simplifies the relations that describe skin friction, static pressure, and Stanton number.

In Hiemenz flow, the velocity field is described [4] by a similarity solution

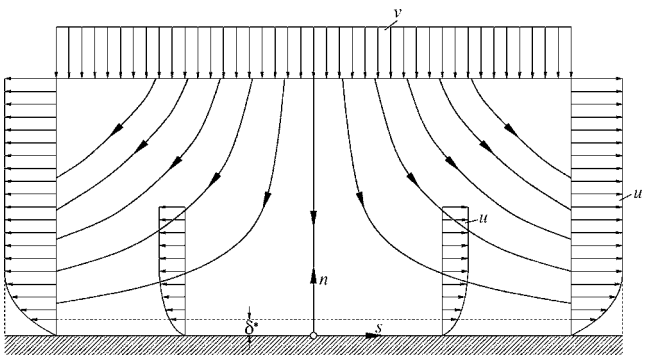

Fig. 6 Hiemenz flow, or plane stagnation-point flow, following Schlichting [4]

$$u = \frac{s\varphi'(\eta)}{L} \quad v = -\frac{\varphi(\eta)}{\sqrt{\mathrm{Re}\, L}} \quad \eta = n\sqrt{\frac{\mathrm{Re}}{L}} \tag{2}$$

Far from the surface, the slope of φ is 1, and the displacement thickness δ^* is the distance along the abscissa between φ and a line of slope 1 passing through the origin. As tabulated by Schlichting [4], $\eta = 4.6 \rightarrow \varphi = 3.9521$, and

$$\delta^* = \int_0^\infty \left(1 - \frac{u}{u_\infty}\right) dn = \int_0^\infty (1 - \varphi')\, d\eta \frac{dn}{d\eta} = 0.6479\sqrt{\frac{L}{\mathrm{Re}}} \tag{3}$$

The displacement thickness (physically, the distance by which the solid surface would have to be displaced to maintain the same mass flow rate in a hypothetical inviscid flow) is constant along s. The skin friction coefficient is evaluated from the tables with $\eta = 0 \rightarrow \varphi'' = 1.2326$, and

$$C_f = \frac{\mu U_o/b_x\, \partial u/\partial n|_{n=0}}{(1/2)\rho U_o^2} = 2\varphi''(0)\frac{s/L}{\sqrt{\mathrm{Re}\, L}} = 2.4652\frac{s/L}{\sqrt{\mathrm{Re}\, L}} \tag{4}$$

varies linearly with s and is zero at the stagnation point. The surface pressure varies from the stagnation point with the square of the velocity at the edge of the boundary layer

$$C_p = \frac{p}{(1/2)\rho U_o^2} = 1 - u^2 = 1 - \left(\frac{s}{L}\right)^2 \tag{5}$$

A similarity solution can be applied to the energy equation for Hiemenz flow to obtain a Stanton number relation for direct comparison to heat transfer measurements. The similarity solution for constant surface temperature is attributed to Squire [11]. As pointed out by Kays and Crawford [12], the heat transfer coefficient is constant along s for the constant temperature solution. Since the similarity variable is independent of s, Hiemenz flow has the interesting characteristic that the constant heat flux and constant surface temperature solutions are identical. Consequently, the Stanton number is uniform along s whether the surface is constant temperature or constant heat flux. Although the temperature field can be solved by White [13], for example, we are looking only for Stanton number. Unlike the flow solution, the heat transfer solution is not exact because viscous dissipation, which occurs over the entire domain, is neglected. The s dependent terms of the energy equation drop out, leaving

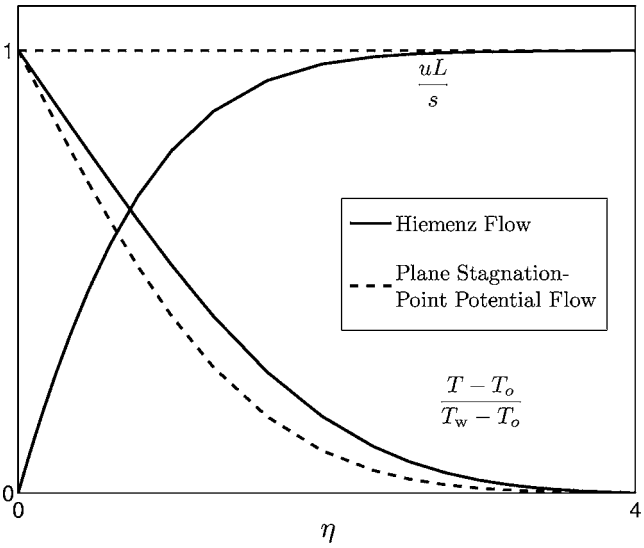

Fig. 8 Momentum and thermal boundary layers in Hiemenz flow and plane stagnation-point potential flow

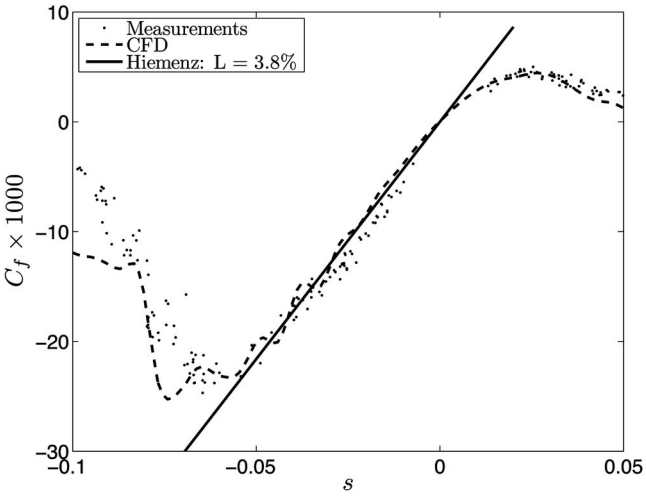

Fig. 9 Skin friction measurements from 15% to 60% span with CFD calculations and a Hiemenz analytical solution fit to measurements. The extent of the stagnation region is about $-0.06 < s < 0.02$.

$$\frac{d^2\theta}{d\eta^2} = -\Pr \varphi \frac{d\theta}{d\eta} \quad \theta = \frac{T-T_o}{T_w-T_o} \tag{6}$$

which can be integrated twice to obtain the dimensionless temperature profile. One boundary condition is the surface condition; the dimensionless surface temperature profile relates to a surface heat flux as

$$\left.\frac{d\theta}{d\eta}\right|_{\eta=0} = -\frac{qb_x}{k(T_w-T_o)}\sqrt{\frac{L}{\mathrm{Re}}} = -\mathrm{St}\,\Pr\sqrt{\mathrm{Re}\,L} \tag{7}$$

where q is constant. The remaining boundary condition is $\theta \to 0$ for large η, and

$$\theta = 1 - \mathrm{St}\,\Pr\sqrt{\mathrm{Re}\,L}\int_0^\eta e^{-\Pr\,\Phi(h)}dh \tag{8}$$

with $\Phi = \int_0^\eta \varphi(h)dh$. For large η, θ tends toward zero, and the relationship for Stanton number in Hiemenz flow is

$$\mathrm{St}\,\Pr\sqrt{\mathrm{Re}\,L} = \left[\int_0^\infty e^{-\Pr\,\Phi(\eta)}d\eta\right]^{-1} \approx 0.57\,\Pr^{0.393} \tag{9}$$

which is within 1% for $0.2 < \Pr < 2$.

The Stanton number for plane stagnation-point potential flow is derived using Eq. (1), instead of Eq. (2), for the velocity profile in Eq. (6). The result is an error function solution for surface heat transfer,

$$\mathrm{St}\,\Pr\sqrt{\mathrm{Re}\,L} = \left[\int_0^\infty e^{-(1/2)\Pr\,\eta^2}d\eta\right]^{-1} = \sqrt{\frac{2\,\Pr}{\pi}} \tag{10}$$

To summarize, for Hiemenz flow, the skin friction profile varies linearly with x and is zero at the stagnation point, the static pressure varies as a parabola, and heat transfer is uniform. The thermal boundary layer for Hiemenz flow is thicker than for plane stagnation-point potential flow because the momentum boundary layer is absent, as shown in Fig. 8. Consequently, for equivalent values of wall and freestream temperature, the heat flux in Hiemenz flow is smaller than in plane stagnation-point potential flow. These relations will be used to analyze the measurements and CFD calculations.

Computational Fluid Dynamics Simulation

A two-dimensional model of the cascade was used to evaluate the skin friction, static pressure, and heat transfer near the leading edge of the airfoil at midspan. The 32,000 cell domain extended upstream of the leading edge by $0.7b_x$ and downstream of the trailing edge by $2b_x$. The cells lying adjacent to the airfoil extended about δ^* ($50\ \mu\mathrm{m}/b_x$) from the surface near the stagnation point. The simulation was run in FLUENT 6.2.16. The maximum y^+ value along the airfoil surface was 10 (at the stagnation point where $\tau_w = 0$, y^+ is zero and therefore not a useful parameter at that location). Further grid refinement near the airfoil surface did not change the solution near the stagnation point. The model was run using the Spalart–Allmaras turbulence model with default closure coefficients [14]. A second order upwind scheme was used for the equations solved. Due to the thinness of the boundary layer near the stagnation point, the near-wall turbulence damping terms in the Spalart–Allmaras model reduced the eddy viscosity to negligible levels, and the turbulent solution near the stagnation point was indistinguishable from a laminar solution.

To test the modeling approach, Hiemenz flow was also simulated in FLUENT. Similar grid spacing was used at the surface as was used in the cascade model. The nominal cascade reference velocity $U_o = 34$ m/s was used along with half the leading edge radius of the airfoil $L = 5.3\%$ (as suggested by Panton [10]) to evaluate a and prescribe the far-field velocity. The skin friction, static pressure, and heat transfer values were within 1% full scale of the analytical solution values.

Results and Discussion

The measured skin friction profile along the surface coordinate s is approximately linear near the leading edge, and this profile characterizes the Hiemenz flow that in turn describes the leading edge aerodynamics. Figure 9 shows the skin friction results, representing 240 OFI measurements from 15% to 60% span. The slope of the skin friction measurements can be used to evaluate the parameter L, which along with U_o characterizes Hiemenz flow, as in Eq. (4). The linear region extends mostly into the suction side with little on the pressure side. Positive and negative skin friction values represent direction of the flow toward the pressure and suction sides, respectively, with interpolation of the skin friction measurements yielding $C_f = 0$ along the stagnation line. A fit to the measurements in the linear region yields a value of 3.8% for the parameter L. The CFD shows a narrower linear region, and at

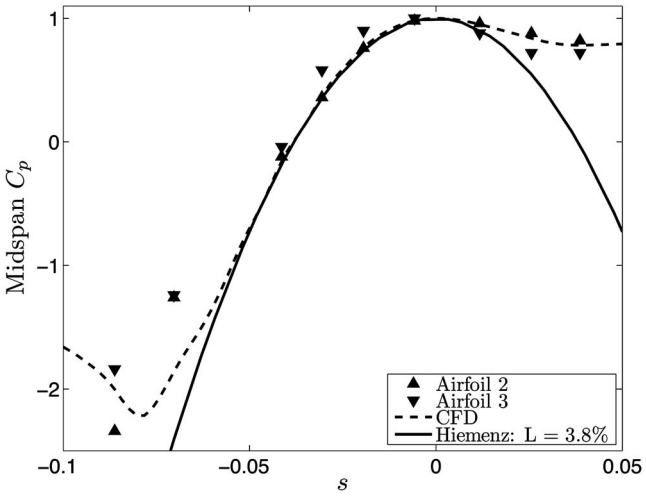

Fig. 10 Measured and calculated midspan static pressure with Hiemenz flow analytical values

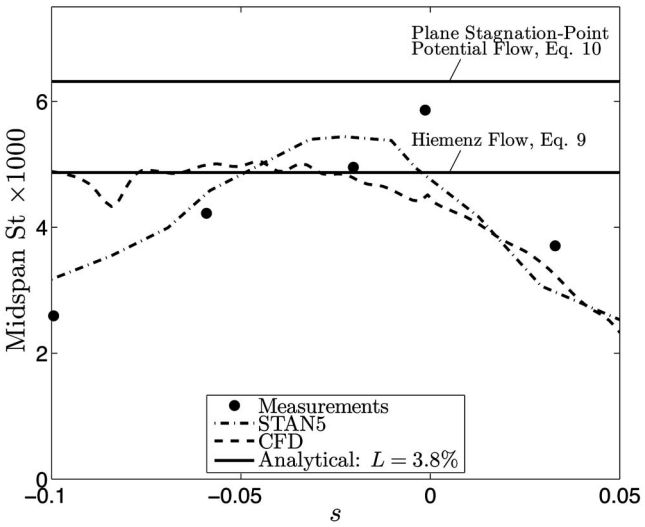

Fig. 11 Measured [3] and calculated midspan Stanton number along with Hiemenz flow and plane stagnation-point potential flow analytical values. The extent of the stagnation region is about $-0.06 < s < 0.02$.

$s=0$, the slope yields a value of 5.0% for the parameter L. The linearity of the skin friction measurements indicates that Hiemenz flow describes the aerodynamics over 70% of the airfoil span and over an arclength of $-0.06 < s < +0.02$, about 55% of the cylindrical portion of the leading edge. This region, where Hiemenz flow describes the aerodynamics, is what we call the stagnation region. End wall effects, where the leading edge shear stress has a spanwise component, were observed within 15% of span at each end wall.

Hiemenz flow, as characterized by the skin friction measurements, indicates the leading edge boundary layer displacement thickness. Based on the measurements with $L=3.8\%$ and using Eq. (3), the displacement thickness in the stagnation region is $\delta^*=0.016\%$ ($45\ \mu m/b_x$). The nickel foil used to measure the skin friction is 50 μm thick, which indicates why the edge of the foil is the source of the OFI measurement complications mentioned earlier.

The static pressure measurements and CFD calculations are consistent with the Hiemenz flow analytical solution as characterized by the parameter $L=3.8\%$ fit to the skin friction measurements. Figure 10 represents the pressure measurements, CFD calculations, and the analytical solution, Eq. (5), for the midspan leading edge pressure distribution. The measurements, CFD calculations, and analytical solution fit well in the stagnation region indicated by the linear skin friction profile. The CFD static pressure profile fits well to the parameter $L=3.8\%$; so it appears that the calculated skin friction profile, for which a larger 5.0% value for L was required to fit the analytical solution, was not accurately resolved.

Approaching $s=-0.1$, there is increased scatter in the pressure measurements due possibly to the abrupt change in static pressure, or the pressure measurements could be affected by wakes generated from the upstream taps, which are holes approximately $8\delta^*$ in diameter. OFI measurements indicate the presence of a wake downstream of the midspan pressure taps when the nickel foil strip was not wrapped around the airfoil leading edge, leaving the leading edge pressure taps uncovered. It is unclear at what point this wake is formed, since the pressure measurements closer toward the stagnation line, where the velocity is lower, do not appear affected. Further down the suction side, by $s=-0.2$, the scatter in the measurements is diminished.

Measurements and calculations indicate that the heat transfer in the stagnation region is not constant along s as predicted with the analytical models (Eqs. (9) and (10)), but plane stagnation-point potential flow provides a Stanton number close to the measured value at the stagnation line. Figure 11 shows the midspan Stanton number measurements and the STAN5 predictions from that study [3]. Also shown are the current CFD calculations and the analytical solutions (Eqs. (9) and (10)), for which L is evaluated based on the skin friction measurements and static pressure measurements and calculations. The STAN5 Stanton number calculations are closest to the measurements overall, but both STAN5 and the current CFD results are very close to the analytical value corresponding to Hiemenz flow at the stagnation line; the measured value at this location is 20% higher. The Stanton number relation for plane stagnation-point potential flow (Eq. (10)), however, yields a value of $St=6.32\times10^{-3}$, which is only 8% higher than the measured value of 5.86×10^{-3}. The results from Eqs. (9) and (10) bound the measurement. Apparently, freestream turbulence is causing thinner momentum and thermal boundary layers than Hiemenz flow can account for, in a small portion of the stagnation region *very* close to the stagnation line. This is consistent with the observation that a heat transfer model, which does not account for a momentum boundary layer, gives a result closer to the measured heat transfer value. An analogous example is the slug flow model used to calculate heat transfer between a flat plate and low Prandtl number fluids (liquid metals) in laminar flow [15].

These results indicate an approach for the prediction of heat transfer at the leading edge stagnation line, where the highest heat transfer levels in turbine cascades usually occur. Surface pressure is typically a reliable CFD calculation available to a turbine designer. Once the Hiemenz or plane stagnation-point potential flow is characterized, the stagnation-point Stanton number can be bracketed using Eqs. (9) and (10), where L is evaluated from the predicted leading edge pressure distribution.

Comparisons With Other Studies

When compared to three other cascade studies, heat transfer predictions based on Hiemenz flow and plane stagnation-point potential flow bound the heat transfer measurements, while for studies of flow over cylinders, some heat transfer measurement values exceed predictions based on the inviscid model. Consider Eqs. (9) and (10) combined to form a range of leading edge heat transfer values; the following is accurate within 1% for $0.2 < Pr < 2$;

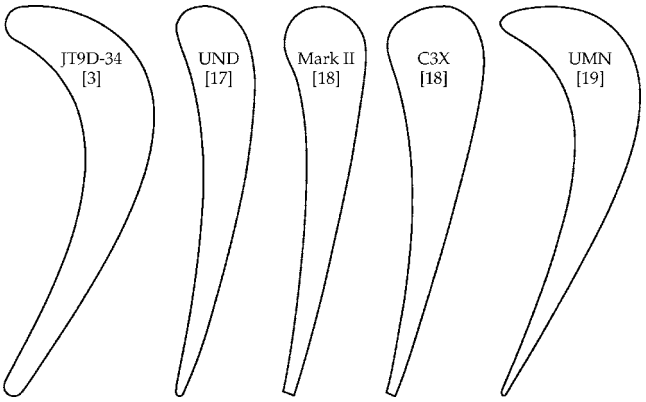

Fig. 12 Airfoil shapes considered for comparison to leading edge heat transfer model (Eq. (11))

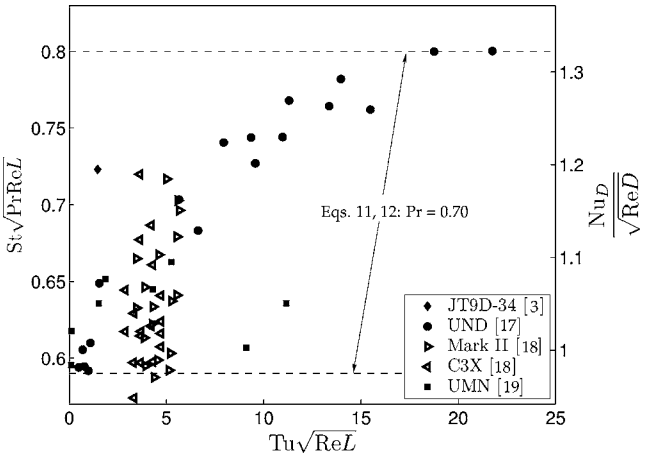

Fig. 13 Cascade heat transfer data from four studies of five airfoils, with all Reynolds numbers based on cascade inlet velocity (choice of length scale does not affect the result)

$$0.57\,\mathrm{Pr}^{-0.107} \leq \mathrm{St}\sqrt{\mathrm{Pr\,Re}\,L} \leq \sqrt{\frac{2}{\pi}} = 0.80 \tag{11}$$

The left side corresponds to the lower heat transfer rates based on Hiemenz flow, and the right side corresponds to higher heat transfer rates based on plane stagnation-point potential flow. Once L has been evaluated for a particular set of Stanton number measurements taken at a given Reynolds number, it is simple to determine whether or not the model fits.

At this point, it is convenient to point out that the parabolic relationship between arclength and static pressure (Eq. (5)) applies also to the stagnation region of a cylinder in crossflow. A value of $L=1/4$ the cylinder diameter is given by Panton [10]. Upon inspection of the pressure profile around a cylinder, that given by Hoerner [16] for example, $C_p=0$ at 30 deg or at $s=\pi/12=0.26$, which characterizes L in terms of the cylinder diameter per Eq. (5), yielding $\pi D=12L$. Further inspection of the pressure profile shows that within 30 deg of the stagnation line, the pressure profile is mainly independent of whether the flow is subcritical or supercritical. The range of Stanton number in Eq. (11) can be interpreted as a range of Frössling number for a cylinder with similar stagnation-region fluid mechanics.

$$1.11\,\mathrm{Pr}^{0.393} \leq \frac{\mathrm{Nu}_D}{\sqrt{\mathrm{Re}D}} \leq \frac{\sqrt{24\,\mathrm{Pr}}}{\pi} = 1.56\sqrt{\mathrm{Pr}} \tag{12}$$

It is important to note that the equivalent cylinder diameter D does not necessarily correspond to the leading edge curvature or radius. The relationship between L and D is dependent on the stagnation-region fluid mechanics, not necessarily the stagnation-region geometry. In the current study, for example, the value of L was found to be 3.8%, which corresponds to $D=14.5\%$, rather different from the geometrical diameter of the airfoil leading edge, 10.6% (see Fig. 2). Another example is Hiemenz flow itself; with a surface of infinite radius of curvature, there is no quantitative relationship between D and L.

Four cascade studies with a total of five airfoils were chosen for comparison with the analytical model in this paper. Figure 12 shows the five airfoil shapes considered for comparison. The first study is by Ames et al. [17], where midspan heat transfer on an inlet guide vane was measured over several Reynolds numbers and inlet turbulence conditions. The parameter L was determined by a fit of Eq. (5) to a pressure profile generated using CFD, the results of which were provided by Professor Ames; the fit resembles Fig. 10 and resulted in $L=12.2\%$. The value of the parameter is high relative to that from the turbine blade featured in the current study, but for the case of the inlet guide vane, Reynolds number was based on the exit velocity and airfoil chord (not inlet velocity and axial chord). As an additional check, the value of L for the inlet guide vane was evaluated from STAN7 heat transfer predictions reported along with the measurements. We expected that the STAN7 predictions could be used to accurately evaluate L, because the STAN5 prediction was very close to the prediction using Hiemenz flow in Fig. 11. The STAN7 predictions reported by Ames used with Eq. (11) resulted in a value of L identical to that evaluated using the pressure profile. The measurements correlate neatly in the range bounded by the models based on Hiemenz flow and plane stagnation-point potential flow (Eq. (11)), as shown in Fig. 13. Larger values of Reynolds number and turbulence intensity tend to put values of $\mathrm{St}\sqrt{\mathrm{PrRe}L}$ closer to the model based on potential flow.

The second study for comparison is by Hylton et al. [18]. In their report, heat transfer to cooled inlet guide vanes was measured, with the cascade inlet flow a nominal 800 K. The results from two different inlet guide vanes were reported for a total of 36 leading edge midspan stagnation-line heat transfer measurements, with Reynolds numbers from 3.5×10^5 to 7.4×10^5. Two values of turbulence intensity were reported: 6.5% and 8.3%. The parameter L was evaluated for each vane using reported STAN5 predictions of stagnation-line heat transfer and Eq. (11), yielding $L=5.9\%$ for the MarkII vane and $L=5.5\%$ for the C3X vane. The measurements are bounded well with the model (Eq. (11)). With the exception of one value of $\mathrm{St}\sqrt{\mathrm{PrRe}L}$ at 0.57, the remaining 35 measurements were between 0.59 and 0.72, with no apparent sensitivity to Reynolds number or to the two similar turbulence intensity levels tested.

The third cascade study for comparison is by Wang et al. [19]. In that study, mass transfer measurements from a turbine blade were reported for a Reynolds number of 2×10^5 and turbulence intensity ranging from 0.2% to 18%. Conveniently, the results were represented in terms of $\mathrm{Nu}_D/\sqrt{\mathrm{Re}D}$. Surprisingly, the eight measurements reported by Wang et al. have values of $\mathrm{Nu}_D/\sqrt{\mathrm{Re}D}$ between 0.95 and 1.05, with no apparent sensitivity to the large range of turbulence levels reported. As with the other two cascade studies, the model still bounds the measurements.

The analytical model bounds most of the reported heat and mass transfer measurements from cylinders considered, but some measurements exceed values predicted with the model. Three studies of cylinders [20–22] were considered for comparison with the analytical model (Eq. (12)). One more study by Mehendale et al. [23], of heat transfer from a rectangular strut with a semicylindrical leading edge, was considered for comparison. Reynolds numbers (where b_x is the cylinder diameter) for the four studies were 0.3×10^5–2.4×10^5, and turbulence levels from 0% to 13% were reported. The lowest turbulence levels in each study coincided with low values of $\mathrm{Nu}_D/\sqrt{\mathrm{Re}}$, consistent with heat transfer

based on Hiemenz flow. About three quarters of the measurements were within the range of the analytical model, but each study reported some values exceeding those in Eq. (12), by up to 26% in the study of Kestin and Wood [22]. The values that exceeded those predicted with the model corresponded to the higher Reynolds numbers and turbulence levels tested in each study.

These cylinder comparisons raise some questions about the model. For the cascade studies, there was varying sensitivity to turbulence levels, which could be explained perhaps by Reynolds number or blade geometry. For the cylinder studies, each one reported heat transfer levels that exceed the model predictions. The study by Mehendale et al. [23] excludes the explanation that the increased heat transfer levels are due to wake shedding from the cylinders. It is clear though that for some conditions, some mechanism for advection exceeds that which would occur in a steady, two-dimensional, plane stagnation-point potential flow. The analytical modeling in this study has been demonstrated, however, to bound the four, open-literature, cascade heat transfer measurements well.

Summary and Conclusion

For a particular plane turbine cascade, measurements and calculations, both analytical and CFD, show that skin friction, surface pressure, and heat transfer near the airfoil leading edge can be represented by Hiemenz flow and plane stagnation-point potential flow. Skin friction follows a linear profile in the stagnation region, similar to Hiemenz flow for 70% of the leading edge span and for 55% of the circular portion of the leading edge arclength. The surface pressure profile in that same region follows that from Hiemenz or plane stagnation-point potential flow. The heat transfer measured at the stagnation line is in close agreement with that evaluated from plane stagnation-point potential flow, using parameters characterized by either the skin friction or surface pressure measurements. For heat transfer prediction at the stagnation line, the calculated pressure profile provides the most reliable evaluation of the parameters that characterize the representative plane stagnation-point potential flow. Furthermore, the Hiemenz flow representation can provide an estimate of the leading edge boundary layer thickness.

The analytical modeling of heat transfer based on Hiemenz flow and plane stagnation-point potential flow was compared to measurements from other studies. For cascades, measurements are bounded well by the model, although there is apparent varying sensitivity to turbulence levels. Measurements from cylinders are mostly bounded by the model, but some heat transfer levels exceed the modeling predictions.

There are two implications of this work for a turbine designer. The first is that leading edge heat transfer levels can be predicted using Eq. (11) or (12), simply with a calculated airfoil pressure profile. The second is that keeping PrRe constant, Eq. (11) shows that it is possible to select a larger value of L such that leading edge Stanton number will be reduced. The designer can then alter the airfoil pressure distribution (i.e., airfoil shape) to get a new parabolic stagnation-region pressure distribution (Fig. 10) to yield the higher value of L, with a resulting decrease in leading edge heat transfer. This would reduce cooling requirements and increase the durability for the leading edges of turbine airfoils.

Acknowledgment

The work reported here was supported by the National Science Foundation under Grant No. 0412929. We thank the NSF and NSF Program Director, Dr. Michael Plesniak, for their sponsorship.

We thank Professor Forrest Ames for sharing detailed measurements and calculations from his experiment.

Nomenclature

- a = velocity profile parameter, U_o/Lb_x, 1/s
- b_x = axial chord, 0.281 m
- CFD = computational fluid dynamics
- C_f = skin friction coefficient, $\tau_w/(1/2)\rho_o U_o^2$
- c_p = constant pressure specific heat, J/kg K
- C_p = static pressure coefficient, $(P-P_o)/(1/2)\rho_o U_o^2$
- D = equivalent cylinder diameter, $12L/\pi$
- Fr = Frössling number, $\mathrm{Nu}_D/\sqrt{\mathrm{Re}}$
- h = integration variable
- k = thermal conductivity, W/m K
- L = length parameter, scaled by b_x
- n = normal coordinate, perpendicular to blade surface, scaled by b_x
- Nu_D = Nusselt number, StPrReD
- p = pressure, Pa
- Pr = Prandtl number, ν/α
- q = heat flux, $\mathrm{W/m^2}$
- r = leading edge radius, scaled by b_x
- Re = Reynolds number, $U_o b_x/\nu$
- s = blade arclength from leading edge attachment line, scaled by b_x
- St = Stanton number, $q/(T_w-T_o)\rho U_o c_p$
- T = temperature, K
- u,v = velocities in s and n directions, scaled by U_o
- U_o = cascade inlet velocity, m/s
- x = axial coordinate, scaled by b_x
- y = pitchwise coordinate, scaled by b_x

Greek Symbols

- α = thermal diffusivity, $\mathrm{m^2/s}$
- δ^* = displacement thickness, scaled by b_x
- η = similarity variable
- θ = dimensionless temperature
- μ = dynamic viscosity, Pa s
- ν = kinematic viscosity, $\mathrm{m^2/s}$
- ρ = density, $\mathrm{kg/m^2}$
- τ = shear stress, Pa
- φ = similarity profile
- Φ = integral of φ

Subscripts

- o = reference
- w = wall

References

[1] Holley, B. M., and Langston, L. S., "Surface Shear Stress and Pressure Measurements in a Plane Turbine Cascade," ASME J. Turbomach., to be published.
[2] Langston, L. S., Nice, M. L., and Hooper, R. M., 1977, "Three Dimensional Flow Within a Turbine Cascade Passage," ASME J. Eng. Power, **99**, pp. 21–28.
[3] Graziani, R. A., Blair, M. F., Taylor, J. R., and Mayle, R. E., 1980, "An Experimental Study of Endwall and Airfoil Surface Heat Transfer in a Large Scale Turbine Blade Cascade," ASME J. Eng. Power, **102**, pp. 257–267.
[4] Schlichting, H., 1960, *Boundary Layer Theory*, 4th ed., MacGraw-Hill, New York.
[5] Bons, J., 2005, "A Critical Assessment of Reynolds Analogy for Turbine Flows," ASME J. Heat Transfer, **127**, pp. 472–485.
[6] Holley, B. M., Becz, S., and Langston, L. S., 2006, "Measurement and Calculation of Turbine Cascade Endwall Pressure and Shear Stress," ASME J. Turbomach., **128**(2), pp. 232–239.
[7] Holley, B. M., 2006, "A Simple and Accurate Interferometric Fringe Analysis Tool for Skin Friction Measurements," *Proceedings of GT2006*, Paper No. GT2006-90581.
[8] Driver, D. M., 2003, "Application of Oil-Film Interferometry Skin-Friction Measurement to Large Wind Tunnels," Exp. Fluids, **34**, pp. 717–725.
[9] Naughton, J. W., and Sheplak, M., 2002, "Modern Developments in Shear-Stress Measurement," Prog. Aerosp. Sci., **38**, pp. 515–570.
[10] Panton, R. L., 1984, *Incompressible Flow*, Wiley-Interscience, New York.
[11] 1938, *Modern Developments in Fluid Dynamics*, Goldstein, S., ed., Oxford University Press, New York.
[12] Kays, W. M., and Crawford, M. E., 1993, *Convective Heat and Mass Transfer*, 3rd ed., McGraw-Hill, New York.

[13] White, F. M., 1974, *Viscous Fluid Flow*, McGraw-Hill, New York.
[14] FLUENT 6.0 User's Guide, 2001, Fluent, Inc., Lebanon, NH.
[15] Mills, A. F., 1995, *Basic Heat and Mass Transfer*, R. D. Irwin, Inc., Chicago.
[16] Hoerner, S. F., 1965, *Fluid-Dynamic Drag*, LCCCN 64-19666.
[17] Ames, F. E., Wang, C., and Barbot, P. A., 2003, "Measurement and Prediction of the Influence of Catalytic and Dry Low NOx Combustor Turbulence on Vane Surface Heat Transfer," ASME J. Turbomach., **125**, pp. 221–231.
[18] Hylton, L. D., Mihelc, M. S., Turner, E. R., Nealy, D. A., and York, R. E., 1983, "Analytical and Experimental Evaluation of the Heat Transfer Distribution Over the Surfaces of Turbine Vanes," NASA CR 168015.
[19] Wang, H. P., Goldstein, R. J., and Olson, S. J., 1999, "Effect of High Free-Stream Turbulence With Large Length Scale on Blade Heat/Mass Transfer," ASME J. Turbomach., **121**, pp. 217–224.
[20] Seban, R. A., 1960, "The Influence of Free Stream Turbulence on the Local Heat Transfer From Cylinders," ASME J. Heat Transfer, **82**, pp. 101–107.
[21] Smith, M. C., and Kuethe, A. M., 1966, "Effects of Turbulence on Laminar Skin Friction and Heat Transfer," Phys. Fluids, **9**(12), pp. 2337–2344.
[22] Kestin, J., and Wood, R. T., 1971, "The Influence of Turbulence on Mass Transfer From Cylinders," ASME J. Heat Transfer, **93**, pp. 321–327.
[23] Mehendale, A. B., Han, J. C., and Ou, S., 1991, "Influence of High Mainstream Turbulence on Leading Edge Heat Transfer," ASME J. Heat Transfer, **113**, pp. 843–850.

Effect of a Cutback Squealer and Cavity Depth on Film-Cooling Effectiveness on a Gas Turbine Blade Tip

Shantanu Mhetras
Diganta Narzary
Zhihong Gao
Je-Chin Han
e-mail: jc-han@tamu.edu

Department of Mechanical Engineering,
Texas A&M University,
College Station, TX 77843-3123

Film-cooling effectiveness from shaped holes on the near tip pressure side and cylindrical holes on the squealer cavity floor is investigated. The pressure side squealer rim wall is cut near the trailing edge to allow the accumulated coolant in the cavity to escape and cool the tip trailing edge. Effects of varying blowing ratios and squealer cavity depth are also examined on film-cooling effectiveness. The film-cooling effectiveness distributions are measured on the blade tip, near tip pressure side and the inner pressure side and suction side rim walls using pressure sensitive paint technique. The internal coolant-supply passages of the squealer tipped blade are modeled similar to those in the GE-E^3 *rotor blade with two separate serpentine loops supplying coolant to the film-cooling holes. Two rows of cylindrical film-cooling holes are arranged offset to the suction side profile and along the camber line on the tip. Another row of shaped film-cooling holes is arranged along the pressure side just below the tip. The average blowing ratio of the cooling gas is controlled to be 0.5, 1.0, 1.5, and 2.0. A five-bladed linear cascade in a blow down facility with a tip gap clearance of 1.5% is used to perform the experiments. The free-stream Reynolds number, based on the axial chord length and the exit velocity, was 1,480,000 and the inlet and exit Mach numbers were 0.23 and 0.65, respectively. A blowing ratio of 1.0 is found to give best results on the pressure side, whereas the tip surfaces forming the squealer cavity give best results for* $M=2$. *Results show high film-cooling effectiveness magnitudes near the trailing edge of the blade tip due to coolant accumulation from upstream holes in the tip cavity. A squealer depth with a recess of* 2.1 mm *causes the average effectiveness magnitudes to decrease slightly as compared to a squealer depth of* 4.2 mm. [DOI: 10.1115/1.2776949]

Keywords: gas turbine, blade tip, film cooling, pressure sensitive paint, E3 blade, cascade

Introduction

The concept of cooling a surface subjected to high mainstream temperatures by perforating the surface with several discrete holes and passing cold air (film cooling) through them is a popular technique used in several applications. The surface under test can be maintained at a cooler temperature due to formation of a thin protective film of relatively colder air on the surface. This technique has been successfully employed for cooling of gas turbine blades subjected to very high mainstream gas temperatures. A high and uniform film-cooling effectiveness on the blade surface will ensure superior performance and thermal fatigue life for the blade, thus making it an important parameter in its design. Hot gases from the combustor enter the turbine, resulting in a significant heat load on the turbine components. One of the regions more susceptible to thermal failure is the blade tip due to its severe environment and difficulty in cooling. Large leakage flow occurs on the tip due to a high-pressure differential from pressure to suction side. This leakage mass flow can be reduced by using a labyrinthlike recessed cavity also known as the squealer tip. The presence of film cooling on the tip further reduces heat transfer from the mainstream gas to the blade tip. A comprehensive compilation of the available film-cooling techniques used in the gas turbine industry has been encapsulated by Han et al. [1].

Experimental investigations performed in the general area of film cooling on a blade tip are limited with few papers available in open literature. Film cooling on a blade tip was first studied by Kim and Metzger [2] and Kim et al. [3] by using a 2D rectangular tip model to simulate leakage flow between the tip and the shroud. Various film-cooling configurations were examined using a transient liquid crystal technique and the results for heat transfer coefficients and film-cooling effectiveness were reported. Kwak and Han [4,5] studied the local heat transfer distribution and film-cooling effectiveness using hue detection based transient liquid crystal technique on the blade tip for plane and squealer tip geometry. A GE-E^3, five-blade linear cascade was used similar to the one used in the present paper. They used three tip gap clearances (1.0%, 1.5%, and 2.5% of blade span) along with three average blowing ratios (0.5, 1.0, and 2.0) for the coolant. Increasing blowing ratio increased film effectiveness but overall heat transfer coefficients decreased. Their results also showed that the squealer geometry showed higher film-cooling effectiveness and lower heat transfer coefficients compared to the plane tip geometry due to its smaller leakage flow.

Ahn et al. [6] presented film-cooling effectiveness results using the pressure sensitive paint (PSP) technique on a plane and squealer blade tip with one row of holes on the camber line and another row of angled holes near the pressure side tip. They used the same high flow cascade as the present study and investigated the effects of tip gap clearance (1.0%, 1.5%, and 2.5% blade span) and blowing ratio ($M=0.5$, 1, and 2). They noted that higher blowing ratios give higher effectiveness. Results with plane tip

Contributed by Turbomachinery Division of ASME for publication in the JOURNAL OF TURBOMACHINERY. Manuscript received August 13, 2006; final manuscript received April 7, 2007; published onlineFebruary 12, 2008. Review conducted by Karen A. Thole. Paper presented at the AIAA Heat Transfer Conference 2006.

showed clear traces of the coolant path, while for squealer tip, coolant accumulation effects were observed on the cavity floor. Christophel et al. [7,8] studied film cooling and heat transfer using the infrared technique on a plane tip under low-speed conditions. They used four different coolant flow rates (0.47%, 0.58%, 0.68%, and 1.0% passage flow) for two tip gaps. A row of holes was located on the pressure side just below the tip with two more dirt purge holes on the tip itself. They found that a smaller tip gap and larger coolant flow showed better cooling. They also found that higher blowing ratios resulted in higher augmentations on tip heat transfer but with an overall net heat flux reduction when combined with adiabatic effectiveness measurements. Mhetras et al. [9] studied film-cooling effectiveness on all surfaces of a squealer tipped blade in a linear high flow cascade using the PSP technique. Coolant was injected through shaped holes near the pressure side similar to the present study and cylindrical holes on the cavity floor. The shaped holes on the pressure side near the tip showed a large coolant spread, consequently resulting in good film coverage. The coolant from the tip holes was directed toward the pressure side inner squealer rim wall to provide additional cooling.

Some experimental investigations have also been performed to study heat transfer on the blade tip under rotating conditions. Heat transfer coefficients on the blade tip and the shroud were measured by Metzger et al. [10] using heat flux sensors in a rotating turbine rig. Dunn and Haldeman [11] measured time-averaged heat flux at a recessed blade tip for a full-scale rotating turbine stage at transonic vane exit conditions. Their results showed that the heat transfer coefficient at the mid- and rear portions of the cavity floor is of the same order as the blade leading edge value. Rhee and Cho [12,13] investigated the mass transfer characteristics for a flat tip on the tip, shroud, and near tip regions. Heat transfer on the tip under rotating conditions was found to be about 10% lower than the stationary case due to relative motion between the shroud and tip. Heat transfer using heat flux gages on a rotating tip was studied by Molter et al. [14] for a high-pressure transonic turbine stage. They performed heat transfer and pressure measurements on a flat as well as a squealer tip and found that at the fundamental vane-crossing frequency, wake/shock disturbances can be significant on the tip surface.

There are many papers available in open literature, which discuss heat transfer coefficients on the blade tip and near tip regions. Several of these papers present results under engine representative mainstream flow conditions. Local heat transfer coefficients on a turbine blade tip model with a recessed cavity (squealer tip) were studied by Yang and Diller [15] in a stationary transonic linear cascade. Bunker et al. [16] utilized a hue detection based liquid crystal technique to obtain local heat transfer distributions on a plane blade tip in a stationary cascade. They studied the effects of tip gap clearance and free-stream turbulence intensity levels. Azad et al. [17,18] used transient liquid crystal technique to study heat transfer. They compared squealer tip and plane tip geometry and concluded that the overall heat transfer coefficients were lower for squealer tip case. Bunker and Bailey [19] studied the effect of squealer cavity depth and oxidation on turbine blade tip heat transfer. Azad et al. [20] and Kwak et al. [21] investigated the heat transfer on several different squealer geometries. A suction side squealer tip was found to give the lowest heat transfer among all cases studied. Heat transfer coefficient distributions for plane and squealer tip and near tip regions were presented by Kwak and Han [22,23] in two papers. By using a squealer tip, heat transfer was found to decrease on the tip and near tip regions.

A few of the many papers on blade tip heat/mass transfer performed under low-speed conditions are also discussed. Investigations comparing a rotating and stationary shroud were performed by Mayle and Metzger [24]. They noted that the effect of shroud rotation could be neglected to measure the blade tip heat transfer over the entire range of parameters considered in the study. Heyes et al. [25] studied tip leakage flow on plane and squealer tips in a linear cascade and concluded that the use of a squealer tip, especially a suction side squealer tip, was more beneficial than a flat tip. Heat transfer coefficients and static pressure distributions of a large-scale turbine blade tip were measured by Teng et al. [26] in a low-speed wind tunnel facility using a transient liquid crystal technique. Mass transfer technique was used by Papa et al. [27] to study local and average mass/heat transfer distributions on a squealer tip and winglet-squealer tip in a low-speed wind tunnel. Jin and Goldstein [28,29] also used this technique on a simulated high-pressure turbine blade tip and near tip surfaces. They observed that the average mass transfer from the tip surface was much higher than that on pressure and suction side surfaces. Saxena et al. [30] investigated the effect of various tip sealing geometries on blade tip leakage flow and heat transfer of a scaled up high-pressure (HP) turbine blade in a low-speed wind tunnel facility using a steady state liquid crystal technique. They noted that the trip strips placed against the leakage flow produce the lowest heat transfer on the tips compared to all the other cases.

Some numerical investigations have also been carried out to study heat transfer and film-cooling effectiveness on blade tip. The effects of tip clearance and casing recess on heat transfer and stage efficiency for several squealer blade tip geometries were predicted by Ameri et al. [31]. Ameri and Rigby [32] also calculated heat transfer coefficients and film-cooling effectiveness on turbine blade models. Numerical results for heat transfer and flow obtained by Ameri and Bunker [33] were compared to the experimental results from Bunker et al. [16] for a power generation gas turbine. Numerical techniques were also utilized by Yang et al. [34,35] to study flow and heat transfer past a turbine blade with plane and squealer tip. Film-cooling effectiveness for flat and squealer blade tips with film-cooling holes on the tip pressure side were predicted by Acharya et al. [36]. Hohlfeld et al. [37] predicted film-cooling flow from dirt purge holes on a turbine blade tip. They found that the flow exiting the dirt purge holes helped in blocking the leakage flow across the gap. As the blowing ratio increased for a large tip gap, tip cooling increased only slightly, whereas film cooling on the shroud increased significantly. The effects of different hole locations on film-cooling effectiveness and heat transfer were predicted by Yang et al. [38].

The main focus of the present study was to investigate the film-cooling effectiveness from the pressure side and tip injection on a cutback squealer tipped blade. Film cooling on the squealer rim walls and the squealer cavity floor was determined at two different cavity depths. An optimal arrangement of film-cooling holes was used to maximize film coverage. In addition, the pressure side rim wall near the trailing edge was removed to allow accumulated coolant in the squealer cavity to escape and cool the trailing edge tip region. The combined effect of the above mentioned design was tested under relatively high-pressure ratios and free-stream exit Mach numbers. By maximizing film-cooling coverage, contact of the hot gases with the squealer tip surfaces can be reduced, thus reducing the blade metal temperature. This will prevent blade tip oxidation as well as marginally reduce the heat flux into the blade.

A scaled up blade tip model of a first stage rotor blade (GE-E^3) of a modern aircraft gas turbine was used in this study, with a row of nine shaped film-cooling holes on the near tip pressure side and another set of ten cylindrical holes on the cavity floor. The squealer rim profile, pressure side and tip hole geometries, ejection angles, and cavity depth are different from Mhetras et al. [9] and are optimized for better film coverage. Film-cooling effectiveness was studied on the rim, cavity floor, inner cavity walls, and the near tip pressure side. Moreover, the PSP technique is based on mass transfer analogy, which eliminates any heating/conduction errors present in other optical measurement techniques such as liquid crystal and IR camera. The experimental results for pressure and effectiveness will aid future engineers to design more efficient turbine blades and help to calibrate CFD codes.

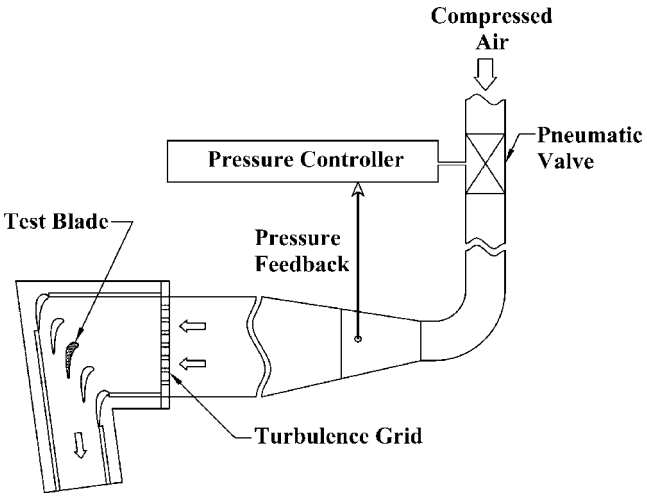

Fig. 1 Schematic of test section and blowdown facility

Experimental Setup

The test section consisted of a five-blade linear cascade with blade tip profiles placed in a blow-down loop. A schematic of the test section and the blow-down loop is shown in Fig. 1. The inlet cross section of the test section was 31.1 cm (width) $\times$12.2 cm (height). A turbulence-generating grid (rectangular bar mesh type) with a porosity of 57% was placed before the inlet. Turbulence intensity was recorded 6 cm upstream of the middle blade (or 20.7 cm downstream of the grid) using a hot-wire probe. Turbulence intensity (Tu) at this location was found to be 9.7% due to the presence of the grid and turbulence length scales were estimated to be 1.5 cm, which is slightly larger than the grid bar size. The bottom and sides on the test section were machined out of 1.27 cm thick polycarbonate sheets, whereas a 1.27 cm thick acrylic plate was used for the top for better optical access to the blade tip. The top plate also acted as a shroud for the blades. Flow conditions in adjacent passages of the center blade were ensured to be identical by adjusting the trailing edge tailboards for the cascade. A comprehensive discussion on the flow conditions, including flow periodicity in the cascade and pressure distribution along the blade, has been reported by Azad et al. [17,18] and Kwak and Han [22,23].

During the blow-down test, the cascade inlet air velocity and exit velocity were 78 m/s and 220 m/s, respectively. The Reynolds number based on the axial chord length and exit velocity was 1.48×10^6. Overall pressure ratio (P_t/P) was 1.29 (where P_t is inlet total pressure and P is exit static pressure) and inlet and exit Mach numbers were 0.23 and 0.65, respectively. The blow-down facility could maintain steady flow in the cascade for about 40 s. Compressed air stored in tanks entered a high flow pneumatic control valve, which could maintain steady flow by receiving downstream pressure feedback. The control valve could maintain a velocity within $\pm3\%$ of desired value.

A three times scaled model of the GE-E^3 blade was used with a blade span of 12.2 cm and an axial chord length of 8.61 cm. Since the blades were placed in a linear cascade, they were machined for a constant cross section for its entire span corresponding to the tip profile of the actual GE-E^3 blade. Figure 2 shows the blade profiles, the inlet and exit angles for air, and the blade tip and shroud definitions. The test blade was made using stereo lithography (SLA) as conventional machining methods were unsuitable for such a complicated geometry. The four guide blades placed in the test section were made of aluminum. Figure 3 shows the film cooling measurement blade with the internal passage geometry. The passages are numbered from 1 to 6 with Passage 1 closest to leading edge and Passage 6 closest to trailing edge. Coolant was

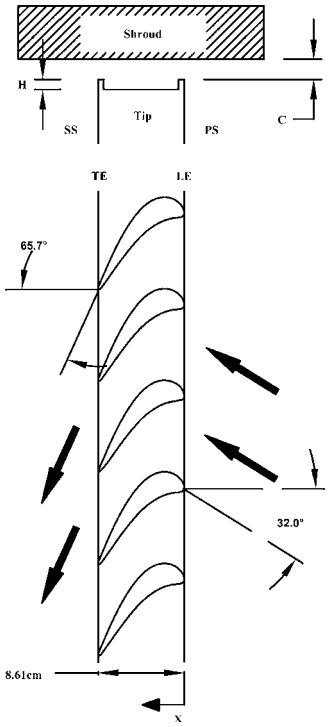

Fig. 2 Definition of blade tip and shroud

supplied to the test blade through two loops with three serpentine passages with a 3 mm wall thickness in each loop as shown. The design of the passages was based on the E^3, Stage 1, high pressure turbine (HPT) rotor blade cooling system as discussed by Halila et al. [39]. The leading edge impingement wall in their design was removed to simplify the passage flow analysis. Figure 4 shows the geometry and orientation of the film-cooling holes on the pressure side and on the squealer blade tip. Ten cylindrical tip holes with a diameter of 1.27 mm (L/d=3.34) were provided on the tip. Out of these ten holes, four were drilled such that they break out at 45 deg along the camber line of the blade on the cavity floor. The remaining six holes were drilled at 45 deg along a curve offset to the suction surface of the blade by 5.08 mm and were equally spaced by 18.3 mm. The holes were inclined to the cavity floor in

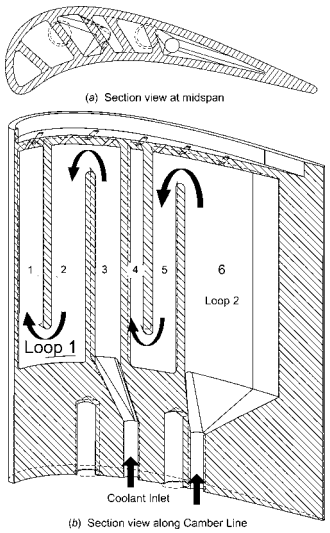

Fig. 3 Internal passage geometry of test blade

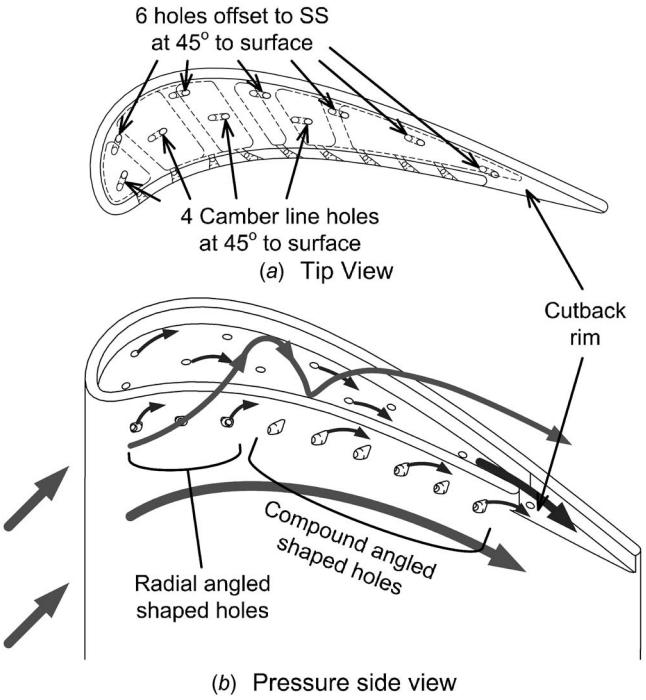

Fig. 4 Orientation of tip and PS holes

the direction of the bulk fluid flow. The first five tip holes were connected to Loop 1 (near LE) and the remaining five to Loop 2 (near TE).

Nine film-cooling holes with a diameter of 1.27 mm were provided for coolant to pass through the airfoil pressure side. The pressure side holes have a laidback and fan-shaped design expanding by 10 deg in three directions (10-10-10) with the expansion starting from the middle of the hole length and were located 9.5 mm below the tip surface with a hole-to-hole spacing of 8.9 mm. This design is similar to the design used by Mhetras et al. [9]. The first three holes near the leading edge were drilled at a radial angle of 45 deg to maximize the coolant spread, whereas the remaining six holes were drilled at a compound angle of 45 deg to the blade span and 45 deg with respect to the airfoil pressure surface with $L/d=4$. Figure 5 shows the detailed views of the shaped holes. All nine holes on the near tip pressure side in the study by Mhetras et al. [9] were drilled at a compound angle of 45 deg. Coolant to the first four holes was supplied through Loop 1, while the remaining five holes were connected to Loop 2. Two squealer tipped blades with the same hole geometry but with recesses of 4.2% and 2.1% of blade span were used to investigate

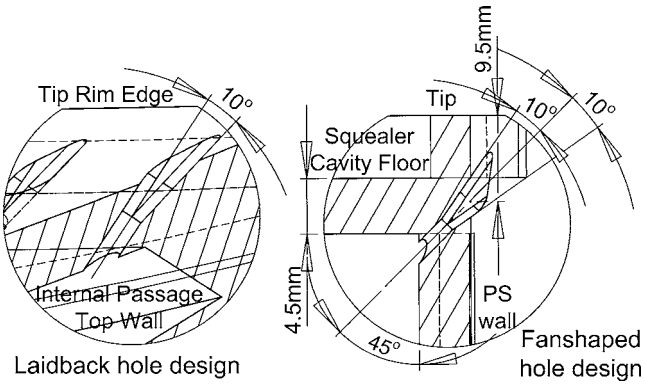

Fig. 5 Detailed geometry of a PS shaped hole

the effect of cavity depth. The pressure side rim wall near the trailing edge is cutback by about 25% of the blade chord for both blades to allow accumulated coolant to escape. The complete blade geometry including the blade profiles, cooling holes, and passage design can be provided by the authors to researchers or turbine blade designers for CFD validation.

This study was performed for a tip gap of 1.5% of blade span (12.2 cm), which was maintained on the middle three blades. Coolant injection through tip and pressure side holes (TP) as well as pressure side holes (P) only was studied. Experiments were performed with four different average blowing ratios (M) of 0.5, 1.0, 1.5, and 2.0. The blowing ratio was defined as $M=\rho_c Vc/\rho_m V_m$. If the density is the same, the ratio is reduced to a velocity ratio. During testing, it was observed that the leakage flow velocity could vary from hole to hole on the tip and near tip surfaces. The mainstream mass flux at each hole location was measured locally by static pressure measurement from PSP on the tip surface and pressure taps on the near tip pressure surface. The coolant mass flow for all holes was determined for a particular blowing ratio from the local mainstream mass flux and the coolant flow rate for each loop was set by adding the coolant mass flows for each individual open hole in that loop.

Film Cooling Effectiveness Measurement Theory and Data Analysis

Data for film-cooling effectiveness were obtained by using the PSP technique. PSP is a photoluminescent material that emits light when excited, with the emitted light intensity inversely proportional to the partial pressure of oxygen. This light intensity can be recorded using a charge-coupled device camera and can then be calibrated against the partial pressure of oxygen. Details of using PSP for pressure measurement are given in Ref. [40]. The image intensity obtained from PSP by the camera during data acquisition is normalized with a reference image intensity taken under no-flow conditions. Background noise in the optical setup is removed by subtracting the image intensities with the image intensity obtained under no-flow conditions and without excitation. The resulting intensity ratio can be converted to pressure ratio using the predetermined calibration curve and can be expressed as

$$\frac{I_{\text{ref}}-I_{\text{blk}}}{I-I_{\text{blk}}}=f\left[\frac{(P_{O_2})_{\text{air}}}{(P_{O_2})_{\text{ref}}}\right]=f(P_{\text{ratio}}) \tag{1}$$

where I denotes the intensity obtained for each pixel and $f(P_{\text{ratio}})$ is the relationship between intensity ratio and pressure ratio obtained after calibrating the PSP.

Calibration for PSP was performed using a vacuum chamber at several known pressures varying from 0 atm to 1.8 atm with intensity recorded for each pressure setting. The calibration curve is shown in Fig. 6. The same optical setup was chosen for calibration as well as for data acquisition during the experiments. PSP is sensitive to temperature with higher temperatures resulting in lower emitted light intensities. Hence, the paint was also calibrated for different temperatures. It was observed that if the emitted light intensity at a certain temperature was normalized with the reference image intensity taken at the same temperature, the temperature sensitivity can be minimized. During testing, it was ensured that temperatures of mainstream air, coolant, and test section were the same while taking reference, air and nitrogen images to minimize uncertainty. Thermocouples (T-type) located upstream of the test section and in the coolant flow recorded temperatures of air and nitrogen gas. Experiments were conducted in an air-conditioned room (20°C) and temperatures of mainstream air, coolant air, and nitrogen gas were maintained at 20°C.

To obtain film-cooling effectiveness, air and nitrogen were used alternately as coolant. Nitrogen, which has nearly the same molecular weight as that of air, displaces the oxygen molecules on the surface causing a change in the emitted light intensity from

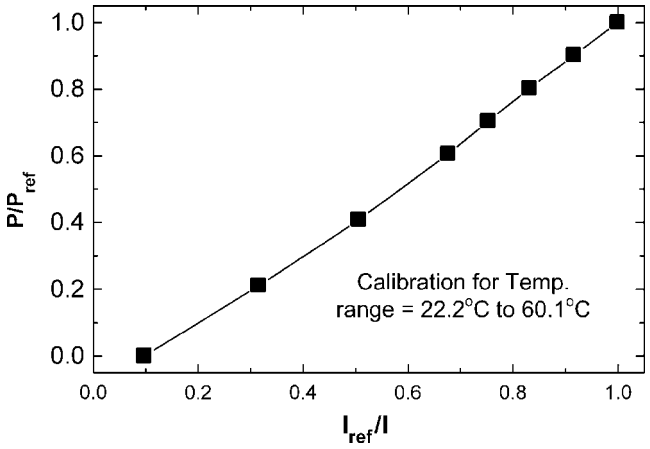

Fig. 6 Calibration curve for PSP

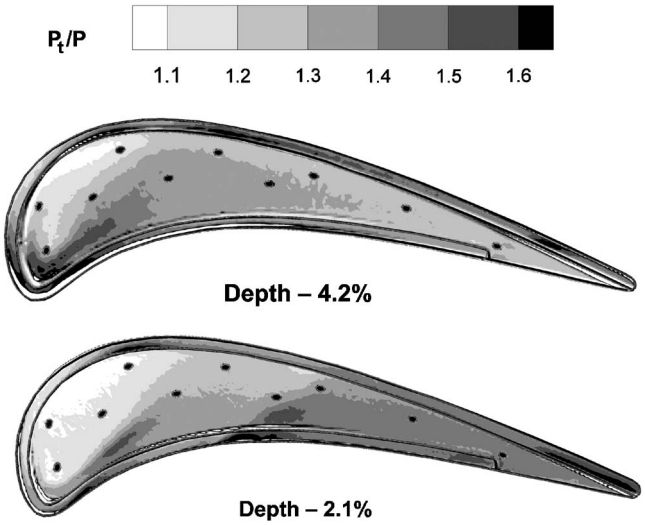

Fig. 7 Pressure ratio on tip

PSP. By noting the difference in partial pressure between the air and nitrogen injection cases, the film-cooling effectiveness can be determined using the following equation:

$$\eta = \frac{C_{\text{mix}} - C_{\text{air}}}{C_{\text{N}_2} - C_{\text{air}}} = \frac{C_{\text{air}} - C_{\text{mix}}}{C_{\text{air}}} = \frac{(P_{\text{O}_2})_{\text{air}} - (P_{\text{O}_2})_{\text{mix}}}{(P_{\text{O}_2})_{\text{air}}} \tag{2}$$

where C_{air}, C_{mix}, and C_{N_2} are the oxygen concentrations of mainstream air, air/nitrogen mixture, and nitrogen on the test surface, respectively. The definition for film effectiveness in Eq. (2) based on mass transfer analogy is of similar form as that for adiabatic film-cooling effectiveness given in

$$\eta = \frac{T_{\text{mix}} - T_m}{T_c - T_m} \tag{3}$$

The accuracy of the PSP technique for measuring film-cooling effectiveness has been compared by Wright et al. [41] on a flat plate with compound angled ejection holes using steady state infrared (IR) technique and steady state temperature sensitive paint (TSP) technique. Data were obtained for a range of blowing ratios and shows reasonable agreement with all three techniques. Results from IR and TSP techniques were within $\pm 8\%$ of the PSP measurements for the same set of conditions with the comparison improving at higher blowing ratios. Larger uncertainties for heat transfer techniques such as IR and TSP methods were observed due to lateral heat conduction in the flat plate as corrections for heat conduction were not included in the presented results.

The center test blade under investigation was layered with PSP using an air brush. This coated surface was excited using a strobe light fitted with a narrow bandpass interference filter with an optical wavelength of 520 nm. A dual fiber optic guide was used to get a uniform incident light distribution on the test surface. Upon excitation from this green light, the PSP coated surface emitted red light with a wavelength higher than 600 nm. A 12 bit scientific grade CCD camera (Cooke Sensicam QE with CCD temperature maintained at $-15\,^{\circ}\text{C}$ using two-stage peltier cooler) was used to record images and was fitted with a 35 mm lens and a 600 nm longpass filter. The filters were chosen to prevent overlap between the wavelength ranges such that the camera filter blocked the reflected light from the illumination source. Coolant mass flow to each loop was set using two separate rotameters to a flow rate corresponding to the blowing ratio. A pneumatic valve was opened and the pressure controller was set to the desired flow rate for the mainstream air. The images were taken when the mainstream flow was fully developed, i.e., after the initial developing time for flow. The camera and the strobe light were triggered simultaneously using a transistor-transistor logic (TTL) signal from a function generator at 10 Hz. A total of 140 TIF images were captured for each experiment with air and nitrogen injection and the pixel intensity for all images was averaged. The image resolution obtained from the camera was 0.6 mm/pixel. After the images were captured, the pneumatic valve was closed. The duration of a single experiment was about 30 s. A computer program was used to convert these pixel intensities into pressure using the calibration curve and then into film-cooling effectiveness.

Uncertainty calculations were performed based on a confidence level of 95% and are based on the uncertainty analysis method of Coleman and Steele [42]. Lower effectiveness magnitudes have higher uncertainties. For an effectiveness magnitude of 0.3, uncertainty was around $\pm 2\%$, while for effectiveness magnitude of 0.07, uncertainty was as high as $\pm 10.3\%$. This uncertainty is the result of uncertainties in calibration (4%) and image capture (1%). The absolute uncertainty for effectiveness varied from 0.01 to 0.02 units. Thus, relative uncertainties for very low effectiveness magnitudes can be very high ($>100\%$ at effectiveness magnitude of 0.01). However, it must be noted that very few data points exist with such high relative uncertainty magnitudes. Uncertainties for the blowing ratios are estimated to be 4%.

Tip Pressure Ratio Distributions

Figure 7 shows the pressure ratio (P_t/P) distributions on the blade tip for the two cavity depths tested obtained from PSP measurements. A higher pressure ratio indicates a higher surface velocity. The pressure side squealer rim acts as a backward facing step to the leakage flow, causing the formation of a recirculation zone inside the squealer cavity. Flow reattachment on the tip can be observed near the leading edge from the sharp gradient in the pressure ratio distributions. As expected, the reattachment length is much shorter for a cavity depth of 2.1%, resulting in a large low velocity region near the leading edge. The downstream cavity region is completely engulfed by the recirculation vortex. Higher pressure ratios can be observed on the cavity floor toward the trailing edge for the 2.1% cavity depth, indicating that the recirculation velocity is higher. Pressure ratio predictions matching pressure gage data under rotating conditions have been presented by Molter et al. [14]. However, their pressure distributions do not resemble the distributions presented in the paper, which may be due to different loading conditions for both blades. The turbine studied by Molter et al. [14] had a high-pressure transonic blade. The resulting blade loading characteristics are different for the E^3 blade and may explain the differing pressure distributions between both these studies.

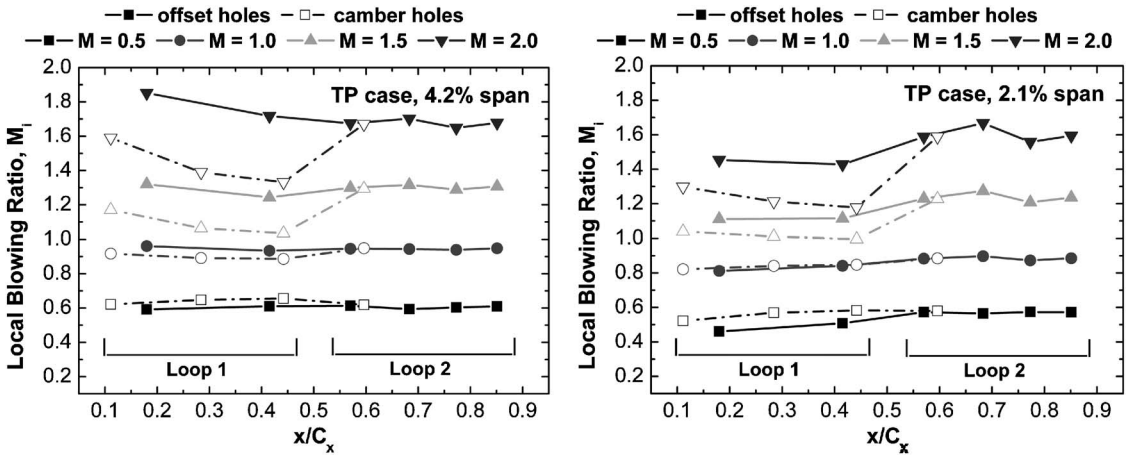

Fig. 8 Local *M* for tip holes for TP cases for 4.2% and 2.1% cavity depths

Local Blowing Ratios

To better explain the results for effectiveness, local blowing ratios through each hole on the tip and airfoil pressure side have been plotted in Figs. 8 and 9, respectively. Local mass flux on the surface of the blade was found using the inlet total pressure and local static pressure. The local surface static pressure distribution for the tip was found using PSP (Fig. 7), whereas static pressure taps located at 97% of blade span were used to measure static pressure on the near tip pressure side. The static pressure in the passages inside the blade was measured using 14 static pressure taps on the pressure and suction side inner passage walls located 3.18 mm below the passage top wall. Local blowing ratio for each hole was calculated by using the pressure differential across it. A constant discharge coefficient C_D for all open holes in a loop was assumed. It should be noted that the constant C_D assumption for all holes in the loop may not be true as C_D depends on not only the geometry but also the external and internal flow conditions. It is assumed that the deviation in the discharge coefficients from hole to hole is not significant and hence an average value can be assumed without introducing a significant error. By measuring the total mass flow rate of the coolant and pressure differential for each hole and using the average discharge coefficient, the coolant mass flow for each hole was determined and the local blowing ratio, M_i, was calculated.

Figure 8 shows the local blowing ratios for the tip (TP cases) for both cavity depths. It can be clearly observed that the local blowing ratios for the holes along the camber line are much lower than the holes offset to the suction side for high blowing ratios. At low blowing ratios, this difference is small. A higher mainstream mass flux due to higher velocities along the camber line near the leading edge causes this uneven distribution even though the coolant mass flow rate through these holes is higher than the corresponding offset holes. The local blowing ratio distributions for both cavity depths are similar with a depth of 2.1%, giving lower blowing ratios for the first few holes near the leading edge. A bigger high-pressure zone as observed in Fig. 7 may explain this behavior. Figure 9 shows the local blowing ratios for the TP and P cases and for both cavity depths for the holes located on the near tip pressure side. Pressure in Passage 1 closest to leading edge is higher due to stagnation of the coolant causing high local blowing ratio for the first two pressure side holes located on Passage 1, as can be observed from Fig. 9. Similarly, the local blowing ratio for the sixth hole in Loop 2 is higher than the other holes in the same loop due to stagnation inside Passage 4. The local blowing ratio gradually decreases with increasing chord due to the increase in the mainstream velocity on the pressure side as the flow approaches the throat region. A nonuniform blowing ratio distribution exists between the tip and pressure side holes for TP cases. The local M_i through the pressure side holes is higher for higher blowing ratios as compared to tip holes, but at lower blowing ratios, M_i is higher for tip holes. However, it should be noted that the average mass flow through the tip holes for all blowing ratios is higher than the pressure side holes. The average difference in total mass flow between all tip and all pressure side holes is

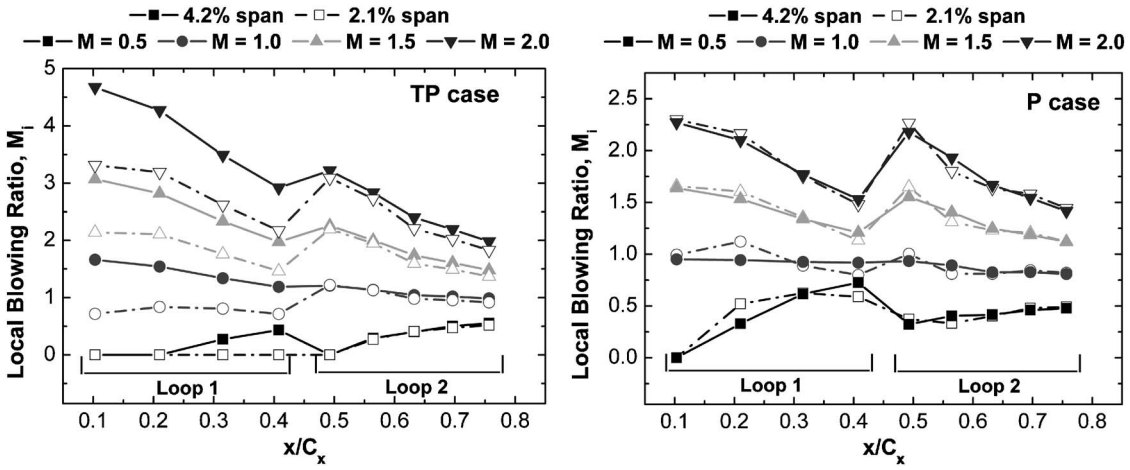

Fig. 9 Local *M* for PS holes for TP and P cases for 4.2% and 2.1% cavity depths

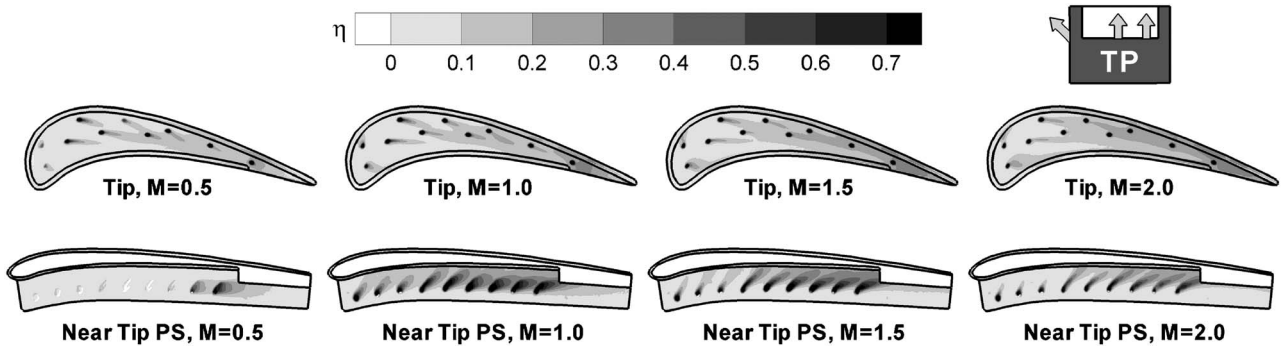

Fig. 10 Film-cooling effectiveness distribution on tip and near tip pressure sides for TP cases for a depth of 4.2%

~60% for $M=0.5$ and decreases to ~5% for $M=2.0$. Local blowing ratios for the near tip pressure side holes in Fig. 9 for the 2.1% cavity depth are lower than that for corresponding holes for the 4.2% cavity depth for TP cases. However, the local blowing ratios for P cases for both cavity depths are almost identical as the cavity depth does not impact the upstream flow as well as the internal passage flow distributions.

Film-Cooling Effectiveness Results

Tip and Pressure Side Injection (TP Cases). The depth of the squealer cavity is viewed as one of the key parameters affecting the film-cooling effectiveness distribution. The flow field inside the squealer cavity depends on the cavity depth, and, consequently, the film coverage is affected. The following section discusses the film-cooling effectiveness results for TP cases for the two cavity depths. Figure 10 shows the film-cooling effectiveness contours for the tip and pressure side injection (TP case) and a cavity depth of 4.2%—the upper row shows the tip side and the bottom row shows the near tip pressure side. On the cavity floor region, the film coverage is seen to be improving with the blowing ratio. Coolant gets accumulated inside the squealer cavity as the ejecting coolant mass flow increases with blowing ratio. This effect is more pronounced in the region between the midchord and the trailing edge due to the contracting squealer passage. The accumulated coolant can be observed to cover the trailing edge cutback region resulting in high effectiveness. Effectiveness levels as high as 0.4 can be observed in the cutback region for $M=2$. These levels are much higher than the effectiveness levels observed by Mhetras et al. [9] on a full squealer without any rim cutback. The peak level as observed by them for $M=2.0$ near the trailing edge for the TP case was around 0.25. For the full squealer case, the coolant coverage near the trailing edge squealer rim is primarily due to coolant carryover from the pressure side. In the current design, both the pressure and tip injection contribute toward the film-cooling effectiveness. Thus, the current cutback design is successful in providing better coverage on the trailing edge portion of the tip.

The coolant film streaks follow the mainstream flow direction inside the cavity. Even though the injection angle may be different, the mainstream flow momentum is strong enough to deflect the jets in its flow direction. The coolant trace near the upstream holes (hole 1 offset to the suction side and hole 1 along the camber line) shows larger spreading and is deflected toward the rims walls. For the 4.2% cavity depth, the coolant ejecting from the first hole offset to the suction side is deflected along or toward the suction side rim, whereas the coolant from the other holes travels toward the pressure side rim. This directional nature can be observed at all the blowing ratios. Reattachment of the mainstream flow may occur between these two holes. The pressure side rim of the squealer acts as a backward facing step in the mainstream flow path. The flow after reattachment recirculates inwards toward the pressure side rim, which may explain the coolant flow directions. The first hole offset to the suction side is outside this recirculation zone and remains unaffected. Detailed flow visualizations in the squealer cavity for a blade tip have been done by Ameri and Rigby [32] and Yang et al. [35,38] using numerical analysis. The flow visualizations presented in these papers confirm the three-dimensional flow structure along with the formation of the recirculation vortex in the squealer cavity.

The rim tip region of a blade is highly susceptible to failure from oxidation due to high metal temperatures. Hence, a uniform coolant distribution is desired to reduce metal temperatures. The distributions in Fig. 10 reveal relatively high effectiveness levels close to the trailing edge on both the pressure and suction side rims. Coolant carryover from the pressure side holes may explain the high effectiveness on the pressure side rim. On the suction side rim, effectiveness levels as high as 0.35 are observed for $M=2.0$ after the midchord region. The leakage flow escapes to the suction side primarily through this region. The accumulated coolant in the leakage flow helps in providing good coverage on the suction side rim. The effectiveness levels on the suction side rim though are fairly insensitive at high blowing ratios.

On the near tip pressure side (bottom row, Fig. 10), a blowing ratio of 1.0 gives better effectiveness distribution than 1.5 and 2.0 due to more coolant spread, although the maximum effectiveness levels occurring close to the hole exits are comparable for all three. High effectiveness magnitudes can be observed on the near tip pressure side downstream of the midchord. The compound angled shaped holes provide excellent film coverage. The first three holes on the pressure side inserted at a radial angle of 45 deg provide a better coolant spread for $M=1.0$ than the compound angles used in Ref. [9] near the leading edge. For all the blowing ratios considered, the effectiveness is lower near the upstream holes due to the higher static pressure near the leading edge of the blade. This is quite apparent at $M=0.5$, where the cooling effectiveness is almost negligible near the upstream holes. More coolant is diverted to the tip holes as observed from the local blowing ratio distributions in Figs. 8 and 9 for $M=0.5$ due to higher surface pressures on the pressure side. Some mainstream ingestion may also occur for the first three pressure side holes for $M=0.5$. At $M=2$, the coolant momentum is very high causing liftoff of the jet from the surface. Local blowing ratios are as high as 4.5 (Fig. 9) for the first hole closest to the leading edge. Lift- off is indicated by a region of low effectiveness immediately downstream of the hole.

Figure 11 shows the effectiveness distributions for the tip and near tip pressure sides with a cavity depth of 2.1% of blade span for the TP case. In the cavity floor region, the trend is similar to the one observed for the larger cavity depth, i.e., increasing effectiveness with increasing blowing ratio due to coolant accumulation. A smaller cavity depth results in a shorter reattachment length for the leakage flow entering the tip gap (Fig. 7). The low

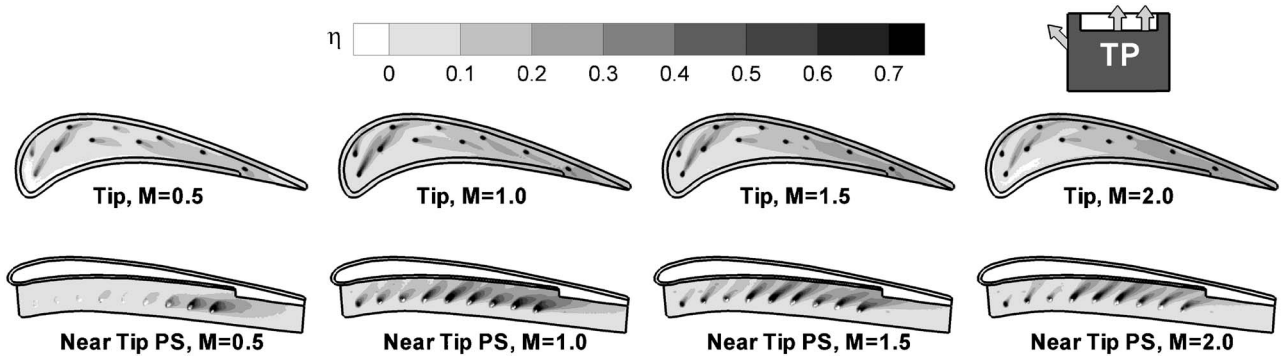

Fig. 11 Film-cooling effectiveness distribution on tip and near tip pressure sides for TP cases for a depth of 2.1%

pressure ratio region is large enough to encompass the first two holes along the camber line and offset to the suction side. Thus, the coolant streaks injecting from these holes follow the mainstream flow path and are not diverted to the pressure side rim by the recirculation vortex as observed for the other holes. Strong traces can be observed from these upstream holes. Film effectiveness on the upstream cavity floor is higher for the smaller cavity depth, whereas in the downstream region the effectiveness is higher for the larger cavity depth. Due to the narrow aspect ratio of the cavity for the smaller squealer depth, the vortex may be squeezed resulting in large velocity and viscous shear gradients from the tip to the cavity floor. This may cause a relatively faster rotating vortex. This has a damaging impact on the coolant coverage resulting in lower effectiveness levels downstream of the blade midchord as compared to a 4.2% cavity depth (Fig. 10). The strong trace from the upstream holes is also felt by the suction side rim tip (a local maximum at about $x/C_x=0.2$), resulting in higher effectiveness as compared to the 4.2% cavity depth. However, the peak magnitudes are lower at about 0.25 units. The pressure side tip rim exhibits similar behavior as that for the 4.2% cavity depth. Downstream of the midchord, both the pressure and suction side rims show more or less similar magnitude. The near tip pressure side distribution for the smaller cavity depth is similar to the larger cavity depth with the 2.1% cavity depth giving slightly lower effectiveness levels. Lower pressures on the tip result in larger nonuniformity in the local blowing ratios between the tip and pressure sides, as observed in Figs. 8 and 9. Thus, the blowing ratios for the near tip pressure side holes are lower than those for the larger cavity depth, resulting in slightly lower effectiveness levels.

Figures 12 and 13 show film-cooling effectiveness distribution on the inner rim walls for the TP case with 4.2% and 2.1% cavity depths, respectively. The effectiveness distribution on both pressure and suction side inner rim walls follows similar trends as seen for the cavity floor and rim, with the highest effectiveness in each case being near the trailing edge. The effectiveness distribu-

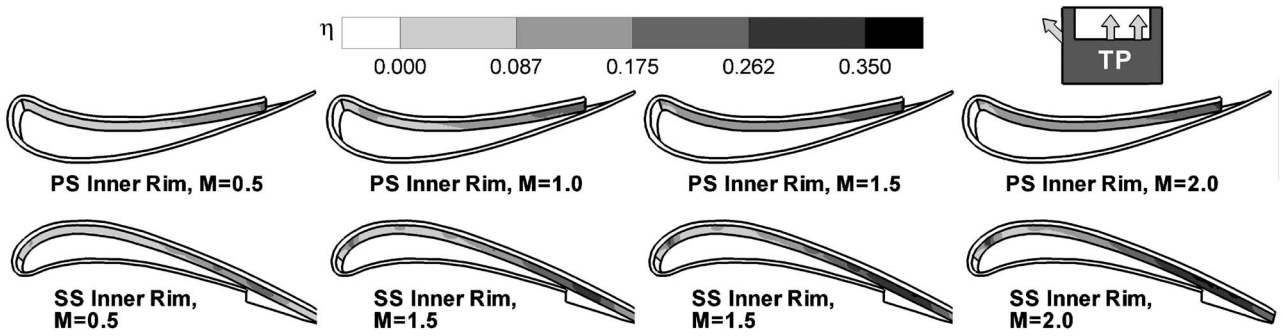

Fig. 12 Film-cooling effectiveness distribution on inner rim walls for PS and SS for TP cases for a depth of 4.2%

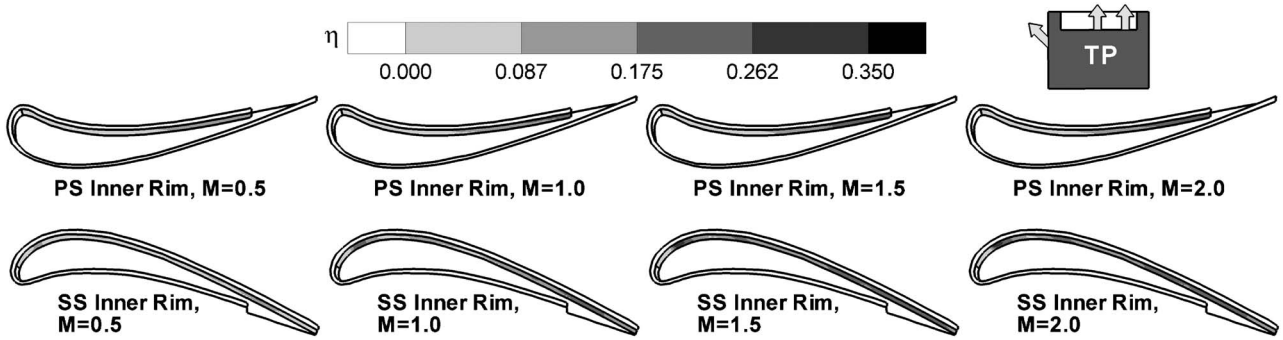

Fig. 13 Film-cooling effectiveness distribution on inner rim walls for PS and SS for TP cases for a depth of 2.1%

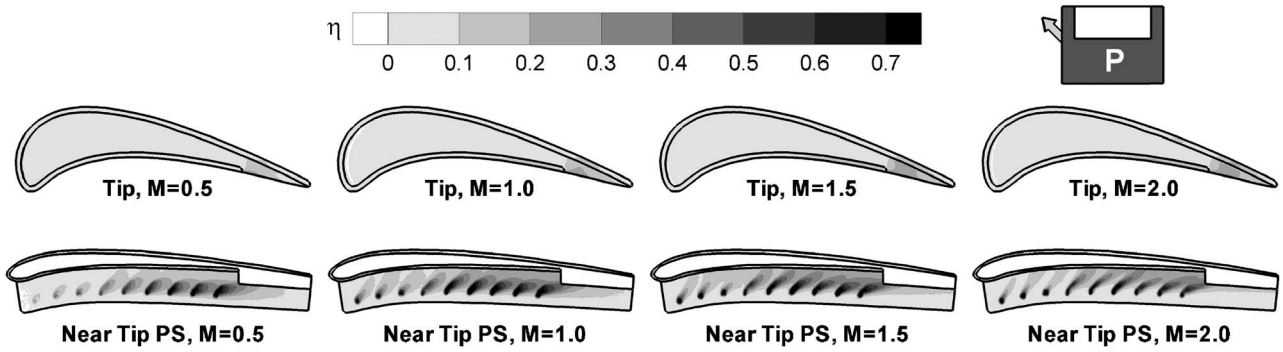

Fig. 14 Film-cooling effectiveness distribution on tip and near tip pressure sides for P cases for a depth of 4.2%

tion shows an increasing trend with higher blowing ratios and also increases as the recirculating flow inside the squealer cavity moves towards the trailing edge. Local high effectiveness levels can be observed on the suction side inner rim near the offset hole locations as the ejecting jets impinge laterally on these walls. Film effectiveness on the inner rim walls is lower for the smaller cavity depth. A smaller mass of coolant may get entrained in the recirculation vortex inside the squealer cavity, which may explain these lower magnitudes.

Pressure Side Injection Only (P Cases). Figures 14 and 15 show the film-cooling effectiveness distributions for the P case with cavity depths of 4.2% and 2.1% of span, respectively. Most of the squealer cavity floor remains unprotected as almost no coolant from the pressure side holes gets entrained in the recirculation vortex. Slight traces can be observed on the pressure side rim due to some coolant carryover. The effectiveness magnitudes for the PS rim are comparable to the TP case. Provision of the cutback helps the coolant from the compound shaped holes to cool the rims and the cutback surface. Minor traces can also be observed on the suction side rim. In general, cases with a 4.2% cavity depth give higher effectiveness magnitudes in the cutback region with magnitudes increasing with blowing ratio. Optimal film-cooling effectiveness on the near tip pressure side is observed for $M=1.5$, as opposed to $M=1$ for TP cases. Effectiveness data for $M=1.0$ for the TP case are comparable to data for $M=1.5$ for the P case. The local blowing ratios for these cases for the near tip pressure side holes are similar, which may explain this result. Comparison between the TP and P cases shows that on the pressure side, the effectiveness levels for $M=0.5$ and 2 are higher for the P case. For $M=0.5$, local blowing ratios (Fig. 9) for the TP case are very low as compared to the P case which explains the higher effectiveness for the P case. On the other hand, for $M=2.0$, local blowing ratios for the TP case are very high, causing lift-off and resulting in lower effectiveness. For the 2.1% cavity depth, the effectiveness levels are marginally lower than for 4.2% cavity depth, both on the pressure side and the rim. Effectiveness on the inner rim walls (Figs. 16 and 17) is seen only near the cutback, mainly on the suction side. The effectiveness level is similar to the one on the cutback cavity floor, which is about 0.1. As observed earlier, the lower cavity depth gives marginally lower effectiveness values.

Averaged Film-Cooling Effectiveness Results. Figures 18 and 19 depict the variation of averaged film-cooling effectiveness along the axial chord for the TP and P cases, respectively. The averaged values are obtained by averaging the effectiveness magnitudes at a given x/C_x location. For the near tip pressure side holes, the averaged results were obtained by averaging from the base of the holes to the tip. Data are shown for all six surfaces for each case. In general, for TP cases, average effectiveness increases with increasing axial chord distance for all surfaces. Very close to the trailing edge ($x/C_x>0.9$), the effectiveness magnitudes start dropping. Beyond $x/C_x=0.8$ (immediately after pressure side rim cutback) for the TP case, the coolant coverage in the cavity floor and the suction side rim region is better than the near tip pressure side region. This is particularly true at higher blowing ratios for both the cavity depths. This is due to the leakage flow diverting the pressure side coolant traces downstream of the pressure side rim cutback on to the cavity floor. For all surfaces other than the near tip pressure side, effectiveness increases with increasing blowing ratio for both TP and P cases similar to that observed from the contour plots and from Fig. 20 which shows the area averaged film-cooling effectiveness results. For the near tip pressure side, highest results are obtained for $M=1.0$ for the TP case and $M=1.5$ for the P case. For $M=1.0$, average effectiveness levels are more than 60% higher than the cavity floor for both

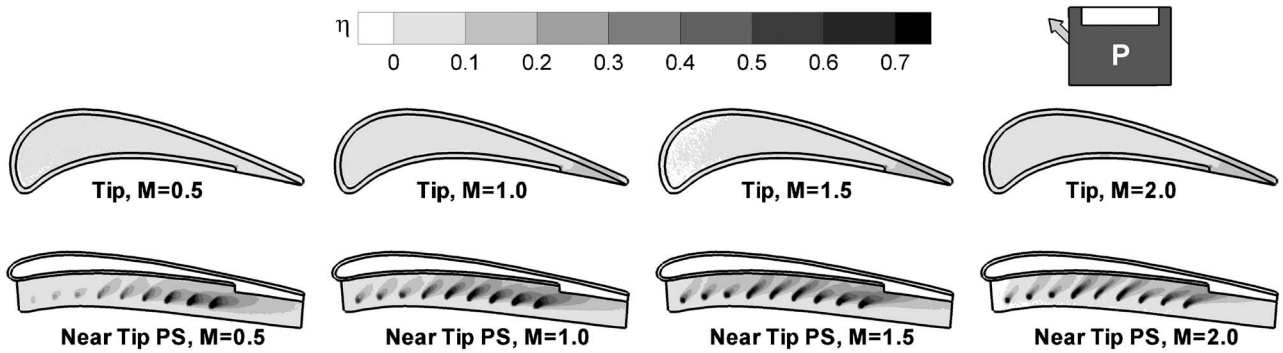

Fig. 15 Film-cooling effectiveness distribution on tip and near tip pressure sides for P cases for a depth of 2.1%

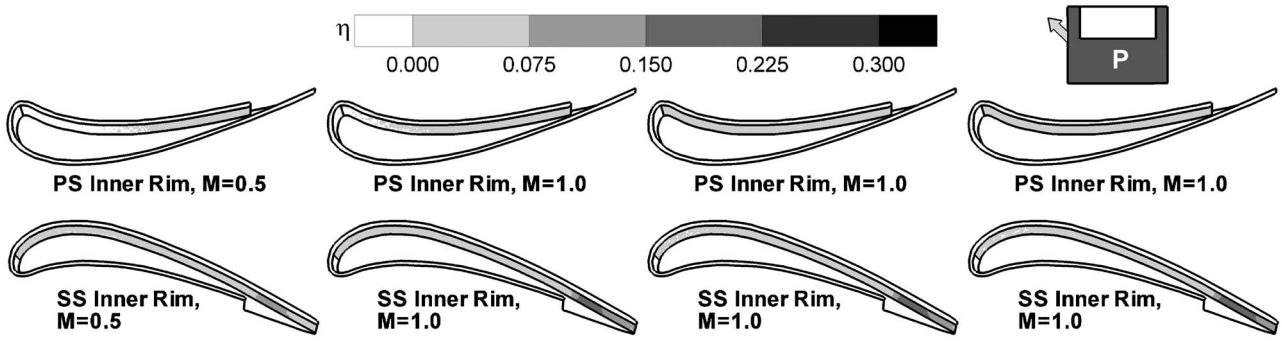

Fig. 16 Film-cooling effectiveness distribution on inner rim walls for PS and SS for P cases for a depth of 4.2%

cavity depths. For the P cases, the near tip pressure side effectiveness values are much higher than the rest of the blade tip regions, particularly at low blowing ratios. Similar to the TP case, a larger cavity depth gives higher effectiveness.

Film-cooling effectiveness comparisons with the cooling design presented by Mhetras et al. [9] give similar average effectiveness levels at all surfaces. However, comparisons with Ahn et al. [6] who used normal holes on the tip indicate that inclined holes used in the present study and in Ref. [9] give much higher effectiveness levels on the tip than normal holes. CFD data by Yang et al. [38] on the squealer tip with normal injection also shows much lower average effectiveness magnitudes.

Conclusions

A parametric study has been performed for measuring film-cooling effectiveness on a squealer blade tip. Effectiveness was measured on the cavity floor, rim, inner rim walls, and near tip pressure side. The effects of squealer cavity depth, coolant injection from the pressure side and tip and pressure side, and varying blowing ratio have been studied. Major findings from the experimental results are listed below.

1. The cutback squealer rim results in higher effectiveness in

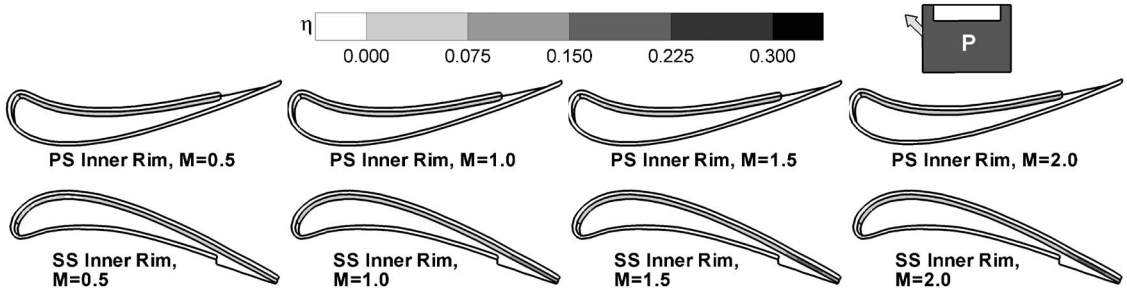

Fig. 17 Film-cooling effectiveness distribution on inner rim walls for PS and SS for P cases for a depth of 2.1%

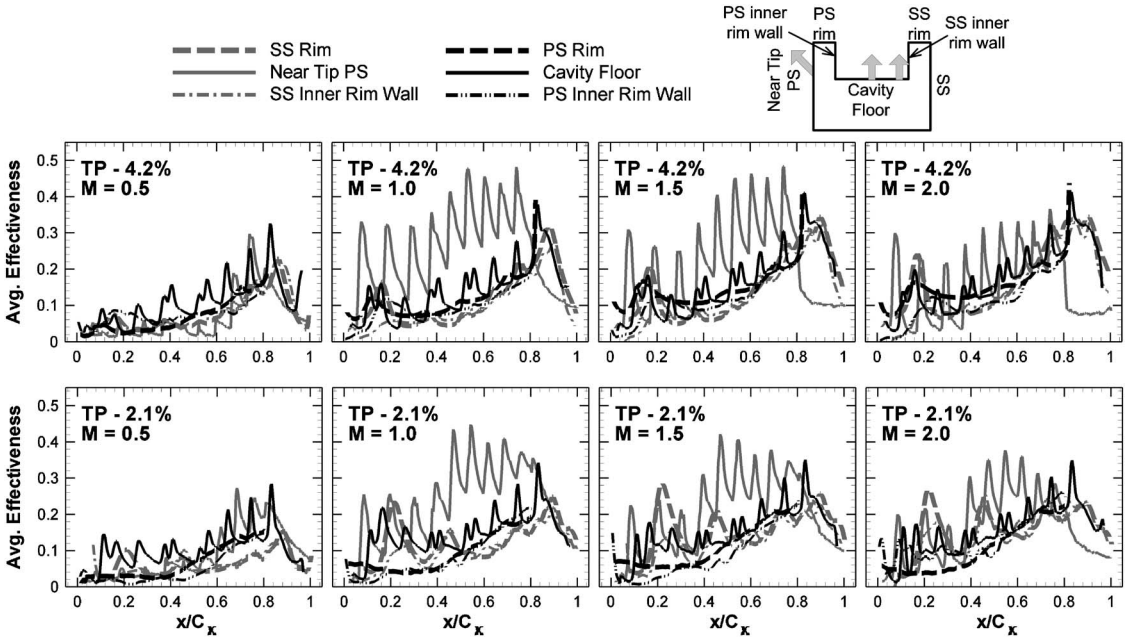

Fig. 18 Averaged film-cooling effectiveness for TP cases

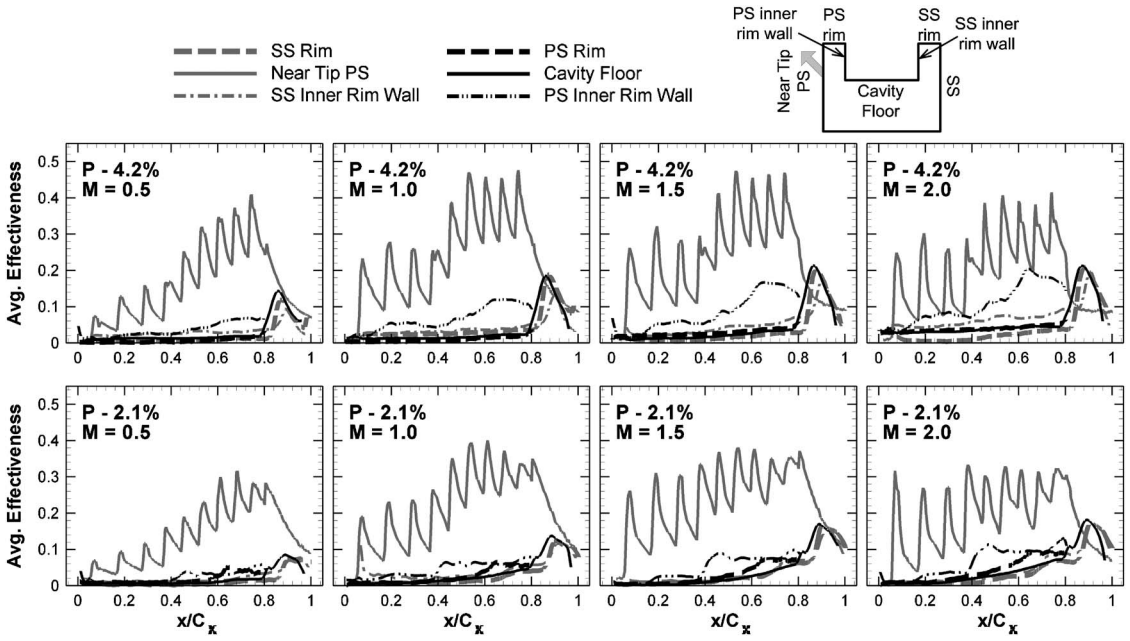

Fig. 19 Averaged film-cooling effectiveness for P cases

the trailing edge region of the blade tip as compared to a full squealer.

2. In general, a larger cavity depth gives higher effectiveness on all tip surfaces for both tip and pressure side injection (TP) and only pressure side injection (P) cases.
3. Higher blowing ratios give higher effectiveness on the tip rim, cavity floor, and inner rim walls. For the near tip pressure side, $M=1$ and 1.5 shows best results.

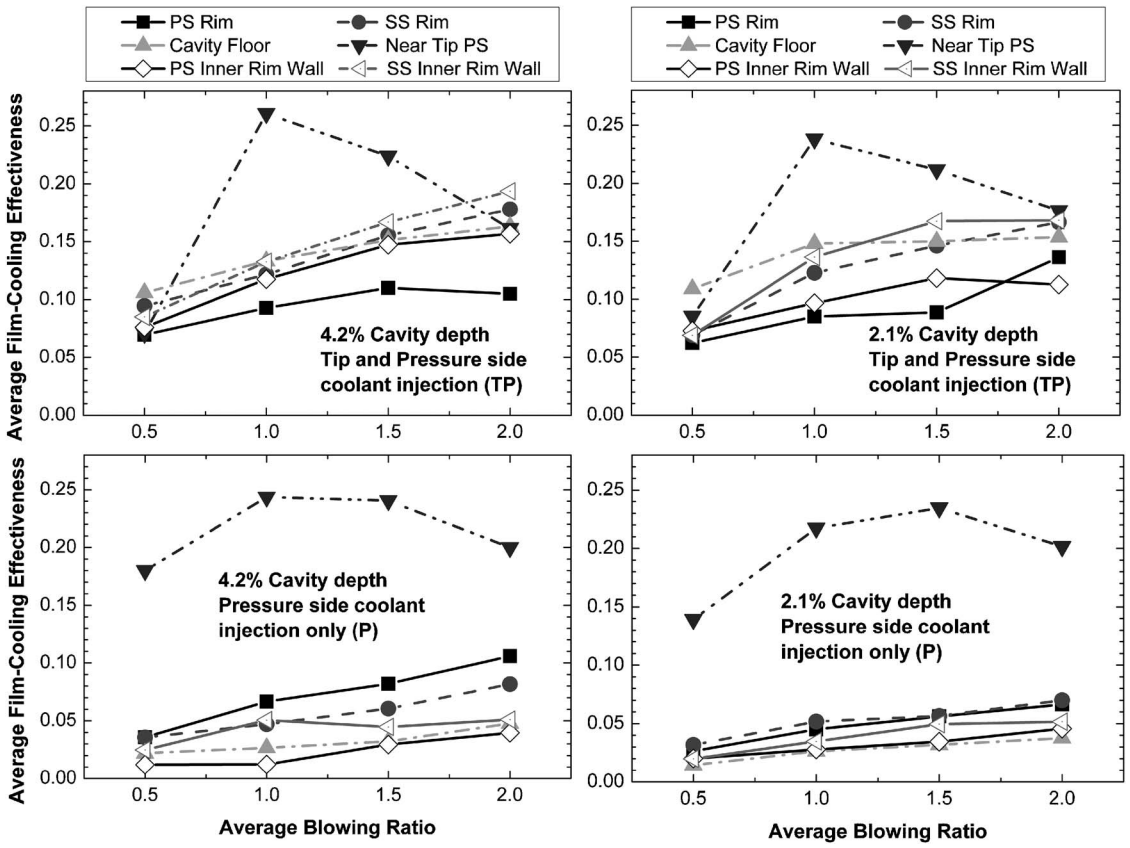

Fig. 20 Area averaged film-cooling effectiveness

4. Coolant accumulation results in increasing effectiveness from blade leading edge to trailing edge.
5. The tip rim and inner and outer squealer rim walls show high and uniform effectiveness due to the combined effect of tip and pressure side coolant injection.
6. Coolant injection from only the pressure side gives poor film-cooling performance on the cavity floor and inner rim walls.
7 Presence of serpentine passages to supply coolant to the holes results in a large variation of local blowing ratios, which can have a significant impact on film-cooling performance.

Acknowledgment

This work was prepared with the partial support of NSF under Grant No. CTS-9903972 and State of Texas Advanced Technology Program. This paper was presented at the 2006 ASME-AIAA Joint Thermophysics and Heat Transfer Conference in San Francisco (AIAA-2006-3404).

Nomenclature

C = tip clearance gap (1.5% span)
C_D = discharge coefficient
C_o = oxygen concentration
C_x = axial chord length of the blade (8.61 cm)
d = diameter Of film cooling holes (1.27 mm)
I = pixel intensity for an image
M = blowing ratio ($=\rho_c V_c / \rho_m V_m$)
M_i = local blowing ratio ($=\rho_{c,\mathrm{local}} V_{c,\mathrm{local}} / \rho_{m,\mathrm{local}} V_{m,\mathrm{local}}$)
P = local static pressure
P_t = total pressure
P_{O_2} = partial pressure of oxygen
PS = blade pressure side
SS = blade suction side
T_c = temperature of coolant at loop inlet
Tu = turbulence intensity level at the cascade inlet
x = axial distance (cm)
V_m = local mainstream velocity at hole location
V_c = coolant velocity
η = local film-cooling effectiveness
ρ_c = density of coolant air
ρ_m = density of mainstream air

Subscript

air = mainstream air with air as coolant
mix = mainstream air with nitrogen as coolant
ref = reference image with no mainstream and coolant flow
blk = image without illumination (black)

References

[1] Han, J. C., Dutta, S., and Ekkad, S. V., 2000, *Gas Turbine Heat Transfer and Cooling Technology* 1st ed., Taylor & Francis, New York, Vol. 1, Chaps. 2 and 3.
[2] Kim, Y. W., and Metzger, D. E., 1995, "Heat Transfer and Effectiveness on Film Cooled Turbine Blade Tip Model," ASME J. Turbomach., **117**(1), pp. 12–21.
[3] Kim, Y. W., Downs, J. P., Soechting, F. O., Abdel-Messeh, W., Steuber, G. D., and Tanrikut, S., 1995, "A Summary of the Cooled Turbine Blade Tip Heat Transfer and Film Effectiveness Investigations Performed by Dr. D. E. Metzger," ASME J. Turbomach., **117**(1), pp. 1–11.
[4] Kwak, J. S., and Han, J. C., 2003, "Heat Transfer Coefficient and Film-Cooling Effectiveness on a Gas Turbine Blade Tip," ASME J. Heat Transfer **125**, pp. 494–502.
[5] Kwak, J. S., and Han, J. C., 2003, "Heat Transfer Coefficient and Film-Cooling Effectiveness on the Squealer Tip of a Gas Turbine Blade," ASME J. Turbomach. **125**, pp. 648–657.
[6] Ahn, J., Mhetras, S. P., and Han, J. C., 2005, "Film-Cooling Effectiveness on a Gas Turbine Blade Tip," ASME J. Heat Transfer **127**, pp. 521–530.
[7] Christophel, J. R., Thole, K. A., and Cunha, F. J., 2005, "Cooling the Tip of a Turbine Blade Using Pressure Side Holes—Part 1: Adiabatic Effectiveness Measurements," ASME J. Turbomach. **127**, pp. 270–277.
[8] Christophel, J. R., Thole, K. A., and Cunha, F. J., 2005, "Cooling the Tip of a Turbine Blade Using Pressure Side Holes—Part 2: Heat Transfer Measurements," ASME J. Turbomach. **127**(2), pp. 278–286.
[9] Mhetras, S. P., Yang, H., Gao, Z., and Han, J. C., 2005, "Film-Cooling Effectiveness On Squealer Rim Walls and Squealer Cavity Floor of a Gas Turbine Blade Tip Using Pressure Sensitive Paint," ASME Paper No. GT-2005-68387.
[10] Metzger, D. E., Dunn, M. G., and Hah, C., 1991, "Turbine Tip and Shroud Heat Transfer," ASME J. Turbomach., **113**(3), pp. 502–507.
[11] Dunn, M. G., and Haldeman, C. W., 2000, "Time-Averaged Heat Flux for a Recessed Tip, Lip, and Platform of a Transonic Turbine Blade," ASME J. Turbomach., **122**(4), pp. 692–697.
[12] Rhee, D., and Cho, H. H., 2006, "Local Heat/Mass Transfer Characteristics on a Rotating Blade With Flat Tip in a Low Speed Annular Cascade—Part I: Near Tip Surface," ASME J. Turbomach., **128**(1), pp. 96–109.
[13] Rhee, D., and Cho, H. H., 2006, "Local Heat/Mass Transfer Characteristics on a Rotating Blade with Flat Tip in a Low Speed Annular Cascade—Part II: Tip and Shroud," ASME J. Turbomach., **128**(1), pp. 110–119.
[14] Molter, S. M., Dunn, M. G., Haldeman, C. W., Bergolhz, R. F., and Vitt, P., 2006, "Heat-Flux Measurements and Predictions for the Blade Tip Region of a High Pressure Turbine," ASME Paper No. GT2006-90048.
[15] Yang, T. T., and Diller, T. E., 1995, "Heat Transfer and Flow for a Grooved Turbine Blade Tip in a Transonic Cascade," ASME Paper No. 95-WA/HT-29.
[16] Bunker, R. S., Baily, J. C., and Ameri, A. A., 2000, "Heat Transfer and Flow on the First Stage Blade Tip of a Power Generation Gas Turbine: Part 1: Experimental Results," ASME J. Turbomach., **122**(2), pp. 263–271.
[17] Azad, G. M. S., Han, J. C., Teng, S., and Boyle, R., 2000, "Heat Transfer and Pressure Distributions on a Gas Turbine Blade Tip," ASME J. Turbomach., **122**(4), pp. 717–724.
[18] Azad, G. M. S., Han, J. C., and Boyle, R., 2000, "Heat Transfer and Pressure Distributions on the Squealer Tip of a Gas Turbine Blade," ASME J. Turbomach., **122**(4), pp. 725–732.
[19] Bunker, R. S., and Baily, J. C., 2001, "Effect of Squealer Cavity Depth and Oxidation on Turbine Blade Tip Heat Transfer," ASME Paper No. 2001-GT-0155.
[20] Azad, G. M. S., Han, J. C., Bunker, R. S., and Lee, C. P., 2002, "Effect of Squealer Geometry Arrangement on a Gas Turbine Blade Tip Heat Transfer," ASME J. Heat Transfer, **124**(3), pp. 452–459.
[21] Kwak, J. S., Ahn, J., Han, J. C., Pang Lee, C., Bunker, R. S., Boyle, R., and Gaugler, R., 2002, "Heat Transfer Coefficients on Squealer Tip and Near Tip Regions of a Gas Turbine Blade with Single or Double Squealer," ASME J. Turbomach. **125**, pp. 778–787.
[22] Kwak, J. S., and Han, J. C., 2003, "Heat Transfer Coefficient on a Gas Turbine Blade Tip and Near Tip Regions," J. Thermophys. Heat Transfer, **17**(3), pp. 297–303.
[23] Kwak, J. S., and Han, J. C., 2003, "Heat Transfer Coefficient on the Squealer tip and Near Squealer Tip Regions of a Gas Turbine Blade," ASME J. Heat Transfer, **125**(4), pp. 669–677.
[24] Mayle, R. E., and Metzger, D. E., 1982, "Heat Transfer at the Tip of an Unshrouded Turbine Blade," *Proceedings of the seventh International Heat Transfer Conference*, Hemisphere, New York, pp. 87–92.
[25] Heyes, F. J. G., Hodson, H. P., and Dailey, G. M., 1991, "The Effect of Blade Tip Geometry on the Tip Leakage Flow in Axial Turbine Cascades," ASME 91-GT-135.
[26] Teng, S., Han, J. C., and Azad, G. M. S., 2001, "Detailed Heat Transfer Coefficient Distributions on a Large-Scale Gas Turbine Blade Tip," ASME J. Heat Transfer, **123**(4), pp. 803–809.
[27] Papa, M., Goldstein, R. J., and Gori, F., 2003, "Effects of Tip Geometry and Tip Clearance on the Mass/Heat Transfer From a Large-Scale Gas Turbine Blade," ASME J. Turbomach., **125**(1), pp. 90–96.
[28] Jin, P., and Goldstein, R. J., 2003, "Local Mass/He at Transfer on a Turbine Blade Tip," Int. J. Rotating Mach. **9**(2), pp. 81–95.
[29] Jin, P., and Goldstein, R. J., 2003, "Local Mass/He at Transfer on Turbine Blade Near-Tip Surfaces," ASME J. Turbomach. **125**, pp. 521–528.
[30] Saxena, V., Nasir, H., and Ekkad, S. V., 2004, "Effect of Blade Tip Geometry on Tip Flow and Heat Transfer for a Blade in a Low Speed Cascade," ASME J. Turbomach. **126**, pp. 130–138.
[31] Ameri, A. A., Steinthorsson, E., and Rigb′y, L. D., 1999, "Effects of Tip Clearance and Casing Recess on Heat Transfer and Stage Efficiency in Axial Turbines," ASME J. Turbomach., **121**(4), pp. 683–693.
[32] Ameri, A. A., and Rigby, D. L., 1999, "A Numerical Analysis of Heat Transfer and Effectiveness on Film Cooled Turbine Blade Tip Models," Report No. NASA/CR 1999–209165.
[33] Ameri, A. A., and Bunker, R. S., 2000, "Heat Transfer and Flow on the First Stage Blade Tip of a Power Generation Gas Turbine: Part 2: Simulation Results," ASME J. Turbomach., **122**(2), pp. 272–277.
[34] Yang, H., Acharya, S., Ekkad, S. V., Prakash, C., and Bunker, R., 2002, "Flow and Heat Transfer Predictions for a Flat-Tip Turbine Blade," ASME Paper No. 2002-GT-30190.
[35] Yang, H., Acharya, S., Ekkad, S. V., Prakash, C., and Bunker, R., 2002, "Numerical Simulation of Flow and Heat Transfer Past a Turbine Blade with a Squealer-Tip," ASME Paper No. 2002-GT-30193.
[36] Acharya, S., Yang, H., Ekkad, S. V., Prakash, C., and Bunker, R., 2002, "Numerical Simulation of Film Cooling on the Tip of a Gas Turbine Blade," ASME Paper No. 2002-GT-30553.
[37] Hohlfeld, E. M., Christophel, J. R., Couch, E. L., and Thole, K. A., 2003,

"Predictions of Cooling Flow Dirt Purge Holes Along the Tip of a Turbine Blade," ASME Paper No. 2003-GT-38251.
[38] Yang, H., Chen, H. C., and Han, J. C., 2004, "Numerical Prediction of Film Cooling and Heat Transfer With Different Film Hole Arrangements on the Plane and Squealer Tip of a Gas Turbine Blade," ASME Paper No. 2004-GT-53199.
[39] Halila, E. E., Lenahan, D. T., and Thomas, T. T., 1982, "Energy Efficient Engine, High Pressure Turbine Test Hardware Detailed Design Report," Report No. NASA CR-167955.
[40] McLachlan, B., and Bell, J., 1995, "Pressure-Sensitive Paint in Aerodynamic Testing," Exp. Therm. Fluid Sci., **10**, pp. 470–485.
[41] Wright, L. M., Gao, Z., Varvel, T. A., and Han, J. C., 2005, "Assessment of Steady State PSP, TSP and IR Measurement Techniques for Flat Plate Film Cooling," ASME Paper No. HT-2005–72363.
[42] Coleman, H. W., and Steele, W. G., 1989, *Experimentation and Uncertainty Analysis for Engineers*, Wiley, New York, pp. 47–131.

Modeling of Rough-Wall Boundary Layer Transition and Heat Transfer on Turbine Airfoils

M. Stripf

A. Schulz

H.-J. Bauer

Lehrstuhl und Institut für Thermische Strömungsmaschinen, Universität Karlsruhe (TH), Kaiserstr. 12, 76128 Karlsruhe, Germany

A new model for predicting heat transfer in the transitional boundary layer of rough turbine airfoils is presented. The new model makes use of extensive experimental work recently published by the current authors. For the computation of the turbulent boundary layer, a discrete element roughness model is combined with a two-layer model of turbulence. The transition region is modeled using an intermittency equation that blends between the laminar and turbulent boundary layer. Several intermittency functions are evaluated in respect of their applicability to rough-wall transition. To predict the onset of transition, a new correlation is presented, accounting for the influence of freestream turbulence and surface roughness. Finally, the new model is tested against transitional rough-wall boundary layer flows on high-pressure and low-pressure turbine airfoils.
[DOI: 10.1115/1.2750675]

Introduction

Increasing surface roughness is well known to have a major effect on the long-term efficiency and total cost of ownership of gas turbine engines. Besides increasing aerodynamic losses, surface roughness causes an augmentation of heat transfer to the thermally loaded parts, which in turn results in a reduction of lifetime. It is thus desirable to predict the heat transfer distribution on the rough surfaces in order to optimize the cooling layout not only for smooth surfaces but also for increasing surface roughness during the service life of the engine.

Several recent experimental studies on rough turbine airfoils indicate that real blade and vane surfaces can be very rough, with roughness heights reaching into the fully rough regime [1,2], and that the roughness effect is twofold: (i) it increases heat transfer and skin friction in the turbulent boundary layer and (ii) the laminar-to-turbulent transition is moved upstream [3–10]. The change in transition location can be critical especially on aft-loaded airfoils, where transition with a smooth surface usually occurs on the suction side close to the trailing edge but is moved considerably upstream by the increased surface roughness. Here, heat transfer can easily increase by a factor of 10 in regions where the boundary layer becomes turbulent due to the roughness. Therefore, correctly modeling the roughness-affected transition is seen to be crucial.

Review of Roughness and Transition Models

Modeling the transitional boundary layer on a rough surface consists of the correct calculation of the laminar and fully turbulent regions of the rough-wall boundary layer, the transitional region between the two boundary layer states, and the onset of the transitional region. In the laminar boundary layer, the effect of surface roughness on heat transfer was shown to be negligible (e.g., [9]) and the roughness effect on the laminar momentum boundary layer is expected to be small compared to its effect on the turbulent boundary layer. Therefore, the major tasks are modeling the rough-wall turbulent boundary layer and the transition process.

Contributed by the International Gas Turbine Institute of ASME for publication in the JOURNAL OF TURBOMACHINERY. Manuscript received June 27, 2006; final manuscript received July 2, 2006; published online February 12, 2008. Review conducted by David Wisler. Paper presented at the ASME Turbo Expo 2006: Land, Sea and Air (GT2006), May 8–11, 2006, Barcelona, Spain.

Roughness Models for Turbulent Boundary Layers. Current methods that incorporate the effect of surface roughness into the calculation of turbulent boundary layers usually take one of the following approaches:

1. In integral methods, the skin friction law is adjusted by adding an equivalent sand grain roughness term that reflects the downward shift in the velocity profile. The derivation and application of this method to skin friction and heat transfer calculations is shown by Dvorak [11] and Dirling [12].
2. The mixing length formulation of eddy viscosity models is modified to account for roughness. Following the idea of Rotta [13], Cebeci and Chang [14] introduce an effective wall displacement Δy, which is a function of the equivalent sand grain roughness height k_s. The eddy viscosity in the vicinity of the wall is then calculated from

$$\mu_t = l^2 \frac{\partial U}{\partial y} \tag{1}$$

with

$$l = \kappa(y + \Delta y)\left[1 - \exp\left(-\frac{y + \Delta y}{A}\right)\right] \tag{2}$$

and

$$\Delta y = 0.9\frac{\nu}{u_\tau}\left[\sqrt{k_s^+} - k_s^+ \exp\left(\frac{-k_s^+}{6}\right)\right] \tag{3}$$

   Feiereisen and Acharya [15] modify the Cebeci and Chang [14] model in order to incorporate directly measurable roughness quantities (centerline average roughness, correlation length and rms deviation of surface slope angles) instead of the equivalent sand grain roughness. Methods similar to the Cebeci and Chang [14] model are proposed by Granville [16] and Krogstad [17].
3. The effect of roughness is indirectly accounted for by the use of modified wall functions. Guo et al. [18] derive a wall function from the Cebeci and Chang [14] model and use it for heat transfer calculations on rough nozzle guide vanes. Another example of this method is given by Jouini et al. [19], who derive a different formulation of the wall function.
4. One- or two-equation turbulence models are altered to account for roughness. Lee and Paynter [20] modify the Spalart-Allmaras one-equation turbulence model by introducing an effective wall displacement similar to the Cebeci

Table 1 Transition onset correlations

Researchers	Correlation
Abu-Ghannam and Shaw [51]	$Re_{\theta,t}=163+\exp\{F(\lambda_\theta)-[F(\lambda_\theta)/6.91]Tu_t\}$ $F(\lambda_\theta)=6.91+12.75\lambda_\theta+63.64\lambda_\theta^2$ for $\lambda_\theta<0$ $F(\lambda_\theta)=6.91+2.48\lambda_\theta-12.27\lambda_\theta^2$ for $\lambda_\theta>0$
Mayle [32]	$Re_{\theta,t}=400Tu_t^{-0.625}$
Schiele [47]	$Re_{\theta,t}=500(Tu^*)^{-0.65}$ $Tu^*=0.5(Tu_1+Tu_t)$ for flat plates $Tu^*=Tu_t$ for turbine airfoils
Menter et al. [52]	$Re_{\theta,t}=803.73[Tu_t+0.6067]^{-1.027}F(\lambda_\theta,K)$ $F(\lambda_\theta,K)=1-[-10.32\lambda_\theta-89.47\lambda_\theta^2-265.51\lambda_\theta^3]$ $\exp[-Tu_t/3]$ for $\lambda_\theta\leq 0$ $F(\lambda_\theta,K)=1+[0.0962(K\times 10^6)+0.148(K\times 10^6)^2$ $+0.0141(K\times 10^6)^3][1-\exp(-Tu_t/1.5)]$ $+0.556[1-\exp(-23.9\lambda_\theta)]\exp(-Tu_t/1.5)$ for $\lambda_\theta>0$

and Chang [14] model. Wilcox [21] incorporates the roughness effects directly into the ω boundary condition of the k-ω turbulence model. Hellsten and Laine [22] extend Menter's k-ω shear stress transport (SST) model in a way similar to Wilcox's suggestion but with additional modifications necessary for the SST version. A modified version of a two-layer k-ε turbulence model is provided by Durbin et al. [23].

5. The discrete element method (DEM), which is based on a suggestion by Schlichting [24], accounts for the roughness directly in the boundary layer equations. Blockage factors α_x and α_y are introduced to reflect the blockage of the individual roughness elements. Additional sink terms in the momentum and energy equation reflect the form drag of the individual elements and the heat transfer to the elements. In this way, the total flow resistance and heat transfer is comprised of the flat surface portion between the roughness elements and the portion transferred to the elements themselves. Early implementations of this method are given by Finson and Wu [25] and Christoph and Pletcher [26]. However, Taylor et al. [27] showed that the blockage factor α_x the authors [25,26] use reflects the maximum blockage instead of the correct average blockage. Other interesting modifications of the model are given by Lin and Bywater [28], Tarada [29], Hosni et al. [30] and McClain [31], which differ mainly in the correlations used in the form drag and additional heat transfer terms and the turbulence model used. Because the discrete element model will be used in the current approach, the underlying conservation equations (Eq. (9)–(13)) are provided later in this paper.

A shortcoming of models 1–4 is that they rely on the equivalent sand grain roughness k_s, which is defined to reproduce the correct skin friction and velocity profile of a certain rough surface. A problem arises when the same k_s is being used to calculate heat transfer because the mechanisms for momentum and energy transport to a rough surface are different. Although part of the momentum transfer to a rough surface is due to the pressure forces that act on the roughness elements, there is no counterpart to this mechanism in heat transfer. The discrete element method overcomes this problem because it considers the different physical characteristics of the individual roughness elements. It is easy, for instance, to consider roughness elements with a thermal conductivity that is different from the base material's conductivity. No matter which roughness model is used to calculate the rough-wall turbulent boundary layer, additional modeling is required to predict transition.

Transition Modeling. Boundary layer transition can occur in one of the following three modes (see [32]): natural transition, bypass transition, and separated flow transition. The present paper concentrates on the bypass transition, where the first stage of the natural transition—the Tollmien-Schlichting instability—is completely bypassed and transition is triggered by large disturbances in the external flow and/or surface roughness. Two different concepts are generally applied to predict this kind of transition:

1. Low Reynolds number (LRN) turbulence models are used, where the wall damping functions are optimized in order to predict the correct onset of transition. This method is attractive because it can be easily implemented in existing CFD codes. Sieger et al. [33] compare a large variety of LRN k-ε turbulence models and conclude that Schmidt and Patankar's [34] extensions of the Lam and Bremhorst [35] and Launder and Sharma [36] models give the best results when applied to turbine airfoils. Tarada [29] combines a LRN k-ε model with the discrete element roughness model and calculates transitional boundary layers on rough turbine airfoils. One shortcoming of this method is the extreme sensitivity of the transition onset location to the values of the additional constants (C_k and $C_{\varepsilon 3}$ in Eqs. (7) and (8)) needed in the transport equations for k and ε.
2. The onset of transition is determined using a correlation to relate the major factors affecting transition to the momentum thickness Reynolds number (see Table 1 for an overview of common transition onset correlations). The progress of transition is then described with an intermittency model, which is based on Emmons' [37] turbulent spot theory. Here, turbulent spots having the shape of an arrowhead are formed at the onset of transition, which are then transported downstream while they grow in size until they coalesce and form a fully turbulent boundary layer. To describe the flow in the transitional region, Emmons introduces the intermittency γ, which characterizes the fraction of time during which the flow at one point on the surface is turbulent. Thus, for a laminar boundary layer $\gamma=0$, whereas for a fully turbulent boundary layer $\gamma=1$. With Narasimha's [38] assumption that the production of turbulent spots occurs randomly along a single line at the onset of transition x_t, Solomon et al. [39] give the following expression for γ:

$$\gamma = 1 - \exp\left[-n \int_{x_t}^{x} \frac{\sigma}{\tan\alpha}\left(\frac{1}{U_e}\right) dx \int_{x_t}^{x} \tan\alpha dx \right] \quad (4a)$$

where n is the spot formation rate, α is the spreading half angle, and σ is the propagation parameter of the turbulent spot. The first and second integrals in Eq. (4a) thus reflect

Table 2 C_d and Nu_d correlations for roughness elements

Researchers	C_d correlation	Nu_d correlation
Taylor et al. [27]	$C_d=(\mathrm{Re}_d/1000)^{-0.125}$ $\mathrm{Re}_d<6\times10^3$ $C_d=0.6$ $\mathrm{Re}_d>6\times10^3$	$\mathrm{Nu}_d=2.475\,\mathrm{Re}_d^{0.4}\mathrm{Pr}^{0.36}$ $\mathrm{Re}_d<10^2$ $\mathrm{Nu}_d=1.403\,\mathrm{Re}_d^{0.5}\mathrm{Pr}^{0.37}$ $10^2<\mathrm{Re}_d<10^3$ $\mathrm{Nu}_d=0.963\,\mathrm{Re}_d^{0.6}\mathrm{Pr}^{0.36}$ $10^3<\mathrm{Re}_d<2\times10^5$ $\mathrm{Nu}_d=0.060\,\mathrm{Re}_d^{0.84}\mathrm{Pr}^{0.36}$ $\mathrm{Re}_d>2\times10^5$
Tarada [29] (Nu_d) Tarada [48] (C_d)	$C_d=\max[C_{dp},C_{dp}(\mathrm{Re}_d/\mathrm{Re}_{dc})^{-0.289}]+16(\beta_x^{-1}-1)/\mathrm{Re}_d$ $C_{dp}=\min\{0.182+0.0542/L_c^{1/2},1.1-0.7\exp[-0.597(k/\bar{d})^{0.419}]\}$ $\mathrm{Re}_{dc}=\min(4.35\times10^2/L_c^{1/2},\ 5\times10^3)$	$\mathrm{Nu}_d=0.8\,\mathrm{Re}_d^{0.4}\mathrm{Pr}^{0.36}$ $\mathrm{Re}_d<10^2$ $\mathrm{Nu}_d=0.25\,\mathrm{Re}_d^{0.65}\mathrm{Pr}^{0.36}$ $10^2<\mathrm{Re}_d<10^3$ $\mathrm{Nu}_d=0.36\,\mathrm{Re}_d^{0.6}\mathrm{Pr}^{0.36}$ $10^3<\mathrm{Re}_d<2\times10^5$ $\mathrm{Nu}_d=0.022\,\mathrm{Re}_d^{0.84}\mathrm{Pr}^{0.36}$ $\mathrm{Re}_d>2\times10^5$
McClain et al. [49]	$C_d=(a/b)^{0.73}(\mathrm{Re}_d/1000)^{-0.125}$ $\mathrm{Re}_d\le6\times10^4$ $C_d=0.6(a/b)^{0.73}$ $\mathrm{Re}_d>6\times10^4$	$\mathrm{Nu}_d=1.7\,\mathrm{Re}_d^{0.49}\mathrm{Pr}^{0.4}$ $\mathrm{Re}_d\le13776$ $\mathrm{Nu}_d=0.0605\,\mathrm{Re}_d^{0.84}\mathrm{Pr}^{0.4}$ $\mathrm{Re}_d>13776$

the streamwise and spanwise spreading of turbulent spots, respectively. An alternative expression for γ is given by Byvaltsev and Kawaike [40], who modified Eq. (4*a*), using dimensionless terms

$$\gamma=1-\exp\left[-\varphi\int_{x_t}^{x}\frac{\sigma}{\sigma_{\lambda_\theta=0}\tan\alpha}\left(\frac{1}{U_e}\right)dx\int_{x_t}^{x}\tan\alpha\frac{U_{e,t}}{x_t^2}dx\right] \tag{4b}$$

with $\varphi=n\sigma_{\lambda_\theta=0}x_t^2/U_{e,t}$. For the prediction of transitional boundary layers on turbine airfoils, the authors achieved good results by assuming $\varphi=1$. Correlations for α and σ are given by Gostelow et al. [41]. D'Ovidio et al. [42] recently validated Gostelow's correlation for α with new experimental data and updated the correlation for σ leading to the following expressions:

$$\alpha=4+\left[\frac{22.14}{0.79+2.72\exp(47.63\lambda_\theta)}\right] \tag{5}$$

$$\sigma=0.024+\left[\frac{0.604}{1+5.0\exp(66\lambda_\theta)}\right] \tag{6}$$

The spot formation rate n in Eq. (4*a*) is usually correlated in terms of the nondimensional breakdown parameter N,

$$N=\frac{n\sigma\theta_t^3}{\nu} \tag{7}$$

Two correlations are taken into account in this work, with the first one being developed by Solomon et al. [39] by combining the work of Gostelow et al. [41] and Fraser et al. [43],

$$N=8.6\times10^{-4}\exp(2.134\lambda_{\theta t}\ln\mathrm{Tu}_t-59.23\lambda_{\theta t}-0.564\ln\mathrm{Tu}_t)\quad\lambda_{\theta t}\le0$$

$$N=8.6\times10^{-4}\exp(-0.564\ln\mathrm{Tu}_t-10\sqrt{\lambda_{\theta t}})\quad\lambda_{\theta t}>0 \tag{8a}$$

The second one was recently presented by Roberts and Yaras [44], who suggest the following correlation, which is based on the boundary layer shape factor H:

$$\log_{10}(N)=\frac{0.55H_t-2.2}{1-0.63H_t+0.14H_t^2}\quad\text{for}\quad1.6\le H_t\le8.5 \tag{8b}$$

An advantage of the intermittency-based concept over the use of extended LRN turbulence models is that it can be easily tuned to experimental data by modifying the transition onset correlations. In the current investigation, this is made use of to incorporate the effect of roughness.

Description of Proposed Model

The proposed model combines the discrete element roughness model (DEM) with an intermittency-based transition model. The choice of models is motivated by the advantages mentioned above.

Transport Equations and Turbulence Model. The starting point for the current investigation is the following set of rough-wall boundary layer equations as derived by Taylor et al. [27] and Tarada [29]:

Continuity:

$$\frac{\partial}{\partial x}(\rho\beta_x U)+\frac{\partial}{\partial y}(\rho\beta_y V)=0 \tag{9}$$

Momentum:

$$\rho\beta_x U\frac{\partial U}{\partial x}+\rho\beta_y V\frac{\partial U}{\partial y}=-\beta_x\frac{\partial P}{\partial x}+\frac{\partial}{\partial y}\left[\beta_y(\mu+\mu_t)\frac{\partial U}{\partial y}\right]-\frac{1}{2}\frac{\rho C_d U^2 d}{L_x L_z} \tag{10}$$

Energy:

$$\rho\beta_x U\frac{\partial H}{\partial x}+\rho\beta_y V\frac{\partial H}{\partial y}=\frac{\partial}{\partial y}\left[\beta_y\left(\frac{\mu}{\mathrm{Pr}}+\frac{\mu_t}{\mathrm{Pr}_t}\right)\frac{\partial H}{\partial y}\right]+\frac{\partial}{\partial y}\left\{\beta_y\left[(\mu+\mu_t)-\left(\frac{\mu}{\mathrm{Pr}}+\frac{\mu_t}{\mathrm{Pr}_t}\right)\right]U\frac{\partial U}{\partial y}\right\}+\frac{\pi k_f\mathrm{Nu}_d(T_r-T)}{L_x L_z} \tag{11}$$

The terms describing the form drag of the roughness elements and the heat transfer to these elements need additional empirical information in form of drag coefficients C_d and Nusselt numbers Nu_d. Several correlations were proposed by different researchers, which are consistent with each other in that they relate C_d and Nu_d to the local element Reynolds number $\mathrm{Re}_d(y)=U(y)d(y)/\nu(y)$ (see Table 2). In the present work, the correlations of McClain et al. [49] are used because they showed the best agreement with the experimental data.

The eddy viscosity μ_t is modeled using the two layer k-ε turbulence model presented by Sieger et al. [45], which combines the one-equation k-l model of Rodi et al. [46] and the standard k-ε model. The model was successfully tested by Schiele [47] against flat plate and turbine airfoil experimental data and is therefore used in the proposed model. Following Tarada [29], additional source terms are added to the k and ε transport equations to account for vortex shedding effects at the roughness elements. The

one-equation near-wall model of Rodi et al. [46] is used without additional modification. Switching between the two models is performed, where the viscosity ratio reaches a value of $\mu_t/\mu=16$. The k-ε model equations with the additional roughness source terms are as follows:

Kinetic energy of turbulence:

$$\rho\beta_x U\frac{\partial k}{\partial x}+\rho\beta_y V\frac{\partial k}{\partial y}=\frac{\partial}{\partial y}\left[\beta_y\left(\mu+\frac{\mu_t}{\sigma_k}\right)\frac{\partial k}{\partial y}\right]+\beta_y\mu_t\left(\frac{\partial U}{\partial y}\right)^2-\rho\beta_x\varepsilon+\frac{\rho C_k U^3 d}{L_x L_z} \tag{12}$$

Dissipation:

$$\rho\beta_x U\frac{\partial \varepsilon}{\partial x}+\rho\beta_y V\frac{\partial \varepsilon}{\partial y}=\frac{\partial}{\partial y}\left[\beta_y\left(\mu+\frac{\mu_t}{\sigma_\varepsilon}\right)\frac{\partial \varepsilon}{\partial y}\right]+\frac{\varepsilon}{k}\left[\beta_y C_{\varepsilon 1}\mu_t\left(\frac{\partial U}{\partial y}\right)^2-\rho\beta_x C_{\varepsilon 2}\varepsilon+C_{\varepsilon 3}\frac{\rho C_k U^3 d}{L_x L_y}\right] \tag{13}$$

The eddy viscosity μ_t is determined by the following relation:

$$\mu_t=\rho C_\mu\frac{k^2}{\varepsilon} \tag{14}$$

For viscosity ratios $\mu_t/\mu\leq 16$, Rodi's one-equation model is used. The dissipation rate in the k equation, Eq. (12), is then calculated from

$$\varepsilon=\frac{\sqrt{\overline{v'^2}}k}{l_{\varepsilon,v}} \tag{15}$$

and the eddy viscosity is given by

$$\mu_t=\gamma\rho l_{\mu,v}\sqrt{\overline{v'^2}} \tag{16}$$

Note that Eq. (16) contains the intermittency factor γ, which is used to model the boundary layer transition and which varies from 0.0 for a laminar boundary layer to 1.0 for a fully turbulent boundary layer.

The length scales $l_{\mu,v}$ and $l_{\varepsilon,v}$ are described by the following correlations which were determined from DNS data (see [46]):

$$l_{\mu,v}=C_{l,\mu}y=0.30y \tag{17}$$

$$l_{\varepsilon,v}=1.3y\left(1+2.12\frac{\nu}{\sqrt{\overline{v'^2}}y}\right)^{-1} \tag{18}$$

In Eq. (17), $C_{l,\mu}=0.30$ is used instead of Rodi's original value of 0.33 because it was found to give better consistency with experimental data [47]. The velocity scale $\overline{v'^2}$ can be determined from the k equation, Eq. (12), using the following empirical relationship, which was again derived from DNS data:

$$\frac{\overline{v'^2}}{k}=4.65\times 10^{-5}y^{*2}+4.00\times 10^{-4}y^{*} \tag{19}$$

with the dimensionless wall distance $y^*=\sqrt{k}y/\nu$.

The standard coefficients in the k-ε model are used ($C_\mu=0.09$, $C_{\varepsilon 1}=1.44$, $C_{\varepsilon 2}=1.92$, $\sigma_k=1.0$, $\sigma_\varepsilon=1.3$), and the coefficients in the additional roughness source terms are $C_k=0.04$ and $C_{\varepsilon 3}=0.0$. The value for C_k corresponds to the value used by Finson and Clarke [50] and is much higher than the one used by Tarada [29], who varied C_k between 3×10^{-5} and 5×10^{-5}. The reason for this difference is that Tarada optimized C_k to correctly predict the onset of transition, whereas in the current work C_k is optimized to give the best agreement with experimental heat transfer and shear stress data in fully turbulent boundary layers.

After the solution of the transport equations with an implicit and forward marching finite-volume boundary layer code based on the method by Patankar and Spalding [51], the skin friction coefficient is calculated from

$$C_f=\frac{\beta_x\mu\left.\frac{\partial U}{\partial y}\right|_{y=0}+\frac{1}{L_x L_z}\int_0^\infty\frac{1}{2}\rho U^2 C_d dy}{0.5\rho U_e^2} \tag{20}$$

The Stanton number $\mathrm{St}=h/(\rho c_p U_e)$ is determined using

$$\mathrm{St}=\frac{-\beta_x k_f\left.\frac{\partial T}{\partial y}\right|_{y=0}+\frac{1}{L_x L_z}\int_0^\infty\pi k_f \mathrm{Nu}_d(T_r-T)dy}{\rho U_e c_p(T_w-T_e)} \tag{21}$$

Transition Zone Model. To describe the boundary layer in the transition zone an intermittency model is used to calculate γ in Eq. (16). In addition it is used to switch off the roughness terms of the DEM in the laminar boundary layer with a simple blending function for the roughness height k:

$$k_{\mathrm{eff}}=\min(k,3\gamma k) \tag{22}$$

This is done for several reasons: (1) the effect of roughness on the laminar boundary layer is small and the effect on heat transfer is negligible (Stripf et al. [9]), (2) the DEM underestimates heat transfer in the laminar boundary layer, and (3) the roughness model can be substituted with other models without changing the conditions in the laminar boundary layer at the onset of transition.

Four intermittency model variations are evaluated for usability in rough-wall transitional flows, all using the same spot spreading angle and propagation rate correlations given in Eqs. (5) and (6):

1. the Solomon, Walker, and Gostelow (SWG) intermittency equation (Eq. (4*a*)) with the spot formation rate correlation (Eq. (8*a*)) from the same authors (SWG model).
2. same as the SWG model, but the effective pressure gradient parameter used in Eqs. (5), (6), and (8*a*) is limited as follows (SWGL model):

$$\lambda_{\theta,\mathrm{eff}}=\max(\lambda_\theta,-0.01)\qquad \frac{k}{\delta_1}<1.0$$

$$\lambda_{\theta,\mathrm{eff}}=\min[\max(\lambda_\theta,-0.01),0.06]\qquad \frac{k}{\delta_1}\geq 1.0$$

3. the Solomon, Walker, and Gostelow intermittency equation (Eq. (4*a*)) with the spot formation rate correlation (Eq. (8*b*)) from Roberts and Yaras (SWGRY model) [44].
4. the Byvaltsev and Kawaike intermittency equation (Eq. (4*b*)) (BK model) [40].

Before a new correlation for the transition onset can be developed, a suitable intermittency model will be selected by manually adjusting the transition onset location until a best fit to the experimental data is achieved. In anticipation of the model validation presented below, the rough high-pressure turbine-vane test cases of Stripf et al. [9] are used for this purpose.

Figure 1 shows the results of the post-diction of measured heat transfer distributions for a smooth and two rough surfaces. Also shown are the underlying intermittency distributions together with the acceleration parameter K. In the decelerated boundary layer regions, all of the models predict an increase in heat transfer that is too steep compared to the measured distributions. There are probably two reasons for this behavior. First, the transition length in decelerated boundary layers is longer for the thermal boundary layer than for the momentum boundary layer (see [32]). And second, the rapidly changing pressure gradient has a delayed effect on the transitional boundary layer. Both effects are not modeled in the current approach, and some differences from the experimental data should be expected. For increasing surface roughness and accelerated boundary layers, all of the models compare reasonably well to the experimental data. A best fit is achieved using the SWG and SWGL models, where the latter one achieves better predictions for the very rough surfaces and transition occurring in

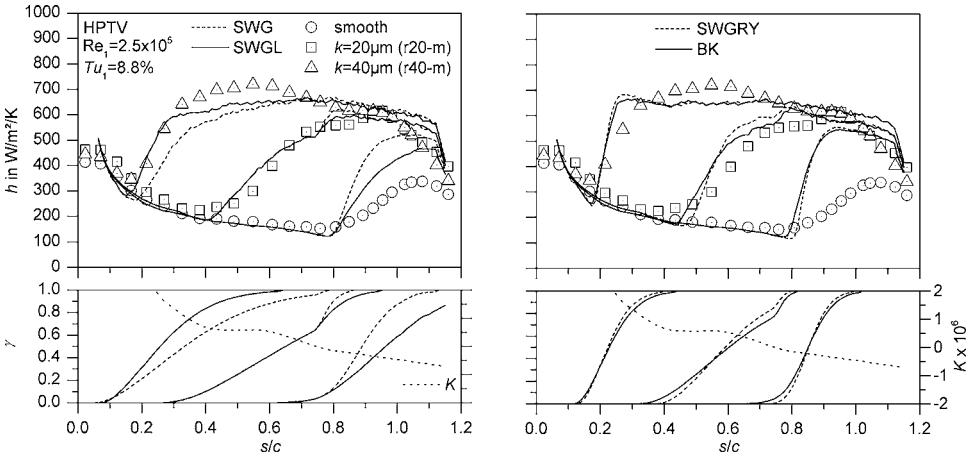

Fig. 1 Comparison of transition zone models—high-pressure turbine vane test cases, suction side [9]

highly accelerated regions. This finding is affirmed by the investigation of additional experimental data from a low-pressure turbine-vane, which was tested by the current authors in the same test rig as in Stripf et al. [9]. Figure 2 shows the results of the post-diction of low-pressure turbine-vane data, which further motivates the use of the SWGL model for the derivation of the rough-wall transition onset correlation.

It should be noted that the choice of the SWGL model implies that no effect of surface roughness on the rate of production of turbulent spots is modeled. At least for high turbulence levels and accelerated boundary layers, this seems to be a functional approach until we have more data available on the transitional rough surface momentum boundary layer.

Transition Onset Model. Developing the rough-wall transition onset correlation begins with selecting a suitable correlation for smooth surfaces. Many suggestions to correlate the momentum thickness Reynolds number at the onset of transition $\mathrm{Re}_{\theta,t}$, have been made by various researchers, considering the two important parameters: turbulence intensity and pressure gradient. Although the pressure gradient has been shown to influence the start of transition for low turbulence intensity ($\mathrm{Tu}_t < 3\%$), it is negligible for higher freestream turbulence levels [32]. Table 1 summarizes some characteristic transition correlations available in the open literature.

In the course of this work, a variety of smooth surface test cases [55–60], including flat plate and turbine airfoil data, are post-dicted using the SWGL model, and by manually varying the transition onset location until a best fit to the experimental data is achieved. Figure 3 shows the resulting momentum thickness Reynolds numbers at the onset of transition for all smooth surface test cases. Open symbols denote data from flat plate experiments and closed symbols mark turbine airfoil data. Furthermore, the different correlations are shown in their zero pressure gradient versions.

For $\mathrm{Tu}_t < 2.0\%$, the correlations from Schiele [47], Abu-Ghannam and Shaw [52], and Menter et al. [53] show little difference from each other and compare well to the experimental data, even though the latter two are shown in their zero pressure gradient version. The correlation presented by Mayle [32] gives an accurate prediction for $\mathrm{Tu}_t > 3.0\%$ but tends to predict an early transition for low turbulence intensities.

In the current work, the correlation developed by Schiele [47] will be used because it gives accurate predictions over the full range of turbulence intensities

$$\mathrm{Re}_{\theta,t,s} = 500(\mathrm{Tu}^*)^{-0.65} \tag{23}$$

with

$$\mathrm{Tu}^* = 0.5(\mathrm{Tu}_t + \mathrm{Tu}_1) \quad \text{for flat plates}$$
$$\mathrm{Tu}^* = \mathrm{Tu}_t \quad \text{for airfoils}$$

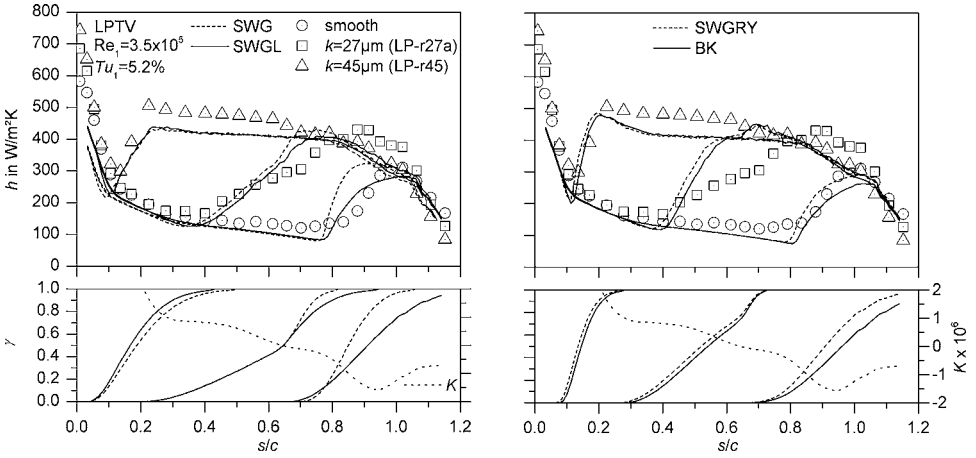

Fig. 2 Comparison of transition zone models—low-pressure turbine vane test cases, suction side

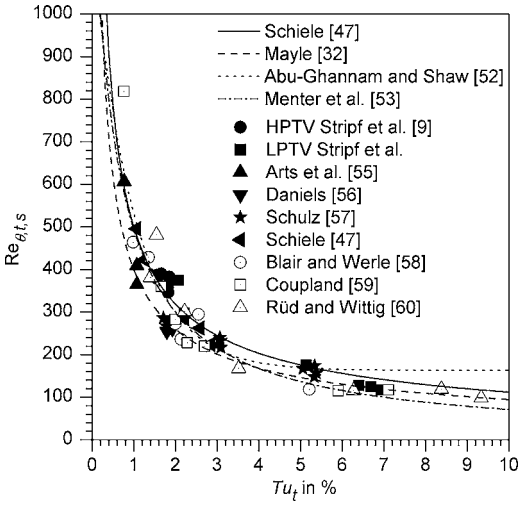

Fig. 3 Smooth surface transition onset correlations

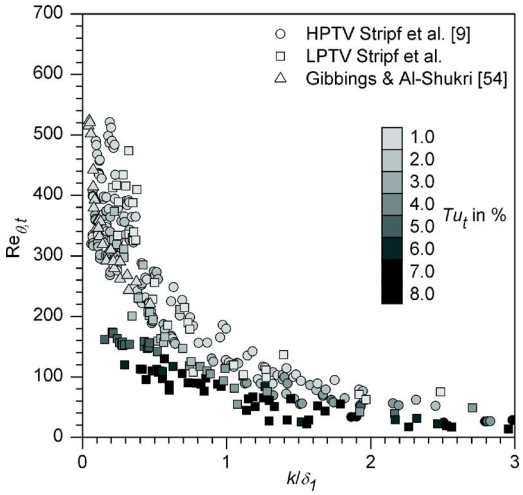

Fig. 4 Rough surface transition onset (all test cases)

The correlation is biased toward the test cases reflecting suction-side transition on modern aft-loaded airfoils and, thus, works well without considering the pressure gradient. In this way, development of the rough-wall correlation is simplified because the problem is reduced to two parameters: turbulence intensity and surface roughness.

The rough-wall transition correlation is developed on the basis of the high-pressure turbine vane test cases reported by the current authors [9] and unpublished data measured in the same test rig but on a low-pressure turbine vane. A large variety of different deterministic rough surfaces made of regularly arranged truncated cones are taken into account. The experimental data include the variation of roughness height, roughness density, Reynolds number, and freestream turbulence level (see Tables 3 and 4). Following the procedure used above for the smooth surfaces, the heat transfer distributions of all rough surface test cases were postdicted using the described model and by manually setting the transition onset location. As the roughness model is switched off in the laminar boundary layer, the values obtained at transition onset are those of a smooth surface. A thickening of the laminar boundary layer due to roughness is therefore not taken into account. The advantage of this approach is that the rough-wall transition onset correlation can be used in existing numerical codes without the need of a roughness model for laminar boundary layers. Figure 4 shows the post-dicted momentum thickness Reynolds numbers $Re_{\theta,t}$ versus the relative roughness height at transition onset for all rough-wall test cases with bypass transition. Circles denote data from the high-pressure turbine vane, and squares stand for data from the low-pressure turbine vane. The turbulence intensity at transition onset increases with darker symbols. In addition, data reported by Gibbings and Al-Shukri [54], is shown as triangles. In contrast to [54], the momentum thickness Reynolds numbers shown here are the ones calculated at the locations reported by Gibbings and Al-Shukri, without taking into account the effect of roughness on the laminar boundary layer. Gibbings and Al-Shukri use the actual measured momentum thickness and come to the surprising result that $Re_{\theta,t}$ increases with increasing surface roughness. In their paper, this is attributed to the thickening effect of the roughness on the laminar boundary layer. Although this result is very interesting, it cannot be used in the current method because the effect of roughness on the laminar boundary layer is not modeled.

Table 3 Surface roughness for the HPTV test cases

Roughness name	k (μm)	d (μm)	$t_1=2t_2$ (μm)	$k/c\times10^{-4}$ (-)
r10-m	10	25	55	1.06
r10-s	10	25	70	1.06
r10-ss	10	25	100	1.06
r20-m	20	50	110	2.13
r20-s	20	50	140	2.13
r20-ss	20	50	200	2.13
r40-m	40	100	220	4.26
r80-m	80	200	440	8.52

Table 4 Surface roughness for the LPTV test cases

Roughness name	k (μm)	d (μm)	t_1 (μm)	t_2 (μm)	$k/c\times10^{-4}$ (-)
LP-r17	17	60	110	55	1.50
LP-r27a	27	80	120	100	2.38
LP-r27b	27	80	180	150	2.38
LP-r27c	27	80	240	200	2.38
LP-r45	45	200	440	220	3.97
LP-r90	90	200	440	220	7.94

Several roughness parameters have been taken into account throughout this work, including the roughness Reynolds number k^+, but the relative roughness height k/δ_1 resulted in the least data scatter and was thus selected for forming the new correlation.

Although the combined effect of roughness and turbulence intensity can be clearly seen in Fig. 4, data scatter is still high. As the roughness parameter k/δ_1 only considers the roughness height but not the roughness density, this is not surprising. The approach followed in this work is to use only those test cases for the correlation which feature roughness densities which result in a maximum roughness effect at a given roughness height. The new correlation can then be used to give a conservative appraisal of the momentum thickness Reynolds number at transition onset. As the type of surface roughness encountered on real turbine airfoils is expected to vary significantly, depending on the operational area and type of operation, the maximum roughness height might be the only parameter known a priori to the turbine designer.

Figure 5 shows the test cases with roughness densities producing maximum roughness effects for a given roughness height. In order to construct the new correlation, the test cases are classified with respect to the turbulence intensity at transition onset. Considering Eq. (23) as boundary condition for $k=0$ and making sure that data from test cases not resulting in a maximum effect on transition lie on the upper right of the corresponding correlation curve, the following equations for the momentum thickness Reynolds number can be deduced:

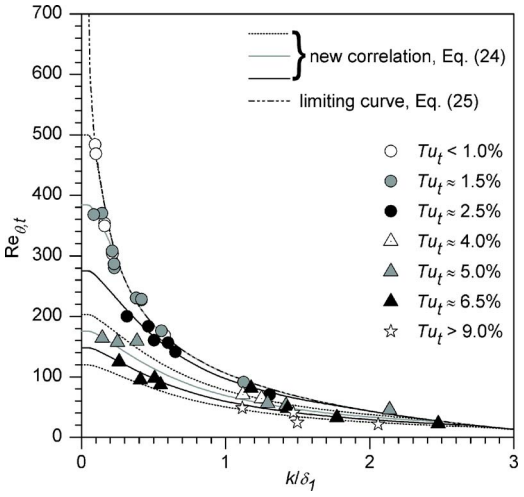

Fig. 5 Rough surface transition onset correlation

$\frac{k}{\delta_1} \leq 0.05$:

$$\mathrm{Re}_{\theta,t} = \mathrm{Re}_{\theta,t,s} = 500(\mathrm{Tu}^*)^{-0.65} \tag{24a}$$

$\frac{k}{\delta_1} > 0.05$:

$$\mathrm{Re}_{\theta,t} = \min\left\{\left[\frac{1}{\mathrm{Re}_{\theta,t,s}} + f_1\left(\frac{k}{\delta_1} - 0.05\right)^{1.4}\right]^{-1}, \quad \mathrm{Re}_{\theta,t,l}\right\} \tag{24b}$$

$$\mathrm{Re}_{\theta,t,l} = -181 + 286.3\left(\frac{k}{\delta_1}\right)^{-0.354} \tag{25}$$

$$f_1 = \min[\max(0.007, 0.005 + 9 \times 10^{-4}\mathrm{Tu}^*), 0.0125] \tag{26}$$

Figure 5 shows the resulting correlation curves for the seven distinct turbulence levels with experimental data. For low turbulence intensity, the data points lie on the limiting curve given by Eq. (25). All the high turbulence intensity curves end on the limiting curve as they reach high roughness values. This is reasonable because the effect of turbulence intensity should vanish for very rough surfaces. Equations (24)–(26) are valid for three-dimensional distributed roughness with relative roughness heights $k/\delta_1 \leq 3$.

Model Validation

The overall model will be validated using the high pressure turbine vane test cases reported by Stripf et al. [9] and additional unpublished data which was measured in the same test section as in [9] but on a low pressure turbine cascade.

High-Pressure Turbine Vane. The experimental setup, measuring technique, and airfoil characteristic used in the following test cases are presented in detail in [9]. An overview of the rough surfaces is presented in Table 3 and together with Fig. 6 gives a clear definition of the surface geometries. Note that the extension –m stands for a roughness density that has a maximum effect on transition.

Figure 7 shows the comparison between measured and calculated suction side heat transfer distributions for two different inlet Reynolds numbers Re_1 and three different inlet turbulence intensities Tu_1. Only the suction side, heat transfer is considered here, because the pressure-side boundary layer stays laminar under most test conditions due to the high acceleration and is therefore less interesting for the validation (see [9]). For the suction side, the onset of transition is correctly predicted by the proposed model (Eqs. (23)–(26)) and the transition zone is well described by the SWGL intermittency model. In the turbulent boundary layer, the discrete element roughness model shows the right level of heat transfer for most of the rough surfaces. However, some deviation is seen in the highly accelerated or decelerated turbulent boundary layer at the high Re_1 cases. Here, heat transfer is underestimated by ~12% in the accelerated boundary layer for the r40-m surface, whereas it is overestimated by the same amount in the decelerated region for r40-m and r80-m.

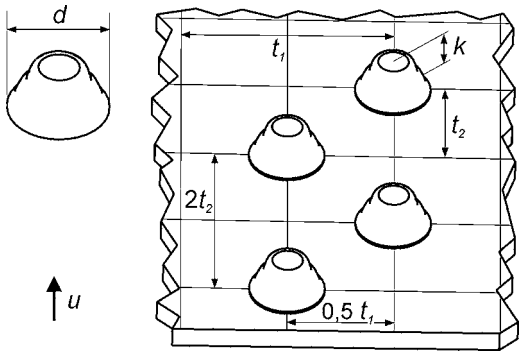

Fig. 6 HPTV test cases, influence of roughness density

In Fig. 8, measurements for different roughness densities at constant roughness height are shown. Because the roughness density is not accounted for in the transition onset correlation, the only difference in the heat transfer calculations occurs in the turbulent boundary layer, where the discrete element model predicts different levels of heat transfer due to the different roughness densities. The largest deviation in transition onset is seen for the r20-ss surface with the lowest roughness density. However, this is acceptable as the model is designed to rather predict an early than a late onset of transition.

Low-Pressure Turbine Vane. Additional test cases with similar surface roughness variations (see Table 4) will be used to further validate the model. The test section and measuring technique are the same as described by Stripf et al. [9] and the airfoil characteristic can be seen in Fig. 9, where the suction side distribution of the acceleration parameter is shown.

Figure 10 gives an overview of measured and calculated heat transfer distributions. A good overall agreement can be observed with the tendency of an early transition prediction. For high turbulence intensity ($\mathrm{Tu}_1 = 11.2\%$) and high Reynolds numbers, the predicted heat transfer in the accelerated laminar boundary layer is too low, which is mainly visible for the smooth or low surface roughness cases. The effect is well known to the research community and several suggestions exist to account for it [61,62]. However, they all change the momentum thickness at the start of transition so that the transition onset correlation has to be adjusted to the individual "laminar model" used. Hence, in favor of a more general correlation, the effect of turbulence on the accelerated laminar boundary layer is not considered here.

For $\mathrm{Tu}_1 = 11.2\%$ and $\mathrm{Re}_1 = 4.5 \times 10^5$, transition seems to occur slightly too far downstream for the three highest surface roughnesses. However, taking into account that heat transfer in the laminar boundary layer is 25% underpredicted, the transition onset location is well described.

Heat transfer augmentation in the turbulent boundary layer due to surface roughness is well predicted, except for the LP-r45 rough surface at high Re_1, where heat transfer is underestimated. For this surface, the roughness elements have a large base diameter compared to the roughness height and the diameter at the crest of the truncated cone is still large. Therefore, the heat transfer at the top area of the truncated cone cannot be neglected in contrast to all other surfaces, where the top area is sufficiently small and the roughness elements more closely resemble full cones. The discrete element method does not account for this heat flux to the top area of the roughness element and underestimates

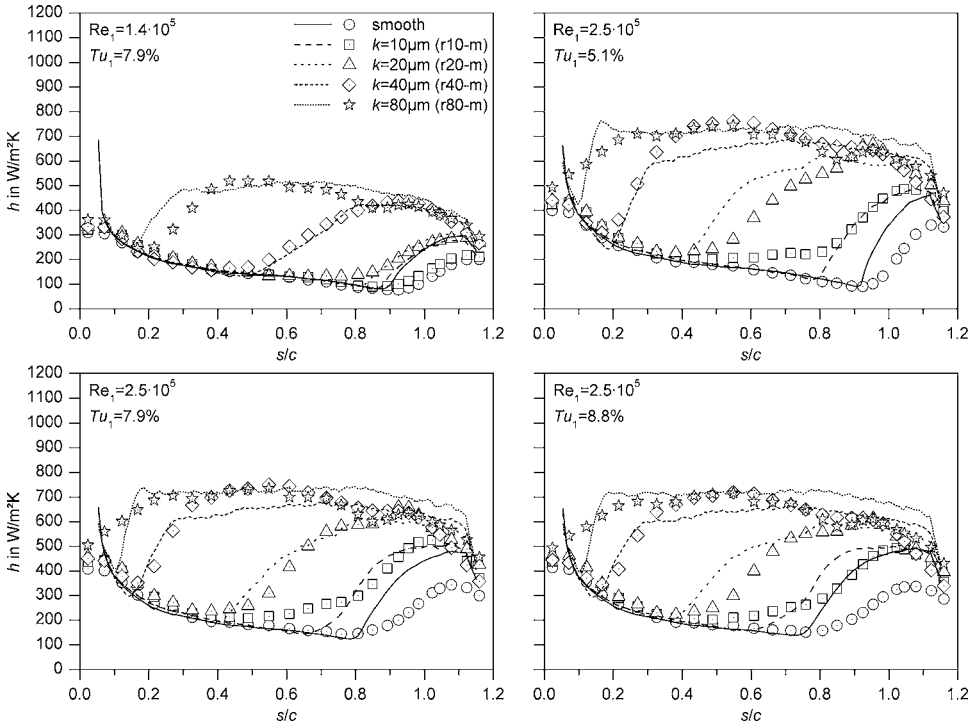

Fig. 7 Roughness geometry

the heat transfer in those cases.

Additional test cases with varying roughness density at constant roughness height are shown in Fig. 11. Again, it can be seen that the proposed transition onset correlation predicts an early transition in cases where the roughness density does not lead to a maximum effect on transition. In the turbulent boundary layer, the effect of roughness density on heat transfer is correctly reflected in the calculation. However, in the accelerated part of the boundary layer, calculated heat transfer coefficients are 15–20 % too low, which is the same behavior as described above, for the high-pressure turbine vane test cases.

Summary and Conclusion

A method to calculate the heat transfer distribution in the transitional boundary layer on rough surfaces has been presented. The method includes a newly developed correlation for the onset of laminar-turbulent transition and an existing intermittency model from Solomon et al. [39], which was slightly modified to give better results on rough turbine airfoils. The new transition onset correlation is constructed to give exact predictions for rough surfaces that, for a given roughness height, feature a roughness density that leads to a maximum effect on transition. For other roughness densities, the correlation predicts an early transition if the maximum roughness height is used as input. The same should be true if the maximum roughness height of real stochastic surfaces is used, although more experimental data are desirable to validate and finely adjust the correlation for this kind of surfaces. Since the method presented is based entirely on heat transfer data, further validation against rough surface momentum boundary layer data from turbine airfoils is desirable as soon as they become available.

In addition, the discrete element model (DEM) is used to account for the effects of roughness in the turbulent boundary layer. The DEM is switched off in the laminar boundary layer, in order not to influence the calculated conditions at the onset of transition. This way, the discrete element roughness model can easily be substituted for a different roughness model without invalidating the new transition onset correlation. However, the authors believe that the discrete element model is the most promising one to account for the effects of real turbine roughness on heat transfer.

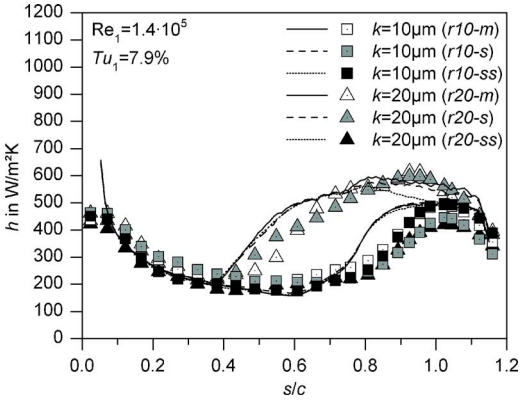

Fig. 8 HPTV test cases—suction side, influence of roughness height

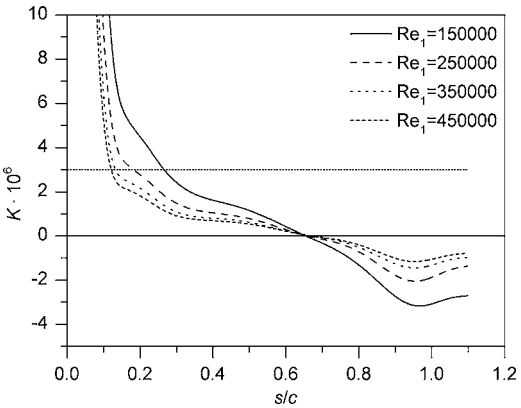

Fig. 9 Acceleration parameter *K* on the LPTV suction side

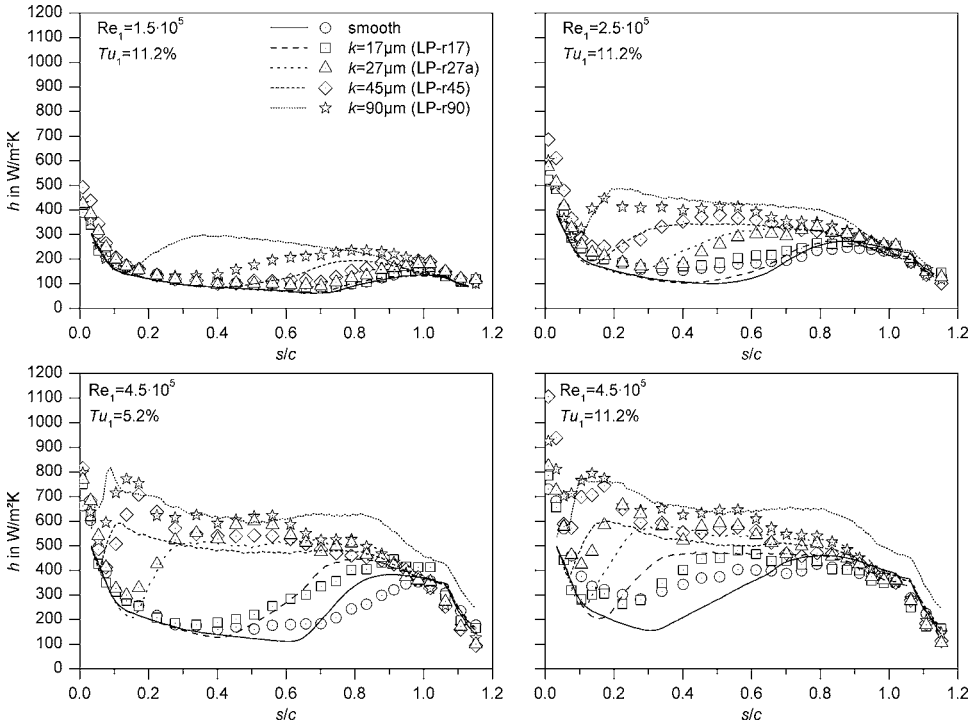

Fig. 10 LPTV test cases—suction side, influence of roughness height

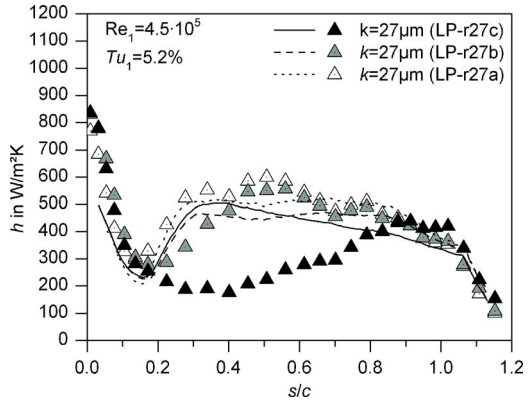

Fig. 11 LPTV test cases, influence of roughness density

Recent model extensions from McClain [31] and McClain et al. [49] show promising results for randomly rough surfaces. The overall model has been successfully validated, using test cases from high- and low-pressure turbine vane suction sides with deterministic rough surfaces of varying roughness density.

Acknowledgment

Financial support from the State of Baden-Württemberg in the frame of the research cooperative "Power Plant Technology of the 21st Century" is gratefully acknowledged.

Nomenclature

a, b = widths of elliptical element (here $a=b$) (m)
A = van Driest damping length (m)
C_d = local element drag coefficient
c = chord length (m)
C_f = skin friction coefficient
c_p = specific heat at constant pressure (J/kg/K)
d = local element diameter (m)
h = heat transfer coefficient (W/m^2/K)
H = boundary layer shape factor $H=\delta_1/\theta$
H = stagnation enthalpy (J/kg)
k = turbulent kinetic energy (m^2/s^2)
k, k_s = roughness height, sand roughness height (m)
k^+ = roughness Reynolds number $k^+=k\cdot u_\tau/\nu$
k_f = thermal conductivity of fluid (W/m/K)
K = acceleration parameter $K=\nu/U_e^2\cdot dU_e/dx$
l = mixing length (m)
$l_{\varepsilon,v}, l_{\mu,v}$ = length scales in the turbulence model (m)
L_x, L_z = element spacings (m)
n = spot formation rate (m^{-1} s^{-1})
N = nondimensional breakdown parameter
Nu_d = local element Nusselt number
P = static pressure (Pa)
Pr, Pr_t = Prandtl number, turb. Prandtl number
Re = Reynolds number
Re_d = local element Reynolds number
Re_θ = momentum thickness Reynolds number
s = surface length (m)
St = Stanton number
T = fluid temperature (K)
T_r = local roughness element temperature (K)
t_1, t_2 = roughness element spacings (Fig. 8) (m)
Tu = turbulence intensity (%)
u_τ = shear stress velocity (m/s)
U, V = streamwise and wall normal velocity (m/s)
v' = wall normal fluctuations (m/s)
x, y, z = coordinates (m)

Greek

α_x, α_y = blockage factors $[\alpha_x=\alpha_y=\pi d^2/(4L_xL_z)]$
α = spot spreading half angle (deg)
β_x, β_y = openage factors $(\beta_x=\beta_y=1-\alpha_x=1-\alpha_y)$
δ_1 = displacement thickness (m)
ε = dissipation rate (m^2/s^3)
γ = intermittency factor

κ = von Karman constant, $\kappa=0.4$
λ_θ = pressure gradient parameter $\lambda_\theta=(\theta^2/\nu)(dU_e/dx)$
μ = dynamic viscosity (Ns/m^2)
μ_t = eddy viscosity (Ns/m^2)
ν = kinematic viscosity (m^2/s)
θ = momentum thickness (m)
ρ = density (kg/m^3)
σ = spot propagation parameter

Subscripts

1 = at cascade inlet
e = at boundary layer edge
s = smooth
t = at transition onset

References

[1] Bogard, D. G., Schmidt, D. L., and Tabbita, M., 1998, "Characterization and Laboratory Simulation of Turbine Airfoil Surface Roughness and Associated Heat Transfer," ASME J. Turbomach., **120**, pp. 337–342.

[2] Bons, J. P., Taylor, R. P., McClain, S. T., and Rivir, R. B., 2001, "The Many Faces of Turbine Surface Roughness," ASME J. Turbomach., **123**, pp. 739–748.

[3] Turner, A. B., Tarada, F. H. A., and Bayley, F. J., 1985, "Effects of Surface Roughness on Heat Transfer to Gas Turbine Blades," AGARD-CP-390, Paper No. 9.

[4] Hoffs, A., Drost, U., and Bölcs, A., 1996, "Heat Transfer Measurements on a Turbine Airfoil at Various Reynolds Numbers and Turbulence Intensities Including Effects of Surface Roughness," ASME Paper No. 96-GT-169.

[5] Abuaf, N., Bunker, R. S., and Lee, C. P., 1997, "Effects of Surface Roughness on Heat Transfer and Aerodynamic Performance of Turbine Airfoils," ASME Paper No. 97-GT-10.

[6] Bunker, R. S., 1997, "Separate and Combined Effects of Surface Roughness and Turbulence Intensity on Vane Heat Transfer," ASME Paper No. 97-GT-135.

[7] Boyle, R. J., Spuckler, C. M., Lucci, B. L., and Camperchioli, W. P., 2000, "Infrared Low Temperature Turbine Vane Rough Surface Heat Transfer Measurements," ASME Paper No. 2000-GT-0216.

[8] Blair, M. F., 1994, "An Experimental Study of Heat Transfer in a Large-Scale Turbine Rotor Passage," ASME J. Turbomach., **116**, pp. 1–13.

[9] Stripf, M., Schulz, A., and Wittig, S., 2005, "Surface Roughness Effects on External Heat Transfer of a HP Turbine Vane," ASME J. Turbomach., **127**, pp. 200–208.

[10] Stripf, M., Schulz, A., and Bauer, H.-J., 2005, "Surface Roughness and Secondary Flow Effects on External Heat Transfer of a HP Turbine Vane," ISABE Paper No. 2005-1116.

[11] Dvorak, F. A., 1972, "Calculation of Compressible Turbulent Boundary Layers With Roughness and Heat Transfer," AIAA J., **10**, pp. 1447–1451.

[12] Dirling, R. B., 1973, "A Method for Computing Rough Wall Heat Transfer Rates on Reentry Nosetips," AIAA Paper No. 73-763.

[13] Rotta, J. C., 1962, "Turbulent Boundary Layers in Incompressible Flow," *Progress in Aeronautical Sciences*, Pergamon, London, Vol. 2, pp. 1–120.

[14] Cebeci, T., and Chang, K. C., 1978, "Calculation of Incompressible Rough-Wall Boundary-Layer Flows," AIAA J., **16**, pp. 730–735.

[15] Feiereisen, W. J., and Acharya, M., 1986, "Modeling of Transition and Surface Roughness Effects in Boundary-Layer Flows," AIAA J., **24**, pp. 1642–1649.

[16] Granville, P. S., 1985, "Mixing-Length Formulations for Turbulent Boundary Layers Over Arbitrarily Rough Surfaces," J. Ship Res., **29**, pp. 223–233.

[17] Krogstad, P., 1990, "Modification of the van Driest Damping Function to Include the Effects of Surface Roughness," AIAA J., **29**, pp. 888–894.

[18] Guo, S. M., Jones, T. V., Lock, G. D., and Dancer, S. N., 1998, "Computational Prediction of Heat Transfer to Gas Turbine Nozzle Guide Vanes With Roughened Surfaces," ASME J. Turbomach., **120**, pp. 343–350.

[19] Jouini, D. B., Bergenblock, T. C., and Sjolander, S. A., 1997, "Computation of the Aerodynamic Performance of Axial-Turbine Blades With Surface Roughness," ISABE Paper No. 97-7041.

[20] Lee, J., and Paynter, G. C., 1996, "Modified Spalart-Allmaras One-Equation Turbulence Model for Rough Wall Boundary Layers," J. Propul. Power, **12**(4), pp. 809–812.

[21] Wilcox, D. C., 1993, *Turbulence Modeling for CFD*, DCW Industries Inc., La Cañada, CA.

[22] Hellsten, A., and Laine, S., 1998, "Extension of k-ω Shear-Stress Transport Model for Rough-Wall Flows," AIAA J., **36**(9), pp. 1728–1729.

[23] Durbin, P. A., Medic, G., Seo, J., Eaton, J. K., and Song, J., 2001, "Rough Wall Modification of Two-Layer k-ε," ASME J. Fluids Eng., **123**, pp. 16–21.

[24] Schlichting, H., 1936, "Experimentelle Untersuchungen zum Rauhigkeitsproblem," Ing.-Arch., **7**, pp. 1–34.

[25] Finson, M. L., and Wu, P. K. S., 1979, "Analysis of Rough Wall Turbulent Heating With Application to Blunted Flight Vehicles," AIAA Paper No. 79-0008.

[26] Christoph, G. H., and Pletcher, R. H., 1983, "Prediction of Rough-Wall Skin Friction and Heat Transfer," AIAA J., **21**(4), pp. 509–515.

[27] Taylor, R. P., Coleman, H. W., and Hodge, B. K., 1984, "A Discrete Element Prediction Approach for Turbulent Flow Over Rough Surfaces," Mississippi State University, Report No. TFD-84-1.

[28] Lin, T. C., and Bywater, R. J., 1982, "Turbulence Models for High-Speed, Rough-Wall Boundary Layers," AIAA J., **20**(3), pp. 325–333.

[29] Tarada, F. H. A., 1987, "Heat Transfer to Rough Turbine Blading," Ph.D. thesis, University of Sussex, England.

[30] Hosni, M. H., Coleman, H. W., and Taylor, R. P., 1991, "Measurements and Calculations of Rough-Wall Heat Transfer in the Turbulent Boundary Layer," Int. J. Heat Mass Transfer, **34**, pp. 1067–1082.

[31] McClain, S. T., 2002, "A Discrete-Element Model for Turbulent Flow Over Randomly-Rough Surfaces," Ph.D. thesis, Mississippi State University.

[32] Mayle, R. E., 1991, "The Role of Laminar-Turbulent Transition in Gas Turbine Engines," ASME J. Turbomach., **113**, pp. 509–537.

[33] Sieger, K., Schulz, A., Crawford, M. E., and Wittig, S., 1993, "An Evaluation of Low-Reynolds Number k-e Turbulence Models for Predicting Transition Under the Influence of Free-Stream Turbulence and Pressure Gradient," *Engineering Turbulence Modelling and Measurements*, Vol. 2, Elsevier, New York, pp. 593–602.

[34] Schmidt, R. C., and Patankar, S. V., 1991, "Simulating Boundary Layer Transition With Low-Reynolds-Number k-ε Turbulence Models—Part 2: An Approach to Improving the Predictions," ASME J. Turbomach., **113**, pp. 18–26.

[35] Lam, C. K. G., and Bremhorst, K., 1981, "A Modified Form of the k-ε Model for Predicting Wall Turbulence," ASME J. Fluids Eng., **103**, pp. 456–460.

[36] Launder, B. E., and Sharma, B. I., 1974, "Application of the Energy-Dissipation Model of Turbulence to the Calculation of Flow Near a Spinning Disc," Lett. Heat Mass Transfer, **1**, pp. 131–138.

[37] Emmons, H., 1951, "The Laminar-Turbulent Transition in a Boundary Layer—Part I," J. Aeronaut. Sci., **18**, pp. 490–498.

[38] Narasimha, R., 1957, "On the Distribution of Intermittency in the Transition Region of a Boundary Layer," J. Aeronaut. Sci., **24**(9), pp. 711–712.

[39] Solomon, W. J., Walker, G. J., and Gostelow, J. P., 1996, "Transition Length Prediction for Flows With Rapidly Changing Pressure Gradients," ASME J. Turbomach., **118**, pp. 744–751.

[40] Byvaltsev, P. M., and Kawaike, K., 2005, "A Comparative Study of Two Transition Zone Models in Heat Transfer Predictions," ASME J. Turbomach., **127**, pp. 230–239.

[41] Gostelow, J. P., Melwani, N., and Walker, G. J., 1996, "Effects of Streamwise Pressure Gradient on Turbulent Spot Development," ASME J. Turbomach., **118**, pp. 737–743.

[42] D'Ovidio, A., Harkins, J. A., and Gostelow, J. P., 2001, "Turbulent Spots in Strong Adverse Pressure Gradients: Part 2 – Spot Propagation and Spreading Rates," ASME Paper No. 2001-GT-0406.

[43] Fraser, C. J., Higazy, M. G., and Milne, J. S., 1994, "End-Stage Boundary Layer Transition Models for Engineering Calculations," Proc. Inst. Mech. Eng., Part C: J. Mech. Eng. Sci., **208**, pp. 47–58.

[44] Roberts, S. K., and Yaras, M. I., 2004, "Modeling of Boundary-Layer Transition," ASME Paper No. GT2004-53664.

[45] Sieger, K., Schiele, R., Kaufmann, F., Wittig, S., and Rodi, W., 1995, "A Two-Layer Turbulence Model for the Calculation of Transitional Boundary-Layers," ERCOFTAC Bull., pp. 21–25.

[46] Rodi, W., Mansour, N. N., and Michelassi, V., 1993, "One-Equation Near-Wall Turbulence Modeling With the Aid of Direct Simulation Data," ASME J. Fluids Eng., **115**, pp. 196–205.

[47] Schiele, R., 1999, "Die transitionale Grenzschicht an Gasturbinenschaufeln: Experimentelle Untersuchungen und Entwicklung eine neuen Verfahrens zur numerischen Beschreibung des laminar-turbulenten Umschlags," dissertation, Universität Karlsruhe, Germany.

[48] Tarada, F. H. A., 1990, "Prediction of Rough-Wall Boundary Layers Using a Low Reynolds Number k-ε Model," Int. J. Heat Fluid Flow, **11**(4), pp. 331–345.

[49] McClain, S. T., Hodge, B. K., and Bons, J. P., 2003, "Predicting Skin Friction for Turbulent Flow Over Randomly-Rough Surfaces Using the Discrete-Element Method: Part I—Surface Characterization," ASME Paper No. FEDSM2003-45411.

[50] Finson, M. L., and Clarke, A. S., 1980, "The Effect of Surface Roughness Character on Turbulent Reentry Heating," AIAA Paper No. 80-1459.

[51] Patankar, S. V., and Spalding, D. B., 1970, *Heat and Mass Transfer in Boundary-Layers*, 2nd ed., Intertext, London.

[52] Abu-Ghannam, B. J., and Shaw, R., 1980, "Natural Transition of Boundary-Layers—The Effects of Turbulence, Pressure Gradient and Flow History," J. Mech. Eng. Sci., **22**, pp. 213–228.

[53] Menter, F. R., Langtry, R. B., Likki, S. R., Suzen, Y. B., Huang, P. G., and Völker, S., 2004, "A Correlation-Based Transition Model Using Local Variables: Part I—Model Formulation," ASME Paper No. GT2004-53452.

[54] Gibbings, J. C., and Al-Shukri, S. M., 1997, "Effect of Sandpaper Roughness and Stream Turbulence on the Laminar Layer and its Transition," Aeronaut. J., **101**, pp. 17–24.

[55] Arts, T., and De Rouvroit, M. L., 1992, "Aero-Thermal Performance of a Two Dimensional Highly Loaded Transonic Turbine Nozzle Guide Vane," ASME J. Turbomach., **114**, pp. 147–154.

[56] Daniels, L., 1978, "Film-Cooling of Gas Turbine Blades," Ph.D. thesis, University of Oxford, England.

[57] Schulz, A., 1986, "Zum Einfluß hoher Freistromturbulenz, intensiver Kühlung und einer Nachlaufströmung auf den Wärmeübergang einer konvektiv gekühlten Gasturbinenschaufel," dissertation, Universität Karlsruhe, Germany.

[58] Blair, M. F., and Werle, M. J., 1981, "Combined Influence of Freestream Turbulence and Favorable Pressure Gradients on Boundary Layer Transition and Heat Transfer," United Technologies Research Center, East Hartford, CT, Report-No. R81-914388-17.
[59] Coupland, J., 1993, personal communication, ERCOFTAC Special Interest Group on Transition Test Cases.
[60] Rüd, K., and Wittig, S., 1986, "Laminar and Transitional Boundary Layer Structures in Accelerating Flow With Heat Transfer," ASME J. Turbomach., **108**, pp. 116–123.
[61] Smith, M. C., and Kuethe, A. M., 1966, "Effects of Turbulence on Laminar Skin Friction and Heat Transfer," Phys. Fluids, **9**(12), pp. 2337–2344.
[62] Byvaltsev, P. M., and Nagashima, T., 1998, "Correlation of Numerical and Experimental Heat Transfer Data at the Turbine Blade Surface," JSME Int. J., Ser. B, **41**, pp. 191–199.

Jack L. Kerrebrock
Alan H. Epstein
Ali A. Merchant
Gerald R. Guenette
David Parker
Jean-Francois Onnee
Fritz Neumayer

Gas Turbine Laboratory,
Massachusetts Institute of Technology,
Cambridge, MA 02139

John J. Adamczyk
NASA-Glenn Research Center,
Cleveland, OH 44135

Aamir Shabbir
University of Toledo,
Toledo, OH 43606

Design and Test of an Aspirated Counter-Rotating Fan

The design and test of a two-stage, vaneless, aspirated counter-rotating fan is presented in this paper. The fan nominal design objectives were a pressure ratio of 3:1 and adiabatic efficiency of 87%. A pressure ratio of 2.9 at 89% efficiency was measured at the design speed. The configuration consists of a counter-swirl-producing inlet guide vane, followed by a high tip speed (1450 ft/s) *nonaspirated rotor and a counter-rotating low speed* (1150 ft/s) *aspirated rotor. The lower tip speed and lower solidity of the second rotor result in a blade loading above conventional limits, but enable a balance between the shock loss and viscous boundary layer loss; the latter of which can be controlled by aspiration. The aspiration slot on the second rotor suction surface extends from the hub up to 80% span. The bleed flow is discharged inward through the blade hub. This fan was tested in a short duration blowdown facility. Particular attention was given to the design of the instrumentation to measure efficiency to 0.5% accuracy. High response static pressure measurements were taken between the rotors and downstream of the fan to determine the stall behavior. Pressure ratio, mass flow, and efficiency on speed lines from 90% to 102% of the design speed are presented and discussed along with comparison to computational fluid dynamics predictions and design intent. The results presented here complement those presented earlier for two aspirated fan stages with tip shrouds, extending the validated design space for aspirated compressors to include designs with conventional unshrouded rotors and with inward removal of the aspirated flow.*
[DOI: 10.1115/1.2776951]

1 Introduction

The work reported here is the latest element of a program being conducted by the MIT Gas Turbine Laboratory and its collaborators to develop and validate the technology for the design of axial compressors that incorporates control of flow separation by aspiration (or suction) of the viscous flows at diffusion-limited locations. Prior to the work reported here, two aspirated single-stage fans were designed and tested. The first was a transport engine aspirated transonic fan stage, with a pressure ratio of 1.6 at a tip speed of only 750 ft/s. It was designed and tested in the Blowdown Compressor at MIT as a first step in assessing the utility of aspiration for increasing stage loading [1]. A second, high tip speed stage was designed and tested at NASA Glenn Research Center to assess the feasibility of similarly high loading at a tip speed of 1500 ft/s [2]. Rotor-tip shrouds were used in these designs for two reasons: first, to enable an assessment of the benefits of aspiration without the complications of tip clearance flows; and second, to provide a practical means in a first-stage configuration for transporting the aspirated flow outwards from the suction slots on the rotor blades to the rotor housing. Both fan stages validated the concept of aspiration by approximately doubling the stage work over that achievable in a similar stage without aspiration. They also validated the design system as a means for designing aspirated compressors with unconventional design parameters, without prior empirical knowledge [3].

The new proposition addressed here is that aspiration offers additional benefits in application to compressors, either fans or cores, with counter-rotating blade rows, because of the high levels of work enabled by the swirl that enters the second rotor. This high work results in high aerodynamic loading and high Mach number in the second blade row of such counter-rotating pairs, both of which lead to diffusion problems that can be addressed with aspiration. The result is a potential for higher pressure ratios with fewer blade rows, hence either shorter and lighter compressors or compressors that meet unusual needs.

A configuration of particular interest in this context is the counter-rotating fan studied here. It consists of a counter-swirl-producing inlet guide vane, followed by a high tip speed (1450 ft/s) nonaspirated rotor and a counter-rotating low speed (1150 ft/s) aspirated rotor. There are no stators. The lower tip speed of the second rotor results in a blade loading above conventional limits, but delivers a good balance between the shock loss and viscous boundary layer loss, both of which can be controlled by aspiration. In the context of such counter-rotating fans, viscous flow control via aspiration enables the design of high work, compact and efficient compression systems that are not possible without such viscous flow control. Applications for such fans may be found in variable-cycle engines for multimission aircraft and in high-supersonic cruise aircraft [4,5].

Such counter-rotating configurations are not readily configured with tip shrouds, in part because of high temperatures in some potential applications, so the rotors were designed with conventional tip clearances and with provision for discharging the aspirated flow from the second rotor inward rather than outward as in the previous aspirated stages. In addition to meeting the needs of potential applications, this choice enables a generic assessment of the feasibility of such inward discharge, which, in general, is desirable for energy recovery from the aspirated flow.

To minimize the time and cost of testing this counter-rotating fan, the evaluation has been carried out in a short test duration blowdown facility at MIT. As discussed in more detail below, the several hundred millisecond test duration of this facility enables evaluation of the performance of the compressor in terms of its pressure ratio, mass flow, and efficiency by means of conventional instrumentation such as is used in continuously operating test facilities. The key requirement is for thermocouple response fast enough to achieve essentially steady measurements during the

Contributed by the Turbomachinery Division of ASME for publication in the JOURNAL OF TURBOMACHINERY. Manuscript received September 5, 2006; final manuscript received September 6, 2006; published online February 12, 2008. Review conducted by David Wisler.

Table 1 Nominal fan design objectives

Pressure ratio	3:1
Adiabatic efficiency	87%
Rotor 1 speed range	1400–1500 ft/s
Rotor 2 speed range	1100–1250 ft/s
Specific flow	41.5 lbm/s ft^2
Exit Mach No.	0.5
Exit swirl angle	<15 deg

blowdown time. All temperature measurements reported here meet this requirement. Therefore, the measurements of pressure ratio, mass flow, and efficiency are directly comparable to those that would be obtained for the same configuration in a steady test facility.

Efficiency being an important component of such a comparison, it is important to note that in this paper, to isolate the effect of aspiration on efficiency, we quote the through-flow adiabatic efficiency. Specifically, this is the adiabatic efficiency of the compressor based on the second rotor outflow. This through-flow efficiency includes the effects of shock losses in the core flow and viscous losses that influence the entropy of the outflow of the compressor. It does not embrace the effects of losses that raise the entropy of the aspirated flow or the work associated with it. The overall impact of these (secondary) effects of aspiration can be properly quantified only in the context of a complete engine design, in which the handling of the aspirated flows is explicated. Merchant et al. [6] qualitatively explored the key issues of aspiration on the engine efficiency, and Kirtley et al. [7] have also examined the impact of flow control in the context of efficiency of multistage compressors. This said, we do comment on the impact of bleed on efficiency later in the paper.

The structure of the remainder of this paper is as follows. The aerodynamic design is summarized first, followed by a brief description of the mechanical design of the stage and facility. The overall compressor performance is discussed and compared with the predictions of multistage computational fluid dynamics (CFD) analyses. The operability and off-design behavior are discussed briefly. Lastly, the important conclusions and implications of the results of the test program are enumerated.

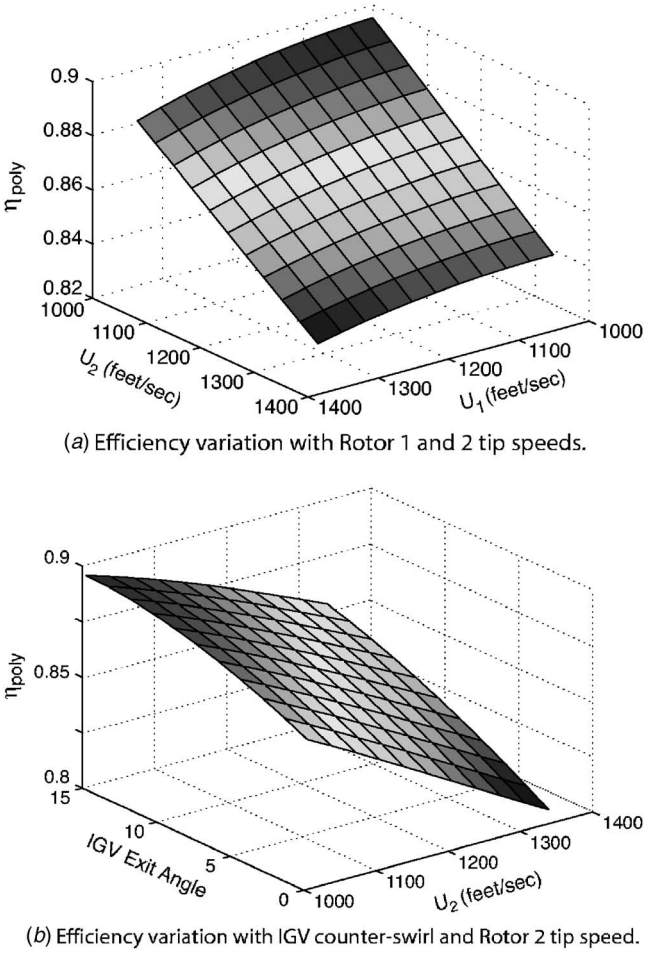

Fig. 1 Design calculations of the effect of rotor speeds and IGV counterswirl on fan efficiency: (*a*) efficiency variation with Rotor 1 and 2 tip speeds; (*b*) efficiency variation with IGV counterswirl and Rotor 2 tip speed

2 Aerodynamic Design

The nominal design objectives for the counter-rotating fan based on engine concept studies are presented in Table 1. The desired pressure ratio was 3:1 with an adiabatic efficiency goal of 87%. The rpm ratio for the rotors was approximately 0.8, and the corresponding tip speed ranges are given in the table. The design point stall margin was 20%. An inlet guide vane was included in the engine concept for off-design operation, and this was exploited in optimizing the performance at the design point. The exit swirl from the second rotor was constrained to less than 15 deg, consistent with either a mechanical strut that could remove the residual swirl or entry into a core.

In contrast to the design of a conventional fan, this design was complicated by the introduction of the second independent rotor with its tip speed and work coefficient as additional design variables. The absence of a vane between the rotors added further complexity to the design effort due to the very high relative supersonic Mach numbers into the second rotor.

In order to clarify the roles of design variables such as rotor speed ratio, a preliminary design study and optimization of design parameters was performed using a one-dimensional model of the fan. Compressibility, area change, shock loss, and airfoil and endwall viscous loss were considered. The design space was explored by parametrically varying rotor speeds, rotor work coefficients, and inlet guide vane swirl. Finally, a constrained optimization yielded the preliminary design.

The parametric study showed that the speed of the second rotor has a strong impact on the efficiency, mainly due to the shock loss at high relative Mach numbers at the rotor face (Fig. 1). The speed of the first rotor has a relatively small impact on the overall efficiency, since the average Mach number varies only from 0.95 to 1.15 over the speed range. In contrast, the average Mach number in the second rotor varies from 1.4 to 1.6. Note that this variation was calculated without any counterswirl in the first rotor. Lowering the blade speed of the second rotor to manage the Mach number, while maintaining the design pressure ratio, results in a higher work coefficient and blade loading than is found in conventional supersonic rotors.

Adding counterswirl via the inlet guide vane increases the relative Mach number into the first rotor, but lowers the relative Mach number into the second rotor and thus its shock losses. As shown in Fig. 1(*b*), the efficiency peaks at about 15 deg of counterswirl. For simplicity, a linear counterswirl variation from 10 deg at the hub to 0 deg at the tip was chosen for the final design.

The optimized 1D design was used as the starting point for a coupled axisymmetric-quasi-3D design of the fan. The basic design parameters are shown in Table 2. The flow path was designed to provide sufficient flow contraction to maintain an acceptable mean line axial velocity decrease. The inlet radius ratio was constrained by the test facility, and the exit radius ratio was selected to achieve an exit Mach number of 0.5 at design conditions. The casing flow path was sloped 2% across each rotor to unload the tip

Table 2 Fan aerodynamic design parameters

Rotor speeds	1450 ft/s	1150 ft/s
Work coefficient	0.34	0.5
Diffusion factor	0.48	0.55
Hub relative Mach	1.0	1.3
Tip relative Mach	1.5	1.45
Blade count	20	29
Avg. solidity	1.9	1.7
Avg. aspect ratio	1.6	1.75
Inlet radius ratio	0.5	0.65

sections, especially that of the second rotor. The aerodynamic design of the blades was carried out using the aspirated blade design methodology described in Merchant [3].

Three-dimensional viscous analysis of the stage, using the multistage average passage APNASA code developed by Adamczyk [8], was a critical component in the design process. The high-supersonic Mach numbers in the blade rows, close blade row spacing, coupled with the very high blade loading demanded higher fidelity blade row matching information than is possible with mixing-plane approaches. While the design was carried out using the quasi-3D design system, modifications to blade geometry such as incidence changes were driven by information from the 3D APNASA solution.

The predicted nominal design point performance for the fan calculated using APNASA is shown in Table 3. The tip clearances for the rotors were approximately 0.6% (Rotor 1) and 0.9% (Rotor 2) of the tip chord. The fan predictions exceeded the efficiency goal by 1.2% at the design pressure ratio and achieved a peak adiabatic efficiency of 89% at a pressure ratio of 3.16.

It is interesting to compare the design parameters of the two rotors shown in Table 2. Although the first rotor parameters are in the range of conventional supersonic fans, the aspect ratio is higher due to a lower average solidity [9]. The average Mach number of the first rotor is also higher than for conventional fans due to the counterswirl from the inlet guide vane. The second rotor has a 40% higher work coefficient and 20% higher average Mach number than the first rotor. The average solidity is also significantly lower than for conventional fans. This is due to a combination of reduced blade count and reduced chord length, both enabled by aspiration.

The detailed design process revealed that a started shock system in the second rotor was critical to meeting the performance goals. This was complicated by three issues: (1) excessive hub boundary layer growth at the shock impingement location leading to shock unstart at the hub, (2) achieving the correct blade throat margin to maintain started flow at design and part speed conditions, and (3) managing the blade metal blockage by keeping the blade count low while maintaining sufficient solidity to meet the high loading requirement. Aspiration was critical in addressing these issues. First, the position of the passage shock was stabilized by aspiration. This approach has been utilized in the form of "shock traps" in supersonic inlets and was also incorporated in previous aspirated compressors [6]. Second, aspiration enabled blade designs with 20% lower solidity at diffusion factors of 0.55. This resulted in reduced blade blockage and enabled a blade design with sufficient throat margin [10]. Increasing the throat margin resulted in a stronger shock system that could be tolerated with aspiration.

Table 3 CFD predicted nominal design point performance

	Rotor 1	Rotor 2	Overall
Pressure ratio	1.92	1.6	3.02
Adiab. efficiency (%)	91.2	86.6	88.2
Poly. efficiency (%)	92.3	87.5	90.0
Aspiration (%)	0	1.0	1.0

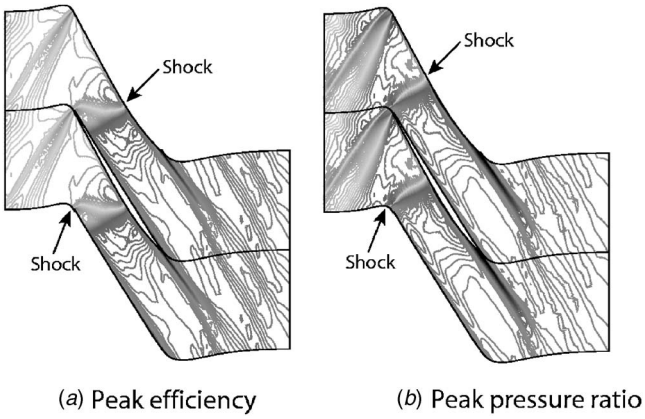

Fig. 2 Contours of Mach number in Rotor 2 at midspan: (*a*) peak efficiency; (*b*) peak pressure ratio

To illustrate the shock locations and boundary layer thicknesses, Fig. 2 presents relative Mach number contours at midspan from the APNASA calculation. The peak efficiency point (Fig. 2(*a*)) has a started shock and a well-attached suction side boundary layer. The peak pressure ratio point, which is the last computed CFD point, shows a spilled shock system. A midspan quasi-3D analysis of the impact of aspiration on the characteristics of the rotor showed that 1% aspiration resulted in a gain of 2% points in efficiency and 6% in pressure ratio before shock unstart.

Figure 3 shows the predicted design speed pressure ratio and adiabatic efficiency with different levels of aspiration (percent of inlet mass flow). The mass flow variation at 0% aspiration indicates that both rotors are unchoked at the computed points. The peak pressure ratio is 3.08 and the peak efficiency potentials is 84%. Comparing the speed lines at 0.5% and 1% aspiration, there is little difference in the peak efficiency, but the pressure ratio at 0.5% aspiration at which the speed line rolls off is 4% lower than at 1% aspiration. The predicted stall margin potentials based on the last computed CFD point, calculated using the method in Wadia et al. [9], are 15% at the design bleed, 11% at 0.5% bleed, and 6% at 0% bleed.

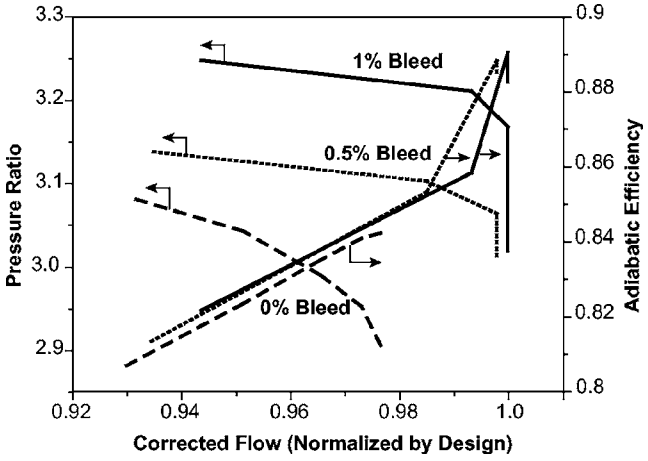

Fig. 3 Predicted fan design speed pressure ratio and efficiency at different levels of aspiration

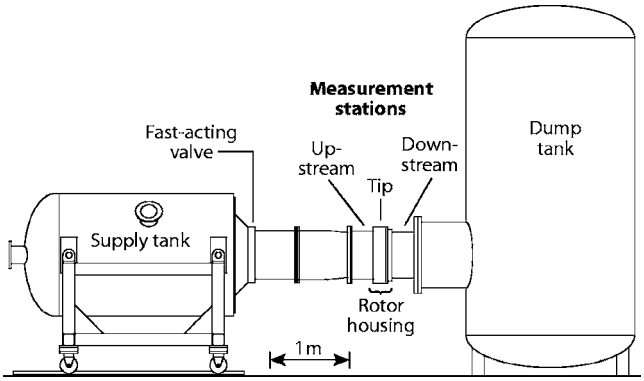

Fig. 4 Blowdown facility

3 Experiment Description

The theory and first application of blowdown compressor testing are described in Kerrebrock [11]. The blowdown facility used in this work is shown in Fig. 4, and its test section details in Fig. 5. The facility consists of a supply tank, initially separated by a fast-acting annular valve from the counter-rotating compressor stages and the dump tank into which they discharge. A choked perforated plate placed between the valve and test section was used to tailor the transient characteristics of the facility to the flow requirements of the compressor. A choked, adjustable area throttle downstream of the stage sets the operating point. For this experiment, a sufficient test time was required to permit accurate measurements of temperatures at the entrance to and exit from the compressor. In this facility, the measurement uncertainty of efficiency is dominated by temperature rise uncertainty. For these experiments, the target for efficiency measurement was 0.5%, which requires measurement of the temperature rise to about the same accuracy. Such instrumentation had been demonstrated for blowdown turbine stage testing [12]. The temperature measurement response time established a 100 ms test time requirement. This short test time precludes aeromechanical problems with the test hardware over the life of a typical test program.

A characteristic of blowdown compressors as used at MIT is that the decrease of the temperature of the gas in the supply tank during the test time is matched by slowing of the rotor, which is driven by its angular inertia, so that the Mach number of rotation is nearly constant during the blowdown. The relatively long test time of these experiments required the addition of a flywheel on each of the spindles carrying the rotors.

The test section, consisting of the two rotors, each on an independent, electric motor-driven spindle, is shown in Fig. 5. The need to provide sufficient inertia to drive these high work stages for the required test time sized the flywheel inertia. The desire to keep the rotating systems' critical speeds above their operating range thus imposed a minimum hub-to-tip ratio on the first rotor of about 0.5. The tungsten flywheels, around which the test section was designed, failed during proof test, necessitating their replacement with maraging steel units. The resultant reduction in flywheel inertia was compensated for by reducing the inlet pressure and thus the test Reynolds number by about 20%.

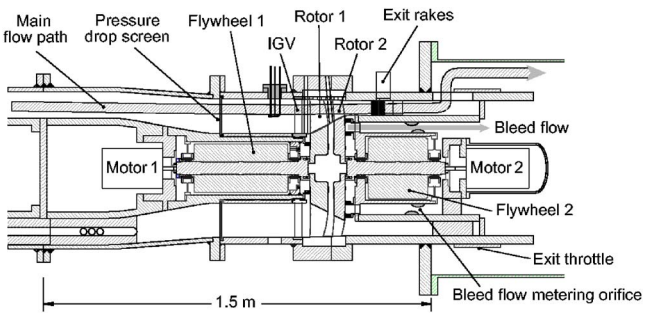

Fig. 5 Counter-rotating fan test section

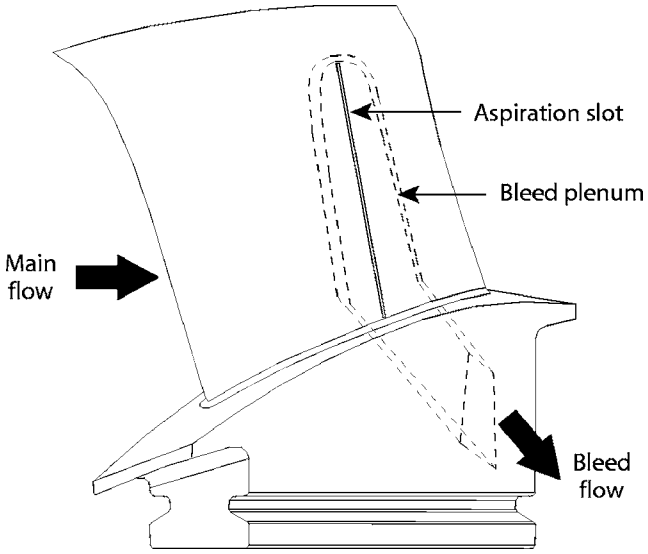

Fig. 6 Aspiration passage geometry in Rotor 2

The first rotor is an integrated bladed steel disk. The second rotor dovetails steel blades to a steel disk. Steel was chosen for the second rotor blades to ease construction of the hollow airfoils. They were fabricated by milling a bleed passage within a partially finished blade, e-beam welding on a cover, and then finish machining. The bleed air is removed through a passage electrodischarge-machined through the rear blade tang, as shown in Fig. 6. The bleed flow path was designed to choke the suction surface slot so as to establish the bleed flow rate. Details of the mechanical design were given by Parker [13].

Primary performance instrumentation consisted of static and total pressure probes and rakes, and stagnation temperature rakes located ahead of the first inlet guide vanes (IGV) and behind the second rotor. (This test section did not have torque meters.) Also, high frequency response wall static pressure transducers were located in the casing between the two rotors and just downstream of the second rotor. The rotor speeds and tank pressures were recorded as well. The pressure across an annular orifice in the bleed flow path downstream of the second rotor was measured to monitor the aspirated bleed flow, but programatic constraints precluded proper bleed flow path calibration so the bleed flow estimates in this paper are from the bleed flow path design CFD calculations.

For these tests, a gas mixture of CO_2 and argon with a ratio of specific heats γ of 1.4 was used in place of air to reduce the speed of sound (and thus mechanical stresses) while maintaining aerodynamic and thermodynamic similarity with air at flight conditions. During data reduction, the mixture was treated as real gas with properties estimated from NIST data (γ changes by about 3% from the stage inlet to outlet). Details of the construction and calibration of the instrumentation along with the test error analysis were given by Onnee [14].

4 Blowdown Operation

Insofar as we are aware, this is the first two-rotor configuration tested in a transient facility and some effort was required to realize the desired test behavior. Given fixed rotor inertia and geometry, the operating condition of the fan during the test time is set by the initial rotor speeds, the supply tank pressure and temperature, and throttle areas downstream of the second rotor and in the bleed flow path (which are adjustable).

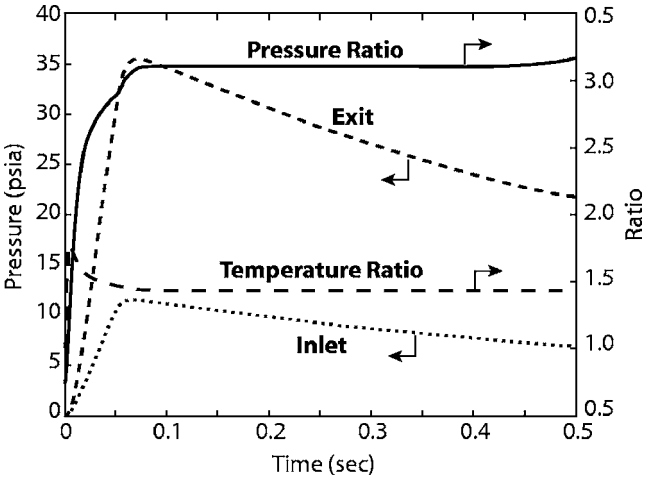

Fig. 7 Typical variation of flow conditions during a blowdown test

Figure 7 shows a typical simulated test time history. While the pressures and temperatures vary during the test, the pressure and temperature ratios across the stage remain close to constant for a sufficient period to enable accurate measurement of the fan performance. The useful test time is after the initial startup transient, from 250 ms to approximately 350 ms. The rise of the dump tank pressure then results in unchoking of the throttle and eventual stall of the fan.

The corrected flow is derived from a survey of the stagnation and static pressures upstream of the IGVs and is essentially a measure of the Mach number at that point. Corrected speed is derived from the measured rotative speed and the measured temperature upstream of the first rotor. All of the measured values, including the rotative speed, are variable in time during the run, so a point on the map is defined by selecting a time near the middle of the test time, when the rotative and flow Mach numbers are nearly constant, and calculating the operating point from the values measured at that time as averaged over three rotor revolutions. Typical variation in corrected speed and weight flow during the nominal 100 ms test time is shown in Fig. 8, which shows a variation of less than $\pm 0.5\%$ in corrected speed and $\pm 1.6\%$ in corrected flow.

After this 100 ms test period, the operating point changes as the throttles unchoke, resulting in the fan stalling after several hundred milliseconds. Conceptually, data from this period could be used to map out the stage behavior over the operating line followed. Such analysis has yet to be done, however, and all data reported herein are those averaged over the 100 ms matched test time.

5 Results and Discussion

In this section, we present and discuss the overall fan performance map. The experimental results are compared and reconciled with CFD calculations carried out using APNASA. The stall behavior of the fan is also discussed from a first principles analysis. In order to assist in understanding the measured performance of the fan, a simple one-dimensional model, which includes shock loss, diffusion loss, and a coupling of the mass flow to the rotor speed (assuming that both rotors operate with a unique incidence condition), was used. The model was calibrated by adjusting the blade metal angles to match the design pressure ratio. The corresponding predicted efficiency from the loss model was found to be in reasonable agreement.

5.1 Overall Fan Performance. The overall measured performance of the counter-rotating compressor is summarized in Figs. 9 and 10, which, respectively, show the pressure ratio and efficiency as functions of corrected speed and corrected flow. The pressure ratio was derived by area averaging the measured upstream/downstream spanwise pressure profiles. The reported efficiency was calculated from total enthalpy and entropy from NIST tables based on area-averaged total pressure and temperature [13,14]. The predicted APNASA performance was calculated from area averaging the flow solution. Excluding the effect of the boundary layers outside the radius of the hub and tip rake measurements resulted in an increase of about 0.3% in the predicted efficiency.

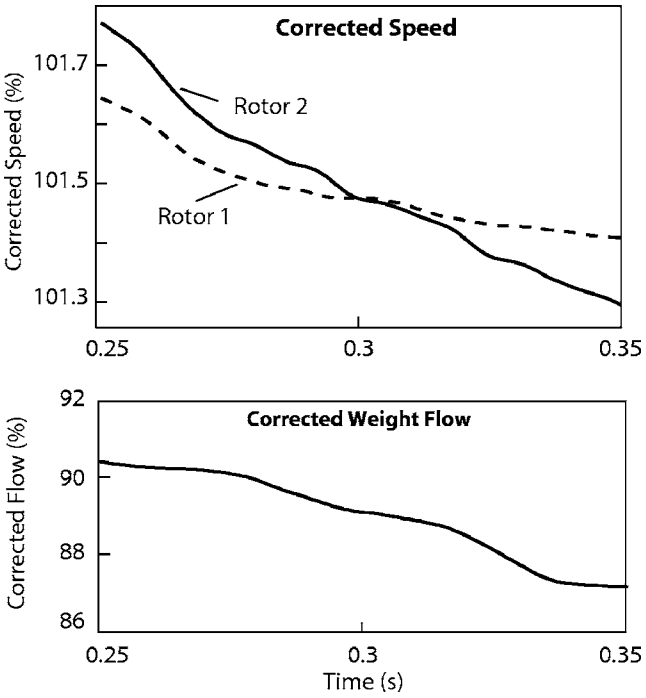

Fig. 8 Measured corrected rotor speed variations

The nominal speeds of the two rotors as percent of the design speed are both shown (R1, top red, and R2, bottom green). The design speed ratio between the rotors was maintained on each of the speed lines, and perturbations from the design speed ratio were tested at the individual points indicated on the map. The operating points on the speed lines were obtained by adjusting the downstream throttle setting. The APNASA calculations presented are all predictions made prior to the start of the test program. Because of the complexity of the dual-shaft test rig, it was diffi-

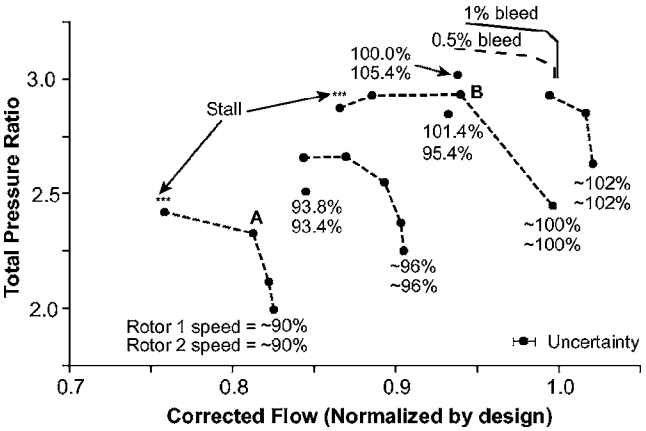

Fig. 9 Compressor pressure ratio as predicted by APNASA (solid lines) and as measured (points)

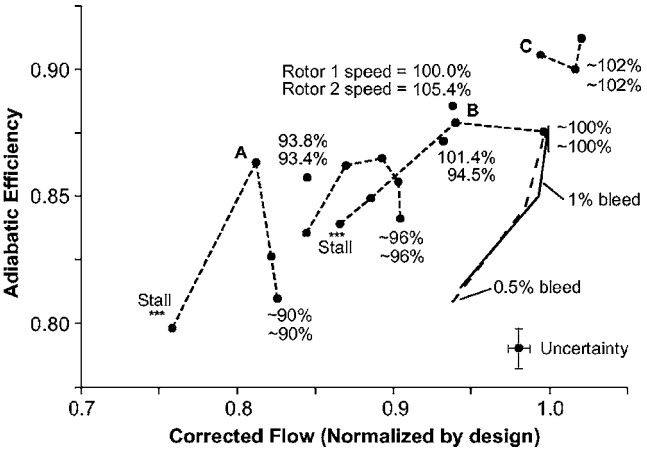

Fig. 10 Adiabatic efficiency as predicted using APNASA (solid lines) and as measured (points)

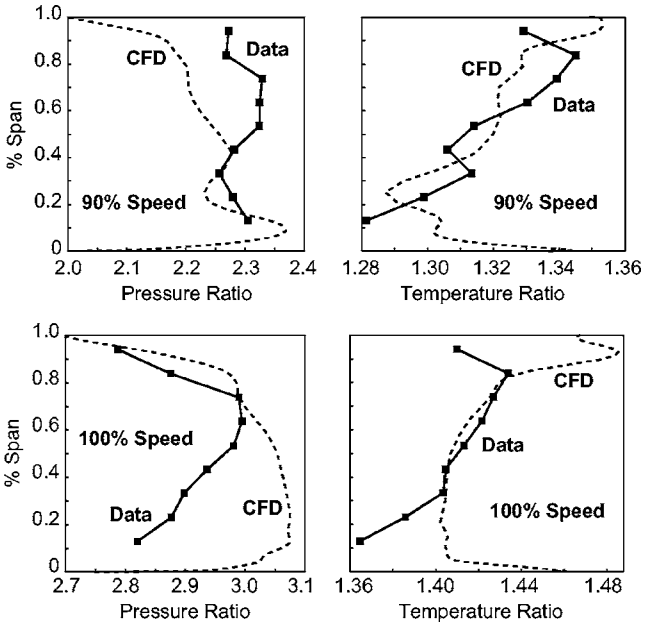

Fig. 11 Spanwise pressure and temperature distributions

cult at first to set operating points to a precision greater than 2% in speed and mass flow prior to the test (although the precision improved with experience and there was no difficulty in reducing the data to 0.1% precision). The predictions were made at an inlet Reynolds number of 2.6×10^6, while tests were run at about 1.6×10^6 at design speed. The rotor-tip clearances used in the calculations were 0.6% and 0.9% of the tip chord for the first and second rotors, respectively, while that in the tests is estimated to 60% smaller than the calculation. The effect of the tighter clearance on the efficiency is estimated to be 0.6% increase based on the tip leakage model by Denton [15]. Thus, the CFD solutions are not exactly at the test conditions, but resource limitations precluded rerunning the CFD at the measured operating points.

Figure 9 shows that the fan achieved a peak pressure ratio of 2.94 at design speed. This is 3% below the predicted design pressure ratio and implies a difference of approximately 1% in the temperature ratio. Comparing this to the predicted peak efficiency points, the measured pressure ratio is 7% below the pressure ratio predicted for 1% aspiration, and 4% below the pressure ratio predicted for 0.5% aspiration. This implies a difference of approximately 2% between the measured and predicted temperature ratios. The one-dimensional fan model described above was used to relate the sensitivity of the stage temperature ratio or work to the flow angle deviation. The model indicated that the stage was very sensitive to changes in exit flow angles, and a rotor deviation change of approximately 1 deg was sufficient to explain the observed differences between the measured and predicted performances. The increase in deviation may be caused by lower than design aspirated flow. An additional point to note is the strong coupling between the rotors due to the absence of a stator, which typically constrains the absolute flow angle into a downstream rotor. Thus, in the counter-rotating compressor, a change in deviation of the first rotor will have a greater impact on the downstream rotor and, thus, the overall stage performance than in a conventional multistage compressor.

The measured choking mass flow at the design speed is within 1% of the predicted design mass flow. The measurements show a flow range of 14% from choke to stall, which is approximately twice the range of the predicted speed line. Typical supersonic stages show a mass flow variation of about 7% at design speed conditions [9,16]. At 102% design speed, the measured choking mass flow is about 2% higher than design. This flow is determined solely by the choking mass flow in the first rotor, and the increase in corrected flow is consistent with the speed increase of the first rotor. At 90% speed, the measured flow range from choke to stall is 10%, and the measured choking flow rate is within 2% of the value predicted by APNASA. It should be noted that the rotor geometry changes with mechanical speed; specifically, the stagger in supersonic fans increases as the blade speed drops, so the choking mass flow will drop as well. Variations in the geometry due to mechanical speed variations were not accounted for in the CFD calculations, which may explain the lower choking mass flow in the predictions.

The peak stage adiabatic efficiency measured was 91% (Fig. 10). As the stage is throttled to stall on the nominal design speed line (100% and 102% design speed lines), the variation in efficiency is qualitatively in agreement with the trend predicted by the APNASA calculation, although the lowest measured efficiency is about 3% points higher than the lowest predicted efficiency. At 90% speed, only one efficiency prediction was available, and this is about three to six points lower than the measurement, depending on the operating point chosen for comparison.

The CFD and test data spanwise distribution of the Rotor 2 exit temperature and pressure are given in Fig. 11 for Point B on the 100% speed line and point A on the 90% speed line. At 100% speed, the CFD overpredicts the pressure rise along the inner half of the span while under predicting the temperature rise. At 90% speed, the outer span pressure rise is overpredicted. The relatively low work at the hub suggests that there may be some separation there.

Given the sensitive supersonic operating condition of both rotors, the measured and predicted performances are in good agreement. Thus, we conclude that the overall aspirated compressor aerodynamic design system gives useful results even in new and unusual sectors of design space such as that selected for this fan.

5.2 Casing Static Pressure Measurements. In the tests to date, the outer casing static pressure measurements provide the only independent assessment of the performance of the first rotor. At nominal design speed, the first rotor is choked at the stage choking mass flow. Here, the measured ratio of wall static to upstream total pressure is 1.39, while the value predicted by APNASA is 1.41. At the stall point, the measured static pressure ratio is 1.45 and the predicted value at the last computed point is 1.44. At 90% speed, the measured normalized static pressure is 1.3 and the predicted value is 1.31. This comparison indicates that this measure of first rotor performance is in agreement with prediction at both speeds.

5.3 Speed Ratio Perturbations. Although the stage was nominally designed and tested for a speed ratio of 0.8, the speed

Table 4 Comparison of casing static pressures at speed ratio perturbations about the design speed

% Speed	Rotor 1	Rotor 2	Overall
100–100	1.41	1.82	2.57
100–105	1.38	1.89	2.61
101–95	1.46	1.73	2.52

ratio will change in many engine applications. Two speed ratio perturbations were examined about Point B on the compressor map (Figs. 9 and 10). Increasing the speed of the second rotor while maintaining the speed of the first rotor results in an increase in pressure ratio and efficiency. The second rotor effectively acts as a throttle for the first rotor, so increasing the speed ratio moves the operating point of the first rotor closer to choke. This can be seen in the decrease in the normalized static pressure downstream of the first rotor shown in Table 4. Note that the overall flow rate does not change even though the first rotor is being throttled down. This unusual behavior can be explained by noting that an increase in the exit deviation of Rotor 1, caused by throttling down, can change the absolute flow angle without necessarily changing the axial velocity (mass flow). The overall result is that the inlet corrected flow of Rotor 2 can change as the blade speed is increased without changing the overall mass flow rate of the compressor. This behavior does not occur in a conventional multistage machine since stators constrain the absolute flow angles into downstream rotors.

Conversely, decreasing the speed ratio results in throttling up of the first rotor, moving it closer to stall. The static pressure rise downstream of the first rotor at 100–95% speeds is greater than the normalized static pressure at the stall point of the stage at the design speed ratio. Thus, changes in speed ratio can have a large impact on the stage performance, in particular, that of the first rotor. The design implication is that the first rotor must be designed with the appropriate stall margin to withstand the throttling effect caused by reductions in the speed ratio, as required in an engine application.

5.4 Stall Behavior. As is common practice, high frequency response pressure measurements on the outer casing downstream of the stage were used to detect rotating stall. The quasisteady test window contains about 20 revolutions of the first rotor and 16 revolutions of the second rotor. Stall was detected during the test time for operating points with a sufficiently closed throttle. The rotating stall frequency observed was approximately 35% of the first rotor speed.

Figure 12 shows the measured stall margin of the fan as defined in Ref. [9]. The stalling pressure ratio was taken as the last operating point on each speed line. (Note that stall was not observed on the 95% and 102% speediness, so these are excluded from this discussion.) The fan exhibits a stall margin of at least 25% on the three speed lines depending on the operating pressure ratio. The stall margin at peak efficiency on the speed lines is approximately 12%. At the nominal design speed, the stall margin is 15% at a pressure ratio of 2.8 and adiabatic efficiency of 88%.

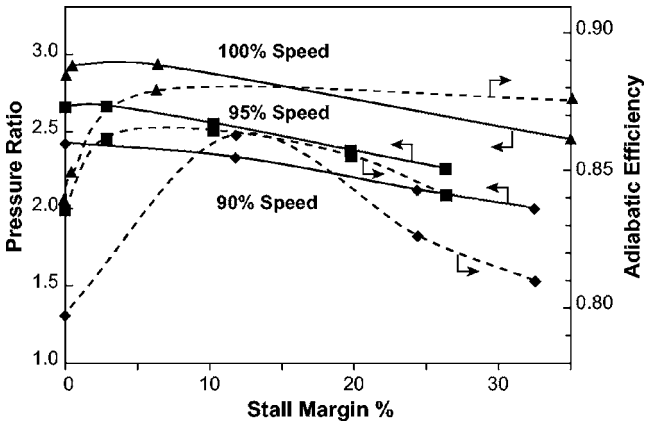

Fig. 12 Measured stall margin versus pressure ratio

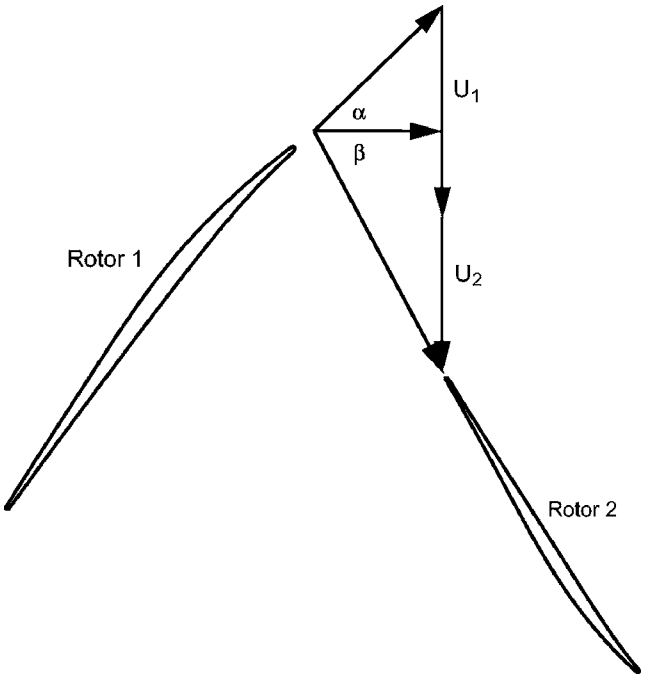

Fig. 13 Velocity triangles in the frame of reference of the first rotor

This is the first counter-rotating fan reported in the literature and, for a high pressure ratio supersonic fan, this stage has considerable flow range and stall margin. This behavior merits some examination. Cumpsty [17] presented a simple explanation that a steeper pressure rise characteristic smoothes out nonuniformities in the flow and therefore is advantageous in delaying stall. The slope of the ideal characteristic of a vaneless counter-rotating fan is

$$\frac{\partial \psi}{\partial \phi_{\text{inlet}}} = -\left(\frac{U_2}{U_1}\right)\tan(\alpha) - \left(1 - \frac{U_2}{U_1}\right)\tan(\beta)$$

Here, U is the blade speed, α is the relative exit angle of Rotor 1, and β is the blade relative inlet angle of Rotor 2. For simplicity, it is assumed that there is no inlet swirl and the axial velocity is constant. Substituting appropriate flow angles and speeds (note that U_1 and U_2 are defined with opposite signs here) in this equation shows that a counter-rotating fan such as this has at least a 50% steeper characteristic compared to a conventional two-stage compressor with the same average work coefficient.

A similar conclusion can be drawn by using the analysis of Smith [18] who showed that a rotor with a sum of absolute and relative angles $\geq$90 deg has a greater ability to damp incoming total pressure disturbances. Such a combination of flow angles also results in a region of high loss in one frame of reference, becoming a region of excess stagnation enthalpy in the frame of reference downstream. The second rotor of the counter-rotating fan exhibits this condition when viewed from the frame of reference of the upstream rotor, as shown in Fig. 13 (the sum of the angles at the mean line is approximately 110 deg). Thus, the second rotor will reduce an incoming stall cell or total pressure disturbance from the first rotor potentially extending the operating

range of the stage.

Another factor which may make the instability behavior of a counter-rotating fan different than that of a conventional geometry is the effect of counter-rotation on the dynamic (i.e., transient) interaction between blade rows. This effect is well known for multispool compressors, in which, for example, the (corotating) disturbances from low spool rotating stall degrade the high pressure compressor stability. When compressors rotate in opposite directions, the influence of rotating disturbances is markedly reduced [19]. Similar interaction may apply for counter-rotating fans, but appropriate analysis remains to be done.

5.5 Comments on Stage Efficiency. The test data and CFD efficiency predictions presented in Fig. 10 and subsequent discussion are that for the Rotor 2 exit flow (the "through flow") in the area mapped by the instrumentation rakes. As can be seen in Fig. 11, this excludes the hub and tip end wall flows. Using the CFD solutions as a guide, inclusion of these flows reduces the overall efficiency by about 0.3%. Also as noted, the tests were run at relatively tight tip clearances, so that opening up the clearances to the values used in the CFD calculations would add an additional 0.6% in loss. Taken together, these imply that the measured through-flow efficiency should be debited by 0.9%. In this case the peak efficiency on the 100% speed line would be 87%, while the 102% speed line reaches 90%.

An engine designer is concerned with more than the compressor through-flow efficiency and must consider all of the power debits on the compressor, which includes the Rotor 2 bleed flow. In this experimental design, the bleed flow is taken radially inward through the blades and disk and so recovers some of its energy since this configuration behaves as a radial inflow turbine. However, the bleed fluid suffers total pressure drops in passing through the choked bleed slot on the blade surface, in the passage within the blade and disk, and in deswirling into the stationary frame. We have estimated (but not measured) the net effect of these factors to be the equivalent of about a 0.5% loss in efficiency. More careful design of the bleed system may reduce this loss by, for example, not choking the bleed slot and reducing the internal passage Mach numbers. If this bleed air is used elsewhere in the engine, the impact of this penalty would decrease, Kerrebrock [20].

6 Conclusions

This study is the first public report of the detailed aerodynamic design and test of a vaneless counter-rotating compressor stage. In this design, aspiration on the second rotor enabled high loading at a low rotor mechanical speed compatible with high Mach number flight. The authors conclude the following from the study:

(1) With aspiration on the second rotor, a counter-rotating vaneless fan has met nominal design objectives of a pressure ratio of 3:1 with rotor speeds of 1450 ft/s and 1150 ft/s on the first and second rotors, and an adiabatic efficiency of better than 87%.
(2) The aerodynamic design approach developed on this, and two previous aspirated compressors, is capable of producing aerodynamic designs for aspirated compressors for new and unique design requirements for which there is no prior experimental experience.
(3) Blowdown testing is a practical and low-cost approach to verification of new and unusual compressor designs.
(4) Vaneless counter-rotating compressors may offer high efficiency, lightweight solutions to compression system requirements.

Clearly more research can and should be done on counter-rotating designs before development. This work would include expanding the test and analysis envelope to include a complete engine operating map, assessment of mechanical robustness criteria such as deterioration and aeromechanics, and, for aspirated implementations, integration of the compressor bleed with the engine secondary flow system.

Acknowledgments

This research was funded by DARPA and the U.S. Air Force Office of Scientific Research. GE Aircraft Engines collaborated in the early phases of the design. TURBOCAM of Dover NH fabricated the blade rows. Kulite Semiconductor Products provided the pressure instrumentation.

References

[1] Schuler, B. J., Kerrebrock, J. L., and Merchant, A., 2005, "Experimental Investigation of an Aspirated Fan Stage," ASME J. Turbomach., **127**(2), pp. 340–348.
[2] Merchant, A., Kerrebrock, J. L., Adamczyk, J. J., and Braunscheidel, E., 2005, "Experimental Investigation of a High Pressure Ratio Aspirated Fan Stage," ASME J. Turbomach., **127**(1), pp. 43–51.
[3] Merchant, A. A., 1999, "Design and Analysis of Axial Aspirated Compressor Stages," Ph.D. thesis, Massachusetts Institute of Technology, Cambridge.
[4] Johnson, J. E., 1995, "Variable Cycle Engine Developments at General Electric-1955-1995," Prog. Astronaut. Aeronaut., **165**, pp. 105–158.
[5] Brear, M. J., Kerrebrock, J. L., and Epstein, A. H., 2006, "Propulsion System Requirements for Quiet, Long Range, Supersonic Aircraft," ASME J. Fluids Eng., **128**(2), pp. 370–377.
[6] Merchant, A., Epstein, A. H., and Kerrebrock, J. L., 2004, "Compressors With Aspirated Flow Control and Counter-Rotation," Paper No. AIAA-2004-2514.
[7] Kirtley, K. R., Graziosi, P., Wood, P., Beacher, B., and Shin, H. W., 2004, "Design and Test of an Ultra-Low Solidity Flow-Controlled Compressor Stator," ASME J. Turbomach., **127**, pp. 689–698.
[8] Adamczyk, J. J., 1985, "Model Equation for Simulating Flows in Multistage Turbomachines," ASME Paper No. 85-GT-226.
[9] Wadia, A. R., Szucs, P. N., and Crall, D. W., 1988, "Inner Workings of Aerodynamic Sweep," ASME J. Turbomach., **120**, pp. 671–682.
[10] Wadia, A. R., and Copenhaver, W. W., 1996, "An Investigation of the Effect of Cascade Area Ratios on Transonic Compressor Performance," ASME J. Turbomach., **118**, pp. 760–770.
[11] Kerrebrock, J. L., Epstein, A. H., Haines, D. M., and Thompkins, W. T., 1974, "The MIT Blowdown Compressor Facility," ASME J. Eng. Power, **96**(4), pp. 394–406.
[12] Keogh, R. C., Guenette, G. R., and Sommer, T. P., 2000, "Aerodynamic Performance Measurements of a Fully-Scaled Turbine in a Short Duration Facility," ASME Paper No. IGTI 2000-GT-486.
[13] Parker, D., 2005, "Design and Operation of a Counter-Rotating Compressor Blowdown Test Facility," S.M. thesis, Massachusetts Institute of Technology, Cambridge.
[14] Onnee, J-F, 2005, "Aerodynamics Performance Measurements in a Counter-Rotating Aspirated Compressor," S.M. thesis, Massachusetts Institute of Technology, Cambridge.
[15] Denton, J. D., 1993, "Loss Mechanisms in Turbomachines," ASME J. Turbomach., **115**, pp. 621–656.
[16] Wennerstrom, A. J., 1984, "Experimental Study of a High-Throughflow Transonic Axial Compressor Stage," ASME J. Eng. Gas Turbines Power, **106**, pp. 553–559.
[17] Cumpsty, N. A., 1989, *Compressor Aerodynamics*, Longmans, London.
[18] Smith, L. H., 1958, "Recovery Ratio—a Measure of the Loss Recovery Potential of Compressor Stages," Trans. ASME, **80**, pp. 517–524.
[19] Longley, J. P., Day, I. J., Shin, H. W., Wisler, D. C., Plumley, R. E., Silkowski, P. D., Greitzer, E. M., and Tan, C. S., 1996, "Effects of Rotating Inlet Distortion on Multistage Compressor Stability," ASME J. Turbomach., **118**(2), pp. 181–188.
[20] Kerrebrock, J. L., 2000, "The Prospects for Aspirated Compressors," AIAA Paper No. 2000-2472.

Advanced Aerodynamic Optimization System for Turbomachinery

Bo Chen[1]
e-mail: b-chen04@mails.tsinghua.edu.cn

Xin Yuan

Key Laboratory for Thermal Science
and Power Engineering of Ministry of Education,
Department of Thermal Engineering,
Tsinghua University,
Beijing 100084, People's Republic of China

To further improve the efficiency of turbomachinery, an advanced aerodynamic optimization system has been developed for the turbomachinery blade optimization design. The system includes parametric modeling, evaluation system, and optimization strategy modules. The nonuniform rational B-spline technique is successfully used for parametric modeling of different blade shapes. An in-house viscous flow code, which combines the lower-upper symmetric-Gauss-Seidel Gaussian elimination (LU-SGS-GE) implicit scheme and the modified fourth-order monotone upstream-centered schemes for conservation laws total variation diminishing (MUSCL TVD) scheme, has been developed for flow field evaluation, which can be replaced by other computational fluid dynamics codes. The optimization strategy is defined by different cases in the system. Parallel optimization technique was used to accelerate the optimization processes. Three test cases were optimized to improve the efficiency by using the system. These cases are the annular turbine cascades with a subsonic turbine blade, a transonic turbine blade, and a subsonic turbine stage. Reasonably high efficiency and performance were confirmed by comparing the analytical results with those of the previous ones. The advanced aerodynamic optimization system can be an efficient and robust design tool to achieve good blade optimization designs in a reasonable time. [DOI: 10.1115/1.2776953]

Keywords: turbomachinery, aerodynamics, NURBS, optimization design

1 Introduction

In the aerospace and power generation industries, engineers are challenged to design the highest quality systems while reducing the cost and the duration of design cycles in order to achieve reactivity to market demands and business changes.

Traditionally, computational fluid dynamics (CFD) has been used in an analysis mode for cut-and-try approaches in designing, in which the design process is guided by the designer's expertise, with eventually a large scattering of results. Recently, computers and CFD codes have become more and more powerful in calculating the three-dimensional (3D) flow fields in terms of accuracy, sensitivity, and efficiency. Meanwhile, optimization methods have been developed in order to reduce the number of calls of computationally extensive programs. Coupling CFD codes with optimization tools is multidisciplinary and an efficient way to carry out turbomachinery designs. It enables designers to reduce the design cycles of turbomachinery blade design programs, where the impressive results of entire airplane optimizations are available [1,2].

However, the blade design has its own specific design problems [3]. Large optimization environments can simply be created, which are theoretically powerful but practically useless. The designers' intuitions cannot be implemented as easily and completely as originally assumed. In this case, optimization environments must involve special geometry modification tools for the handling of 3D designs, as well as mesh generation tools and CFD solvers. A sound interface programming is needed. Thus, optimization is often seen to be nothing else than a black box, respecting many constraints, producing many possible solutions, involving heaps of optimization parameters, and finding out quickly the optimal blade design.

A considerable amount of research has been conducted on blade design of turbomachinery. 2D/3D blade-to-blade inverse methods employing specified flow quantities (Mach number distribution, pressure distribution, pressure load distribution, etc.) have been commonly used in the past few decades [4–9]. However, the inverse design lacks direct control on parameters that indicate improvement of performance, and the specification of the aerodynamic duty in terms of local variables to achieve global aerodynamic optimum is not clear and needs more deliberation. In the meantime, the blade design coupled with optimization algorithms and CFD solver has been developed [10–12]. Owing to the sophistication of internal flows in turbomachinery, many flow features are fully 3D and cannot be predicted by quasi-3D approach [13]. With the development of the in-house 3D Navier–Stokes solver, full 3D blade design using optimization techniques is becoming desirable and practical.

In the present study, an advanced aerodynamic optimization system for turbomachinery blade design has been developed. There are three basic components of the system, parametric modeling module based on nonuniform rational B-spline (NURBS) technique, optimization strategy module, and evaluation system module. Each of these modules has its sub-blocks chosen in order to carry out different optimization schemes. The parametric modeling module would be discussed, particularly its principles and advantages. Details of the other two modules would be recounted in the following sections as well. Some blade design optimization cases with the above aerodynamic optimization system have been completed. In the present paper, we will show three turbine blade optimization cases, which are the annular turbine cascades with a subsonic turbine blade, a transonic turbine blade, and a subsonic turbine stage. Reasonably high efficiency and performance were confirmed by comparing the analytic results with those of the previous designs. From these three practical cases, the advanced aerodynamic optimization system shows its validity for the aerodynamic design of different turbomachinery blades.

[1]Corresponding author.

Contributed by the Turbomachinery Division of ASME for publication in the JOURNAL OF TURBOMACHINERY. Manuscript received November 7, 2006; final manuscript received March 15, 2007; published online February 12, 2008. Review conducted by Aspi Wadia.

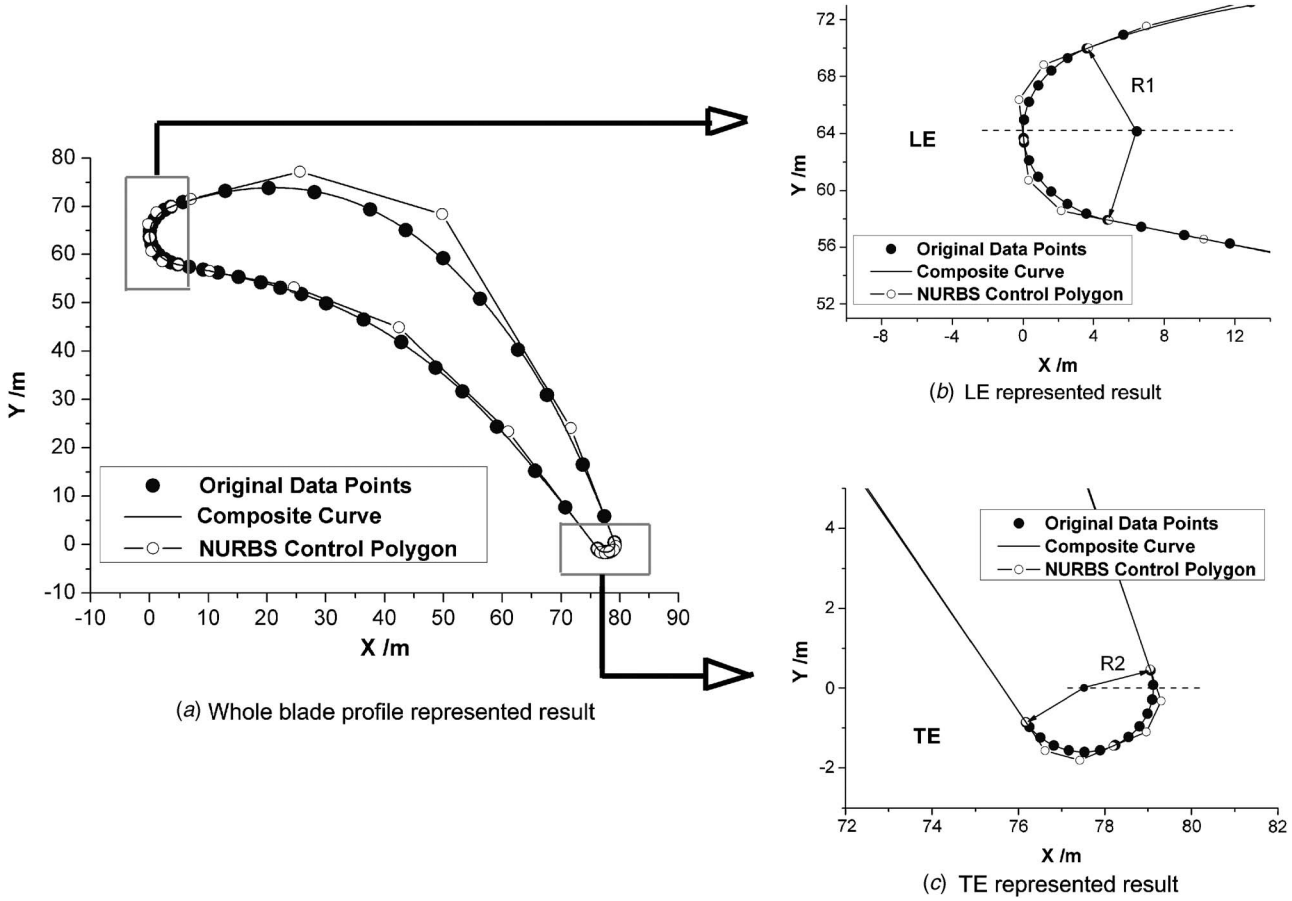

Fig. 1 Subsonic turbine blade profile represented with NURBS

2 Blade Three-Dimensional Geometric Representation and Deformation Module

In blade design optimization processes, one problem is how to choose design variables and reduce their number while maintaining the freedom and the quality of blade representations. The design variables can be derived from the geometric parametrization of blade curves and surfaces. Compressor blades of gas turbine engines are usually thin, low cambered, and have a round leading edge (LE) and a round or sharp trailing edge (TE), whereas turbine blades are highly cambered and have round LE and TE. Therefore, the geometric representation of such blades with one or two functions is quite a challenge.

Bezier [14] curves were first used in representing blade geometry, probably because of their easy implementation, but they have several limitations. First, they are nonrational functions and cannot represent conics (e.g., LE and TE circles) exactly; second, they are global in nature, i.e., when a control point is moved, the entire blade shape is modified. Later B spline was introduced to

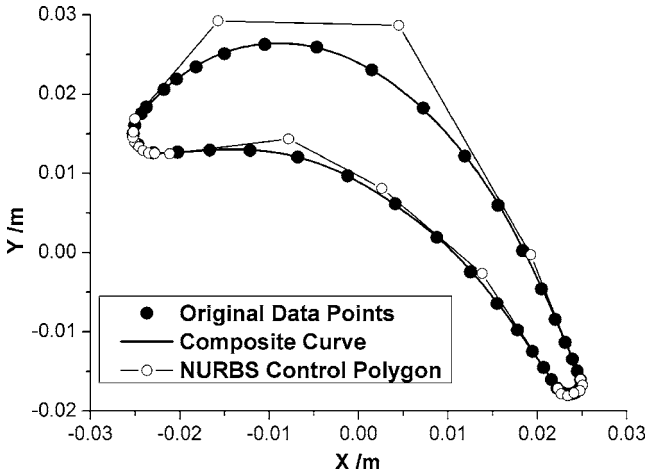

Fig. 2 Transonic turbine blade profile represented with NURBS

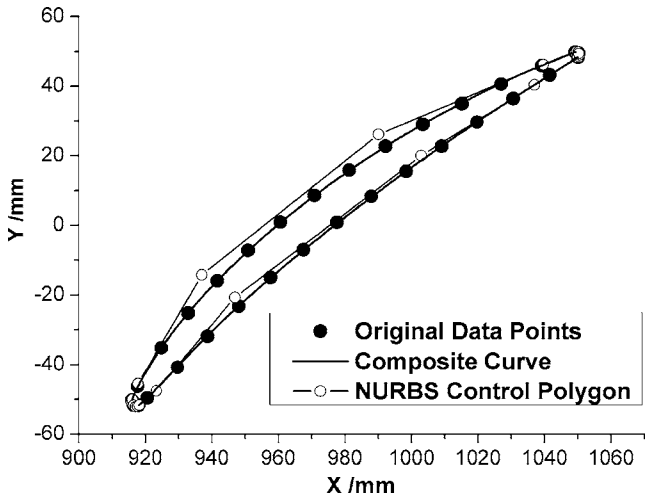

Fig. 3 Compressor blade profile represented with NURBS

overcome the global nature of Bezier polynomials, with more complex interpolation functions that can capture local characteristics. However, B spline cannot represent conics exactly as well so that the blade LE and TE cannot be represented exactly. NURBS is now widely used in geometric representations, with its powerful rational interpolation functions, which can overcome the shortcoming of Bezier curves as well as B splines. Using a single NURBS function with at most 13 control points and weights, Trepanier et al. [15] were successful in representing, rather accurately (up to manufacturing tolerance) and efficiently, the geometry of two-dimensional airfoils used in wing sections.

In this work, NURBS composite curves were used to represent blade control sections, and this parametrization involves the solution of an inverse problem for the control points, where the error in the representation is minimized using sequential quadratic programming (SQP). Meanwhile, NURBS curves were used to represent the blade stacking line so that deformation, such as lean, sweep, and twist of blades, could be achieved. Later, NURBS skinned surface technology was introduced to reconstruct blades with different shapes of blade profile. The whole geometric representation and deformation module for turbomachinery cascades is demonstrated.

2.1 Blade Profile Represented Using Nonuniform Rational B Spline. The NURBS curve is given by a sum over all control points, n, of a B-spline basis function $N_{i,p}(u)$ times the control point coordinates P_i times a weight ω_i so that the coordinates of the blade profile or the blade stacking line are determined once the control points and the corresponding weights are specified. A NURBS curve is defined such that [16]

$$A(u) = \sum_{i=0}^{n} R_{i,p}(u) P_i \tag{1}$$

with

$$R_{i,p}(u) = \frac{N_{i,p}(u)\omega_i}{\sum_{j=0}^{n} N_{j,p}(u)\omega_j} \tag{2}$$

where P_i are the control point coordinates, ω_i their respective weights, $N_{i,p}(u)$ the pth-degree B-spline basis functions, and $A(u)$ the position of a point on the curve. The basis functions are obtained through a knot vector, which defines the functions' break points, of the form

$$\{\underbrace{0, \ldots, 0}_{p+1}, u_{p+1}, \ldots, u_{m-p+1}, \underbrace{1, \ldots 1}_{p+1}\}$$

This work used a so-called composite curve, i.e., NURBS curves with different degrees merge into one curve so that they can be represented and controlled by a common function, to represent the blade profile. This method can efficiently reduce the number of variables, which affects the scale of a design optimization process. NURBS is quite convenient in representing a circular arc with a second-degree NURBS curve by giving a start angle, an end angle, and an arc radius. So, in representing LE and TE, the solution of an inverse problem is not considered. The pressure side and suction side of a blade profile are always third-degree curves whose functions are often impossible to find. In this work, two third-degree NURBS curves are used to represent the pressure side and suction side of blade profiles, respectively, and so the parametrization involves the solution of an inverse problem for the control points and weights, where the error between NURBS curves and original profile data has to be minimized. Weights of control points play a less important role in NURBS curves' representation than that of control points, and reducing the number of variables is quite important as well. In this work, weights are not used as design variables and are set equal to 1. This initial presumption was appropriate with results of experiments for different kinds of blade profiles.

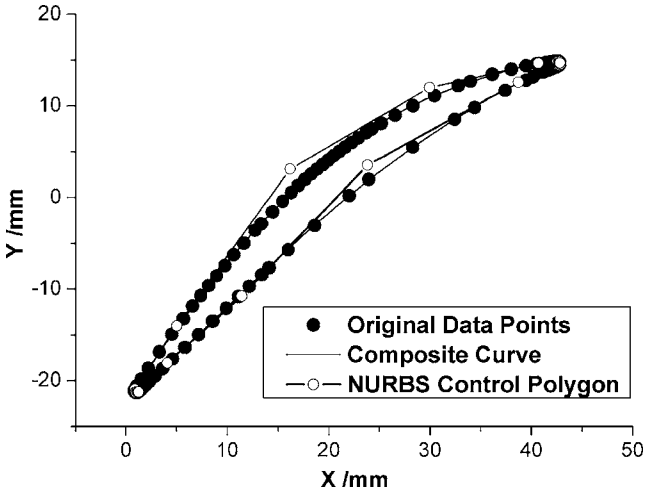

Fig. 4 Fan blade profile represented with NURBS

The error in the representation can be minimized using optimization tools, such as SQP, and this optimization problem can be specified by introducing a cost function of the form

$$F(X) = k \times \varepsilon_{\text{av}} + \varepsilon_{\max} \tag{3}$$

where

$$\varepsilon_{\max} = \left(\max_{1 \le j \le m} e_j\right)/L_{\text{blade}} \quad \text{and} \quad \varepsilon_{\text{av}} = \left(\frac{1}{m}\sum_{j=1}^{m} e_j\right) \Big/ L_{\text{blade}}$$

X is the vector of design variables (in this case the positions of control points of the approximation curve: $X = \{x_1, y_1, x_2, y_2, \ldots, x_n, y_n\}$), $\varepsilon_{\max}$ is the maximum error, ε_{av} is the average discrete error, e_j is the distance between the original curve and its approximation computed at m sampling points, L_{blade} is the length of a blade, and k is a weight factor. In the present calculations, m varies between 100 and 200, and $k=2$. This choice of a cost function accelerates convergence of the optimization process by including both the maximum error, which controls the quality of the final approximation, and the average error, which is also called mean error and globally compares the quality of different solutions [17,18].

The optimization process of blade parameterization using NURBS is carried out in a "blade profile fitting system" (BPFS) using ISIGHT, a commercial code that can provide excellent optimization environments. SQP was selected as the optimization tool. In this work, as the grid input files of IN-HOUSE CODE and NUMECA, a commercial CFD code, both of which are used for 3D flow calculation in the future blade optimization designs, list the blade profile's pressure side and suction side data separately, two third-degree composite NURBS curves are used to parametrize both sides of the blade, respectively. Each composite curve was combined by three curves, two conic curves for LE and TE, and a third-degree curve with six control points. As the two conic curve variables do not take part in the optimization process, the number

Table 1 Representation experiment result of different kinds of blade profiles

Blade profile kind	Total runs	Initiale $F(X)$	Finiale $F(X)$	Improvemente (%)
Subsonic turbine blade	311	0.01996	0.00201	89.91
Transonic turbine blade	223	0.03465	0.00244	92.96
Compressor blade	187	0.02804	0.00192	93.15
Fan blade	305	0.02281	0.00172	92.74

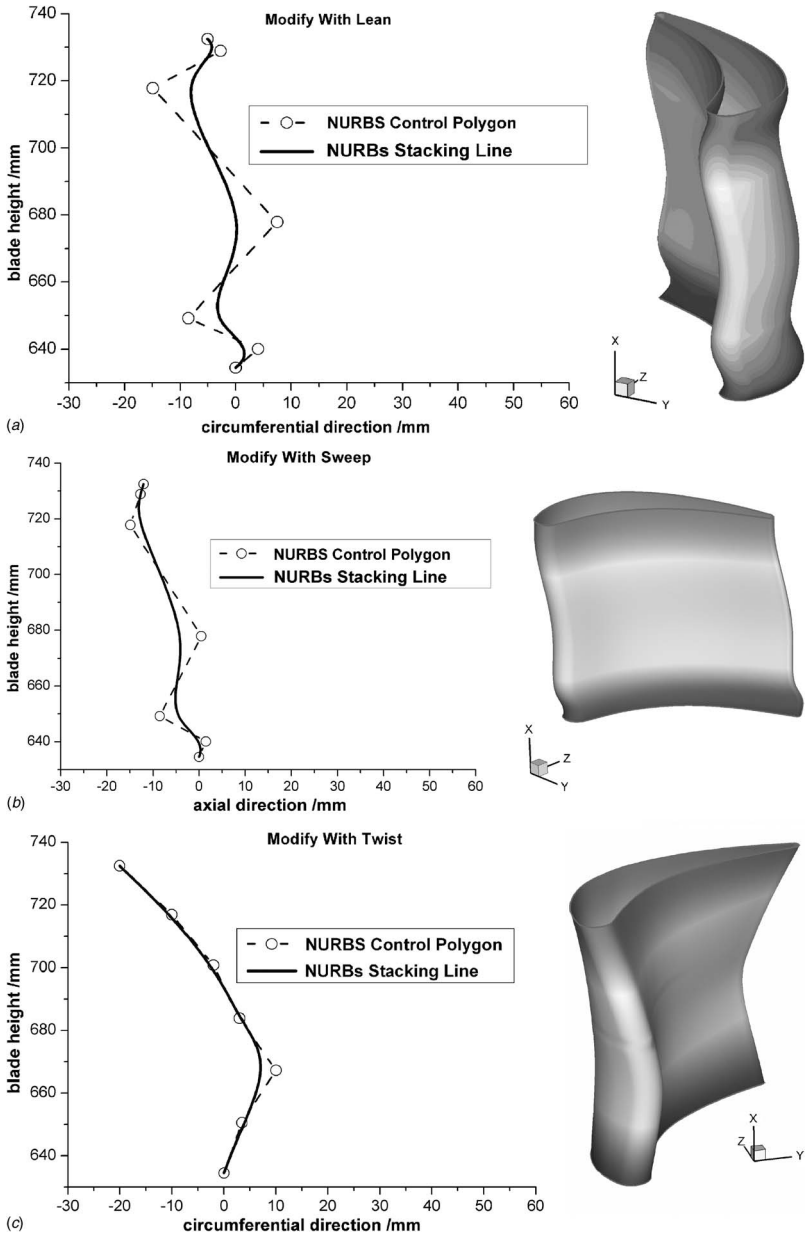

Fig. 5 Stacking line represented using NURBS for blade deformation: (*a*) lean of the blade, (*b*) sweep of the blade, and (*c*) twist of the blade

of variables of each third-degree curve is 6. So there are 12 variables around a blade section profile for the fitting process. With this method, different kinds of blade profiles were represented successfully in BPFS, and the operation of this optimization process is quite easy, with the three steps below:

- original data points are given;
- An initial guess is obtained for the NURBS control points assuming that all the weights are equal to 1; and
- the positions of control points are optimized using SQP so as to minimize the error between the composite curve and the original data.

Figure 1 shows a subsonic turbine blade profile represented by a composite curve. Both Figs. 1(*b*) and 1(*c*) show the LE and the TE represented by NURBS curves. Attention should be paid to notice that NURBS curves in Figs. 1(*b*) and 1(*c*) representing LE and TE are third degree, because degree elevation algorithm was used to change conic NURBS curves into third degree NURBS

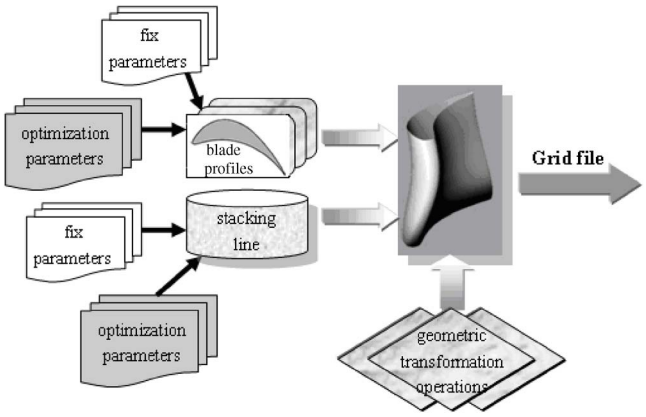

Fig. 6 3D blade deformation system

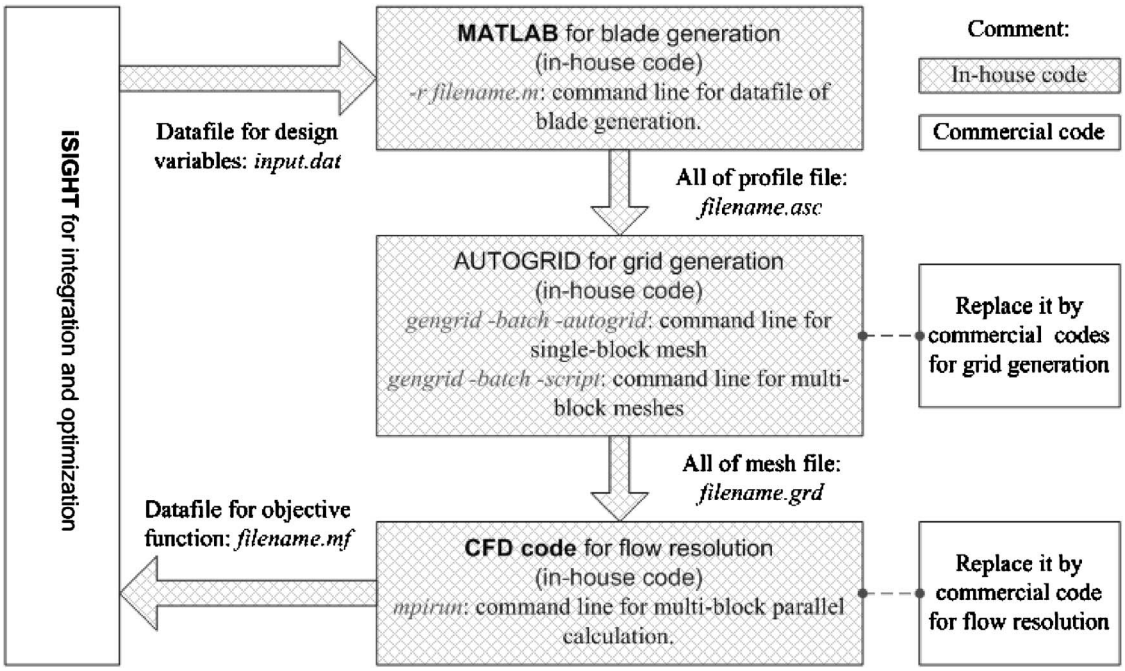

Fig. 7 Integration among NURBS, ISIGHT, and CFD codes

curves. Also, BPFS is fit for other kinds of blade profiles, such as compressor blade profile and fan blade profile. The same optimization processes were done to represent another three typical blade profiles. Figures 2–4 show the other three kinds of blade profiles represented by composite curves in BPFS, respectively.

Table 2 Major parameter specification for case 1

Hub radius	634.5 mm
Tip radius	734.5 mm
Blade number	56
Inlet total temperature	343.26 K
Inlet total pressure	144,417.6 Pa
Inlet flow angle	0 deg
Outlet static pressure	125,564.3 Pa

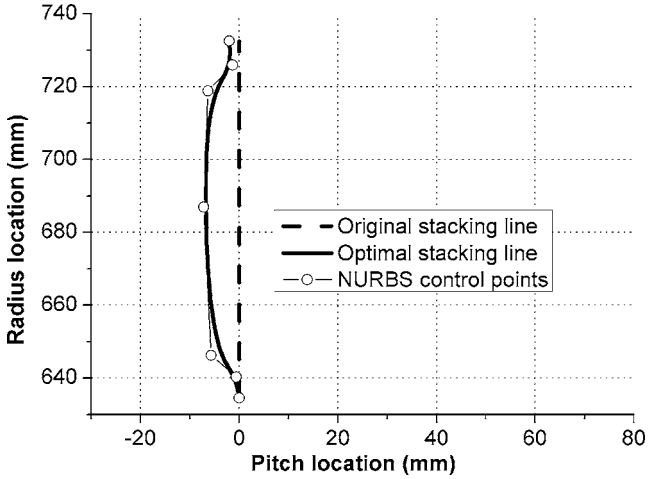

Fig. 8 Stacking line before and after optimization: (*a*) original and (*b*) after optimization

Table 1 shows the representation result of the different blade profiles. All calculations were performed on a Compaq Pentium 4 running at 1.8 GHz clock speed.

From the table and the figures listed, composite curve method was proved to be successful in representing, rather accurately (up to manufacturing tolerance) and efficiently, the geometry of two-dimensional blade profiles. Here, attention should be paid to realize that variables of a whole blade profile are more than 12 and the number is 16 including LE and TE variables.

2.2 Blade Stacking Line Represented Using Nonuniform Rational B Spline. In turbine and compressor cascade designs, it is very important to reduce the loss near the cascade endwalls, which contributes to the overall cascade loss significantly [19]. One of the efficient methods to reduce this loss is to modify the blade stacking line with lean, sweep, and/or twist. Lean is the bending of blades in the circumferential direction and this gives the bowed blade (the concept of which was published in the 1960s by Deich et al. [20]), which has been considered by numerous researchers as the appropriate blade design to reduce the loss of turbine cascades. Sweep is the bending in the axial direction. Twist as spiral deformation over the blade height is very important in adjusting the flow angles, and in this work, this modification can be adjusted by a NURBS curve or application to each profile section individually, which would be described in the next section.

In this work, blade stacking line represented by NURBS can modify the blade with lean, sweep, and twist and this parametrization did not need a solution of inverse problems. With NURBS parametrization, variables of stacking line, i.e., positions of NURBS control points excluding their corresponding weights, can be given to blade 3D design optimization programs. Figures 5(*a*)–5(*c*) show the blade stacking line with lean, sweep, and twist, respectively. Lean and sweep can be controlled by a third-degree NURBS curve with seven control points, and twist can be controlled by another third-degree NURBS curve with seven or fewer control points, which can be defined by designers according to the needs and scales of optimization processes.

2.3 Skinned Surface and Three-Dimensional Blade Deformation. Skinned surface technology was needed when blade profiles are different along the height of a blade and designers want to interpolate sections into given profiles. In this work, multiple two-dimensional slices of control sections, i.e., given blade profiles represented by composite curves, are placed at the hub, tip, and several span locations, and a 3D blade surface is constructed by NURBS skinning technology. Meanwhile, geometric transformation operations such as translation, resizing, and rotation are applied to these control sections. Twist of 3D blade is achieved by means of NURBS stacking line for twist, so the rotation translation operation applying to each control section individually is another efficient way to adjust the blade flow angles. The geometric transformation matrices are given by

$$A_1^i = \begin{bmatrix} 1 & 0 & 0 & \Delta x_i \\ 0 & 0 & 0 & \Delta y_i \\ 0 & 0 & 0 & 0 \\ 0 & 0 & 0 & 1 \end{bmatrix} \quad A_2^i = \begin{bmatrix} sx_i & 0 & 0 & 0 \\ 0 & sy_i & 0 & 0 \\ 0 & 0 & 1 & 0 \\ 0 & 0 & 0 & 1 \end{bmatrix}$$

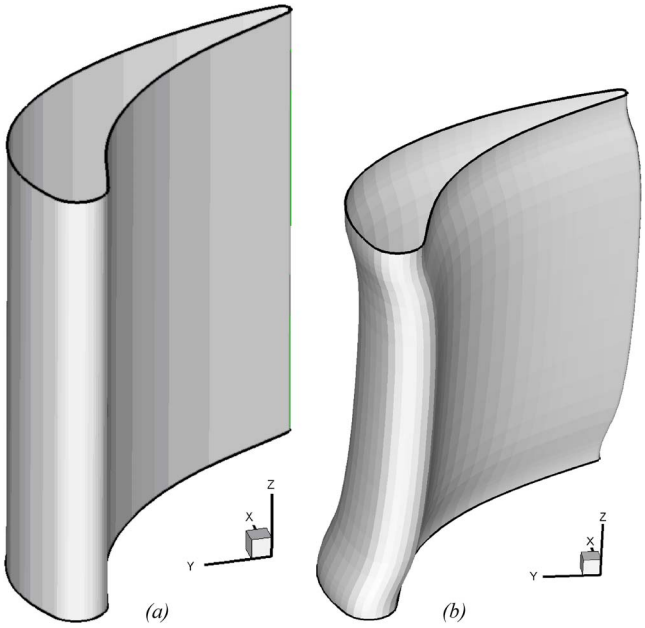

Fig. 9 Yamamoto's 3D blade surface

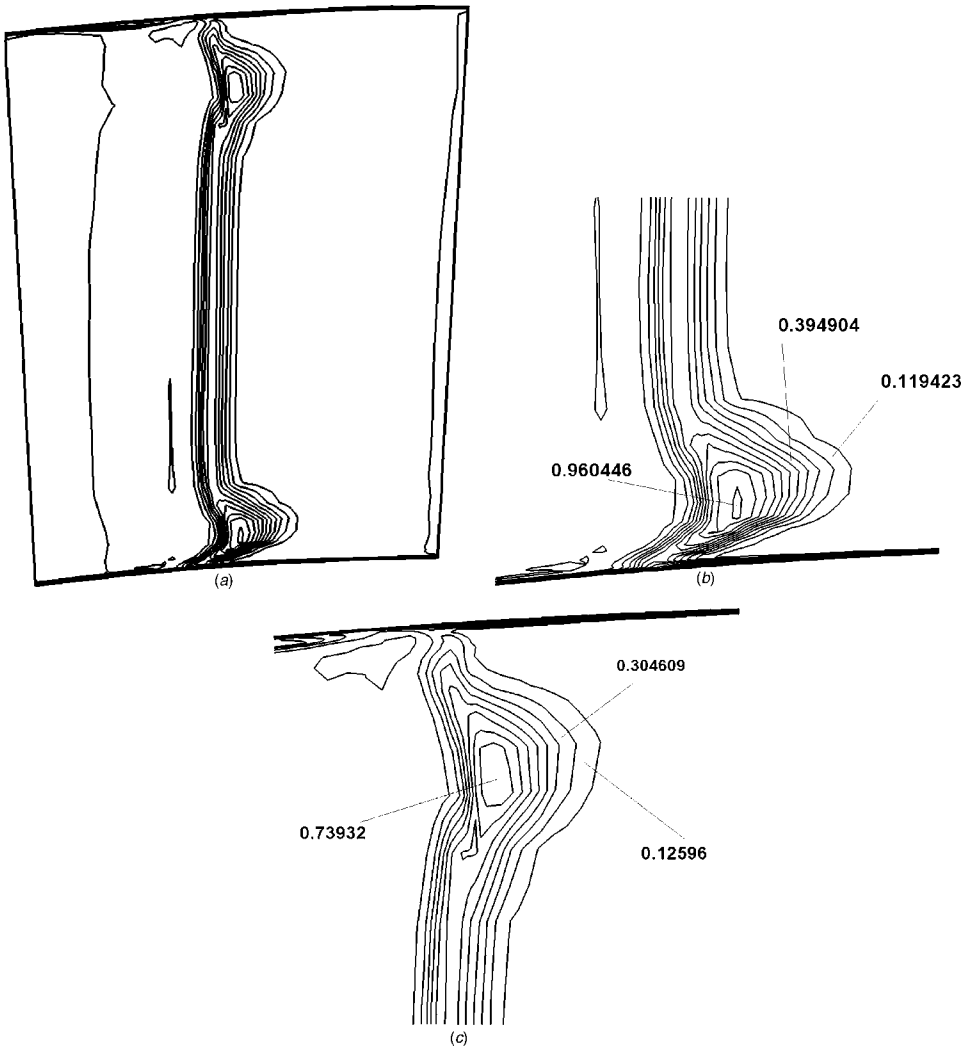

Fig. 10 Total pressure loss coefficient contours before optimization: (*a*) exit section, (*b*) end wall, and (*c*) tip

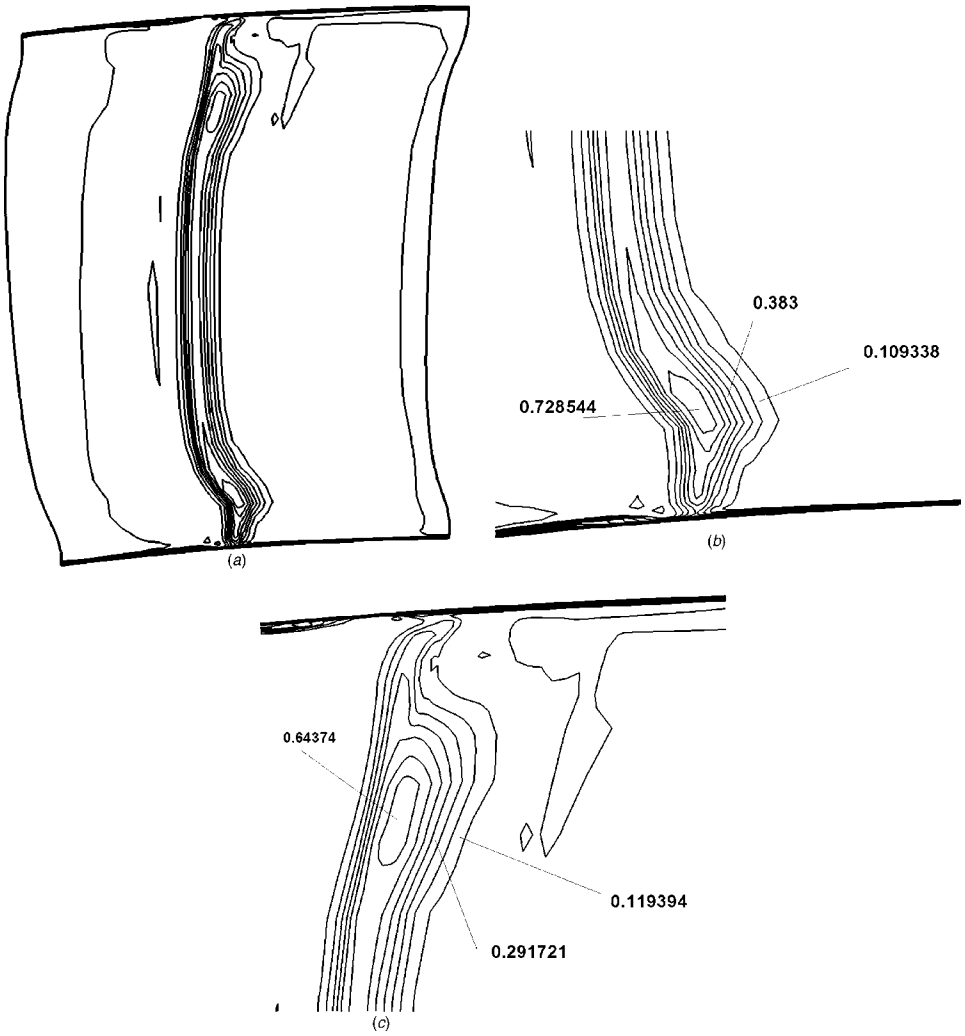

Fig. 11 Total pressure loss coefficient contours after optimization: (*a*) exit section, (*b*) end wall, and (*c*) tip

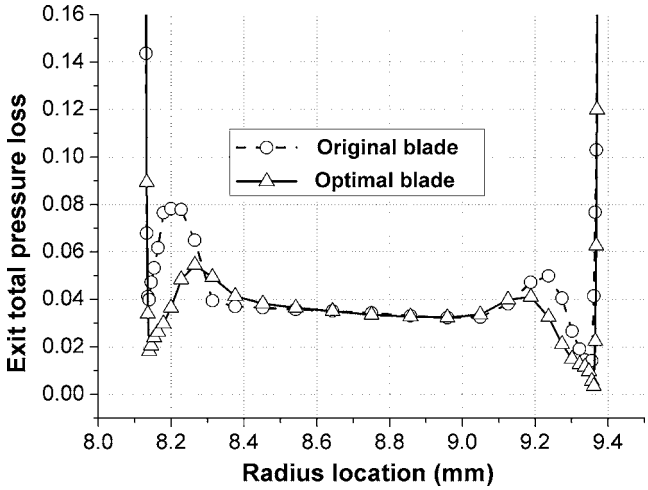

Fig. 12 Exit total pressure loss distributions

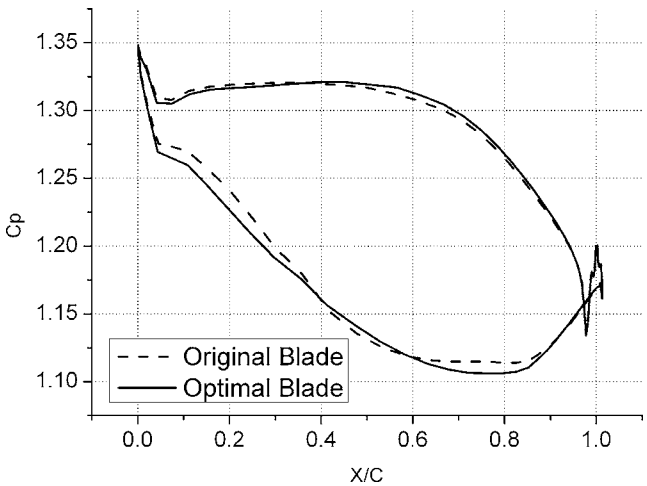

Fig. 13 Comparison of static pressure coefficients

$$A_3^i = \begin{bmatrix} \cos(\theta_z^i) & -\sin(\theta_z^i) & 0 & 0 \\ -\sin(\theta_z^i) & \cos(\theta_z^i) & 0 & 0 \\ 0 & 0 & 1 & 0 \\ 0 & 0 & 0 & 1 \end{bmatrix}$$

where A_1^i, A_2^i, A_3^i and are translation, resizing, and rotation matrices of the ith control section, respectively, Δx_i and Δy_i are the axial and circumferential movements, respectively, sx_i and sy_i are the axial and circumferential scaling factors, respectively, and θ_z^i is the rotation angle.

With the skinned blade surface and NURBS stacking line, a 3D blade deformation can be easily achieved according to different blade optimization design objects. Figure 6 shows the whole 3D blade parametric modeling module. With this module, designers can choose design variables such as blade profile variables, stacking line variables, or both of them to generate grid files for blade optimization designs.

3 Evaluating the System by Parallel Computation

A 3D viscous flow analyzed code proposed in our laboratory, which solves the Navier–Stokes equations and the low-Reynolds-number q-omega two-equation turbulence model, is used to predict the effect of full 3D viscous flow through turbomachinery. The code combines the LU-SGS-GE implicit scheme and the modified fourth-order MUSCL TVD scheme [21]. On the other hand, commercial CFD software, for instance, FINE/TURBO, can also be used to evaluate the viscous flow fields.

The in-house or commercial codes are accelerated by grid overlapping and multidomain treatment for distributed parallel computation. The parallelization is implemented on AMD Opteron 246×2 plus DDR400 cluster computer system where the interconnection is realized through a Fast Ethernet (1 Gbit/s) switch.

Table 3 Major parameter specification for case 2

Hub radius	696.86 mm
Tip radius	821.86 mm
Blade number	112
Inlet total temperature	290 K
Inlet total pressure	96,400 Pa
Inlet flow angle	−30 deg
Outlet static pressure	51,521.97 Pa

4 Optimization Strategy and System Integration

The basic idea of the integrated optimization strategy is to accelerate the design of the new blade by reducing the number of design variables, approximating the performance of the blade using knowledge acquired during previous designs, and taking the most from the robustness of exploratory algorithms and the efficiency of numerical algorithms for optimization. The commercial software ISIGHT is used for automatic process integration, DOE study, and optimizer implementation. The overall scheme of the optimization strategy and system integration is shown in Fig. 7. The optimization strategy can be integrated and optional in the following:

- DOE is used to explore the high-dimensional design space and screen the most influential variables as design variables.
- Genetic algorithm (GA) or adaptive simulated annealing (ASA) is applied to the optimization problem to estimate the potential global optimum.
- Response surface model (RSM) for approximation is constructed by interpretation of the data obtained from design of experiments (DOE) and GA studies.
- SQP optimization is applied to the RSM model for local refinement iteratively.

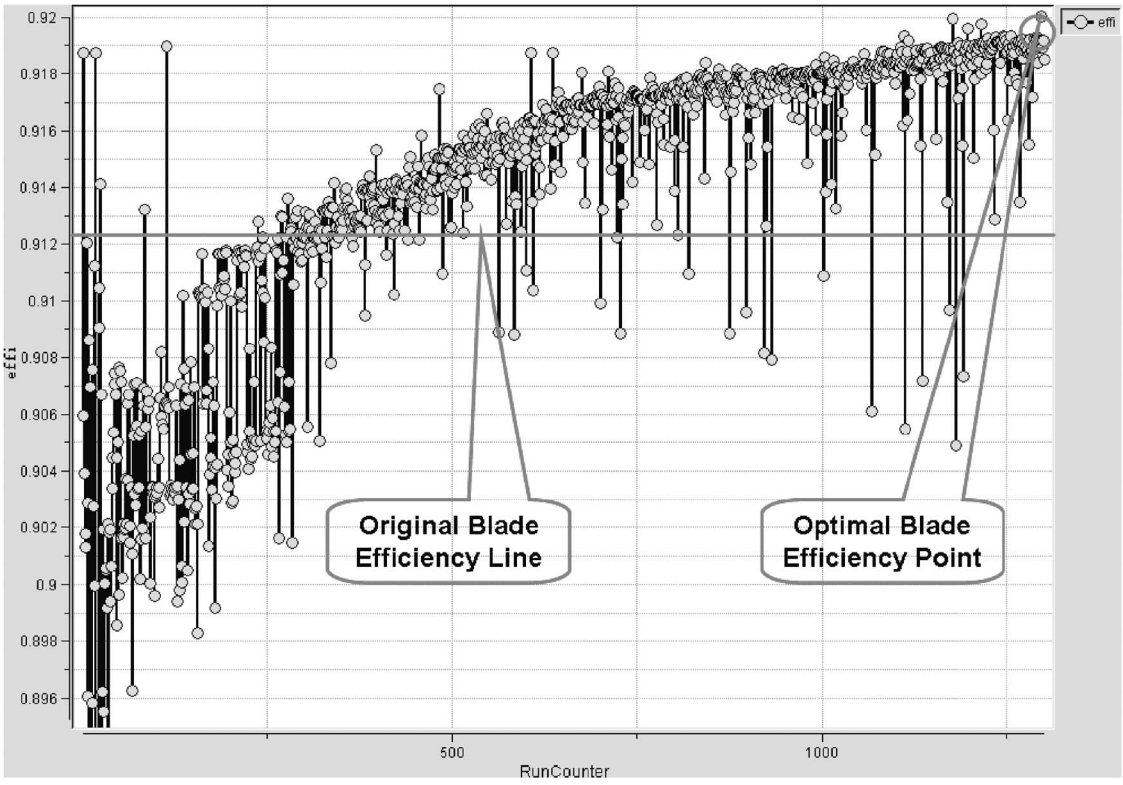

Fig. 14 The evaluating history of the GA strategy

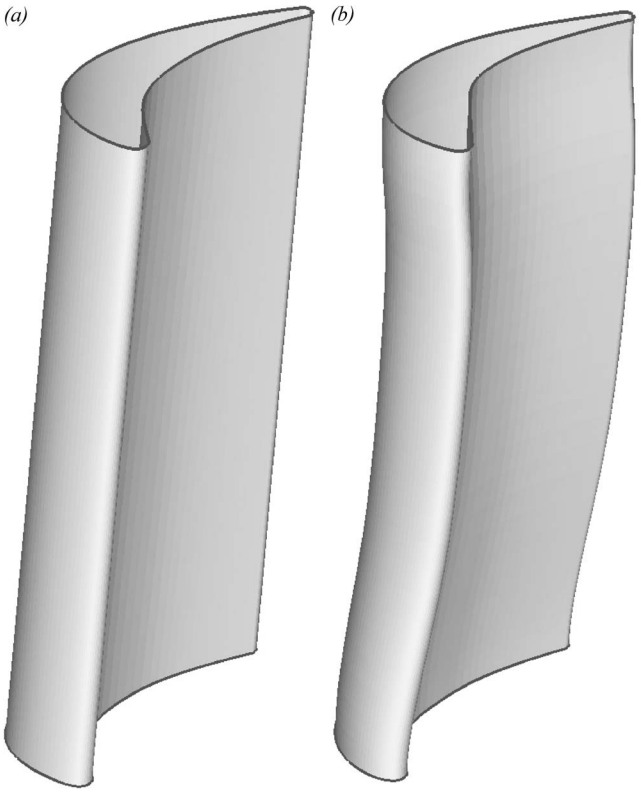

Fig. 15 VKI-LS-59 3D blade surface: (*a*) original and (*b*) after optimization

- Whenever an optimal point from the RSM based SQP optimization in the previous step is obtained, the exact 3D Navier–Stokes CFD solver is restarted to correct and update RSM.
- The above steps are run iteratively until the final global optimum is obtained.

5 Results

In this work, three test cases are performed. They are the annular turbine cascades with a subsonic blade, a transonic blade, and one subsonic turbine stage to achieve optimization processes, respectively.

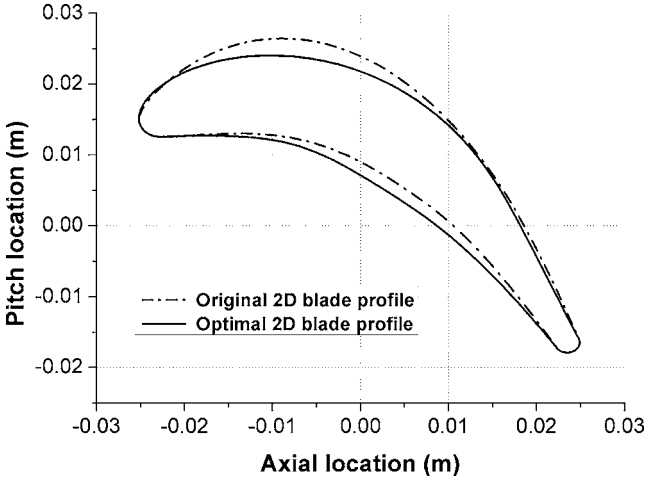

Fig. 16 Bottom profile comparison

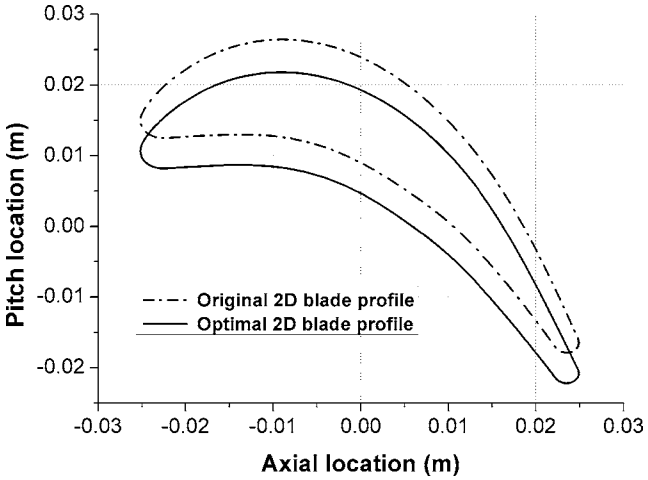

Fig. 17 Middle profile comparison

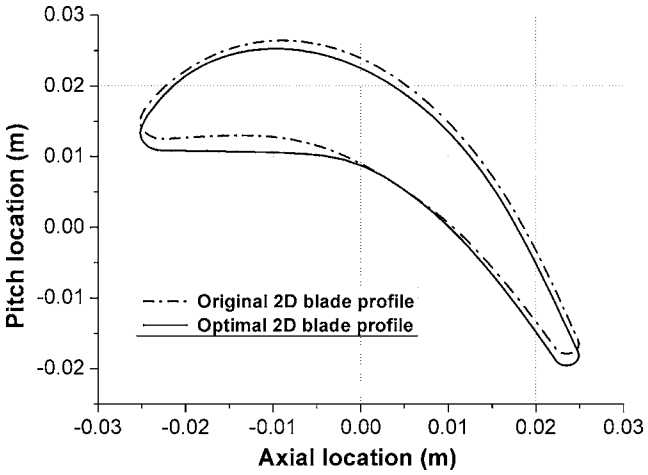

Fig. 18 Top profile comparison

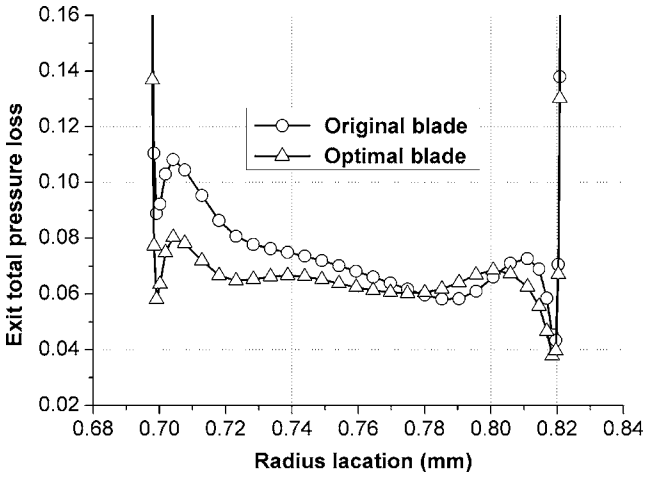

Fig. 19 Exit total pressure loss distributions

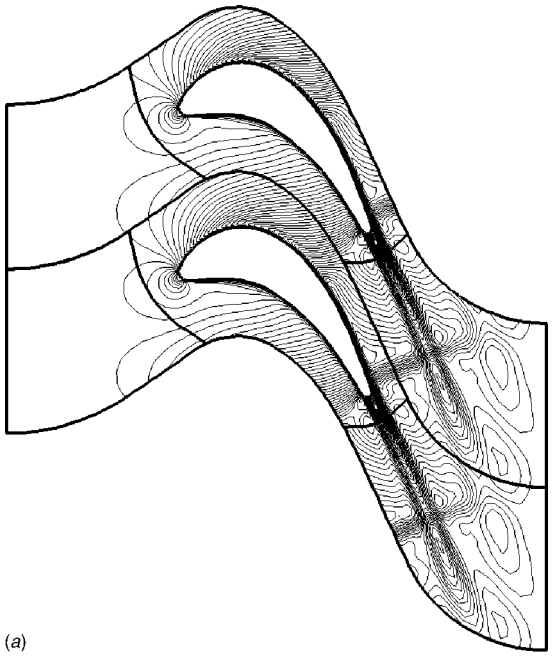

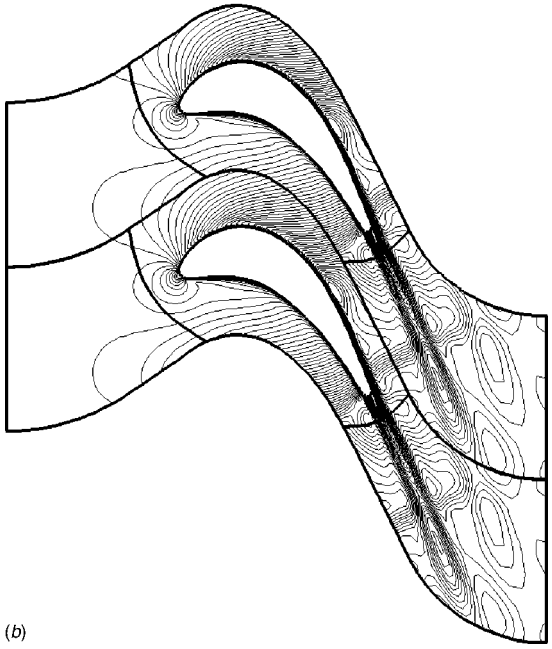

Fig. 20 Mach number contours at the blade middle span: (*a*) original blade and (*b*) optimal blade

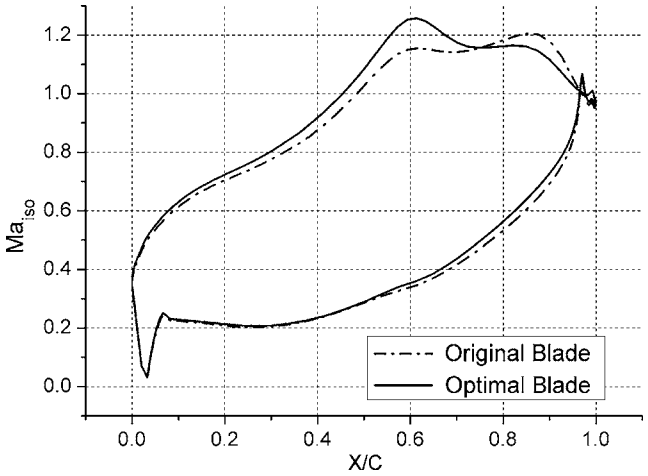

Fig. 21 Isentropic Mach number along the blade

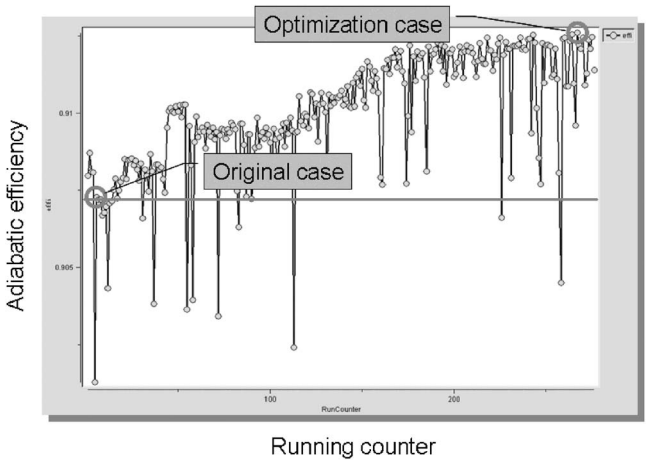

Fig. 22 The evaluating history of the ASA strategy

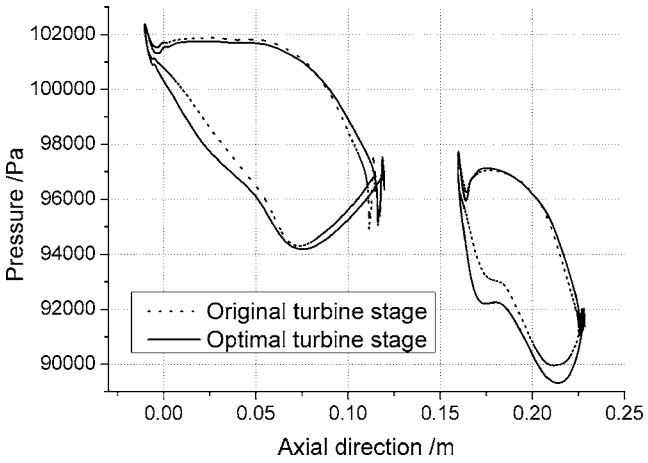

Fig. 23 Comparison of static pressure distributions

5.1 Subsonic Turbine Blade. This is a straight turbine blade and is arranged as an annular turbine cascade. Table 2 shows the major blade specification and inlet/outlet boundary conditions.

The initial blade is a straight blade with the same profiles along the radius direction. In this case, the NURBS technique is only used for 3D stacking line and so the number of design variables is 11. The optimization strategy chooses the ASA algorithm with 150 running times. The evaluating code uses the IN-HOUSE CODE. The flow field analysis in this example uses a C-type mesh with 129 $\times 25 \times 49$ grid points; the computational region is divided into eight blocks. These are for accelerated optimization process with the parallel calculating technique. The single running time of the optimization case takes about 60 min; the total optimization CPU

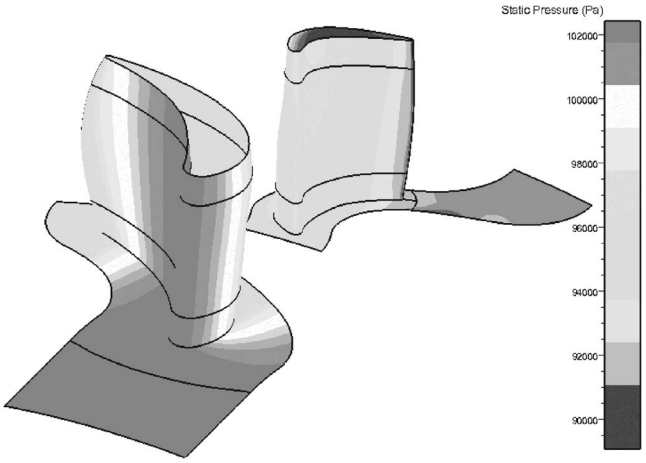

Fig. 24 Original case

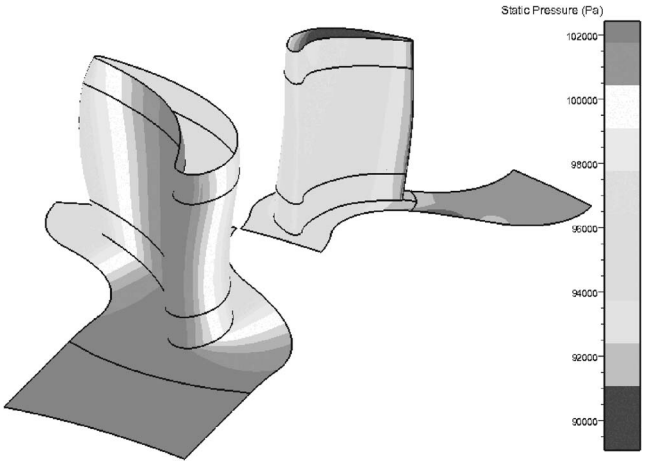

Fig. 25 Optimal case

time is about 150 h. After optimization, the adiabatic efficiency increases by 0.58% for this example.

Figure 8 shows the 3D stacking line before and after optimization. The stacking line shows the couple S-type style. Figure 9 shows the blade 3D surface before and after optimization.

Figures 10 and 11 show the exit total pressure loss contours before and after optimization. Figure 12 shows the exit total pressure loss distribution curve. From these pictures, the optimization result that the passage vortices near end walls have been weakened obviously is clear. Figure 13 shows that the performance of the static pressure along the blade middle span has been improved.

5.2 Transonic Turbine Blade. The second optimization case selects the VKI-LS-59 blade and is arranged as an annular turbine cascade. Table 3 shows the major blade specification and inlet/outlet boundary conditions for this case. In this work, the commercial CFD code, NUMECA, was used to achieve the flow field calculations during the optimization process.

The definition parameters for profiles of control sections and stacking line were treated as input variables. In this case, the blade includes three key profiles, the button one, the top one, and the middle one. So the design variables in the optimization process are 16 variables for each profile and there are three profiles, and 11 stacking line variables for the lean of the blade. So the total number of the design variables is 59.

In this case, the initial blade is a straight blade with the same profiles along the radius direction. The flow field analysis in this example uses H-O-H-type mesh with $17 \times 53 \times 161$ grid points. The objective function is the total pressure coefficient defined in the software, and there are four restrictions. Mass flow was restricted to be not less than the initial condition one and the areas of the three key profiles are restricted to change at the level of 3%. The optimization strategy chose GA as the optimization method with 1300 running times. The single running time of the optimization case takes about 70 min with the 1 GHz CPU and 13 CPUs take part in the optimization processes. GA design technique is executed in parallel in order to shorten the optimization period.

Figure 14 shows the evaluating history of this case by using the GA strategy. Figure 15 shows the initial blade and the optimal blade shapes, respectively. Figures 16–18 show the three key blade profiles, the bottom one, the middle one, and the top one, before and after the optimization process.

The blade key profiles are all changed after optimization. Figure 19 shows the exit total pressure loss distribution curve. Figure 20 shows the Mach number contour comparison at the middle span of the initial and optimal blades. Figure 21 shows the isentropic Mach number along the middle span of the blade before and after optimization.

After optimization, the efficiency changes from 91.23% to 92.07%, and the improvement is 0.84%. Figure 19 shows that the exit total pressure loss near the hub and at the middle of the blade has been obviously weakened, but passage vortices near the shroud have been strengthened. The optimal blade shape is like the double S type and Fig. 20 shows that shock wave flow field at the middle span of the blade has been improved obviously before and after optimization.

5.3 Subsonic Turbine Stage. The third optimization example is an annular turbine stage, which includes a stator blade and a rotor blade. The NURBS technique is used for 2D blade profiles and 3D stacking line of stator and rotor blades. Ninety-nine control parameters are used for the whole stage optimization.

The optimization strategy chooses the ASA method with 276 running times. The evaluating code uses NUMECA. An H-O-H type mesh is used for the flow analysis in this example with 423,108 coarse grid points for optimization and 751,280 fine grid points for final prediction. The single running time of the optimization case takes about 28 min and the total CPU time for the optimization process of one stage is about 128 h and 48 min.

Figure 22 shows the evaluating history of this case by using the ASA method. Figure 23 shows the pressure distribution along the middle span of the stator blade and the rotor blade. Figures 24 and 25 show the 3D blade surface and the static pressure contours before and after optimization. After optimization, the adiabatic efficiency of the turbine stage increases by 0.5% for this stage example.

6 Conclusions

An advanced aerodynamic optimization system for turbomachinery has been developed and used for the blade design optimization. The present system integrates three modules; these are the parametric modeling module, the evaluation system module, and the optimization strategy module. The NURBS technique has been successfully used for blade shape representation and 3D geometric deformation. The in-house viscous flow code and commercial CFD code are selected to run for evaluation of flow field. The above modules are integrated to construct the whole advanced aerodynamic optimization system. Three turbine blade optimization cases, which are the annular turbine cascades with a subsonic blade, a transonic turbine blade, and a subsonic turbine stage, are discussed. Reasonably high efficiency and performance were confirmed by comparing the analytical results with those of the previous designs. From these three practical cases, the advanced aerodynamic optimization system shows its validity for blade aerodynamic design of turbomachinery.

The advanced aerodynamic optimization system can be an efficient and robust design tool to achieve good aerodynamic blade design optimization in a reasonable time.

Acknowledgment

This work was partly supported by the National Natural Science Foundation of China (No. 50676043) and the Specialized Research Fund for the Doctoral Program of Higher Education (No. 20050003063).

References

[1] Dornberger, R., Stoll, P., and Buche, D., 2000, "Multidisciplinary Turbomachinery Blade Design Optimization," Paper No. AIAA-2000-0838.
[2] Reuther, J. J., Alonso, J. J., Jameson, A., Rimlinger, M. J., and Saunders, D., 1999, "Constrained Multipoint Aerodynamic Shape Optimization Using an Adjoint Formulation and Parallel Computers," J. Aircr., **36**(1), pp. 51–60.
[3] Havakechian, S., and Greim, R., 1999, "Recent Advances in Aerodynamic Design of Steam Turbine Components," VGB Conference.
[4] Schwering, W., 1971, "Design of Cascades for Incompressible Plane Potential Flows With Prescribed Velocity Distribution," ASME J. Eng. Power, **93**(3), pp. 321–329.
[5] Lecomte, C., 1974, "Calculation of Cascade Profiles From the Velocity Distribution," ASME J. Eng. Power, **96**, pp. 407–412.
[6] Leonard, O., and Van den Braembussche, R. A., 1992, "Design Method for Subsonic and Transonic Cascade With Prescribed Mach Number Distribution," ASME J. Turbomach., **114**(3), pp. 553–560.
[7] Meauze, G., 1982, "An Inverse Time Marching Method for the Definition of Cascade Geometry," ASME J. Eng. Power, **104**(3), pp. 650–656.
[8] Dang, T., and Isgro, V., 1995, "Euler-Based Inverse Method for Turbomachinery Blades, Part I: Two-Dimensional Cascades," AIAA J., **33**(12), pp. 2309–2315.
[9] Dang, T., Damle, S., and Qiu, X., 2000, "Euler-Based Inverse Method for Turbomachine Blades, Part 2: Three-Dimensional Flows," AIAA J., **38**(11), pp. 2007–2013.
[10] Goel, S., Cofer, J., and Singh, H., 1996, "Turbine Airfoil Design Optimization," ASME Paper No. 96-GT-158.
[11] Niizeki, Y., Sasaki, T., Horibata, Y., Fukuyama, Y., and Kobayashi, T., 1999, "Optimization System for Compressor Aerodynamic Design," *Proceeding of the IGTC*, pp. 475–482.
[12] Ashihara, K., and Goto, A., 2001, "Turbomachinery Blade Design Using 3D Inverse Design Method, CFD, and Optimization Algorithm," ASME Paper No. 2001-GT-0358.
[13] Denton, J. D., and Dawes, W. N., 1999, "Computational Fluid Dynamics for Turbomachinery Design," Proc. Inst. Mech. Eng., Part C: J. Mech. Eng. Sci., **213**(2), pp. 107–124.
[14] Farin, G., 1993, *Curves and Surfaces for Computer Aided Geometric Design*, 2nd ed., Academic, Boston.
[15] Trepanier, J.-Y., Lepine, J. L., and Pepin, F., 2000, "An Optimized Geometric Representation for Wing Profiles Using NURBS," Can. Aeronautics Space J., **46**(2), pp. 12–19.
[16] Lepine, J., Guibault, F., and Trepanier, J.-Y., 2001, "Optimized Nonuniform Rational B-Spline Geometrical Representation for Aerodynamic Design of Wings," AIAA J., **39**(11), pp. 2033–2041.
[17] Piegl, L., and Tiller, W., 1997, *The NURBS Book*, Springer, New York.
[18] Ghaly, W. S., and Mengistu, T. T., 2003, "Optimal Geometric Representation of Turbomachinery Cascades Using NURBS," Inverse Probl. Eng., **11**(5), pp. 359–373.
[19] Yamamoto, A., 1987, "Production and Development of Secondary Flow and Losses Within Two Types of Straight Turbine Cascades, Part I: A Stator Case," ASME J. Turbomach., **102**(2), pp. 186–193.
[20] Deich, M. E., Gubarev, A. B., Filipov, G. A., and Wang, Z., 1962, "A New Method of Profiling the Guide Vane Cascades of Turbine Stages with Small Diameter-Span Ratio," Teploenergetika (8), pp. 42–46.
[21] Yuan, X., and Daiguji, H., 2001, "A Specially Combined Lower-Upper Factored Implicit Scheme for Three-Dimensional Compressible Navier–Stokes Equations," Comput. Fluids, **30**(3), pp. 339–363.

Numerical Study of Instability Mechanisms Leading to Transition in Separation Bubbles

Brian R. McAuliffe
Aerodynamics Laboratory,
Institute for Aerospace Research,
1200 Montreal Road, Building M-2,
Ottawa, ON K1A 0R6, Canada

Metin I. Yaras
Department of Mechanical and Aerospace Engineering,
Carleton University,
1125 Colonel By Drive,
Ottawa, ON, K1S 5B6, Canada

In this paper, transition in a separation bubble is examined through numerical simulation. The flow Reynolds number and streamwise pressure distribution are typical of the conditions encountered on the suction side of low-pressure turbine blades of gas-turbine engines. The spatial and temporal resolutions utilized in the present computations correspond to a coarse direct numerical simulation, wherein the majority of turbulence scales, including the inertial subrange, are adequately resolved. The accuracy of the simulation results is demonstrated through favorable comparisons to experimental data corresponding to the same flow conditions. The results of the simulation show linear Tollmien-Schlichting (T-S) instability growth downstream of the point of separation, leading to the roll up of spanwise vorticity into discrete vortical structures, characteristic of Kelvin-Helmholtz (K-H) instability growth. The extent of cross-stream momentum exchange associated with packets of amplified T-S waves is examined, along with details of the time-periodic breakdown into turbulence occurring upon the development of the K-H instability. Reynolds-averaged properties of the separation bubble are presented and provide evidence of the strong three-dimensional nature of the reattachment process.
[DOI: 10.1115/1.2750680]

1 Introduction

The process of laminar-to-turbulent transition in a separation bubble shares characteristics with both attached boundary layers and free shear layers. The Tollmien-Schlichting (T-S) instability, typically associated with attached-flow boundary-layer transition, is a viscous instability whereby two-dimensional disturbances amplify and develop, through vortex stretching, into three-dimensional structures that burst into turbulent spots [1]. Through lateral and longitudinal growth, these spots eventually merge, yielding a fully turbulent flow state at the end of the transition zone [2]. In a number of recent studies [3–9], experimental evidence suggests that this instability mechanism may play a significant role in the breakdown to turbulence in separation bubbles.

The inviscid Kelvin-Helmholtz (K-H) instability is the dominant mechanism leading to transition in free shear layers. The transition process driven by this mode of instability results from breakdown to turbulence in regions of high shear created by vortical structures that result from the roll up of the free shear layer [10,11]. The roll up is the result of a small disturbance creating a finite curvature in the shear layer, with the centrifugal force produced by this curvature altering the pressure field in a way that amplifies the ripple in the inviscidly unstable velocity field. Roll up of the shear layer occurs in a direction consistent with the vorticity of the layer. A vortex pairing instability is sometimes observed in K-H transition. Experimental and computational studies have revealed that under certain conditions, K-H instability may play a dominant role in the transition process of separation bubbles [12–18].

Knowledge of whether the transition process in a separation bubble is dominated by the T-S or K-H mechanism may be critical for accurate prediction of the extent of the bubble and the characteristics of the turbulent boundary layer immediately downstream of the reattachment point. Chandrasekhar [19] presents an inviscid stability analysis for a hyperbolic tangent velocity profile $[U=U_0\tanh(y/d)]$, which is a reasonable approximation to a separated shear layer. He demonstrates that the shear layer is inviscidly unstable to disturbances in the range of $0<\kappa d<1$, where κ is the wave number. More recent studies have shown a correlation of the dominant instability frequency when formulated as a Strouhal number ($\mathrm{Sr}_{\theta s}$), using the momentum thickness and edge velocity at separation as the characteristic length and velocity scales, respectively. Talan and Hourmouziadis [20] observed that when transition occurred via the K-H mechanism, $\mathrm{Sr}_{\theta s}$ was in the range of 0.010–0.014. McAuliffe and Yaras [18] observed values in the range 0.008–0.013. Ripley and Pauley [21] and Muti Lin and Pauley [13] give values of $\mathrm{Sr}_{\theta s}$ in the range of 0.005–0.008 based on the vortex shedding frequency. However, vortex pairing is observed in their simulations, and the instability frequency is approximately twice the quoted shedding values ($0.010<\mathrm{Sr}_{\theta s}<0.016$). The stability parameters κd and $\mathrm{Sr}_{\theta s}$are related to each other, and it can be readily demonstrated that the range of 0–1 for κd corresponds to a range of 0–0.0398 for $\mathrm{Sr}_{\theta s}$.

Recently, through a study with experimental and computational components, Roberts and Yaras [5,22] demonstrated that transition of a separated shear layer through the K-H instability does not preclude the presence of T-S activity in the shear layer. They highlighted the possibility of an interaction between the two instability modes, with the roll up of shear-layer vorticity into vortical structures occurring at the dominant T-S frequency. The present effort is a follow-up of that study, focusing on numerical simulation of another separation-bubble transition case that was experimentally observed by Roberts and Yaras [5] to have significantly more pronounced T-S activity. Through analysis of the present findings within the context of those documented by Roberts and Yaras [5,22], a better understanding of the relative roles of the T-S and K-H instability mechanisms in separation-bubble transition is realized.

2 Experimental Setup

The experiments against which the simulations are compared were performed in a closed-circuit wind tunnel on a flat-plate test surface of 1220 mm length and 762 mm width. Streamwise pres-

Contributed by the International Gas Turbine Institute of ASME for publication in the JOURNAL OF TURBOMACHINERY. Manuscript received July 13, 2006; final manuscript received December 14, 2006; published online February 12, 2008. Review conducted by David Wisler. Paper presented at the ASME Turbo Expo 2006: Land, Sea and Air (GT2006), May 8–11, 2006, Barcelona, Spain.

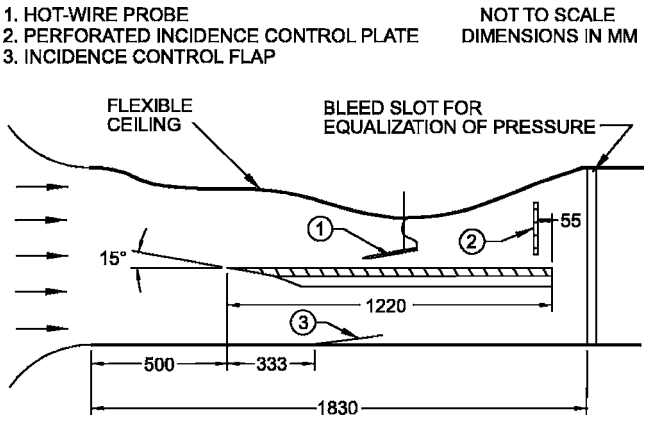

Fig. 1 Schematic of test section

sure gradients were imposed on the test surface using a contoured wall that forms the ceiling of the test section (Fig. 1). This test configuration has been used by the present research group extensively in studies of attached and separated boundary layers [3–5,23–25]. Boundary layer measurements were made at midspan of the test surface using a hot-wire anemometer with a single tungsten sensor of 5 μm dia and 1.3 mm length. The separation bubble and the upstream and downstream boundary layers were measured through wall-normal traverses at multiple streamwise locations, complemented by streamwise traverses performed within the separation-bubble region.

3 Numerical Method

3.1 Computational Domain and Boundary Conditions. The computational domain was selected to contain the measured separation bubble of ~125 mm length and is shown in Fig. 2. The domain width is 60 mm and was selected such that a turbulent spot generated at the experimental location of transition onset would span half the domain once it has convected to the experimental location of transition completion. The width of the turbulent spot was estimated based on Gostelow et al.'s [26] correlation for the spot spreading angle.

The experimental streamwise pressure distribution was imposed along the upper boundary of the computational domain, which was placed well within the freestream. The upper boundary was shaped such that fluid does not enter the domain through this boundary, allowing the use of the outflow boundary condition.

The domain inflow plane is located 400 mm downstream of the test-plate leading edge. This location is upstream of the suction peak and, therefore, allows for the growth of instabilities in the adverse-pressure-gradient boundary layer prior to separation. The prescribed inlet velocity profile is that measured in the experiment at the same streamwise location. The freestream turbulence and laminar boundary layer fluctuations associated with this measured velocity profile were not explicitly imposed on the inflow and freestream boundaries of the computational domain. Instead, the simulated freestream turbulence of 0.1% intensity was allowed to develop through round-off errors associated with the finite-precision computations. The turbulence intensity measured in the freestream flow over the separation bubble was 0.7%. Based on earlier experimental studies [24], the effect of this discrepancy between the measured and simulated freestream turbulence intensities on the transition process is expected to be small. The integral length scale associated with this simulated freestream turbulence is 20 mm, which is on the same order as the measured value of 40 mm. As well, the simulated freestream-turbulence frequency spectrum has a distribution similar to that of the experiment, albeit with a lower energy content.

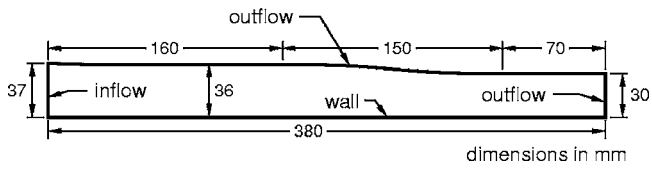

Fig. 2 Schematic of computational domain

The rear outflow boundary of the domain is situated ~150 mm downstream of the point of reattachment. An area-averaged constant static pressure condition was specified for this outflow boundary. The location of this boundary was chosen such that absence of a convective boundary condition, which allows for transient flow structures to leave the domain with minimal deformation, does not affect the flow field within and immediately downstream of the separation bubble.

No-slip smooth-wall conditions were specified along the lower boundary of the domain, and periodic flow conditions were imposed onto the two surfaces bounding the domain in the spanwise direction.

3.2 Solution Method. The simulations were performed using the ANSYS-CFX commercial CFD software package (version 5.7.1). Central differencing was used for discretization of the spatial derivatives, and time discretization was realized through second-order Euler backward differencing. Solutions of the continuity and momentum equations at each time step were converged through an algebraic multigrid scheme within eight iterations. The spatial and temporal resolutions summarized below were chosen such that the turbulence scales in the turbulent boundary layer downstream of the separation bubble are resolved down to about 40 times the Kolmogorov scale. Roberts and Yaras [22] demonstrated that this level of resolution is sufficient to perform coarse direct numerical simulations (DNS) of the transition process in separation bubbles, i.e., without explicit modeling of subgrid turbulence. Their simulation demonstrated good agreement with experiment with regard to the shape and extent of the separation bubble, the streamwise velocity spectra, and the laminar-to-turbulent breakdown process. The present simulations were therefore performed in this coarse DNS framework. However, the spatial and temporal resolution is comparable to those of other studies of similar flow phenomena for which the simulations have been referred to as DNS [27–29].

3.3 Spatial Grid. The domain shown in Fig. 2 was discretized using a structured grid of 381, 61, and 51 nodes in the streamwise, spanwise, and wall-normal directions, respectively. Equal node spacing of 1 mm was used in the streamwise and spanwise directions, and the nodes were distributed with an expansion factor of 1.1 in the wall-normal direction. Based on the turbulent boundary layer near the domain outlet, y^+ of the first node off the wall is about 0.6. The corresponding x^+ and z^+ value is 24. A grid refinement study was performed, whereby the spanwise spacing was refined to $z^+=16$, the streamwise spacing in the transition region was refined to $x^+=12$, and the nodes were clustered toward the separated shear layer. This refinement did not yield any significant changes in the characteristics of the separation bubble presented in this paper.

3.4 Simulation Time-Step and Simulation Duration. A time step of 0.2 ms was used for the simulation, which corresponds to a Courant number ($U\Delta t/\Delta x$) within the separated shear layer of ~1.0. The simulation was started on a two-dimensional grid to establish a separation bubble within ~1000 time steps, which was used as an initial condition for the three-dimensional domain. Approximately 2000 time steps were then required to reach the long-term values of the turbulence statistics, after which the simulation was continued for another 2048 time steps. The simulation required 2540 CPU hours to complete on a cluster of four Intel Pentium 4 processors. The presented results are based

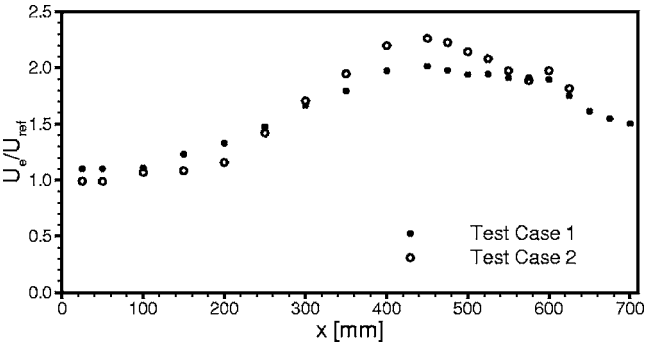

Fig. 3 Experimentally measured freestream velocity distributions

on the data of the last 2048 time steps, corresponding to 1280 CPU hours. From this data set, five evenly spaced x–y planes and two x–z planes of data were extracted at each time step for averaging and analysis.

4 Results and Discussion

The present discussion of the instability and transition processes observed in the simulated separation bubble is supplemented by experimental results from two sets of measurements. The measured freestream velocity distributions for these two cases are shown in Fig. 3. Test cases 1 and 2 respectively correspond to the Cp1 and Cp4 pressure distributions identified in earlier publications of this research group [5]. Test case 2 is noted to have a stronger initial acceleration and a stronger deceleration prior to separation, as compared to test case 1. The flow Reynolds number based on the length of the test plate and the midspan freestream velocity just downstream of the leading edge (x=25 mm) is 350,000, and the freestream turbulence intensity at the test-surface leading edge is 0.7%.

Table 1 Measured separation bubble characteristics

	Test case 1	Test case 2
x_s (mm)	498	525
L_b (mm)	127	100
$\mathrm{Re}_{\theta s}$	258	309
$\eta_{\min} \times 10^6$	−1.6	−2.3
f_{MA} (Hz)	170	200
f_{MA} (Eq. (1))	150	120
κd	0.40–0.44	0.34–0.41
$\mathrm{Sr}_{\theta s}$	0.0106	0.0110

Previously published [5] characteristics of the measured separation bubbles are summarized in Table 1. The momentum thickness Reynolds number based on conditions at the point of separation is fairly similar for the two cases. The time-averaged bubble length L_b is notably shorter in test case 2 due to the differences in the adverse pressure gradients imposed on the boundary layer, as demonstrated by the lowest observed values of the acceleration parameter upstream of separation ($\eta_{\min}$). Figure 4 presents measured velocity-fluctuation time traces at various streamwise locations through the separation bubble, at a fixed distance of 2 mm from the test surface. The streamwise coordinate used for comparison in Fig. 4 is the distance from the separation location, $x' = x - x_s$, normalized by the time-averaged length of the separation bubble L_b. In test case 2, presented in the right column of Fig. 4, a periodic wave motion is observed to develop slowly in the separated shear layer. The dominant frequency of this motion is ~200 Hz, which is somewhat larger than the value of 120 Hz predicted for the growth of T-S waves in the preseparated boundary layer through the correlation of Walker [30]

$$f_{\mathrm{MA}} = \frac{3.2 U_e^2}{2\pi\nu\,\mathrm{Re}_{\delta^*}^{3/2}} \tag{1}$$

A recent numerical study of test case 2 by Roberts and Yaras [22] demonstrated excellent agreement with experimental results with respect to the time-averaged size and shape of the separation bubble, the frequency spectra of streamwise velocity fluctuations, and the location of breakdown to turbulence. Roberts and Yaras

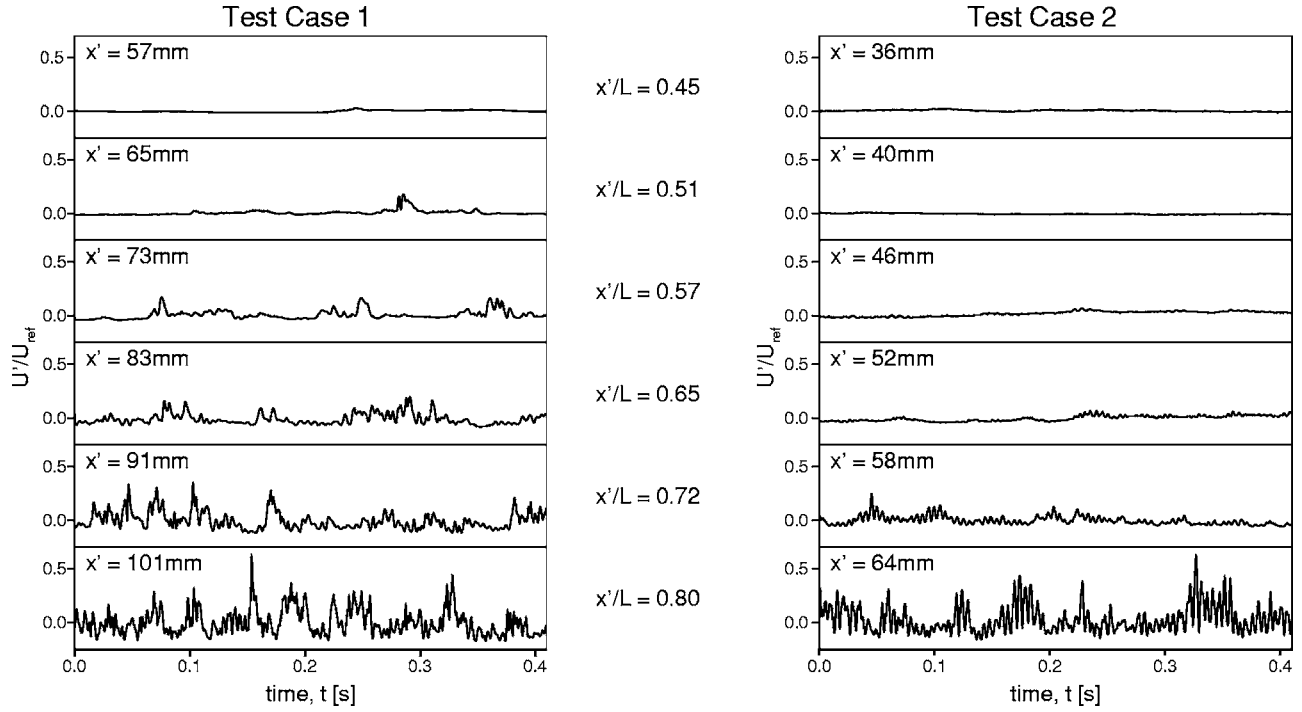

Fig. 4 Sample hot-wire velocity-fluctuation time traces

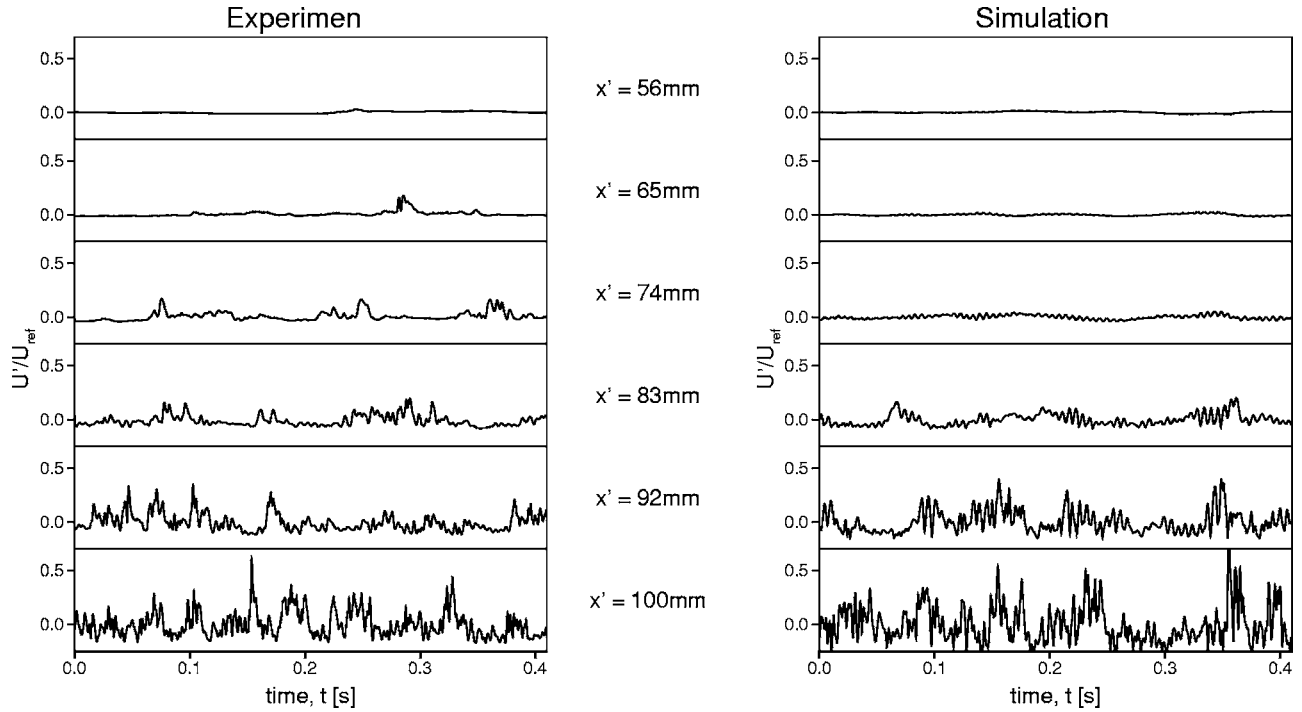

Fig. 5 Comparison of measured and computed velocity-fluctuation time traces for test case 1 (y=2 mm)

[22] used the same numerical scheme as for test case 1 described in the present paper. Through their simulation, the breakdown to turbulence noted in the range $0.72 \leq x'/L_b \leq 0.80$ in Fig. 4 was observed to be linked to the K-H instability. Specifically, transition to turbulence was noted to be associated with vortical structures that developed through roll up of the shear-layer vorticity near the downstream end of the separation bubble and shed downstream periodically. The frequency of vortex shedding was found to coincide with the frequency of maximum amplification rate of the T-S waves in the separated shear layer, raising the possibility of a coupling between the two instability mechanisms.

For test case 1, small-amplitude fluctuations are seen up to $x'/L_b=0.45$, as with test case 2. Beyond this point, the two test cases begin to differ, with isolated regions (packets) of amplified disturbances appearing more distinctly in the time traces of test case 1. The frequency of maximum amplification rate in these wave packets is ~170 Hz, which is in reasonable agreement with the correlation of Walker (Eq. (1)) for T-S waves, yielding a value of 150 Hz. The values of Chandrasekhar's stability parameter, κd, and the Strouhal number equivalent, $\mathrm{Sr}_{\theta s}$, are noted to be within the range of K-H instability in both test cases (Table 1). The present numerical simulation of test case 1 is intended to shed further light on the spatial and temporal development of the packets of strong T-S amplification, and on their role in the breakdown of the separated shear layer into turbulence.

Figure 5 presents the measured and computed velocity-fluctuation time traces at several locations along the separated shear layer for test case 1. The agreement between the two sets of velocity traces is good, with the exception of the packets of amplified velocity fluctuations appearing somewhat later in the simulation than in the experiment. The fact that the simulated freestream turbulence intensity was slightly lower than the measured value may explain this discrepancy. Measured and predicted frequency spectra of velocity fluctuations are given in Fig. 6 for several streamwise locations and compare favorably with the exception of more pronounced peaks at the dominant T-S frequency in the simulation. In both the measured and predicted spectra, the power spectral density at the high end of the frequency range is observed to remain relatively low until about $x'=101$ mm. This trend, and the fact that the growth rate of disturbances at the

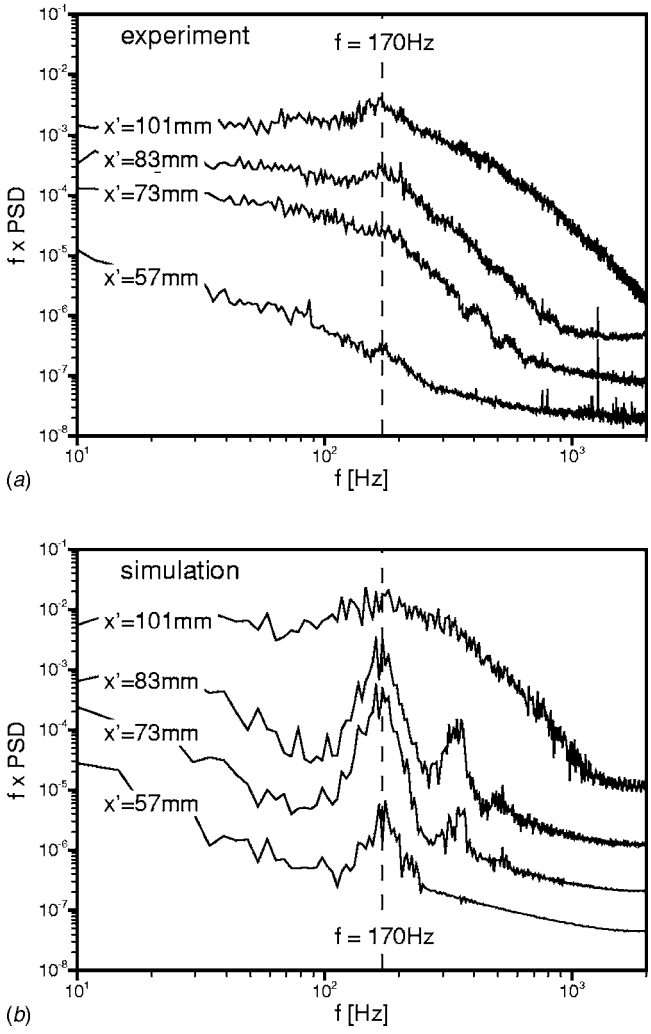

Fig. 6 Disturbance spectra in the separation bubble: (a) experiment and (b) simulation (test case 1)

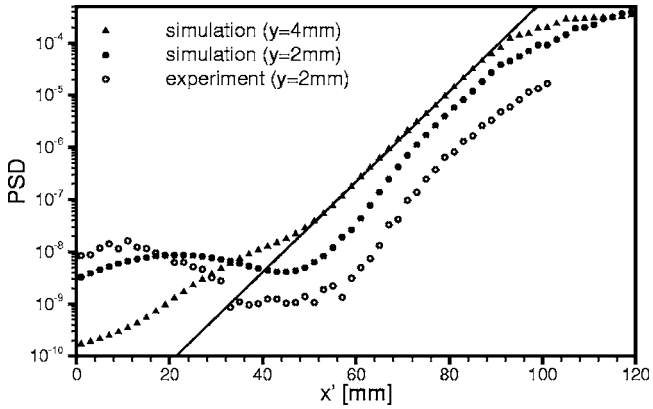

Fig. 7 Instability growth rates at the dominant frequency (test case 1)

dominant frequency remains close to linear until about $x'=90$ mm (Fig. 7), suggests that the isolated packets of high-amplitude velocity fluctuations observed in both measured and computed velocity time traces (e.g., $x'=83$ mm in Fig. 5) represent instability growth prior to breakdown into turbulence. To describe the physics associated with the subsequent amplification and damping of fluctuations within these packets, profiles of instantaneous streamwise velocity and $u'v'$ during a period of amplified instability at $x'=85$ mm are presented in Fig. 8 along with the velocity-fluctuation time traces at 2 mm and 4 mm from the surface. The profiles shown are associated with peaks and troughs of the velocity signal at 4 mm from the surface. At the start of the period shown in Fig. 8, the streamwise velocity profiles have relatively high levels of reverse flow (10–15% of edge velocity) with low levels of $u'v'$. The inherent instability of this velocity profile causes an increase in the amplitude of fluctuations and also results in the shear layer moving closer to the surface. The peaks of these amplified fluctuations are noted to correspond to large negative values of $u'v'$ in the region of highest vorticity, located near the velocity-profile inflection points, which facilitate cross-stream momentum exchange, resulting in a diminished reverse flow and, hence, reduced inflectional shape of the velocity profile. This modification of the velocity profile then leads to a reduction in the amplitude of the velocity fluctuations.

Given that the packets of T-S waves within the separated shear layer do not amplify to the point of bursting into turbulent spots, eventual breakdown into turbulence in the simulation of test case 1 occurs as the separated shear layer rolls up into vortical structures, as demonstrated in Fig. 9, which presents instantaneous velocity vector fields in x-y and x-z planes. The level of velocity fluctuation with respect to the local time-mean velocity magnitude is illustrated through vector shading. The presence of high-frequency velocity fluctuations is found to correlate with regions of high levels of shear that develop between pairs of spanwise oriented vortical structures, an example of which is evident at $x'=95$ mm in Fig. 9. The noted vortical structures are similar to those encountered in separation bubbles where the dominance of the K-H mechanism in the transition process is more certain, such as test case 2 [22]. This observation demonstrates the significance of K-H instability in the transition process even in instances of considerable amplification of T-S waves in separated shear layers.

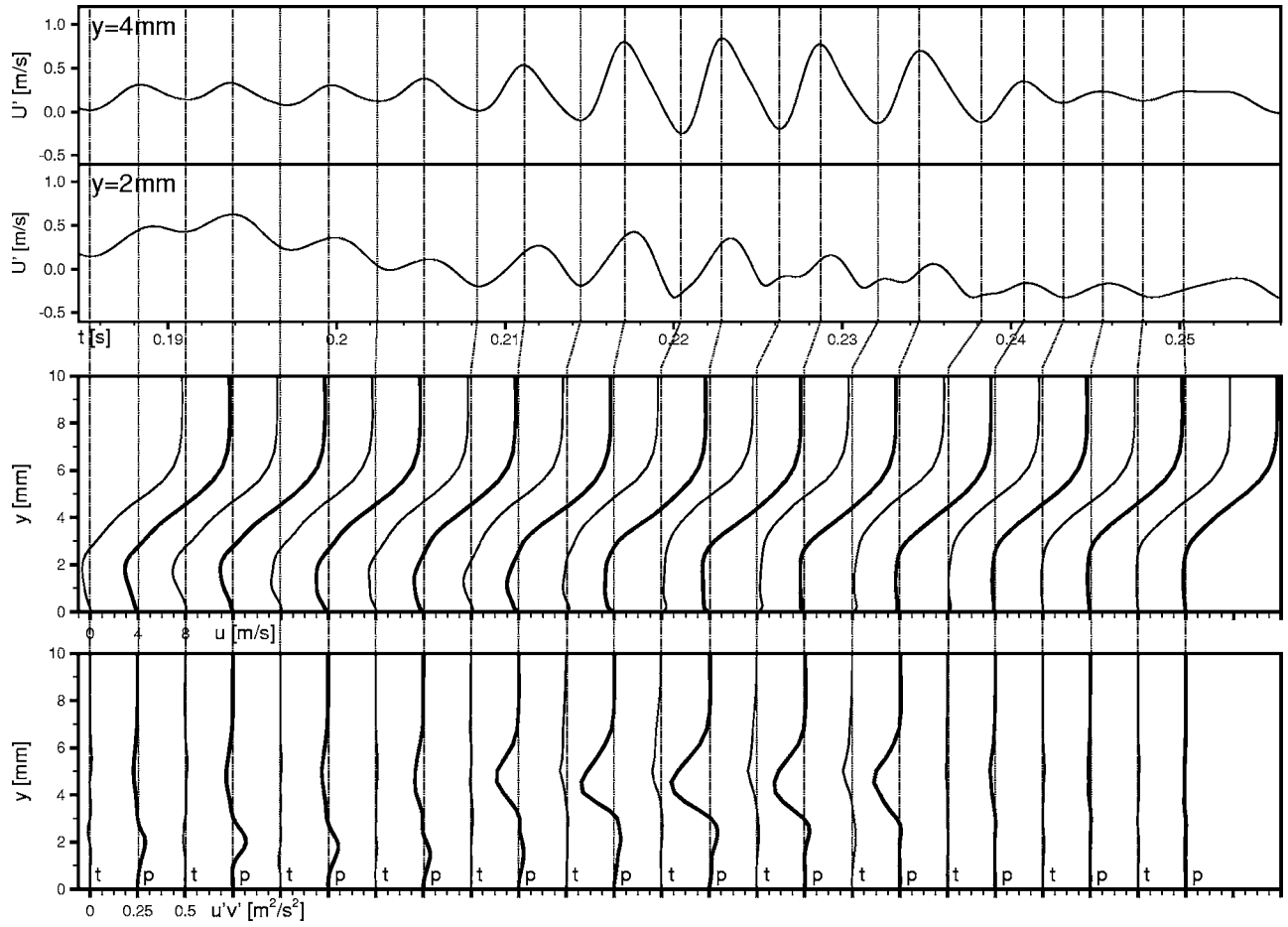

Fig. 8 Effects of instability growth on velocity profiles at $x'=85$ mm for test case 1 (p=peak, t=trough)

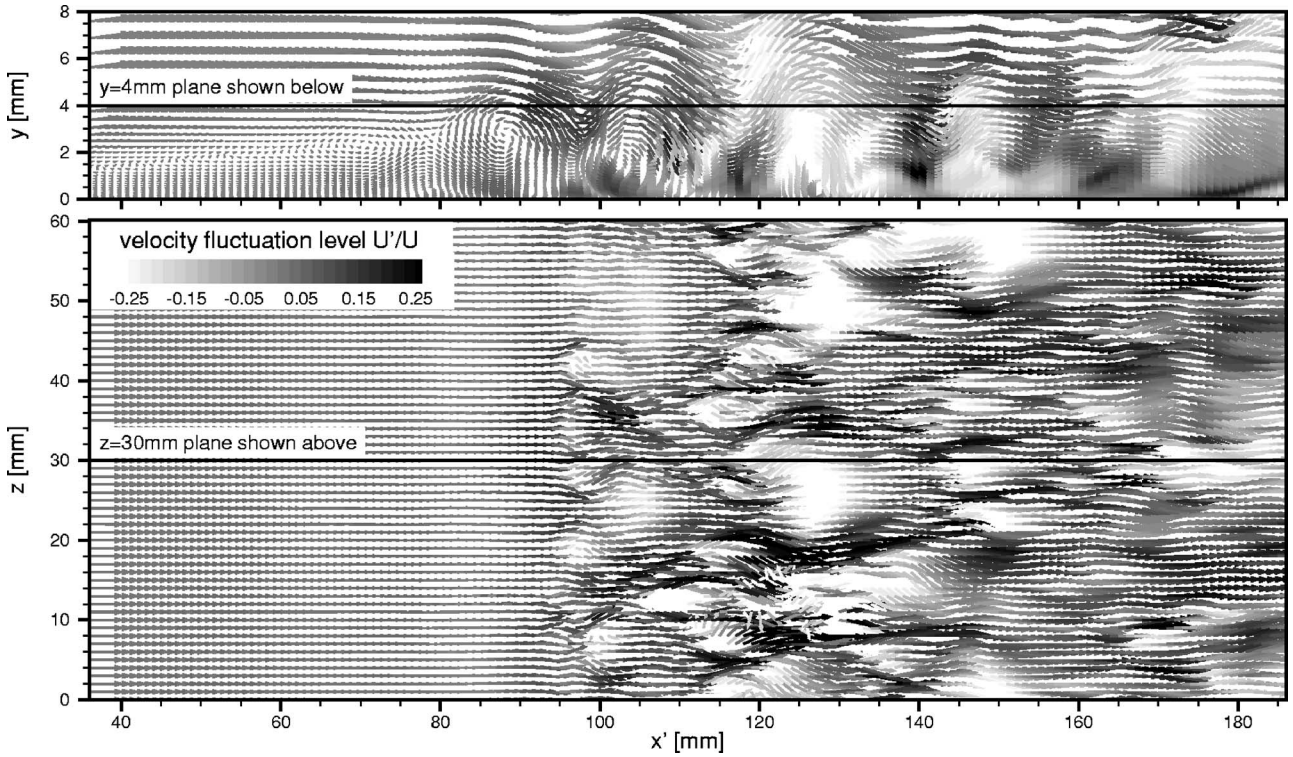

Fig. 9 Instantaneous vector field through the transition region of test case 1 (*x-y* plane at *z*=30 mm and *x-z* plane at *y*=4 mm)

As shown in Fig. 10, simulated streamwise velocity fluctuations are in reasonable agreement with experiment through the separation-bubble region. The velocity fluctuations upstream and downstream of reattachment are more dispersed and extend farther from the wall in the simulations. This is likely caused by the higher energy content about the T-S frequency (Fig. 6), which yields an overprediction of the power spectral density across the frequency spectrum downstream of breakdown into turbulence. The lower intensity of random fluctuations associated with the simulated freestream turbulence may have allowed for the greater concentration of energy about the T-S frequency.

Unlike the point measurements of streamwise velocity obtained with the hot-wire probe, the simulation results provide an opportunity to examine fluctuations in the spanwise and wall-normal directions as well as cross correlations of fluctuations of all three velocity components. These results are presented in Fig. 11. The uppermost plot in Fig. 11 presents the time-mean velocity field through the bubble region with correct streamwise–to–wall-normal proportions. All other plots in the Fig. 11 have a modified wall-normal scaling to allow better visualization of the bubble structure and distribution of the turbulence statistics. Streamlines through the bubble region are presented in the second plot from the top in Fig. 11, and show the displacement effect of the bubble on the freestream flow as well as the time-mean recirculation within the bubble. Fluctuation levels in the velocity field are shown in plots of velocity rms fluctuation (U_{rms}) and normal Reynolds stress components ($\overline{u'u'}$, $\overline{v'v'}$, $\overline{w'w'}$) in Fig. 11. All quantities are normalized by the freestream velocity at the streamwise location of separation (U_{es}). A double-peak distribution is present in U_{rms}, $\overline{u'u'}$, and $\overline{w'w'}$ in the aft part of the bubble, with the outer peak occurring along the line of maximum shear and the inner peak occurring along the line of maximum reverse flow within the time-averaged bubble region.The highest fluctuation levels are observed slightly downstream of the time-mean reattachment point. The double-peak profiles observed in these results are consistent with the predictions of Dovgal et al. [31], and Rist and Maucher [32] using linear stability theory. The rate of growth of wall-normal fluctuations ($\overline{v'v'}$) with streamwise distance reaching a peak along the rear portion of the time-mean dividing streamline of the separation bubble is consistent with the substantial cross-stream momentum exchange that should prevail in this

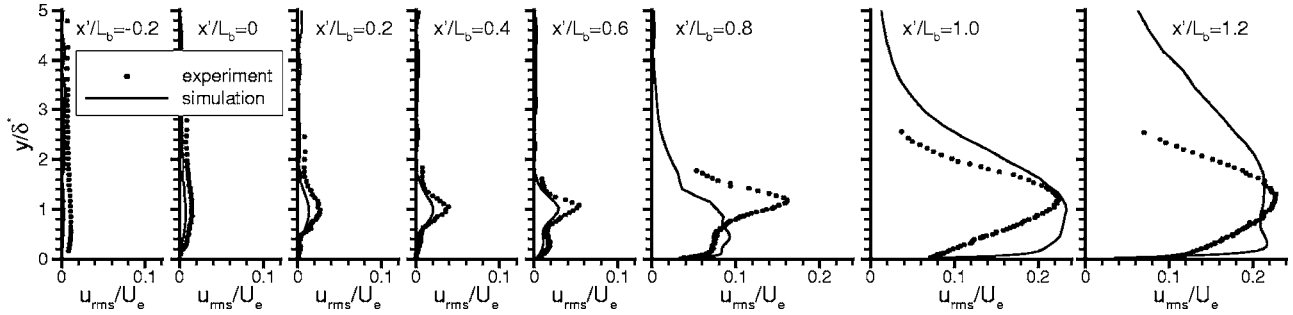

Fig. 10 Streamwise velocity fluctuation profiles in the separation-bubble region (test case 1)

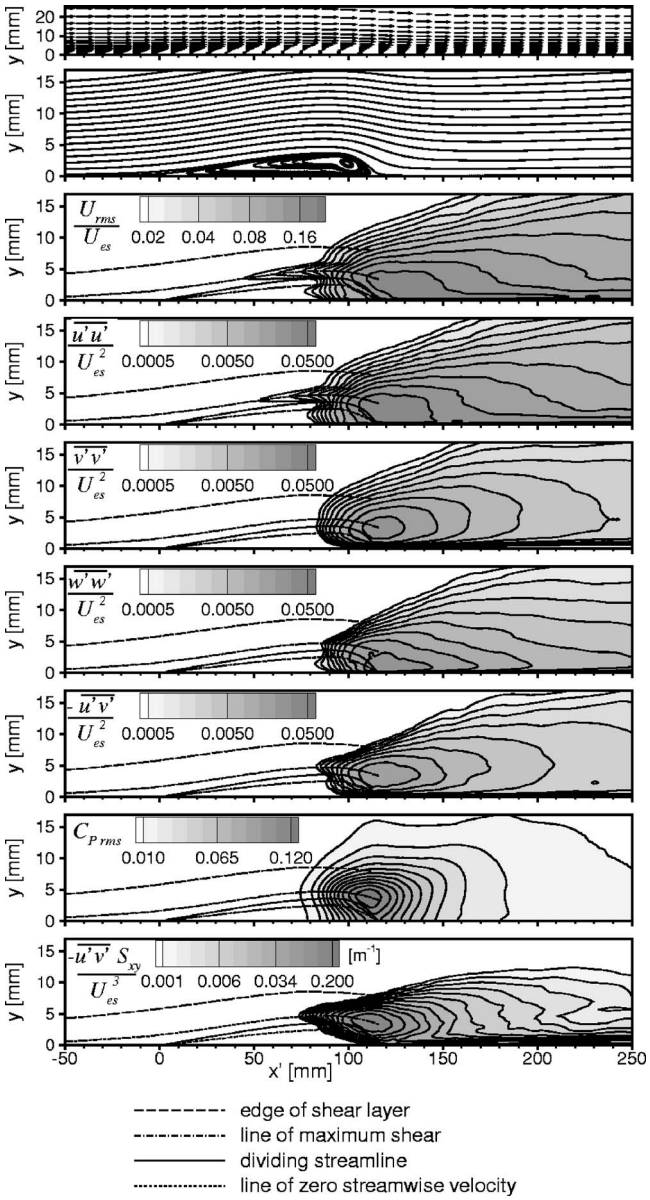

Fig. 11 Turbulence statistics for test case 1

region to reattach the separated shear layer. The peak value in $\overline{w'w'}$ is comparable to those in $\overline{u'u'}$ and $\overline{v'v'}$, which is consistent with the three-dimensional nature of the structures responsible for the turbulence, as illustrated in Fig. 9. As expected, the velocity fluctuations in the rear portion of the separation bubble and downstream of the reattachment point are accompanied by pressure fluctuations ($C_{P\mathrm{rms}}$). The pressure fluctuations are observed to decrease at a faster rate downstream of the reattachment point than the velocity fluctuations.

The effects of turbulence within a wall-bounded shear layer can be characterized by an increase in the net momentum transfer towards the wall due to turbulent mixing, for which the Reynolds shear-stress component $\overline{u'v'}$ is a measure. As observed in Fig. 11, this Reynolds stress component begins to increase within the rear portion of the separated shear layer at about $x'=80$ mm and peaks at the streamwise location of the time-mean reattachment point. Similar levels and distributions of $\overline{u'v'}$ were observed by Volino [6] and by McAuliffe and Yaras [18] in experiments of separation-bubble transition within a single-passage low-pressure turbine cascade and over a low-Reynolds-number airfoil, respectively. The energy transfer facilitated by the $\overline{u'v'}$ Reynolds shear stress component is quantified by $-\overline{u'v'}S_{xy}$, which is the work done by this shear stress on the time-mean flow field through the strain rate S_{xy}. This energy transfer is noted to reach its peak on the line of maximum shear, at the streamwise location of the time-mean reattachment point. Downstream of the reattachment point, the highest levels of $-\overline{u'v'}S_{xy}$ are observed close to the surface, which is a characteristic of turbulent boundary layers in which $-\overline{u'v'}S_{xy}$ is commonly referred to as the production of turbulent kinetic energy [1,33]. The fact that the magnitude of $-\overline{u'v'}S_{xy}$ begins to increase in the separated shear layer at about $x'=75$ mm, which is upstream of the location of breakdown into turbulence ($x'=90$ mm), suggests that the packets of amplified T-S waves observed within the separated shear layer are also instrumental in the cross-stream momentum exchange. The mechanism associated with this cross-stream momentum exchange was illustrated through instantaneous velocity profiles in Fig. 8.

5 Conclusions

Transition in a separation bubble has been examined through direct numerical simulation (DNS). The spatial and temporal resolutions correspond to a coarse DNS wherein turbulence scales down to the inertial subrange have been resolved. Good agreement has been achieved with experimental results obtained under the same flow conditions.

Linear instability growth is observed in the separated shear layer in the form of packets of wave activity, with a dominant frequency that corresponds to that of maximum Tollmien-Schlicting (T-S) instability growth rate within the boundary layer prior to separation. This T-S activity in the separated shear layer is followed by roll up of spanwise vorticity into discrete vortical structures, as is typical for the Kelvin-Helmholtz (K-H) instability. Both instabilities occur at the same frequency, which is consistent with the results of another test case with less pronounced T-S amplification in the separated shear layer, which was recently studied by this research group. The breakdown to turbulence is observed over a narrow streamwise extent and is demonstrated to occur in a time-periodic manner within a region of high shear that develops between pairs of roll-up vortices. Despite the dominance of the K-H instability mechanism in the ultimate breakdown into turbulence, which provides the cross-stream mixing for the reattachment of the separated shear layer, the packets of amplified T-S waves are demonstrated to contribute considerably to the cross-stream momentum exchange in the separated shear layer.

Acknowledgment

The authors gratefully acknowledge the financial support of Pratt & Whitney Canada in this project. The first author would also like to thank the Natural Sciences and Engineering Research Council of Canada for financial support through a postgraduate scholarship. Dr. J. E. D. Gauthier of Carleton University is also acknowledged for providing the computational resources for the simulation.

Nomenclature

C_P = pressure coefficient $=(P-P_{es})/0.5\rho U_{es}^2$
d = characteristic length of tanh velocity profile $=2\theta$
f = frequency
L_b = separation bubble length $=x_r-x_s$
P = static pressure
S_{xy} = x-y component of strain rate tensor $=\frac{1}{2}((\partial u/\partial y)+(\partial v/\partial x))$
$\mathrm{Sr}_{\theta s}$ = instability Strouhal number $=f_{\mathrm{MA}}\theta_s/U_{es}$
t = time
U = velocity magnitude
U_0 = characteristic velocity of tanh velocity profile

u = x-velocity component
v = y-velocity component
w = z-velocity component
x = streamwise coordinate (=0 mm at test surface leading edge)
x' = separation-referenced streamwise coordinate $=x-x_s$
y = wall-normal coordinate (=0 mm on test surface)
z = spanwise coordinate (=381 mm at midspan of test surface)
Re_{δ^*} = displacement thickness Reynolds number $=U_e\delta^*/\nu$
Re_θ = momentum thickness Reynolds number $=U_e\theta/\nu$
δ^* = displacement thickness
η = acceleration parameter $=(\nu/U_e^2)(dU_e/dx)$
κ = wave number $=2\pi/\Lambda$
Λ = wavelength
ν = kinematic viscosity
ρ = density
θ = momentum thickness

Subscripts

e = boundary layer edge
MA = maximum amplification rate
min = minimum value observed upstream of separation
r = reattachment
ref = reference condition ($x=25$ mm, $y=25$ mm, at midspan of test surface)
rms = root mean square
s = separation

Superscripts

$+$ = wall-scale coordinate
$'$ = fluctuation quantity
$\overline{a}$ = time-mean quantity of variable a

Acronyms

DNS = direct numerical simulation
K-H = Kelvin-Helmholtz
PSD = power spectral density
T-S = Tollmien-Schlichting

References

[1] Schlichting, H., and Gersten, K., 2000, *Boundary Layer Theory*, 8th ed., Springer-Verlag, Berlin.
[2] Mayle, R. E., 1991, "The Role of Laminar-Turbulent Transition in Gas Turbine Engine," ASME J. Turbomach., **113**, pp. 509–537.
[3] Roberts, S. K., and Yaras, M. I., 2003, "Effects of Periodic Unsteadiness, Free-Stream Turbulence and Flow Reynolds Number on Separation-Bubble Transition," ASME Paper No. GT2003-38626.
[4] Roberts, S. K., and Yaras, M. I., 2005, "Boundary-Layer Transition Affected by Surface Roughness and Free-Stream Turbulence," ASME J. Fluids Eng., **127**, pp. 449–457.
[5] Roberts, S. K., and Yaras, M. I., 2006, "Effects of Surface Roughness Geometry on Separation-Bubble Transition," ASME J. Turbomach., **128**, pp. 349–356.
[6] Volino, R. J., 2002, "Separated Flow Transition Under Simulated Low-Pressure Turbine Airfoil Conditions—Part 1: Mean Flow and Turbulence Statistics," ASME J. Turbomach., **124**, pp. 645–655.
[7] Volino, R. J., 2002, "Separated Flow Transition Under Simulated Low-Pressure Turbine Airfoil Conditions—Part 2: Turbulence Spectra," ASME J. Turbomach., **124**, pp. 656–664.
[8] Volino, R. J., and Murawski, C. G., 2003, "Separated-Flow Transition in a Low Pressure Turbine Cascade—Mean Flow and Turbulence Spectra," ASME Paper No. GT2003-38727.
[9] Volino, R. J., and Bohl, D. G., 2004, "Separated Flow Transition Mechanism and Prediction with High and Low Freestream Turbulence Under Low Pressure Turbine Conditions," ASME Paper No. GT2004-53360.
[10] Huang, L. S., and Ho, C. M., 1990, "Small-Scale Transition in a Plane Mixing Layer," J. Fluid Mech., **210**, pp. 475–500.
[11] Estevadeordal, J., and Kleis, S. J., 1999, "High-Resolution Measurements of Two-Dimensional Instabilities and Turbulence Transition in Plane Mixing Layers," Exp. Fluids, **27**, pp. 378–390.
[12] Malkiel, E., and Mayle, R. E., 1996, "Transition in a Separation Bubble," ASME J. Turbomach., **118**, pp. 752–759.
[13] Muti Lin, J. C., and Pauley, L. L., 1996, "Low-Reynolds-Number Separation on an Airfoil," AIAA J., **34**, pp. 1570–1577.
[14] Watmuff, J. H., 1999, "Evolution of a Wave Packet Into Vortex Loops in a Laminar Separation Bubble," J. Fluid Mech., **397**, pp. 119–169.
[15] Spalart, P. R., and Strelets, M. K., 2000, "Mechanisms of Transition and Heat Transfer in a Separation Bubble," J. Fluid Mech., **403**, pp. 329–349.
[16] Yang, Z., and Voke, P. R., 2001, "Large-Eddy Simulation of Boundary-Layer Separation and Transition at a Change of Surface Curvature," J. Fluid Mech., **439**, pp. 305–333.
[17] Abdalla, I. E., and Yang, Z., 2004, "Numerical Study of the Instability Mechanism in Transitional Separating-Reattaching Flow," Int. J. Heat Fluid Flow, **25**, pp. 593–605.
[18] McAuliffe, B. R., and Yaras, M. I., 2005, "Separation-Bubble-Transition Measurements on a Low-Re Airfoil Using Particle Image Velocimetry," ASME Paper No. GT2005-68663.
[19] Chandrasekhar, S., 1961, *Hydrodynamic and Hydromagnetic Stability*, Clarendon Press, Oxford.
[20] Talan, M., and Hourmouziadis, J., 2002, "Characteristic Regimes of Transitional Separation Bubbles in Unsteady Flow," Flow, Turbul. Combust., **69**, pp. 207–227.
[21] Ripley, M. D., and Pauley, L. L., 1993, "The Unsteady Structure of Two-Dimensional Steady Laminar Separation," Phys. Fluids A, **5**, pp. 3099–3106.
[22] Roberts, S. K., and Yaras, M. I., 2006, "Large-Eddy Simulation of Transition in a Separation Bubble," ASME J. Fluids Eng., **128**, pp. 232–238.
[23] Yaras, M. I., 2001, "Measurements of the Effects of Pressure-Gradient History on Separation-Bubble Transition," ASME Paper No. 2001-GT-0193.
[24] Yaras, M. I., 2002, "Measurement of the Effects of Freestream Turbulence on Separation-Bubble Transition," ASME Paper No. GT-2002-30232.
[25] Roberts, S. K., and Yaras, M. I., 2005, "Modeling Transition in Separated and Attached Boundary Layers," ASME J. Turbomach., **127**, pp. 402–411.
[26] Gostelow, J. P., Melwani, N., and Walker, G. J., 1996, "Effects of Streamwise Pressure Gradients on Turbulent Spot Development," ASME J. Turbomach., **118**, pp. 737–743.
[27] Na, Y., and Moin, P., 1998, "Direct Numerical Simulation of a Separated Turbulent Boundary Layer," J. Fluid Mech., **374**, pp. 379–405.
[28] Alam, M., and Sandham, N. D., 2000, "Direct Numerical Simulation of 'Short' Laminar Separation Bubbles With Turbulent Reattachment," J. Fluid Mech., **403**, pp. 223–250.
[29] Kalitzin, G., 2003, "DNS of Fully Turbulent Flow in a LPT Passage," Int. J. Heat Fluid Flow, **24**, pp. 636–644.
[30] Walker, G. J., 1989, "Transitional Flow On Axial Turbomachine Blading," AIAA J., **27**, pp. 595–602.
[31] Dovgal, A. V., Kozlov, V. V., and Michalke, A., 1994, "Laminar Boundary Layer Separation: Instability and Associated Phenomena," Prog. Aerosp. Sci., **30**, pp. 61–94.
[32] Rist, U., and Maucher, U., 2002, "Investigations of Time-Growing Instabilities in Laminar Separation Bubbles," Eur. J. Mech. B/Fluids, **21**, pp. 495–509.
[33] Panton, R. L., 2001, "Overview of the Self-Sustaining Mechanisms of Wall Turbulence," Prog. Aerosp. Sci., **37**, pp. 341–383.

Improving Film Cooling Performance Using Airfoil Contouring

Atul Kohli
Pratt & Whitney,
400 Main Street, M/S 165-16,
East Hartford, CT 06108
e-mail: atul.kohli@pw.utc.com

David G. Bogard
Mechanical Engineering Department,
The University of Texas,
Austin, TX 78713
e-mail: dbogard@mail.utexas.edu

In this study, a computational fluid dynamics (CFD)-based optimization process is used to change the contour of the airfoil near a suction-side cooling hole in order to improve its film effectiveness characteristics. An overview of the optimization process, which includes automated geometry, grid generation, and CFD analyses, is provided. From the results for the optimized geometry, it is clear that the detachment of the cooling jet is much reduced and the cooling jet spread in the spanwise direction is increased substantially. The new external contour was then tested in a low-speed wind tunnel to provide a direct measure of the predictive capability. Comparisons to verification test data indicate that good agreement was achieved for both pressure and film cooling effectiveness behavior. This study proves that despite its limitations, current Reynolds averaged Navier-Stokes (RANS) methodology can be used a viable design tool and lead to innovative concepts for improving film cooling effectiveness. [DOI: 10.1115/1.2750681]

Introduction

Advancements in film cooling technology have been key in enabling higher combustor exit temperatures required for improved performance of gas turbine engines. Significant advances in film cooling technology have come about as a result of hole shaping. A lot of experimental research over the past few decades focused on film effectiveness measurements to quantify the effects of governing geometry and flow parameters, a review of which can be found in Bunker [1].

The majority of experimental data available in literature is for film cooling on a flat plate. These studies have provided invaluable understanding of the complex flow phenomena that exist in film cooling flows by being able to vary governing parameters in a controlled manner. For example, the study by Pedersen et al. [2], three decades ago, showed the effect of density ratio on film effectiveness using foreign gas injection. More recently, the study of Gritsch et al. [3] studied the effect of internal cross-flow and hole shape using a single hole on a flat plate with high Mach number flow. Increasingly, experimental studies on film cooling are being reported on engine relevant geometry and conditions. For example, Ganzert et al. [4] made effectiveness and aerodynamic loss measurements on the suction side of an airfoil at realistic Mach numbers.

CFD capabilities and speed have also improved over the years. Zerkle and Leylek [5] clearly showed the importance of modeling both the plenum and cooling for good film effectiveness predictions. This study and that by Kohli and Thole [6] showed that RANS, when used with a two-equation turbulence model, typically overpredicts the film effectiveness at the centerline of the cooling jet and underpredicts the amount of lateral spreading that leads to merging of cooling jets from a row of cooling holes. This deficiency of RANS CFD with two-equation models has been echoed by other researchers and led them to focus on better turbulence models, LES, and time-accurate calculations. However, despite its limitations, RANS remains the method of choice especially in a turbine design environment over higher fidelity methods that are computationally intensive.

Contributed by the International Gas Turbine Institute of ASME for publication in the JOURNAL OF TURBOMACHINERY. Manuscript received July 13, 2006; final manuscript received August 24, 2006; published online February 12, 2008. Review conducted by David Wisler. Paper presented at the ASME Turbo Expo 2006: Land, Sea and Air (GT2006), May 8–11, 2006, Barcelona, Spain.

Although most film cooling research has been directed at finding hole shapes that improve effectiveness, this study focuses on the external shape of the airfoil in conjunction with film cooling. To the authors knowledge, there have been no reported studies in the literature that have performed a coupled aerothermal optimization. This study is an example of where an optimization process resulted in a novel concept that was patented by Kohli et al. [7].

In this study, a CFD-based optimization process is used to change the contour of the airfoil near a cooling hole to improve the film effectiveness without increasing the aerodynamic mixing losses. An overview of the optimization process, automated geometry, grid generation, and CFD analyses is provided. A round film cooling hole on the suction side of a vane, which has been well documented in previous low speed tests by Ethridge et al. [8], was used for this investigation. The new external contour that was predicted to improve film cooling effectiveness was then tested in the low-speed wind tunnel. Comparisons to verification test data show that despite its limitations RANS-based CFD can be used as an effective design tool for film cooling applications.

Airfoil Shape Optimization Process

In order to meet the stringent life requirements for future turbine airfoils, it is important to have a physics-based design system in place that can be used to predict the behavior of new cooling schemes. As part of this effort, this study used computer-based optimization methods to optimize a suction-side film cooling configuration using CFD. A key aspect of this program is the parametric definition of the cooling hole geometry in order to completely automate the geometry and grid generation process to allow integration with an optimizer as seen in Fig. 1.

The optimization software used for this study was iSIGHT®, which is commercially available. All the geometry parameters describing the problem, which included the airfoil and the cooling hole, were inputs to the process. Using the parametric input, geometry and mesh generation was automated using a commercial geometry and meshing tool called ICEM®. The Pratt & Whitney in-house CFD code was then used to solve each configuration and provide results for the objective functions (film effectiveness and pressure loss) that were used to rank different configuration. A gradient-based technique called MMFD (modified method of feasible directions) was used to arrive at the optimum parameters defining the airfoil contour for maximum film effectiveness. β-spline parameters both upstream and downstream of the cooling

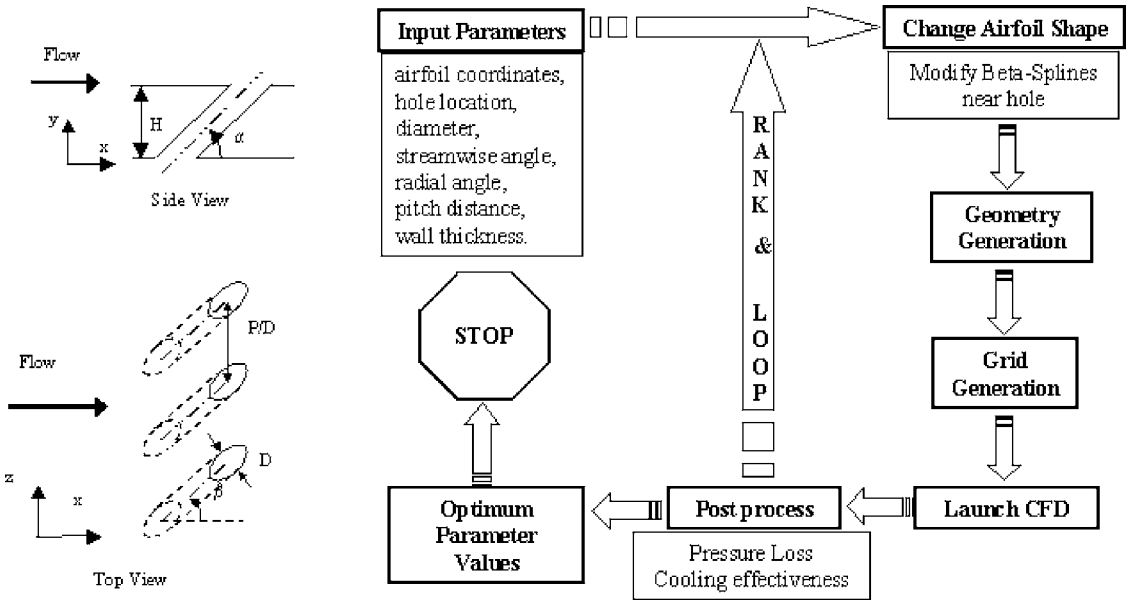

Fig. 1 Schematic of the parametric definition of the cooling hole and flowchart of the optimization process

hole were perturbed during the optimization. The overall pressure loss and average effectiveness was monitored for each configuration. Since negligible changes were observed in the pressure loss at such low Mach number conditions, the objective of the optimization run was limited to increasing cooling effectiveness. The average effectiveness was calculated over a region that covered one hole pitch and extended 20 diameters downstream of the cooling hole. The pressure in the plenum was fixed such that the cooling holes were operating at a blowing ratio of $M \sim 0.85$.

This study used Pratt & Whitney's, multiblock, structured 3D RANS code described collectively by Ni [9], Ni and Bogoian [10] and Davis et al. [11]. Numerical closure for turbulent flow is obtained via the k-ω turbulence model as described by Wilcox [12]. The code is accurate to second order in space and time, and multigrid techniques were used to obtain rapid convergence. The CFD model included all the details of the cooling hole geometry. Flow through the supply plenum, cooling hole and main gas path are all part of the calculation, as shown in Fig. 2. For the main flow-path inlet, the total pressure and total temperature were specified. At the exit, the appropriate static pressure was specified. Coolant total pressure and temperature were specified at the inlet to the plenum. A turbulence level of 1% was specified at both the flow-path and plenum inlets. Periodic conditions were specified in the spanwise direction to simulate a row of cooling holes.

A structured multiblock mesh topology was used for this problem with attention to boundary layers consistent with the use of a low Reynolds number k-ω turbulence model. Both the airfoil and cooling hole were meshed using a O-H topology. A total of 686,400 grid points were used for this study. The grid counts used in the main flowpath were $231 \times 33 \times 37$ in the H sector and $165 \times 25 \times 37$ in the O sector in the streamwise (x), pitchwise (y), and spanwise (z) directions, respectively. The plenum used a $49 \times 33 \times 37$ grid in the x, y, and z directions, respectively. The H mesh in the cooling hole had dimensions of $33 \times 17 \times 13$ along the flow direction, major axis, and minor axis, respectively. In addition, the O mesh used in the cooling hole to resolve the boundary layers had 13 grid points in the wall-normal direction. Figure 3 shows the mesh near the cooling hole. The viscous grid provides near-surface values of y^+ of the order 1 on no-slip boundaries and ~ 7 grid points per momentum thickness. Mesh independence was verified for this mesh configuration with prior studies using very similar airfoil and film cooling configurations. Keep in mind that, in order to rank configurations, the optimization procedure uses only the change in the calculated objective for each configuration. Therefore, in order to complete the optimization in a reasonable time, each solution was run for a fixed number of iterations.

The low-speed cascade geometry was redesigned by performing the airfoil shape optimization for low-speed conditions. The cooling configuration for the baseline geometry consists of five showerhead, two pressure-side, and three suction-side rows of holes as documented by Polanka et al. [13]. The current study optimized the airfoil surface for the first row of suction-side holes

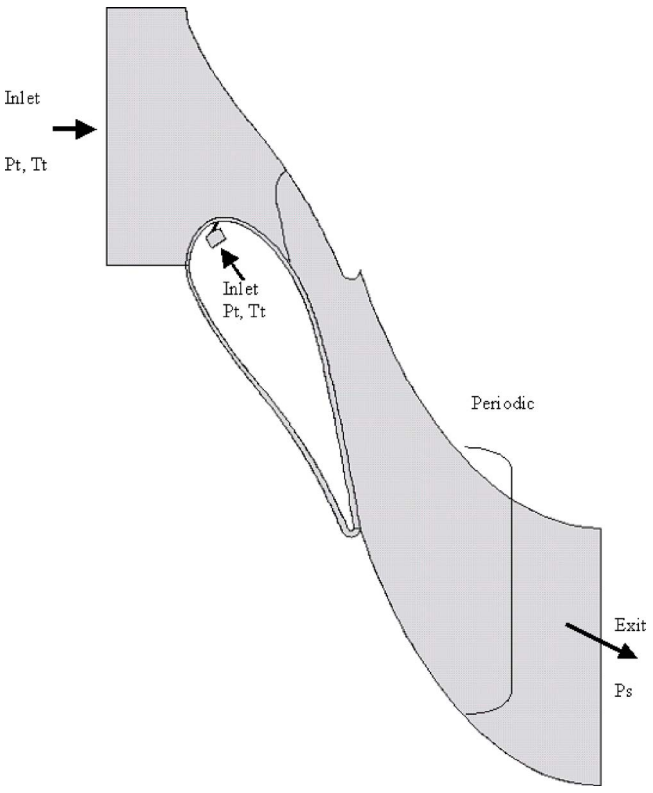

Fig. 2 Schematic of computational domain with boundary conditions

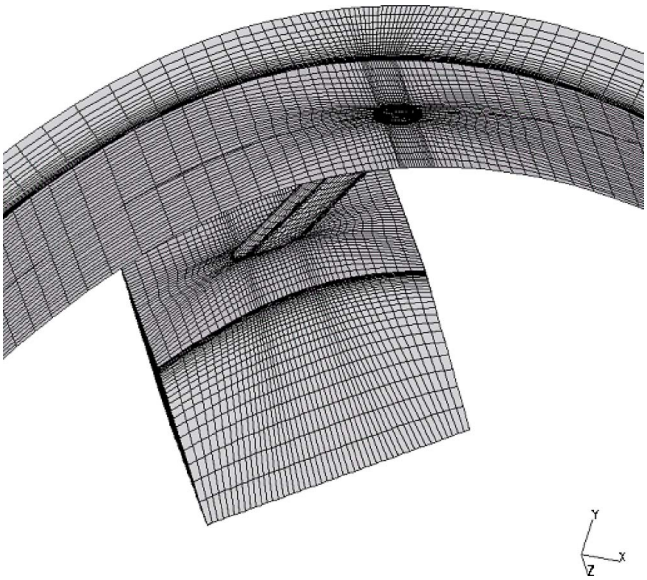

Fig. 3 Mesh near the film cooling hole

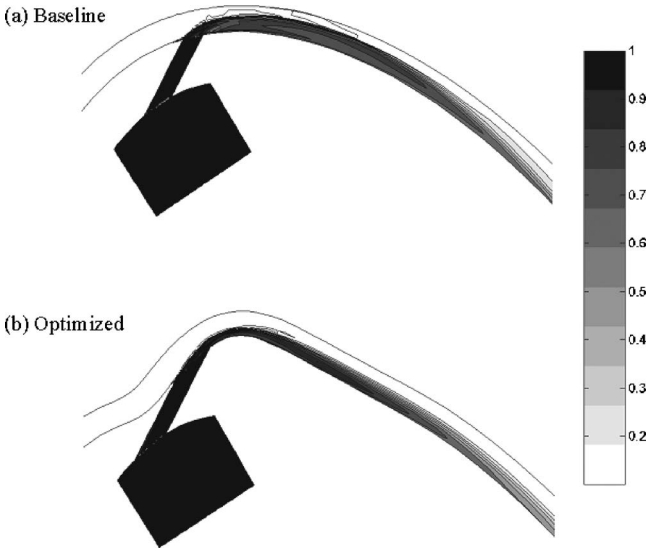

Fig. 5 Centerline temperature contours for (*a*) baseline and (*b*) optimized geometry show how the optimized airfoil contour changed the trajectory of the cooling jet

that are purely axial with a 50 deg surface angle that have a pitchwise spacing of $P/D=5.5$ and are located at $x/C=0.16$. Figure 4 shows the optimization history, with the average effectiveness for each run. The calculations were performed in parallel on four SUN Ultra60 machines. Each configuration took about 8 h of wall time, and the whole optimization process took several weeks of run time as 64 configurations were analyzed. As shown in Fig. 4, the average effectiveness of the optimized airfoil shape was predicted to be ~6% better than the baseline.

To explain the increase in effectiveness for the optimum geometry compared to the baseline, temperature contours along the hole centerline of the two cases are shown in Fig. 5. The change in the airfoil shape and its effect on the trajectory of the film cooling jet is clearly evident by looking at the results for the optimum geometry. Because the cooling jet has a lower trajectory, it does not disperse as rapidly thereby improving its cooling effectiveness. Remember that the cooling holes for this row are inclined at 50 deg to the surface and, due to the change in airfoil shape, behave equivalent to cooling holes at shallower angles. The contour of the optimized airfoil shows a slight depression with respect to the nominal shape upstream of the cooling hole. Downstream of the hole, the optimized contour extends beyond the nominal shape to cause a slight "bump." These changes in geometry increase the amount of local convex curvature and the Coanda effect experienced by the cooling flow immediately downstream of the injection location. There is also a corresponding and significant increase in the acceleration of the main flow (discussed in the next section) as it moves past the cooling hole. Therefore, the film cooling jet trajectory is shallower for the optimized contour.

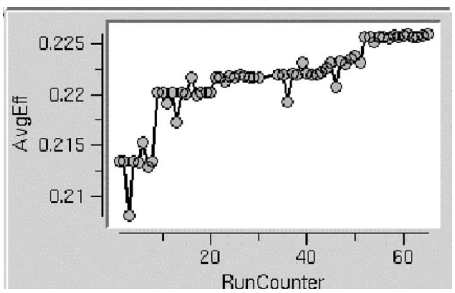

Fig. 4 Optimization history showing average effectiveness of each configuration

To see what effect the change in trajectory of the film cooling jet has on surface effectiveness, please see Fig. 6, which shows the results for both baseline and optimized geometry. For the baseline geometry, the effectiveness contours indicate warmer temperature immediately downstream of the cooling hole and colder temperatures further downstream. This behavior is consistent with a slight detachment and reattachment of the cooling jet for the baseline geometry and is expected because of the steep injection angle and reasonably high blowing ratio. From the surface effectiveness results for the optimized geometry, it is clear that the detachment of the cooling jet is much reduced and the coldest temperatures now occur near the cooling hole. In addition, the cooling jet is spread substantially more in the spanwise direction. Thus, not only is the optimized contour helping change the trajectory of the film cooling jet, it is also causing enhanced spreading the in the lateral direction. Given the fact that, due to manufacturing and design constraints, film cooling holes are operated at suboptimum conditions, these predictions suggest that airfoil contouring can be used to improve their performance.

To provide a direct measure of the predictive capability, an experimental validation was undertaken and is described in the next section. As a reminder, based on what we know from literature, these predictions have many limitations and may not provide very good quantitative answers. However, the question that this

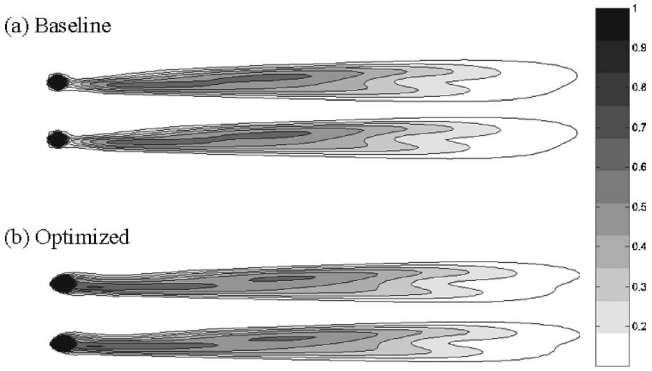

Fig. 6 Surface temperature contours for the (*b*) optimized geometry indicate reduced detachment and increased spreading compared to the (*a*) baseline

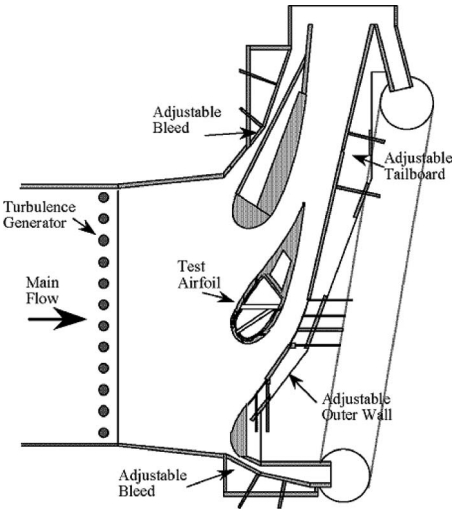

Fig. 7 Schematic of the low-speed cascade test facility

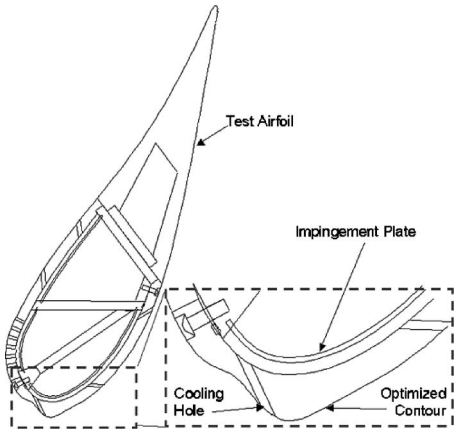

Fig. 8 Detailed view of the test airfoil

study is trying to answer is: Can we use RANS CFD to make engineering decisions based on ranking film cooling configurations? Or, will this approach mislead us because of all its limitations?

Experimental Validation of Optimized Shape

The airfoil shape optimized for the first row of suction-side holes was tested in the low-speed cascade at the University of Texas. Adiabatic effectiveness tests were conducted for the first row of holes on the suction side of the vane for the baseline geometry and the optimized geometry to provide a direct validation of the predictions. Experiments were conducted using cryogenically cooled air to obtain a density ratio for the coolant of DR=1.6. Figure 7 shows a schematic of the cascade facility that has been documented by Polanka et al. [13]. The cascade consists of a central test airfoil and two periodic passages. Periodicity is achieved by adjusting the bleeds, sidewalls, and tailboards shown in the schematic to achieve the target pressure distribution on the central test airfoil and by locating the stagnation point correctly on the adjacent leading edges. There is a turbulence generator capable of producing engine-relevant turbulence levels of 20%. The tests reported in this study were conducted with low mainstream turbulence of nominally Tu=0.5%. Viewing ports in the side, top, and bottom walls allow surface temperature measurements on the test airfoil using a IR camera. The uncertainty in effectiveness (95% confidence interval) was $\partial\eta = \pm 0.04$ for $M > 0.4$, $\partial\eta = \pm 0.02$ for $M < 0.4$, and $\partial\bar{\eta} = \pm 0.02$ for all $\bar{\eta}$.

Key dimensions and aerodynamic conditions associated with the test airfoil are tabulated in Table 1. The airfoil is scaled up a factor of nine from engine scale, and exit conditions are set to match engine-relevant Reynolds number. A detailed view of the test airfoil with the optimized suction side contour is shown in Fig. 8. The showerhead, suction side, and pressure side cooling holes have separate plenums to allow independent control of blowing parameters on different parts of the airfoil. The showerhead and pressure-side holes were not used in these tests, and these holes were taped over. A range of blowing ratios were tested, including blowing ratios below and above the blowing ratio that provided maximum adiabatic effectiveness.

Table 1 Characteristic dimensions and test conditions

Axial Chord	29.3 cm
Span	54.9 cm
Inlet Mach number	0.012
Exit Mach number	0.085
Exit Reynolds number	1.06×10^6

For these tests, coolant was supplied to all three rows of holes on the suction side, and the total flow rate to all three rows of holes was measured. The local blowing ratio for the first row of holes was determined using previously established correlations for the fraction of flow coming from different rows of holes at a given plenum pressure. Measurements of the surface temperature were made with an IR camera from upstream of the first row of holes to about 20D downstream (just before the second row of holes). Three holes were imaged near the center of the array of holes on the test airfoil. Lateral averages were calculated over two pitches between holes.

Figure 9 shows the predicted pressure distribution for the optimized airfoil shape compared to test data. The CFD predictions were used to guide the placement of the pressure taps for the test so as to capture the areas of strong acceleration near the cooling hole induced by the change in airfoil shape. As seen in Fig. 9, the predictions agree well with the data. For reference, the cooling hole is located at an axial chord of 1.9 in. It is clear from the pressure distribution that the airfoil contour decelerates the flow upstream of the cooling hole. It then causes the flow to accelerate significantly as it goes by the cooling hole. It is this significantly strong acceleration that changes the trajectory of the detached cooling jet. Remember that this acceleration comes about due to an increase in the convex curvature. Although there is a significant region further downstream where the flow then decelerates back to the nominal pressure distribution, but this does not cause any flow separation. Once the cooling jet is attached to the surface due to the acceleration and the convex curvature, it is able to with-

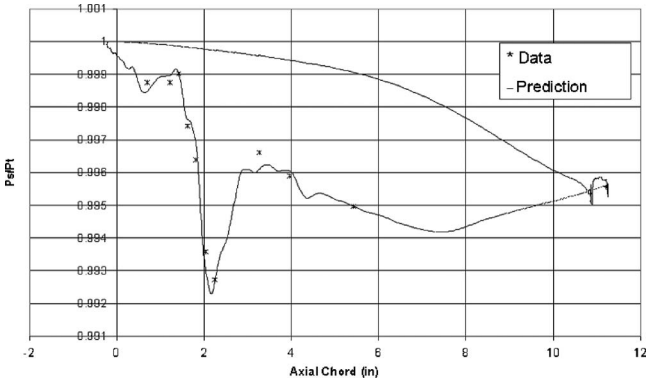

Fig. 9 Comparison of the predicted and measured pressure distribution between cooling holes for the optimized geometry

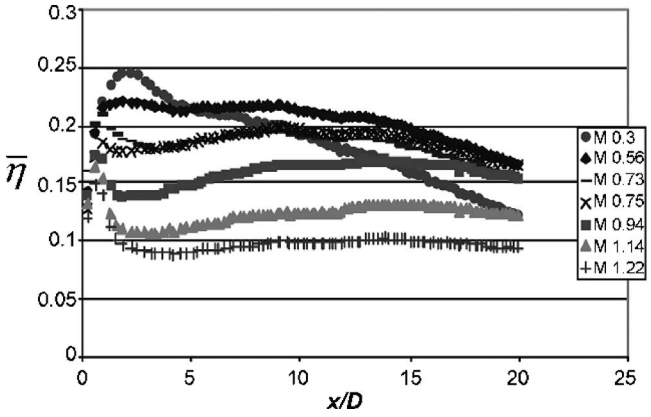

Fig. 10 Laterally averaged effectiveness for the baseline airfoil at various blowing ratios

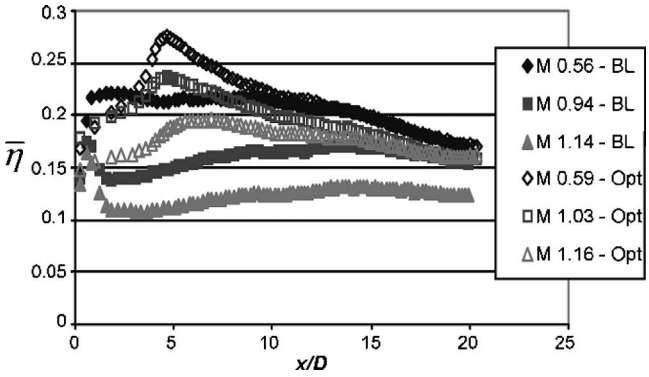

Fig. 12 Average effectiveness of baseline and optimized geometries for three different blowing ratios

stand an adverse pressure gradient. This demonstrates the importance of what happens immediately downstream of the cooling hole to its film cooling performance.

Results from the baseline airfoil are shown in Fig. 10 in terms of the laterally averaged adiabatic effectiveness $\bar{\eta}$. Maximum adiabatic effectiveness was obtained at a blowing ratio of $M=0.6$ with values generally above $\bar{\eta}=0.2$. For this blowing ratio, there is evidently slight separation near the hole (indicated by the decrease in $\bar{\eta}$ near the hole compared to the $M=0.3$ case). As the blowing ratio is increased to $M=1.22$, the performance degrades to $\bar{\eta}<0.1$ presumably due to coolant jet separation. These results are similar to previous measurements of the first suction-side holes (Ethridge et al. [8]).

Corresponding results for the optimized geometry are presented in Fig. 11. Maximum $\bar{\eta}$ levels are similar to the baseline geometry, but good performance is maintained at higher blowing ratios. Remember that the airfoil contour optimization was performed at one blowing ratio of $M\sim0.85$, and the predictions suggested about a 6% increase in the value of the spatially averaged effectiveness over $x/D=0-20$. In comparison, the experimental results indicate an increase of ~16% (from 0.19–0.22) at a similar blowing ratio. Thus, although the CFD-based optimization correctly suggested an increase in effectiveness, the value of this increase was not predicted correctly.

To make a direct comparison between the baseline and optimized airfoils, Fig. 12 shows the film effectiveness for both at low, medium, and high blowing ratios. As is evident in Fig. 12, the most dramatic difference between the baseline and optimized geometry is at the highest blowing ratio of nominally $M=1.15$, where the optimized geometry provides performance only slightly degraded from the maximum $\bar{\eta}$ levels at $M=0.6$. The optimized contour has clearly changed the separated behavior that the cooling jet shows for the baseline airfoil. Further comparison between the two geometries is presented in Fig. 13 in which the $\bar{\eta}$ level at $x/D=5$ and 15 are presented as a function of varying M. Figure 13 clearly shows the improved performance of the optimized geometry for $M>0.6$.

As discussed in the previous section, in addition to the improved separation characteristics, the optimized contour caused increased lateral spreading of the cooling flow. To gain more insight into the differences in performance for the two geometries, Fig. 14 provides contour plots of adiabatic effectiveness for blowing ratios of $M=0.6$, 0.98, and 1.15. At $M=0.6$, both geometries are performing at optimum levels. Near the holes, the optimum geometry clearly has a wider distribution of coolant, which accounts for the improved average adiabatic effectiveness in this region. Downstream, the two geometries provide coolant distributions that are essentially the same. At $M\sim1$, the dramatic decrease of adiabatic effectiveness for the baseline geometry clearly indicates significant separation. In contrast, the optimized geometry appears to remain well attached, resulting in much better performance up to an $x/D=18$. At $M\sim1.2$, separation effects are severe for the baseline geometry, i.e., very low adiabatic effectiveness downstream of the holes. For the optimized geometry, the center and bottom holes show some decrease in performance, suggesting that significant separation is starting to occur.

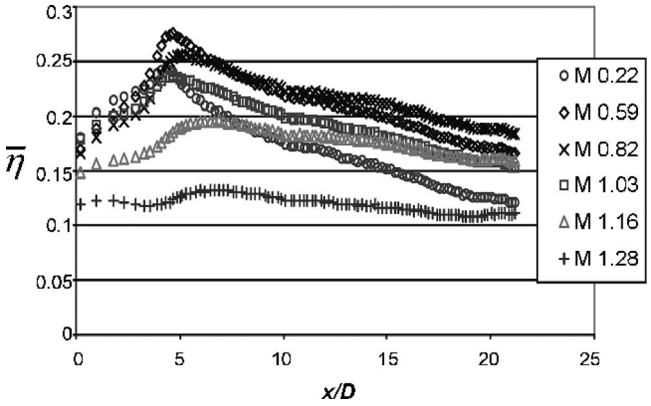

Fig. 11 Laterally averaged effectiveness for the optimized airfoil at various blowing ratios

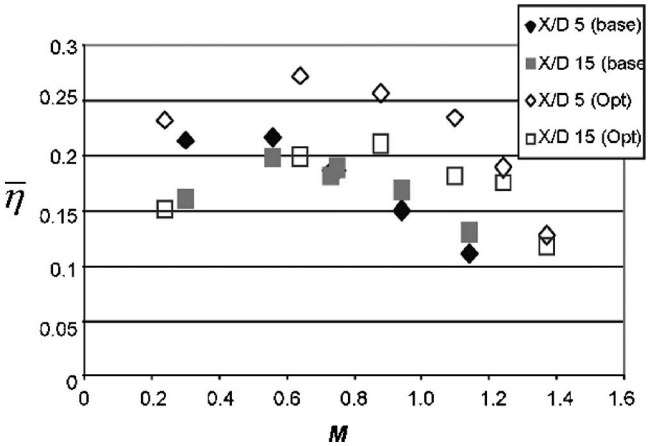

Fig. 13 Comparison of laterally averaged effectiveness near the hole ($x/D=5$) and far from the hole ($x/D=15$) for varying blowing ratios

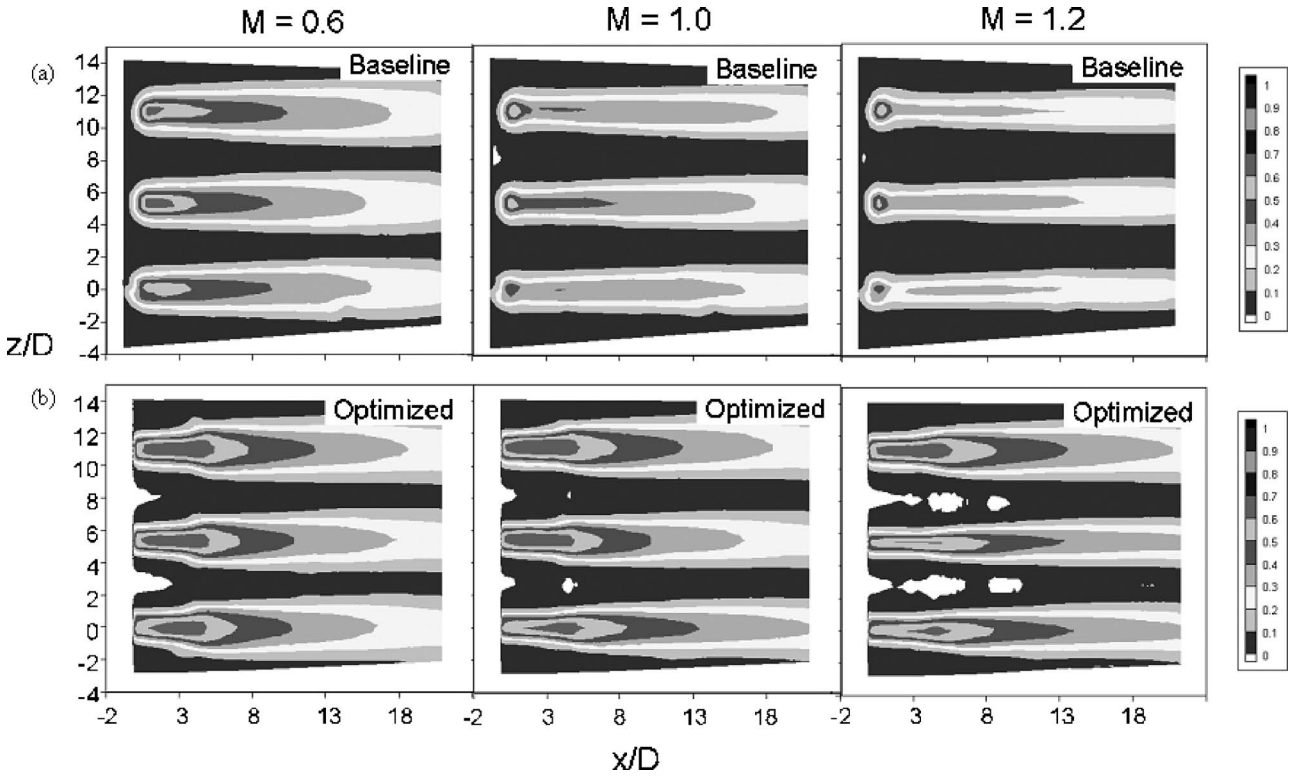

Fig. 14 Surface effectiveness contours for (*a*) baseline and (*b*) optimized geometries for three different blowing ratios

In summary, the optimized geometry has much better film effectiveness at higher blowing ratios compared to the baseline. This is attributed to the increased acceleration and convex curvature as a result of the change in airfoil shape near the cooling hole. The optimized geometry prevents detachment of the cooling jet from the surface and increases the lateral spreading of the jet.

Conclusions

An optimization procedure was used to optimize the airfoil shape with film cooling so as to maximize adiabatic effectiveness with no impact on aerodynamic losses. An increase in effectiveness was achieved by changing the shape of the airfoil such that the flow accelerates as it approaches the cooling jet exiting the cooling hole. This local acceleration causes the film cooling jet to hug the airfoil surface thereby reducing the entrainment of hot gas into the film layer. Once the cooling jet is attached to the surface due to the acceleration and the convex curvature, it is able to withstand an adverse pressure gradient. This demonstrates the importance of what happens immediately downstream of the cooling hole to its film cooling performance.

To prove this concept for increased cooling effectiveness, a low-speed cascade test was performed. The experimental pressure distribution data were in very good agreement with the predictions. The optimized airfoil did show an improved effectiveness compared to the baseline. The experimental results were consistent with the predictions in that optimized airfoil resisted separation and showed improved lateral spreading leading to an increase in film effectiveness. However, the level of this increase was ~16% as measured in the tests, whereas the computations predicted a 6% increase. These results indicate that RANS CFD can be used for making engineering decisions on ranking film cooling configurations but are not quantitatively accurate. And despite its limitations, RANS remains a viable method and can be used to discover innovative ideas to improve the state of the art, as was clearly demonstrated in this study.

Acknowledgment

The authors would like to thank Pratt & Whitney for permission to publish this work. The authors appreciate the funding for this study provided by the USAF Research Laboratory, Propulsion Directorate with Matthew Meininger as contract monitor. The first author would like to acknowledge the contribution of Joel Wagner and Andrew Aggarwala of Pratt & Whitney who were co-inventors of this concept.

Nomenclature

C = Axial chord of vane
CFD = computational fluid dynamics
D = diameter of cooling hole
DR = density ratio $=\rho_c/\rho_\infty$
H = wall thickness
P = pitchwise distance between cooling holes
M = blowing ratio $=(\rho_c U_c)/(\rho_\infty U_\infty)$
RANS = Reynolds averaged Navier-Stokes
TL = turbulence level $=(u^2\ \text{rms}+v^2\ \text{rms})^{1/2}/U_\infty$
U = mainstream velocity
x = axial coordinate
y = wall normal coordinate
z = spanwise or lateral coordinate
α = streamwise angle of cooling hole
β = radial angle of cooling hole
η = film effectiveness $=(T_{aw}-T_\infty)/(T_c-T_\infty)$
ρ = density

Subscripts

aw = adiabatic wall
c = coolant
∞ = mainstream
rms = root-mean-square

Superscripts

- = lateral average

References

[1] Bunker, R. S., 2005, "A Review of Shaped Hole Turbine Film-Cooling Technology," ASME J. Heat Transfer, **127**(4), pp. 441–453.

[2] Pedersen, D. R., Eckert, E. R. G., and Goldstein, R. J., 1977, "Film Cooling With Large Density Differences Between the Mainstream and the Secondary Fluid Measured by the Heat-Mass Transfer Analogy," ASME J. Heat Transfer, **99**, pp. 620–627.

[3] Gritsch, M., Schulz, A., and Wittig, S., 2003, "Effect of Internal Coolant Crossflow on the Effectiveness of Shaped Film-Cooling Holes," ASME J. Turbomach., **125**(3), pp. 547–554.

[4] Ganzert, W., Fottner, L., and Hildebrandt, T., 2000, "Systematic Experimental and Numerical Investigations on the Aerothermodynamics of a Film Cooled Turbine Cascade With Variation of the Cooling Hole Shape—Part I: Experimental Approach," ASME Turbo Expo, Munich, ASME, Paper No. 2000-GT-295.

[5] Zerkle, R. D., and Leylek, J. H., 1994, "Discrete-Jet Film Cooling: A Comparison of Computational Results With Experiments," ASME J. Turbomach., **113**, pp. 358–368.

[6] Kohli, A., and Thole, K. A., 1997, "A CFD Investigation on the Effects of Entrance Crossflow Directions to Film-Cooling Holes," National Heat Transfer Conference, Baltimore.

[7] Kohli, A., Wagner, J. H., and Aggarwala, A. S., 2003, "Film Cooled Article With Improved Temperature Tolerance," U.S. Patent No. 6,547,524 B2.

[8] Ethridge, M. I., Cutbirth, J. M., and Bogard, D. G., 2001, "Scaling of Performance for Varying Density Ratio Coolants on an Airfoil With Strong Curvature and Pressure Gradients," ASME J. Turbomach., **123**, pp. 231–237.

[9] Ni, R. H., 1982, "A Multiple-Grid Scheme for Solving the Euler Equations," AIAA J., **20**(11), pp. 1565–1571.

[10] Ni, R. H., and Bogoian, J. C., 1989, "Prediction of 3-D Multistage Turbine Flowfield Using a Multiple-Grid Euler Solver," AIAA Paper No. 89-0203.

[11] Davis, R. L., Shang, T., Buteau, J., and Ni, R. H., 1996, "Prediction of 3-D Unsteady Flow in Multi-Stage Turbomachinery Using an Implicit Dual Time-Step Approach," AIAA Paper No. 96-2565.

[12] Wilcox, D. C., 1998, *Turbulence Modeling for CFD*, 2nd ed., DCW Industries, La Canada, CA.

[13] Polanka, M. D., Witteveld, V. C., and Bogard, D. G., 1999, "Film Cooling Effectiveness in the Showerhead Region of a Gas Turbine Vane—Part 1: Stagnation Region and Near-Pressure Side," Paper No. 99-GT-48.

Flow Physics and Profiling of Recessed Blade Tips: Impact on Performance and Heat Load

Bob Mischo
e-mail: bob.mischo@lsm.iet.mavt.ethz.ch

Thomas Behr

Reza S. Abhari

Turbomachinery Laboratory,
Swiss Federal Institute of Technology,
CH-8092 Zürich, Switzerland

In axial turbine, the tip clearance flow occurring in rotor blade rows is responsible for about one-third of the aerodynamic losses in the blade row and in many cases is the limiting factor for the blade lifetime. The tip leakage vortex forms when the leaking fluid crosses the gap between the rotor blade tip and the casing from pressure to suction side and rolls up into a vortex on the blade suction side. The flow through the tip gap is both of high velocity and of high temperature, with the heat transfer to the blade from the hot fluid being very high in the blade tip area. In order to avoid blade tip burnout and a failure of the machine, blade tip cooling is commonly used. This paper presents the physical study and an improved design of a recessed blade tip for a highly loaded axial turbine rotor blade with application in high pressure axial turbines in aero engine or power generation. With use of three-dimensional computational fluid dynamics (CFD), the flow field near the tip of the blade for different shapes of the recess cavities is investigated. Through better understanding and control of cavity vortical structures, an improved design is presented and its differences from the generic flat tip blade are highlighted. It is observed that by an appropriate profiling of the recess shape, the total tip heat transfer Nusselt number was significantly reduced, being 15% lower than the flat tip and 7% lower than the base line recess shape. Experimental results also showed an overall improvement of 0.2% in the one-and-a-half-stage turbine total efficiency with the improved recess design compared to the flat tip case. The CFD analysis conducted on single rotor row configurations predicted a 0.38% total efficiency increase for the rotor equipped with the new recess design compared to the flat tip rotor.
[DOI: 10.1115/1.2775485]

Introduction

Tip clearance between the blade tip of a rotor and the casing is necessary for a free rotation of the rotor blade row. The gap, however, allows fluid to cross the blade tip from the pressure side of the blade to the suction side due to the pressure difference on the pressure and the suction side. This flow is associated with two main problems. Firstly, roughly one-third of all the aerodynamic losses in a rotor row are related to the tip leakage vortex, which forms when the tip leakage over the blade tip enters the passage flow again on the blade suction side. It both creates mixing loss when it mixes with the main flow and perturbs the pressure field on the blade tip wall that is responsible for the blade lift. Furthermore, the fluid crossing the gap is not turned by the blade and therefore no work is extracted from it. It is therefore interpreted as lost work extraction. Secondly, the fluid crossing the tip clearance has a higher temperature than most of the fluid in the main flow due to hot streak migration, resulting in a high thermal load for the blade tip. In fact, blade tips burn away if not adequately cooled and are hence one of the limiting factors for the blade lifetime.

Additionally, it is desirable to minimize the tip clearance gap height in order to improve the performance through reduction of the tip leakage mass flow. This reduced gap height, however, increases the risk of the rotor blade rubbing the casing sometime during the operational envelope. This can occur, for example, if the rotor expands further than the casing due to transients, a rotor dynamic excursion, an ovalization of the casing, or through casing thermal distortions. In the case of a severe blade rub with a flat tip, catastrophic coolant loss could occur if the tip wears off. Even in a case of a relatively minor rub for a flat tip, any cooling holes located on the tip may be damaged, resulting in an inadequate cooling eventually leading to blade tip burnout.

One solution in the blade tip design optimization to this stated problem is to use a recessed blade tip (see Fig. 2) instead of a simple flat tip. The recess cavity inside the blade tip has several beneficial features. Since material at the upper surface of the blade is moved to a lower radius from the axis of rotation, blade root mechanical stresses can be lowered. Also in case of a tip rub, i.e., when the rotor blade touches the casing during rotation, only the thin cavity rim is damaged. Wear damage to the casing is also limited and since the purge holes for the blade tip cooling are located inside the cavity, the rubbing does not damage the outlet of the holes. Efficient cooling is hence assured even if rubbing occurs. Finally, the recess cavity may act as a labyrinth seal, which could be beneficial in reducing tip clearance mass flow. Unlike for the case of a flat blade tip, the more complex flow physics for a recessed blade tip is less well understood. Also, systematic design procedures for cavity size and shape are not available. The aim of this study is to better understand aerodynamics and heat transfer physics of recess cavities and provide new design boundaries for a standard, highly loaded rotor blade representative of a high pressure turbine. A three-dimensional computational fluid dynamics (CFD) tool has been extensively used for this purpose.

The tip clearance flow has been investigated recently with a number of contributions in the open literature. An important contribution always referred to is the work by Rains [1], who studied tip clearance flow for axial flow pump motivated by concerns of cavitation. Moore and Tilton [2] investigate the tip leakage flow both experimentally and analytically. The flow structure inside the gap and heat transfer to the blade have been discussed. A flow

Contributed by the International Gas Turbine Institute of ASME for publication in the JOURNAL OF TURBOMACHINERY. Manuscript received June 27, 2006; final manuscript received August 18, 2006; published online February 29, 2008. Review conducted by David Wisler. Paper presented at the ASME Turbo Expo 2006: Land, Sea and Air (GT2006), Barcelona, Spain, May 8–11, 2006, Paper No. GT2006-91074.

model assuming the gap losses coming from complete mixing behind the vena contracta leading to uniform flow conditions at the gap outlet is presented. Bindon [3] measured and investigated the tip clearance loss formation. He could divide the total end wall loss into loss generated inside the tip gap, mixing loss of the tip leakage vortex, and secondary and end wall losses. He concluded that not only tip leakage mass flow is important for loss generation (48% of overall loss seen in mixing loss), but also the flow structure inside the gap would play a significant role (39% of overall loss generated inside the gap). Furthermore, he showed a conceptual model for tip clearance loss formation. Morphis and Bindon [4] investigated loss for different blade tip geometries. They found that the overall loss remained unchanged although gap losses strongly varied between the base line sharp edged flat tip and differently contoured blade tips. Whereas the sharp edge case showed high losses inside the gap with a strong separation bubble at the pressure side lip, the contoured cases showed less losses since no separation bubble was formed on the gap inlet but, in turn, an increased tip gap mass flow was found.

In a study of different squealer tips by Heyes et al. [5], it was also concluded that the separation bubble with the associated vena contracta is effectively sealing the gap, and by reducing tip mass flow the tip clearance losses may be decreased. In this study, a flow model for squealer tips is included as well as a model for the flow at the gap exit which is represented as a combination of an isentropic jet between the casing and gap midheight and a wake formed behind the separation bubble. A computational study by Ameri [6] on heat transfer on the blade tip showed that a flat tip with sharp edges performs best in terms of efficiency and total pressure loss compared to a mean camberline squealer tip and a flat tip with radiused blade tips. Further computational studies by Tallman and Lakshminarayana [7,8] on the experimentally investigated linear cascade by Morphis and Bindon [4] discuss the effect of tip clearance height and relative casing wall movement on the flow physics in the tip gap. A further experimental investigation on the tip clearance flow physics due to moving casing wall is presented in a two-part study by Yaras and Sjolander [9,10]. It was found that the moving belt simulating relative casing motion significantly decreased tip gap mass flow. Also, the tip passage vortex is drawn to the suction side, providing a throttling effect [11]. Furthermore, a reduced pressure difference driving the flow into the gap was observed.

In a recent study, detailed heat transfer to recessed blade tip was first investigated by Dunn and Haldemann [12]. A recessed blade tip was equipped with heat flux gauges and experimentally investigated in a full stage rotating turbine. Nusselt number was shown for different vane/blade spacings. It was found that the leading edge Nusselt number on the cavity bottom was in excess of the blade stagnation value.

Computational Method

The following section describes the computational tools used for this study. The computational tools for preprocessing and the solver are all developed in-house. These tools interact in parts with commercial products for postprocessing.

Grid Generator. The numerical grids used were generated with the in-house developed grid generator called MESHBOUND. The multiblock structured grid generator uses a two-dimensional NURBS library as input data to mesh the computational domain boundaries. Using a set of geometrical transformations, the interior block boundaries are defined according to the intended grid topology. High grid quality, i.e., smooth gridlines, limited aspect ratio, skewness, and cell-to-cell ratios are achieved using both nonlinear interpolation algorithms with flexible clustering specification and two-dimensional Poisson-type elliptic partial differential equations during the meshing of each block. Several topologies are implemented and these partition the computational domain for a blade tip with recess area into 18 blocks. Especially, the use of up- and downstream wake blocks with adjustable sizes and grid density helps keep low grid skewness in the trailing edge area and prevents the numerical diffusion of the shed wake. An example of a grid for a recess case is shown below in Fig. 1.

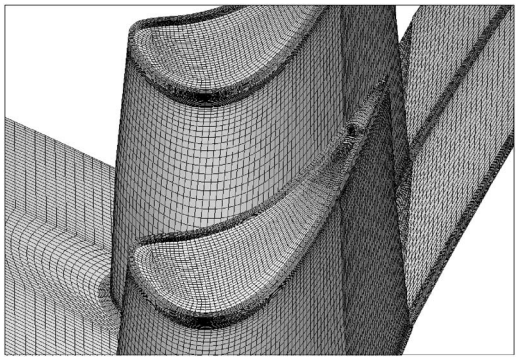

Fig. 1 Three-dimensional computational grid turbine rotor blade with standard recess cavity

The densely packed tip region grid block spans over about the top 10% the blade span.

Numerical Solver. The numerical flow solver used for this study is called MBSTAGE3D, a three-dimensional, structured Navier–Stokes solver for multistage turbomachinery applications. The time marching algorithm used in MBSTAGE3D is a Jameson-type algorithm [13,14], i.e., an explicit method with a residual-averaging technique applied for improving stability. The time discretization is accomplished by a five-stage Runge-Kutta technique, which is of fourth-order accuracy. All computations discussed here were conducted with the algebraic Baldwin–Lomax turbulence model [15] together with logarithmic wall function developed by Sommer et al. [16] to compute the turbulent viscosity at the wall.

Extensive postprocessing necessary to gain understanding of flow physics is achieved through 3D, 2D, 1D, and scalar investigation of the flow fields of interest. The 3D visualizing is done with TECPLOT, a collection of integrators and the 3D data generation subroutines for TECPLOT are developed in-house.

Computational Model. The computational domains for this study model a single pitch of the rotor blade row. The grids show a high resolution in the blade tip area in order to capture the flow gradients in this region. Since logarithmic wall functions are used, $y+$ values are allowed to approach values for around 50–100. This helps in keeping the number of grid points at about 900,000 points, since clustering near walls does not need to be as aggressive as in two layer turbulence model computations. Hence, the high number of grid points in the blade tip area leads to homogeneous mesh density with smooth cell-to-cell ratio distribution.

Uniform profiles of mean absolute total pressure, total temperature, as well as pitch and yaw flow angles at the stator exit are prescribed as boundary conditions on the rotor inlet plane. End wall boundary layers at hub and casing are modeled through a power law. Radial equilibrium with a prescribed static pressure at the casing is used as outlet boundary condition. A moving wall boundary condition is applied at the casing.

Experimental Approach

In order to perform the intended computational and experimental study, a previously designed axial turbine test case has been utilized. The geometry of the one-and-a-half-stage, unshrouded turbine models a highly loaded ($\Delta H/U^2=2.36$), low aspect ratio gas turbine environment. The air loop of the test rig is of a quasiclosed type and includes a radial compressor, a two-stage water to air heat exchanger, and a calibrated venturi nozzle for mass flow measurements. Before the flow enters the turbine section, it

Table 1 Main parameter of "LISA" 1.5 stage axial turbine research facility at design operating point

Turbine	
Rotor speed (rpm)	2700
Pressure ratio (1.5 stage, total to static)	1.60
Turbine entry temperature (TET) (°C)	55
Total inlet pressure (p_{t0}) [bar abs norm]	1.4
Mass flow (kg/s)	12.13
Shaft power (kW)	292[a]
Hub/tip diameter (mm)	660/800
First stage	
Pressure ratio (first stage, total to total)	1.35
Degree of reaction (−)	0.39
Loading coefficient $y=\Delta h/u^2$ (−)	2.36[b]
Flow coefficient $f=c_x/u$ (−)	0.65
Rotor geometry	
Blade height (mm)	69.3
Tip clearance/span (%)	1.0

[a]From torquemeter.
[b]From five-hole-probe measurement.

passes through a 3 m long straight duct, which contains flow straighteners to ensure an evenly distributed inlet flow field. Downstream of the turbine, the air loop is open to atmospheric conditions. A dc generator absorbs the turbine power and controls the rotational speed of the turbine. An accurate torque meter measures the torque that is transmitted by the rotor shaft to the generator. The turbine entry temperature (TET) is controlled to an accuracy of 0.3% and the rotor speed is kept constant within ± 0.5 min^{-1} by the dc generator. More information on the turbine design (Behr et al. [17]) as well as on the operation of the experimental facility (Sell et al. [18]) can be found in the open literature (see also Table 1).

Flow Physics and Design Improvement

The following section describes in detail the flow physics in a flat tip and in a nominal recess tip being representative of modern designs. Here, the differences between the flat tip and the nominal recess design are presented. The detailed investigation of the three-dimensional flow field for a nominal recess case having a length L of 80% axial chord and a depth D of twice the tip gap height allowed us to identify key flow features. A sensitivity study of variations of the tip recess geometry parameters shown in Fig. 2 and its impact on the flow features was then performed on this nominal recess design to find the new and improved recess design for experimental evaluation.

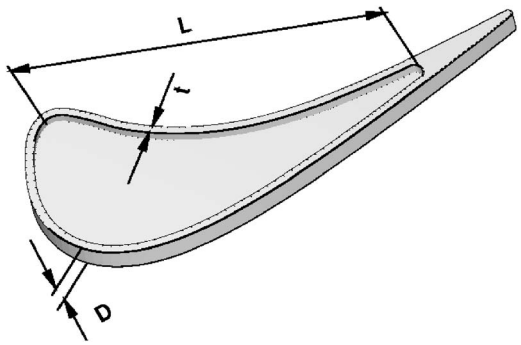

Fig. 2 Geometrical parameters studied for improved recess cavity design

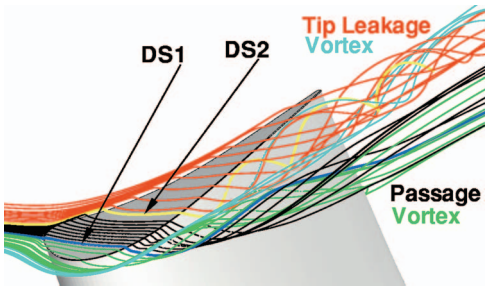

Fig. 3 Three-dimensional CFD predicted flow over flat tip blade

Parametric Study. The geometrical parameters varied in this study were the length L of the recess cavity, the depth D of the cavity, and the shape of the recess rim which most generally can be any function of the two former parameters. In this study, however, the shape was mostly a function of the length.

From the parametric study, it could be shown that the recess cavity walls offered additional surface that would generate additional power, which needs to be added to the main power generated by the outer blade wall. It was also observed that the tip leakage flow for all the recessed cases was lower than for the flat tip. The overall mass flow through the computational domain remained unchanged, suggesting that the change in the leakage mass flow occurred prior to the suction side throat region, hence resulting in a constant corrected flow through the rotor. It is important to also note that variations in total pressure loss coefficients followed those of the tip gap mass flow. The relation between aerodynamic loss and tip leakage mass having been verified necessitated further reduction of the tip leakage mass flow as an important design criteria. The changes with depth were strongly nonlinear, with an optimum depth leading to minimum tip leakage mass flows being identified. This is also an important difference in the tip leakage mass flow evolution in a flat tip case where the tip leakage mass flow varies linearly with the gap height. The changes in recess length were almost linear.

Test Cases. The understanding of the detailed flow physics is therefore particularly important in the design process and will be investigated next on behalf of three major test cases. The first case is a flat tip blade. The second test case is a nominal recess cavity with a length of 80% axial chord and twice as deep as the tip gap, the rim thickness being kept constant. This test case represents a current design for recess cavities. The final test case is the newly designed recess geometry based on the extensive physical modeling and geometric perturbation.

Tip Region Flow Physics

In this part, the three-dimensional predicted flow fields in the blade tip region are described for the three test cases described above. First, the flat tip computation will be presented.

Flat Tip. The flat tip flow field presented in Fig. 3 shows two main flow structures. The first one is the tip passage vortex which forms when incidence driven fluid enters the tip gap from the suction side at leading edge and leaves it again after 20% axial chord. Furthermore, tip leakage occurring on the pressure side between leading edge and 15% axial chord crosses the tip gap and mixes with the incidence flow in the tip passage vortex. The feeding of the tip passage vortex is well organized, with the flow past a dividing streamline triggering the formation of the tip passage vortex. The succeeding pressure side leakage flow feeding the tip passage vortex can also be identified.

The second main flow feature observed is the tip leakage vortex that forms from the tip leakage flow crossing the gap from the pressure side starting at 15% axial chord. The dividing streamline

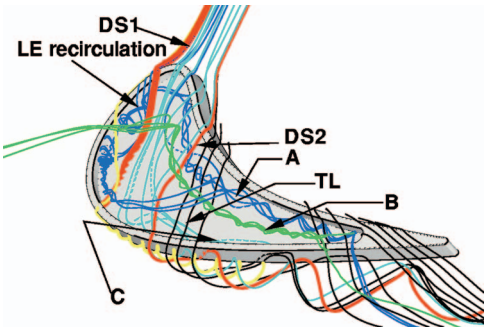

Fig. 4 Three-dimensional CFD predicted flow through nominal recess cavity

between the pressure side leakage feeding the tip passage vortex and the tip leakage vortex outer fluid layer can be identified. The outer fluid layers in the tip leakage vortex result from the main part of the pressure driven, low gap shear loss generating leakage jet. The tip leakage vortex core is formed by blade tip boundary layer fluid.

Cutting plane orthogonal to the blade mean camberline reveals the well known gap flow structure. When the tip leakage flow enters the gap from the pressure side, a separation bubble is formed, leading to a vena contracta. The leakage jet leaving the vena contracta would then form the wake fluid in the lower part of the gap. This wake creates mixing loss and is found later in the tip leakage vortex core. The leakage jet above the wake part is often modeled as an isentropic jet; it forms the outer fluid layers around the tip leakage vortex core depending on the axial position when it left the gap on the suction side.

Nominal Recess Cavity. In the following section, it is attempted to physically model the flow structure in a typical nominal recess region. It should be noted that the following flow structure is dependent on the aerodynamic design of the turbines, varying somewhat for different blade rotor designs and not exactly matching the following descriptions. Despite of this limitation, it is believed that many of the flow features remain the same for modern axial high work turbines, with the sensitivities and the trade studies relating to geometrical variation remaining applicable. In total, six main flow features influencing the cavity flow were identified.

Starting at the leading edge of the pressure side, fluid above the blade leading edge stagnation point fluid of the passage enters the cavity. It crosses the cavity with low loss and at the flow angle of fluid at leading edge, and impinges on the corner between the cavity bottom and cavity suction side wall shortly following the peak suction. After hitting the corner wall, this pressure side leading edge jet rolls up into a vortical structure *C* and moves downstream inside the cavity, partly leaving the cavity and entering the suction passage flow again. The boundary layer on the recess rim entering the cavity along the whole pressure side due to the tip clearance pressure gradient and on the first 20% axial chord on the suction side immediately rolls up into a vortex *A* in the corner between the cavity bottom and the cavity walls, stretching along the whole pressure side to the end of the cavity and reaching up to 20% of axial chord on the suction side cavity wall. After 10% of the axial chord, this suction side part of the vortex *A* is lifted off the cavity bottom by an incidence driven suction side leakage jet *C* entering the cavity. A third important flow feature is vortex *B* which forms when casing boundary layer fluid rolls up against the pressure side tip leakage jet *TL*. This vortex stays on the casing wall and deflects the pressure tip leakage inside the cavity, as shown in Fig. 4. Between the above two vertical flow structures, a dividing streamline *DS*1 establishes.

Downstream of the 20% axial chord, the flow behavior of the pressure side leakage is similar to the flat tip case with the difference that the leakage is deflected by the cavity vortices and interacts with them. After leaving the gap on the suction side, this fluid forms again the outer layer of the tip passage vortex and the tip leakage vortex. The core of the tip passage vortex is formed by the same incidence tip leakage that lifts off the cavity corner vortex when entering and leaving the cavity between 10% and 20% axial chord. The core of the tip leakage vortex is wake fluid behind the separation bubble on the suction side rim that forms when the pressure side leakage jet leaves the cavity.

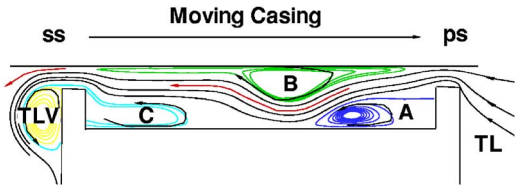

Fig. 5 Two-dimensional CFD predicted flow through nominal recess cavity

To additionally clarify the flow features inside the cavity, a cutting plane orthogonal to the camberline located downstream of the formation of the vortex formed by the pressure side leading edge jet is shown in Fig. 5. The three main cavity vortices above are referenced. Between the casing vortex *B* and the rim boundary layer roll up vortex *A*, the pressure side leakage crosses the cavity, lifting up vortex *C* caused by the pressure side leading edge cavity jet. Two separation bubbles form, one at the pressure side rim edge to the outer blade wall when the tip leakage jet enters the gap, and the other on the suction side rim edge with the cavity wall when the tip leakage leaves the cavity again. The tip leakage jet is recognizable as a low entropy zone between the higher entropy zones where the vortices are located. The casing vortex is rather squeezed; this explains why downstream of the blade gradually more and more fluid from the neighboring vortices mix in.

New Recess. The nominal design showed many vortical structures inside the recess cavity. Particularly, the front part of the cavity is affected by these structures. As seen above, the boundary layer fluid leaking from the rim into the cavity rolls up in a vortex along the corner between cavity bottom and cavity rim wall. The aim of the new design was to eliminate the recirculation zone in the front part of the blade to minimize aerodynamic losses and reduce the head transfer coefficient.

The new design follows the dividing streamline that separates the recirculation zone from the pressure side leading edge jet. In Fig. 6, the effect of the new design on the cavity flow pattern is showed. The recirculation on the leading edge is suppressed. The pressure side leading edge jet now spreads inside the whole cavity. The casing boundary layer fluid rolls up into vortex *B* and interacts with the fluid from the pressure side leading edge jet.

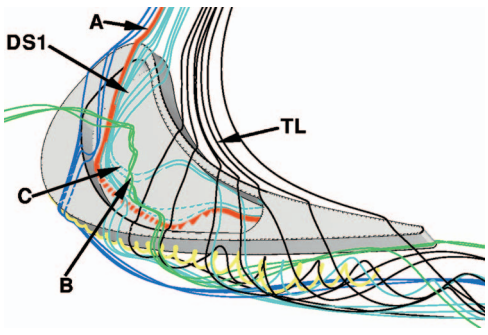

Fig. 6 Three-dimensional CFD predicted flow through new recess cavity

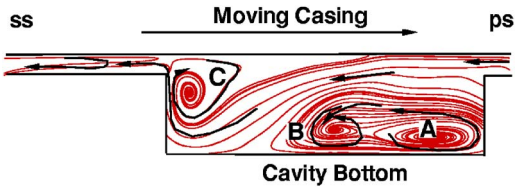

Fig. 7 Two-dimensional CFD predicted flow through new recess cavity

The fluid trapped in the recirculation in the nominal design now enters the cavity and is pushed out again by the pressure side leading edge jet. After leaving the cavity, it feeds the tip passage vortex. The two-dimensional cutting plane shown in Fig. 7 illustrates the vortical pattern inside the cavity.

Vortices *A* and *B* are actively interacting. Therefore, vortex *B* is not confined to the casing anymore but can occupy the whole cavity volume. Vortex *C* is formed by the fluid that led to the suction side leading edge recirculation in the nominal case. It is formed when this fluid separates on the cavity rim while being pushed out of the cavity by the pressure side leading edge jet.

Computational Performance Results

In the following section, the computational results regarding the aero-thermal performance of the three test cases introduced above are presented. For the aerodynamic performance, the tip leakage mass flow is investigated since it is intensively related to the total pressure loss. Nusselt number distribution and integrated heat flux vector on the blade tip walls are compared to assess the impact of the new design on heat transfer.

Aerodynamics: Tip Leakage Mass Flow. In the following, the variations of accumulated tip gap mass flow from leading to trailing edge for the pressure and the suction side for the three investigated test cases are shown separately. On the pressure side (Fig. 8), the most important feature is the progressive growth of the accumulated tip gap mass flow from leading edge to trailing edge, for the flat tip compared to a linear increase as long as the recess cavity opens behind the rim. Downstream of the cavity trailing edge, the accumulated tip gap mass flow also varies nonlinearly and is similar to the flat tip case for both recess designs.

The linear increase may be explained through the average static pressure variation at the tip gap entry on pressure side and its exit on the suction side (Fig. 9). The static pressure decreases both for pressure and for the suction side nonuniformly in the flat tip case. For the recess cases, however, static pressure remains at constant level whenever tip leakage enters the cavity, which is the case for the entire pressure side gap and also for the front part of the suction side, where incidence fluid enters into the cavity. The recess cavity acts like a reservoir where pressure remains constant. The sealing effect and the resulting reduction of the accumulated tip gap mass flow are clearly observed. The nominal recess case showed a reduction of 23% in the leakage mass flow when compared to the flat tip; the new design had 25% less mass flow crossing the gap compared to the flat tip.

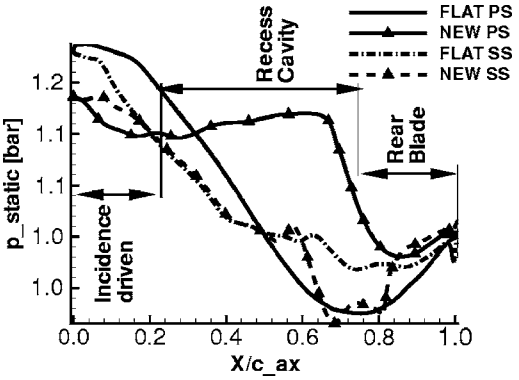

Fig. 9 CFD predicted tip rim static pressure

The accumulated tip clearance mass flow on the gap exit for the blade suction side is shown for flat tip blade, the nominal recess, and the new design in Fig. 10.

The incidence driven tip leakage mass flow is much more intense in the recess cases than in the flat tip case. Incidence leakage reaches for all three cases from leading until 22% axial chord. However, the amount of mass flow entering the recess cavities is almost double the one for the flat tip. This sustains again the cavity in acting as a reservoir to be filled up with fluid. The difference in the amount of mass flow additionally having entered the cavity compared to the flat tip gap almost exactly matches with the reduction in total cumulated tip leakage mass flow over the entire suction side. No large differences in tip gap mass flow are noted between the nominal and the new recess designs.

Heat Transfer

In the following, Nusselt number distributions between the flat tip and both recess cases are compared. High Nusselt numbers occur on the leading edges in all three cases. This is where hot fluid meets the blade tip first and heat transfer is highest. On the pressure side edges Nusselt number has the same magnitude in all three cases. The thin rim of the nominal recess shows a similar distribution on the suction side front part compared to the new design. When the tip leakage vortex forms (at about 25% axial chord), the value of the Nusselt number drops for both the flat tip case and the nominal recess case. This observation, however, cannot be made for the suction side rim of the new design. Both the flat tip and the nominal recess show high Nu numbers at the leading edge. In the new design, however, Nu number values do not reach as high on the cavity bottom. In Fig. 11, a clear difference between the new design and the flat tip as well as the nomi-

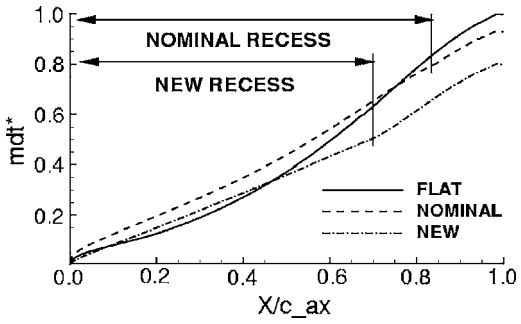

Fig. 8 Pressure side CFD predicted normalized tip mass flow

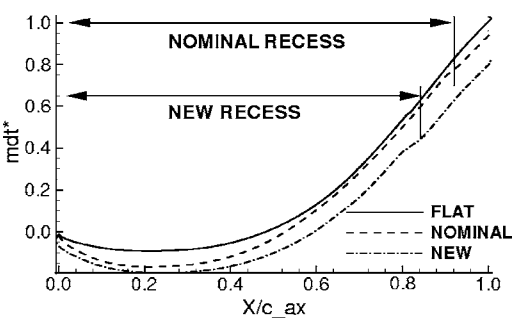

Fig. 10 Suction side CFD predicted normalized tip mass flow

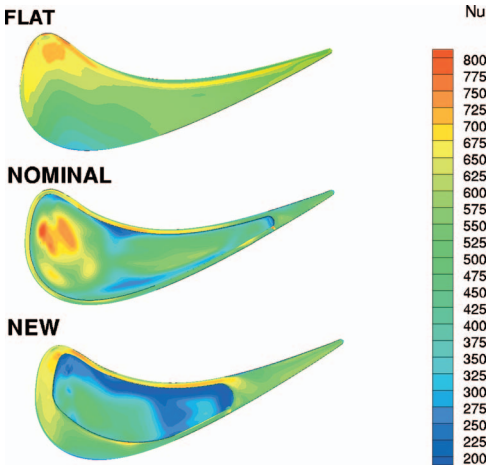

Fig. 11 CFD predicted blade tip nusselt number distribution

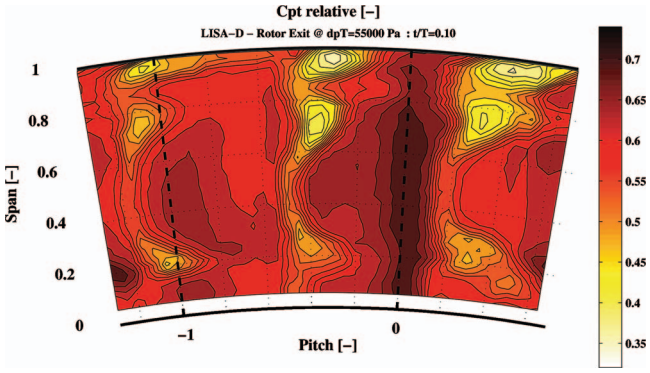

Fig. 13 Experimental relative total pressure coefficient distribution at 14% axial chord downstream rotor blade trailing edge for flat tip blade

nal recess case can be seen. The blocking of the suction side recirculation zone by a thicker rim has not led to higher Nusselt numbers on the rim.

The integrated heat flux vector on the blade tip gives the heat load for three test cases. In Fig. 12, where heat load is split according to the affected wall type, a clear observation can be made. The overall predicted tip heat load is highest for the flat tip and lowest for the new design. The reduction of heat load between the flat tip and the new design (about 14%) is about twice as high than between the nominal and the new recess design (7%). However, it must be noted that the new design also has higher regions of heat load than the nominal design. This is the case for the tip rim and the cavity walls to which the cavity rim walls and the remaining rear flat blade tip portion belong. Increasing the rim thickness as well as a deeper and shorter cavity are the reasons for this increased heat load. However, it has also been shown that changing the flow field on the leading edge inside the cavity through the elimination of the suction side recirculation zone has proved effective in reducing heat load on the cavity bottom.

Validation With Experimental Results

In the following section, the previous results from CFD predictions are compared to experimental results. The flat tip and the new recess design blades have been experimentally evaluated at ETHZ axial turbine facility LISA.

Aerodynamic Performance. First, the predicted and experimental relative total pressure coefficients for the flat tip and the new recess design are compared in 2D axial cutting planes located 14% axial chord downstream of the rotor trailing edge. The experimental data for the flat tip blade shown in Fig. 13 are snapshots at a given point in time of an unsteady flow. Therefore, unsteady flow features are resolved which are not present in the single row steady state CFD results. The fact regarding unsteady data also explains the modulation of the low relative total pressure zones identifying the secondary flow vortices and the tip leakage vortex.

The CFD predictions from a single row steady state computation are shown in Fig. 14. The computationally predicted relative total pressure coefficient resolves in sufficiently good accuracy the secondary flow structures measured by the experiment. The hub and tip passage vortices are captured both in their spatial extension and in their magnitude. Also, the trailing edge wake of the rotor blade is captured in the CFD results. The region associated with the tip clearance vortex is, however, overpredicted compared to the experiment.

In a second step, CFD predicted and measured pitch averaged radial distributions of relative flow yaw angle at 14% of the axial chord downstream of the rotor blade trailing edge for the flat tip blade are shown in Fig. 15. It can be seen that the variation in the relative yaw angle due to the tip leakage vortex between 80% span and 100% span is largely overpredicted by the computational result. The magnitude of relative yaw angle variation due to the hub and tip secondary flow structure is well predicted.

Next, experimental and CFD predicted data for the new recess design are compared. The experimental data shown in Fig. 16 are again snapshots of unsteady data. The snapshots for the flat blade tip and the new recess design were both taken at the same point in time.

The CFD predicted relative total pressure coefficients from steady state computations are shown in Fig. 17. It can again be seen that the predicted CFD results resolve the same features that are also captured by the measured flow field. Predicted relative total pressure coefficients showing the hub and tip passage vortices agree well with the experimental data. The overprediction of the tip leakage vortex noted in the flat tip case is also found in the new recess design case. Compared to the computationally pre-

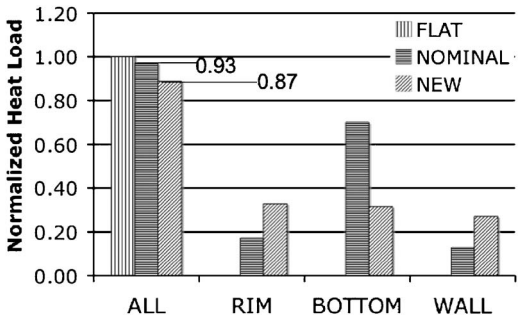

Fig. 12 CFD predicted normalized heat load for flat tip, nominal recess, and new recess

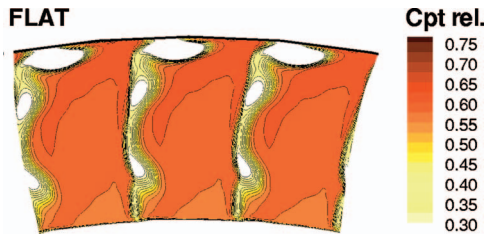

Fig. 14 CFD predicted relative total pressure coefficient distribution at 14% axial chord downstream rotor blade trailing edge, flat tip blade

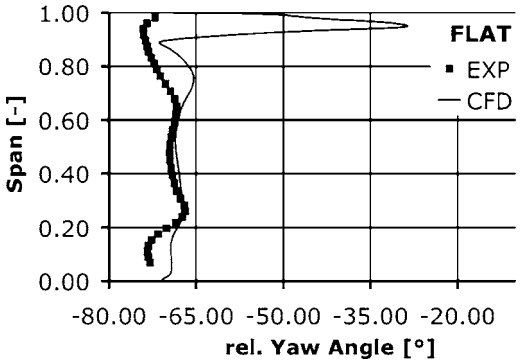

Fig. 15 Steady CFD prediction versus pitch averaged experimental relative yaw angle at 14% axial chord downstream rotor blade trailing edge, flat tip blade

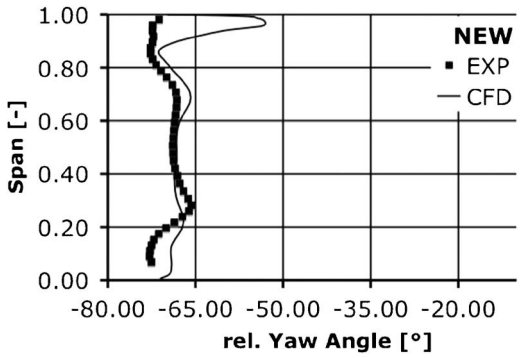

Fig. 18 CFD predicted versus experimental pitch averaged relative yaw angle at 14% axial chord downstream rotor blade trailing edge for new recess tip blade

dicted relative total pressure coefficient for the flat tip case, it can be noted that the spatial extension of the tip leakage vortex core for the new recess design has been reduced.

The measured and predicted pitch averaged relative flow yaw angle distributions for the new design are presented in Fig. 18. The CFD predicted relative flow angle distribution matches the experimental data up to about 80% of the span. The part from 80% span to 100% span is influenced by the tip leakage vortex. Whereas the secondary flow features on hub and tip are correctly predicted, the difference in flow angle due to the tip leakage vortex is very much overpredicted.

The reasons for the overpredicted flow angles in Figs. 15 and 18 could be threefold. First, the actual unsteady flow field shows modulation of the vortex core responsible for over- and underturning. The time averaged experimental data take this modulation into account, whereas the steady state CFD computations cannot capture such a time dependent variation of the flow angles. Furthermore, multirow effects leading to distorted rotor inlet flow profiles are not taken into account in the CFD boundary condition specification either. Finally, the use of the algebraic turbulence model does not capture the right mixing of the vortex with the main flow. These issues will be addressed in greater detail in a subsequent paper.

In Fig. 19, the experimentally measured relative yaw angle distributions for the flat tip and the new recess design are presented for the tip region from 60% span to the casing at 100% span. It can be seen that the new recess design shows less overturning than the flat tip blade. This result clearly illustrates that the recess cavity influences the tip leakage vortex, which is responsible for the stated overturning.

Change in Turbine Efficiency. Experimentally measured performance data show that the new recess design has an overall improvement of 0.2% in the one-and-a-half-stage turbine total efficiency compared to the flat tip case at exactly the same overall turbine operating conditions. The CFD analysis conducted on single rotor row configurations predicted a 0.38% total efficiency increase for the rotor equipped with the new recess design compared to the flat tip rotor, which is in good quantitative agreement with the experimental data.

Heat Load. The predicted heat transfer data are qualitatively compared to data presented by the Ohio State University Gas Turbine Laboratory [12]. A turbine blade with a recess cavity similar to the nominal design presented here was equipped with heat transfer gauges to measure heat transfer on the cavity bottom near leading edge, trailing edge, and in the middle. Also, the rim was equipped with several gauges. Nusselt numbers were reported

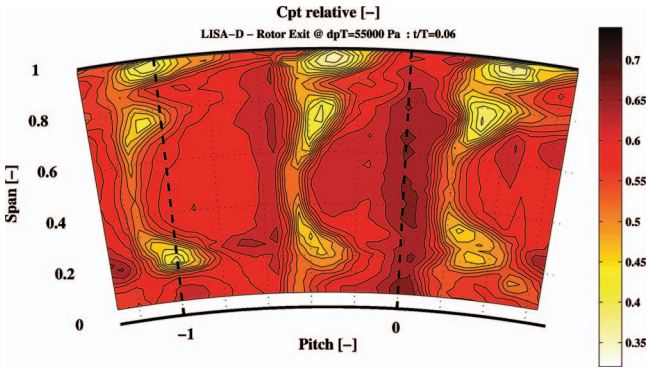

Fig. 16 Experimental relative total pressure coefficient distribution at 14% axial chord downstream rotor blade trailing edge, new recess tip blade

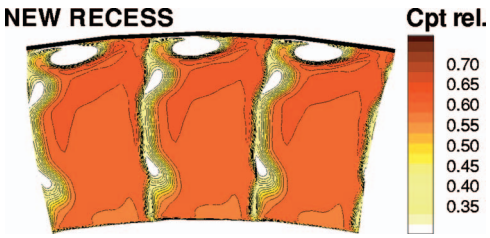

Fig. 17 CFD predicted relative total pressure coefficient distribution at 14% downstream rotor blade trailing edge for new recess tip blade

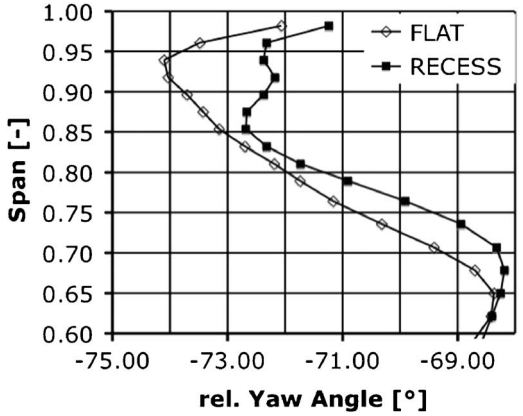

Fig. 19 Experimental pitch averaged relative yaw angle at 14% axial chord downstream rotor blade trailing edge for new recess tip blade

for different vane/blade spacings. The trend in the variation of Nu number according to the investigated location is similar. The highest Nu number is found in the leading edge region. The second heat flux gauge was positioned 12.5% blade axial chord from peak suction downstream, reporting almost half of the Nu number at leading edge. This can also be observed in the nominal recess case in Fig. 11. Finally, the third heat gauge at 62% blade axial chord corresponding to 80% cavity axial chord reports almost the same Nu number for all vane spacings that was reported for the low vane spacing on the previous one for the short spacing.

Conclusion

A computational design optimization for a nominal recess cavity commonly used in axial turbine rotor blades has been presented. From extensive parametric study, a new recess cavity design is presented. Extensive aerodynamic and heat transfer comparisons between the new design and the flat tip blade and the nominal recess tip are presented. The computational data were compared to experimental data from ETHZ where the 3D flow structures and the performance of rotor blades with flat tip and the new recess design were measured. Qualitative comparisons to the experimental data from OSU have also been used to validate the predicted heat transfer data. The following concluding statements can be drawn from this study.

1. A better understanding of the three-dimensional flow inside recess cavities was gained. Three cavity vortices were found to govern the leakage flow through the cavity.
2. Change of the cavity geometry influenced the generation and the interaction of the main recess vortices. A particular recirculation at the suction side front responsible for high heat transfer could be eliminated and lead to a new design with improved heat transfer behavior.
3. The beneficial effect of creating an aerodynamic seal has been shown for both recess designs. Tip leakage mass flow could be lowered by as much as 25% in the new recess design compared to the flat tip. CFD showed increased power output for the new design too. Experimental measurements showed a 0.2% increase in the turbine efficiency between the flat tip and the new recess tip at design point.
4. The heat load on the blade tip is found to be a balance between the heat load on the different blade tip components, i.e., the tip rim, the cavity rim walls, the cavity bottom, and the rear flat blade tip. The new recessed design is about 7% lower on the overall heat load compared to the base line recessed design and 13% lower compared to the flat tip.
5. To the best of the author's knowledge, this is the first time that detailed profiling of blade tip recess cavity is shown to improve performance and reduce heat load.

Acknowledgment

The authors would like to thank Dr. Burdet and Dr. Mokulys for their valuable contributions to this work.

Nomenclature

X (axial), Y,Z = Cartesian coordinates

R (radial), θ, X = cylindrical coordinates

$c_{ax} = X_{TE\ blade} - X_{LE\ blade}$ = blade axial chord

$h = (R_{blade\ tip} - R_{hub})/(R_{hub} - R_{casing})$ = tip clearance height

L = recess length

D = recess depth

$t(L,D)$ = recess rim thickness

p_s = static pressure

p_{tr} = relative total pressure

p_{t0} = turbine inlet total pressure

$p_{s,turbine,exit}$ = turbine exit static pressure

$\dot{m} = \int_A \mathbf{c} \cdot d\mathbf{A}$ = mass flow

$mdt^* = \dot{m}_{tip}/\dot{m}_{flat\ tip}$ = normalized tip gap mass flow

$C_{pt} = (p_{tr} - p_{s,turbine,exit})/(p_{t0} - p_{s,turbine,exit})$ = total pressure coefficient

$M = \int_A r \cdot \mathbf{p}_\theta \cdot d\mathbf{A}$ = torque

K_f = thermal conductivity of fluid

T_∞ = rotor inlet total temperature

T_w = wall temperature

q_w = wall heat flux

$Nu = q_w c_{ox}/K_f(T_w - T_\infty)$ = Nusselt number

$\eta_m = (\omega M/\dot{m})/\{c_p T_{in}[1 - (p_{t,out}/p_{t,in})^{(\kappa-1)/\kappa}]\}$ = efficiency

References

[1] Rains, D. A., 1954, "Tip Clearance Flows in Axial Flow Compressors and Pumps," Hydrodynamics and Mechanical Engineering Laboratories, California Institute of Technology, Report No. 5.

[2] Moore, J., and Tilton, J. S., 1988, "Tip Leakage Flow in a Linear Turbine Cascade," ASME J. Turbomach., **110**, pp. 18–26.

[3] Bindon, J. P., 1989, "The Measurement and Formation of Tip Leakage Loss," ASME J. Turbomach., **111**, pp. 257–263.

[4] Morphis, G., and Bindon, J. P., 1992, "The Development of Axial Turbine Leakage Loss for Two Profiled Tip Geometries Using Linear Cascade Data," ASME J. Turbomach., **114**, pp. 198–203.

[5] Heyes, F. J. G., Hodson, H. P., and Dailey, G. M., 1992, "The Effect of Blade Tip Geometry on the Tip Leakage Flow in Axial Turbine Cascades," ASME J. Turbomach., **114**, pp. 643–651.

[6] Ameri, A. A., 2001, "Heat Transfer and Flow on the Blade Tip of a Gas Turbine Equipped With a Mean-Camberline Strip," ASME Paper No. 2001-GT-0156.

[7] Tallman, J., and Lakshminarayana, B., 2000, "Numerical Simulation of Tip Clearance Flows in Axial Flow Turbines, With Emphasis on Flow Physics, Part I—Effect of Tip Clearance Height," ASME J. Turbomach., **123**, pp. 314–323.

[8] Tallman, J., and Lakshminarayana, B., 2000, "Numerical Simulation of Tip Clearance Flows in Axial Flow Turbines, With Emphasis on Flow Physics, Part II—Effect of Outer Casing Relative Motion," ASME J. Turbomach., **123**, pp. 324–333.

[9] Yaras, M. I., and Sjolander, S. A., 1992, "Effects of Simulated Rotation on Tip Leakage in a Planar Cascade of Turbine Blades: Part I—Tip Gap Flow," ASME J. Turbomach., **114**, pp. 652–659.

[10] Yaras, M. I., and Sjolander, S. A., 1992, "Effects of Simulated Rotation on Tip Leakage in a Planar Cascade of Turbine Blades: Part II—Downstream Flow Field and Blade Loading," ASME J. Turbomach., **114**, pp. 660–667.

[11] Basson, A. H., and Lakshminarayana, B., 1995, "Numerical Simulation of Tip Clearance Effects in Turbomachinery," ASME J. Turbomach., **109**, pp. 545–549.

[12] Dunn, M. G., and Haldemann, C. W., 2000, "Time Averaged Heat Flux for a Recessed Blade Tip, Lip and Platform of a Transonic Turbine Blade," ASME Paper No. GT2000-0197.

[13] Jameson, A., and Baker, T. J., 1984, "Multigrid Solutions of the Euler Equations for Aircraft Configurations," AIAA Paper No. 84-0093.

[14] Tatsumi, S., Martinelli, L., and Jameson, A., 1995, "A New High Resolution Scheme for Compressible Viscous Flow With Shocks," AIAA Paper No. 95-0466.

[15] Baldwin, B., and Lomax, H., 1978, "Thin Layer Approximation and Algebraic Model for Separated Turbulent Flows," AIAA Paper No. 78-257.

[16] Sommer, T. P., So, R. M. C., and Lai, Y. G., 1992, "A Near-Wall Two-Equation Model for Turbulent Heat Fluxes," Int. J. Heat Mass Transfer, **35**(12), pp. 3375–3387.

[17] Behr, T., Kalfas, A. I., and Abhari, R. S., "Unsteady Flow Physics and Performance of a One-and-1/2-Stage Unshrouded High Work Turbine," ASME Paper No. GT2006–90959.

[18] Sell, M., Schlienger, J., Pfau, A., Treiber, M., and Abhari, R. S., 2001, "The 2-stage Axial Turbine Test Facility LISA," ASME Paper No. 2001-GT-049.

Boundary Layer Transition on the High Lift T106A Low-Pressure Turbine Blade With an Oscillating Downstream Pressure Field

Maciej M. Opoka[1]
e-mail: Maciej.Opoka@rolls-royce.com

Richard L. Thomas

Howard P. Hodson

Whittle Laboratory,
University of Cambridge,
Cambridge, UK

This paper presents the results of an experimental study of the interaction between the suction surface boundary layer of a cascade of low-pressure (LP) turbine blades and a fluctuating downstream potential field. A linear cascade equipped with a set of T106 LP turbine blades was subjected to a periodic variation of the downstream pressure field by means of a moving bar system at low-speed conditions. Measurements were taken in the suction surface boundary layer using 2D laser Doppler anemometry, flush-mounted unsteady pressure transducers and surface shear stress sensors. The Reynolds number, based on the chord and exit conditions, was 1.6×10^5. *The measurements revealed that the magnitudes of the suction surface pressure variations induced by the oscillating downstream pressure field, just downstream of the suction peak, were approximately equal to those measured in earlier studies involving upstream wakes. These pressure field oscillations induced a periodic variation of the transition onset location in the boundary layer. Two turbulence levels were investigated. At a low level of inlet freestream turbulence of 0.5%, a separation bubble formed on the rear part of the suction surface. Unsteady measurements of the surface pressure revealed the presence of high-frequency oscillations occurring near the start of the pressure recovery region. The amplitude of these fluctuations was of the order of 7–8% of exit dynamic pressure, and inspection of the velocity field revealed the presence of Kelvin-Helmholtz-type shear layer vortices in the separated free shear layer. The frequency of these shear layer vortices was approximately one order-of-magnitude greater than the frequency of the downstream passing bars. At a higher inlet freestream turbulence level of 4.0%, which is more representative of real engine environments, separation was prevented by an earlier onset of transition. Oscillations were still observed in suction surface shear stress measurements at a frequency matching the period of the downstream bar, indicating a continued influence on the boundary layer from the oscillating pressure field. However, the shear layer vortices seen in the lower turbulence intensity case were not so clearly observed, and the maximum amplitude of suction surface pressure fluctuations was reduced.*
[DOI: 10.1115/1.2751142]

Introduction

Today, there is a trend to increase the lift coefficients of low-pressure (LP) turbine blades. This is to achieve engine weight and cost reductions. The blade loading is often expressed in the form of a Zweifel coefficient. This typically rises from conventional values of 0.8 to levels approaching 1.2. As the lift coefficient increases, the adverse pressure gradient on the rear part of the suction surface becomes ever more aggressive

$$Z = \frac{S}{C_{ax}} \frac{\tan\alpha_2 - \tan\alpha_1}{0.5\ \mathrm{s}^2\ \alpha_2} \tag{1}$$

The Reynolds numbers of LP turbine blades range from about 0.5×10^5 in the final stage at high altitude in small business jet applications to about 5×10^5 at sea-level takeoff in the first stage of the largest turbofans. Between takeoff and cruise altitude, the Reynolds number might fall by a factor of between 3 and 4. Given these Reynolds numbers and the lift coefficients of modern LP turbines, boundary layer transition and separation play important roles in determining engine performance at different operating conditions. In this context, it is well known that the turbulence and mean velocity perturbations associated with the interaction of wakes from an upstream blade row with a downstream blade row play an important role in the transition process in many LP turbines.

In the multistage environment, the relative motion of the adjacent blade rows gives rise to a variety of unsteady interactions. The potential influence of a blade extends both upstream and downstream. It decays exponentially with a length scale of the order of the blade pitch. The rate of decay of the wakes is much lower than that of the potential fields. As a result, the interaction of wakes with downstream blade rows has received far more attention in the literature.

It will be shown below that the unsteady perturbations in the velocity field due to the oscillating potential field of the downstream blade row can be of a comparable magnitude to the unsteady perturbations caused by an upstream wake [1]. Recently, Lou and Hourmouziadis [2] described the behavior of a separation, formed on a flat plate under an adverse pressure gradient, which is typical of LP turbines. The unsteady modulation of separation size (in length and in height) was attributed to the effect of periodic freestream velocity oscillations. This work was carried out at a low level of freestream turbulence. In real multistage turbomachines, significantly higher turbulence levels might be

[1]Currently at Rolls Royce Deutschland, Dahlewitz, Germany.

Contributed by the International Gas Turbine Institute of ASME for publication in the JOURNAL OF TURBOMACHINERY. Manuscript received June 27, 2006; final manuscript received January 15, 2007; published online February 29, 2008. Review conducted by David Wisler. Paper presented at the ASME Turbo Expo 2006: Land, Sea and Air (GT2006), May 8–11, 2006, Barcelona, Spain.

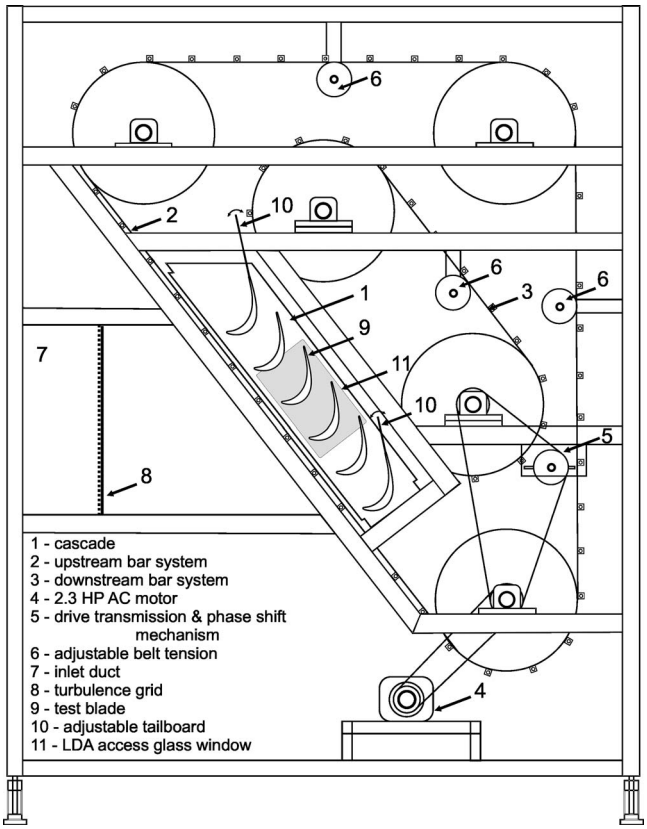

Fig. 1 T106A LP turbine bar-passing rig

found. In spite of the high freestream turbulence, the suction side separation can still be present, especially at lower Reynolds numbers, as shown in Opoka and Hodson [3]. However, the transition mechanism in the separated shear layer may differ.

The current paper presents an exploration of the often-neglected effect of upstream propagating potential fields from the downstream bladerow at low and elevated freestream turbulence intensities.

Experimental Setup

Previous studies of LPT cascades at the Whittle Laboratory have used a single system of moving belts and bars, for example Curtis et al. [4] and Stieger et al. [1]. These experiments produced flows representative of a single stage of a turbomachine suitable for wake–boundary layer interaction studies.

In order to facilitate replication of a downstream potential field, the facility of Stieger et al. [1] was redesigned to accommodate a system of moving belts and bars situated downstream of the cascade.

Bar Passing Rig. The general arrangement of the test facility is shown in Fig. 1. The basic rig characteristics are summarized in Table 1. The cascade (1) consists of six T106 profiles, assembled with a pitch-chord ratio known as configuration A. The T106 profile is a high lift LP turbine blade. It is a high turning profile with a design exit Mach number of 0.59. As shown in the schematic of the velocity triangles (see Fig. 2), the inlet conditions were chosen to reproduce those of a 50% reaction turbine. The Zweifel coefficient is of the order of 1.05.

The upstream moving bar system (2) that is shown in Fig. 1 is used to generate viscous wakes. The downstream moving bar system (3) was designed to reproduce the stator suction surface pressure oscillations associated with the potential fields of a downstream rotor.

This dual belt system was driven by a 2.3 HP AC motor (4)

Table 1 Characteristic dimensions of T106A cascade

Cascade properties	
Profile	T106A
Number of blades in the cascade	6
Real chord – C (mm)	198
Axial chord – C_{ax} (mm)	170
Cascade pitch – s (mm)	158.2
Pitch to chord ratio – $s/C=\tau$	0.799
Blade aspect ratio – h/C	1.884
Design inlet flow angle α_1 (°)	−37.7
Design exit flow angle α_2 (°)	63.2
Downstream bar diameter – D (mm)	47.5
Downstream bar to trailing edge (mm)	112
Downstream bars pitch (mm)	237

with feedback control. The drive from the upstream system was transmitted onto the downstream system through the belt (5). For the current work, no bars were fitted to the upstream system. The test facility was attached to the outlet of an open cycle low-speed wind tunnel, where a centrifugal fan supplied the airflow. The set of gauzes and honeycomb inserts in the tunnel made the flow uniform before delivering it into the cascade test section through the inlet duct (7).

Because the propagation of the unsteady potential field depends on the flow Mach number, it is impossible to reproduce an exactly equivalent unsteady pressure field in a low-speed facility, such as the one used here. Being conscious of the limitation of such an approach, inviscid numerical predictions for the T106 LP turbine repeating stage design, with pitch and chord ratios of 1:1.5 and a blade row gap equal to 43% of the downstream rotor blade pitch (40% of rotor C_{ax}), were carried out by Antoranz and de la Calzada [5]. These were followed by a series of simulations in which the downstream rotor was replaced with a cylindrical bar. The bar diameter and the spacing between stator trailing edge and the bar center were chosen to match the amplitude of pressure oscillations seen on the stator suction surface as induced by the real rotor blade. The downstream bar system was designed following the results of these simulations.

Test Conditions and Cascade Equipment. The flow delivered from the wind tunnel is characterized by low turbulence levels of the order of 0.5%. To reach levels of inlet freestream turbulence

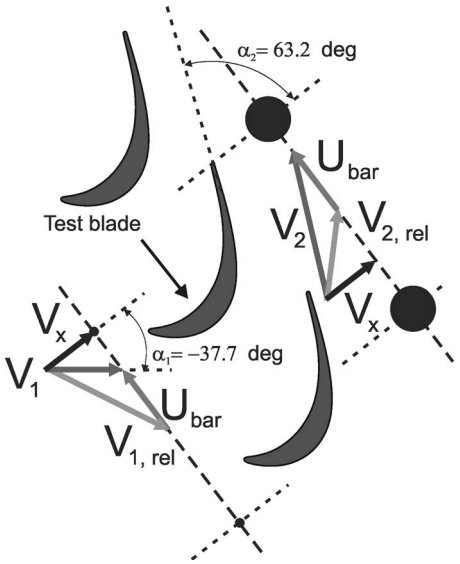

Fig. 2 T106A cascade, with downstream bars shown at time $t/\tau_0=0.0$

intensity more representative of the multistage environment (2–4%, see [6]), a turbulence grid was used. The turbulence grid (see (8) in Fig. 1) was based on the work of Roach [7]. The grid was located at a distance of three axial chords upstream of the test blade (9). This provided an inlet freestream turbulence intensity (FSTI) of 4.0%, measured in the absence of the cascade, at a location corresponding to the leading edge of the test blade. It should be mentioned that the turbulence grid was not parallel to the cascade inlet plane. Therefore, the decay of turbulence varies across the cascade in the pitchwise direction. The correlation of Roach predicts the turbulence levels at the leading edges of the top and bottom blades to be equal to 5.65% and 2.95%, respectively. Although these turbulence levels differ, the levels are such that the differences in blade boundary layer behavior, which result from the varying inlet turbulence intensity, do not seriously affect the cascade periodicity at the Reynolds number investigated here.

Total and static pressure probes at the inlet, and wall tappings at the outlet from the cascade were used to monitor the flow conditions and check the level of inlet uniformity and outlet periodicity. Adjustable tailboards (10), shown in Fig. 1, extending from the trailing edge of the top and bottom blades were used to ensure that the outlet flow was periodic.

The pitch ratio for the cascade and the downstream bar system was 1:1.5, as shown in Fig. 2, for which the initial position of time ($t/\tau_0=0.0$) has been presented. A ratio of 1:1.5 is similar to that found in many LP turbines.

Measuring Techniques and Data Presentation. The cascade flow conditions were monitored with a 16 channel Scanivalve DSA 3017. The T106 test blade (9) shown in Fig. 1 was equipped with surface pressure tappings. The tappings had a diameter of 0.3 mm and were located at midspan. The time mean levels of surface static pressure were measured using a Scanivalve system. Surface flush-mounted, fast response Kulite pressure transducers (model XCS-062) were used to acquire unsteady suction surface pressures at blade midspan. A detailed description of the Kulite signal acquisition procedure may be found in Stieger et al. [1].

A sheet of 50 hot-film sensors spaced at intervals of 2.54 mm in the streamwise direction was fitted on the blade suction surface at midspan. The array was manufactured by Senflex. The sensors were used to measure the quasi wall shear stress distribution using the procedure described in Hodson et al. [8]. Each sensor was connected to a Dantec C-series anemometer. The signal outputs from each anemometer were first acquired with filter settings that provided only the mean component. Then, a band-pass filter was used to acquire the fluctuating part.

During the acquisition of the hot-film and pressure transducer data, the logging frequency was 10 kHz and 128 ensembles of 4096 samples were acquired. The bar-passing frequency was equal to ~28 Hz. The data in this paper are presented as pressure coefficient and normalized quasi wall shear stress, both as ensemble averaged. These are defined by Eqs. (2) and (3), respectively. The signal of the hot-film gauges was normalized for each gauge, separately. Raw hot-film signals were extracted from the first ensemble of acquired data

$$\langle C_{p2is}\rangle = \frac{P_{01} - \langle P_{S(s,t)}\rangle}{P_{01} - P_{S2}} \tag{2}$$

$$\langle \tau_w\rangle_{\mathrm{ND}} = \frac{\langle \tau_w(s)\rangle - \langle \tau_w(s)\rangle_{\min}}{\langle \tau_w(s)\rangle_{\max} - \langle \tau_w(s)\rangle_{\min}} \tag{3}$$

One of the cascade sidewalls was equipped with a glass window (11) to allow laser beam access (see Fig. 1). Two-dimensional, suction surface boundary layer surveys were performed with a Dantec LDA system. This included a 5 W Argon ion laser (Coherent Innova 70) and Dantec FibreFlow System with a beam expander. To avoid interruption of the laser beams by the blade surface, the laser probe axis was inclined with respect to the blade suction surface. The size of the measuring volume was equal to approximately $0.08\times0.08\times1.00$ mm.

The LDA system was operated in backscatter mode. The Dantec burst spectrum analysers (BSAs) and photo multiplier tubes were controlled with LABVIEW software. The acquisition was triggered by each bar-passing event. Data were collected in the dead time mode with a dead time interval that ensured statistical independence of the acquired data.

The seeding for the LDA was generated using a TSI six jet atomizer with Shell Odina Oil. The mean particle size was ~1.5 μm. The data rate during the acquisition varied between 1.5 and 5 kHz.

During the post-processing of laser signals, a coincidence filter was used. The velocity bias resulting from periods of higher or lower velocity was removed using a residence time weighting factor as defined in Eq. (4) (see [9])

$$\eta_i = \frac{t_{ri}}{\sum_{j=1}^{N} t_{rj}} \tag{4}$$

The LDA data was ensemble averaged by first dividing the wake passing period into 128 time bins. Each time bin was evaluated based on a nominal average of 500 samples. The weighting factor, mean, variance, and cross moments were then calculated for each time bin according to Eqs. (5)–(7)

$$\langle u\rangle = \sum_{i=1}^{N} \eta_i u_i \tag{5}$$

$$\langle u'^2\rangle = \sum_{i=1}^{N} \eta_i (u_i - \langle u\rangle)^2 \tag{6}$$

$$\langle u'v'\rangle = \sum_{i=1}^{N} \eta_i (u_i - \langle u\rangle)(v_i - \langle v\rangle) \tag{7}$$

The traverses were performed perpendicular to the suction surface, in the boundary layer region, between 0.1 mm and 16 mm above the wall at 45% of the blade span. The complete traverse consisted of 21 stations, with the first millimeter above the wall being traversed in five steps. From these LDA measurements, the time-dependent ensemble mean turbulent kinetic energy, displacement thickness, momentum thickness, and shape factor values were derived using Eqs. (8)–(11). The edge of the boundary layer was defined as the height where the velocity was equal to 98% of the freestream value. The LDA data were normalized with the cascade isentropic exit velocity (V_{2is})

$$\langle \mathrm{TKE}\rangle = \frac{1}{2}(\overline{\langle u'^2\rangle} + \overline{\langle v'^2\rangle}) \tag{8}$$

$$\langle \delta^*\rangle = \int_{y=0}^{\langle\delta\rangle} \left(1 - \frac{\langle u\rangle}{\langle U_e\rangle}\right) \mathrm{d}y \tag{9}$$

$$\langle \theta\rangle = \int_{y=0}^{\langle\delta\rangle} \frac{\langle u\rangle}{\langle U_e\rangle}\left(1 - \frac{\langle u\rangle}{\langle U_e\rangle}\right) \mathrm{d}y \tag{10}$$

$$\langle H_{12}\rangle = \frac{\langle \delta^*\rangle}{\langle \theta\rangle} \tag{11}$$

$$\mathrm{Re}_{2,is} = \frac{\rho\overline{V_{2,is}}C}{\mu} \tag{12}$$

$$\phi = \frac{\overline{V_{x1}}}{U_{\mathrm{bar}}} \tag{13}$$

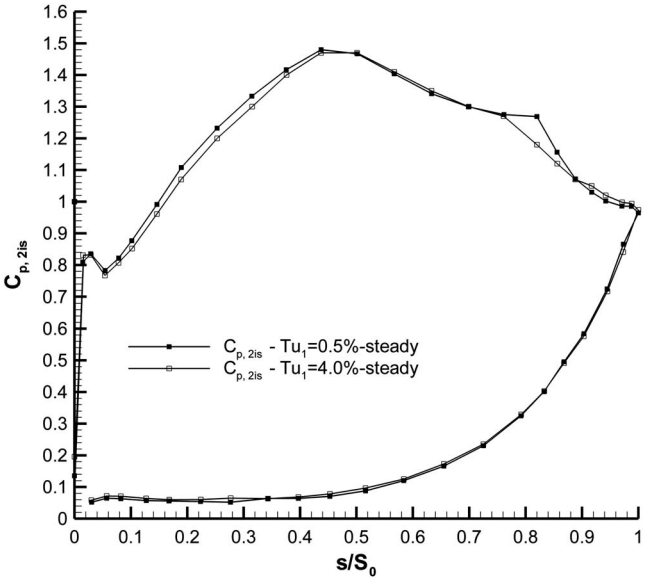

Fig. 3 Steady-state surface pressure coefficient Cp_{2is}, $Re_{2is}=1.6\times10^5$, $Tu_1=0.5\%$ (black) and 4.0% (grey)

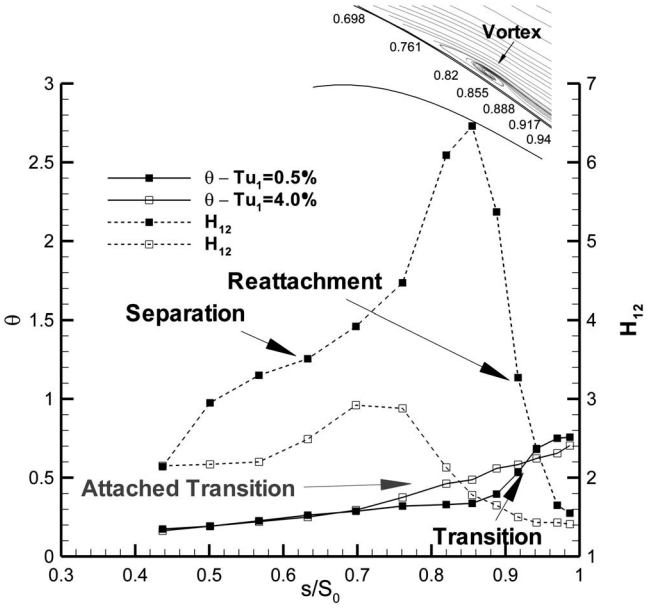

Fig. 4 Steady flow suction surface boundary layer momentum thickness (θ) and shape factor (H_{12}), $Re_{2is}=1.6\times10^5$, $Tu_1=0.5\%$ (black), and 4.0% (grey)

$$F_{\text{red}} = \frac{fC}{V_{2,is}} \tag{14}$$

The data presented in this paper were acquired at a Reynolds number of $Re_{2is}=1.6\times10^5$, based on the exit isentropic velocity and the real chord, as given by Eq. (12). The flow coefficient, defined by Eq. (13), was equal to 0.83. The reduced frequency of the potential disturbance, defined by Eq. (14), was set to 0.46. The background flow was characterized by two levels of inlet freestream turbulence intensity ($Tu_1=0.5\%$ and 4.0%).

Uncertainty Analysis. At the exit from the cascade, the exit dynamic pressure varied by $<2.5\%$ over the five passages. Over the central passages, the variation was $<1\%$.

The inclination of the laser probe with respect to the suction surface of the blade was of the order of 5 deg. This was to avoid any obstruction of the laser beams by the blade wall. The velocity measured with the inclined LDA probe is insignificantly different from that measured with a noninclined probe ($<0.5\%$), and for this reason, it was considered unnecessary to apply a correction to the measurements. The 2D LDA data were processed with a coincidence window set to 0.005 ms. The step resolution of the traversing system was 0.025 mm.

The mean pressure levels were measured using a Scanivalve DSA 3107 array with a ±2500 Pa range. The discretization error on this measurement is 0.17 Pa, which corresponds to 0.2% of the exit dynamic pressure at $Re_{2is}=1.6\times10^5$. The sensitivity of the Kulite transducer system was approximately equal to 500 Pa/V with a discretisation error of 0.05 Pa.

Steady Flow Results

Time Mean Surface Pressure Coefficient. The measured steady flow distributions of the surface pressure coefficient, at the Reynolds number Re_{2is} of 1.6×10^5 are presented in Fig. 3. The data were measured using the DSA 3017, which was connected to surface pressure tappings via the Scanivalve. Symbols are shown at each pressure tapping and sensor position. The black line and filled symbols are attributed to the lower case of FSTI ($Tu_1=0.5\%$) and the higher FSTI case (4.0%) is (and will be in the other figures) represented by empty symbols and/or grey lines.

The peak suction point occurred for both cases at a surface position of $s/S_0=0.44$. Downstream of this point, the boundary layer flow develops under the influence of an adverse pressure gradient.

For the lower freestream turbulence case, the suction surface boundary layer was observed to separate at a surface distance of $s/S_0=0.63$. From this point, the pressure "plateau" extended up to a distance of $s/S_0=0.82$. The end of the pressure plateau indicates the onset of the transition process. Transition manifests through the pressure recovery region. Downstream of $s/S_0=0.9$, the boundary layer was fully reattached.

In the case of the higher freestream turbulence, the distribution of the surface pressure coefficient between $s/S_0=0.6$ and $s/S_0=0.8$ did not develop a full pressure plateau, as observed previously. This might suggest the absence of the separation bubble due to attached flow transition.

Boundary Layer Integral Parameters. In Fig. 4, time mean boundary layer momentum thickness (θ) and shape factor (H_{12}) calculated from the LDA data are shown. Once again, both FSTI cases are presented at the Re_{2is} of 1.6×10^5. For the lower turbulence intensity case (filled symbols), at a surface distance of $s/S_0=0.63$, the laminar boundary layer separates with a shape factor, H_{12}, of 3.5. The momentum thickness (θ), increases slowly in a region between $s/S_0=0.63$ and $s/S_0=0.82$, which corresponds to the end of the pressure plateau in Fig. 3. Within the above region, and further downstream up to $s/S_0=0.86$, the shape factor (H_{12}) continuously rises. At a surface distance of $s/S_0=0.86$, following the end of the pressure plateau, the shape factor suddenly drops. Here, a rapid increase of momentum thickness begins. Downstream of $s/S_0=0.94$, the streamwise gradient of momentum thickness becomes milder. Transition is completed. Therefore, it can be concluded that transition occurred through a laminar separation. The boundary layer leaving the blade trailing edge is attached and fully turbulent ($H_{12}<1.6$).

To the top right of Fig. 4, streamlines of the time mean velocity field illustrate the separation bubble described above. The large vortex, with a center at $s/S_0=0.84$, appears due to breakdown of the separated shear layer. It is because of its particular location that it is often referred to as recovery vortex.

For the case of the higher FSTI, the transition process differs.

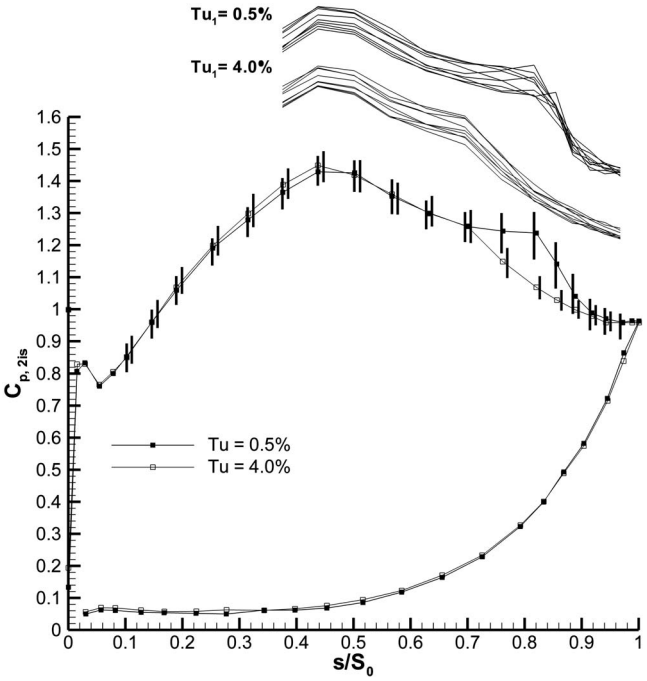

Fig. 5 Ensemble-averaged suction surface pressure coefficient, $Re_{2is}=1.6\times10^5$, $F_{red}=0.46$, $\phi=0.83$, $Tu_1=0.5\%$ (black), and 4.0% (grey)

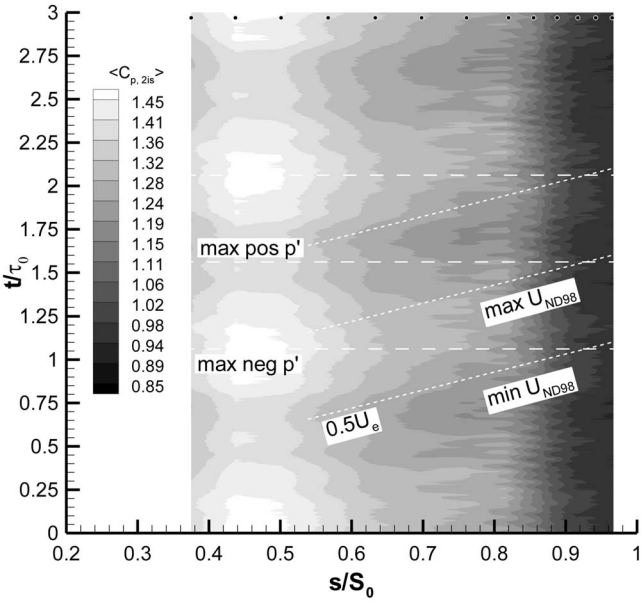

Fig. 6 Ensemble-averaged suction surface pressure coefficient, $Re_{2is}=1.6\times10^5$, $F_{red}=0.46$, $\phi=0.83$, and $Tu_1=0.5\%$

The higher levels of freestream disturbance enhance the exchange of momentum between the freestream and the boundary layer region. The boundary layer flow, after passing the point of the peak suction, is characterized by a lower shape factor H_{12} (mainly due to the reduction of the displacement thickness δ^*) even though it experiences a similar adverse pressure gradient. The momentum thickness shows no sensitivity to freestream turbulence over the distance between $s/S_0=0.44$ and $s/S_0=0.70$. At a surface distance of $s/S_0=0.70$, the curve of the momentum thickness departs from that of the lower freestream turbulence. This rise of momentum thickness indicates that the transition process has begun. Therefore, the suction surface boundary layer at the higher FSTI, although inflexional, will not undergo separation, as was observed in the lower freestream turbulence case. In fact, no reverse flow was observed in the boundary layer and the shape factor did not exceed a value of 3.0.

Unsteady Flow Results

Ensemble-Averaged Surface Pressure Coefficient and Velocity at the Boundary Layer Edge. The effect of the downstream potential field was investigated at flow coefficient $\phi=0.83$ and reduced frequency $F_{red}=0.46$. Figure 5 presents data acquired at $Re_{2is}=1.6\times10^5$ and both FSTI levels, $Tu_1=0.5\%$ and $Tu_1=4.0\%$. The suction surface time mean distributions of the unsteady pressure coefficient are shown, and the pressure surface data are copied from Fig. 3. Additionally, here, at each measurement station, vertical lines have been superimposed. These lines represent the peak-to-peak variation of the ensemble-averaged suction surface pressure coefficient, measured during one period of downstream bar interaction. The vertical lines representing the case of the higher FSTI are shifted in the downstream direction by 0.01 of s/S_0, to avoid overlapping of the two cases.

At both FSTI levels, on the front part of the blade, the peak-to-peak variation of the pressure is of the order of 8.0% of the exit dynamic pressure. After passing the peak suction point, the variation in pressure increases as the distance to the disturbance source is reduced. For the case of $Tu_1=0.5\%$, the maximum peak-to-peak perturbation (15% exit dynamic pressure) is observed in the region of the separation bubble between $s/S_0=0.75$ and $s/S_0=0.85$. At $s/S_0=0.90$, in the region of the turbulent boundary layer downstream of reattachment, the magnitude of pressure variation is less than that observed over the earlier part of the blade. This is true for both levels of FSTI. At the higher FSTI level ($Tu_1=4.0\%$), the maximum peak–to-peak perturbation (10% exit dynamic pressure) is located at $s/S_0=0.70$. To comprehend the significance of this influence, it should be recalled that surface pressure variations induced by passing wakes ahead of the separation at low FSTI [1] were approximately equal to those currently observed. Opoka and Hodson [3], who continued the work of Stieger at the higher FSTI (4.0%), reported a 10% pressure perturbation due to the upstream wake. This reveals that the strength of both the wake and the potential field interactions are of a comparable order.

The data in Fig. 5 were compared to the results of the aforementioned inviscid predictions of Antoranz and de la Calzada [5]. The measured maximum pressure oscillation was ~50% above the predicted value, but occurred at a similar location. The reasons for this discrepancy require further investigation. Dring et al. [10], investigated a single stage of an axial turbine with an axial gap between the blade rows set to 0.15 and 0.65 of the axial chord. At the smaller axial gap, they reported a peak-to-peak pressure variation on the stator suction surface of the order of 30% of exit dynamic pressure. Increasing the axial gap reduced the surface pressure oscillations by a factor of 10.

On the top of Fig. 5, two sets of lines represent the pressure coefficient distributions at ten equally spaced time intervals. In both cases of FSTI, the observed pressure perturbation at the peak suction point is approximately twice the value seen near the trailing edge of the blade. At the lower FSTI, the separation point and the end of the pressure plateau oscillate about their steady flow positions. For the higher FSTI, the pressure plateau becomes more pronounced than in steady flow. This might indicate the transient appearance of a short separation bubble.

The data from Fig. 5 have been replotted in the form of a space-time diagram in Fig. 6. The horizontal lines superimposed onto Fig. 6 indicate time instances at which the maxima of the positive and negative pressure perturbations were observed between the peak suction point $s/S_0=0.44$ and $s/S_0=0.64$. The maximum decrease of surface pressure is located at approximately

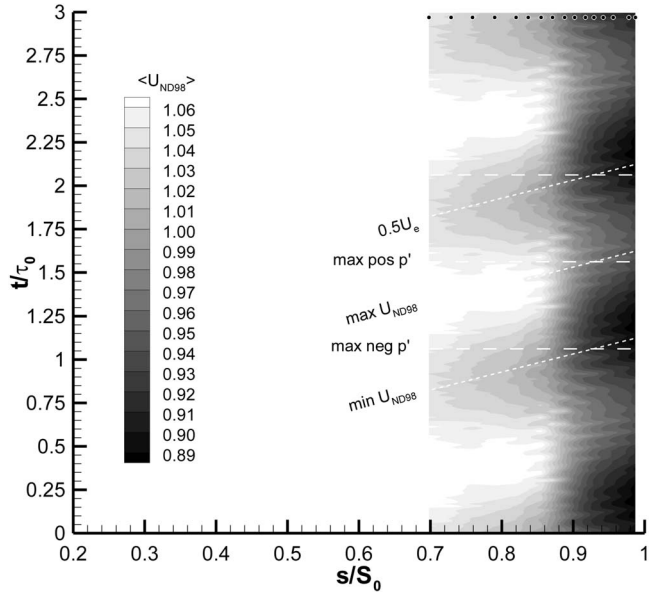

Fig. 7 Ensemble-averaged nondimensional velocity at the edge of the boundary layer $Re_{2is}=1.6\times10^5$, $F_{red}=0.46$, $\phi=0.83$ and Tu=0.5%

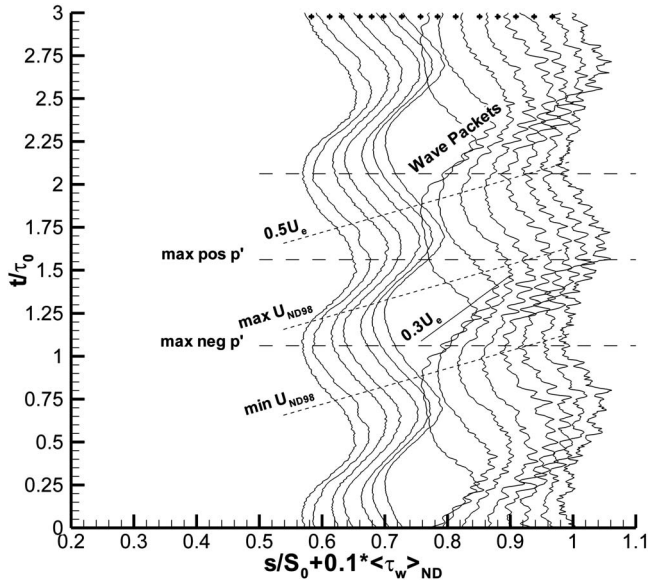

Fig. 8 Traces of normalized ensemble-averaged surface quasi-wall shear stress, $Re_{2is}=1.6\times10^5$, $F_{red}=0.46$, $\phi=0.83$, and $Tu_1=0.5\%$

$t/\tau_0=0.10$, and the maximum increase occurs a half period later at $t/\tau_0=0.6$. These lines shall be superimposed onto other figures as a visual aid to conveying the impact of the potential field influence. The three inclined lines are explained in the following paragraph.

Figure 7 illustrates the distribution of the nondimensional ensemble-averaged velocity at the boundary layer edge with the horizontal lines superimposed from Fig. 6. The inclined lines indicate the paths of the maxima and minima of the velocity perturbations. The angle of inclination of these lines corresponds to a celerity equivalent to a half of the local freestream velocity. This celerity is thought to be related to the speed of the downstream bar in the cascade pitchwise direction (see Fig. 2). This speed is of the order of 0.54 of the exit velocity. As the bars are passing downstream of the cascade, and their potential field propagates upstream, the blade passage exit area is partially blocked ($d_{bar}/s=0.33$). At the time $t/\tau_0=0.0$, the distance between the centre of the bar and the trailing edge is the smallest (see Fig. 2). This is when the rear part of the suction surface begins to strongly decelerate. In Fig. 6, downstream of $s/S_0=0.6$, pressure changes (especially pressure minima) appear to follow the velocity trends, albeit with a phase advance. Along the region between surface locations $s/S_0=0.60$ and $s/S_0=0.82$, the highest values of the oscillating surface pressure coefficient (C_{p2is}) appear during the period of acceleration. Note that the terms acceleration and deceleration relate to temporal, rather than spatial gradients of velocity. Deceleration of the flow velocity can be viewed in the region from the maximum velocity line to the minimum velocity line.

In both Figs. 6 and 7 in the vicinity of $s/S_0=0.80$, high-frequency oscillations appear and persist up to the trailing edge of the blade. These oscillations, as well as the remaining case of the higher FSTI will be discussed below.

Mechanism of Unsteady Transition at Lower FSTI. In the steady flow, at a $Re_{2is}=1.6\times10^5$ and FSTI of $Tu_1=0.5\%$, the process of suction surface transition was observed to begin in the separated shear layer at $s/S_0=0.82$. The end of the pressure plateau region indicated the start of transition, while the process itself manifested through a rapid growth of the boundary layer momentum thickness (see Figs. 3 and 4). The reattachment point was located at a surface distance of $s/S_0=0.92$.

Ensemble-Averaged Quasi Wall Shear Stress at Low FSTI. A space-time diagram in Fig. 8 shows traces of normalized ensemble-averaged quasi wall shear stress. Black circles at the top of Fig. 8 represent the position of each sensor. The data were measured at the same flow conditions as the data shown in Figs. 6 and 7. Because of the nature of normalizing the hot-film data, information on the relative amplitudes between neighboring sensors is not retained. Thus, only qualitative impressions can be inferred from Fig. 8.

Upstream of $s/S_0=0.70$, the flow in the near wall region of the separated boundary layer is laminar. The frequency of the oscillations in the plot is equal to the downstream bar passing frequency (28 Hz). The peaks and valleys of these oscillations align with the superimposed velocity lines. However, the phase of the shear stress does not coincide with the phase of the velocity in the freestream. The phase lag relative to the freestream velocity is approximately equal to a quarter of the period of the potential field interaction. The lag means that the maximum positive shear stress perturbations occur during deceleration of the edge of the boundary layer, and that the maximum negative shear stress perturbations occur during the acceleration of the velocity at the edge of the boundary layer.

The above-mentioned phase lag represents the time of viscous diffusion, during which freestream oscillations penetrate through the boundary layer. The growth of the boundary layer between $s/S_0=0.56$ and $s/S_0=0.70$ might be deduced from the increasing value of the phase lag between the line of maximum velocity and the peaks of the quasi wall shear stress.

In Fig. 8, at a surface distance $s/S_0=0.74$, a new region of increased quasi wall shear stress appears at about half way between the superimposed lines of minima and maxima of the freestream velocity. However, the first appearance of this high shear stress pattern coincided with the minimum velocity line. The increased destabilisation or, perhaps, increased receptivity introduced by the deceleration process forces the transition onset location to move upstream from its steady flow location of $s/S_0=0.82$. From this location ($s/S_0=0.74$), high-frequency oscillations begin to develop into wave packets that travel downstream at approximately one-third of the freestream velocity. They can be seen throughout the region of elevated quasi wall shear stress downstream of $s/S_0=0.74$. The fact that they survive the ensemble-averaging process indicates that these instabilities are

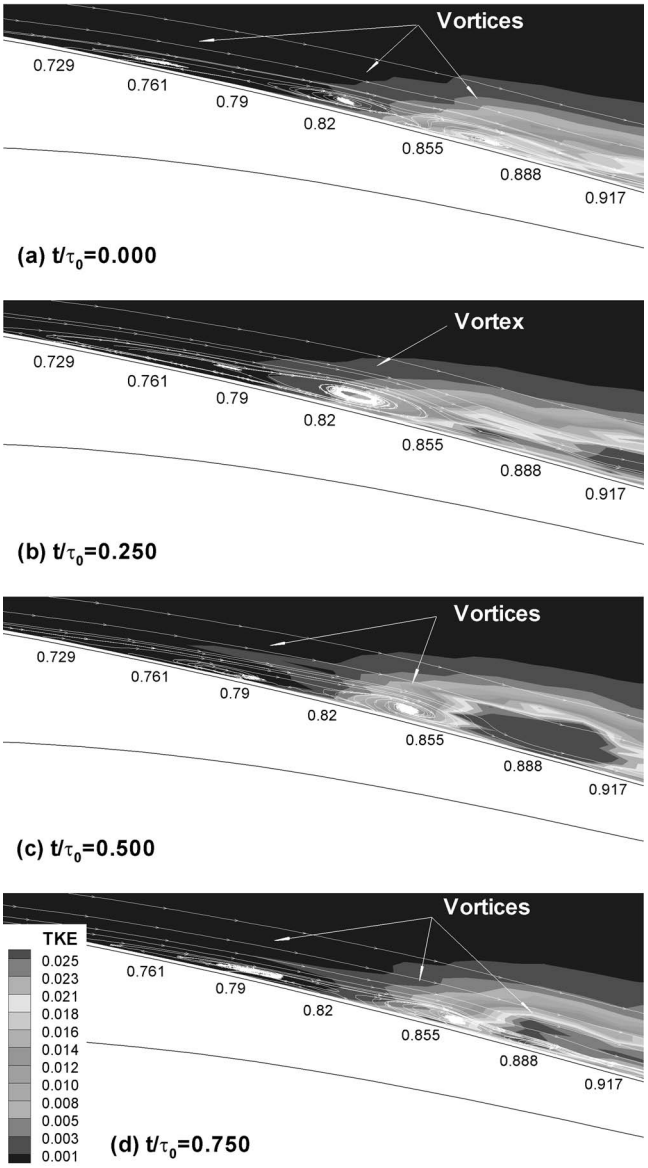

Fig. 9 Streamlines calculated from ensemble-averaged 2D LDA data, $Re_{2is}=1.6\times105$, $F_{red}=0.46$, $\phi=0.83$, and $Tu_1=0.5\%$

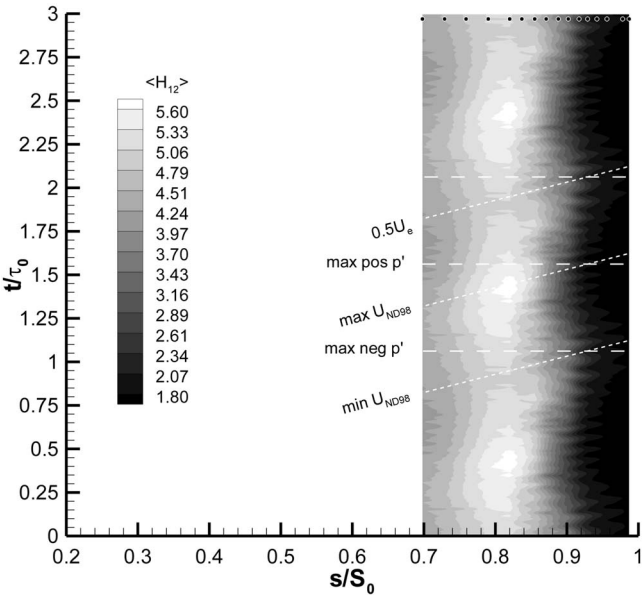

Fig. 10 Ensemble-averaged boundary layer shape factor, $Re_{2is}=1.6\times10^5$, $F_{red}=0.46$, $\phi=0.83$, and $Tu_1=0.5\%$

phase locked to the cyclic effects of the downstream bars.

The wave packet frequency at $s/S_0=0.90$ was ~14 times greater (392 Hz) than the downstream bar passing frequency (28 Hz). Such wave packets were observed in the past by Obremski and Fejer [11] and recently by Lou and Hourmouziadis [2], both of whom investigated transition along a flat plate with unsteady periodic flows for the case of attached and separated boundary layer, respectively. Here, as in the case of [2], no calmed region was observed.

During the remaining part of the cycle, identifiable as regions of lower quasi wall shear stress, Fig. 8 shows that acceleration allows the onset of transition to return to its steady-state location at $s/S_0=0.82$. Downstream of a surface location of approximately $s/S_0=0.90$, oscillations are observed throughout the whole period.

Unsteady 2D Velocity Field on the Suction Surface at Low FSTI. Figure 9 shows streamlines calculated from the measured velocity field imposed on a contour field of the turbulent kinetic energy (TKE) defined by Eq. (8). These are presented at four equally spaced time instances spanning one full period. In steady flow, the center of the vortex inside the separation bubble was located at $s/S_0=0.84$, as identified in the streamlines that are shown at the top of Fig. 4. Under unsteady flow conditions, the position of the vortex inside the separation bubble oscillates. Also, more than one vortex is present for a majority of the period within the region from $s/S_0=0.73$ to $s/S_0=0.89$. It is suggested that the instability wave packets observed at surface position $s/S_0=0.74$ (see Fig. 8) are due to fluctuations in the separated shear layer. These fluctuations are amplified in the shear layer and proceed into a Kelvin-Helmholtz-type of breakdown, involving a rolling up of the shear layer into a continuous sequence of spanwise vortices. The vortices are shed from the separation region into the turbulent flow following the reattachment of the bubble.

The nature of the interaction is similar to that observed by Stieger et al. [1], who examined the case of incoming wakes on the same T106 profile at the same FSTI. The frequencies at which the separation bubbles shed vortices are similar in both cases. The higher peak-to-peak pressure perturbation (30% exit dynamic pressure) associated with the traveling vortex in the case of Stieger et al. [1] is believed to be due to stronger forcing provided by the wake negative jet.

The contour field in Fig. 9 presents the turbulent kinetic energy calculated from LDA data (see Eq. (8)). The elevated levels of TKE appear at surface distance $s/S_0=0.85$ due to transition. The peak values of TKE are found between surface distance of $s/S_0=0.85$ and $s/S_0=0.92$. These high TKE regions are due to the breakdown of the vortices.

Ensemble-Averaged Boundary Layer Parameters at Low FSTI. Figure 10 shows the unsteady distribution of the boundary layer shape factor. The peak values of the shape factor are above 5.5, which is indicative of a relatively tall separation bubble. At $s/S_0=0.82$, one can observe periodic oscillations of the maximum shape factor values. This indicates the changing thickness of the bubble. No values fall below ~4.75, and it can therefore be stated that the modulating separation bubble is present throughout the full period of potential field interaction.

Unfortunately, there are no velocity data illustrating the unsteady behavior of the separation point. However, the position of the pressure plateau on the lines of C_{p2is} (upper) imposed on the top right in Fig. 5, suggests an influence on the separation point. The reattachment point, preceding the appearance of the turbulent flow ($H_{12}<2.0$) in Fig. 10, fluctuates at the bar-passing frequency

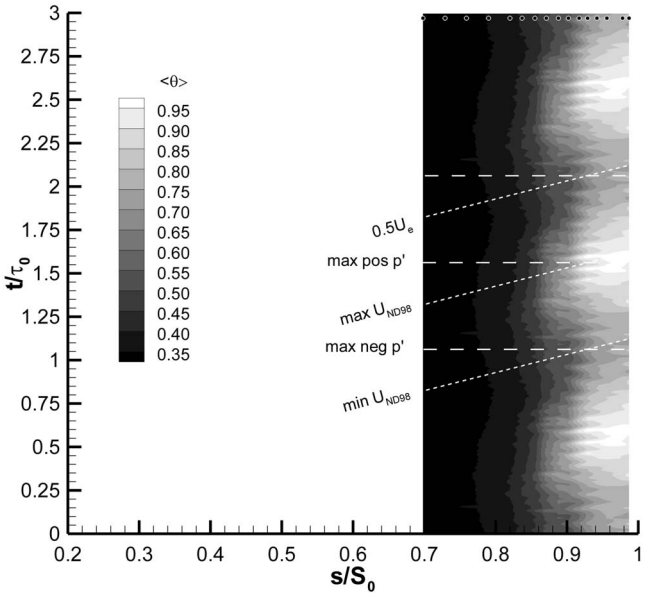

Fig. 11 Ensemble-averaged boundary layer momentum thickness, $Re_{2is}=1.6\times10^5$, $F_{red}=0.46$, $\phi=0.83$, and $Tu_1=0.5\%$

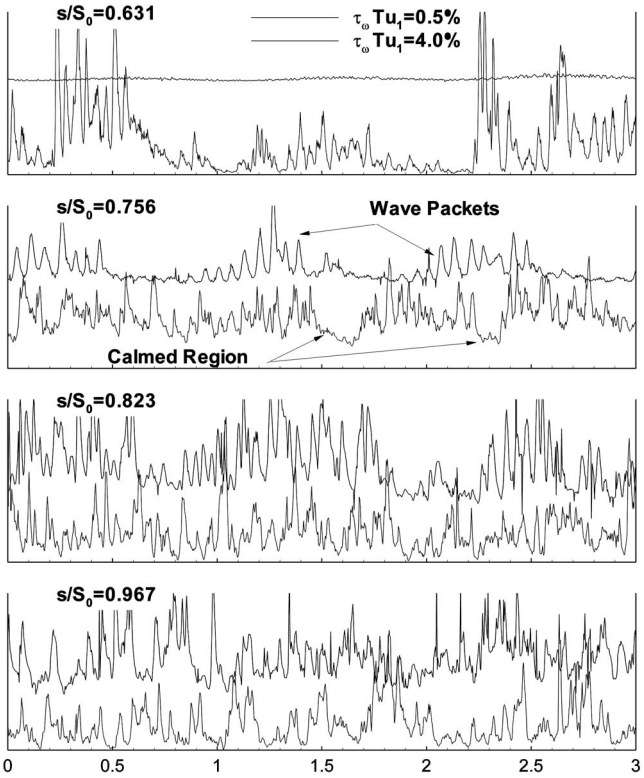

Fig. 12 Comparison between traces of normalized raw quasi-wall shear stress for $Tu_1=0.5\%$ (black) and $Tu_1=4.0\%$ (grey), illustrating effect of a downstream potential field at $Re_{2is}=1.6\times10^5$ for six surface locations $s/S_0=0.63$, 0.75, 0.82, and 0.96

about $s/S_0=0.90$. These oscillations are in phase (with regards to the min-max velocity cycle) with the front part of the bubble between $s/S_0=0.70$ and $s/S_0=0.75$.

In Fig. 10, the tallest bubble occurs along the line of maximum velocity ($s/S_0=0.82$, between $t/\tau_0=0.35$ and $t/\tau_0=0.4$; see also Figs. 9(*b*) and 9(*c*). Similarly, the lowest values of the shape factor are distributed along the line of minimum velocity, for which the most downstream reattachment was observed. The earliest reattachment location occurs at about $t/\tau_0=0.35$, just before the maximum shape factor values are observed.

Figure 11 presents a space-time diagram of the ensemble-averaged boundary layer momentum thickness (θ) calculated from the LDA measurements. The absolute values of momentum thickness can be seen to oscillate with the bar-passing period. The most rapid growth of the boundary layer momentum thickness is observed just before and then along the line of maximum velocity at the boundary layer edge, in a similar manner to the quasi wall shear stress of Fig. 8, which was discussed earlier. This is a consequence of the developing transition process enhancing the growth of the boundary layer. The bulk of the boundary layer momentum thickness near to the trailing edge is associated with this early transition, initiated at around $s/S_0=0.74$, as shown in Fig. 8.

In summarizing Figs. 10 and 11, it is noted that the tallest bubble results in the greatest loss of momentum. The most shallow separation bubble is stretched and reattaches further downstream. At this time, the momentum thickness has the same value as in steady flow. A comparison of the shape factor values presented here with those in Fig. 4 shows that the potential field of the downstream bars, in penetrating the rear part of the blade passage, tends to reduce the size (height and length) of the separation bubble, as at no point does the unsteady shape factor reach the maximum steady-state value of 6.5 and no value above 3.0 is observed downstream of $s/S_0=0.92$.

Effect of Freestream Turbulence on Transition. Figure 12 compares individual traces of raw hot-film signals, at both cases of FSTI during three periods of the interaction cycles. Four surface locations have been chosen for this discussion. At each presented surface distance, the upper lines represent data of the lower FSTI case, and the lower lines the higher FSTI case.

For the first plot of Fig. 12, at $s/S_0=0.63$, the data for the lower FSTI case indicate the laminar character of the flow. In the same plot, periodic patterns of transitional flow occur in the case of the higher FSTI. The most obvious turbulent spots appear at times between $t/\tau_0=0.25$ and $t/\tau_0=0.5$ and in subsequent periods at a similar phase. Once again, this early transition is due to deceleration of the outer part of the boundary layer, which destabilizes and/or increases the receptivity of the boundary layer. In fact, the attached flow transition in the high turbulence case starts at $s/S_0=0.6$ and develops as it progresses downstream. In contrast to the lower FSTI case, calmed regions are observed for the higher FSTI case. This is because the spots are formed before the boundary layer could separate, which makes the case of the higher FSTI more relevant to the work of Obremski and Fejer [11].

Twelve percent of suction surface length further downstream, at $s/S_0=0.756$, the trace of the high FSTI indicates transitional flow within the boundary layer at most times. Also, there is evidence of a calmed region just after $t/\tau_0=1.5$ and 2.5. In the case of the low FSTI, the flow remains laminar between the times of $t/\tau_0=0.5$ and $t/\tau_0=1.0$. During the remaining part of the cycle, the boundary layer begins to undergo transition during the decelerative phase, and hence, wave packet fluctuations become observable at approximately $t/\tau_0=0.1$, 1.1, 2.1, etc. As the flow develops further, these fluctuations grow and develop higher-frequency components, which are indicative of natural breakdown. The remaining laminar regions also begin to undergo transition (see $s/S_0=0.823$). Breakdown to turbulence occurs rapidly across the remainder of the surface, resulting in a turbulent wall-shear stress characteristic throughout the entire period at the trailing edge, $s/S_0=0.967$.

Trailing-Edge Boundary Layer. The two different transition modes (attached at the higher FSTI and separated at the lower FSTI) were also examined in terms of the boundary layer momentum thickness measured near to the trailing edge at $s/S_0=0.96$.

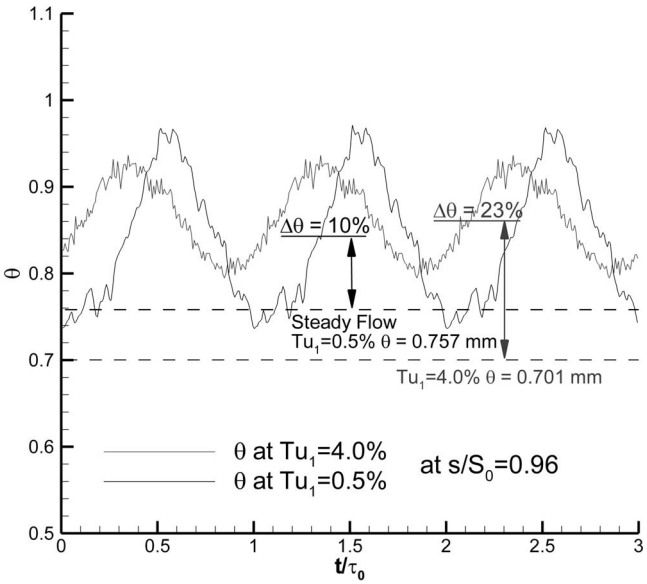

Fig. 13 Ensemble-averaged boundary layer momentum thickness measured with LDA at $s/S_0=0.96$, $Re_{2is}=1.6\times10^5$, $F_{red}=0.46$, $\phi=0.83$, $Tu_1=0.5\%$, and $Tu_1=4.0\%$

The ensemble-averaged data are presented in Fig. 13.

At low FSTI, the time mean of θ rises by ~10% in comparison to the steady flow value (dashed line). The minimum value equals the steady flow value. The maximum value of θ appears in phase with the peak shear stress at $t/\tau_0=0.60$.

In the case of the higher FSTI, the time mean θ was raised by ~23% relative to the corresponding steady flow value. This is mainly due to an earlier transition onset, which increases the turbulent wetted area and, therefore, the amount of momentum loss in the boundary layer. As was shown in Fig. 12, the transition was well developed at $s/S_0=0.63$.

Conclusions

The potential field of a downstream blade row has an important impact on the boundary layer of the upstream blade. It was shown that the transition on the suction surface responds to the freestream velocity changes driven by the downstream pressure field. In these experiments, the passage of a downstream bar behind the cascade exit alters the pressure distribution inside the blade channel. The oscillatory influence on the pressure distribution forces the flow to accelerate and decelerate with a period equal to the bar-passing period. During the decelerating phase, transition was promoted further upstream than in steady flow. This raised the momentum loss in the boundary layer.

At the lower FSTI, which in some ways is representative of higher FSTI at even lower Reynolds numbers than that examined here, transition in the separated shear layer was observed to develop from the initiation of Kelvin-Helmholtz instabilities, leading to the formation of free shear layer vortices. These vortices induced surface pressure perturbations with an amplitude of the order of 7–8% of the exit dynamic pressure. Upstream of the separation, the surface pressure oscillations induced by the downstream pressure field were approximately equal to the magnitude of those measured in earlier studies involving an upstream wake.

At elevated freestream turbulence, which is more representative of real multistage machines at the Reynolds number investigated, the boundary layer undergoes transition 10% of surface length earlier. It is an attached flow transition and calmed regions form. Regions of high and low wall shear stress appear in response to modulation of the freestream velocity induced by the potential field of the downstream passing bar. The time-mean and ensemble-mean momentum thickness of the boundary layer was increased at both freestream turbulence levels.

Acknowledgment

The work reported in this paper was conducted as a part of the project on "Unsteady Transitional Flows in Turbomachines" (UTAT), which was funded by European Commission under Contract No. GRD1-2001-40192. The numerical work of Antonio Antoranz and Pedro de la Calzada from ITP is acknowledged. Furthermore, the authors would like to thank Trevor Chandler, Alistair Ross, and David Grey for their preparation of the test facility.

Nomenclature

C = profile chord (m)
D = downstream bar diameter (mm)
F = reduced frequency
P = pressure (Pa)
S = surface length (mm)
T = period (s)
U = velocity (m/s)
Re = Reynolds number
Tu = turbulence intensity (%)
d = upstream bar diameter (mm)
h = blade span (mm)
s = blade pitch, surface length (mm)
t = time (s)
α = flow angle (deg)
δ = displacement thickness (mm)
θ = momentum thickness (mm)
ϕ = flow coefficient
ρ = density (kg/m^3)
τ = shear stress or period (s)

Subscripts

∞ = freestream
0 = total
1 = inlet
2 = outlet
p = pressure
w = wall
ax = axial
is = isentropic
red = reduced

Acronyms

LP = low pressure
2D = two-dimensional
LDA = laser Doppler anemometry
FSTI = freestream turbulence intensity
TKE = turbulent kinetic energy

Other

$\langle x \rangle$ = ensemble-averaged x
$\bar{x}$ = time mean x

References

[1] Stieger, R., Hollis, D., and Hodson, H. P., 2004, "Unsteady Surface Pressures Due to Wake Induced Transition in a Laminar Separation Bubble on a LP Turbine Cascade," ASME J. Turbomach., **126**, pp. 544–550.
[2] Lou, W., and Hourmouziadis, J., 2000, "Separation Bubbles Under Steady and Unsteady Main Flow Conditions," ASME Paper No. 2000-GT-027.
[3] Opoka, M. M., and Hodson, H. P., 2005, "An Experimental Investigation on the Unsteady Transition Process on the High Lift T106A Turbine Blade," Paper No. 1277 ISABE, Munich.
[4] Curtis, E. M., Hodson, H. P., Banieghbal, M. R., Howell, R. J., and Harvey, N. W., 1997, "Development of Blade Profiles for Low Pressure Turbine Applications," ASME J. Turbomach., **119**, pp. 531–538.
[5] Antoranz, A., and de la Calzada, P., 2002, "Downstream Cylindrical Rods

Design for Whittle Lab Low Velocity Cascade," ITP Internal Report in UTAT Project No. 13/05/02
[6] Halstead, D. E., Wisler, D. C., Okiishi, T. H., Walker, G. J., Hodson, H. P., and Shin, H. W., 1997, "Boundary Layer Development in Axial Compressors and Turbines—Part 3: LP Turbines," ASME J. Turbomach., **119**, pp. 225–237.
[7] Roach, P. E., 1987, "The Generation of Nearly Isotropic Turbulence by Means of Grids," Int. J. Heat Fluid Flow, **8**(2), pp. 82–92.
[8] Hodson, H. P., Huntsman, I., and Steele, A. B., 1994, "An Investigation of Boundary Layer Development in a Multistage LP Turbine," ASME J. Turbomach., **116**, pp. 375–383.
[9] George, W. K., 1975, "Limitations to Measuring Accuracy Inherent in the Laser-Doppler Signal," *Proc LDA Symposium Copenhagen* (A76-45326 23-25), Skovlunde, pp. 20–63.
[10] Dring, R. P., Joslyn, H. D., Hardin, L. W., and Wagner, J. H., 1982, "Turbine Rotor-Stator Interaction," ASME J. Eng. Power, **104/729**, pp. 729–742.
[11] Obremski, H. J., and Fejer, A. A., 1967, "Transition in Oscillating Boundary Layer Flows," J. Fluid Mech., **29**(1), pp. 93–111.

Control of Shroud Leakage Loss by Reducing Circumferential Mixing

Budimir Rosic
e-mail: br241@cam.ac.uk

John D. Denton

Whittle Laboratory,
Cambridge University,
Cambridge, CB30DY, UK

Shroud leakage flow undergoes little change in the tangential velocity as it passes over the shroud. Mixing due to the difference in tangential velocity between the main stream flow and the leakage flow creates a significant proportion of the total loss associated with shroud leakage flow. The unturned leakage flow also causes negative incidence and intensifies the secondary flows in the downstream blade row. This paper describes the experimental results of a concept to turn the rotor shroud leakage flow in the direction of the main blade passage flow in order to reduce the aerodynamic mixing losses. A three-stage air model turbine with low aspect ratio blading was used in this study. A series of different stationary turning vane geometries placed into the rotor shroud exit cavity downstream of each rotor blade row was tested. A significant improvement in flow angle and loss in the downstream stator blade rows was measured together with an increase in turbine brake efficiency of 0.4 %. [DOI: 10.1115/1.2750682]

Introduction

In low aspect ratio HP turbines with shrouded blades, leakage losses contribute significantly to overall losses. Leakage flow reduces turbine performance primarily by reducing extracted work in the rotor blades. Along with this, Wallis et al. [1] identified four other loss-generating mechanisms through which the shroud leakage flows affect turbine performance. They are due to mixing in the inlet shroud cavity; mixing through the labyrinth seal; mixing loss in the exit cavity due to the velocity difference between the cavity re-entry flow and the main flow; and nonideal incidence onto the downstream blade row. In recent years, the physics of the leakage flow path, and its interaction with the mainstream flow, has been intensively investigated by many authors, among others Denton and Johnson [2], Wallis et al. [1], Giboni et al. [3], Peters et al. [4], and Pfau et al. [5].

Denton and Johnson [2] showed that the shroud leakage flow undergoes little change in swirl velocity as it passes over the shroud. The difference in the swirl velocity between the unturned shroud leakage flow and the main passage flow downstream of the blade row is significant, and entropy is generated in the mixing process. At the same time, the unturned leakage flow alters the incidence and secondary flows in the downstream blade row. Gier et al. [6] presented a similar leakage-associated loss breakdown as Wallis et al. [1]. For the shroud geometry investigated, they estimated that the reentry mixing losses and the "subsequent-row" losses (incidence and secondary flow losses) together contribute to 60% of total cavity related losses. Wallis et al. [1] recognized the reduction of the reentry mixing losses as a promising strategy for reducing aerodynamic losses. They used a turning device, a row of bladelets fixed on the rotor shroud to turn the leakage flow by extracting useful work from the leakage flow. Because of the mechanical constraints of the model turbine, and the mainstream flow ingress into the shroud cavity, the effectiveness of the turning device was poor and a drop in overall efficiency was measured. They also tested a series of flat turning vanes fixed onto the casing above the shroud and aligned to the machine axis, in order to turn the leakage flow in the axial direction. They measured an improvement in the turbine efficiency and reduced tangential velocity in the casing region at the rotor exit plane. This reduced the spanwise extent of the casing secondary flows in the downstream stator blade row.

The experimental study presented in this paper further explored the idea of turning the rotor shroud leakage flow in the direction of the main blade passage flow in order to reduce the aerodynamic mixing losses in the circumferential direction. A series of different stationary turning vane geometries placed into the rotor shroud exit cavity downstream of each rotor blade row was tested, using a three-stage air model turbine with low aspect ratio blading.

Model Turbine and Experimental Methods

The experiments were carried out using a low speed multistage air turbine, that was designed to represent the first few stages of a high-pressure steam turbine (Fig. 1). Atmospheric air enters the inlet section radially and passes through a flow straightener before entering the turbine. Air is drawn through three turbine stages by a fan downstream of the turbine. Both stator and rotor blades were shrouded. The operating point, determined by the flow coefficient ϕ and rotational speed, is set by the fan power and dynamometer brake. The flow coefficient is calculated using the axial velocity at turbine inlet, which is measured indirectly using a mass flow measurement in the exhaust section and a density measurement at inlet.

Experiments were performed on 50% reaction blading at the design operation condition (ϕ=0.384). The key turbine geometry and operating parameters are presented in Table 1. The blade parameters are taken at blade midheight. The blading was designed to represent typical HP steam turbine conditions, and all parameters satisfy that condition. The Reynolds number, based on exit velocity and true chord, is significantly lower than that in a real turbine. The Mach number is also lower, but as the flow in a real HP turbine is well subsonic, this is not felt to be significant.

A detailed diagram of the stage geometry used in this study is presented in Fig. 2. To allow for the axial movement of the rotor shaft relative to the casing, the rotor sealing arrangement has opened inlet and exit shroud cavities. Using two ~0.75 mm clearance radial seals resulted in an overshroud leakage flow of ~1.5%. The stator hub sealing geometry uses a previously reported sealing arrangement [1] designed to minimize leakage flow. It comprises two axial abradable balsa wood seals each

Contributed by the International Gas Turbine Institute of ASME for publication in the JOURNAL OF TURBOMACHINERY. Manuscript received July 14, 2006; final manuscript received July 14, 2006; published online March 21, 2008. Review conducted by David Wisler. Paper presented at the ASME Turbo Expo 2006: Land, Sea and Air (GT2006), May 8–11, 2006, Barcelona, Spain.

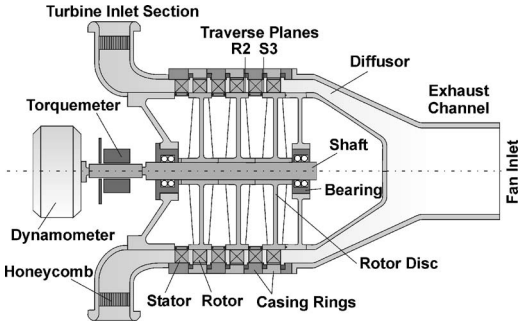

Fig. 1 Schematic of model turbine

forming an axial clearance of ~0.5 mm with the shroud. The actual clearance cannot be measured, and the 0.5 mm is a best estimate subject to some uncertainty.

The time-mean flow properties of the main passage were obtained using a five-hole pneumatic probe. The properties were measured by performing full-span area traverses over one blade pitch at an axial distance of 6 mm and 17 mm downstream of the third stator and the second rotor trailing-edge tip, respectively (the traverse plane positions are shown in Fig. 1). The traverse grid was 37×37 uniformly spaced points in both the radial and pitchwise directions.

Experimental results are presented in the form of spanwise distribution of the pitchwise mass-averaged yaw angle and total pressure coefficient contours. In the model turbine, a repeating stage condition develops downstream of the second stage [7], and therefore, the experimental results downstream of rotor 2 and stator 3 are given.

Total pressure was nondimensionalized by the total pressure drop across the whole turbine to give a total pressure coefficient C_{p0}. The measurement plane covers one pitch from 2% to 97% span. The white areas on the contour plots of experimental data indicate regions not covered by the traverses.

Table 1 Turbine geometrical and operational parameters

Design operating point data		
Flow coefficient, ϕ	0.384	
Stage loading, Ψ	1.0	
Design speed (rpm)	830	
Inlet Mach number	0.045	
Number of stages	3	
Inter blade row spacing (mm)	25 mm	
Blade height, h (mm)	75 mm	
Hub to tip ratio	0.85	
Blade parameters	**Stator**	**Rotor**
Blade number	40	38
True chord, l (mm)	89.73	105
Aspect ratio, h/l	0.836	0.714
Pitch to chord ratio	0.81	0.728
Reynolds number[a]	2.53×10^5	2.97×10^5

[a]Based on true chord and exit velocity.

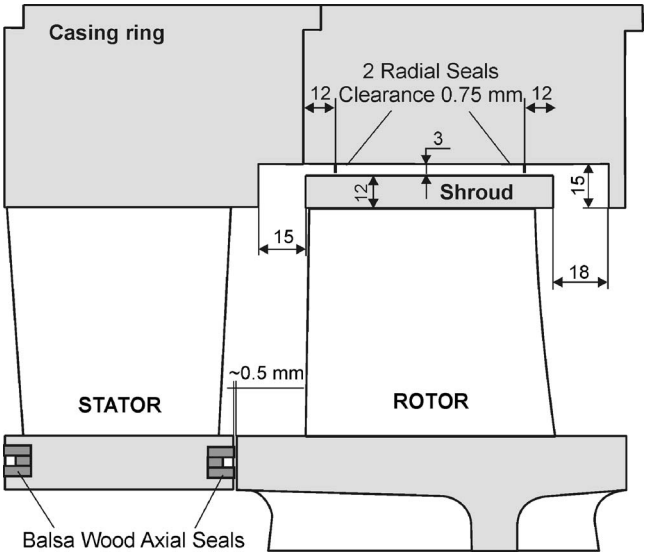

Fig. 2 Stage geometry with open shroud cavities

Numerically Predicted Shroud Leakage Offset Loss

In order to quantify the influence of each of the identified shroud leakage loss mechanisms on turbine performance, a set of numerical tests was performed. The tests were completed using Denton's 3D multiblock Reynolds-averaged Navier-Stokes (RANS) finite volume solver TBLOCK, which was run in steady mode using the mixing-plane approach. The code was calibrated against experiments, and capabilities of the solver in predicting the flow in the multistage turbine with shrouded blades were demonstrated in work of Rosic et al. [8].

In order to separate the contribution of each leakage loss mechanism, the flow in a 1.5 stage turbine was analyzed and five different calculations were performed. First, only the main blade passage with clean end walls, as a datum configuration, was calculated (Fig. 3(*a*)). The second calculation added the inlet cavity without the leakage flow, thus reducing the turbine efficiency by 0.2% compared to the first test case. A similar calculation, including only the shroud exit cavity, reduced further the efficiency by 0.25%. The fourth test combined both cavities and the shroud with a single radial seal above it. The seal clearance and, therefore, the leakage flow were set to zero. This case included effects of the both cavities and windage loss caused by the rotating shroud and gave a 0.5% reduction in efficiency. Finally, in the fifth test case the seal gap was opened and a shroud leakage flow of ~1.7% was predicted. The overall drop in efficiency in this case was 2.6%, compared to the datum configuration. The area averaged pitchwise entropy generated through the domain is presented in Fig. 3(*b*). The significant influence of the flow in the downstream stator is obvious. Classical shroud leakage theory states that the efficiency drop due to the reduced work extraction resulting from the tip leakage flow is directly proportional to the mass fraction of the leakage. This suggests that the lost efficiency due to the generation of entropy apart from the dissipation of the seal jet for this configuration is 2.6%–1.7%=0.9%. Test case 4, as described above, showed that the loss due to the cavities and windage above the shroud was equal to 0.5%. This means that 0.9%–0.5% =0.4% is the lost efficiency that can be attributed to the reentering leakage flow and incidence and secondary flow losses in the downstream stator blade row.

This fact marks the control of the leakage losses related to the reentry mixing and the downstream blade row as one of the most promising ways for further improvement of turbine performance. Figure 3(*c*) summarizes the contribution of all aforementioned loss shroud leakage mechanisms to the overall turbine performance reduction.

Influence of Shroud Leakage Flow on the Mainstream Flow Field

In order to evaluate the quality of the shroud leakage flow control strategy presented in this paper, flow in the turbine with different rotor shroud geometry and leakage flow fraction was analyzed.

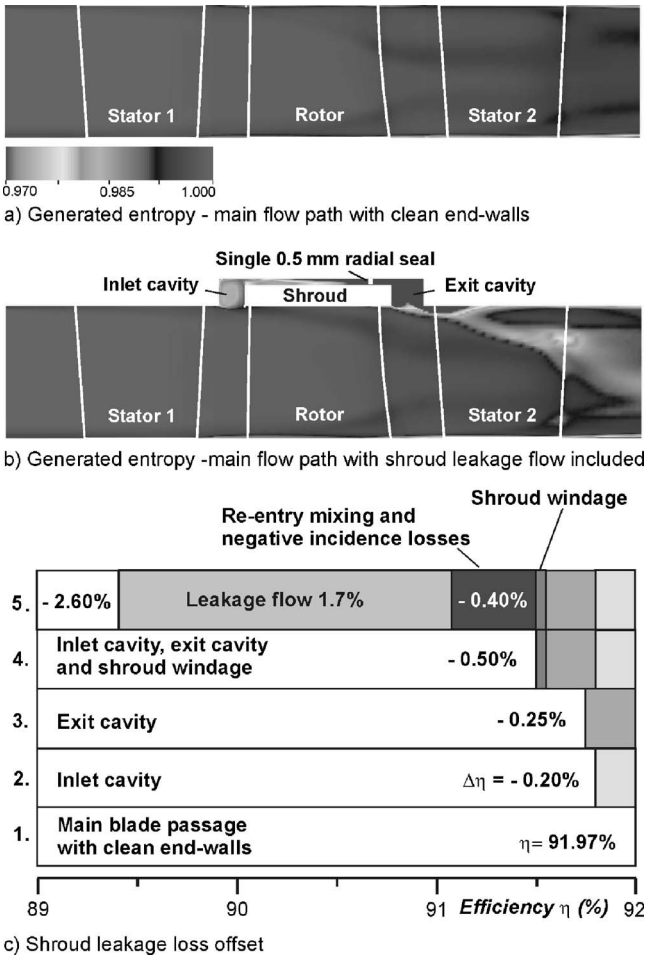

Fig. 3 Shroud leakage loss mechanism breakdown (CFD)

Figure 4(*a*) shows measured contours of the total pressure coefficient downstream of stator 3, for the stage configuration with the open rectangular shroud cavities as shown in Fig. 2. The most distinctive flow feature is a strong loss core at the midspan position and a weaker loss core toward the hub. As is typical for a low aspect ratio blade and 3D blade design with compound lean, strong secondary flows migrate from the hub and casing to the midspan on the blade suction surface. This process is intensified by the influence of the cavity flows and the leakage flow (~1.5% in this study). Because of the radial pressure gradient the spanwise penetrations of the hub and casing, secondary flows are nonsymmetric, and the loss core associated with the casing passage vortex merges with other low momentum fluid from the blade wake to form the strong midspan loss core. Although the seal clearances on the hub were minimized, evidence of leakage flow was present and the loss core associated with the hub secondary flows, located at ~20% of span was intensified.

In the case with the closed rotor shroud cavities and the minimized leakage flow (~0.7%), the C_{p0} contours downstream of stator 3 are shown in Fig. 4(*b*). The influence of the leakage flow is reduced. The loss core at midspan is weakened, and the radial migration of the casing secondary flows is reduced. The wake area is more spread out toward the casing. The location of the hub loss core stays unchanged. A detailed analysis of the turbine flow in these two configurations with open and closed cavities, together with CFD comparisons for the same geometries, were given by Rosic et al. [8].

Although the influence of the leakage flow was minimized in the second case with the closed shroud cavities, it cannot be considered representative for the "no leakage" case. Because of the mechanical constrains of the model turbine, the configuration without rotor leakage flow cannot be tested experimentally. This idealized configuration was modeled and tested numerically using TBLOCK. The flow domain consisted of all three stages with the hub leakage flow modeled and the clean casing end walls with no leakage flow. The predicted C_{p0} contours downstream of stator 3 are shown in Fig. 4(*c*). In this case, the loss core associated with the casing secondary flow did not migrate radially and there is almost no evidence of the midspan loss core. Figure 4 suggests that the flow in shrouded low aspect ratio turbines is dominated by the leakage flow and that reduction in the leakage flow reduces the intensity of the secondary flow and its radial migration toward the midspan in the downstream blade row.

Turning Vanes

In order to analyze the effect of turning the leakage flow into the axial direction, a series of stationary turning vanes was fixed onto the casing wall close to the downstream edge of the shroud exit cavity, as is shown in Fig. 5. The vanes were made from

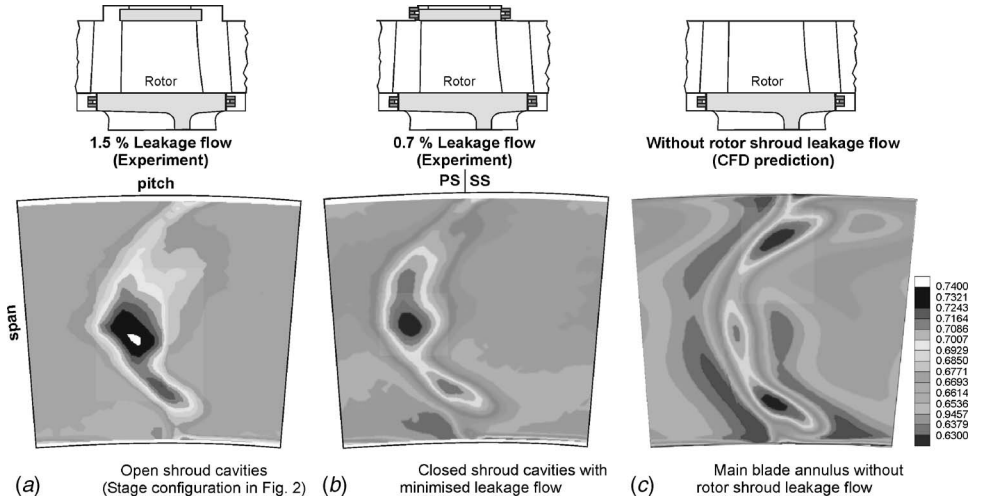

Fig. 4 Measured C_{p0} distribution downstream of the stator 3, for the configurations with open (*a*) and closed (*b*) rotor shroud cavities, and predicted distribution for the case with the clean casing end wall (*c*)

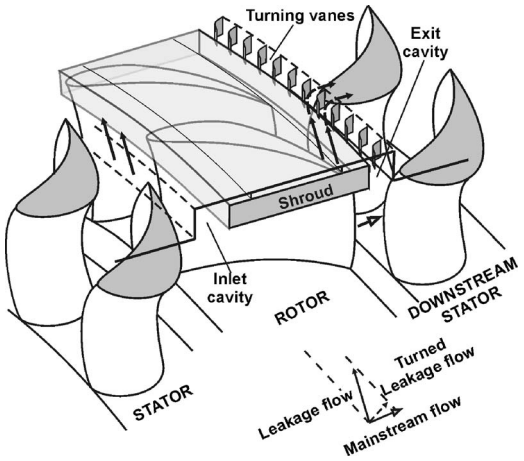

Fig. 5 Schematic of shroud geometry and turning vanes in shroud exit cavity

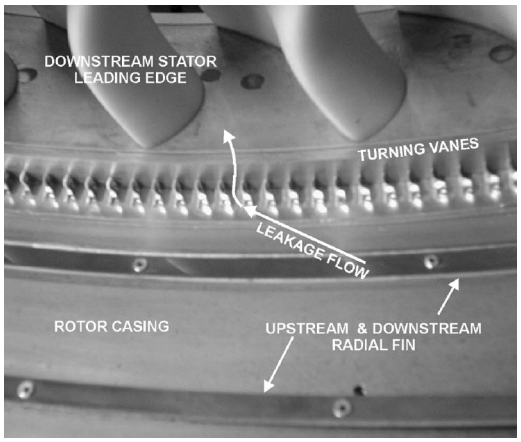

Fig. 7 Turning vanes in the shroud exit cavity

0.5 mm thick, 8×8 mm aluminum plates (Fig. 6). In order to analyze the effectiveness of the turning vanes, the number of the turning vanes per rotor blade pitch was varied in this study from 2 to 8. As mentioned above, the unturned leakage flow maintains its swirl velocity over the shroud. Hence, the leakage flow approaches the exit cavity with the flow angle approximately equal to the flow angle at the stator exit. To minimize the loss caused by the leakage flow separation on the turning vane leading edge, the turning vanes were bent and formed to 70 deg (the design stator exit flow angle) from the turbine axis (Fig. 6). The downstream edge of the turning vane is flat and aligned to the axial direction. Figure 7 shows the turning vanes assembly in the shroud exit cavity and location of the radial fins and the downstream stator leading edge. The turning vanes were mounted in the exit cavity downstream of each rotor blade row.

Experimental Results

The flow interaction between the mainstream and the shroud leakage flow in the case with the open rotor shroud exit cavity is highly three-dimensional and circumferentially nonuniform. Essentially, the rotor blade-to-blade pressure gradient extends downstream of the trailing edge allowing the main passage flow to enter periodically the cavity close to the blade pressure surface. The incoming flow rolls up and forms the cavity vortex, which travels along the cavity and reenters the mainstream in the wake region close to the blade suction side. The leakage flow enters the cavity, mixes with the cavity fluid, and deflected from the cavity downstream end wall, reenters the main passage close to the suction side. The mixing of the ingested flow and the unturned shroud leakage flow favorably modifies the tangential momentum of the reentry leakage jet. In spite of that, the leakage jet approaches the downstream stator blade row with the strong negative incidence. The leakage jet hits the stator blade on the suction side, increasing the static pressure in this region. On the pressure side, flow is accelerated and the static pressure decreases. Although the modified leading-edge loading is such as to reduce the pressure gradient driving secondary flow, the streamwise vorticity associated with the leakage jet is in a direction to increase the secondary flow. This streamwise vorticity is mainly due to the difference in tangential velocity between the leakage jet and mainstream flow. The effects of the vorticity are dominant, and in the case of low aspect ratio blades, the result is increased radial migration of the secondary flows and a strong loss core around midspan as shown in Fig. 8(*a*). The effects of skewed inlet boundary layers on the downstream blade row secondary flows were analyzed by Bindon [9], Boletis et al. [10], and Walsh and Gregory-Smith [11].

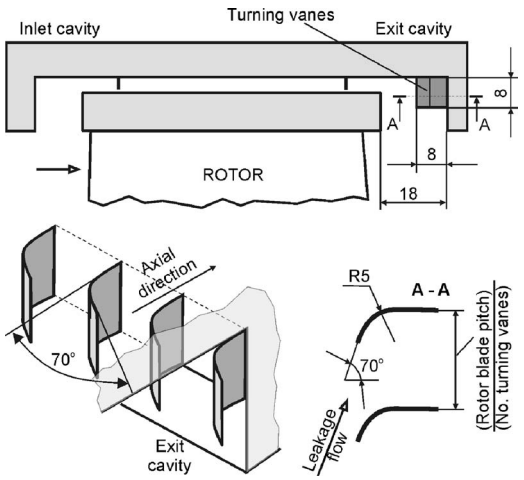

Fig. 6 Turning vanes—geometry and details

In order to reduce the difference in tangential velocity, initially two turning vanes per rotor blade pitch were mounted into the shroud exit cavity of all three rotor rows. As a result, a portion of the leakage flow was turned toward the axial direction before it reentered the mainstream flow. This improved the flow angle onto the downstream stator leading edge, and consequently, the intensity and radial migration of the casing secondary flows were reduced. The central loss core (Fig. 8(*b*)) is weaker, and the wake is more spread out. In the case with four turning vanes per rotor blade pitch, the effectiveness of the vanes in turning the leakage flow was improved and a further weakening of the loss core was measured, as shown in Fig. 8(*c*). Reducing the vane-to-vane spacing further, with eight turning vanes per rotor blade pitch, the central loss core at the midspan almost disappeared (Fig. 8(*d*)), and the low total pressure region stretched out, covering most of the blade span at the trailing edge. This wake structure is similar to that presented in Fig. 4(*c*), for the test case with simulated flow without rotor shroud leakage flow, where the secondary flow loss core stays close to the casing.

For the same set of the turning vane configurations, the spanwise distribution of the pitchwise mass-averaged yaw angle measured downstream of stator 3 is presented in Fig. 9. The change in the yaw angle between the shroud configurations with the open and closed cavities (Figs. 4(*a*) and 4(*b*)) is given in Fig. 9(*a*). The flow field above 30% of the blade span undergoes a significant change caused by the increased leakage flow in the case with open cavities. Close to the casing, the flow is overturned, and at midspan, it is underturned in the case of the open cavities compared to the case with minimized leakage flow and closed cavities. These

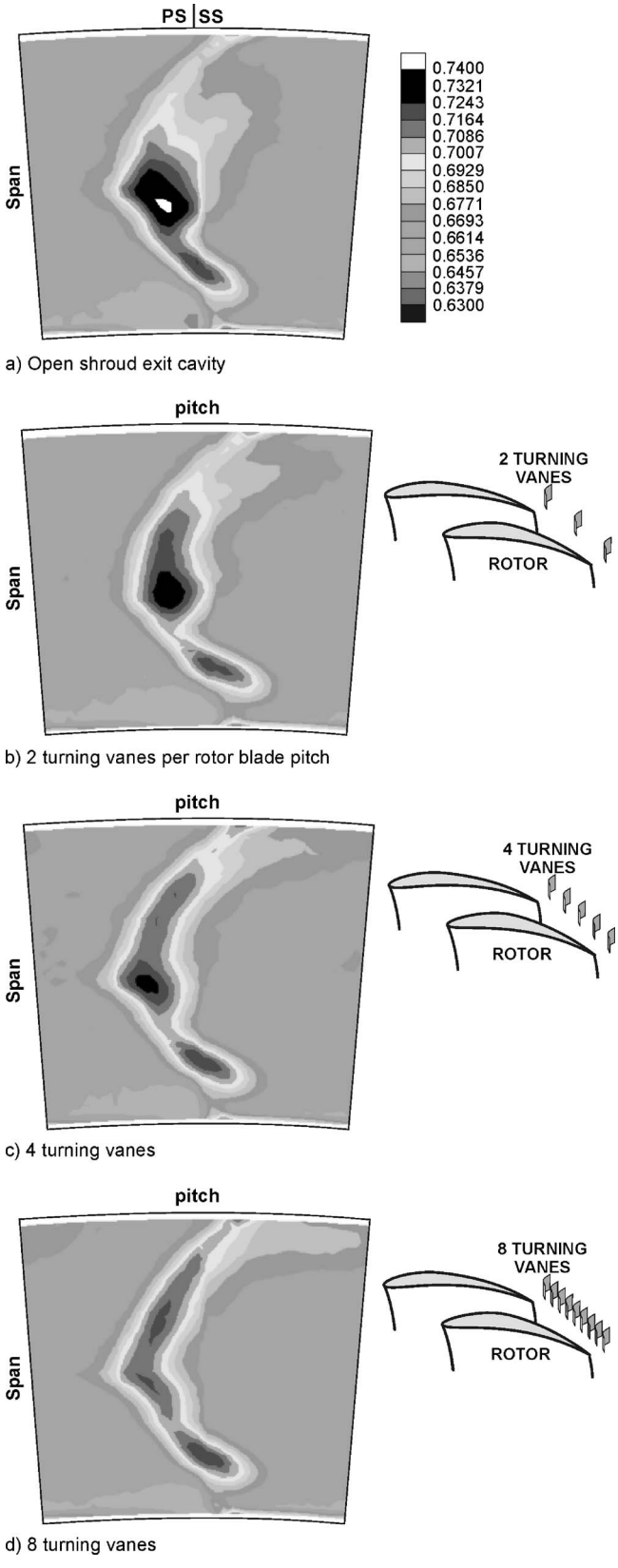

Fig. 8 C_{p0} contours downstream stator 3, for different number of turning vanes in shroud exit cavity

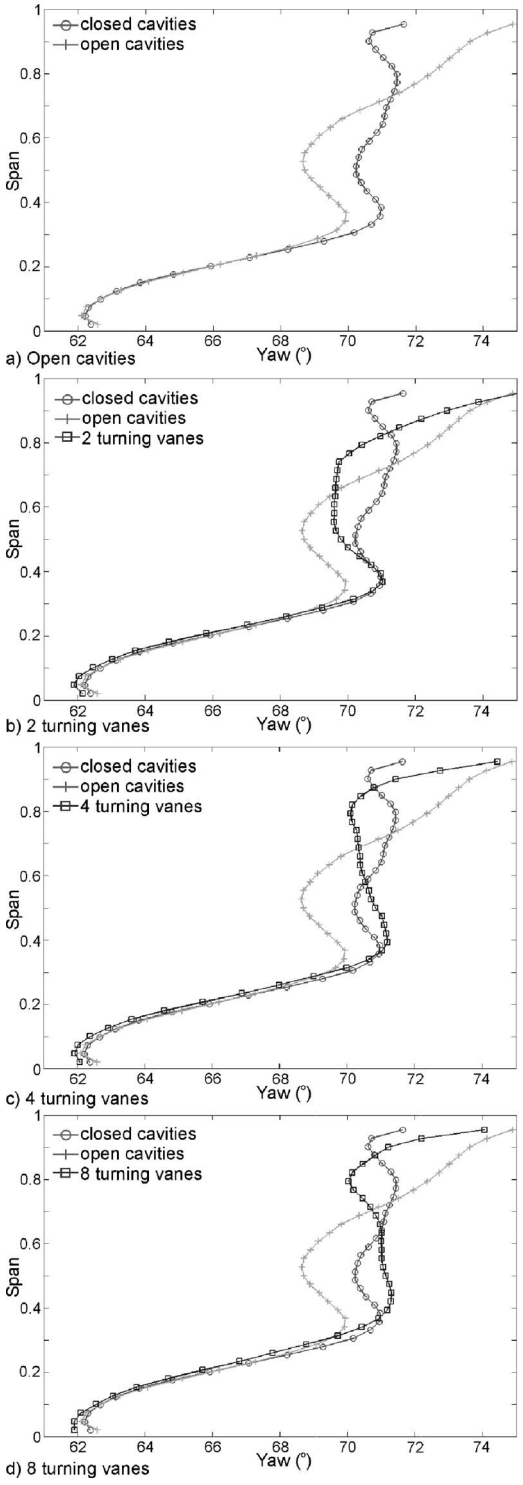

Fig. 9 Pitchwise-averaged yaw angle downstream stator 3, for different number of turning vanes in shroud exit cavity

two distributions are used to analyze the effectiveness of the turning vanes placed in the open shroud exit cavity. With two turning vanes per blade pitch mounted in the cavity (Fig. 9(*b*)), the underturning at the midspan and overturning in the casing region are reduced. Four turning vanes improved the yaw angle further, and the flow angle is shifted toward the flow angle distribution measured for the case with the closed cavities (Fig. 9(*c*)). The same trend is continued with the increased number of the turning vanes, and yaw angle distribution for eight turning vanes is shown in Fig. 9(*d*). In this study, a configuration with ten turning vanes per rotor blade pitch was also tested. The total pressure contours and the yaw angle did not show significant difference from the configura-

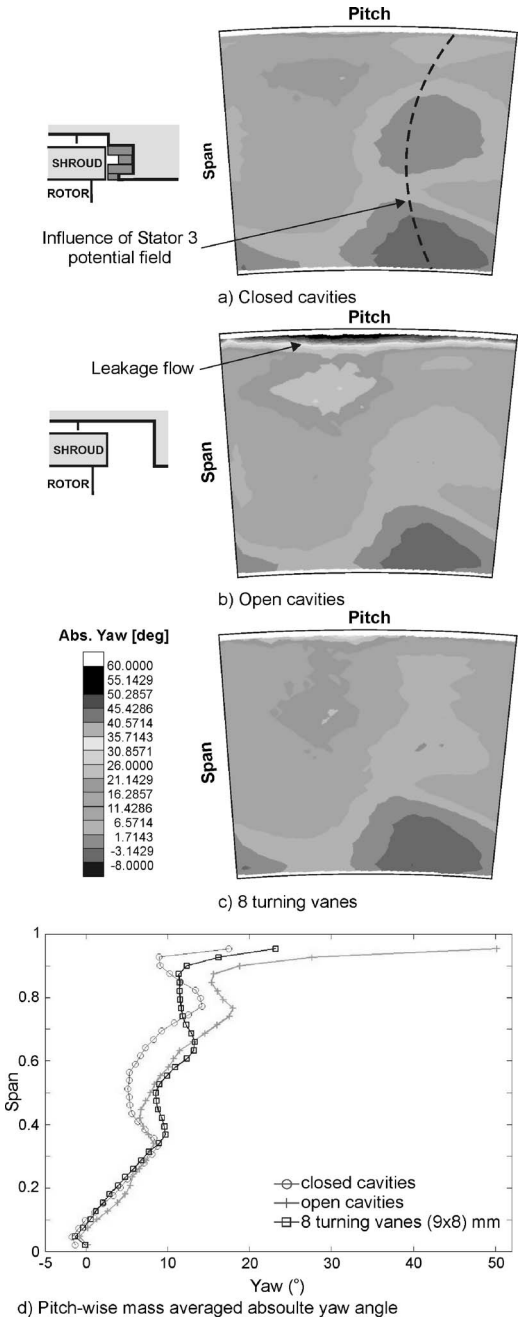

Fig. 10 Absolute yaw angle distribution downstream of the rotor 2 in the case with eight turning vanes

tion with eight vanes presented here. Figure 10 shows the measured absolute yaw angle distribution downstream of the rotor 2 for the case with eight turning vanes, compared to the open cavity case without turning vanes and the case with closed cavities.

Contours of absolute yaw angle in the case with closed shroud cavities and minimized influence of leakage flow are shown in Fig. 10(*a*). The area of the high yaw angle close to the casing in the case of the open cavities represents the leakage jet (Fig. 10(*b*)) and indicates the significant difference in tangential velocity between leakage and mainstream flows. The difference in tangential velocity creates a highly skewed boundary layer at the inlet of the downstream stator. It is responsible for the increased secondary flow and radial migration of the low momentum end-wall fluid. The presence of turning vanes in the exit shroud cavity almost completely eliminated the high swirl of the leakage flow in the

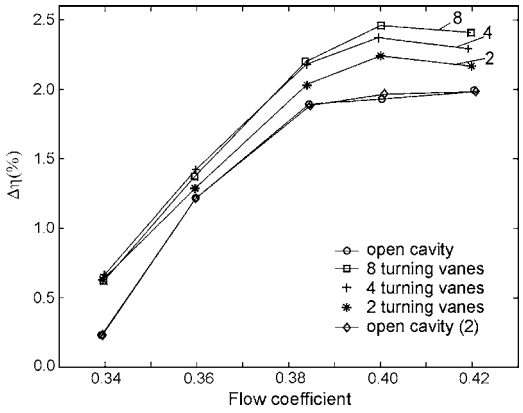

Fig. 11 Change in overall turbine efficiency for different number of turning vanes

casing region as shown in Fig. 10(*c*). This distribution of yaw angle is similar to that in the case with closed cavities and minimized leakage flow. Figure 10(*d*) shows the pitchwise averaged absolute yaw angle for these three geometries. The reduced overturning in the casing region in the case with turning vanes is evident.

The overall turbine efficiency was also measured for each turning vane configuration, and the results are plotted in Fig. 11. The efficiency for the case with open cavities without turning vanes was measured before and after (open cavity (2)), the study with turning vanes was completed. The achieved level of agreement between these two measurements shows that the repeatability of the efficiency measurements was high enough to capture changes in efficiency caused by the presence of the turning vanes in the exit cavity. The measured turbine efficiency confirmed the effectiveness of the turning vanes in improving the main blade flow field that was demonstrated using the total pressure and yaw angle distributions. The configuration with eight turning vanes showed an efficiency improvement at the design flow coefficient of ~0.4%. This efficiency improvement agrees with the predicted offset loss associated with the mixing losses of the reentering leakage flow, and the losses in the downstream stator blade row (Fig. 3).

L-Shape Turning Vanes

The presence of turning vanes in the shroud exit cavity inevitably increases the "wetted area" and, therefore, the related friction loss. Despite vane profiling to accommodate approaching leakage flow angle, a flow visualization experiment performed in the intervane channel indicated a highly turbulent and separated flow structure. The turning vane shown in Fig. 6 also reduces the allowed rotor axial movement relative to the casing. To minimize the effects discussed above, the vane geometry presented in Fig. 6 was modified resulting in a set of L-shape turning vanes, which were then tested experimentally. The geometry of the L-shape vanes is shown in Fig. 12. The wetted area is reduced and the

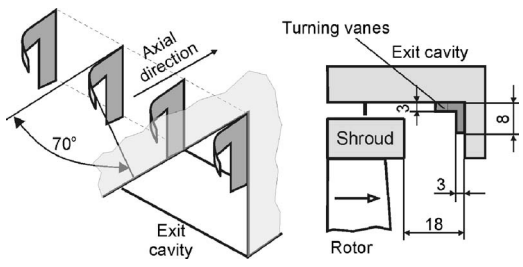

Fig. 12 L-shape turning vanes

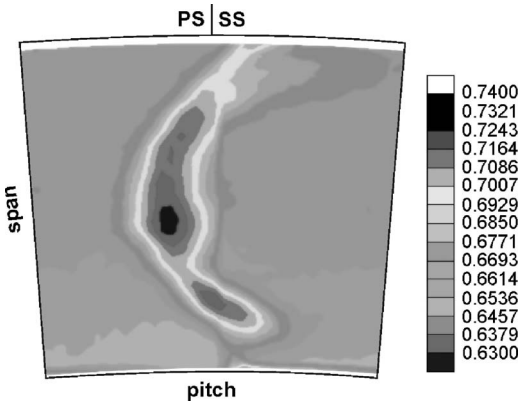

Fig. 13 C_{p0} contours downstream stator 3, for L-shape turning vanes

axial movement of the rotor is unrestricted.

Figure 13 shows C_{p0} contours measured downstream of stator 3 in the case with six L-shape vanes per rotor blade pitch mounted in the shroud exit cavity. The casing secondary flow radial migration and the central loss core are significantly reduced compared to the case with an open cavity without turning vanes (Fig. 8(*a*)). However, the six L-shape vane configuration is not as effective as the configuration with eight rectangular turning vanes. This can be seen by comparing the C_{p0} contours presented in Figs. 13 and 8(*d*).

The pitchwise-averaged yaw angle distribution also confirms the improved flow field downstream of stator 3 (Fig. 14). The results are very similar to those with four rectangular vanes (Fig. 9(*c*)). Both the overturning in the region close to the casing and the underturning at midspan are reduced. This analysis demonstrates that these very small changes in the geometry can have a significant effect on the mainstream flow field and turbine performance. It also confirms that a reduction in the leakage flow tangential velocity can be successfully achieved using the turning vane concept described and tested in this study.

Conclusions

The flow in shrouded low aspect ratio turbines is dominated by the leakage flow. The numerical study presented in this paper quantified the influence of each of the identified shroud leakage loss mechanisms on turbine efficiency. The reduction of the losses associated with the mixing of the reentering leakage flow, and incidence and secondary flow losses in the downstream stator blade row, was identified as a promising strategy for reducing overall aerodynamic losses.

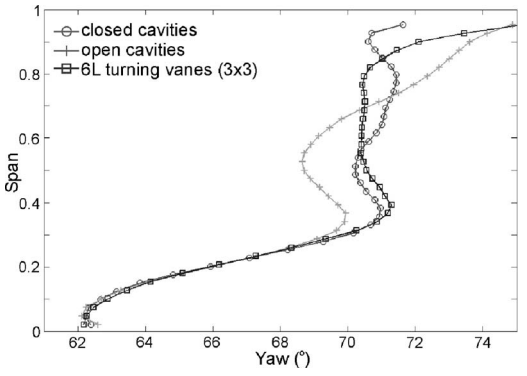

Fig. 14 Pitchwise-averaged yaw angle downstream stator 3, for L-shape turning vanes

An experimental study was undertaken to test a set of turning vanes placed in the shroud exit cavity designed to turn the rotor shroud leakage flow in the direction of the main blade passage flow. The results demonstrated that it is possible to improve the flow field in the downstream blade row, and overall turbine performance, by reducing the aerodynamic mixing losses in the circumferential direction. The effectiveness of the turning vanes depends primarily on their geometry and the vane-to-vane spacing. It was shown that the configuration with eight turning vanes per rotor blade pitch significantly improved the loss and flow angle distribution downstream of the stator blade rows, together with an increase in the turbine efficiency of 0.4%. The turning vanes with minimized turning area (L-shape vanes), which do not restrict the rotor axial movement also proved to be effective in turning the shroud leakage flow.

Acknowledgment

The authors would like to thank Siemens Power Generation for funding this work. Also, we would like to thank B. Gurney and N. Hooper, of the Whittle Laboratory, for technical assistance, and A. Peterson and K. Reid for support during the paper writing.

Nomenclature

h, h_0 = blade height, total enthalpy
l, l_x = chord length, axial chord
p_0 = total pressure
$p_{0,\text{in}}, p_{0,\text{ex}}$ = turbine inlet and exit total pressure
V, V_x = absolute velocity, axial velocity
U = blade speed
η = efficiency
3D = three-dimensional
HP = high pressure
LE, TE = leading and trailing edge
PS, SS = pressure side, suction side
$\phi = U/V_x$ = flow coefficient
$\Psi = \Delta h_0/U^2$ = stage loading
$C_{p0} = (p_{0,\text{in}} - p_0)/(p_{0,\text{in}} - p_{0,\text{ex}})$ = total pressure coefficient

References

[1] Wallis, A. M., Denton, J. D., and Demargne, A. A. J., 2000, "The Control of Shroud Leakage Flows to Reduce Aerodynamic Losses in a Low Aspect Ratio, Shrouded Axial Flow Turbine," ASME Paper No. 2000-GT-475.
[2] Denton, J. D., and Johnson, C. G., 1976, "An Experimental Study of the Tip Leakage Flow Around Shrouded Turbine Blades," CEGB Report No. R/M/N848, Marchwood Engineering Laboratories, UK.
[3] Giboni, A., Wolter, K., Menter, J. R. P., and Pfost, H., 2004, "Experimental and Numerical Investigation Into the Unsteady Interaction of Labyrinth Seal Leakage Flow and Main Flow in a 1.5 Stage Axial Turbine," ASME Paper No. GT2004-53024.
[4] Peters, P., Menter, J. R., Pfost, H., Giboni, A., and Wolter, K., 2005, "Unsteady Interaction of Labyrinth Seal Leakage Flow and Downstream Stator Flow in a Shrouded 1.5 Stage Axial Turbine," ASME Paper No. GT2005-68065.
[5] Pfau, A., Kalfas, A. I., and Abhari, R. S., 2004, "Making Use of Labyrinth Interaction Flow," ASME Paper No. GT2004-53797.
[6] Gier, J., Stubert, B., Brouillet, B., and de Vito, L., 2003, "Interaction of Shroud Leakage Flow and Main Flow in a Three-Stage LP Turbine," ASME Paper No. GT2003-38025.
[7] Lewis, K. L., 1993, "The Aerodynamics of Shrouded Multistage Turbines," Ph.D. thesis, Cambridge University, Engineering Department.
[8] Rosic, B., Denton, J. D., and Pullan, G., 2005, "The Importance of Shroud Leakage Modeling in Multistage Turbine Flow Calculations," ASME Paper No. GT2005-68459.
[9] Bindon, J. P., 1979, "The Effect of Hub Inlet Boundary Layer Skewing on the Endwall Shear Flow in an Annular Turbine Cascade," ASME Paper No. 79-GT-13.
[10] Boletis, E., Sieverding, C. H., and Van Hove, W., 1983, "Effects of a Skewed Inlet End Wall Boundary Layer on the 3-D Flow Field in and Annular Turbine Cascade," AGARD Conference Viscous Effects in Turbomachines, Copenhagen.
[11] Walsh, J. A., and Gregory-Smith, D. G., 1990, "Inlet Skew and the Growth of Secondary Losses and Vorticity in a Turbine Cascade," ASME J. Turbomach., **110**, pp. 633–642.

Roque Corral[1]
Head of Technology and Methods Department,
Industria de TurboPropulsores S.A.,
28830 Madrid, Spain
e-mail: Roque.Corral@itp.es

Fernando Gisbert
School of Aeronautics,
UPM,
28040 Madrid, Spain
e-mail: Fernando.Gisbert@itp.es

Profiled End Wall Design Using an Adjoint Navier–Stokes Solver

A methodology to minimize blade secondary losses by modifying turbine end walls is presented. The optimization is addressed using a gradient-based method, where the computation of the gradient is performed using an adjoint code and the secondary kinetic energy is used as a cost function. The adjoint code is implemented on the basis of the discrete formulation of a parallel multigrid unstructured mesh Navier–Stokes solver. The results of the optimization of two end walls of a low-pressure turbine row are shown.
[DOI: 10.1115/1.2751143]

Introduction

The exponential growth of the computational power during the past decades has paved the way to undertake much of the present turbomachinery designs with the aid of simulation tools. This has allowed a rapid evaluation of the proposed designs, and thus a significant reduction of the whole design cycle time. Within this context, it is realistic to tackle methodologies that refine a given design optimizing an objective function at a reasonable computational cost. Evolutionary or genetic algorithms are still prohibitive in terms of CPU time, requiring hundreds, if not thousands, of evaluations of the cost function to reach an optimum [1,2]. Nevertheless, these algorithms provide valuable information, especially when the problem requires multiobjective optimization, and may become the only way to reach an acceptable optimum when the objective function is noisy. However, for regular enough cost functions, gradient-based optimization methods may obtain the optimum with much less computational effort. A gradient-based optimization method, requires two main building blocks: a nonlinear Navier–Stokes solver to evaluate the optimized geometry, and an efficient tool to compute the gradient.

The nonlinear solver [3], known as Mu^2s^2T, has been used to evaluate the different designs. It uses hybrid unstructured grids to discretize the spatial domain and an edge-based data structure to compute the fluxes. A second-order numerical scheme, with Roe's matricial artificial viscosity, conforms the spatial discretization scheme, which is marched in time with an explicit five-stage Runge–Kutta. Jacobi preconditioning and multigrid are used to accelerate steady-state convergence, and dual time stepping is used for unsteady flows. Turbulence effects are modeled using either the $k-\omega$ or the algebraic Baldwin–Lomax model. The code has been parallelized using Message Passing Interface (MPI).

Efficient gradient evaluation for aerodynamic configurations is performed with the aid of adjoint Navier–Stokes solvers. Without such tools, the gradient must be evaluated by solving the linear Navier–Stokes equations as many times as free design parameters are considered in the optimization, what makes this approach prohibitive when the number of parameters is high, as it is the case for current turbomachinery designs. Nagel and Baier [4] undertook the optimization of a low pressure turbine (LPT) vane and its end walls, performing hundreds of cost function evaluations to reach an optimum. The use of aerodynamic adjoint solvers was pioneered by Pironneau [5] and later introduced by Jameson [6] and Jameson et al. [7–9], who used it first for two-dimensional airfoil optimizations, then for wings and finally for complete aircraft configurations. Nowadays, adjoint codes are widely used in optimization problems in both the discrete and continuous approaches. In the continuous approach, the adjoint equations are formulated and then discretized in the computational domain [10]. The discrete approach, instead, linearizes the discrete Navier–Stokes equations and develops the adjoint discrete problem from them [11–13]. This second approach is more suitable when a linear code exists [14], as the adjoint code routines can always be cross-checked against their linear counterparts. The existence of a linearized version of the code [15] has favored this latter approach.

Once the building blocks of the method are in place, a cost function and a set of parameters to control it must be chosen. The main target of the three-dimensional design of vanes, and to a lesser extent, of rotor blades, is the minimization of secondary losses, measured both in terms of total pressure losses and secondary kinetic energy. This goal can be achieved by modifying the axial and tangential lean of the airfoil and/or the turbine end walls. In this work, we have focused on the additional reduction in losses that may be obtained removing the constraint that the end wall is axisymmetric. It has been shown that by altering the end wall shape it is possible to modify the secondary vortex system and reduce the vortex strength downstream of the row [16,17]. This reduction impacts on both total pressure losses and secondary kinetic energy, but it has been observed that the sensitivity for the latter is larger. The end walls are perturbed with a series of sines and cosines at different axial locations of the row, as shown in Fig. 1, whose amplitudes need to be determined during the design phase of the airfoil.

The design of a profiled end wall involves tens of parameters and may become a huge task for the designer if it is not properly automatized. In its most primitive form, the designer has to obtain the sensitivities of the secondary losses with regard to the design parameters, which means tens of evaluations of the cost function, each requiring the solution of the 3D Reynolds-averaged Navier–Stokes equations in the flow domain, discretized with a grid of $\sim 10^6$ points. The designer has to choose a proper combination of the perturbations and evaluate the design again. The designer not only has to monitor the secondary losses but also traverse the solution to find local separations and other unexpected features. The automatization of this task would not only speed up the design, but it could potentially improve the final design.

The paper outlines how the adjoint solver is derived from the baseline Navier–Stokes solver and how the optimization algorithm is used to design the end walls of low-pressure turbine rows. Comparisons between optimizer results and manually obtained solutions are also performed.

[1]Also associate professor at the Department of Propulsion and Thermofluid Dynamics of the School of Aeronautics, UPM.

Contributed by the International Gas Turbine Institute of ASME for publication in the JOURNAL OF TURBOMACHINERY. Manuscript received July 28, 2006; final manuscript received July 31, 2006; published online March 21, 2008. Review conducted by David Wisler. Paper presented at the ASME Turbo Expo 2006: Land, Sea and Air (GT2006), May 8–11, 2006, Barcelona, Spain.

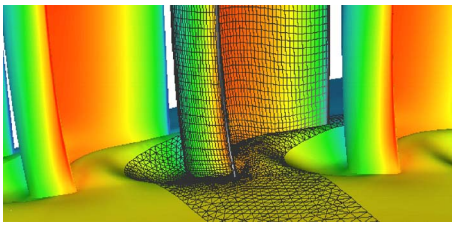

Fig. 1 Detail of an end-wall design

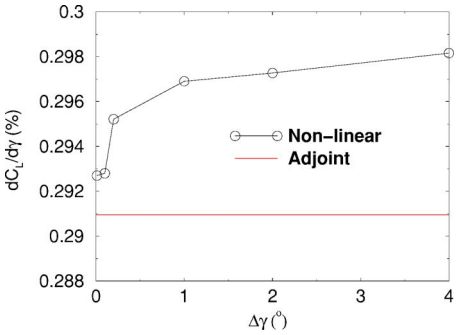

Fig. 2 Sensitivity of the lift coefficient to the stagger angle, T106 blade ($M_{is,\text{exit}}=0.59$)

Derivation of the Adjoint Discrete Equations

The optimization problem consists in minimizing a cost function $f(\mathbf{U}_j, \boldsymbol{\varphi}_k)$, where the variables $\mathbf{U}_j$ must fulfill the steady-state discrete Navier–Stokes equations, that can be schematically written as

$$\mathbf{R}_i(\mathbf{U}_j, \boldsymbol{\varphi}_k) = 0 \tag{1}$$

and $\boldsymbol{\varphi}_k$ represents the geometric parameters that are modified to control the objective function f. The restrictions imposed by the discrete Navier–Stokes equations can be absorbed by the functional, by multiplying each of them by a Lagrange multiplier $\boldsymbol{\psi}_i$,

$$g(\mathbf{U}_j, \boldsymbol{\varphi}_k) = f(\mathbf{U}_j, \boldsymbol{\varphi}_k) + \boldsymbol{\psi}_i^T \mathbf{R}_i(\mathbf{U}_j, \boldsymbol{\varphi}_k) \tag{2}$$

Since the steady state is fulfilled, the problems of minimizing f and g are equivalent. The gradient of g is obtained by differentiating Eq. (2)

$$\frac{dg}{d\boldsymbol{\varphi}_k} = \left(\frac{\partial f}{\partial \mathbf{U}_j}\right)^T \frac{\partial \mathbf{U}_j}{\partial \boldsymbol{\varphi}_k} + \frac{\partial f}{\partial \boldsymbol{\varphi}_k} + \boldsymbol{\psi}_i^T \left(\left[\frac{\partial \mathbf{R}_i}{\partial \mathbf{U}_j}\right] \frac{\partial \mathbf{U}_j}{\partial \boldsymbol{\varphi}_k} + \frac{\partial \mathbf{R}_i}{\partial \boldsymbol{\varphi}_k} \right) \tag{3}$$

which shows us two strategies to proceed when evaluating the gradient:

1. The standard or classical approach is to linearize Eq. (1) to obtain

$$\left[\frac{\partial \mathbf{R}_i}{\partial \mathbf{U}_j}\right] \frac{\partial \mathbf{U}_j}{\partial \boldsymbol{\varphi}_k} + \frac{\partial \mathbf{R}_i}{\partial \boldsymbol{\varphi}_k} = 0 \tag{4}$$

and remove the dependence of the Lagrange multipliers in Eq. (3). The gradient of the modified objective function, g, is then

$$\frac{dg}{d\boldsymbol{\varphi}_k} = \left(\frac{\partial f}{\partial \mathbf{U}_j}\right)^T \frac{\partial \mathbf{U}_j}{\partial \boldsymbol{\varphi}_k} + \frac{\partial f}{\partial \boldsymbol{\varphi}_k} \tag{5}$$

which states that the linear discrete Navier–Stokes equations must be evaluated for nominal variations of every geometric parameter, $\boldsymbol{\varphi}_k$, to obtain the flow sensitivities, $\partial \mathbf{U}_j / \partial \boldsymbol{\varphi}_k$. This is especially unsuitable for complex geometries where the number of parameters is very large, of the order of hundreds.

2. Alternatively, the Lagrange multipliers can be chosen to remove the dependence on $\partial \mathbf{U}_j / \partial \boldsymbol{\varphi}_k$, giving rise to the need to solve the adjoint discrete Navier–Stokes equations

$$\left[\frac{\partial \mathbf{R}_i}{\partial \mathbf{U}_j}\right]^T \boldsymbol{\psi}_i + \frac{\partial f}{\partial \mathbf{U}_j} = 0 \tag{6}$$

to obtain the Lagrange multipliers. In Eq. (6), the analytic expression for the cost function is usually known, hence, the cost function sensitivity $\partial f / \partial \mathbf{U}_j$ can be obtained analytically. The gradient in Eq. (3) then yields

$$\frac{dg}{d\boldsymbol{\varphi}_k} = \boldsymbol{\psi}_i^T \frac{\partial \mathbf{R}_i}{\partial \boldsymbol{\varphi}_k} + \frac{\partial f}{\partial \boldsymbol{\varphi}_k} \tag{7}$$

which shows that one single evaluation of the adjoint equations can be used to determine the gradient by simply multiplying the adjoint variables, i.e., the Lagrange multipliers $\boldsymbol{\psi}_i$, by the variation of the steady-state equations with the geometric parameters, $\partial \mathbf{R}_i / \partial \boldsymbol{\varphi}_k$. This term is evaluated using the complex variable method, which states that

$$\frac{\partial \mathbf{R}_i}{\partial \boldsymbol{\varphi}_k} = \lim_{\varepsilon \to 0} \frac{\mathcal{I}[\mathbf{R}_i(\mathbf{U}_j, \boldsymbol{\varphi}_k + i\varepsilon)]}{\varepsilon}$$

and requires only one evaluation of the discrete Navier–Stokes equations, which consumes orders of magnitude less CPU time than the resolution of Eq. (4). The additional term $\partial f / \partial \boldsymbol{\varphi}_k$ is also evaluated with the same method.

Equations (4) and (6) show that the linear and adjoint problems share the same eigenvalues, namely the ones of the matrix $[\partial \mathbf{R}_i / \partial \mathbf{U}_j]$, which is transposed in the adjoint problem. Therefore, the asymptotic convergence of both problems must be the same when analogous iterative schemes are used.

Equation (7) also shows the physical meaning of the adjoint variables. For a constant value of $\partial \mathbf{R}_i / \partial \boldsymbol{\varphi}_k$ along the grid, the nodes with a larger value of $\boldsymbol{\psi}_i$ will have a larger impact on the gradient than those nodes with smaller values. Thus, efficient geometry changes must perturb zones of the domain where the adjoint solution is comparatively large.

Results

The adjoint operators for the spatial discretization, Runge–Kutta, residual smoothing, and multigrid operators have been constructed [18]. The adjoint code implementation has been debugged with the aid of an in-house linear solver, by ensuring that $\boldsymbol{\psi}^T[A]\mathbf{u} = \mathbf{u}^T[A]^T\boldsymbol{\psi}$, where the matrix $[A]$ represents a generic operator, e.g., the spatial discretization, multigrid operators, etc. On the other hand, we have compared the sensitivities obtained by the adjoint code and the ones obtained by numerical differentiation, using the nonlinear version of the code.

The sensitivity of the lift coefficient C_L to variations in the stagger angle γ has been assessed for a two-dimensional viscous solution of the T106 blade [19] ($\gamma = 59.28$ deg, $M_{is,\text{exit}} = 0.59$).

These results are shown in Fig. 2. The sensitivities obtained by the adjoint code and by a second-order differentiation scheme are very similar for both approaches. The discrepancies could be attributed to the incomplete linearization of the artificial viscosity terms or to the lack of linearization of the turbulent equations, since the turbulent viscosity is kept constant in the adjoint code.

Figure 3 compares the convergence of the T106 case for the nonlinear and adjoint solvers. The convergence rate of both codes is about the same. However, the asymptotic convergence rate is more clearly seen in the adjoint solver probably due to its linear nature. This result was expected, since the linear and the adjoint problems share the same eigenvalues, and thus, the asymptotic convergence rate should coincide. In this case, 20–30 multigrid

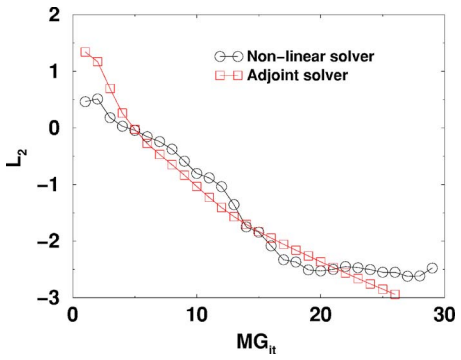

Fig. 3 Comparison of the convergence history of the T106 case for the nonlinear and adjoint solvers

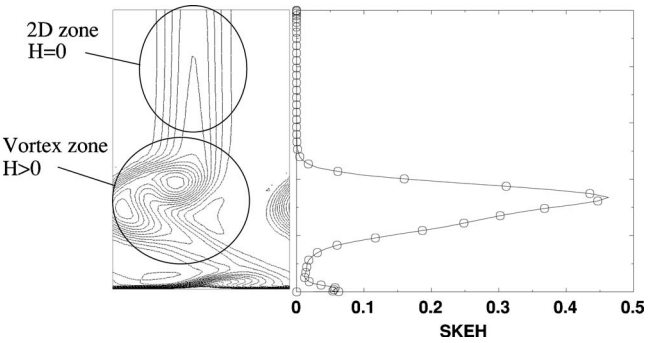

Fig. 4 Secondary flow pattern for a 3D straight cascade. Left: Total pressure ISO contours. Right: Mass-averaged nondimensional SKEH distribution.

iterations are enough to converge the problem for engineering purposes. The CPU cost to obtain the nonlinear solution and the adjoint solution is roughly the same.

Cost Function Definition. Keeping in mind that the final target is to minimize the production of secondary losses while the mean flow at the row exit remains unaltered, a proper cost function needs to be chosen. The cost function selected to drive the optimization is the mass-averaged SKEH (that is the product of the secondary kinetic energy and the helicity) at an axial plane cut. The nondimensional secondary kinetic energy for a node i is defined as

$$\mathrm{SKE}_i = \frac{(\mathbf{v}_i - \mathbf{v}_{pi})^2}{\mathbf{v}_{\mathrm{exit}}^2} \tag{8}$$

where $\mathbf{v}_{\mathrm{exit}}$ is the exit mass-averaged velocity, and $\mathbf{v}_{pi}$ is the projection of the velocity vector at the i node over the circumferentially mass-averaged velocity $\mathbf{v}_m$,

$$\mathbf{v}_{pi} = \frac{\mathbf{v}_i \cdot \mathbf{v}_m}{\mathbf{v}_m^2}\mathbf{v}_m$$

being $\mathbf{v}_i$ the local velocity. The nondimensional helicity H_i is defined as

$$H_i = \frac{|\mathbf{v}_i \cdot \boldsymbol{\omega}_i|}{\mathbf{v}_{\mathrm{exit}}^2/\ell_c} \tag{9}$$

where $\boldsymbol{\omega}_i$ is the local vorticity vector and ℓ_c is a characteristic length, typically the blade chord. The nondimensional SKEH value is obtained multiplying Eqs. (8) and (9)

$$\mathrm{SKEH}_i = \frac{(\mathbf{v}_i - \mathbf{v}_{pi})^2|\mathbf{v}_i \cdot \boldsymbol{\omega}_i|}{\mathbf{v}_{\mathrm{exit}}^4/\ell_c} \tag{10}$$

The aim of multiplying the SKE_i by the helicity is clearly seen in a straight 3D cascade. In such a configuration, the secondary flow is confined next to the end wall and just the wake velocity deficit exists at midspan (see Fig. 4), where the vorticity is perpendicular to the velocity, the helicity vanishes, and the contribution of the wake to the SKEH is null. In the region where the secondary vortex is located, $\mathbf{v}_i$ and $\boldsymbol{\omega}_i$ are almost aligned; therefore $H>0$, contributing to increase the SKEH. Therefore, multiplying the SKE by the helicity the phenomenon we want to minimize, which is the strength of the vortex, is isolated.

End wall perturbations may give rise to large adverse pressure gradients that may eventually promote massive separations of the flow. These detached bubbles are essentially a two-dimensional feature, and hence, the SKEH is unable to detect them since $\mathbf{v}_i \cdot \boldsymbol{\omega}_i \simeq 0$. However, they induce large variations of the swirl angle. Even if the flow is attached, the swirl angle needs to be limited somehow; otherwise, it will increase the losses in the downstream row, since changes in the swirl angle will give rise to changes in the incidence that will not be possible to absorb modifying the geometry of the downstream row. To account for these phenomena in the optimization process, we have introduced a penalty function that grows exponentially with the difference in the swirl angle between the baseline and the actual case. It is expressed as

$$F_p = f_1 e^{-[(\bar{\beta}_s - \beta_t + f_2)/f_3]} \tag{11}$$

being f_1, f_2, and f_3 factors to conform the shape of the penalty function, β_t the target swirl angle, and $\bar{\beta}_S$ the mass-averaged swirl angle in the region of interest. Thus, when $\bar{\beta}_S < \beta_t$, the penalty function grows, and the new cost function $\overline{\mathrm{SKEH}} + F_p$ moves further away from the minimum.

Optimization Method. The optimization method used in this work consists of a projected gradient search combined with a Broyden's method to improve the final convergence to the desired optimum [20]. This method has been selected because its simplicity and capability to deal with complicated constraints that are not known a priori, i.e., constraints that require the complete simulation of the system to know if they are satisfied. These kinds of constraints are frequent in turbomachinery problems, e.g., a fixed mass flow or a fixed power. Another important advantage of this method is that it requires only the computation of the functions involved and its gradients and no Hessian matrices are needed.

Designing LPT End Walls. The adjoint code has been used to compute the derivatives of the SKEH with regard to the geometry changes. The geometry of the end walls is modified by adding a perturbation to the axisymmetric baseline surface that consists of a Fourier series

$$P(x,\theta) = C(x) + \sum_{j=1}^{j=n_F}\left[A_j(x)\sin\left(j2\pi\frac{\theta}{\theta_b}\right) + B_j(x)\cos\left(j2\pi\frac{\theta}{\theta_b}\right)\right] \tag{12}$$

where θ_b is the blade pitch. The perturbations are specified at some fixed axial locations, which remain constant during the whole optimization process. In this work, six axial locations have been perturbed using the previous expression.

Two different optimized solutions are presented for the hub end wall of a LPT vane, one with a single harmonic perturbation ($n_F=1$), which is compared to a manual design with the same degrees of freedom, and the other with multiple harmonics ($n_F=4$). All the perturbation amplitudes are restricted to a maximum value of a 10% of the axial chord.

This case has an aspect ratio $\Lambda \simeq 5$, the exit Mach number is ~ 0.6, and the Reynolds number based on the exit conditions and the axial chord is 1.2×10^5. The domain has been discretized using a semi-unstructured mesh of 590,000 points. The construction

of this mesh involves the radial smoothing of a two-dimensional grid previously constructed along specified radial planes [21]. Hence, obtaining the perturbed grids is a time-consuming task that will influence the overall optimization time as the number of design parameters grow.

Computational Cost. All the cases presented in this paper have been computed in two PIV at 3 GHz. The process is fully parallelized except for the construction of the grid. Both the manual design and the single harmonic optimized case consider the same number of design parameters, 18.

The manual design consists of evaluating the gradient by solving the Navier–Stokes equations as many times as the number of parameters, and then evaluating the gradient components by finite difference. The Navier–Stokes equations are evaluated twice for each parameter, with different values of the perturbation, to keep the sensitivity of the cost function to variations in the design parameters. Once the gradient is calculated, the new geometry is evaluated, but just another optimization step is performed, and only the most representative parameters (i.e., those with larger sensitivities) are varied. The whole design requires ~400 h of CPU time to reach a solution (50 runs of the nonlinear solver), but the whole process is not fully automatic and the designer has to drive the optimization, increasing the design time even more. The optimizer consumes 60 h of CPU time to reach the final solution (eight cost function evaluations), that supposes roughly an order of magnitude less time than the manual process. Besides, the process is fully automatized, avoiding the designer the tedious task of manually postprocessing all solutions.

When considering the multiple harmonics case, the final solution is obtained in ~80 h, which represents 30% more CPU time, even though the number of parameters has been increased from 18 to 54. Since the number of optimizer iterations for both problems is the same, the increase in the CPU time is produced due to the larger number of parameters. Hence, the construction of the semi-unstructured grid for each perturbation parameters noticeably influences the total CPU time, but its impact is smaller than the evaluation of 36 additional cost functions each time the gradient is computed, which is another advantage derived from the use of the adjoint Navier–Stokes solver.

Single Harmonic Perturbation. The solution obtained with the optimizer is compared to the one proposed by the aerodynamic designer. The main difference between both approaches is that during the manual design, smaller maximum perturbation amplitudes have been allowed, and hence, the flow is not as much disturbed as it is in the optimized solution. There are also flow effects that are taken into account when performing the manual design and that cannot be controlled by the optimizer, such as suction-side flow separation next to the hub. This effect can only be indirectly addressed in the optimization process by means of the swirl angle penalty function of Eq. (11).

The radial distribution of SKEH for the axisymmetric baseline case and the profiled end walls may be seen in Fig. 5. A pure two-dimensional region with SKEH$\simeq$0 between the 15% and 50% of the span is clearly distinguished. It may be seen that the SKEH is appreciably reduced in the optimized solution, with the peak value divided approximately by a factor of 2. The reduction is smaller for the manual design, due to the smaller amplitude of the perturbations, but the manual design allows a better control of the solution downstream of the perturbations. Both the swirl angle (Fig. 6) and especially the total pressure (Fig. 7) are improved in the manual design, while the same is not true for the optimized solution. Although the swirl angle is modified with respect to the base case, the variations are controlled by the penalty function. A more restrictive selection of the penalty function parameters would produce a swirl angle distribution closer to the baseline case. The total pressure losses have increased with the proposed design. This is an indication of the separation that takes place in the trailing-edge region next to the hub and cannot be directly

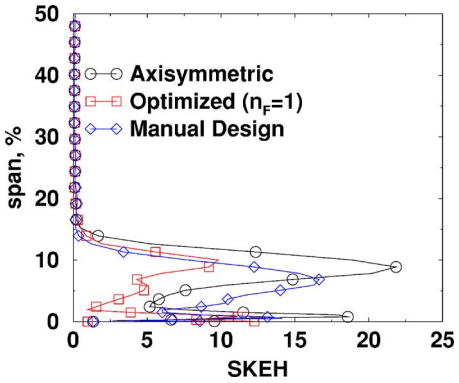

Fig. 5 Comparison of the baseline, optimized solution and manual design cases: Mass-averaged nondimensional SKEH at the outlet for the single harmonic case

controlled since there is no mechanism to reflect its impact on the penalty function. Thus, it is possible to weaken the vortex strength reducing the secondary losses, at the expense of increasing simultaneously the primary losses. This situation could be avoided by redefining the cost function. A reliable loss indicator that reflects both the total pressure loss and the mixing of the flow is the mixed-out average of the total pressure [22], but it has not been used in this work to maintain the same cost function used in manual designs.

Figure 8 represents the flow migration in the hub for this case, that is certainly unusual. This may be noted by looking at the

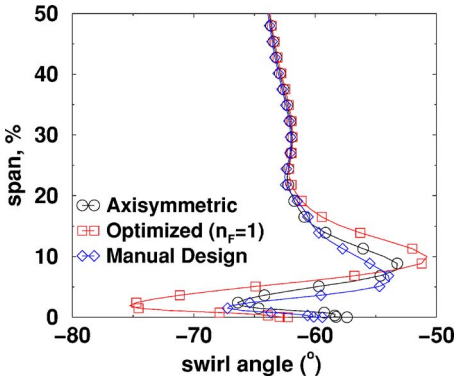

Fig. 6 Comparison of the baseline, optimized solution and manual design cases: Mass-averaged swirl angle at the outlet for the single harmonic case

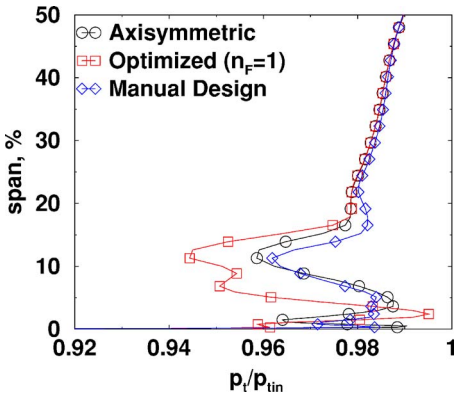

Fig. 7 Comparison of the baseline, optimized solution and manual design cases: Mass-averaged nondimensional total pressure at the outlet for the single harmonic case

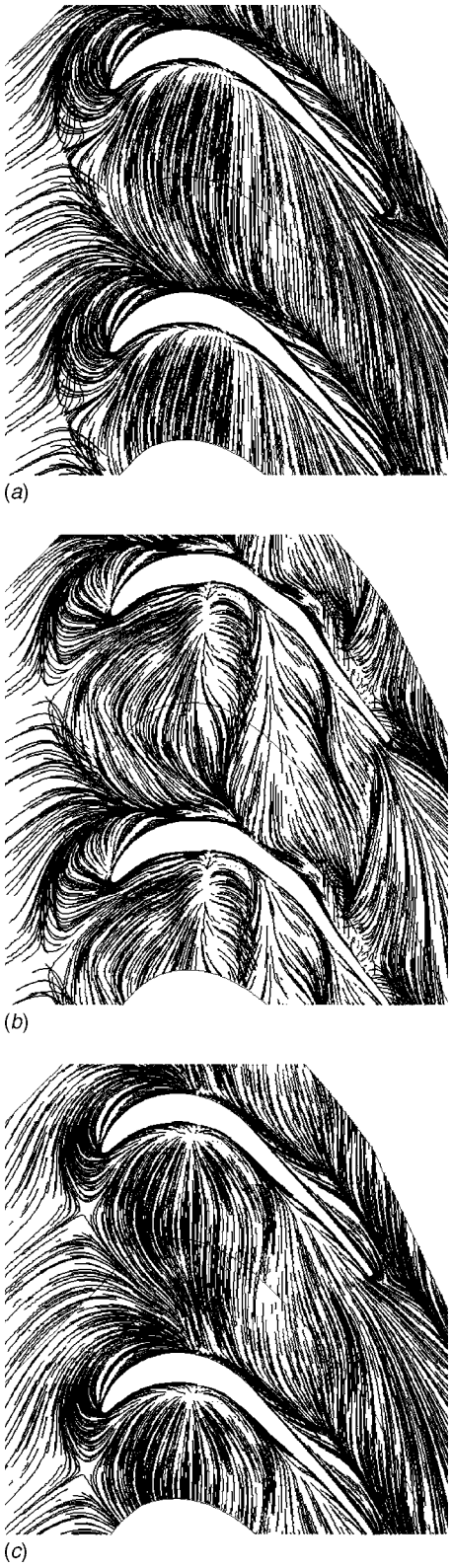

Fig. 8 Detail of the hub boundary layer flow migration for the single harmonic case. (*a*): Axisymmetric, (*b*): Optimized solution, and (*c*): Manual design.

slope of the streamlines close to the hub, which head directly to the ss. The differences in the migration patterns between the baseline and optimized cases are clear. The flow migration for the optimized case is much weaker than the original one, except when approaching the blade trailing edge. It gets stronger because of the almost complete disappearance of the suction side leg of the horseshoe vortex and the passage vortex, that in the axisymmetric case prevent the flow from turning too much in that region. This effect is also seen in the manual design, but it is weaker due to the smaller end wall perturbations. In that design, the suction-side vortex is still present. Also, saddle point of the optimized case has moved toward the suction side, the blade is less front loaded and the horseshoe vortex is weakened. This effect has not been reproduced in the manual design.

The pressure distribution in the blade-hub intersection for the optimized single harmonic case (Fig. 9(*a*)) shows a reduction of the loading between the leading edge and A, due to the change of incidence, a pressure rise in the ss at B, followed by a sharp decrease that ends at C, both associated with the bump located close to the ss, then the flow separates (between C and D), and finally, the pressure sharply rises again. The perturbations intended to be applied just for the suction side also modify the pressure side distribution and the flow separates at the rear part of the blade due to the adverse pressure gradient. These adverse effects may be caused by a poor control of the end wall geometry due to an insufficient number of harmonics and may be minimized with the use of a higher number of control parameters. The manual design roughly follows the same geometry obtained with the optimizer. There are two positive bumps, one next to the pressure side and the other above the suction side next to the trailing edge, and one negative bump, above the suction side at the beginning of the perturbation. The negative bump placed near the trailing edge in the pressure side is not obtained with the optimizer. As the amplitudes of the perturbations for the manual design are smaller than for the optimized case, the effect of the nonaxisymmetric end wall in the pressure distribution is less noticeable, as it occurs in the other distributions (Fig. 5–7).

Multiple Harmonic Perturbation. The multiple harmonic perturbation case consists of four Fourier harmonics for each axial location, yielding a total number of 54 control parameters for the end wall. The axial locations of the perturbations have remained constant.

By adding more control parameters, all the distributions presented in the single harmonic case are improved. Figure 10 compares the final SKEH distribution to the base solution. It is seen that the core distribution is greatly modified. The peak value has been divided by four and displaced toward the hub at 5% of the span. The swirl angle underturning has also been reduced by two degree regions in the core region of the span (see Fig. 11), while maintaining acceptable overturning values next to the hub, due to the use of the penalty function. The total pressure distribution (Fig. 12) shows the same trend as the SKEH. The peak of the losses has been displaced toward the hub about a 7% and, contrary to the previous case, its value has not been increased. The pressure distribution in the blade-hub intersection shows how it is possible to decouple the effects of the pressure and suction side of the blade by adding more control parameters in the circumferential direction. Thus, in Fig. 13, we see how the pressure side distribution is not affected very much except for the pressure bump around D. The suction side distribution shows an overall behavior similar to the single harmonic case, but eliminating the undesirable bumps, that are seen in the latter. A pressure drop between A and B is followed by a rise at C, but the difference between the multiple and single harmonic distribution is that the sharp pressure rise next to the trailing edge (after D in Fig. 9) is not produced. Hence, the flow separation that leads to higher pressure losses in the single harmonic case is minimized.

The optimizer (Fig. 13, top) has placed four bumps across the channel, whose effect is the isolation of the vortices generated in the passage. This effect reduces the interaction of the vortices with the main stream and weakens their strength. The migration of the hub boundary layer (Fig. 14) also shows this phenomenon. We see

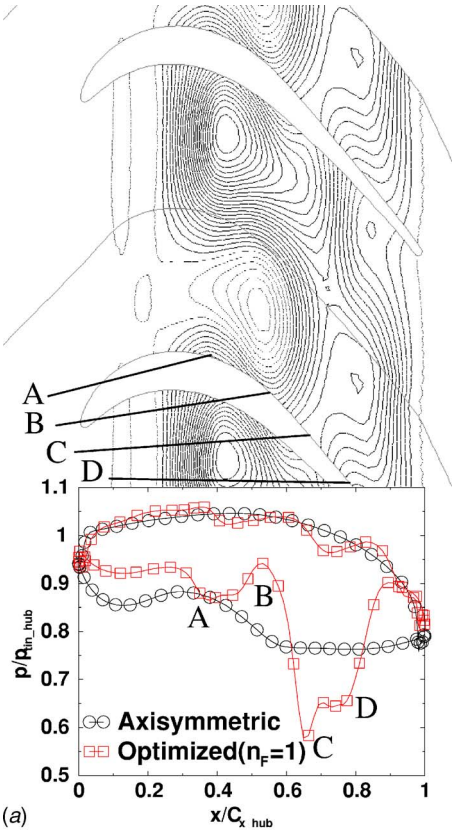

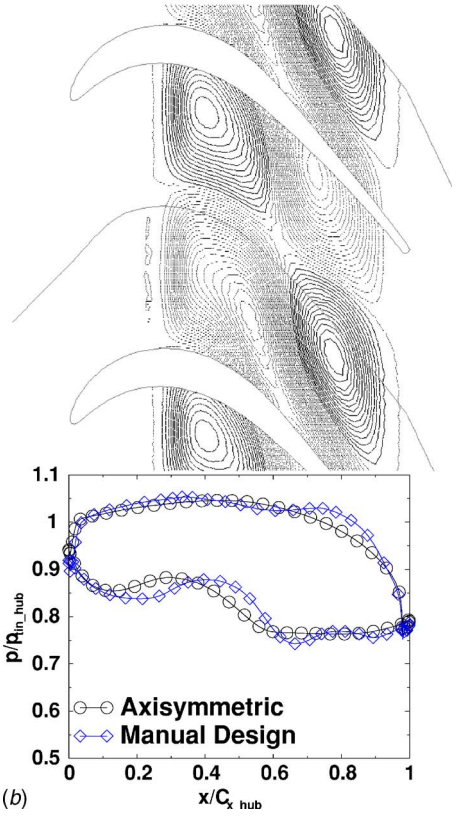

Fig. 9 Isolines (solid positive and dotted negative) of the hub surface perturbation (*a*) and comparison of the baseline and optimized nondimensional pressure distribution on the blade-hub intersection (*b*), for the single harmonic case (*a*), and for the manual design (*b*)

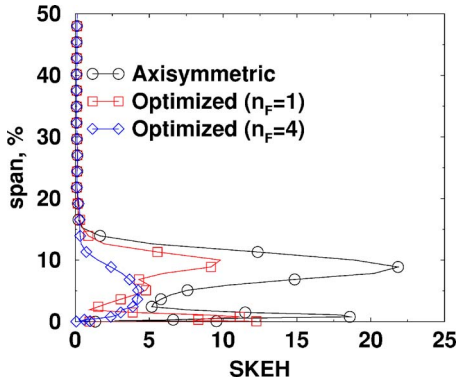

Fig. 10 Comparison of the baseline and optimized mass-averaged nondimensional SKEH at the outlet for the multiple harmonic case

how the streamlines are guided through the bumps in the rear part of the channel and how the suction side vortices are confined next to the suction side wall.

Both the single and the multiple harmonic solutions consider fixed axial locations for the geometry perturbations. The solutions could be enhanced if the number of axial stations were increased to improve the end wall control. By placing them in zones where the adjoint solution has larger values, such as next to the leading edge (see Fig. 15), smaller geometry changes could lead to larger

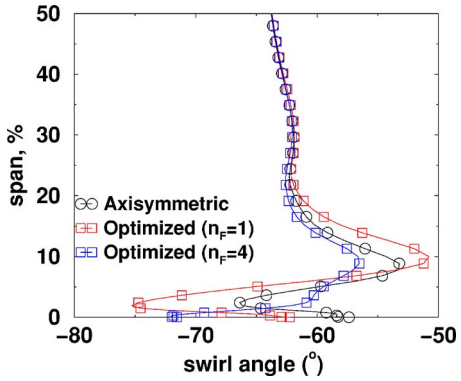

Fig. 11 Comparison of the baseline and optimized mass-averaged swirl angle at the outlet for the multiple harmonic case

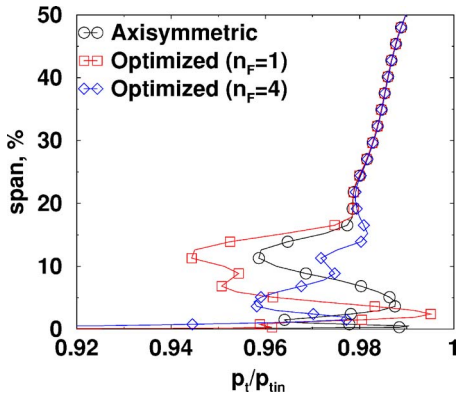

Fig. 12 Comparison of the baseline and optimized mass-averaged nondimensional total pressure at the outlet for the multiple harmonic case

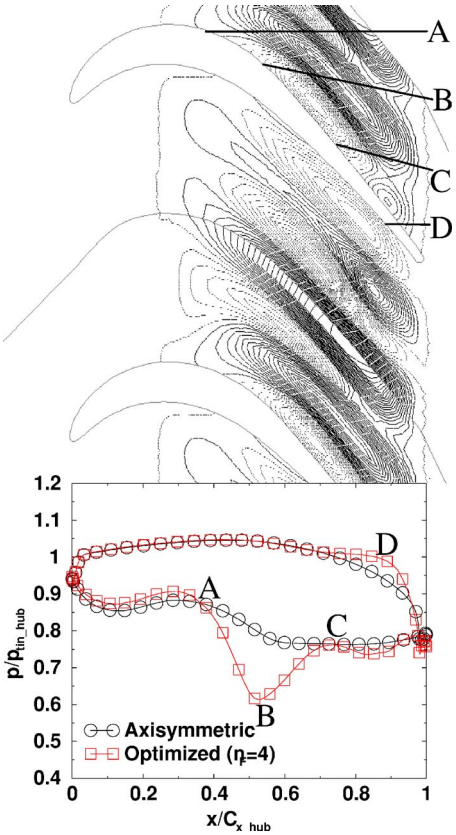

Fig. 13 Isolines (solid positive and dotted negative) of the hub surface perturbation (top) and comparison of the baseline and optimized nondimensional pressure distribution on the blade-hub intersection (bottom) for the multiple harmonic case

changes in the flow configuration. However, this issue has not been addressed in this work to keep the same restrictions as the designers.

Conclusions

We have presented an efficient method for the resolution of the adjoint Navier–Stokes and have demonstrated the equivalence between the linear and adjoint approach to compute the sensitivities. The adjoint solver has been used in conjuction with a gradient-based optimization method to minimize the secondary losses of a LPT vane using nonaxisymmetric end walls. The selected cost function is based on the secondary kinetic energy, which has a large sensitivity to variations in the secondary flow pattern. However, additional restrictions based on the limitation of the exit swirl angle need to be included to avoid the generation of losses in the downstream rows.

A vane of a LPT has been the subject of this optimization process with two sets of design parameters. The first has a single harmonic perturbation per axial location of the perturbation function, whereas the second has four harmonics. The SKEH has been greatly reduced in both cases, but the latter design has shown better results in terms of both SKEH reduction and flow control close to the end wall. The end wall has also been designed by expert designers finding similar solutions to the ones encountered by the optimizer. However, even in the best cases, small details of the flow, which are important for the designer, as small separation regions in the corners, are not prevented by the selected cost function. Future work will concentrate on improving the cost function to fulfill all the designer's criteria in a systematic way.

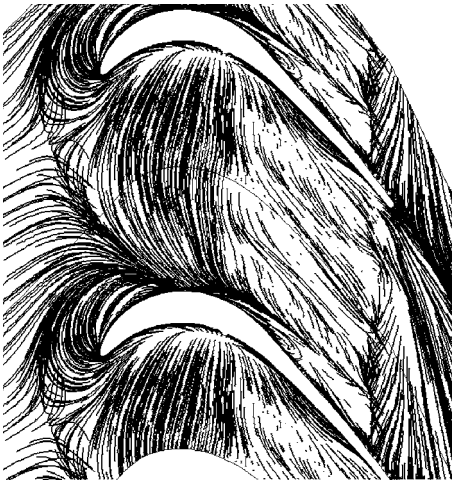

Fig. 14 Detail of the hub boundary layer flow migration for the multiple harmonic case

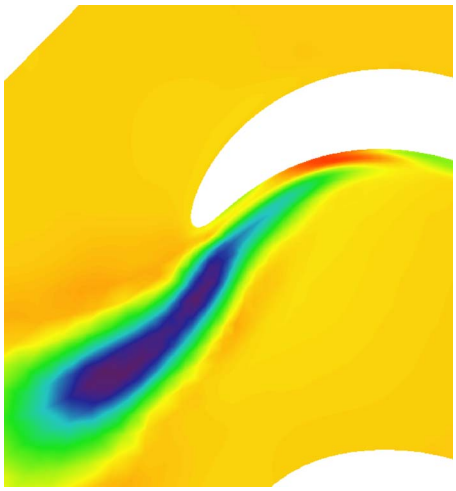

Fig. 15 Detail of the adjoint solution in the boundary layer region for the multiple harmonic case

Acknowledgment

The authors wish to thank ITP for permitting the publication of this paper and for its support during the project. The second author wants to thank ITP for allowing him the use of its facilities. This work has been partially funded by the Spanish Ministry of Science and Technology under PROFIT Grants No. FIT-100300-2003-11 and No. FIT-370200-2004-21, and by ITP under Contract No. DT-ITP-03-009 to the School of Aeronautics of the UPM.

References

[1] van den Braembussche, R., Alsalihi, Z., and Verstraete, T., 2004, "Fast Multidisciplinary Optimization of Turbomachinery Components," *Applications to Aeronautics and Turbomachinery*, Lecture Series 2004-07: Optimization Methods & Tools for Multicritieria/Multidisciplinary Design, von Karman Institute for Fluid Dynamics, Nov.

[2] Giannakoglou, K., Papadimitrou, D., and Kampolis, I., 2004, "Coupling Evolutionary Algorithms, Surrogate Models and Adjoint Methods in Inverse Design and Optimization Problems," *Applications to Aeronautics and Turbomachinery*, Lecture Series 2004-07: Optimization Methods & Tools for Multicritieria/Multidisciplinary Design, von Karman Institute for Fluid Dynamics, Nov.

[3] Corral, R., Crespo, J., and Gisbert, F., 2004, "Parallel Multigrid Unstructured Method for the Solution of the Navier–Stokes Equations," AIAA Paper 2004-0761.

[4] Nagel, M. G., and Baier, R.-D., 2005, "Experimentally Verified Numerical Optimization of a Three-Dimensional Parametrized Turbine Vane With Non-axisymmetric End Walls," ASME J. Turbomach., **127**, pp. 380–387.

[5] Pironneau, O., 1974, "On Optimum Design in Fluid Mechanics," J. Fluid

Mech., **64**, pp. 97–110.
[6] Jameson, A., 1988, "Aerodynamic Design via Control Theory," J. Sci. Comput., **3**, pp. 233–260.
[7] Jameson, A., Pierce, N., and Martinelli, L., 1998, "Optimum Aerodynamic Design Using the Navier Stokes Equation," Theor. Comput. Fluid Dyn., **10**, pp. 213–237.
[8] Kim, S., Alonso, J., and Jameson, A., 2002, "Design Optimization of High Lift Configurations Using a Viscous Continuous Adjoint Method," AIAA Paper 2002-0844.
[9] Jameson, A., Shankaran, S., Martinelli, L., and Haimes, B., 2004, "Aerodynamic Shape Optimization of Complete Aircraft Configurations using Unstructured Grids," AIAA Paper 2004-0533.
[10] Anderson, W. K., and Venkatakrishnan, V., 1997, "Aerodynamic Design Optimization on Unstructured Grids With a Continuous Adjoint Formulation," Institute for Computer Applications in Science and Engineering, Jan. Technical Report No. TR-97-9.
[11] Anderson, W., and Bonhaus, D., 1999, "Airfoil Design on Unstructured Grids for Turbulent Flows," AIAA J., **37**(2), pp. 185–191.
[12] Elliott, J., and Peraire, J., 1997, "Practical Three-Dimensional Aerodynamic Design and Optimization Using Unstructured Meshes," AIAA J., **35**(9), pp. 1479–1485.
[13] Giles, M., Duta, M., Müller, J., and Pierce, N., 2003, "Algorithm Developments for Discrete Adjoint Methods," AIAA J., **122**(2), pp. 198–205.
[14] Giles, M. B., and Pierce, N. A., 2000, "An Introduction to the Adjoint Approach to Design," Flow, Turbul. Combust., **65**, pp. 393–415.
[15] Corral, R., Escribano, A., Gisbert, F., Serrano, A., and Vasco, C., 2003, "Validation of a Linear Multigrid Accelerated Unstructured Navier-Stokes Solver for the Computation or Turbine Blades," AIAA Paper No. 2003-3326.
[16] Rose, M., and Martin, G., 1994, "Non-Axisymmetric Endwall Profiling in the HP NGVs of an Axial Flow Gas Turbine," ASME Paper No. 94-GT-249.
[17] Harvey, N., Rose, M., Shahpar, S., Taylor, M., Hartland, J., and Gregory-Smith, D., 1999, "Non-Axisymmetric Turbine End Wall Design—Part I: Three-Dimensional Design System," ASME J. Turbomach., **122**, pp. 278–285.
[18] Corral, R., and Gisbert, F., 2005, "Non Axisymmetric End-Wall Design Using an Adjoint Navier-Stokes Solver," AIAA Paper No. 2005-4025.
[19] Wood, J., Strasizar, T., and Hathaway, M., 1990, "Test Case E/CA-6, Subsonic Turbine Cascade T106," Test Cases for Computation of Internal Flows, AGARD-AR-275, July.
[20] Martel, C., 2000, "Nonlinear Constrained Optimization of Turbomachinery Problems," Escuela Técnica Superior de Ingenieros Aeronáuticos, Dec. Tech. Rep. No. ETSIA FM/00-01.
[21] Contreras, J., Corral, R., Fernández-Castañeda, J., Pastor, G., and Vasco, C., 2002, "Semiunstructured Grid Methods for Turbomachinery Applications," ASME Paper No. 2002-GT-30572.
[22] Prasad, A., 2005, "Calculation of the Mixed-Out State in Turbomachine Flows," ASME J. Turbomach., **127**, pp. 564–572.

Three-Dimensional Finite Element Analysis of Dovetail Attachments With and Without Crowning

J. R. Beisheim
Development Group,
ANSYS, Inc.,
Canonsburg, PA 15317

G. B. Sinclair
Department of Mechanical Engineering,
Louisiana State University,
Baton Rouge, LA 70803

*The stress analysis of dovetail attachments presents some challenges. These stem from the high stress gradients present, the contact inequalities attending conforming contact, and the nonlinearities inherent in Coulomb friction laws. Obtaining converged contact stresses in the presence of these phenomena is demanding, especially in three dimensions. In Beisheim and Sinclair (2003, ASME J. Turbomach., **125**, pp. 372–379), a submodeling approach with finite elements is employed to meet these challenges when friction is not present. Here we extend this approach to treat contact when friction is present. Converged stresses are obtained by using two successive submodels. Comparing these stresses with two-dimensional analysis elucidates some of the truly three-dimensional aspects of the stress analysis of dovetail attachments. Further comparisons of contact stresses when crowning is added indicate the possible alleviation of fretting fatigue that may be afforded by this means.* [DOI: 10.1115/1.2751486]

1 Introduction

1.1 Motivation and Background. Single tooth attachments or "dovetails" are used to secure fan and compressor blades to disks in gas turbines. A section through a typical dovetail is shown in Fig. 1(*a*). Therein the base of the blade is pulled as a result of the centripetal acceleration of its remainder, while it is restrained by contact with the disk on two flats (e.g., $C-C'$) in Fig. 1(*a*). At the edges of these contact regions, fretting can occur when loads vary. This fretting can lead to fatigue crack initiation and ultimately to failures (e.g., in the disk at C, the blade at C'). The ultimate intent of this work is to try to devise a means of reducing the incidence of such failures.

In attempting to realize this objective, an understanding of the stresses acting at the edges of contact is key. Such an appreciation, however, is not readily achieved. Even with the aid of finite element codes and restricting attention to two-dimensional aspects, the literature gives testimony to the difficulty of obtaining converged contact stresses: see Boddington et al. [1], Kenny et al. [2], Papanikos and Meguid [3], Meguid et al. [4], and Sinclair et al. [5]. These difficulties stem from the high stress gradients involved together with the nonlinearities attending conforming contact (i.e., the nonlinearities involved in determining contact extents and whether slip occurs or not). Only [5] explicitly meets convergence checks, which it does via a submodeling approach (Fig. 2). Resulting normal contact stresses show sharp peaks near the edges of contact (Fig. 3), but nonetheless peak stresses that would appear to have converged (close-up of Fig. 3: coarse, medium, and fine submodel grids formed by successively having element sides).

Converged, and otherwise verified, two-dimensional stresses at the edges of contact have helped in gaining an appreciation of the physics leading to fatigue in dovetail attachments. This physics is described in some detail in Sinclair and Cormier [6]: here we summarize the aspects pertinent to the present study.

The key contributor to fatigue in dovetail attachments identified in [6] is a *pinching mechanism* occurring during unloading when friction is present. During loading up, the attachment can be shown to slip. Under these circumstances, stresses can be expected to behave as in classical Hertzian contact. That is, from Poritsky [7], with peak values obeying

$$\sigma_c \propto \sigma_0 \quad \tau_c = \mu\sigma_c \quad \sigma_h = \pm 2\tau_c \tag{1}$$

where σ_c and τ_c are the normal and shear contact stresses (positive as in Fig. 1(*b*)), respectively, σ_h is the hoop stress, σ_0 is the applied stress acting at the top of the blade section (Fig. 1(*a*)), and μ is the coefficient of friction ($0 \le \mu \le 0.4$ in typical attachments; Hamdy and Waterhouse [8]). The finite element results of [5] are in close accord with the analytical results of Poritsky [7] and (1), with tensile σ_h occurring at C in the disk, C' in the blade (Fig. 1(*a*)). During unloading, stresses completely reverse themselves if $\mu=0$ (confirmed in [5]). However, when $\mu \neq 0$, the blade can stick to the disk. The angular periodic arrangement of the blades can then produce pinching because the sides of a representative geometry are not parallel (i.e., the outer near-vertical boundaries of the disk in Fig. 1(*a*) are not parallel). Under these circumstances, we have the following, somewhat unexpected, behavior:

$$\sigma_0 \downarrow \ \sigma_c \uparrow \tag{2}$$

That is, the normal contact stress actually increases with unloading. As a consequence, we further have

$$\tau_c \downarrow \ \sigma_h \downarrow \tag{3}$$

That is, now the shear stress drops dramatically for two reasons: first, because there is less load to oppose ($\sigma_0 \downarrow$), second, because the normal contact stress is now doing more to oppose it ($\sigma_c \uparrow$). As a result, because the hoop stress is largely produced by the shear stress, it too drops dramatically. Moreover, during loading up, the location of the peak tensile hoop stress is just outside of contact: during unloading with pinching, this location can move inside the contact region (because $\sigma_c \uparrow$) and the hoop stress actually becomes compressive. These effects are illustrated in Fig. 4. They essentially reveal that minor oscillations in applied loading/rpm (σ_0) can lead to relatively major oscillations in tensile hoop stresses at the edges of contact. These significantly fluctuating hoop stresses are then the harbinger of fatigue failures in dovetail attachments.

Contributed by the International Gas Turbine Institute of ASME for publication in the JOURNAL OF TURBOMACHINERY. Manuscript received August 10, 2006; final manuscript received September 5, 2006; published online March 21, 2008. Review conducted by David Wisler. Paper presented at the ASME Turbo Expo 2004: Land, Sea and Air (GT2004), Vienna, Austria, June 14–17, 2004. Paper No. GT2004-53222.

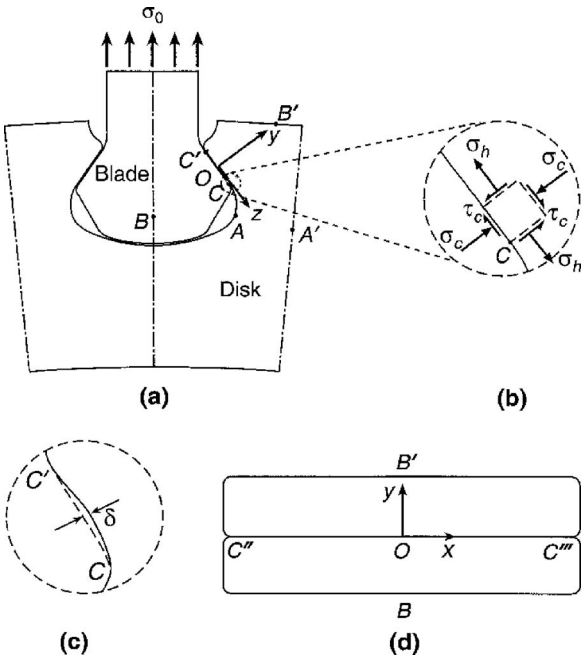

Fig. 1 Dovetail attachment configuration: (*a*) section of overall attachment, (*b*) close-up of disk near lower contact point with stresses acting, (*c*) in-plane crown on blade flat, and (*d*) out-of-plane section *BB′*

One potential means of alleviating these fluctuations is via *precision crowning* (Sinclair and Cormier [9,10]). We summarize the pertinent elements of this approach here.

Basically, precision crowning seeks to reduce the peak hoop stress $\sigma_h^{\max}$ during loading up when friction is present. This is because if $\sigma_h^{\max}$ is less at maximum load, there is less hoop stress to fluctuate. Further, because during loading up

$$\sigma_c \downarrow \Rightarrow \tau_c \downarrow \Rightarrow \sigma_h \downarrow \tag{4}$$

(see (1)); this objective is tantamount to reducing the peak contact stress $\sigma_c^{\max}$ during loading up. This latter reduction can be achieved with a small crown of height δ (Fig. 1(*c*)). This produces

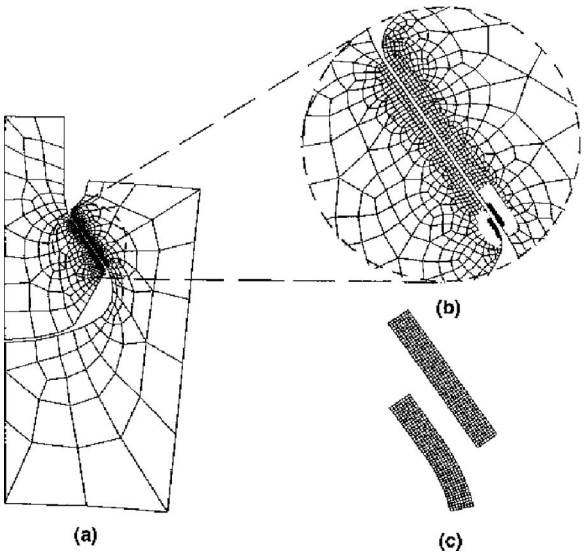

Fig. 2 Finite element grids: (*a*) coarse global grid, (*b*) close-up of coarse global grid with submodel region shown shaded solid, and (*c*) coarse submodel grid

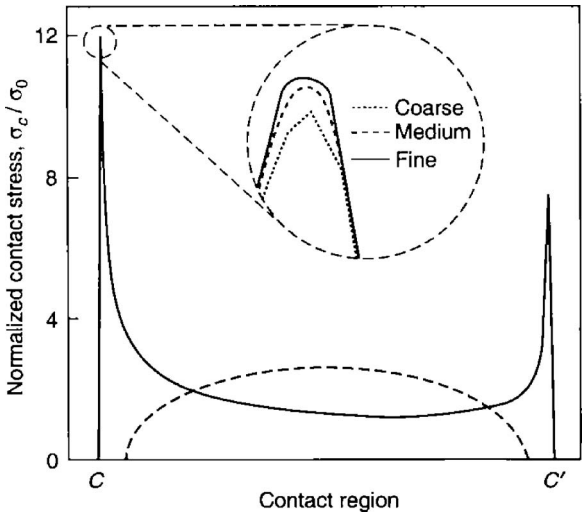

Fig. 3 Contact stress distributions (μ=0)

Hertzian-like contact stresses (shown dashed in Fig. 3 for $\delta=\delta_0$, a baseline value). It also produces companion reductions in $\sigma_h^{\max}$ and $\Delta\sigma_h$, the fluctuation in the hoop stress accompanying unloading: see Table 1, assembled from [9] for a range of crown heights and an uncrowned (δ=0) attachment. From this table it would appear that reduction of hoop stress fluctuations by a factor of 3 is available with crowning. Moreover, there is a range of crown heights that would be effective, namely,

$$\delta = 2\delta_0 \pm \delta_0 \tag{5}$$

While the baseline δ_0 is of the order of the elastic approach in Hertzian contact, the high nominal stresses present in dovetail attachments mean that it is not so small as to be unrealizable in

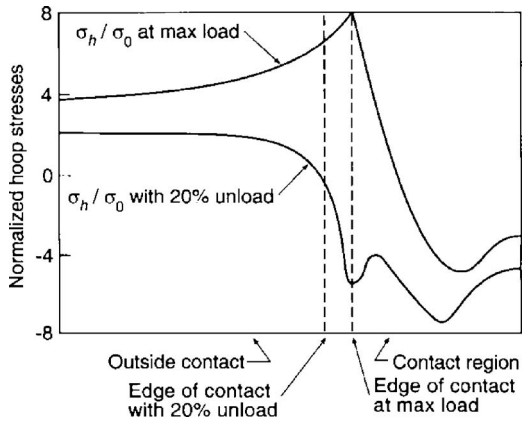

Fig. 4 Hoop stress variations near the edge of contact for 20% unloading (μ=0.4)

Table 1 Reduction in edge-of-contact stresses with in-plane precision crowning (μ=0.4)

			$\Delta\sigma_h/\sigma_0$	
$\frac{\delta}{\delta_0}$	$\frac{\sigma_c^{\max}}{\sigma_0}$	$\frac{\sigma_h^{\max}}{\sigma_0}$	20% unload	40% unload
0	9.0	8.0	13.2	20.7
1	2.3	3.0	3.0	4.4
2	3.2	3.7	3.7	5.9
4	4.5	4.0	4.4	7.4

practice (δ_0=25 μm in [9]), especially given the tolerance implicit in (5).

To be consistent, crowning also needs to be implemented in the out-of-plane direction (Fig. 1(*d*), no crown included). In [9], such out-of-plane crowning is assessed with a limited two-dimensional analysis of sections as in Fig. 1(*d*) and indicated to be similarly effective in reducing $\sigma_c^{\max}$; hence, implicitly, $\sigma_h^{\max}$, $\Delta\sigma_h$.

There are, however, some open questions regarding [9]'s assessment of the effectiveness of crowning. The first question occurs because the out-of-plane configuration is really loaded by shear transfer. That is, as in beam theory,

$$p = -\frac{dV}{dz} \tag{6}$$

where p is the nominal pressure between the blade and the disk and V is the shear stress resultant on sections such as BB' (Fig. 1). The shear stresses attending V are not admitted in a plane strain state. In [9], these shears are simulated with body force fields and then plane strain analysis is used. This analysis is necessarily confined to the frictionless case, the further shears attending friction also being absent from a plane strain treatment. While such an approach can be expected to be qualitatively similar to the true stresses in the out-of-plane section (Fig. 1(*d*)), it remains to be seen just how well they agree quantitatively, and what are the effects of friction.

The second question occurs because there are some truly three-dimensional effects on the stresses in dovetail attachments, whereas the analysis in [9] is limited to two dimensions. These three-dimensional stresses act in the "corners" of the contact region (e.g., when $x \to C'''$, $z \to C'$ in Fig. 1). While the heightened concentration of the contact stress that is induced at such corners can also be expected to be reduced by crowning, it remains to be seen just how big are such reductions.

1.2 Objective and Scope. Here, then, we seek to develop a means for the three-dimensional analysis of dovetail attachments in the presence of friction. This should enable us to provide some answers to the questions raised by [9].

To this end, we follow a previous pilot three-dimensional study of dovetail attachments without friction effects (Beisheim and Sinclair [11]). The analysis in [11] uses finite elements with submodeling to achieve convergence. We extend this analysis to handle friction.

We begin in Sec. 2 with a description of the actual, dovetail-attachment, test piece analyzed. This is the same test piece as analyzed in [11] so that we can draw on [11] for frictionless results. Next, in Sec. 3, we describe the submodeling analysis. This transpires to take a second submodel over that needed in [11]. Continuing in Sec. 4, we demonstrate convergence and error control for contact and hoop stresses. We then present stress results to quantify the differences between two-dimensional and three-dimensional analysis, and the effects of crowning. We close in Sec. 5 with some remarks in light of these results.

2 Attachment Configurations

2.1 Without Crowning. Figure 5 shows the geometry of a test piece used in the industry to simulate a dovetail attachment and analyzed in [11] without friction. Now we consider a representative coefficient of friction (μ=0.2) and a maximum (μ=0.4 [8]).

In Fig. 5, the blade base simulates the bottom of an actual blade including its contacting flats with a disk, while the disk segment simulates that portion of an actual disk to which a blade is attached. At the edges of contact, there are blend radii that are of the order of 5% of the blade base thickness. The applied stress σ_0 then simulates the effects of rotation of the remainder of the blade. After this load is transferred to the disk segment, this segment must be further restrained. In practice, this is achieved by attaching the segment to the center of the disk. In this test piece, the segment is restrained by two pieces that are held fixed: an outer restraining ring shown in Fig. 5, and a platform not shown in Fig. 5. The platform is attached to the top surface of the portion of the disk segment shown in Fig. 5.

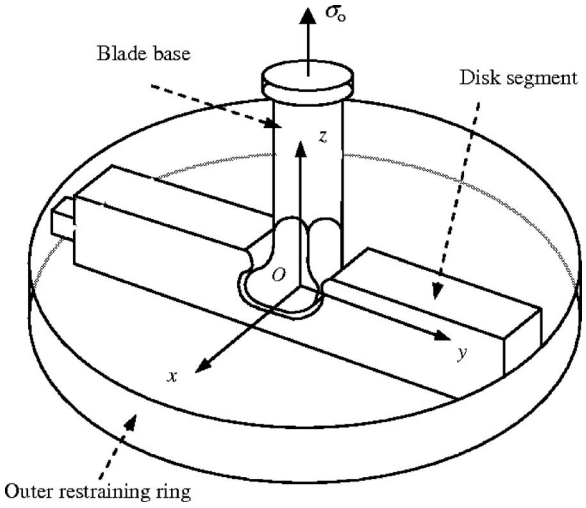

Fig. 5 Dovetail attachment test piece

To describe the geometry of the test piece more precisely, we use a rectangular Cartesian coordinate system with coordinates (x,y,z). The origin O of this coordinate system is located at the bottom of the blade beneath the center of the circular cross section. The z-axis is aligned with the center of the blade base, while the x- and y-axes are also central. Thus, the planes x=0 and y=0 are planes of symmetry with the present axial loading σ_0. This enables us to focus attention on just the quadrant of the blade base and the disk segment confined within $x \geq 0$ and $y \geq 0$. We further simplify the problem by excluding the geometry of the platform by modeling this as a rigid contact surface. Thus, it only enters as boundary conditions on the top of the disk segment. We also simplify the analysis by replacing the outer ring by an effective stiffness in the y direction.

In general, then, we seek the stresses $\sigma_x, \sigma_y, \sigma_z, \tau_{xy}, \tau_{xz}, \tau_{yz}$, and their associated displacements u, v, w, throughout the blade and disk, satisfying: the stress equations of equilibrium in the absence of body forces; the stress-displacement relations for a homogeneous and isotropic, linear elastic solid; and the following boundary conditions. Symmetry boundary conditions are applied to the surfaces at x=0 and y=0 for our quarter-symmetry model. A tensile normal traction σ_0 is applied to the top surface of the blade base, while the shear tractions there are taken to be zero (Fig. 5). On the surface of the disk segment where the outer ring is connected, $\sigma_y = -kv$ while the shear tractions are taken to be zero (the stiffness k in this condition is determined to apparently within 0.2% via a submodel of the outer ring in [11]). With the exception of the contact surfaces to be described next, stress-free boundary conditions are applied on all other surfaces.

The contacting surfaces between the platform and the disk, and the contacting surfaces between the blade and the disk, must each comply with the following contact conditions and constraints. First, the contact conditions require that the normal stresses and displacements on the contacting surfaces be equal. Second, the shear stress resultant is limited to μ times the normal stress when slip occurs, or less than this value if no slip occurs and tangential displacements are matched. Third, the contact constraints require that the normal stress be nowhere tensile inside the contact region and that there be no interpenetration outside the contact region.

In particular, we seek the normalized peak contact stress and hoop stress defined by

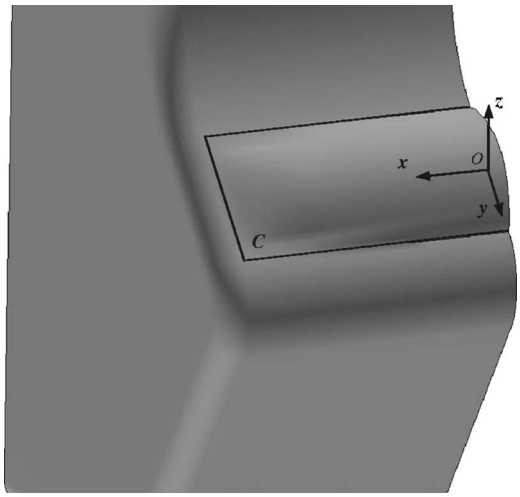

Fig. 6 Crowning profile

$$\bar{\sigma}_c^{\max} = \sigma_c^{\max}/\sigma_0 \quad \bar{\sigma}_h^{\max} = \sigma_h^{\max}/\sigma_0 \tag{7}$$

In actual dovetail attachments, it is the fluctuation in the hoop stress that accompanies unloading that can be expected to be of greatest import for fatigue failure. However, here in this test piece, unloading fluctuations in the hoop stress are not representative of those in actual attachments. This is because the test piece configuration lacks the periodic symmetry of an actual disk, and hence the pinching mechanism largely responsible for hoop stress fluctuations. Nonetheless, we can expect the maximum stresses of (6) to reflect the sort of fluctuations likely to be experienced in actual attachments (cf. Table 1, wherein $\sigma_c^{\max}/\sigma_0$ is 52% $\pm$9% of $\Delta\sigma_h/\sigma_0$ with a 40% unload).

2.2 With Crowning. In large part, we use the same test piece configuration (Fig. 5) when studying the effects of precision crowning. The only change here is to the blade on the contacting flat surface between the blade and the disk. On this flat, as a first simple crown, the blade is now given an elliptic parabaloid profile, the elliptical version of the Hertz approximation to a hemispherical cap (half of this profile is sketched in Fig. 6). That is, in terms of the rectangular coordinates of Fig. 6, a crown of height z, where

$$z = \delta\left(1 - \frac{x^2}{a^2} - \frac{y^2}{b^2}\right) \tag{8}$$

Here, δ continues as the central crown height, and a, b are the extents of the crown in the x, y directions, respectively.

Following [9], we take a and b to be about 7/8 of their respective available extents on the original contact flat. This leaves 1/8 of these extents available on which smooth blended transitions back to the original surface can be made (as in Fig. 1(*c*)).

Also following [9], we wish to take δ to be sufficiently small so that contact spreads throughout most of the available region, yet not so small that contact spreads off the crown. We want contact spread out as much as possible so that the nominal contact stress, and hence $\bar{\sigma}_c^{\max}$, is reduced as much as possible. We want the contact not to spread off the crown so as to avoid the large peak stresses that could then occur at the edges, even with blend radii there (cf. Fig. 3).

To obtain an initial estimate of δ, we compute the crown height for elastic contact of an elliptic parabaloid. From Johnson [12], this is

$$\frac{\delta}{b} = \frac{3\pi}{4}\frac{(1-\nu^2)p}{E}K\left(\sqrt{1-\frac{b^2}{a^2}}\right) \tag{9}$$

for $a \geq b$. In (9), E is Young's modulus, ν is Poisson's ratio, p is the average contact pressure, and K is the complete elliptic integral of the first kind. To set the minimum δ to avoid contact spreading off the crown, we evaluate (9) for the maximum pressure. This occurs for the frictionless case because then there are no contact shear tractions to help balance the load. We use the estimate in (9) to initiate finite element studies of crowning effects. Ultimately, this leads to the following range of acceptable crown heights:

$$\delta = \delta_0 \pm \frac{\delta_0}{5} \tag{10}$$

where δ_0 continues as our baseline crown height. For the present test configuration, $\delta_0 = 120$ μm (or 4.7 thousandths of an inch).

3 Finite Element Analysis

3.1 Global Analysis. Eight-node hexahedral (brick) elements are used to discretize most of the blade and disk (SOLID45, ANSYS [13]). We use low-order brick elements to facilitate interpolation with the bicubic surface when submodeling. Away from the contact region, some higher-order tetrahedral elements are used to discretize the curved neck of the blade as they provide a better fit to the geometry (SOLID92, ANSYS [13]). We place a boundary layer of elements around the region of interest on both the blade and disk. The boundary layer has a depth of three-eighths the smallest radius of curvature of the blade, a depth that is somewhat more conservative than the value previously tested in the numerical analysis of conforming contact problems (see [5]). Inside this boundary layer, we create uniform grids of elements and systematically refine these grids by halving element sides. Outside this boundary layer, we only approximately systematically refine the global grids. We do this by specifying the number of elements along the edges of the blade and disk away from the region of interest. We then use the VMESH command in ANSYS [13] to automatically mesh the rest of the region. The resulting global coarse grid is shown in Fig. 7(*a*). The numbers of spatial elements for this coarse global grid (C) and the successive medium (M) and fine (F) global grids is set out in Table 2. While the systematic halving of element sides would see successive three-dimensional grids increase these numbers of elements by factors of 8, here the approximately systematic scheme used away from the contact region leads to factors of 7.0 and 7.3.

To police the contact constraints of Sec. 2.1, we use surface-to-surface contact elements (TARGE170 and CONTA173, ANSYS [13]). These surface elements overlay the spatial elements on the contact surfaces within the boundary layer. An important input parameter for these contact elements in ANSYS is the normal contact stiffness factor (FKN). This factor controls the stiffness of the contacting surfaces, which affects the amount of penetration of the contact surface into the target surface. We override the default value of 1 with a value of 10 in order to help limit penetration while still maintaining good convergence of the contact algorithm in ANSYS. Otherwise, we use the default nonlinear convergence criteria in ANSYS. The numbers of contact elements for the C, M, and F grids are included in Table 2; these increase by nearly a factor of 4 between grids, consistent with systematic halving of element sides in two dimensions.

With these finite element grids, we judge any stress component sought, say σ, to be *converging* if

$$|\sigma^c - \sigma^m| > |\sigma^m - \sigma^f| \tag{11}$$

where superscripts denote the grid used in the computation. This particular convergence check has been demonstrated to be effective in determining whether or not stress fields are converging in contact problems in contrast to just a two-grid check (see [5]).

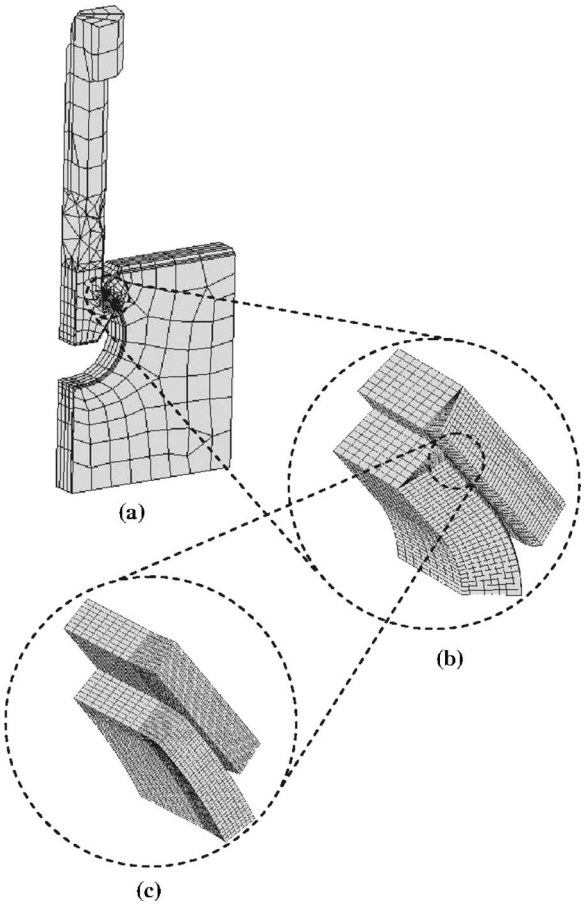

Fig. 7 Coarse finite element grids for dovetail attachment test piece: (*a*) global grid, (*b*) first submodel grid, and (*c*) second submodel grid

Further, σ is judged to have *converged* if the estimated discretization error $\hat{e}_d$ is less than the error level sought e_s. Thus,

$$\hat{e}_d = \frac{\sigma^f - \sigma^m}{\sigma^f} \quad |\hat{e}_d| < e_s \tag{12}$$

for converged σ. Typically in practical stress analysis, $e_s = 0.01$ (1%) represents an excellent level of accuracy, $e_s = 0.05$ (5%) a good level, and $e_s = 0.1$ (10%) a satisfactory level. Here, we seek to determine the peak stresses of interest to within a good level (5%). If not all results have converged as in (12) with $e_s = 0.05$, as can be expected to be the case here, then we proceed to submodel.

3.2 Submodel Analysis. While submodeling enables finite element analysis to resolve peak contact stresses with far less computation than that involved in direct discretization of the entire configuration, it only does this reliably if the additional source of error involved, namely, error in submodel boundary conditions, is controlled. To do this, we follow Cormier et al. [14] and subsequent developments [15–17]: the approach therein has been found to offer significant computational advantages over others in the literature (see [14]), and to be effective in resolving three-dimensional contact stresses in dovetail attachments (see [11]).

Table 2 Number of elements for each finite element grid

Grid	Spatial	Contact	Total
C	2,127	487	2,614
M	14,990	1,943	16,933
F	108,870	7,765	116,635
SC	9,216	1,152	10,368
SM	73,728	4,608	78,336
SF	589,824	18,432	608,256
SSC	19,968	4,992	24,690
SSM	159,744	19,968	179,712

In essence the approach adopted for error control in submodeling entails the following. As with the global analysis, we continue to employ three grids when submodeling to gauge convergence. Now, though, the exact or true error e_e can be separated into two parts as follows:

$$e_e = \frac{\sigma_e - \sigma^{\text{fs}}_{\text{fbc}}}{\sigma_e} = \frac{\sigma_e - \sigma^{\text{fs}}_{\text{ebc}}}{\sigma_e} + \frac{\sigma^{\text{fs}}_{\text{ebc}} - \sigma^{\text{fs}}_{\text{fbc}}}{\sigma_e} = e_{\text{sd}} + e_{\text{bc}} \tag{13}$$

Here σ_e is the exact or true value of σ, and $\sigma^{\text{fs}}_{\text{fbc}}$ its determination on the fine submodel grid using boundary conditions drawn from the fine global grid: that is, our best available estimate of σ_e. Further, $\sigma^{\text{fs}}_{\text{ebc}}$ is σ determined on the fine submodel grid using exact or true boundary conditions. Thus, e_{sd} is the true submodel discretization error while e_{bc} is the true boundary condition error in the submodel. Of course, we do not know σ_e, or even $\sigma^{\text{fs}}_{\text{ebc}}$. Hence we must estimate these quantities. We do this with

$$\hat{e}_d = \frac{\sigma^{\text{fs}}_{\text{fbc}} - \sigma^{\text{ms}}_{\text{fbc}}}{\sigma^{\text{fs}}_{\text{fbc}}} \quad \hat{e}_{\text{bc}} = \frac{\sigma^{\text{fs}}_{\text{fbc}} - \sigma^{\text{fs}}_{\text{mbc}}}{\sigma^{\text{fs}}_{\text{fbc}}}, \tag{14}$$

where $\sigma^{\text{ms}}_{\text{fbc}}$ is σ computed on the medium submodel grid with boundary conditions from the fine global grid, while $\sigma^{\text{fs}}_{\text{mbc}}$ is σ computed on the fine submodel grid with boundary conditions from the medium global grid. We then judge σ to be *converging* when the analogue of (11) holds on the submodel grids, and to have *converged* when

$$|\hat{e}_d + \hat{e}_{\text{bc}}| < e_s \tag{15}$$

If (15) is not complied with, successive submodeling can be applied.

Further general descriptions of this submodeling approach may be found in [14,15,17], and a description of how it is applied in three-dimensional contact of dovetail attachments in [11]. In particular, this last reference details the rationale and implementation of displacements with bicubic surfaces in submodel boundary conditions, as well as how to size submodel regions in three dimensions. With the approach, a series of two-dimensional test problems were solved in Cormier et al. [14] and peak stresses determined to within 2%. These problems involved up to five submodels. Also in [11], three-dimensional peak contact stresses were determined to within 3%, using a single submodel.

Here, it transpires that we need two submodels because we are also seeking to resolve the hoop stress σ_h in addition to the contact stress σ_c, and the former is typically harder to resolve because of discontinuities in its slope. The coarse grids for these two successive submodels are shown in Figs. 7(*b*) and 7(*c*): the corresponding numbers of spatial and contact elements are included in Table 2. Herein SC, SM, and SF denote the first submodel coarse, medium, and fine grids, respectively, while SSC and SSM the coarse and medium grids, respectively, for the second submodel. With the second submodel, a convergence check analogous to (11) is actually applied to the three grids SF, SSC, and SSM. This enables us to avoid a further grid for the second submodel, a grid that could be expected to be quite time-consuming to run.

One important note when using submodeling with contact analyses is to continually verify the contact conditions at the contact surfaces, while systematically refining your grids. This is necessary for the following reason.

In the ANSYS software, one surface of the "contacting surface pair" is designated the "contact surface" and the other surface the "target surface." In general, it is recommended in the ANSYS docu-

Table 3 Convergence of normalized peak stresses without crowning

	$\bar{\sigma}_c^{\max}$		$-\bar{\sigma}_h^{\max}$	
Grid	$\mu=0.2$	$\mu=0.4$	$\mu=0.2$	$\mu=0.4$
C	12.6	11.6	7.6	7.5
M	21.9	16.3	13.8	13.2
F	26.2	23.5	18.6	18.1
SC	32.5	27.8	27.7	28.2
SM	41.1	35.9	36.2	36.4
SF	45.1	40.3	42.7	43.0
SSC	45.8	41.4	42.3	44.2
SSM	46.8	41.7	42.2	43.9

mentation that the contact surface contain a more refined mesh than the target surface. As the element sizes get smaller with each submodel grid, this distinction becomes more important. As the element size begins to approach the actual amount of displacement at the contact surface, if the target surface happens to be more refined than the contact surface, some nodes on the target surface may not properly detect the contact surface. This results in a zero-valued force at these nodes, and ultimately produces contact stresses that are zero, or approximately zero, at these locations.

The obvious solution to this in the ANSYS software is to refine the contact surface more than the target surface. An alternative solution is to define "symmetric contact" conditions for the contacting surface pair. Symmetric contact involves defining each surface of the contacting surface pair as both the contact surface and target surface, a double definition that can slow run times but will avoid the problem mentioned above.

4 Results

4.1 Without Crowning. Table 3 sets out the maximum magnitudes of the normalized contact and hoop stresses $\bar{\sigma}_c^{\max}$ and $\bar{\sigma}_h^{\max}$ computed on our global and submodel sequences of grids (from nodal values). These values enable convergence to be checked. On the last three grids (SF, SSC, SSM), $\bar{\sigma}_h^{\max}$ is converging in the sense of (11) for both friction cases, $\mu=0.2$ and 0.4. On these same grids, $\bar{\sigma}_c^{\max}$ is also converging for $\mu=0.4$, but not in compliance with (11) for $\mu=0.2$. However, on the grid sequence SC, SF, SSM, $\bar{\sigma}_c^{\max}$ for $\mu=0.2$ is converging. Because if anything, this latter sequence represents a more stringent convergence check (with element extents being quartered instead of just halved), we judge $\bar{\sigma}_c^{\max}$ for $\mu=0.2$ to be converging as well.

Given that stresses are converging, we can estimate the discretization error $\hat{e}_d$ using (14) to see if stresses have converged sufficiently. For $\bar{\sigma}_c^{\max}$, this yields

$$\hat{e}_d = 2.1\% \quad \text{and} \quad 0.7\% \tag{16}$$

for $\mu=0.2$ and 0.4, respectively. These errors need to be taken in conjunction with boundary condition errors from both submodels. Using (14), errors from the latter source are: for the first submodel,

$$\hat{e}_{\text{bc}} = -1.9\% \quad \text{and} \quad -0.3\% \tag{17}$$

for $\mu=0.2$ and 0.4, respectively, and for the second submodel,

$$\hat{e}_{\text{bc}} = 1.7\% \quad \text{and} \quad 1.5\% \tag{18}$$

for $\mu=0.2$ and 0.4, respectively. The total combined error estimate $\hat{e}$ is then the signed arithmetic sum of these contributions, that is

$$\hat{e} = \hat{e}_d + \sum \hat{e}_{\text{bc}} \tag{19}$$

For $\bar{\sigma}_c^{\max}$, this yields

$$\hat{e} = 1.9\% \tag{20}$$

for both $\mu=0.2$ and 0.4. This error estimate represents a good level of accuracy ($<5\%$) and meets our accuracy objective.

Proceeding similarly for $\bar{\sigma}_h^{\max}$ yields (from Table 3)

$$\hat{e}_d = 0.2\% \quad \text{and} \quad 0.7\% \tag{21}$$

for $\mu=0.2$ and 0.4, respectively. Using (14) then to estimate boundary condition errors for both submodels and combining with $\hat{e}_d$ of (21) via (19) yields

$$\hat{e} = -0.1\% \quad \text{and} \quad 0.8\% \tag{22}$$

for $\mu=0.2$ and 0.4, respectively. These error estimates represent an excellent level of accuracy ($<1\%$) and again meet our accuracy objective.

Both $\bar{\sigma}_c^{\max}$ and $\bar{\sigma}_h^{\max}$ of Table 3 are converging on the first submodel sequence of grids (though barely so for $\bar{\sigma}_h^{\max}$). However, corresponding discretization errors are large, being about 10% for $\bar{\sigma}_c^{\max}$ and 15% for $\bar{\sigma}_h^{\max}$. This prevents meeting our overall error level of less than 5% and necessitates the second submodel here.

The converged contact and hoop stresses in Table 3 are in accord with expected trends. The contact stresses are expected to decrease with increasing friction because the frictional shear tractions balance more of the applied load under this scenario: in Table 3, $\bar{\sigma}_c^{\max}$ decreases by 11% as $\mu=0.2\rightarrow\mu=0.4$. The hoop stresses are expected to be comparable to the contact stresses and probably increase with increasing friction (cf. (1)): in Table 3, $\bar{\sigma}_h^{\max}$ is 90% of $\bar{\sigma}_c^{\max}$ when $\mu=0.2$ and increases by 5% as $\mu=0.2\rightarrow\mu=0.4$.

Focusing on the contact stress, Fig. 8 presents normalized contact stresses $\bar{\sigma}_c$ along three radial rays $r_i(i=1,2,3)$ within the contact zone for $\mu=0$. On r_1 (Fig. 8(*b*)), there is good agreement between plane strain analysis and three-dimensional (3D) analysis. The difference in the maximum stresses is 7%, while the average difference in stresses is less than 4%. Here, then, a two-dimensional (2D) analysis is certainly appropriate.

On r_2 (Fig. 8(*c*)), there is qualitative agreement between plane strain analysis with simulated shear transfer and 3D analysis (the former analysis is only applicable for $\mu=0$, hence the results in Fig. 8 are for $\mu=0$). However, quantitatively there are significant differences. These are most pronounced for the maximum stresses which have a 30% discrepancy. Here, then, a 2D analysis is really not sufficiently accurate.

On r_3 (Fig. 8(*d*)), some essentially three-dimensional aspects of the contact stress distribution make their presence felt. The peak $\bar{\sigma}_c$ along this ray is significantly higher than along either of the other rays (r_1, r_2). To quantify this increase, we define

$$\lambda = K_T^{3D}/K_T^{2D} \tag{23}$$

where $K_T=\bar{\sigma}_c^{\max}/\bar{\sigma}_c^{\text{average}}$ is the stress concentration factor for the contact stresses, and the superscripts distinguish plane strain analysis (on r_1) from 3D (on r_3). From [11] and the present study we then have

$$\lambda = 2.14 \quad \text{and} \quad 2.46 \tag{24}$$

for $\mu=0$ and 0.2, respectively. Clearly marked stress increases occur because of these three-dimensional effects.

Some support for the degree of 3D stress increase evident in (24) is available from the analysis of a flat, smooth, rigid punch with rectangular planform pressed into an elastic half-space. This problem is singular. If the coordinate system shown in Fig. 6 is rotated clockwise through 180 deg about the z-axis, then placed with origin in the corner at C, the following singular stresses can be identified. As the edge at $x = 0$ is approached away from the corner,

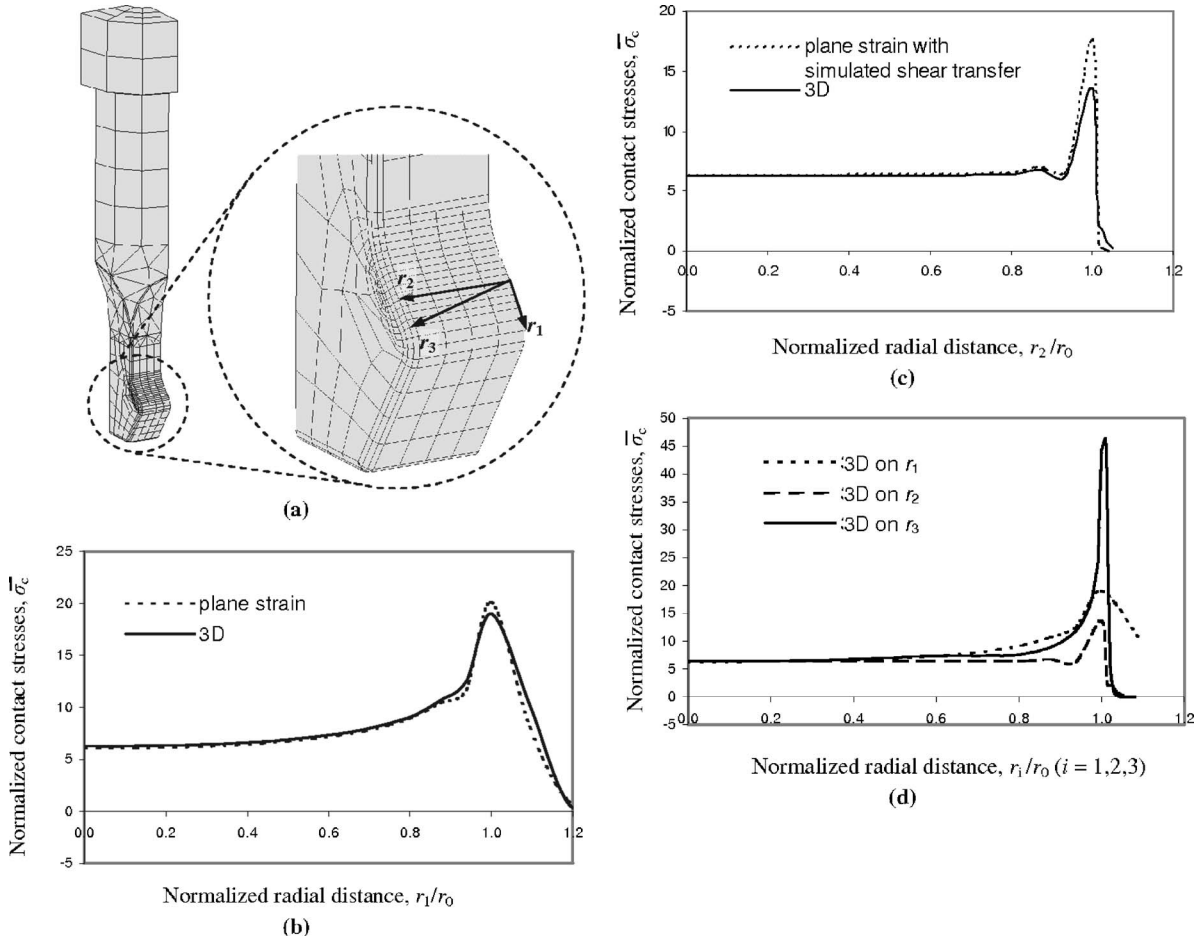

Fig. 8 Contact stress results: (*a*) blade segment with lines along which stresses are taken, (*b*) comparison of plane strain and 3D stresses, (*c*) comparison of plane strain with simulated shear transfer and 3D stresses, and (*d*) 3D "corner" effect on stresses (μ=0)

$$\sigma_c = O(1/\sqrt{x}) \text{ as } x \to 0 (y \neq 0) \tag{25}$$

This singular character is effectively identified in Sadowsky [18] and Aksentian [19]. As the corner at $x=y=0$ is approached,

$$\sigma_c = O\left[\frac{(x^2+y^2)^{0.15}}{\sqrt{xy}}\right] \text{ as } x,y \to 0 \tag{26}$$

This last singular character is identified in Morrison and Lewis [20]. Making the changes of variable $x=r\cos\theta, y=r\sin\theta$, reveals that it is stronger than at the edges, being $O(r^{-0.7})$ instead of $O(r^{-0.5})$. Thus, the singular character in this problem is in accord with higher stresses in the corner ($\lambda > 1$). Furthermore, integrating these singular stresses over intervals near the edge so that the average stress in the interval mirrors the K_T^{2D} found in [11], then comparing with the corresponding K_T^{3D} for an average in the corner, leads to[1]

$$\lambda = 2.54 \tag{27}$$

This is somewhat higher than the λ in (24) because our contact region is not quite rectangular, though it is nearly so (the corner is rounded so that it moves in 2% of the radial distance to a sharp corner).

[1]The stresses used to do this averaging are taken from Brothers [21] and integrated with a numerical quadrature scheme that recognizes the singularities of (25) and (26).

4.2 With Crowning. Table 4 sets out the maximum magnitudes of $\bar{\sigma}_c^{\max}$ and $\bar{\sigma}_h^{\max}$ computed on just our global sequence of grids. These values are for the baseline crown height $\delta_o = 120$ μm. They show that both stresses are converging in the sense of (11) for both values of μ, though $\bar{\sigma}_h^{\max}$ for $\mu=0.4$ barely so.

Given stresses are converging, we can estimate $\hat{e}_d$ using (14) to see if they have converged sufficiently. For $\bar{\sigma}_c^{\max}$, this yields

$$\hat{e}_d = 1.8\% \quad \text{and} \quad 4.8\% \tag{28}$$

for $\mu=0.2$ and 0.4, respectively. These estimates represent good levels of accuracy. For $\bar{\sigma}_h^{\max}$, this yields

$$\hat{e}_d = 6.6\% \quad \text{and} \quad 17.0\% \tag{29}$$

Table 4 Convergence of normalized peak stresses with crowning ($\delta=\delta_0$)

	$\bar{\sigma}_c^{\max}$		$-\bar{\sigma}_h^{\max}$	
Grid	μ=0.2	μ=0.4	μ=0.2	μ=0.4
C	24.8	23.2	18.4	19.7
M	26.7	25.7	24.1	24.9
F	27.2	27.0	25.8	30.0

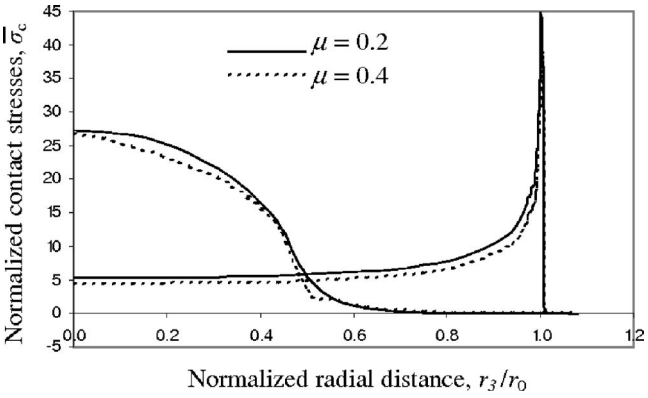

Fig. 9 Contact stress with and without crowning along r_3 of Fig. 8

for μ=0.2 and 0.4, respectively. These estimates represent one satisfactory result and one unsatisfactory result. A submodel could be employed to try and improve the errors in $\bar{\sigma}_h^{\max}$. This would entail a different sequence of grids to that used in our submodeling without crowning because peak stresses now occur in the center of contact rather than at the edge. Here, since we can only infer the effects of crowning for this test configuration anyway (recall the earlier discussion regarding pinching), we simply use the good results for $\bar{\sigma}_c^{\max}$ to this end.

The $\bar{\sigma}_c^{\max}$ in Table 4 represent reductions of 42% and 35% over corresponding values in Table 3 for μ=0.2 and 0.4, respectively. These are comparable reductions to those reported in [9] (see Table 1, wherein $\bar{\sigma}_c^{\max}$ is reduced by 64% for δ_o and μ=0.4). The reductions for the full 3D treatment are increased over the 2D analysis in [9] because of the λ-factor. However, they are also reduced because the area of contact sees a greater reduction with crowning in 3D analysis than in 2D. With a different crowning profile than the simple one of (8), these contact area reductions in going from 2D to 3D analysis could themselves be reduced, thereby resulting in a greater alleviation of 3D contact stresses with crowning. Such different crowning profiles merit further analysis.

Continuing to focus on the contact stress, Fig. 9 presents $\bar{\sigma}_c$ along r_3 within the contact region for both μ=0.2 and 0.4. For both values of μ, these three-dimensional stresses show a very similar redistribution with crowning to that found earlier in [9] for two-dimensional stresses (Fig. 3). Varying the crown height as in (10) shows comparable reductions in $\bar{\sigma}_c^{\max}$ can be achieved. In particular, for μ=0 and $\delta=4\delta_o/5$, the peak remains central, while for μ=0.4 and $\delta=6\delta_o/5$, the contact still spreads over half of the available region.

5 Concluding Remarks

When friction is present in the three-dimensional analysis of dovetail attachments, converged stresses can be expected to be more challenging to obtain. Here, this challenge is met with two successive submodels that result in overall error estimates that are less than 2%. In particular, the critical, peak, hoop stress needed to track pinching effects is determined to within 1% using this approach. Thus submodeling, or if need be successive submodeling, looks to be an effective means of analyzing the three-dimensional contact stresses in dovetail attachments.

There is a plane in which two-dimensional plane-strain analysis suffices (r_1 of Fig. 8). However, for other planes there are no really appropriate two-dimensional approaches and three-dimensional analysis is required. Moreover, the truly three-dimensional stresses so computed can be significantly higher ($>2\times$) than peak plane-strain stresses. It follows that three-dimensional analysis is required if one is to obtain a full appreciation of the contact stresses in dovetail attachments.

When crowning is added, the maximum contact stress is reduced by more than one-third for the three-dimensional test configuration treated here. This sort of reduction can be expected to lead to significant drops in the hoop stress fluctuations accompanying unloading in actual dovetail attachments. Thus, this three-dimensional study confirms the promise of alleviation of fatigue failures in dovetail attachments reported in the earlier two-dimensional study [9].

Acknowledgment

We are most grateful to General Electric Aircraft Engines of Cincinnati for providing the funding for this research. We also appreciate being furnished specifications for the dovetail test piece application by Pratt & Whitney. In addition, we are grateful to ANSYS for providing access to their software, which is used exclusively throughout.

References

[1] Boddington, P. H. B., Chen, K., and Ruiz, C., 1985, "The Numerical Analysis of Dovetail Joints," Comput. Struct., **20**, pp. 731–735.
[2] Kenny, B., Patterson, E. A., Said, M., and Aradhya, K. S. S., 1991, "Contact Stress Distributions in a Turbine Disk Dovetail Type Joint—A Comparison of Photoelastic and Finite Element Results," Strain, **27**, pp. 21–24.
[3] Papanikos, P., and Meguid, S. A., 1994, "Theoretical and Experimental Studies of Fretting-Initiated Fatigue Failure of Aeroengine Compressor Discs," Fatigue Fract. Eng. Mater. Struct., **17**, pp. 539–550.
[4] Meguid, S. A., Refaat, M. H., and Papanikos, P., 1996, "Theoretical and Experimental Studies of Structural Integrity of Dovetail Joints in Aeroengine Discs," J. Mater. Process. Technol., **56**, pp. 668–677.
[5] Sinclair, G. B., Cormier, N. G., Griffin, J. H., and Meda, G., 2002, "Contact Stresses in Dovetail Attachments: Finite Element Modeling," J. Eng. Gas Turbines Power, **124**, pp. 182–189.
[6] Sinclair, G. B., and Cormier, N. G., 2002, "Contact Stresses in Dovetail Attachments: Physical Modeling," J. Eng. Gas Turbines Power, **124**, pp. 325–331.
[7] Poritsky, H., 1950, "Stresses and Deflections of Cylindrical Bodies in Contact With Applications to Contact of Gears and Locomotive Wheels," J. Appl. Mech., **17**, pp. 191–201.
[8] Hamdy, M. M., and Waterhouse, R. B., 1981, "The Fretting Wear of Ti-6Al-4V and Aged Inconel 718 at Elevated Temperatures," Wear, **71**, pp. 237–248.
[9] Sinclair, G. B., and Cormier, N. G., 2003, "Contact Stresses in Dovetail Attachments: Alleviation via Precision Crowning," J. Eng. Gas Turbines Power, **125**, pp. 1033–1041.
[10] Sinclair, G. B., and Cormier, N. G., 2001, "Precision Crowning of Blade Attachments in Gas Turbines," U.S. Patent No. 6,244,822B1 (also, in 2003, U.K. Patent No. GB 2,345,943B).
[11] Beisheim, J. R., and Sinclair, G. B., 2003, "On the Three-Dimensional Finite Element Analysis of Dovetail Attachments," ASME J. Turbomach., **125**, pp. 372–379.
[12] Johnson, K. L., 1989, *Contact Mechanics*, Cambridge University Press, Cambridge, U.K.
[13] *ANSYS Advanced Analysis Techniques*, Revision 6.0, 2001, ANSYS Inc., Canonsburg, PA.
[14] Cormier, N. G., Smallwood, B. S., Sinclair, G. B., and Meda, G., 1999, "Aggressive Submodelling of Stress Concentrations," Int. J. Numer. Methods Eng., **46**, pp. 889–909.
[15] Sinclair, G. B., Beisheim, J. R., Epps, B. P., and Pollice, S. L., 2000, "Towards Improved Submodeling of Stress Concentrations," *Proceedings of the Tenth International ANSYS Conference*, Pittsburgh, PA, CD-ROM.
[16] Sinclair, G. B., and Epps, B. P., 2002, "On the Logarithmic Stress Singularities Induced by the Use of Displacement Shape Functions in Boundary Conditions in Submodelling," Commun. Numer. Methods Eng., **18**, pp. 121–130.
[17] Beisheim, J. R., and Sinclair, G. B., 2002, "Three-Dimensional Submodeling of Stress Concentrations," *Proceedings of the Eleventh International ANSYS Conference*, Pittsburgh, PA, CD-ROM.
[18] Sadowsky, M. A., 1928, "Two-Dimensional Problems in Elasticity Theory," Z. Angew. Math. Mech., **8**, pp. 107–121.
[19] Aksentian, O. K., 1967, "Singularities of the Stress-Strain State of a Plate in the Neighborhood of an Edge," J. Appl. Math. Mech., **31**, pp. 193–202.
[20] Morrison, J. A., and Lewis, J. A., 1976, "Charge Singularity at the Corner of a Flat Plate," SIAM J. Appl. Math., **31**, pp. 233–250.
[21] Brothers, P. W., 1976, "The Rigid Rectangular Punch on the Elastic Half-Space," MS thesis, University Of Auckland, Auckland, New Zealand.

Unsteady Transition Phenomena at a Compressor Blade Leading Edge

Alan D. Henderson
e-mail: alan.henderson@utas.edu.au

Gregory J. Walker
e-mail: greg.walker@utas.edu.au

School of Engineering,
University of Tasmania,
Hobart, 7001, Australia

Jeremy D. Hughes
Rolls-Royce plc,
Derby DE248BJ, UK
e-mail: jeremy.hughes@rolls-royce.com

Wake-induced laminar-turbulent transition is studied at the leading edge of a C4-section compressor stator blade in a 1.5-stage axial compressor. Surface hot-film sensor observations are interpreted with the aid of numerical solutions from UNSFLO, a quasi-three-dimensional viscous-inviscid flow solver. The passage of a rotor wake, with its associated negative jet, over the stator leading edge is observed to have a destabilizing effect on the suction surface boundary layer. This leads to transition closer to the stator leading edge than would have occurred under steady flow conditions. The strength of this phenomenon is influenced by the rotor-stator axial gap and the variability of individual rotor wake disturbances. A variety of transition phenomena is observed near the leading edge in the wake path. Wave packets characteristic of Tollmien-Schlichting waves are observed to amplify and break down into turbulent spots. Disturbances characteristic of the streaky structures occurring in bypass transition are also seen. Examination of suction surface disturbance and wake-induced transitional strip trajectories points to the leading edge as the principal receptivity site for suction surface transition phenomena at design loading conditions. This contrasts markedly with the pressure surface behavior, where transition at design conditions occurs remotely from leading-edge flow perturbations associated with wake chopping. Here, the local receptivity of the boundary layer to the wake passing disturbance and turbulent wake fluid discharging onto the blade surface may be of greater importance. [DOI: 10.1115/1.2751148]

Introduction

The unsteady flow resulting from interactions between adjacent blade rows in axial turbomachinery is well known to influence the boundary layer development on blade surfaces. The unsteady flow experienced by a blade element in an embedded stage is dominated by the relative motion of the upstream blade row. The periodic passage of upstream wakes over a blade surface often results in a flow phenomenon known as "wake-induced" transition as described in Mayle [1], Walker [2], and Halstead et al. [3–5]. Transition occurring between these wake-induced events can often occur by other modes. The resulting multimoded transition was observed in studies of both compressor and turbine blade boundary layers by Halstead et al. [3–5].

The high levels of turbulence within wakes shed from upstream blade rows led some researchers to conclude that wake-induced transition would inevitably be of the bypass type, i.e., that turbulent spots would be directly produced in the boundary layer through local interactions with freestream turbulence [1]. Assuming that wake-induced transition occurs in this way, the onset of transition would be expected to correlate with the wake passing trajectory. However, some researchers observed a time lag between the wake trajectory and the onset of transition. Solomon et al. [6] used a quasi-steady method to predict the unsteady onset of transition on a compressor blade surface. The prediction was directly compared to experimental results obtained from hot-film sensors. Significantly better agreement was found if the predicted onset boundary was based on a disturbance speed of $0.7U$. They proposed that the transition process must involve disturbances traveling more slowly than the freestream.

Hughes and Walker [7] later developed a wavelet analysis technique for detecting instability waves in measurements from hot-film sensors. Results from this analysis showed significant Tollmien-Schlichting (T-S) wave packet activity prior to transition. The dominant wave frequencies were compared to linear stability predictions for the unstable T-S wave frequency having the greatest amplification rate [8]. Reasonable agreement was found, considering that pressure gradient alters the frequency range of disturbances receiving amplification and that maximum amplification ratio is a more appropriate parameter. This provided strong evidence for instability processes retaining a significant role in wake-induced transition on compressor blades. Hughes and Walker [7] varied the freestream turbulence level experienced by a blade element by clocking the upstream inlet guide vane (IGV) blade wakes with respect to the stator blade row and observed wave packet activity in both low- and high-turbulence cases.

The effect of turbulence on transition on a flat plate boundary layer under zero pressure gradient was studied by Boiko et al. [9]. They found that the artificially introduced T-S waves not only received amplification but were also involved in nonlinear processes that lead to the formation of turbulent spots.

Many recent studies of flows with high freestream turbulence have shown that bypass transition involves elongated streaky structures that produce alternating regions of low and high velocity in the spanwise direction [10,11]. These structures are thought to result from freestream turbulence interacting with the boundary layer during a receptivity stage. Once initiated the structures grow in size with the boundary layer. Their propagation velocity is typically $0.7U$, which is characteristically different from T-S wave velocity of between $0.4U$ and $0.5U$. Several different modes of instability have been associated with these streaky structures. Present research suggests that the mode responsible for breakdown to turbulence depends largely on flow conditions [10,11]. There is also suggestion that streaky structures may interact with T-S waves resulting in new disturbances [12], or may be accompanied by three-dimensional T-S wave packets [13].

The flow at the leading edge of turbomachinery blades has been found to substantially influence both freestream turbulence and

Contributed by the International Gas Turbine Institute of ASME for publication in the JOURNAL OF TURBOMACHINERY. Manuscript received September 1, 2006; final manuscript received October 5, 2006; published online March 21, 2008. Review conducted by David Wisler. Paper presented at the ASME Turbo Expo 2006: Land, Sea and Air (GT2006), May 8–11, 2006, Barcelona, Spain.

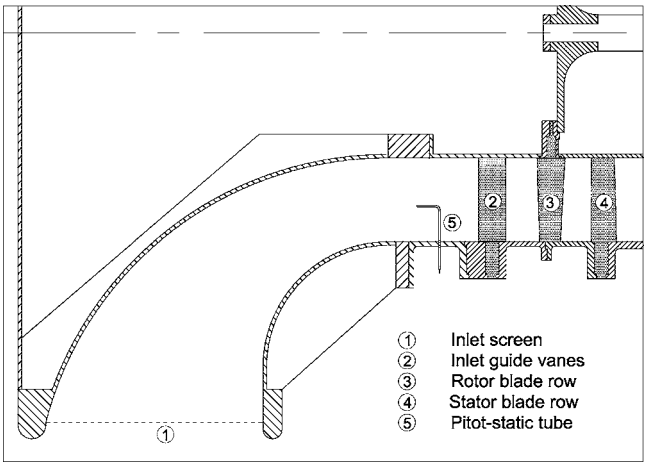

Fig. 1 University of Tasmania research compressor facility

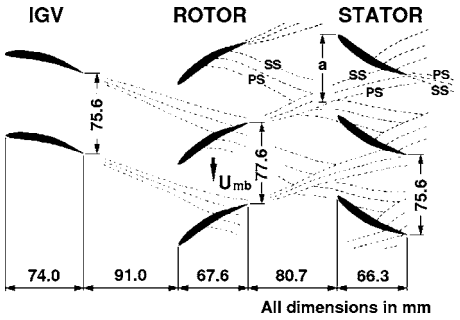

Fig. 2 Cross section of the research compressor showing the midpassage blade row configuration with typical instantaneous wake dispersion pattern

boundary layer development. Hobson et al. [14] observed significant amplification of free-stream turbulence at the leading edge of blades in a two-dimensional compressor cascade. Soranna et al. [15] used particle image velocimetry (PIV) to study an IGV wake as it impinged on a rotor blade leading edge. They found that nonuniform strain rates caused by the rapid distortion of the wake resulted in an anisotropic variation of turbulence properties. They also found that compressive strain along the stagnation streamline enhanced the production of turbulence. Kendall [16] found that leading-edge geometry influenced the development of T-S waves in both terms of frequency and amplitude.

The present study investigates the unsteady transitional flow around a C4 stator blade leading edge. The negative jet effect within the passing wakes of an upstream rotor causes periodic fluctuations in incidence with associated perturbations in the surface pressure distribution. Numerical simulations predict the passing wakes have a destabilizing effect on the suction surface boundary layer. This is supported by comparison with surface hot-film measurements that show the development of instability wave packets.

A variety of transition phenomena at the stator leading edge are observed, depending on the characteristics of incident wake disturbances. The paper will examine their relative frequency and occurrence, and the manner in which they are influenced by axial blade row spacing, compressor loading, and random variations in the amplitude of blade wake disturbances.

Experimental Detail

Research Compressor. The experimental measurements presented in this study were made in the low-speed research compressor at the University of Tasmania (UTAS). The facility comprises of a 1.5-stage axial compressor embedded in an open-loop wind tunnel. Air enters radially through a cylindrical inlet 2.13 m dia and 0.61 m wide. The flow passes through a 6.25:1 contraction, where it is turned through 90 deg to the axial direction. The compressor has three blade rows: inlet guide vanes (IGVs), rotor, and stator, as shown in Figs. 1 and 2. Both IGV and stator blade rows have 38 blades, and the rotor has 37 blades, giving space/chord ratios at midspan of 0.99 and 1.02, respectively. The blades are of British C4 section with a constant chord length of 76.2 mm and an aspect ratio of 3.0. The blade profiles were stacked about a radial axis to achieve free-vortex flow and 50% reaction at midspan position at design flow conditions. The test section annulus is constant in area with hub and casing diameters of 0.69 m and 1.14 m, respectively. Following the test section, the flow passes through a long annular diffuser before discharging through a cylindrical throttle at exit. The throttle opening can be automatically adjusted to achieve the desired flow coefficient. The rotor is directly driven by a 30 kW motor. The speed is controlled by an analog feedback loop with a computer-controlled reference voltage. The variation at a fixed setting is generally less than ± 0.2 rpm. The speed was varied in response to changing atmospheric conditions to maintain constant Reynolds number operation during testing.

Instruments are inserted into the test section through an axial slot in the casing wall. A probe traversing rig allows accurate positioning in axial and radial directions. The IGV and stator blade rows are held in movable rings that allow circumferential traversing (clocking) over two blade pitches via stepper drives. The relative circumferential position of the stationary blade rows is measured by the displacement a shown in Fig. 2. The arrangement also permits relative circumferential traverses of the IGV and stator blade rows to be conducted with circumferentially fixed probes.

Scope of Investigation. Data were obtained for three compressor loadings: high, medium, and low load cases as detailed in Table 1. These load cases, used in previous investigations by Walker and co-workers [17–19], correspond to near stall, design, and maximum flow, respectively. All measurements were performed at midspan position using a constant reference Reynolds number ($\mathrm{Re}_{\mathrm{ref}}=120{,}000$), which corresponds to a typical rotor speed of 500 rpm. The stator inlet Reynolds number (Re_1) for each load case varies with the flow coefficient as shown in Table 1. The test Reynolds numbers are low by comparison to modern controlled diffusion compressor airfoils; but they are, nevertheless, above the critical Reynolds number for C4 blades, due to the characteristically different pressure distributions, which give a roughly linear deceleration over almost the whole suction surface at design conditions.

The surface velocity distributions for the three load cases from Walker et al. [18] are shown in Fig. 3. The measurements were made using two stator blades instrumented with static pressure tappings. Both high and medium load cases show a rapid acceleration to peak suction within $s^*=0.05$ from the leading edge. This is followed by a nearly linear deceleration over the remaining surface. At low loading, the velocity distribution has a more gradual acceleration to peak suction at $s^*=0.3$. The slight discontinuity at $s^*=0.7$ indicates the presence of a separation bubble. Further description of these distributions is provided in publica-

Table 1 Stator operating conditions at midblade height

Loading	ϕ (V_a/U_{mb})	i (deg)	Re_1	Tu_s (%)	Tu_{D_s} (%)
High	0.600	4.1	110000	3.15	5.39
Medium	0.675	1.2	117000	2.27	3.75
Low	0.840	−6.1	130000	2.03	3.07

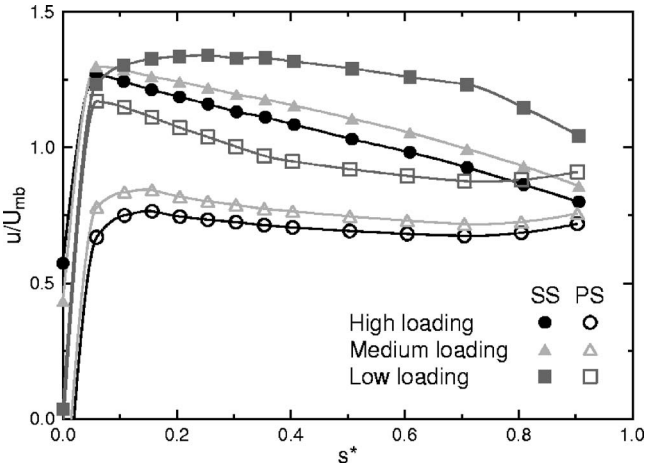

Fig. 3 Measured stator blade surface velocity distributions (from [18])

tions by Walker et al. [17,18].

The turbulence field experienced by the stator blade row was varied by clocking the IGV and stator blade rows. Aligning the IGV wake centers on the stator stagnation streamline ($a/S=0.0$) resulted in a turbulence intensity between rotor wakes of $\sim 2.0-3.0\,\%$ and aligning the wakes in the stator passage ($a/S=0.5$) gave $\sim 0.5-1.5\,\%$.

Measurement Techniques. One stator blade was instrumented with an array of 61 surface mounted hot-film sensors at midspan used in previous studies [18,19]. The hot-film sensors were controlled using TSI-IFA100 constant temperature anemometers. The frequency response of the system was estimated to be better than 30 kHz. All signals were low pass filtered at 20 kHz and sampled at 50 kHz to avoid aliasing. Data acquisition was triggered once per revolution by a precision optical encoder connected to the rotor shaft. At each measurement station a total of five channels were simultaneously acquired 512 times, with each record containing 1024 sample points. Each record spans approximately six rotor passing periods.

Measurements from hot-film sensors were processed to yield quasi-wall shear stress, which is known to be approximately proportional to the wall shear stress, as expressed by

$$\tau_q = \left(\frac{E^2 - E_o^2}{E_o^2}\right)^3 \propto \tau_w \tag{1}$$

This technique was developed by Hodson et al. [20] and has since been used in numerous studies [4,5,7,18,19].

Solomon [21] developed an automated method of interpreting quasi-wall shear stress measurements to identify regions of turbulent, laminar, or relaxing flow. This method was based on intermittency detection using probability density functions and a peak valley counting algorithm. Individual records were then averaged to yield the temporal variation of ensemble-averaged intermittency ($\langle\gamma\rangle$). Walker et al. [18] presented results showing both ensemble-averaged quasi-wall shear stress and ensemble-averaged intermittency, finding the latter a more useful description of the state of the boundary layer.

Unsteady Flow Simulation

The UNSFLO suite of programs developed by Giles and Haimes [22] was designed for studying unsteady flow interactions between adjacent blade rows in compressors and turbines. The flow solver was based on a hybrid approach, solving the thin layer Navier-Stokes equations on an O-mesh around each blade element and the inviscid Euler equations over the remaining flow. This approach neglects the effect of viscous dissipation of wakes convected by the freestream flow. However, Giles and Haimes [22] argue this is compensated to some extent by artificial dissipation in the numerical scheme. The uncertainty associated with dissipation of wakes was not considered to be critical in this study since the simulated wake properties were carefully modeled at the compressor leading edge and the study was primarily concerned with the flow development close to the leading edge.

Model Description. In the present study, UNSFLO was used to model the unsteady flow through a single outlet stator blade row in the UTAS research compressor. The model inlet was located $50\%c$ axially upstream from the blade leading edge, and the outlet was located $50\%c$ axially downstream from the trailing edge. The structured mesh surrounding the O-mesh contained approximately 300×80 quadrilateral elements in the respective axial and circumferential directions. The O-mesh contained 344 elements around the blade surface with 20 elements in the normal direction. Turbulent closure was achieved using the algebraic turbulence model of Cebeci and Smith [23]. The specified locations for transition onset and length were estimated from steady flow solutions using the viscous-inviscid MISES code developed by Drela and Giles [24]. Transition occurred well downstream of the leading edge and was not considered to significantly influence the unsteady laminar flow development in the region of interest around the leading edge.

The incoming rotor wakes were modeled by prescribing a moving velocity defect at the model inlet plane. The wake model parameters were carefully selected to give equal wake width and velocity defect in the plane of the stator leading edge to values predicted using a steady flow model over the same distance: This avoided errors that could be introduced by an unknown level of numerical diffusion acting on the wake as it convected between the model inlet and the stator blade row. This simple approach does not account for viscous wake stretching effects, which may arise due to blade circulation effects in the blade-blade plane, radial variations of whirl velocity, and modification of mixing processes by interaction with wakes from upstream blade rows. However, the model should give a rough approximation of an ensemble-averaged perturbation seen by the stator leading edge corresponding to the low turbulence clocking case with the IGV wake streets aligned in the stator passage ($a/S=0.5$).

The wake model was based on the experimental data and correlation given by Schlichting [25] as

$$\frac{\Delta u}{U} \approx 0.98\left(\frac{C_d d}{x}\right)^{1/2}\left[1-\left(\frac{y}{b}\right)^{3/2}\right]^2 \tag{2}$$

where $\Delta u = U-u$ is the wake velocity defect at a distance y normal to the wake centerline and x downstream from the wake source. The half width of the wake is given by $b \approx 0.567\sqrt{C_d x d}$. The drag coefficient C_d was estimated using a two-dimensional loss prediction using blade chord as the reference length ($d=c$). Schlichting [25] notes Eq. (2) has good agreement with experimental data for $x > 50C_d d$. Fortunately, the relatively large axial spacing between rotor and stator blade rows resulted in rotor wakes traveling a distance of $x=64C_d d$ before reaching the stator leading edge. The wake angle in the rotor relative frame was determined from time-averaged flow angle measurements using a three-hole probe. The wake profile given by Eq. (2) was found to agree well with numerically simulated wakes in a recent study by Wu et al. [26]. The resulting absolute velocity fluctuations are consistent with experimental observations of rotor wake disturbances in the UTAS research compressor reported by Boxhall [27].

The compressor blade configuration used in this investigation had a rotor-stator axial space of $106\%c$, which is relatively large compared to modern gas turbine engines. Gorrell et al. [28] studied the performance of a transonic compressor for three different axial spacings: close ($10\%c$), mid ($26\%c$), and far ($55\%c$). Gorrell et al. [28] reported the mid spacings and far spacings were

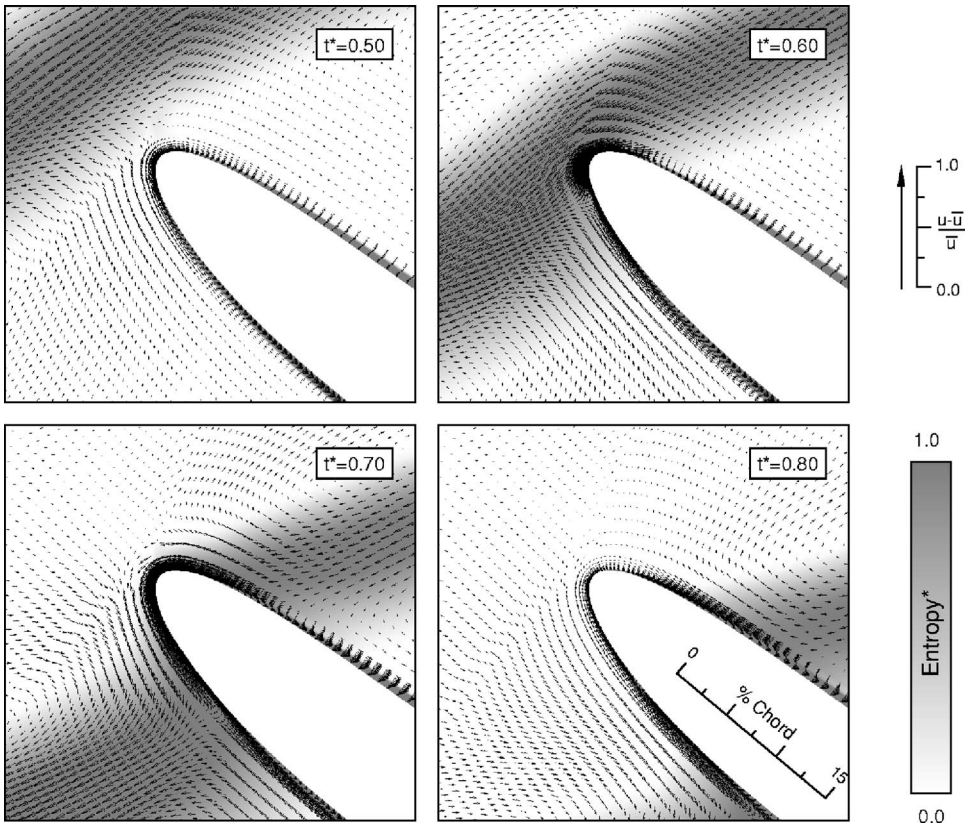

Fig. 4 Unsteady flow field around stator leading edge (UNSFLO). Vectors indicate perturbation from local time-mean velocity. Gray shading indicates fluid entropy relative to the maximum level at the wake center.

representative of current design practice. Lower spacings are desirable to reduce weight and may improve efficiency; however, reducing spacing too much leads to increased noise and vibration.

The large axial spacing used in the current investigation had the advantage of allowing detailed measurement of unsteady flow phenomena such as IGV-rotor wake-wake interactions. It also effectively decoupled the rotor-stator pressure fields. As a result, the unsteady flow experienced by stator blades was essentially dominated by convective disturbances from the upstream rotor wakes rather than pressure field effects. This simplifies the analysis and validation of the numerical model. The numerical predictions will later be applied to investigate the likely unsteady flow behavior at more practical values of axial blade row spacing.

Figure 4 shows the instantaneous UNSFLO solution around the stator leading edge at medium compressor load ($\phi=0.675$) for four different phases of the rotor wake passage. Figure 4 may be interpreted to provide useful information about the unsteady flow behavior. The stator blade is oriented so that the suction surface is the lower surface and the direction of the freestream flow is from top left to bottom right. The vectors show the instantaneous deviation of unsteady flow velocity from the time-mean flow. The rotor wake is clearly indicated by both elevated levels of entropy and the unsteady velocity vectors. An observer moving with the freestream sees a reverse flow within a wake region that is commonly referred to as a "negative jet" (see, for example, [29,30]). The negative jet associated with the rotor wake causes a relative convection of fluid toward the stator pressure surface and away from the stator suction surface.

At $t^*=0.50$, the rotor wake center is $\sim 10\%c$ upstream of the stator leading edge and starts to exhibit distortion from the upstream potential flow field of the blade. At $t^*=0.60$, the local flow deceleration along the stagnation streamline is clearly evident. The leading edge is completely immersed in the wake and the stator experiences a local increase in incidence that is largely confined to the first $5\%c$. Fluid entrainment by the negative jet decreases the suction surface velocity immediately prior to the wake arrival. Conversely, the discharge of the rotor wake jet onto the pressure surface causes an increase in velocity prior to the wake arrival. At $t^*=0.70$, the rotor wake is $\sim 10\%c$ downstream of the stator leading edge. The perturbations at the leading edge are now minimal. The rotor wake has convected further on the suction surface due to the effects of the stator blade circulation. The negative jet causes a reduction in velocity after the wake passage on the pressure surface and an increase in velocity on the suction surface, as shown at $t^*=0.80$. The streamwise extent of contact between the rotor wake fluid and the stator blade is clearly increasing on the pressure surface and decreasing on the suction surface. These phenomena were reported in numerical studies of flow through a compressor stage by Ho and Lakshminarayana [29]. Similar behavior has been observed in turbine cascades, except that the direction of the wake jet is reversed (e.g., [30]). These results show that the wake jet effect causes unsteady flow perturbations on both blade surfaces and entrainment of fluid by the jet causes large-scale vortical flows throughout the blade passage.

Predicted Leading-Edge Boundary Layer Behavior. The UNSFLO solutions were also analyzed to provide information about the temporal variation in boundary layer properties near the stator leading edge. The right-hand side of Fig. 5 shows the temporal variation in dimensionless skin friction factor ($C_f/\overline{C_f}$) at several stations around the leading edge. Here, $\overline{C_f}$ represents a time average over the rotor blade passing period. The fluctuations correlate well with the center of the rotor wake $s^* \sim t^*$ trajectory as indicated by the finely dashed line. The fluctuations are also consistent with the qualitative descriptions made in the previous section. The

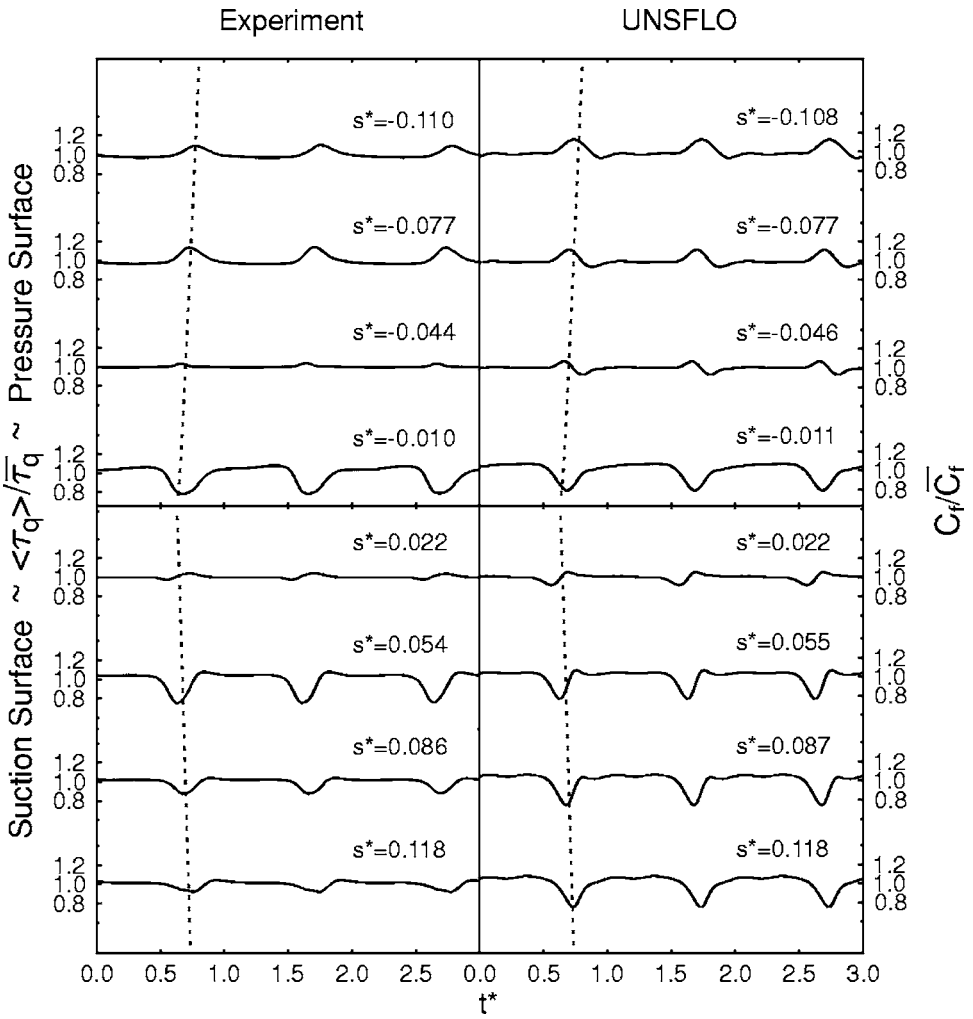

Fig. 5 Left: Temporal variation in dimensionless ensemble-averaged quasi-wall shear stress ($\langle\tau_q\rangle/\overline{\tau_q}$). Right: Temporal variation in dimensionless skin friction factor ($C_f/\overline{C_f}$), medium load case (ϕ=0.675).

left-hand side of Fig. 5 shows experimental hot-film measurements made at similar surface positions to the UNSFLO results. The hot-film measurements have been expressed in terms of dimensionless ensemble-averaged quasi-wall shear stress ($\langle\tau_q\rangle/\overline{\tau_q}$); this nondimensionalization reduces uncertainty from the approximations inherent in Eq. (1). The shear stress perturbations observed in both the experimental and UNSFLO results agree well in terms of shape and character for the region of laminar flow close to the leading edge ($s^* < 0.1$). The agreement starts to deteriorate at $s^* = 0.118$ on the suction surface, where the effects of diffusion from wake-induced turbulence are starting to become evident in the experimental data. Excluding the record at $s^* = -0.01$, which is very close to the time-mean stagnation point location, it is seen that the wake-induced shear stress fluctuations are of opposite phase on the suction and pressure surfaces: There is a decrease in wall shear stress along the wake path on the suction surface and a corresponding increase on the pressure surface near the leading edge.

Figure 6 shows computed values of momentum thickness Reynolds number Re_θ and shape factor $H = \delta^*/\theta$ at several positions near the blade leading edge. On the suction surface, the flow perturbation caused by the passing wakes causes simultaneous increases in both Re_θ and H. This indicates that the boundary layer will be periodically destabilized by the passing wakes as increases in Re_θ and H are both individually destabilizing. Although this effect may not be sufficiently strong to cause local transition, the unsteady flow perturbation will provide suitable conditions for the earlier appearance and enhanced growth of T-S–type wave packets similar to those observed in the unsteady flow flat plate experiments of Obremski and Fejer [31] and the compressor blade studies of Hughes and Walker [7].

The resultant temporal variation of the neutral stability boundary on the stator suction surface, as predicted from the computed fluctuations in Re_θ and H on a quasi-steady assumption is shown on a dimensionless time-space ($t^* \sim s^*$) plot in Fig. 7. For the medium load case, the fluctuation in position of the neutral stability boundary during the rotor wake passage is predicted to be about $6\% s^*$. The results are consistent with observations of wave packet occurrence frequency from the earlier measurements of Hughes and Walker [7] that are reproduced in Fig. 7. The subsequent development of ensemble-averaged turbulent intermittency ($\langle\gamma\rangle$) is indicated by shaded contours.

On the pressure surface, the boundary layer shape factor and momentum thickness Reynolds number are both predicted to decrease during the rotor wake passage. This effect will be stabilizing, however the magnitude of the boundary layer fluctuations on the pressure surface are much less than on the suction surface, and the resulting fluctuations in the neutral stability boundary are less significant.

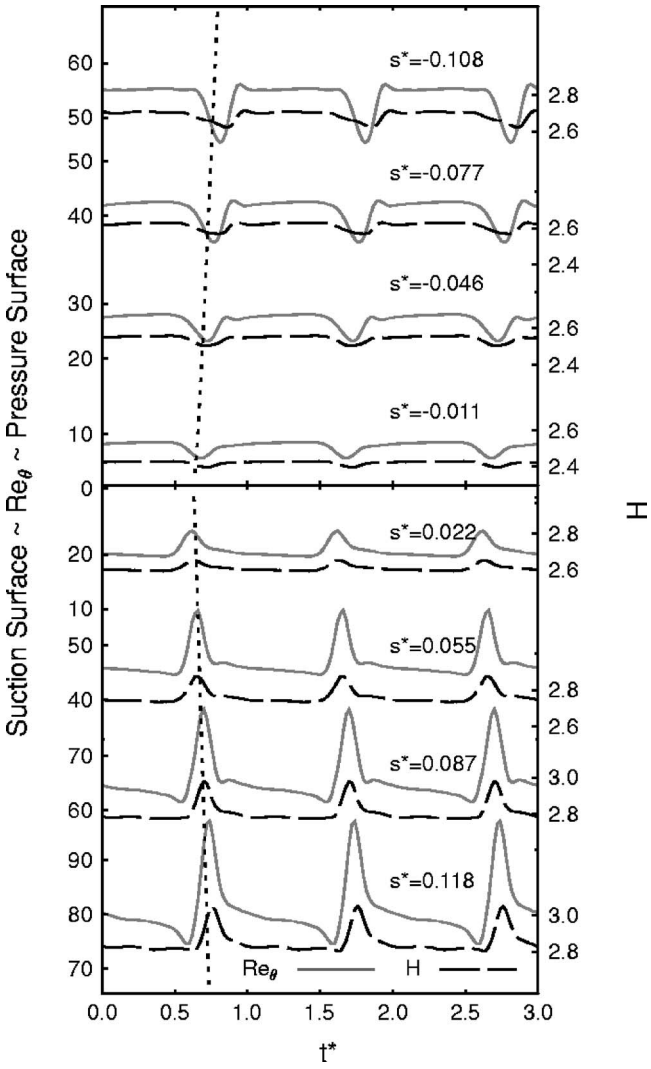

Fig. 6 Temporal variation in momentum thickness Reynolds number and shape factor from UNSFLO computations, medium load case (ϕ=0.675)

Predicted Effect of Varying Rotor-Stator Axial Spacing. Figure 8 compares the predicted temporal variation in dimensionless skin friction factor for axial spacings of 106%c and 41%c. These are respectively the large axial gap (LAG) and short axial gap (SAG) cases reported by Hughes [32]. The SAG case is more typical of blade row spacing in a practical machine. This decrease in axial gap increases the relative velocity defect of the rotor wake at the stator leading edge from $\Delta u/U$=0.13 to $\Delta u/U$=0.21. The change in amplitude of shear stress fluctuations near the stator leading edge in response to the rotor wake passing is comparatively small. The hot-film observations presented in Fig. 9 show the variability of individual wake signatures resulting from random turbulent fluctuations within the wakes to be relatively much greater. In the high freestream turbulence data presented in Fig. 10, the fluctuations in shear stress produced by freestream turbulence are seen to approach the magnitude of those resulting from rotor wake disturbances. The fact that the freestream turbulence is less effective in promoting transition than the wake disturbances is suggestive of a receptivity issue related to turbulence scale.

Transitional Flow Behavior

Further information about the flow development around the leading edge is provided by inspection of individual hot-film traces. A collection of typical hot-film traces for the three loading cases at the low turbulence clocking position (a/S=0.5) is shown in Fig. 9. This corresponds to the IGV wake street passing through the stator passage, so that the stator blades are subjected to relatively pure rotor wake disturbances with intervening regions of low turbulence flow. The traces have been individually scaled to allow disturbance signatures to be followed along the blade surface. The numbering enclosed in brackets on the right-hand side indicates the data set number at each hot-film sensor location. Traces that share equal numbering were acquired simultaneously. This is particularly useful in following the evolution of disturbances along the surface. Particle trajectories at speeds of 1.0U, 0.7U, and 0.5U have been overlaid for reference. In all load cases, the traces show considerable variability in both the amplitude and nature of wake-induced flow events.

The suction surface traces at medium and high loading show typical T-S wave packets as shown by event "A1." These types of wave packets are similar to those observed by Hughes and Walker [7] and in other studies [31,33]. The convection speed of around 0.5U provides further confirmation that these are essentially T-S instability wave phenomena.

The T-S wave packets appear near the leading edge at instants coinciding with a local decrease in shear stress imposed by the wake jet interaction. Recent numerical studies by Zaki and Durbin [34] have shown that inviscid (Kelvin-Helmholtz) instabilities are responsible for the final turbulent breakdown stage of bypass transition. However, these instability waves occur near the outer edge of the boundary layer and have a characteristically higher convection velocity: Zaki and Durbin [34] suggest a speed of about $\frac{2}{3}U$ for this secondary instability.

It is not clear if wave packets exist at the film sensor location of s^*=0.022, since their frequency would likely exceed the cutoff frequency of the low-pass filtering; however, the strong acceleration around the leading edge ($s^*<0.05$) would be expected to stabilize the boundary layer in this region. Transition resulting from this type of event only occurs after a relatively short period of wave amplification. The particular wave packet, indicated by A1 in Fig. 9, eventually breaks down into a turbulent spot at s^*=0.44. Similar behavior in the case of a more turbulent freestream, when the stator blade is immersed in the IGV wake street (a/S=0.0), is exhibited by event A2 in Fig. 10.

In the high load case, the traces show much greater periodicity in wake-induced transition. Breakdown occurs much more rapidly owing to the stronger adverse pressure gradient experienced by the flow.

Significantly different behavior is exhibited by events B1 and B2 shown in Fig. 9 for the medium and low load cases, respectively. Here, the significant increase in shear stress characteristic of a turbulent spot appears quite quickly, with relatively little prior wave packet signature. The convection speed of these events is close to 0.7U. Although characteristic of a turbulent spot, this propagation velocity is also consistent with the "turbulent puff" events and the inviscid secondary instabilities in bypass transition reported by Zaki and Durbin [34]. These are packets of streamwise vortices (Klebanoff modes) induced principally by transverse and normal freestream velocity fluctuations. Boundary layer disturbances of this type were reported by Westin et al. [35] in response to isolated vortical disturbances introduced just upstream of a leading edge. A comprehensive description of instability phenomena and receptivity issues can be found in Boiko et al. [13]. It is possible for various types of instability to occur simultaneously and undergo complex interactions.

Event C, observed on the stator suction surface at low load, appears similar to event B1, in that it also convects with a speed of about 0.7U. However, rapid transition does not occur, and the disturbance appears to be damped by the accelerating flow situation.

Regardless of the type of event preceding transition, it is clear from both the individual film records of Figs. 9 and 10 and the ensemble-averaged intermittency plots of Fig. 7 that turbulent

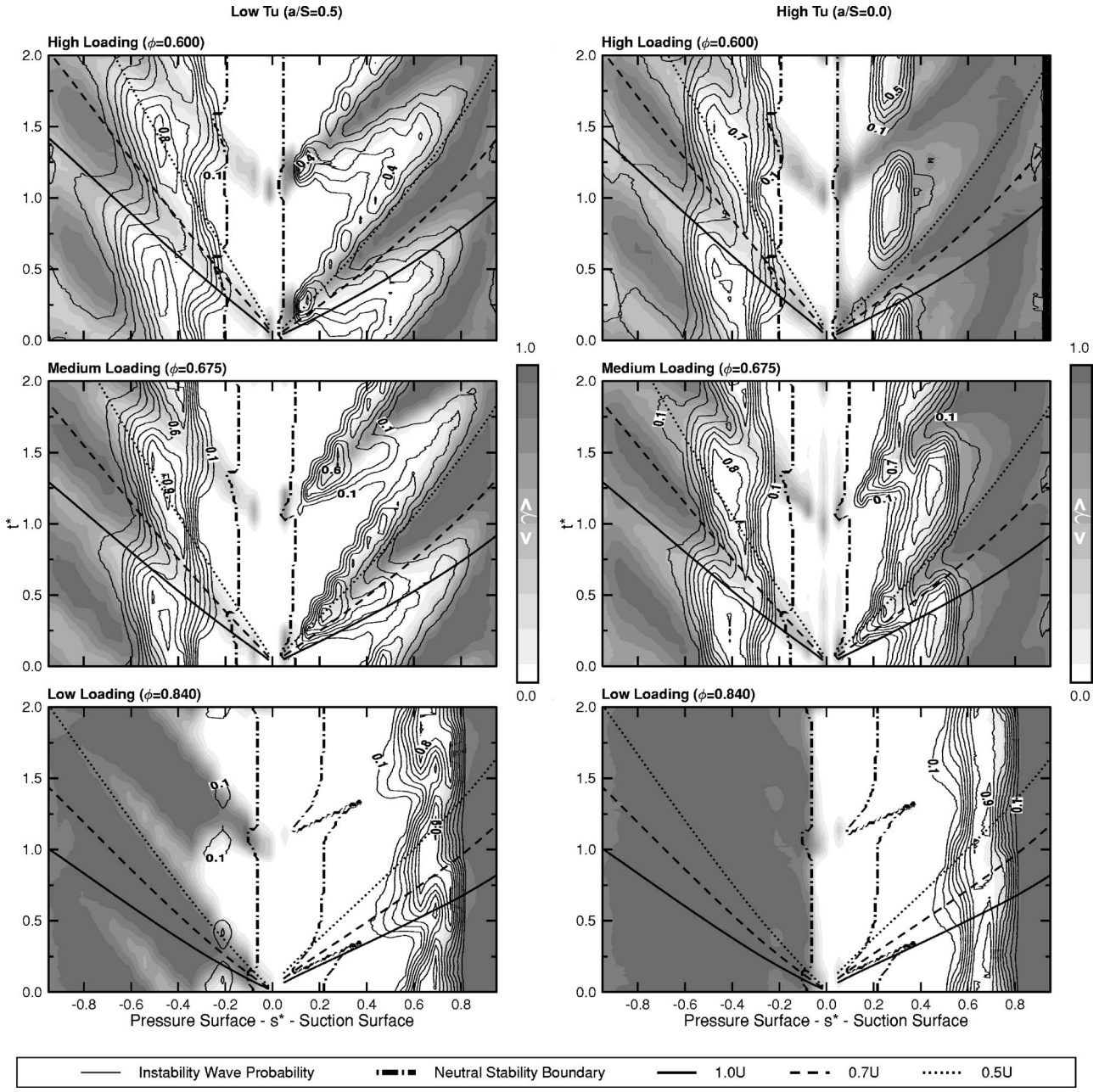

Fig. 7 Stator surface ensemble-averaged intermittency $\langle\gamma\rangle$ (shaded contours) and probability of instability wave occurrence (line contours) with superimposed particle trajectories at different proportions of local freestream velocity (adapted from [7]) and added neutral stability boundary predicted by the present study

breakdown on the stator suction surface significantly lags the rotor wake passage in the freestream. Hence, the simplistic engineering model of bypass transition occurring almost instantaneously in response to disturbances from a turbulent freestream cannot possibly apply. The process of boundary layer transition requires finite intervals of time and distance for its completion. It commences with a region of receptivity to external disturbances that is followed by internal amplification and the appearance of secondary instabilities leading eventually to the high-frequency fluctuation characteristic of a turbulent spot. As seen from Fig. 7, the wake-induced turbulent strips on the stator suction surface generally lie between particle trajectories of $0.5U$ and $0.7U$ originating at the stator leading edge. This strongly suggests that the region close to the leading edge is the most significant receptivity site in this case.

Factors contributing to the importance of the leading edge region as the most significant receptivity site on the suction surface of a compressor blade are as follows:

(a) negative jet effect, which transports turbulent wake fluid from the adjacent upstream blade row away from the surface
(b) destabilizing effect of the upstream blade wake convecting over the blade leading edge
(c) decelerating mean flow (for higher loading conditions), which will promote disturbance amplification within the boundary layer

The flow behavior on the stator pressure surface is characteristically different from the suction surface. Here, the negative jet

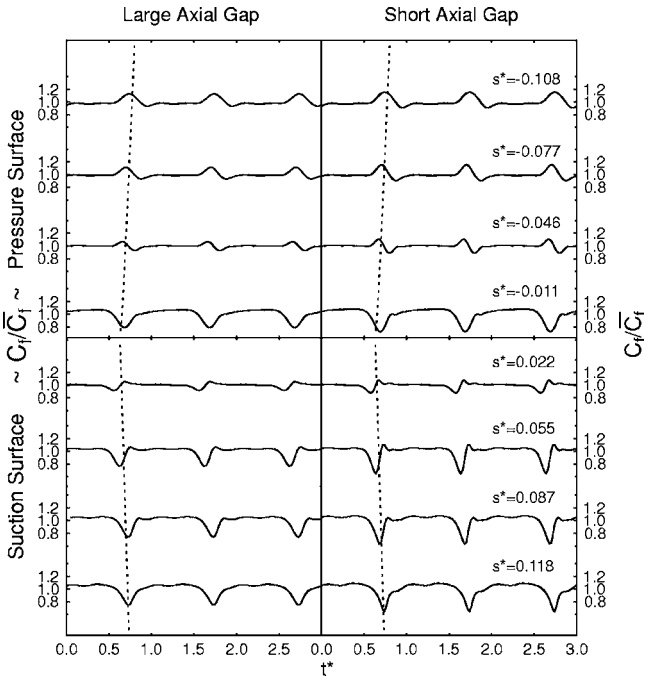

Fig. 8 Predicted temporal variation in shape factor for LAG and SAG cases, medium load case (ϕ=0.675)

causes a discharge of rotor wake fluid onto the blade surface. Perturbations from the wake jet, convecting at about $1.0U$, are clearly evident for the low freestream turbulence case in Fig. 9. At high and medium load, transition does not generally commence until around $s^*=-0.5$, probably due to the boundary layer Reynolds number being too low to sustain turbulent flow ($\mathrm{Re}_\theta \approx 180$ at $s^*=-0.5$). However, a couple of isolated turbulent breakdown events around $s^*=-0.4$ can be seen in these cases. At the low load condition, the large negative incidence produces sufficient destabilization for transition to occur close to the leading edge in the wake path. Outside the wake path, the flow separates due to the high adverse pressure gradient and a turbulent reattachment is observed to develop around $s^*=-0.3$.

For the high turbulence case (a/S=0.0), the hot-film traces on the stator pressure surface are much more confused. They are generally characterized by the superposition of low-frequency fluctuations from damped turbulent disturbances in the freestream. The wake-induced flow features observed in the low turbulence case are still evident, with the exception of the low loading case where the freestream turbulence shortens the separation bubble and causes almost continuous turbulent reattachment around $s^*=-0.1$.

Wake-induced transition phenomena on turbine blades are likely to differ from the compressor blade behavior in several respects. Because of the opposite direction of the wake jet from an adjacent upstream blade row, the leading-edge perturbations produced by wake chopping will be stabilizing on the suction surface and destabilizing on the pressure surface. Turbulent wake fluid will discharge onto the suction surface, rather than the pressure surface as in the compressor blade case. The higher blade loadings in a turbine and the resulting increased distortion (bowing) of the wake in the blade passage, will cause the turbulent wake fluid to be in contact with a relatively larger region of the surface on a turbine blade. The flow will be generally more stable near a turbine blade leading edge due to the acceleration of the bulk flow. This makes the appearance of turbulent flow arising from leading-edge unsteadiness less likely; turbulent patches near the leading edge, if they occur, may be subsequently relaminarized by the strong flow acceleration. The principal receptivity site on a turbine blade suction surface is likely to be near the pressure minimum, which will be remote from leading-edge perturbations. Dovgal and Kozlov [36] reached this conclusion in respect of transition on an airfoil suction surface resulting from acoustic excitation.

Conclusions

Wake-induced laminar-turbulent transition has been studied at the leading edge of a C4-section compressor stator blade in a 1.5-stage axial compressor. Numerical solutions from UNSFLO, a quasi-three-dimensional viscous-inviscid flow solver, were veri-

Fig. 9 Typical raw quasi-wall shear stress traces, IGV wakes in stator passage (a/S=0.5)

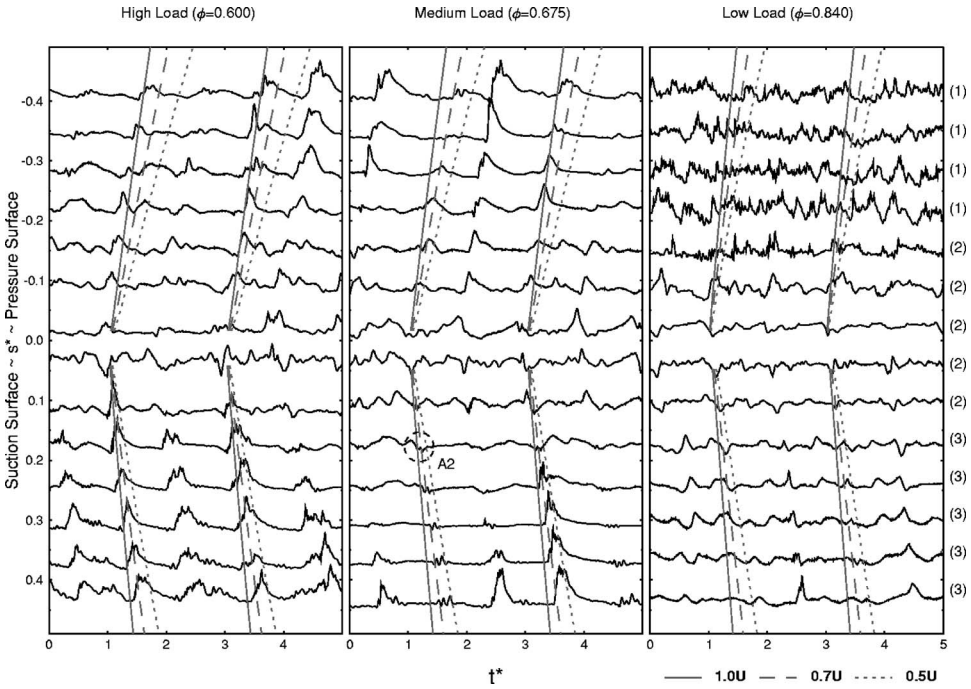

Fig. 10 Typical raw quasi-wall shear stress traces, IGV wakes on stator blade row (a/S=0.0)

fied by comparison with surface hot-film observations. These solutions proved a useful aid to interpretation of the complex shear stress perturbations produced by wake chopping.

The passage of a rotor wake, with its associated negative jet, over the stator leading edge was observed to have a destabilizing effect on the suction surface boundary layer. This leads to transition closer to the stator leading edge than would have occurred under steady flow conditions. The strength of this phenomenon is influenced by the rotor-stator axial gap and the variability of individual rotor wake disturbances.

A variety of transition phenomena were observed near the leading edge in the wake path. Wave packets characteristic of Tollmien-Schlichting waves were observed to amplify and break down into turbulent spots. Disturbances characteristic of the streaky structures occurring in bypass transition were also seen. Examination of suction surface disturbance and wake-induced transitional strip trajectories points to the leading edge as the principal receptivity site for suction surface transition phenomena at design loading conditions. This contrasts markedly with the pressure surface behavior, where transition at design conditions occurs remote from leading-edge flow perturbations associated with wake chopping. Here, the local receptivity of the boundary layer to the wake passing disturbance and turbulent wake fluid discharging onto the blade surface will likely be of greater importance.

The magnitude of leading-edge flow perturbations associated with wake chopping should decrease with increasing axial gap between adjacent blade rows. But this effect should be relatively minor over the range of axial blade row spacings used in practical machines. The variability of wake velocity defect due to large-scale turbulent motion within incident wakes appears of much greater significance.

Wake chopping is likely to have a much smaller influence on unsteady wake-induced transition on the suction surface of turbine blades, due to stabilizing effects of the generally accelerating flow moving the transition region away from the leading edge. This suggests that the design procedures so successfully used to improve turbine blade performance through manipulation of unsteady transition phenomena may not be optimal for compressor blades.

Acknowledgment

The financial support of Rolls-Royce plc is gratefully acknowledged.

Nomenclature

- a = circumferential distance of stator blade leading edge from center of IGV wake street at midspan
- c = blade chord
- E = anemometer output voltage
- E_0 = anemometer output voltage at zero flow
- H = boundary layer shape factor = δ^*/θ
- i = blade incidence
- PS = pressure surface
- Re = compressor inlet Reynolds number=$V_a(c/\nu)$
- $\mathrm{Re}_{\mathrm{ref}}$ = reference Reynolds number=$U_{mb}(c/\nu)$
- Re_1 = stator inlet Reynolds number=$V_1(c/\nu)$
- s = surface length from leading edge
- $s_{\max}$ = surface length from leading edge to trailing edge
- s^* = dimensionless surface length=$s/s_{\max}$
- S = blade pitch
- SS = suction surface
- t = time
- t^* = dimensionless time=t/T
- T = rotor blade passing period
- Tu_D = total disturbance level
- Tu = random disturbance level (turbulence)
- u = streamwise velocity
- U = local free-stream velocity
- U_{mb} = midspan rotor blade speed
- V_a = mean axial velocity at compressor inlet
- V_1 = velocity at stator inlet
- δ^* = boundary layer displacement thickness
- γ = turbulent intermittency
- ν = kinematic viscosity

ϕ = flow coefficient $= V_a / U_{mb}$
τ_q = quasi-wall shear stress
τ_w = wall shear stress
θ = boundary layer momentum thickness

Superscripts, Subscripts, etc.

$\bar{()}$ = time-mean
$\langle\rangle$ = ensemble (phase-lock) average
$()^*$ = dimensionless quantity
$()_s$ = pitchwise average

References

[1] Mayle, R. E., 1991, "The Role of Laminar-Turbulent Transition in Gas Turbine Engines," ASME J. Turbomach., **113**, pp. 509–537.
[2] Walker, G. J., 1993, "The Role of Laminar-Turbulent Transition in Gas Turbine Engines: A Discussion," ASME J. Turbomach., **117**, pp. 207–217.
[3] Halstead, D. E., Wisler, D. C., Okiishi, T. H., Walker, G. J., Hodson, H. P., and Shin, H., 1997, "Boundary Layer Development in Axial Compressors and Turbines—Part I: Composite Picture," ASME J. Turbomach., **119**(1), pp. 114–127.
[4] Halstead, D. E., Wisler, D. C., Okiishi, T. H., Walker, G. J., Hodson, H. P., and Shin, H., 1997, "Boundary Layer Development in Axial Compressors and Turbines—Part II: Compressors," ASME J. Turbomach., **119**(3), pp. 426–444.
[5] Halstead, D. E., Wisler, D. C., Okiishi, T. H., Walker, G. J., Hodson, H. P., and Shin, H., 1997, "Boundary Layer Development in Axial Compressors and Turbines—Part III: LP Turbines," ASME J. Turbomach., **119**(2), pp. 234–246.
[6] Solomon, W. J., Walker, G. J., and Hughes, J. D., 1999, "Periodic Transition on an Axial Compressor Stator: Incidence and Clocking Effects—Part II: Transition Onset Predictions," ASME J. Turbomach., **121**, pp. 408–415.
[7] Hughes, J. D., and Walker, G. J., 2001, "Natural Transtion Phenomena on an Axial Compressor Blade," ASME J. Turbomach., **123**, pp. 392–401.
[8] Walker, G. J., 1989, "Transitional Flow on Axial Turbomachine Blading," AIAA J., **27**(5), pp. 595–602.
[9] Boiko, A. V., Westin, K. J. A., Klingmann, B. G. B., Kozlov, V. V., and Alfredsson, P. H., 1994, "Experiments in a Boundary Layer Subjected to Free Stream Turbulence—Part II: The Role of TS-Waves in the Transition Process," J. Fluid Mech., **281**, pp. 219–245.
[10] Asai, M., Minagawa, M., and Nishioka, M., 2002, "The Instability and Breakdown of a Near-Wall Low-Speed Streak," J. Fluid Mech., **455**, pp. 289–314.
[11] Brandt, L., Schlatter, P., and Henningson, D. S., 2004, "Transition in Boundary Layers Subject to Free-Stream Turbulence," J. Fluid Mech., **517**, pp. 167–198.
[12] Bakchinov, A. A., Westin, K. J. A., Kozlov, V. V., and Alfredsson, P. H., 1998, "Experiments on Localized Disturbances in a Flat Plate Boundary Layer—Part II: Interaction Between Localized Disturbances and TS-Waves," Eur. Phys. J. B, **17**(6), pp. 847–873.
[13] Boiko, A. V., Grek, G. R., Dovgal, A. V., and Kozlov, V. V., 2002, *The Origin of Turbulence in Near-Wall Flows*, Springer, New York.
[14] Hobson, G. V., Wakefield, B. E., and Roberts, W. B., 1999, "Turbulence Amplification With Incidence at the Leading Edge of a Compressor Cascade," Int. J. Rotating Mach., **5**(2), pp. 89–98.
[15] Soranna, F., Chow, Y., Uzol, O., and Katz, J., 2006, "The Effect of IGV Wake Impingement on the Flow Structure and Turbulence Around a Rotor Blade," ASME J. Turbomach., **128**(1), pp. 82–95.
[16] Kendall, J. M., 1991, "Studies on Laminar Boundary-Layer Receptivity to Freestream Turbulence Near a Leading Edge," ASME Fluids Engineering Division (FED), ASME, New York, Vol. 114, pp. 23–30.
[17] Walker, G. J., Hughes, J. D., Köhler, I., and Solomon, W. J., 1998, "The Influence of Wake-Wake Interactions on Loss Fluctuations of a Downstream Axial Compressor Blade Row," ASME J. Turbomach., **120**, pp. 695–704.
[18] Walker, G. J., Hughes, J. D., and Solomon, W. J., 1999, "Periodic Transition on an Axial Compressor Stator: Incidence and Clocking Effects—Part I: Experimental Data," ASME J. Turbomach., **121**, pp. 398–407.
[19] Henderson, A. D., Walker, G. J., and Hughes, J. D., 2006, "Influence of Turbulence on Wake Dispersion and Blade Row Interaction in an Axial Compressor," ASME J. Turbomach., **128**(1), pp. 150–157.
[20] Hodson, H. P., Huntsman, I., and Steele, A. B., 1994, "An Investigation of Boundary Layer Development in a Multistage LP Turbine," ASME J. Turbomach., **116**(3), pp. 375–383.
[21] Solomon, W. J., 1996, "Unsteady Boundary Layer Transition on Axial Compressor Blades," Ph.D. thesis, University of Tasmania, Australia.
[22] Giles, M., and Haimes, R., 1993, "Validation of a Numerical Method for Unsteady Flow Calculations," ASME J. Turbomach., **115**, pp. 110–117.
[23] Cebeci, T., and Smith, A. M. O., 1974, *Analysis of Turbulent Boundary Layers*, Academic Press, New York.
[24] Drela, M., and Giles, M. B., 1987, "Viscous-Inviscid Analysis of Transonic and Low Reynolds Number Airfoils," AIAA J., **25**(10), pp. 1347–1355.
[25] Schlichting, H., 1968, *Boundary-Layer Theory*, 6th ed. McGraw-Hill, New York.
[26] Wu, X., Jacobs, R. G., Hunt, J. C. R., and Durbin, P. A., 1999, "Simulations of Boundary Layer Transition Induced by Periodically Passing Wakes," J. Fluid Mech., **398**, pp. 109–153.
[27] Boxhall, P. J., 1971, "Unsteady Flow Phenomena in an Axial-Flow Compressor," M.Eng.Sc. thesis, University of Tasmania, Australia.
[28] Gorrell, S. E., Okiishi, T. H., and Copenhaver, W. W., 2003, "Stator-Rotor Interactions in a Transonic Compressor—Part I: Effect of Blade-Row Spacing on Performance," ASME J. Turbomach., **125**(2), pp. 328–335.
[29] Ho, Y. H., and Lakshminarayana, B., 1995, "Computation of Unsteady Viscous Flow Through Turbomachinery Blade Row Due to Upstream Rotor Wakes," ASME J. Turbomach., **117**, pp. 541–552.
[30] Stieger, R. D., and Hodson, H. P., 2005, "The Unsteady Development of a Turbulent Wake Through a Downstream Low-Pressure Turbine Blade Passage," ASME J. Turbomach., **127**(2), pp. 388–394.
[31] Obremski, H. J., and Fejer, A. A., 1967, "Transition in Oscillating Boundary Layer Flows," J. Fluid Mech., **29**(1), pp. 93–111.
[32] Hughes, J. D., 2001, "Unsteady Aerodynamics in an Axial Flow Compressor," Ph.D. thesis, University of Tasmania, Australia.
[33] Cohen, J., Breuer, K. S., and Haritondis, J. H., 1991, "On the Evolution of a Wave Packet in a Laminar Boundary Layer," J. Fluid Mech., **225**, pp. 575–606.
[34] Zaki, T. A., and Durbin, P. A., 2005, "Mode Interaction and the Bypass Route to Transition," J. Fluid Mech., **531**, pp. 85–111.
[35] Westin, K. J. A., Bakchinov, A. A., Kozlov, V. V., and Alfredsson, P. H., 1998, "Experiments on Localized Disturbances in a Flat Plate Boundary Layer—Part I: The Receptivity and Evolution of a Localized Free Stream Disturbance," Eur. Phys. J. B, **17**(6), pp. 823–846.
[36] Dovgal, A. V., and Kozlov, V. V., 1983, "Influence of Acoustic Perturbations on the Flow Structure in a Boundary Layer With Adverse Pressure Gradient," Fluid Dyn., **18**(2), pp. 205–209.

Separated Flow Transition on an LP Turbine Blade With Pulsed Flow Control

Jeffrey P. Bons
Daniel Reimann
Matthew Bloxham

Department of Mechanical Engineering,
Brigham Young University,
Provo, UT 84602

Flow measurements were made on a highly loaded low pressure turbine blade in a low-speed linear cascade facility. The blade has a design Zweifel coefficient of 1.34 with a peak pressure coefficient near 47% axial chord (midloaded). Flow and surface pressure data were taken for $\mathrm{Re}_c = 20{,}000$ *with 3% inlet freestream turbulence. For these operating conditions, a large separation bubble forms over the downstream portion of the blade suction surface, extending from 59% to 86% axial chord. Single-element hot-film measurements were acquired to clearly identify the role of boundary layer transition in this separated region. Higher-order turbulence statistics were used to identify transition and separation zones. Similar measurements were also made in the presence of unsteady forcing using pulsed vortex generator jets just upstream of the separation bubble (50%* c_x*). Measurements provide a comprehensive picture of the interaction of boundary layer transition and separation in this unsteady environment. Similarities between pulsed flow control and unsteady wake motion are highlighted.* [DOI: 10.1115/1.2751149]

Introduction

A number of recent studies, summarized by Rivir et al. [1], have shown considerable promise in the arena of low pressure turbine (LPT) separation reduction using embedded flow control devices. LPT separation is a loss-producing phenomenon that is primarily associated with low Reynolds number turbine operation [2–4]. Rivir et al. reviewed progress with a wide variety of flow control devices including passive surface protrusions (delta wings) and recesses (dimples), MEMS actuators, heated wires, electrostatic discharge devices, and vortex generating jets (VGJs). Of the active control devices listed, VGJs are perhaps the most straightforward to implement in an engine since the manufacturing technology required is virtually identical to that currently used for film cooling.

Experiments with vortex generator jets (VGJs), conducted in several low-speed turbine cascade facilities with the same Pack B LPT blade profile [5–8] have demonstrated substantial reductions in separation losses at low (separating) Reynolds numbers (25–65% depending on flow conditions). VGJs are typically configured with a low pitch angle (30–45 deg) and aggressive skew angle (45–90 deg) to the near wall flow direction. Here, pitch angle is defined as the angle the jet makes with the local surface, and skew angle is defined as the angle of the projection of the jet on the surface, relative to the local freestream direction. When operated in the steady mode, it has been shown that the VGJ creates a vortex pair with one very strong leg accompanied by a weak leg of opposite sign [8,9]. The result is a single, dominant, slowly decaying streamwise vortex that energizes the separating boundary layer by effectively bringing high momentum freestream fluid down near the wall. Experimental results have shown steady VGJs to be extremely robust with effective operation over a wide range of flow conditions (Reynolds number and freestream turbulence) and control implementations (chordwise location and blowing ratio) [2,5].

Despite the success of steady VGJ flow control, the real promise for VGJ integration into a gas turbine engine is in the unsteady or pulsed mode. Laboratory tests indicate that the mass flow requirements of VGJs can be reduced to an almost negligible fraction ($<0.01\%$) of the core mass flow through nonsteady forcing [5]. Unlike flow control on external airfoils [10], pulsed VGJs implemented in a LPT cascade exhibit effectiveness for a wide range (three orders of magnitude) of frequency [5]. This finding bodes well for eventual VGJ integration in turbomachinery designs since embedded airfoils are already subject to a highly unsteady environment due to upstream wakes and secondary flows. It may be possible to synchronize VGJ actuation with the rotor passing frequency such that the jet is phased to interact synergistically with the convected wake disturbance.

Several researchers have shown evidence of a "calmed zone" of well-attached laminar flow following the unsteady interaction of a wake disturbance with a separation bubble on a LPT airfoil suction surface [11,12]. Typically, this period of well-behaved flow persists for 20–40% of the wake passing period. It is followed by a gradual return to separated laminar flow prior to the arrival of the next wake disturbance. One possible application of pulsed flow control would be to actuate near the end of the calmed zone, thus preventing the return to a separated state. To optimize the timing of pulsed flow control in this manner, the nature of the unsteady interaction of VGJs and the separated boundary layer must be better understood. Unlike in steady control mode, the flow mechanism responsible for pulsed VGJ separation control effectiveness is yet unclear. An initial study with varying the jet duty cycle from 50% to 1% suggested that the fluid dynamics associated with the starting and ending of the jet are the most critical [5]. It was assumed that these transitions would be punctuated with vortical motions that would perform a comparable role to the streamwise vortices associated with steady VGJs. However, computational studies by Postl et al. [13] showed that while pulsed VGJs generated some freestream entrainment through vortex interaction, the primary mechanism for boundary layer control was turbulent transition. They noted the presence of large amplitude 2D (spanwise) disturbances downstream of the VGJs that accelerated boundary layer transition, and thus reattachment. Subsequent work by Postl et al. [14] suggested that these 2D waves were more efficiently induced by normal jet blowing (versus skewed injection). This finding was corroborated by the recent experimental measurements of Hansen and Bons [9] that showed that normal and skewed pulsed jets have approximately the same

Contributed by the International Gas Turbine Institute of ASME for publication in the JOURNAL OF TURBOMACHINERY. Manuscript received September 1, 2006; final manuscript received November 14, 2006; published online March 21, 2008. Review conducted by David Wisler. Paper presented at the ASME Turbo Expo 2006: Land, Sea and Air (GT2006), Barcelona, Spain, May 8–11, 2006, Paper No. GT2006-90754.

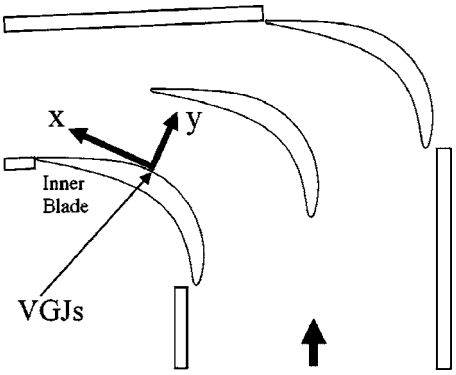

Fig. 1 Linear cascade facility (not actual L1M profiles)

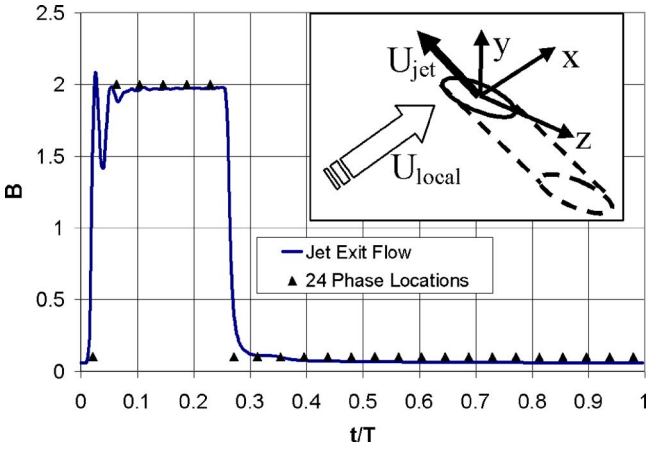

Fig. 2 VGJ exit velocity profile (inset of jet configuration)

effect on a separation bubble in a 2D diffusing flow. Following this, Bons et al. [15] showed that in a LPT cascade, the separation bubble responds in a spanwise uniform (2D) manner to VGJ interaction, with only scant evidence of the vortical disturbance associated with steady control.

The present study is a follow-on to the work of Bons et al. [15], with the objective of providing more details of the fluid interaction of VGJs with the separation bubble. The role of boundary layer transition was specifically investigated since it must be thoroughly documented and understood in order to someday be able to model VGJs in a blade design code. Accurate models are seen as a necessary precursor to the eventual adaptation of flow control in the turbine design system. The present study is conducted without the presence of unsteady wakes in order to focus on the jet interaction exclusively. It is expected that these results will help to guide future experimental and computational work with pulsed VGJs and wakes on LPT blades.

Experimental Configuration

A detailed description of the cascade facility used for this study is found in Eldredge and Bons [8]. The open-loop wind tunnel is driven by a centrifugal blower and produces conditioned exit flow with $\pm 2\%$ velocity uniformity and 0.3% freestream turbulence at the cascade inlet. For the present study, this level of background freestream turbulence was augmented to 3% with a passive square-bar grid located 5.2 axial chords (c_x) upstream of the cascade. At the cascade inlet plane, the freestream turbulence was fairly isotropic with an integral lengthscale of 2 cm. Acceleration in the blade passage causes the turbulence level to decay to below 2% at the exit, while the integral lengthscale increases to nearly 3 cm at the cascade exit plane.

The VGJ-equipped blade is located at the inner corner of the two-passage cascade so that the suction surface will experience uncovered turning as it would in a full linear cascade (note: Fig. 1 is shown with Pack B blading. The full blade shape is not available for public release at this time, but coordinates can be made available to USAF contractors.) Fourteen 0.64 mm diameter pressure taps were drilled into the suction surface of the inner blade and seven on the pressure surface of the middle blade. These static pressure taps are used for verification of the c_p distribution in the controlled passage. All c_p and velocity data were taken over the center 0.15 m of blade span, where the flow was confirmed to be approximately two-dimensional. The inlet bleeds and exit tailboards of the cascade can be adjusted to produce nominally periodic flow through the two passages. Eldredge and Bons [8] showed that proper adjustment of these tunnel walls allowed the two-passage cascade to closely match both the c_p distribution and the boundary layer behavior of a larger eight-blade Pack B linear cascade used by Sondergaard et al. [2].

The blade profile is the midloaded L1M turbine blade designed using the recently implemented design and analysis system for turbine airfoils at the Air Force Research Laboratory by Clark [15,16]. The blades have an axial chord (c_x) of 0.22 m and a span of 0.38 m. The cascade solidity (axial chord/spacing) is 0.99. The design Zweifel load coefficient for the L1M was 1.34. The midloaded design (peak c_p at 47% c_x) does not experience the massive (nonreattaching) separation that plagues the aftloaded Pack B at low Re. Instead, the L1M has a closed separation bubble at least down to $\mathrm{Re}_c = 20{,}000$. The inside corner blade in the cascade (see Fig. 1) was also configured with a single row of 2.3 mm diameter VGJ holes, spaced ten hole diameters apart and located at 50% c_x. The holes were drilled with a 30 deg pitch angle to the blade surface and injected at a 90 deg skew angle from the streamwise direction. The pitch angle lies in the y-z plane and the skew angle lies in the x-z plane (see Fig. 2 inset). A pressurized cavity in the center of the blade provided for both steady and pulsed jet operation over a range of blowing ratios.

The primary tool for flow diagnostics was a single element hot-film anemometer mounted to a 3-axis traverse located atop the cascade. The hot-film element has a diameter of 50.8 μm, a length of 1.02 mm, and a maximum frequency response of roughly 200 kHz. The traverse incorporated a blade-following device that allowed data to be taken at constant wall distance, spanning most of the blade suction surface (from 30% c_x to the blade trailing edge). The follower was used to obtain 15 streamwise profiles with wall distances approximately evenly spaced from 1.5 mm to 20 mm. The uncertainty in velocity was $\pm 1.5\%$ and the follower position was accurate to within ± 0.2 mm. Each profile consisted of 61 streamwise measurement locations, with a spacing ranging between 2.7 mm and 6.9 mm, the smaller steps concentrated in the region of the separation bubble. Flow data were acquired for both no control ($B=0$) and pulsed control cases. For pulsed actuation, the high pressure air line feeding the VGJ plenum was connected to a Parker-Hannifen pulsed valve. The valve was operated at a frequency of 5 Hz with a duty cycle of 25%, the same conditions studied by Bons et al. [15]. The pulse of air exiting the jet holes is essentially a step function. Some attenuation occurs in the jet plenum resulting in a slightly modified jet waveform as shown in Fig. 2. This figure shows the jet hole exit blowing ratio time history as measured with a single-element hot film positioned at the jet exit (with no freestream flow). The $t/T = 0$ station represents the time at which the control signal was sent to the pulsed valve. The peak value of B is approximately 2 and the mean value is 0.5.

Data Processing. Since the goal of this study was to document transition-related phenomena, large data records were taken at each position to assure steady statistics. For the no-control case, this was done using a sampling rate of 10 kHz for 16 s (160,000 data points). Flow intermittency (γ) was calculated using the

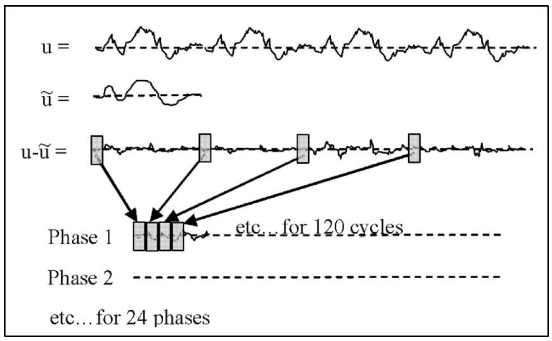

Fig. 3 Data processing flowchart for phase-locked unsteady velocity data

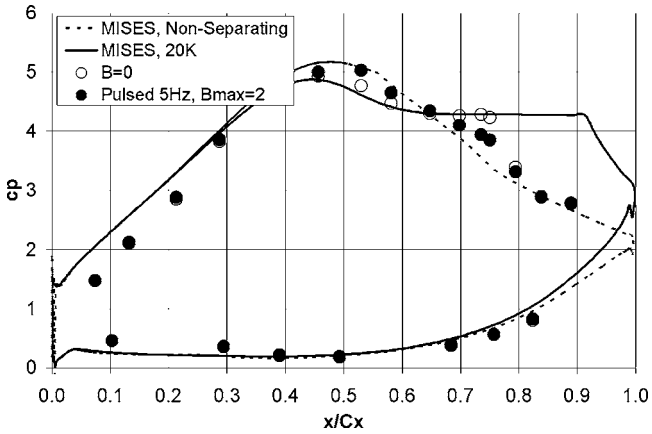

Fig. 4 Experimental L1M c_p distribution for Re_c=20,000 compared to MISES prediction (experimental data for B=0 and 5 Hz pulsed)

methodology developed by Volino et al. [17], which employs both the first and second velocity derivatives as turbulence discriminators. The data is initially high-pass filtered to eliminate low-frequency fluctuations that are common to both laminar and turbulent zones. The absolute value of the first derivative of velocity is then compared to a predetermined threshold based on the local velocity fluctuations. This procedure yields a $\Gamma_1(t)$ distribution, which is the first intermittency discriminator. A second discriminator (Γ_2) based on the absolute value of the second derivative of velocity is then coupled with the first discriminator to yield a final intermittency value. The composite result is low-pass filtered to eliminate erratic transitions between the two states. The only modification that was made to the original Volino formulation was to calculate the high and low-pass filter frequencies using the local mean velocity rather than the freestream velocity (U_∞). By doing this, the cutoff frequencies are more directly tied to the local convective speed of flow disturbances over the hot-film anemometer, thus avoiding erroneous intermittency values in and near the separation bubble.

In addition to the mean and fluctuating velocity, higher order turbulence statistics (skewness and kurtosis) were computed from each data record to provide multiple assessments of the turbulent character of the flow and to help identify the separated flow regimes. In addition, based on the work of Townsend [18], the kurtosis (or flatness) of the first derivative of the instantaneous velocity was computed as well.

In the case of pulsed flow control, the data acquisition time was increased to 24 s at the same frequency (10 kHz). The transistor-transistor logic (TTL) signal from the pulsed valve controller was used to phase-lock the data acquisition with the pulsed VGJ control. To obtain the same turbulence statistics in the case of unsteady control, the data processing methodology shown schematically in Fig. 3 was followed. First, the 120 cycles (24 s $\times$ 5 Hz) of velocity data were averaged to produce an ensemble average mean velocity distribution ($\tilde{u}$) at each point. This ensemble was then subtracted from each of the 120 cycles to eliminate the bulk unsteady motion of the flow from the statistical calculations. The resulting velocity record represents cycle-to-cycle deviations from the ensemble-averaged mean flow. The next step was to divide each cycle into 24 phases of equal length (8.3 ms). The first phases of data from all 120 cycles were then concatenated together to form a continuous velocity deviation signal associated with the first 8.3 ms of jet actuation (a total of 10,000 data points). This data record was evaluated in a manner similar to the no-control velocity data to determine intermittency, skewness, kurtosis, and kurtosis of du/dt. The process was repeated for each of the 24 phases to produce the time variation of turbulent flow statistics and intermittency over one complete pulsing cycle.

Experimental Results

The L1M cascade c_p distribution for Re_c=20,000 is shown in Fig. 4, both with and without flow control. The figure also contains a MISES prediction with and without separation (high and low Re). In the low Re case, forced transition as specified by the Praisner and Clark [19] transition models produced reattachment just before the trailing edge. Uncertainties in the pressure measurements translate to an uncertainty of ± 0.25 in the c_p data at Re_c=20,000. The predicted separation zone is broader than that obtained experimentally, suggesting that the experimental transition location is earlier than expected. This is possibly due to the lower inlet turbulence level (0.5% versus 3%) used in the calculation, as will be discussed later. The pressure distribution with flow control has a reduced separation zone and follows closely the nonseparating MISES calculation, particularly near the peak c_p. From this, it is clear that the pulsed VGJs are effective in the time-average sense at reducing laminar separation.

Baseline (Uncontrolled) Case. Figure 5 contains a series of contour plots showing flow data for the no control (B=0) case. The engine axial direction is left to right (axis units are normalized by c_x). A magnified close-up of the region $0.64 < x/c_x < 0.78$ is included in each plot. Separation is evident beginning around 59% c_x, as identified by the low $u_{\text{mean}}/U_{\text{in}}$ and elevated turbulence that both begin in this region. From this point until approximately 73% c_x, the turbulence level grows in a free shear layer that is removed slightly from the blade surface (note the region of low u_{rms} near wall fluid below the free shear layer from 68% to 73% c_x in the Fig. 5(b) close-up). Near 73% c_x, the elevated u_{rms} region in the free shear layer begins to broaden in the wall normal direction and the intermittency begins to rise above zero, indicating the inception of transition to turbulence. The intermittency value rapidly approaches unity near this location, signaling the fully turbulent character of the separated boundary layer. The transition region is rather abrupt, suggesting a bypass mode. The local turbulence level ($u_{\text{rms}}/U_{\text{in}}$) exceeds 25% in the vicinity of transition. The separation bubble reaches its maximum thickness in the wall-normal direction shortly after the transition to turbulence is complete. The bubble then continues to shrink from 78% to 88% c_x, which corresponds to the region of peak turbulence (near 40%).

The MISES prediction for the separation extent is from 56% to 92% c_x, as determined by the region where local wall shear levels are negative. This is somewhat broader than the region noted in the experiment, though no such precise separation indicator was available in the cascade facility for direct comparison. The overprediction of the separation bubble size by MISES is probably due

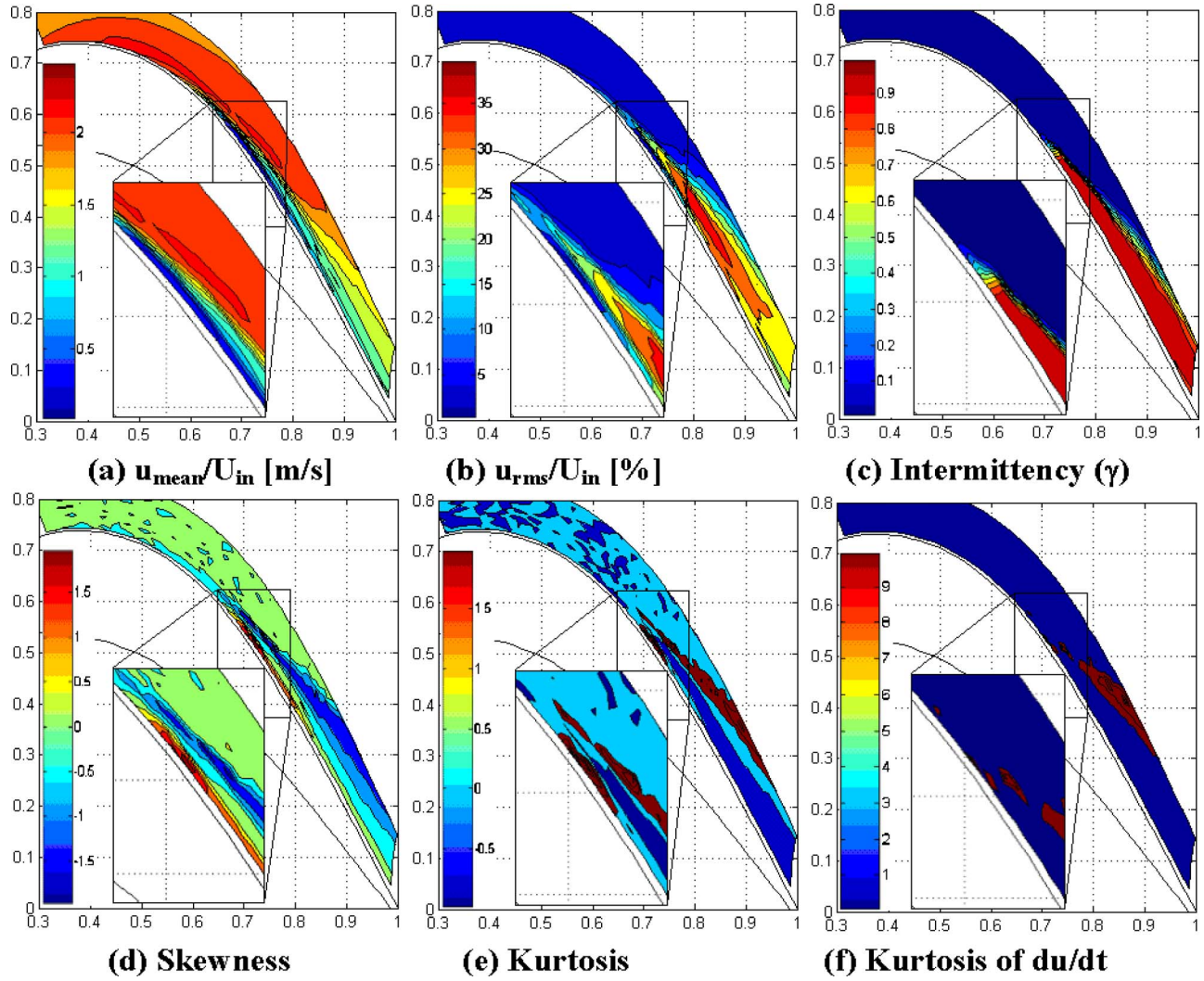

Fig. 5 No control ($B=0$) at $Re_c=20{,}000$. Horizontal axis is axial direction from leading edge normalized by c_x. Vertical axis is pitchwise direction normalized by c_x. Close-up of region $0.64<x/c_x<0.78$.

to the lower freestream turbulence level (0.5%) used in the calculation. A higher turbulence level would create a fuller boundary layer near the separation location, delaying it somewhat. Higher freestream turbulence would also move the detached boundary layer transition prediction (and thus the 92% c_x reattachment point) forward on the L1M suction surface.

The last three contour plots in Fig. 5 provide additional indications of separation and transition, using higher-order statistics. A broad band of negative skewness begins just upstream of the transition zone, eventually extending to the edge of the measurement domain 20 mm from the blade surface. This negative skewness indicates a region of predominantly high velocity flow punctuated by occasional pockets of low momentum fluid. As the shear layer begins to transition from a laminar to a turbulent state, the frequency of lower momentum pockets decreases as indicated by the increasingly negative skewness values. The minimum value of skewness corresponds approximately to the middle of the transition zone, as shown. The skewness eventually returns to zero as the flow becomes fully turbulent.

Figure 5(*d*) also shows a region of elevated positive skewness in the separation bubble where the mean velocity is at a minimum. This positive skewness occurs because the single-element hot-film cannot distinguish reverse flow. Regions of reverse flow register with a positive u velocity since the sensor is only sensitive to the magnitude of the fluid velocity component that is normal to the sensor axis. Since the center of the separation bubble is a region of frequent unsteady oscillations of forward and reverse flow, the anemometer will register all velocity fluctuations as positive velocity excursions. Thus, the instantaneous hot-film data record appears as a low (≈ 0) nominal velocity with occasional bursts of positive velocity. This creates the strong positive skewness shown in the plot. This rectifying of the velocity signal only occurs when the mean velocity is very low, such as in the heart of the separation bubble. Interpreted in this way, the skewness becomes a very useful indicator of separation. This also contributes to the perceived lull in local turbulence level in the near wall region (68% to 73% c_x) below the free shear layer as it transitions from laminar to turbulent.

The final contour plot in Fig. 5(*f*) shows the kurtosis (or flatness) of the local temporal acceleration (du/dt) distribution. The first location where this parameter rises above the background level of zero (corresponding to a Gaussian distribution) is in the separated free shear layer just prior to boundary layer transition ($\approx 73\%$ c_x). It then remains elevated only in the region corresponding to transition values of the intermittency function ($0 < \gamma < 1$). Upstream and downstream of this location, the contour map is devoid of useful information. The absence of color in the contour map suggests that this parameter is an excellent (almost binary) flag for transition. This explains why it has been employed

elsewhere as a transition discriminator [18]. It will become especially useful in sorting out the role of transition in the unsteady flow control case. The kurtosis of the instantaneous velocity signal itself (Fig. 5(*e*)) exhibits a similar peak at the onset of transition. Unfortunately, it was not as consistent in the unsteady forcing case and is not discussed further.

Several correlations have been suggested for predicting detached-boundary layer transition on turbomachinery blading. Praisner and Clark [19] suggested a correlation based exclusively on the momentum thickness Reynolds number at the separation location ($\mathrm{Re}_{\theta\mathrm{sep}}$):

$$s_{\mathrm{tr}} = s_{\mathrm{sep}} + 173 s_{\mathrm{sep}} \mathrm{Re}_{\theta\mathrm{sep}}^{-1.227} \tag{1}$$

Roberts and Yaras [20] offered one based on $\mathrm{Re}_{\theta\mathrm{sep}}$, the surface roughness level (k_{rms}), and the inlet turbulence level and lengthscale (through Taylor's turbulence factor, $\mathrm{TF} = \mathrm{Tu}_{\mathrm{in}}(L/\lambda_{\mathrm{in}})^{0.2}$):

$$\mathrm{Re}_{\mathrm{tr\text{-}sep}} = \left\{ 835 - 36\mathrm{TF}(\%) - [1400 + 25e^{0.45\mathrm{TF}(\%)}]\frac{k_{\mathrm{rms}}}{\theta_{\mathrm{sep}}} \right\} \mathrm{Re}_{\theta\mathrm{sep}}^{0.7} \tag{2}$$

For the present study, the inlet turbulence level was 3%, the integral lengthscale was 20 mm, and the surface roughness was $k_{\mathrm{rms}}=0.6$ μm. The 59% c_x separation location corresponds to a suction surface distance equivalent to 162 mm from the stagnation point. The boundary layer momentum thickness at the point of separation is 0.52 mm at $\mathrm{Re}_c=20{,}000$, giving $\mathrm{Re}_{\theta\mathrm{sep}}=111$. Using these measured values, the two correlations predict transition at 82% c_x and 81% c_x, respectively, somewhat downstream of the transition location indicated in Fig. 5.

Pulsed Jet Injection. As mentioned previously, three-dimensional particle image velocimetry (PIV) data taken by Bons et al. [15] in the same cascade facility indicated that the separation bubble's response to the unsteady jet injection was largely two-dimensional (i.e., spanwise uniform). As such, the unsteady follower data is presented for only one spanwise location (approximately 2*d* above the upper lip of a VGJ hole near the blade midspan). Since the jet injection direction is upwards along the span, the data plane is in the direct path of the jet injection (only 2*d* away from the injection point). Accordingly, the jet event figures prominently in the data presented herein. A second, less-comprehensive set of data taken 2*d* lower in span showed essentially the same flow behavior for the bubble dynamics, although the fluid dynamics near the jet hole were not as prominent, since the jet was convected above the data plane in that case.

The jet hole exit velocity profile in Fig. 2 indicates the locations of the 24 phases used to analyze the unsteady data. Figure 6 shows a series of $\tilde{u}/U_{\mathrm{in}}$ contour plots for ten of the 24 phases that experience the most dynamic change. For compactness, the vertical axis for these plots is the wall-normal distance rather than the pitchwise direction used in Fig. 5. Figure 7 contains the corresponding plots of ensemble-averaged $u_{\mathrm{rms}}/U_{\mathrm{in}}$. Recall that this is the unsteadiness that remains after the bulk unsteady motion corresponding to the 5 Hz pulsing of the jet has been removed. Finally, Fig. 8 is a composite of the three different transition indicators: intermittency, skewness, and kurtosis of the fluid acceleration. These five parameters provide a rich mosaic from which the essential fluid mechanics can be extracted.

The VGJ jet is "ON" for phases 1–6 (as indicated with black arrows in Figs. 6–8) and "OFF" for phases 7–24. Evidence of the jet disturbance at 50% c_x appears as early as Phase 1 in the turbulence data, while the mean velocity contour does not show any signs until Phase 2. Phase 1 straddles the initiation of the pulse, and the mean velocity is not terribly affected at this point. However, the pulse initiation does create considerable high frequency unsteadiness, thus, generating a strong kurtosis signal. In fact, the jet initiation appears to produce the most energetic high frequency unsteadiness compared to the subsequent phases of jet actuation

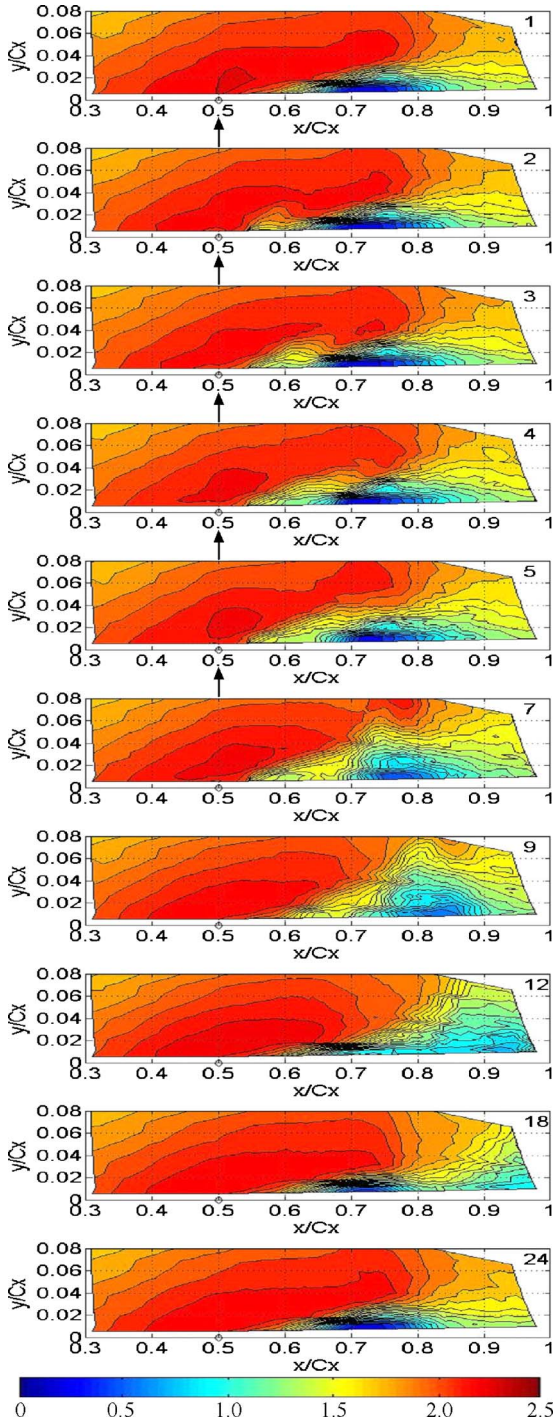

Fig. 6 $\tilde{u}/U_{\mathrm{in}}$ contour plots at ten different phases in unsteady VGJ cycle (phase number is in top right corner)

(e.g., Phases 2–6). A second, less prominent region of elevated kurtosis occurs at the pulse termination (Phases 5–7), but this is substantially weaker. The skewness plots show that this jet initiation event generates a concentrated region of positive and negative skewness that convects downstream intact from Phases 1–3. This signals a region of transition in the flow associated with the jet initiation event. Thus, the starting of the jet does initiate transition in a very localized region, which convects downstream disturbing the flow in its path. This is consistent with the interpretation of Bons et al. [5] that the starting event is the most critical in determining jet effectiveness. However, in that study, the effec-

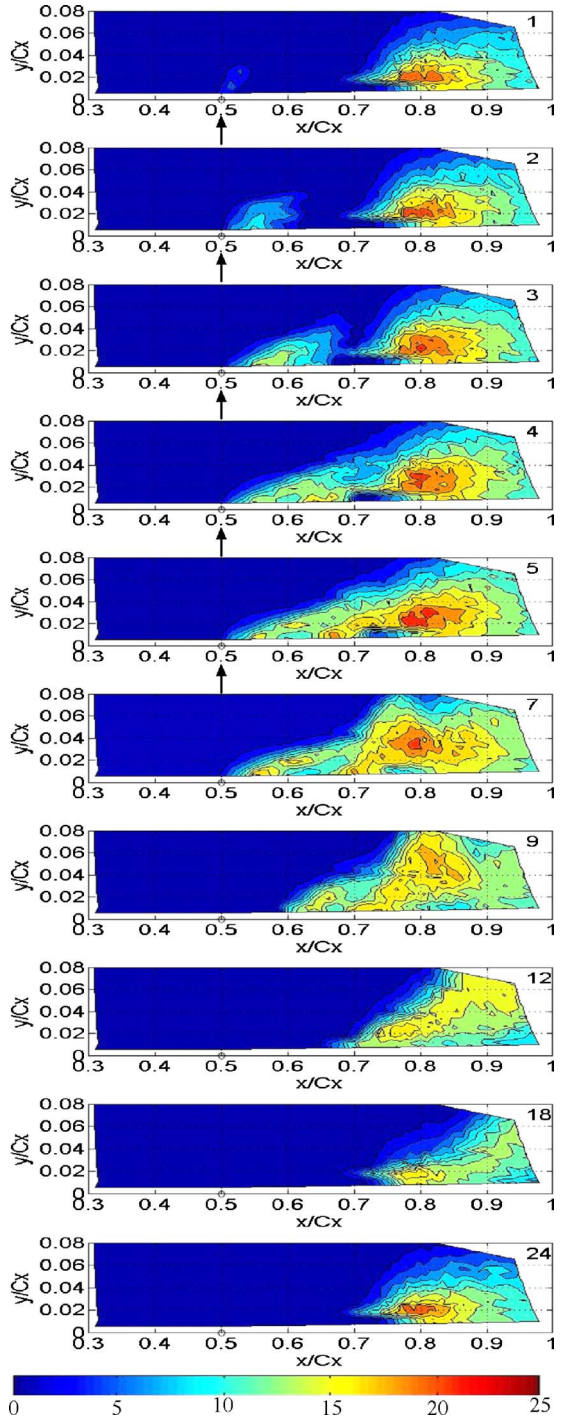

Fig. 7 Ensemble-averaged u_{rms}/U_{in} contour plots at ten different phases in unsteady VGJ cycle

tiveness was attributed to the starting vortex associated with the jet initiation. The present data suggest that the important feature is, instead, the flow unsteadiness that initiates transition upstream of the separation zone.

In the subsequent phases with the jet "ON," the fluid event associated with the jet initiation creates a line of transition in the flow emanating from the jet hole to the moving location of the starting event. Ultimately this creates a boundary layer transition line ($\gamma=1$) that is a full 15% c_x further upstream than the nominal position before the jet arrives. When the more energetic (higher mean momentum) fluid associated with this line of transition finally impacts the separation bubble in Phase 4, the bubble begins to move rapidly downstream. Because this occurs at the upstream end first, the bubble becomes more rounded between Phases 5 and 9. The low velocity region ($\tilde{u}/U_{in}<2$) has a y/c_x extent of 0.06 in Phase 9 versus 0.03 in Phase 5 and the streamwise extent is reduced accordingly. The peak turbulence level in the bubble is dramatically reduced once the high momentum fluid begins to sweep it off the blade (Phases 7–12). Peak turbulence levels drop from 23% in Phase 7 to below 18% in Phase 12. This process continues until the separation bubble is ejected from the trailing edge.

Once the jet is extinguished, the source for instability growth beginning at 50% c_x has been eliminated and the transition line moves downstream, finally stabilizing just beyond 70% c_x (as determined by a composite of Figs. 8(*a*)–8(*c*)). The embryo of the next bubble can be seen in Phase 7 as some residual low momentum fluid is left near 60% c_x. With time, this fluid migrates downstream to 70% c_x and forms the nucleus of the next bubble, which grows from Phases 12 to 24. Note that the separation bubble location just prior to the next jet pulse is very similar to the no-control case (Fig. 5); however, the transition indicators are not equivalent. This reflects the amplified disturbance growth that occurs due to forcing and suggests that the bubble is not responding quasi-steadily to the changing flow conditions.

The unsteady motion of the transition line can also be seen in a time-space plot (Fig. 9). A similar presentation was used by Volino et al. [7] for their synthetic jet data. This figure shows the ensemble-averaged turbulence and intermittency over two jet cycles at a constant wall distance (6 mm) corresponding to the location of the free shear layer when it first begins to transition. The trajectory of the jet initiation is clearly noted as the lower edge of the $\gamma=1$ band emanating from the jet hole at 50% c_x. The local peak in turbulence level at $x/c_x=0.8$ and $t/T=0.2$ corresponds to the jet initiation event. The convection velocity of the jet disturbance from 50% c_x to this location is 2.1 m/s, roughly 70% of the average local velocity between 50% and 80% c_x. The jet termination event convects at approximately the same velocity until it is engulfed in the separation bubble dynamics at $x/c_x=0.73$ and $t/T=0.43$. At this point, the transition line motion decelerates to roughly 20% of the average local velocity between 50% and 80% c_x. The transition line continues to move downstream until $x/c_x=0.83$ and $t/T=0.78$ when a resurgence of the separation bubble redirects the transition back upstream at approximately the same velocity. (This motion is depicted in the intermittency plot with dashed arrows.) The zone of low turbulence coincident with this point of redirection bears resemblance to the "calmed zones" following convected wake disturbances noted by Gostelow and Thomas [11] and Stieger and Hodson [12]. The calmed zone is marked by low turbulence levels and laminar-like boundary layer behavior. Based on these similarities, it is possible that the calmed zone associated with wake passing could be extended by short bursts from an upstream VGJ. This implies that the favorable flow conditions associated with laminar flow over the suction surface could be maintained for a longer duration as well.

Conclusions

Ensemble-averaged hot-film data were taken in a low speed, low pressure turbine cascade both with and without pulsed VGJ control. A novel ensemble-averaging technique was implemented to determine the variation of turbulence-related quantities through the pulsing cycle. Comparisons between the control and no-control data indicate that the nature of the boundary layer/separation bubble interaction is not quasi-steady. The pulsed jets play a critical role in creating premature transition on the blade, thus bringing momentum into the separation zone and reducing its size dramatically. Turbulence parameters such as intermittency,

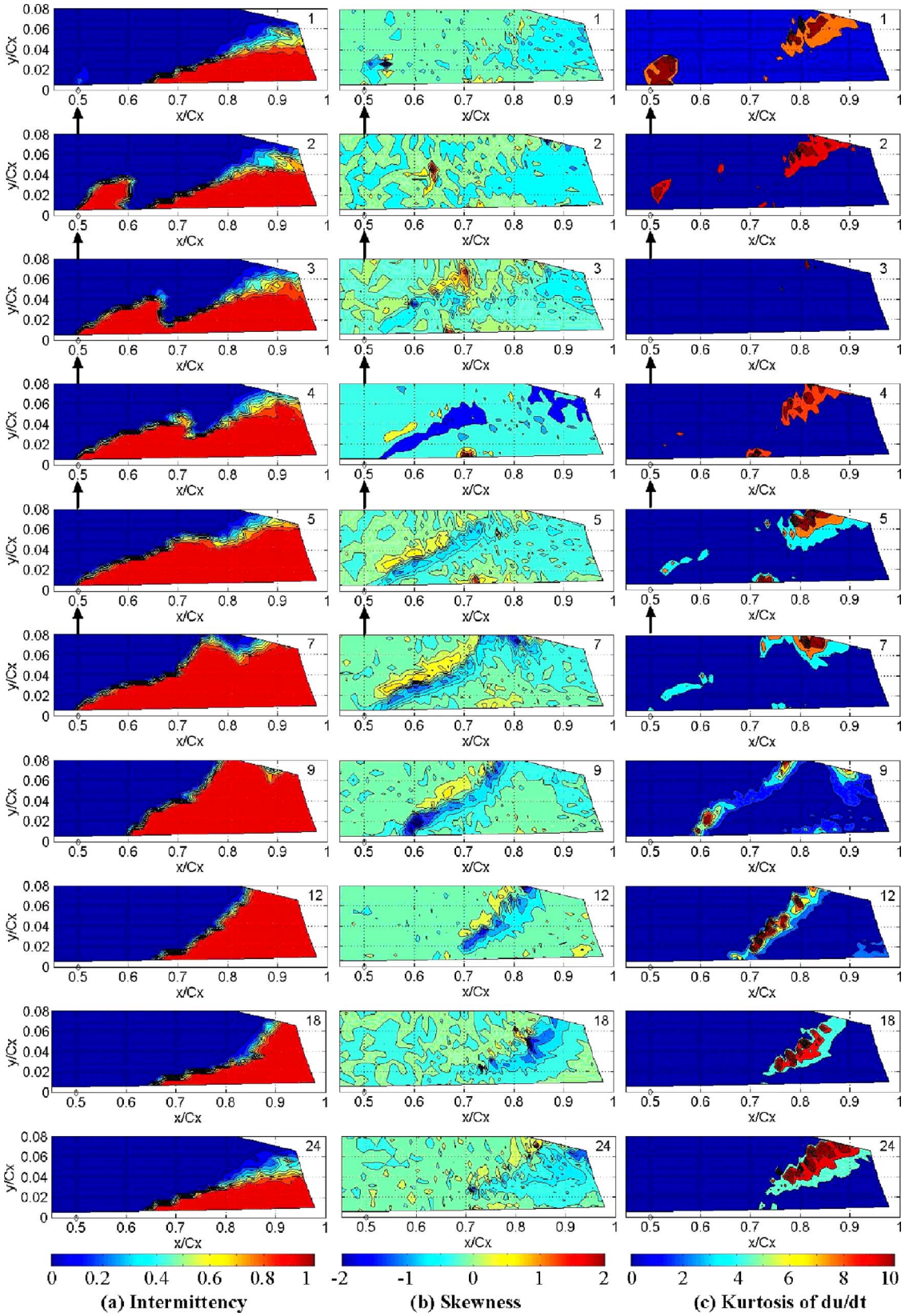

Fig. 8 Ensemble-averaged contour plots of various turbulence parameters at ten different phases in unsteady VGJ cycle

skewness, and kurtosis of the local fluid accelerations allow the transition line to be clearly identified both with and without control. Since the bubble response to unsteady control is similar in many ways to the effect of passing wakes, it appears to be possible to synchronize the two events synergistically, thus improving blade performance.

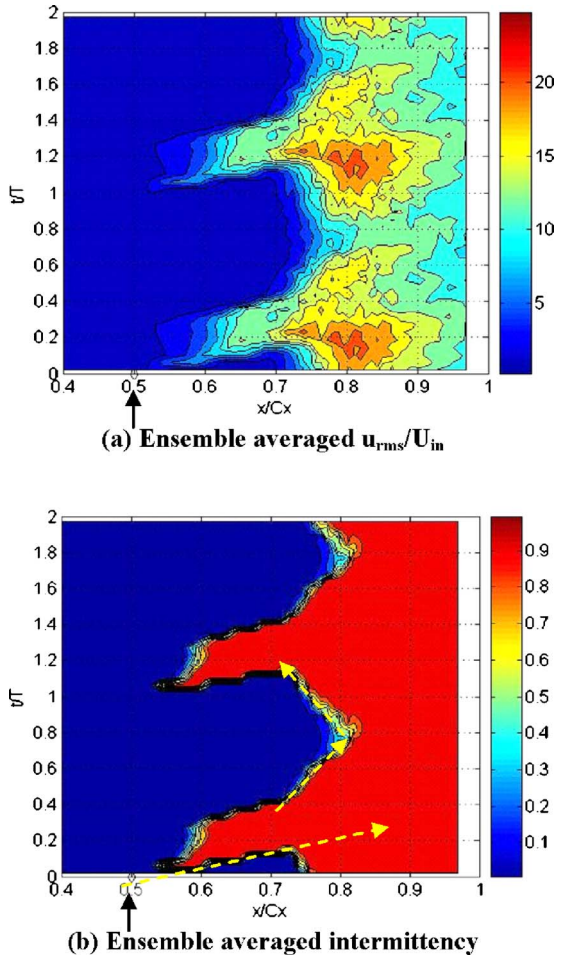

Fig. 9 Time history plots of turbulence and intermittency at y=6 mm (y/c_x=0.027)

Acknowledgment

Financial support from the U.S. Air Force Office of Scientific Research is gratefully acknowledged, with Dr. Thomas Beutner as program manager. In addition, the support of Drs. John Clark and Rolf Sondergaard at the Air Force Research Laboratory during this effort is greatly appreciated. The experimental portion of this study could not have been accomplished without the able assistance of Michael Armstrong.

Nomenclature

B = VGJ blowing ratio, U_{jet}/U_{local}
F^+ = dimensionless forcing frequency, $f/(Ue/\text{SSLJ})$
L = suction surface length, 331.3 mm
MEMS = microelectromechanical systems
P = pressure
Re = Re based on cascade inlet conditions, C_xU_{in}/ν
SSLJ = suction surface length from VGJ to trailing edge
T = forcing period, 200 ms
Tu = turbulence level in the cascade inlet
U = velocity
USAF = United States Air Force
c_p = pressure coefficient $(P_{Tin}-P_{local})/(P_{Tin}-P_{Sin})$
c_x = blade axial chord, 21.9 cm
d = jet hole diameter, 2.3 mm
f = pulsed jet forcing frequency, Hz
k_{rms} = root mean square surface roughness, 0.6 μm
u = instantaneous streamwise velocity component
u_{mean} = mean streamwise velocity component
u_{rms} = root mean square streamwise velocity component
$\tilde{u}$ = ensemble average streamwise velocity
s = streamwise distance along the blade suction surface
t = time
x = axial coordinate from the cascade inlet face
y = local surface normal coordinate

Greek Symbols

Γ = intermittency distribution
λ = integral lengthscale of turbulence at inlet
θ = boundary layer momentum thickness
ν = kinematic viscosity
γ = intermittency

Subscripts

S = static
T = total
in = cascade inlet
jet = VGJ jet
local = local blade conditions
tr = transition
sep = separation

References

[1] Rivir, R. B., Sondergaard, R., Bons, J. P., and Lake, J. P., 2000, "Passive and Active Control of Separation in Gas Turbines," AIAA Paper No. 2000-2235.
[2] Sondergaard, R., Bons, J. P., and Rivir, R. B., 2002, "Control of Low-Pressure Turbine Separation Using Vortex Generator Jets," J. Propul. Power, **18**(4), pp. 889–895.
[3] Sharma, O., 1998, "Impact of Reynolds Number on LP Turbine Performance," *Proc. of 1997 Minnowbrook II Workshop on Boundary Layer Transition in Turbomachines*, Paper No. NASA/CP-1998-206958.
[4] Matsunuma, T., Abe, H., Tsutsui, Y., and Murata, K., 1998, "Characteristics of an Annular Turbine Cascade at Low Reynolds Numbers.," ASME Paper No. 98-GT-518.
[5] Bons, J. P., Sondergaard, R., and Rivir, R. B., 2002, "The Fluid Dynamics of LPT Blade Separation Control Using Pulsed Jets," ASME J. Turbomach., **124**, pp. 77–85.
[6] McQuilling, M., and Jacob, J., 2004, "Effect of Chord Location on Separation Control With Vortex Generator Jets on Low Pressure Turbine Blades," AIAA Paper No. 2004-2205.
[7] Volino, R. J., 2003, "Separation Control on Low-Pressure Turbine Airfoils Using Synthetic Vortex Generator Jets," ASME Paper No. GT2003-38729.
[8] Eldredge, R. G., and Bons, J. P., 2004, "Active Control of a Separating Boundary Layer With Steady Vortex Generating Jets—Detailed Flow Measurements," AIAA Aerospace Sciences Meeting, Reno, NV, Jan. 5–8.
[9] Hansen, L. C., and Bons, J. P., 2004, "Time-Resolved Flow Measurements of Pulsed Vortex-Generator Jets in a Separating Boundary Layer," AIAA Paper No. 2004-2203.
[10] Seifert, A., Bachar, T., Koss, D., Shepshelovich, M., and Wygnanski, I., 1993, "Oscillatory Blowing: A Tool to Delay Boundary-Layer Separation," AIAA J., **31**(11), pp. 2052–2060.
[11] Gostelow, J. P., and Thomas, R. L., 2003, "Response of a Laminar Separation Bubble to an Impinging Wake," ASME Paper No. GT2003-38972.
[12] Stieger, R. D., and Hodson, H. P., 2003, "The Transition Mechanism of Highly-Loaded LP Turbine Blades," ASME Paper No. GT2003-38304.
[13] Postl, D., Gross, A., and Fasel, H. F., 2003, "Numerical Investigation of Low-Pressure Turbine Blade Separation Control," AIAA Paper No. 2003-0614.
[14] Postl, D., Gross, A., and Fasel, H. F., 2004, "Numerical Investigation of Active Flow Control for Low-Pressure Turbine Blade Separation," AIAA Paper No. 2004-0750.
[15] Bons, J. P., Hansen, L. C., Clark, J. P., Koch, P. J., and Sondergaard, R., 2005, "Designing Low-Pressure Turbine Blades with Integrated Flow Control," ASME Paper No. GT2005-68962.
[16] Clark, J. P., 2004, "An Integrated Design, Analysis, and Optimization System for Turbine Airfoils," Air Force Research Laboratory internal report.
[17] Volino, R. J., Schultz, M. P., and Pratt, C. M., 2003, "Conditional Sampling in a Transitional Boundary Layer Under High Freestream Turbulence Conditions," ASME J. Turbomach., **125**, pp. 28–36.
[18] Townsend, A. A., 1948, "Local Isotropy in the Turbulent Wake of a Cylinder," Aust. J. Sci. Res., Ser. A, **1**, pp. 161–174.
[19] Praisner, T. J., and Clark, J. P., 2004, "Predicting Transition in Turbomachinery, Part 1—A Review and New Model Development," ASME Paper No. GT-2004-54108.
[20] Roberts, S. K., and Yaras, M. I., 2005, "Modeling Transition in Separated and Attached Boundary Layers," ASME J. Turbomach., **127**, pp. 402–411.

Aerodynamic and Heat Flux Measurements in a Single-Stage Fully Cooled Turbine—Part I: Experimental Approach

C. W. Haldeman
R. M. Mathison
M. G. Dunn
S. A. Southworth
J. W. Harral

Gas Turbine Laboratory,
The Ohio State University,
Columbus, OH 43235

G. Heitland
Honeywell Aerospace,
Phoenix, AZ 85034

*This paper describes the experimental approach utilized to perform experiments using a fully cooled rotating turbine stage to obtain film effectiveness measurements. Significant changes to the previous experimental apparatus were implemented to meet the experimental objectives. The modifications include the development of a synchronized blowdown facility to provide cooling gas to the turbine stage, installation of a heat exchanger capable of generating a uniform or patterned inlet temperature profile, novel utilization of temperature and pressure instrumentation, and development of robust double-sided heat flux gauges. With these modifications, time-averaged and time-accurate measurements of temperature, pressure, surface heat flux, and film effectiveness can be made over a wide range of operational parameters, duplicating the nondimensional parameters necessary to simulate engine conditions. Data from low Reynolds number experiments are presented to demonstrate that all appropriate scaling parameters can be satisfied and that the new components have operated correctly. Along with airfoil surface heat transfer and pressure data, temperature and pressure data from inside the coolant plenums of the vane and rotating blade airfoils are presented. Pressure measurements obtained inside the vane and blade plenum chambers illustrate passing of the wakes and shocks as a result of vane/blade interaction. Part II of this paper (Haldeman, C. W., Mathison, R. M., Dunn, M. G., Southworth, S. A., Harral, J. W., and Heltland, G., 2008, ASME J. Turbomach., **130**(2), p. 021016) presents data from the low Reynolds number cooling experiments and compares these measurements to CFD predictions generated using the Numeca FINE/Turbo package at multiple spans on the vanes and blades.*
[DOI: 10.1115/1.2750676]

1 Introduction

The high-pressure turbine stage (vanes, blades, and disk) of modern gas turbine propulsion engines has been operating at inlet temperatures near or in excess of metal melting temperature for several years using air bled from the compressor to cool the components. At these elevated temperatures, relatively small changes in surface temperature can lead to changes in the life of the part by about a factor of two [1].

Changes in material properties are often considered as an alternative to changes in cooling schemes. Although advances in materials and material coating have allowed the operating temperatures of turbines to increase, the overall desire to push the operating temperatures even higher has made understanding turbine cooling more important rather than less so. The advent of new materials will not eliminate the need for cooling in the future; rather, they are complementary pushing the operating temperatures of turbines to levels higher than either technique could achieve alone.

Cooling plays a critical role in turbine aerodynamics, heat transfer, life durability, and efficiency. However, cooling designs have been difficult to verify experimentally under realistic operating conditions. Cooling designs are often empirically extrapolated from limited data and are evaluated based on flight hardware inspections many years after design decisions have been made.

Over the last ten years, more complete integration of the experimental, analytical, and computational aspects of turbine design has yielded improved designs. For example, 3D unsteady aerodynamics has been explored using all three sets of tools and is routinely incorporated into turbine designs. Issues such as turbine clocking [2] and structural issues [3,4] have all been successfully handled with this combination of disciplines.

With advances in both the computational and experimental capabilities necessary for investigating cooling effects, the possibility and necessity of performing a film-cooled high-pressure turbine stage measurement program under controlled laboratory conditions has become a possibility. There are multiple approaches that can be undertaken when planning such an experiment, and no one approach will be the "best" for all endeavors. However, the data that are acquired and the applicability of those data to the engine designer are intricately linked to these decisions. Thus, this paper will discuss, in more detail than usual, the modifications that have been made to a specific facility in order to perform relevant cooling experiments. This paper will also discuss, in some detail, the critical work that has previously occurred in this area and will illustrate how this facility addresses some of the limitations of earlier work. In addition, it will describe the overall experimental plan that is being pursued to examine film cooling and its interaction with turbulence and combustor-generated hot streaks. Data from recent measurements will be shown and discussed. This discussion is meant to complement the second part of the paper, which focuses almost entirely on experimental results for a turbine stage operating at a specific condition. In Part II [5], data will be compared to predictions obtained using the NUMECA FINE/TURBO code.

The overall goal of these two papers is to provide details of how these experiments and the accompanying analysis are being

Contributed by the International Gas Turbine Institute of ASME for publication in the JOURNAL OF TURBOMACHINERY. Manuscript received July 13, 2006; final manuscript received July 16, 2006; published online March 24, 2008. Review conducted by David Wisler. Paper presented at the ASME Turbo Expo 2006: Land, Sea and Air (GT2006), May 8–11, 2006, Barcelona, Spain.

conducted and the current level of interaction between the computational and experimental work. In addition, specific results regarding the measured effectiveness of film cooling are provided for the blade.

1.1 Brief Review of Past Work. The film cooling research area has reached a point where the knowledge gained in the more basic studies involving flat plate and cascade facilities can be effectively utilized in full rotating rigs that replicate engine conditions as closely as can presently be done under controlled laboratory conditions. One can now begin to think about how to create fully cooled measurement programs and how to perform the associated analysis and computations. During the initial phase of this work, there were several proof-of-concept, full-rotating experiments [6–8] that provided the basis for much of our current understanding of the issues involved with film cooling research that will be discussed later. The second phase of film cooling research is focused on capturing more of the important characteristics of turbine flow physics, such as interactions with combustor temperature profiles and freestream turbulence. Much of this work will be guided by the needs of the third phase, which will focus on implementation of the new information into the turbine design system.

Film cooling research is not a new area. With some effort, one can find in excess of 2500 references on the subject in the open literature dating back to 1940. There are two abbreviated bibliographies of film cooling research by Kercher [9,10], providing references from 1971 through 1996 and leading-edge film cooling references from 1972 through 1998.

To a turbine designer, one of the difficulties with the existing knowledge base is that a significant portion is specific to simple flow geometries at flow conditions far from those associated with turbine operating conditions. For example, numerous studies appear in the literature for isolated holes or a single row of holes (which may be circular or shaped and have various values of L/D). Elovic and Koffel [11] presented detailed discussion of the 1983 state of the-art regarding the design of turbine airfoil cooling systems. The authors included in their discussion a summary of current practice for predicting both external and internal heat transfer. A significant portion of the methodology described as standard practice almost eighteen years ago is still in use today.

It is not possible here to provide a full review of all the fundamental film-cooling related work done by previous investigators. The focus here will be on the work done with rotating turbines in the 1980s and 1990s that is most relevant to the current work. Of these, there are three main experiments that will be discussed. The first is the 1980 work of Dring et al. [6] who used a low-speed warm turbine that did not operate at turbine design corrected conditions, but was among the earliest of experiments that had rotating cooling, although from only one cooling hole. The comparisons of this data with cascade data pointed out the overall importance of secondary flow effects on the cooling flow. This work was the beginning of the full scale rotating rigs that came on line in the 1980s and 1990s at Calspan [12], Oxford [13], MIT [14], and VKI [15], and later at WPAFB [16].

One of the major cooling experiments was performed at MIT [17] in the mid-1990s. This experiment involved coolant gas directed to a few of the blades contained on the rotor disk and vane trailing-edge injection, but without vane film cooling. The results had a substantial impact on the understanding of film cooling. This work also illustrated many of the problems that were endemic to this type of research and the amount of auxiliary work that had to be developed and undertaken to facilitate these experiments. An example is the development of the double-sided Kapton heat-flux sensors for use where the traditional single-sided heat flux gauge and semi-infinite data reduction models were no longer valid [18]. Problems with the cooling supply, leakages, and timing were all routine problems that had to be overcome.

Takeishi et al. [6] also performed a cooled experiment but was unable to acquire time-accurate measurements. His sampling technique and experimental goals focused on mass transfer in the boundary layer and, thus, provided detailed measurements in the boundary layer, but only at a few locations.

One of the important conclusions of these experiments was that cooling issues tend not to have an overriding characteristic that can be emphasized at the expense of others to reduce experimental complexity. Cooling gas migration along the blade pressure surface is not replicated well in nonrotating facilities [7]. In addition, the entire problem changes when the inlet conditions change from uniform turbine inlet temperatures and low turbulence intensity to nonuniform temperature profiles and relatively high turbulence intensity that more accurately reproduce the combustor exit conditions.

Among the early attempts to create a radial temperature profile generator was that of Haldeman at MIT in the 1980s [19]. The initial manufacture of this device was problematic, and it was not until the mid-1990s that it was successfully used in hot streak-migration work [20,21], almost 20 years after the original analytical work on hot streak migration had been discussed by Kerrobrock and Milkolajczak [22] and Lakshminarayana [23]. Haldeman continued with the passive matrix system and has been successful in using a very different version than attempted initially in a shock tunnel [24] environment. Two other facilities have used an alternative technique (mass injection) to generate temperature profiles [25,26].

At the same time that the experimental facilities were being developed, computational models were also being developed at various locations. The film cooling models of TEXSTAN have evolved since the early version described by Miller and Crawford [27]. The revised film cooling models are derived based on the early work of Tafti and Yavuzkurt [28] with extensions by Neelakantan and Crawford [29,30]. Those references show extensive validation of the models for flat plate conditions. For film-cooled airfoils, very little validation of the Crawford models has been carried out. Weigand et al. [31] evaluated TEXSTAN and a 3D Navier-Stokes code for predicting heat transfer on a fully film-cooled vane for both film cooling effectiveness and heat transfer. They found the boundary layer program provided good agreement with the data, providing the appropriate boundary conditions are used for the velocity loading.

It comes as no surprise that the flow field near a cooling hole of a vane or blade is very complex. Recent modeling techniques appear to have moved into one of two alternative perspectives based on previous work. One group has moved toward the ideal of fully solving the entire flow field within each cooling hole, within the supply plenums, and the external flow over the airfoils. Leylek and Zerkel have reported the results of several studies in this general area [32]. An alternative method championed by Abhari [33] and Abhari et al. [34,35] is the "macromodel," which is an extension of past injection models. The injection model accounts for the penetration and spreading of the coolant jet as well as entrainment of the boundary layer fluid by the coolant. Abhari compared the steady-state predictions of his code to the film cooled linear cascade data of Camci [36].

1.2 Important Design Parameters. The results of much of the detailed cooling research done previously have shown that in addition to the main parameters needed to be matched in a full-scale rotating turbine rig—vane inlet Reynolds number, design corrected speed, flow function, stage pressure ratio, and gas-to-metal temperature ratio—other parameter are also of interest. These include the coolant to core gas temperature ratio, the mass fractions of coolant to core gas, and the blowing ratio. For these experiments, one usually matches the blowing ratio at one location (such as the showerhead holes on the vane); the blowing ratio at other airfoil locations is determined by the geometry of the hardware and the external flow physics. For studies involving nonuniform temperature profiles, there have been a variety of different parameters used in the literature to characterize the incoming profiles.

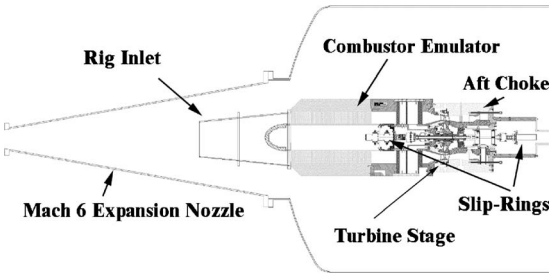

Fig. 1 Honeywell turbine in TTF

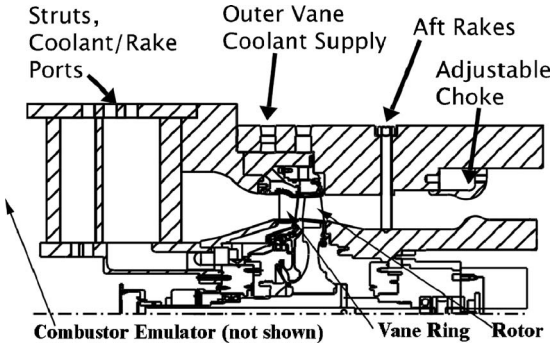

Fig. 2 Turbine stage

The terms noted above govern the input conditions at the vane and blade inlet. There are an equally large number of measures of the overall effectiveness of the film cooling. Several possibilities exist depending on the primary goal, but the major ones used in this work will be the net heat flux reduction and the adiabatic effectiveness. These terms have been defined in the Nomenclature.

2 Experimental Plan

The experimental results presented in this paper are representative of the initial phase of a multiphased measurement program utilizing a fully film-cooled high-pressure turbine stage. Complicating external factors will be added in step-by-step fashion to observe, empirically, which are important for film-effectiveness measures throughout the stage. Each measurement phase has been designed to provide benchmark quality data for computational fluid dynamics (CFD) code validation and model development. The measurements reported here were performed with both the vanes and blades cooled, and a uniform vane inlet temperature profile, with a low freestream turbulence level. A single Reynolds number condition is reported here, but measurements are being acquired over a range of inlet Reynolds numbers at selected turbine operating conditions. A second series of measurements will examine the effects of freestream turbulence on film cooling by inserting a turbulence grid just upstream of the vane inlet and repeating the uniform inlet temperature profile measurements in order to generate an empirical picture of the importance of turbulence throughout the stage. A third series of measurements will focus on the effects of inlet temperature profiles only by removing the turbulence grid and introducing hot streaks and radial profiles. A fourth series of measurements will examine the effects of both temperature profile and turbulence by combining the two operations to see if there are effects that are not predicted by superposition of the individual inlet conditions. The final series of measurements will utilize a uniform inlet temperature profile without the turbulence grid, but with the vane trailing-edge injection turned off.

3 Rig Description

3.1 Overall Rig Description. A modern high-pressure turbine stage manufactured by Honeywell Engines was selected as the research vehicle for this effort. A schematic of the rig housing the turbine located in The Ohio State University (OSU) Turbine Test Facility (TTF) is shown in Fig. 1. The primary components of the experimental configuration, the inlet, the combustor emulator, the turbine stage, the downstream choke, and the two slip ring units (one 200 channels and the other 300 channels, or alternatively specified as 100 and 150 pairs of wires) are shown.

A more detailed description of the flow path in the immediate region of the turbine stage is provided in Fig. 2. The computational domain, which will be described in more detail later, is contained within the inlet and exit rakes shown in Fig. 2.

Coolant flow to the vanes and blades is supplied via three separate cooling paths that can be controlled independently: the rotor path, the vane inner path (which controls the showerhead and cooling holes), and the vane outer path that feeds the trailing edge. The cooling paths within the rig are shown in more detail in Fig. 3. As noted in Fig. 3, the shroud cooling holes are blocked for these experiments. The rig consists of 12 vane doublets (24 vanes total) and 38 blades.

The outer vane path is fed directly from the outside of the rig via two tubes (180 deg apart). The flow then proceeds through a collection of holes until it reaches the main plenum, which is an annular configuration that provides coolant to all vanes and is located at the tip of the red arrow in Fig. 3. The blade and vane inner path cooling flow enters through the struts shown in Fig. 3. There are four struts, two of which are used to supply the vane inner cooling (green/light arrows) and two are used for the blade cooling (blue/medium arrow). Both of these cooling streams move into the diverter system (which combines the two inlets for the vane inner path into one annular plenum and moves the flow out to the vane) and combines the two blade inlets and directs that onto the rotor system via a tangential on board injector (TOBI), which moves the coolant into the rotor frame of reference. The TOBI is also engine hardware, and no changes were made to the flow angles to match for the changes in physical speed between the engine and the rig. All three cooling paths can be controlled separately from outside the rig. During the course of the experiments, off-design variations in all of these parameters will be performed. The data presented in this paper are from a low Reynolds number condition, which represents one of the conditions of interest.

The engine hardware being used for these experiments has complex cooling-hole geometry consisting of shaped holes of

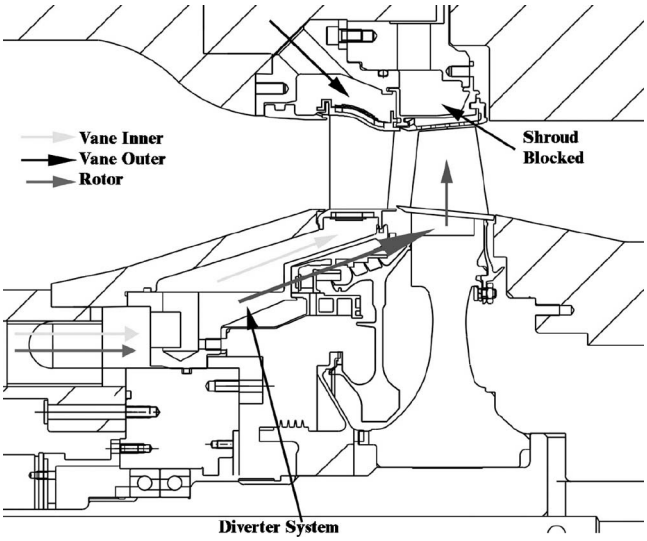

Fig. 3 Turbine cooling paths

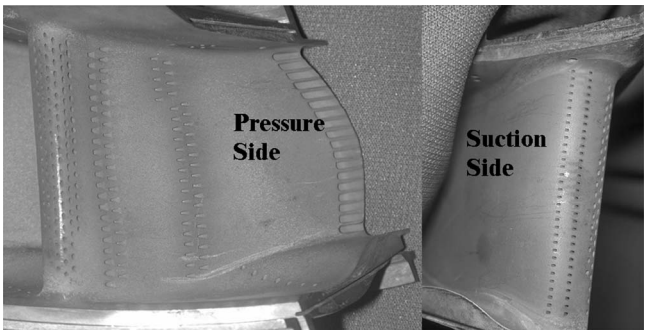

Fig. 4 Vane cooling hole pattern

various dimensions on both the vanes and blades. The vane, shown in Fig. 4, has 12 rows of film holes and a row of trailing-edge slots.

The blade also has a complicated cooling pattern consisting of eight rows of holes spread out along the surface in a 3D pattern. The hole shape and diameters change with location on the airfoil.

As seen in Fig. 5, many of the cooling-hole rows do not cover the entire span of the blade, indicating the 3D nature of the cooling design. During the assembly of the rig, all the blades were flowed using a blowdown rig to check the total area of the cooling holes and representative blades were instrumented. Time did not allow for all the vanes to be flowed, but all the vanes that were instrumented were flowed using this experimental apparatus.

3.2 Instrumentation. The instrumentation package for this rig consists largely of Kulite XCQ-062-100A pressure transducers mounted externally on the blade airfoil (to provide the surface pressure) or internally on the blade to provide the pressure within the airfoil cooling cavities. In addition, the blades are instrumented with double-sided Kapton heat-flux gauges (HFG) and type K butt-welded thermocouples usually 25.4×10^{-6} m or 12.7×10^{-6} m (0.001 in. dia or 0.0005 in. dia). More information about the calibration and construction of the Kapton heat-flux sensors is available in Murphy [37]. The thermocouples and pressure transducers are also used in stage entrance and exit flow path rakes. Of all these instruments, only the thermocouples have a characteristic frequency lower than blade passing and, thus, temperature measurements from these devices are essentially time-averaged values.

Since the focus of these experiments is on the blade, the vane is only instrumented at 50% span with 15 double-sided heat-flux gauges, 16 external pressures, and two internal temperatures and pressures (one set mounted on the outer vane circuit and the other on the inner vane circuit). The heat-flux gauges are spread over two individual vanes, and thin-film heaters are located in one of the vanes so that the metal temperature of the vane can be set for individual experiments and thus the adiabatic wall temperature (see discussion in Part II [5]) can be deduced.

Three spanwise locations are instrumented on the blade (15%, 50%, and 90%). Of the 38 rotor airfoils, 22 are instrumented in some fashion. Two of the airfoils were filled (cooling holes plugged) to provide data for uncooled blades. These airfoils were also instrumented at the 50% and 90% span locations and have cartridge heaters installed in them to provide the uncooled heat transfer and the adiabatic wall temperatures. Several blades had thermocouples mounted in their roots, immediately below the platform surface, with the thermocouple exposed to the coolant gas. These were mounted around the rotor to provide a measure of the uniformity of the gas temperature.

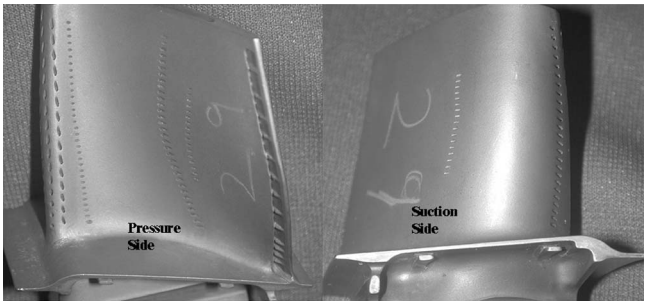

Fig. 5 Blade cooling holes

Fig. 6 Blade suction side, 50% span instruments

At 15% span, there are 13 HFG locations, and at 50% span there are 53 HFG locations (spread over the cooled and uncooled airfoils), 15 external pressures, and 12 internal pressures (cooled airfoils only). At 90% span, there are 39 HFG locations (distributed between cooled and uncooled blades) and 15 external pressures (cooled blades). In addition, there are six HFGs mounted in the recess of the squealer tip and 12 HFGs mounted on the rotor shroud (two circumferential locations of six) and six pressure transducers.

Space will not allow detailed photographs of the instrumentation, but one can see an example of various HFG blades and pressure transducers at the midspan location in Fig. 6.

4 Facility Modifications for Film Cooling Work

As described earlier in the paper, the OSU GTL TTF had to be modified in several ways to meet the requirements of the fully cooled experiments. Since these modifications have not been discussed previously, they are briefly reviewed here.

4.1 Large Cooling Facility (LCF). The most visible addition to the facility is a cooling tank, which provides the source of the cooled air (or Nitrogen) for the turbine rig. A picture of the cooling system is shown in Fig. 7.

This facility consists of a triple-jacketed stainless steel tank, the inner vessel of which is $\sim$1.28 m^3 ($\sim$45 ft^3) in volume and is rated for service from 200 K to 477 K (360 R to 860 R) and vacuum to 2745 KPa (400 psia). The second jacket contains the coolant, which is controlled by one of two chillers (seen on the top of Fig. 7). The outer jacket (the part that is visible in Fig. 7) houses $\sim$0.13 m ($\sim$5 in.) of Perlite insulation. Total residual heat-losses were originally $\sim$500 W, although the addition of extra insulation on the outside has reduced that considerably.

The coolant gas flow exits though a 0.1524 m dia (6 in. dia) sleeve valve designed with an elliptical inlet to provide very high-quality uniform flow. This characteristic is not as important when the facility is used as a cooling facility, but offers smooth flow when the facility is being used in a stand-alone mode as a calibration device. The valve uses a pneumatic activation system that

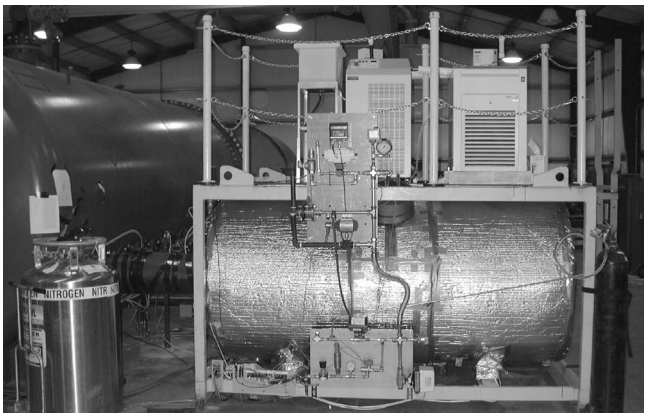

Fig. 7 Large cooling facility

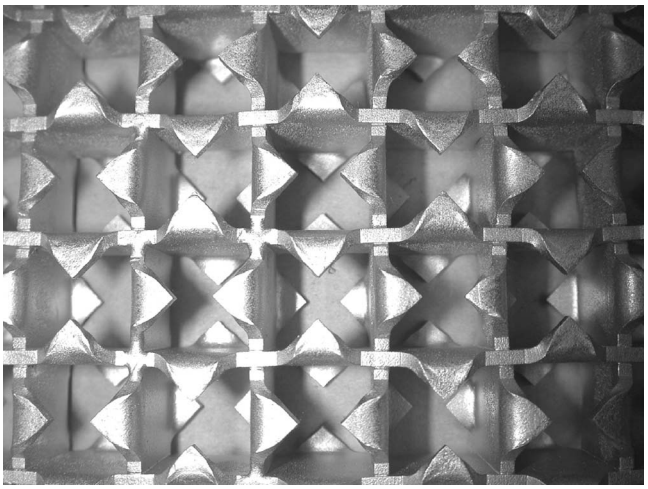

Fig. 9 Turbulence grid

also provides the braking power to keep the valve from slamming into its housing. When connected to the TTF, the cooling circuit is comprised of three main parts as shown in Fig. 8.

The LCF supplies the coolant at about 218 K (392 R) and at pressure ranges from 276 KPa to 827 KPa (40 psia to 120 psia). The flow is then split into three separate circuits by means of venturi-style chokes (discharge coefficients ~1), which are sized to generate the proper mass flow in each circuit (rotor, vane inner, and vane outer). An intermediate heat exchanger is placed in line with the LCF to precool the metal lines leading to the rig and to reduce the overall uncooled length. This device, known as the "supercooler," is a simple passive heat exchanger cooled with liquid nitrogen.

Each cooling circuit consists of two tubes attached to the turbine stage in two locations to stabilize the internal pressure. Temperature control is based on the temperature recorded at the vane and blade inlets, and not the LCF itself.

Coolant mass flows were measured using a variety of methods. The volume of the dump tank was obtained independently through calculations, volume comparisons, and blowdown time constant measurements. This resulted in an installed volume up to the chokes of 1.2873 $m^3 \pm 0.76\%$. This value is then used with calculated blowdown time constants (based on pressure decay rates in the LCF tank) to get the mass flow in each circuit independently. These are verified against the measurements made at the inlet to each cooling sector to check for consistency and leaks.

4.2 Combustor Emulator. As mentioned earlier, the ability to generate nonuniform temperature profiles that more accurately simulate a combustor has been desired of the full-scale rotating rigs since the 1990s. When using the combustor emulator, the TTF facility is operated in blowdown mode, which allows longer run times than can be achieved when operating in the traditional shock-tube mode. This is critical for this experiment because it allows time for the cooling flow start-up and stabilization process. The actual development and operation of this current combustor emulator has been documented by Haldeman et al. [24] and will not be dealt with in great detail here.

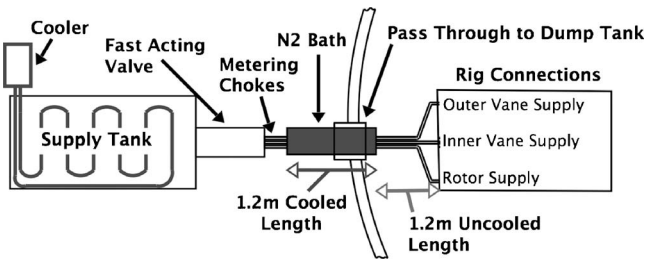

Fig. 8 Schematic of cooling connections

The highlights of this system are as follows:

1. It can provide uniform temperatures, constant radial profiles, or various hot streaks of the same number as the fuel nozzles (order of 20), all without changing the configuration. By changing the initial heater layout, different shape factors in the profile can be generated, and by changing which heaters are used, the number of hot streaks can be varied from run to run without any hardware changes. The location of the hot streaks can also be clocked with respect to the vanes.
2. It allows for the generation of the temperature profiles and freestream turbulence intensity separately (see Sec. 4.3). This is critical if one is examining the independent importance of these effects because standard mass injections systems generate both the turbulence and the temperature profiles at the same time.

As shown in [24], both the matrix and the flow path have a temperature uniformity of about ±3 K at 450 K. The overall effectiveness (measured temperature at the inlet rakes to the matrix temperature) was ~95% (98% predicted), and peak-to-base temperature ratios of 1.68 have been obtained easily. There are many parameters used to characterize the combustor temperature profiles. Here, we will modify those of Chana et al. [26], who proposed two measurements of the profiles: the overall temperature distortion factor (OTDF) and the radial temperature distortion factor (RTDF). But in his case, he was using a mass injection system that injected coolant; thus, his normalizing value was the difference between the average gas temperature and the coolant temperature. In our case, we use the difference between the average gas temperature and the wall temperature (see Nomenclature).

4.3 Turbulence Grid. As a companion to the combustor emulator, a turbulence grid was fabricated based on a design suggested by General Electric Aircraft Engines. Initial turbulence intensity measurements for this grid have been performed by Eaton [38], which vary between 8% and 14% at the vane inlet based on axial distance of the grid from the vane. A photograph of the welded grid is shown in Fig. 9.

This grid is manufactured from 0.002 m (0.080 in.) thick stainless steel plates, with cells 0.0191 m^2 (0.75 $in.^2$) and tabs 0.0064 m (0.25 in.) on an edge. The grid is designed to be moved axially several vane chords so that one can change the nominal turbulence intensity entering the vane ring.

4.4 Data Acquisition Improvements. The addition of double-sided heat-flux gauges, the combustor emulator, and the

cooling system all contribute to a significant increase in the required number of data acquisition channels. The system that has been in place at the Ohio State University Gas Turbine Laboratory has been a 256-channel 100 KHz 12-bit CAMAC-based system. To extend the capabilities, an additional 256 channels of data acquisition has recently been added. The new DAS system (VXI based) is scalable and uses eight channel VX2824B modules. Each channel has an effective output word rate (sample rate) of up to 2.5 Megasamples per second at 16-bit resolution with on-board memory. Each card employs a parallel σ-δ A/D converter architecture. Lower effective sample rates are achieved using hardware decimation. The use of digital filters as anti-alias filters at the lower speeds allows sharper response than their analog counterparts without compromising the Nyquist criteria.

Table 1 Operating conditions

Property	Rig operating point	Rig set point
Total pressure ratio	3.672 ± 0.085	Not available
Corrected speed (rPM)	9719	9719
T_{core}/T_{metal}	1.39	1.40
$T_{cooling}/T_{metal}$	0.883	Rotor=0.893 Vane inner and outer=1
Mass flow ratio (vane inner to vane outer)	1.816	2.44
Mass flow ratio (vane inner to rotor)	1.057	1.03
Reynolds number (Re)	17.6×10^6	17.15×10^6

5 Experimental Procedure and Data

5.1 Facility Operation. Detailed descriptions of how this facility has been operated in the past are available in many papers [39–43] and will not be described here. Only those changes in operational procedure needed for the cooling experiments will be discussed.

For cooled experiments with the combustor emulator, facility operation is much more involved than it was when operating the facility in simple blowdown mode. First, the LCF is chilled to the proper temperature. This can take up to 36 h from a room-temperature start, but the system has remained at temperature for many weeks. The facility dump tank has to be under a vacuum or at least filled with dry air; otherwise, the LCF valve will begin to frost. The heater assembly requires 2–4 h to reach the proper temperature. Hot streaks can be generated more quickly than uniform temperatures. Once the matrix is ~45 min from being ready to run, the supercooler is charged with liquid nitrogen. The LCF valve is opened for a short period of time prior to initiation of the full experiment to prechill the lines. When all the external systems are at the operating point, the main supply tubes are loaded and the rotor is brought up to speed in the vacuum of the dump tank to a value below the operating point. The power to the combustor emulator is turned off, and the cooling supply and DAS are armed.

The firing sequence begins when the fire switch is pushed to start an automated timing circuit. The first valve to open is the LCF. This supplies coolant that chokes at two points in the system: at the main mass-flow setting venturies and also in the blades and vanes at the cooling holes (or close to them) since the tank and the rig are in a vacuum. Then after a brief delay, usually on the order of 1 s, the timer opens the main tunnel fast-acting valve to initiate the primary airflow. This valve closes after ~150 ms and is followed by the closure of the LCF valve, completing the experiment.

Several different A/D systems are required to monitor all of these events. One of these, a standard National Instruments PCI-6071 board based unit, is used to measure the temperature of the combustor emulator, LCF, and cooling tube temperatures. This runs continuously over the course of the day, sampling about once every 5 s, displaying the data, and storing it to a file, monitoring the development of the pre-experiment conditions. The trigger point is marked on this record in order to synchronize these data with the other high-speed data files.

A second National Instruments system (also using 6071 boards) is used to monitor the LCF tank pressure, and cooling temperatures, and rake conditions during the main experiment. This collection of data is usually sampled at between 5 KHz and 10 KHz, and the data is stored to a file, which covers the entire time the LCF is activated. Over 96 National Instruments based channels are used in the monitoring of these systems.

The main data acquisition systems (512 channels) are used just for the 200 ms that the TTF is activated. Data acquisition rates vary from 100 KHz to 2 MHz depending on the individual channel settings. All blade and vane data are collected on these systems so that blade passing frequency and its harmonics can be resolved.

5.2 Results for Cooled Experiment. As mentioned previously, the focus of Part I has been on the experimental apparatus and how the cooled experiments are performed. Part II [5] focuses more on the measurements obtained for the film-cooled turbine stage, and readers are directed there for more detail regarding the pressure and heat transfer data on the vane and blade. The purpose of the remainder of this paper is to examine the measurements obtained that are specifically applicable to supporting components, the combustor emulator, the cooling system, and initiation of the experiment.

The operating point for the data presented in this paper is provided in Table 1. This is a low Reynolds number case and was run with a low mass flow ratio to check for overall system accuracy since this represents one of the more difficult cases to operate.

In Table 1, the rig set point was the desired condition and the rig operating point is the conditions at which the data were obtained. Traditionally, multiple runs can be made to make the operating point coincident with the set point by changing the choke valve to mach the pressure ratio, and changing the chokes in the cooling lines to balance the mass flows and temperatures. At this operating point, the mass flow accuracy for the cooling flows was approximately 0.02–0.04 Kg/s, depending on the circuit, which translates into an overall accuracy of ~0.8% of the core flow (or ~5% of the total coolant flow). The uncertainty arises from difference in the mass flow as measured out of the coolant tank (using an isentropic blowdown model, and the measurements at the vanes and rotor locations). The sources may be due to variations in the total coolant hole area of the blades, slight instrument error, or leaks. Whatever the source is, the overall accuracy is relatively good, given the low mass flows involved, and probably represents the realistic limit on how accurately the cooling mass flow can be measured. Although the overall accuracy does not tend to scale with the mass flow and will stay approximately constant as the mass flows are increased, at engine operating conditions, the accuracy of the mass flow as a percentage of the core flow should be improved. In this particular case, the vane outer mass flow was substantially less than originally designed. The other variations are due to slight increases in the cooling temperatures that are a result of the low mass flow rates.

Figure 10 illustrates the combustor emulator temperature history during the heat-up period. In this case, there was a computer glitch and the acquisition system had to be restarted at about 80 min. One can see that the average temperature in the combustor emulator matrix rises in ~1 h to a peak of 500 K.

The conditions for this run were for a low Reynolds number case, and the temperatures were set specifically low. At the peak heating rate (70 min), the variation in the matrix (highest to lowest temperature) is ~175 K. At 70 min, the core heaters are lowered and the edge heaters remain powered (they would be off for

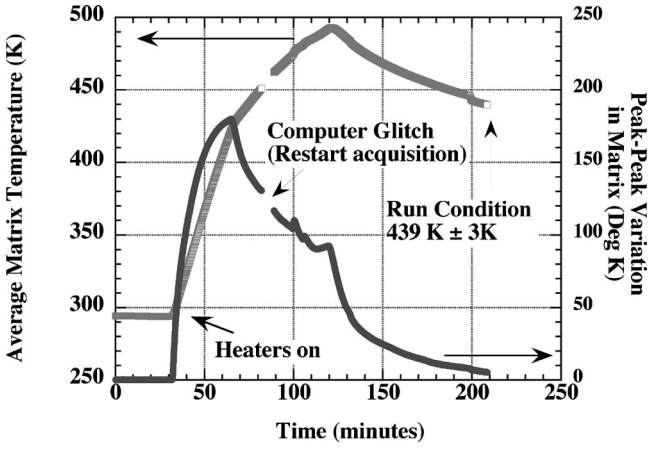

Fig. 10 Overall matrix temperature

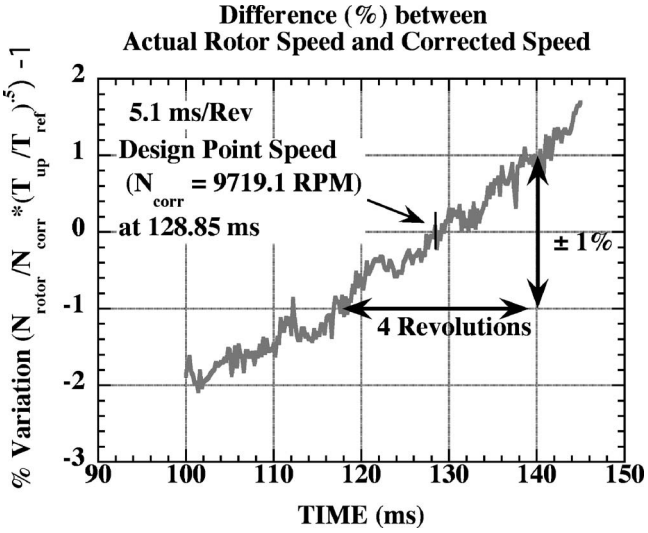

Fig. 12 Corrected speed variation

a hot streak profile) and the uniformity improves until 120 min where the power to all the core heaters are turned off. The matrix becomes rapidly more uniform over the next 30 min, dropping to a peak variation of ~24 K. Over the next hour or so, the matrix equilibrates to the final range of ~5.5 K.

Time histories of the inlet and exit rake temperatures are shown in Fig. 11 covering the time period of the entire 4000 ms that the LCF was activated. Data sampling is initiated when the LCF receives its trigger to start the cooling flow. At this time, there is already a small difference in the rake temperature, with the upstream rakes ~4 K higher in temperature than the downstream rakes. This is attributed to radiation heating of the thermocouple coming from the combustor emulator. By ~500 ms, one can see the downstream rakes stabilizing at ~275 K. This is due to the ~10% mass flow coming from the LCF and exiting through the blade and vane cooling holes. In this case, the main TTF valve is opened at 1500 ms, and one sees the sharp jump in the rake temperatures that is associated with the core flow passing through the heater. The main valve on the TTF has closed by 1700 ms, and the thermocouples return to their initial temperatures until the cooling system is closed at ~3000 ms, where the temperatures come together.

During the main experiment, the corrected speed remains constant to about ±1% over four revolutions with the design point occurring at 128.85 ms (or 1628.5 ms on the scale in Fig. 11), as shown in Fig. 12.

The flow path total pressure upstream of the vane inlet and downstream of the rotor exit are shown in Fig. 13 along with the stage total-to-total pressure ratio during the test time period. All of these measurements are very constant during the flow period of interest (118–140 ms). The upstream and downstream flow path temperatures obtained from the rakes are shown in Fig. 14 and are also uniform over the time period of interest, 118–140 ms. Figures 11–14 demonstrate that the overall operation of the experiment can be controlled very well. The relatively small variation from the design point pressure ratio is easily corrected by changing the choke position.

The final figures are presented to illustrate the measured internal cooling pressures and temperatures. Figure 15 shows a time history of the normalized pressure, scaled in this case by the rig operating point pressure to obtain reasonable values before the core flow starts (P_{local}/P_{OP}) for several different internal pressure transducers placed inside the vanes and blades.

Here, one can also see that the internal pressures are stabilized by ~100 ms, with the exception of the vane outer circuit, which has not stabilized in pressure. The vane outer circuit feeds the trailing edge, and this pressure history may indicate that mass flows in each circuit are not balanced correctly. While the pressure in the outer vane circuit is still rising, the changes during the data window are small. Thus, the primary effect of not being balanced in the mass flows is a variance in the operating point from the experimental goal as outlined in Table 1. A slight change in the

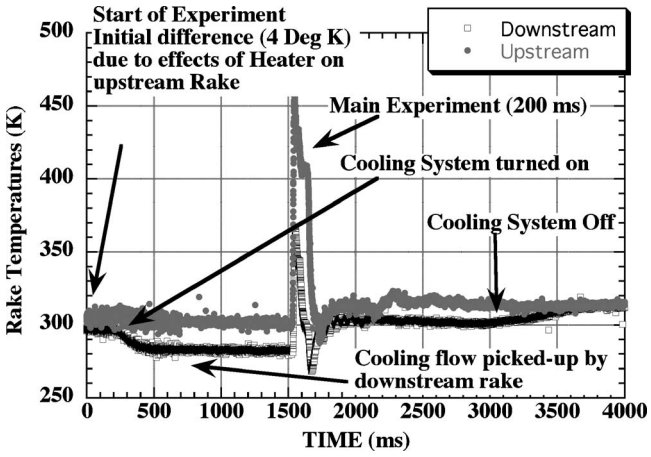

Fig. 11 Cooling experiment time history

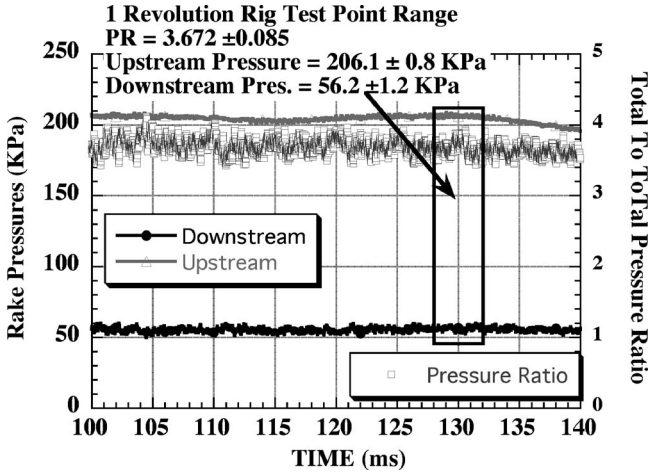

Fig. 13 Overall stage pressures and pressure ratio

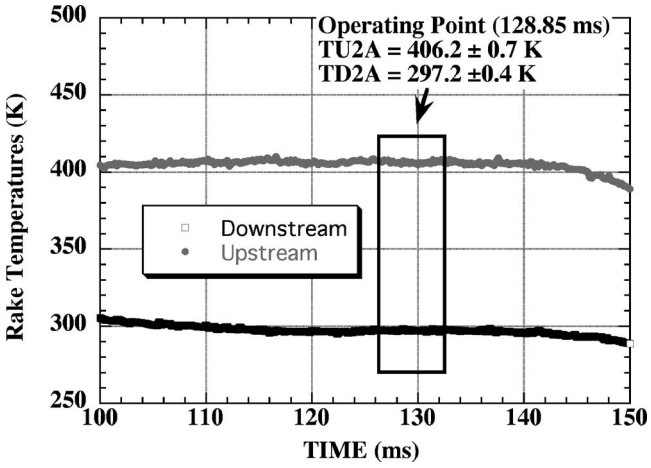

Fig. 14 Rake temperatures at design point

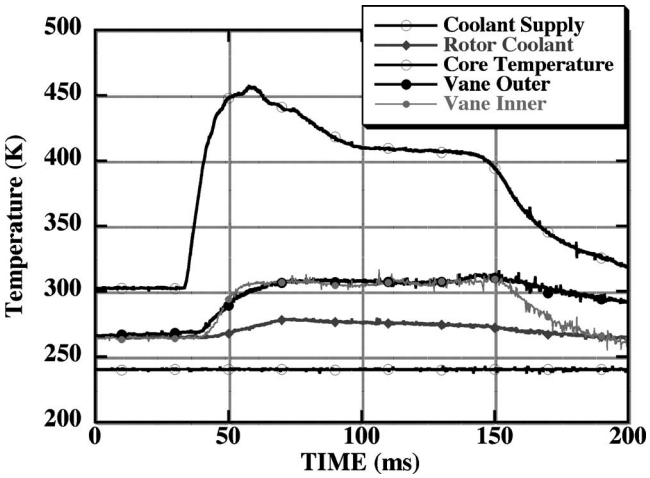

Fig. 16 Internal temperatures

choke (by means of drilling out the hole) in the outer vane coolant line will increase the mass flow here substantially (see Fig. 8). This is primarily an indication that the effective cooling slot area at the vane trailing edge is larger than anticipated. A more detailed discussion of the blowing ratios and mass flows for this experiment are given in Part II [5].

As a companion plot, the vane and blade internal temperatures are shown in Fig. 16. For this particular operational setting, the mass flows were chosen to be low and the temperatures reflect this, with perhaps a partial stalling of the flow during the experiment in the vanes so that the flow slows down and becomes closer to the metal temperature. However, the rotor maintains a higher velocity because it faces a lower external pressure and thus does not increase as much in temperature during the experiment. When running closer to engine design conditions, the higher blowing ratios are obtained by increasing the mass flow rates, which translate into higher pressures in the cooling cavities and should be reflected in smaller increases in coolant plenum temperatures. Low mass flows result in higher coolant temperatures, and thus, this represents a limit for these low Reynolds number conditions. For the higher coolant mass flow rates, the coolant temperatures will be lower due to reduced heat transfer to the coolant flowpath.

Part II [5] compares the time-averaged measured surface pressure distribution with steady predictions for the vane and blade. The reader is referred to Part II [5] for the vane data, but in this part the interaction between the internal and external flow on the blade will be shown as examples of the type of data that is now available to the designer. In Fig. 17, the strong vane passing effects can be seen both on the external pressure transducers and the internal transducers at some locations.

Figure 18 presents the power spectrum of all of the blade internal pressure transducers. A strong signal occurring at vane passing frequency is clearly visible suggesting that the blade internal pressure transducers see the acoustic waves from blade passing. This plot also shows where the sensors are located (see Part II [5] for a better description), but one can see that the three sensors at PI1 location (PRIN33, PRIN34, and PRIN37) all have peak amplitudes at ~0.006, while the two sensors at PI4 (PRIN35 and PRIN38) seem to dominate at about 0.009. This provides some idea of the uniformity across different blades in the frequency spectrum. When comparing these values to those of the external pressure sensors (see Part II [5]), they seem small, but they are still not insignificant. Abhari and Epstein [8] suggested that around the leading edge, one could see interactions between the internal and external flows, which is indicated here.

6 Conclusions

The goal of Part I was to document the basic experimental approach, the goals of the measurement program, and the design and implementation of the various new pieces of hardware required to perform a fully cooled turbine experiment. Flow path

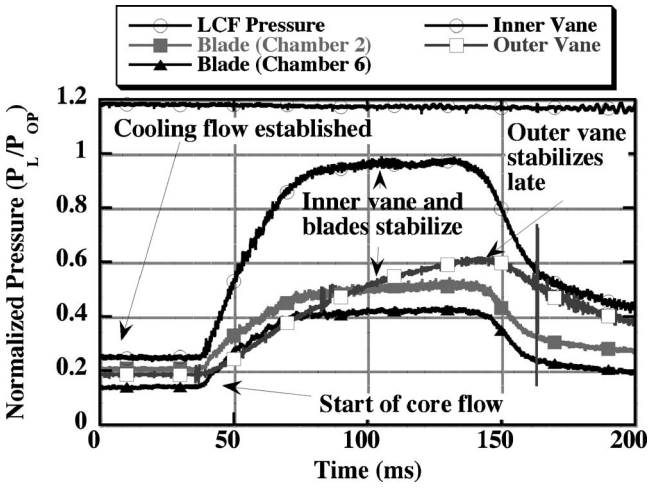

Fig. 15 Cooling gas internal pressures

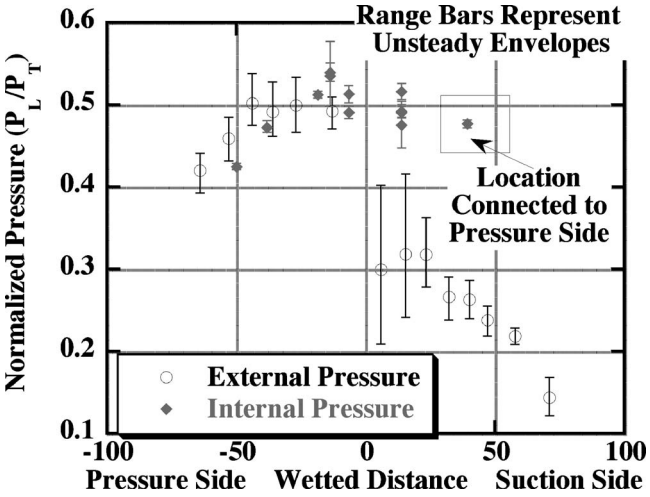

Fig. 17 Normalized rotor pressures

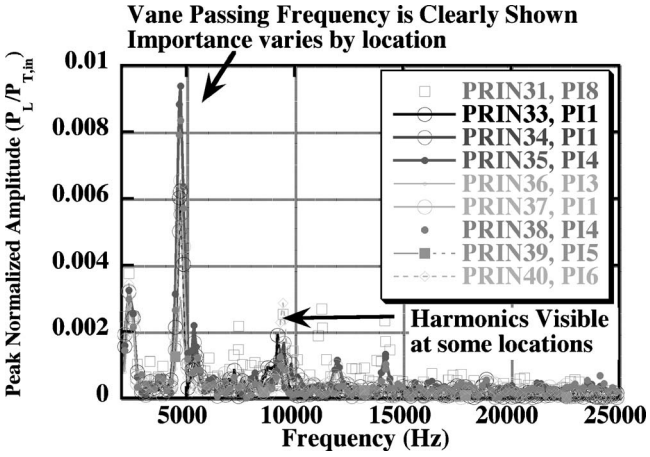

Fig. 18 Power spectrum of internal rotor pressures

measurements have been presented as part of a fully film-cooled turbine stage measurement program as validation of this approach and as an example of the data that are now available from these experiments. The second part of this paper concentrates specifically on the surface pressure and heat flux measurements obtained for the vane and blade surfaces for locations throughout the stage and comparisons of these measurements with predictions.

Measurements presented here for the fully cooled high-pressure turbine stage demonstrate that such measurements can be successfully performed under controlled laboratory conditions. In addition, the measurements presented demonstrate that the flow path conditions are uniform over the operating range of interest.

Acknowledgment

The research reported here was supported by the NASA/DoD URETI for Aeropropulsion and Power at The Ohio State University. The technical monitor for this effort is Ms. Kimlan T. Pham of the NASA Glenn Research Center. The authors would also like to acknowledge the dedicated staff of the OSU GTL for their efforts in preparing the instrumented turbine stage and for helping in completion of the measurements. The authors also thank their friend Reza Abhari, who was heavily involved in the conception and formulation of this experiment when we were all together at Calspan Corporation and at the OSU GTL.

Nomenclature

Experimental Parameters That are Set

PR = pressure ratio measured at rake locations, $P_{T,\mathrm{inlet}}/P_{T,\mathrm{outlet}}$

$\mathrm{TR}_{\mathrm{core}}$ = core to wall temperature ratio, $T_{T,\mathrm{inlet}}/T_{\mathrm{metal}}$

N_{corr} = corrected speed, $N_{\mathrm{phy}}\sqrt{T_{\mathrm{ref}}/T_{T,\mathrm{inlet}}}$ (rpm)

$T_{T,\mathrm{inlet}}$ = total temperature at inlet rake

T_{ref} = reference temperature, 288 K (519 R)

N_{phy} = physical speed of the turbine

FF = flow function, $\dot{m}(P_{\mathrm{ref}}/P_{T,\mathrm{inlet}})\sqrt{T_{T,\mathrm{inlet}}/T_{\mathrm{ref}}}$

P_{ref} = reference pressure, 101.356 KPa (14.7 psia)

TR_x = cooling to wall temperature ratio at location x, $T_{T,\mathrm{inlet}}/T_x$

Mr_x = mass flow fractions, $\dot{m}_x/\dot{m}_{\mathrm{core}}$

BR_x = blowing ratio, $(\rho_x/\rho_\infty)(u_x/u_\infty) \Rightarrow (P_x/P_\infty) \times (\mathrm{Ma}_x/\mathrm{Ma}_\infty)\sqrt{(\gamma_x/\gamma_\infty)(R_\infty/R_x)(T_\infty/T_x)}$

Ma = local Mach number

OTDF = temp profile, $T_{\mathrm{local}}-T_{\mathrm{mean}}/T_{\mathrm{mean}}-T_{\mathrm{wall}}$

RTDF = temp profile, $T_{\mathrm{radial}}-T_{\mathrm{mean}}/T_{\mathrm{mean}}-T_{\mathrm{wall}}$

T_{radial} = temperature at a given radial location averaged circumferentially

Re = Reynolds number, $(\dot{m}/A)(1/\mu)L$

A = choke area

L = characteristic length (1 m)

Experimental Parameters That Are Measured

Net Heat-Flux Reduction

Δq_r = $1-(q_f''/q_0'')$, $\dot{q}_f''/q_0''$= (heat flux of film cooling)/(heat flux without cooling)

Adiabatic Film Effectiveness

η_{ad} = $(T_r-T_{ad})/(T_r-T_c)$, T_c is temperature of coolant

T_r = adiabatic recovery temperature without film cooling

T_{ad} = film-cooled adiabatic surface temperature

References

[1] Han, J.-C., Dutta, S., and Ekkad, S., 2000, *Gas Turbine Heat Transfer and Cooling Technology*, Taylor and Francis, London.

[2] Haldeman, C. W., Krumanaker, M., and Dunn, M. G., 2003, "Influence of Clocking and Vane/Blade Spacing on the Unsteady Surface Pressure Loading for a Modern Stage and One-Half Transonic Turbine," ASME J. Turbomach., **125**, pp. 743–753.

[3] Clark, J. P., Stetson, G. M., Magge, S. S., Ni, R. H., Haldeman, C. W., Jr., and Dunn, M. G., 2000, "The Effect of Airfoil Scaling on the Predicted Unsteady Loading on the Blade of a 1 and 1/2 Stage Transonic Turbine and a Comparison With Experimental Results," ASME Paper No. 2000-GT-0446.

[4] Clark, J. P., Aggarwala, A. S., Velonis, M. A., Gacek, R. E., Magge, S. S., and Price, F. R., 2002, "Using CFD to Reduce Resonant Stresses on a Single-Stage, High-Pressure Turbine Blade," ASME Paper No. 2002-GT-30320.

[5] Haldeman, C. W., Mathison, R. M., Dunn, M. G., Southworth, S. A., Harral, J. W., and Heltland, G., 2008, "Aerodynamic and Heat Flux Measurements in a Single-Stage Fully Cooled Turbine—Part II: Experimental Results," ASME J. Turbomach., **130**(2), p. 021016.

[6] Takeishi, K., Aoki, S., Sato, T., and Tsukagoshi, K., 1991, "Film Cooling on a Gas Turbine Rotor Blade," ASME Paper No. 91-GT-279.

[7] Dring, R. P., Blair, M. F., and Joslyn, H. D., 1980, "An Experimental Investigation of Film Cooling on a Turbine Rotor Blade," ASME J. Eng. Power, **102**, pp. 81–87.

[8] Abhari, R. S., and Epstein, A. H., 1992, "An Experimental Study of Film Cooling in a Rotating Transonic Turbine," ASME Paper No. 92-GT-201.

[9] Kercher, D. M., 1998, "A Film-Cooling CFD Bibliography: 1971–1996," Int. J. Rotating Mach., **4**(1), pp. 66–72.

[10] Kercher, D. M., 2000, "Turbine Airfoil Leading Edge Film Cooling Bibliography," Int. J. Rotating Mach., **6**(5), pp. 313–319.

[11] Elovic, E., and Koffel, W. K., 1983, "Some Considerations in the Thermal Design of Turbine Airfoil Cooling Systems," Int. J. Turbo Jet Engines, **1**, pp. 45–66.

[12] Dunn, M. G., Rae, W. J., and Holt, J. L., 1984, "Measurement and Analysis of Heat Flux in a Turbine Stage—Part II: Discussion of Results and Comparison With Prediction," ASME J. Eng. Gas Turbines Power, **106**, pp. 234–240.

[13] Hildritch, M. A., and Ainsworth, R. W., 1990, "Unsteady Heat Transfer Measurements on a Rotating Gas Turbine Blade," ASME Paper No. 90-GT-175.

[14] Guenette, G. R., Epstein, A. H., Giles, M. B., Hanes, R., and Norton, R. J. G., 1989, "Fully Scaled Transonic Turbine Rotor Heat Transfer Measurements," ASME J. Turbomach., **111**, pp. 1–7.

[15] Denos, R., Arts, T., Paniagua, G., Michelassi, V., and Martelli, F., 2000, "Investigation of the Unsteady Rotor Aerodynamics in a Transonic Turbine Stage," ASME Paper No. 2000-GT-435.

[16] Haldeman, C. W., Dunn, M. G., MacArthur, C. D., and Murawski, C. G., 1992, "The USAF Advanced Turbine Aerothermal Research Rig (ATARR)," *Heat Transfer and Cooling in Gas Turbines* (AGARD Conference Proceedings 527), AGARD, Neuilly Sur Seine, Franace, pp. 20-1–20-14.

[17] Abhari, R. S., and Epstein, A. H., 1992, "An Experimental Study of Film Cooling in a Rotating Transonic Turbine," ASME Paper No. 92-GT-201.

[18] Epstein, A. H., Guenette, G. R., Norton, R. J. G., and Yuzhang, C., 1985, "High Frequency Response Heat Flux Gauge," Rev. Sci. Instrum., **57**(4), pp. 639–649.

[19] Haldeman, C., 1989, "An Experimental Study of Radial Temperature Profile Effects on Turbine Tip Shroud Heat-Transfer," Aeronautical and Astronautical Engineering Dept., MIT, Cambridge, MA.

[20] Shang, T., Guenette, G. R., Epstein, A. H., and Saxer, A. P., 1995, "The Influence of Inlet Temperature Distortion on Rotor Heat Transfer in a Transonic Turbine," AIAA Joint Propulsion Conference, San Diego, CA.

[21] Shang, T., and Epstein, A. H., 1997, "Analysis of Hot Streak Effects on Turbine Rotor Heat Load," ASME J. Turbomach., **119**(July), pp. 544–553.

[22] Kerrebrock, J. L., and Mikolajczak, A. A., 1970, "Intra-Stator Transport of Rotor Wakes and its Effect on Compressor Performance," ASME J. Eng. Power, **92**, pp. 359–368.

[23] Lakshminarayana, B., 1975, "Effects of Inlet Temperature Gradients on Tur-

bomachinery Performance," ASME J. Eng. Power, **97**, pp. 64–74.
[24] Haldeman, C. W., Mathison, R. M., and Dunn, M. G., 2004, "Design, Construction, and Operation of a Combustor Emulator for Short-Duration High-Pressure Turbine Experiments," AIAA Joint Propulsion Conference, Fort Lauderdale, Paper No. AIAA-2004-3829.
[25] Barringer, M. D., Thole, K. A., and Polanka, M. D., 2004, "Developing a Combustor Simulator for Investigating High Pressure Turbine Aerodynamics and Heat Transfer," presented at ASME Turbo Expo, Vienna.
[26] Chana, K. S., Hurrion, J. R., and Jones, T. V., 2003, "The Design, Development and Testing of a Non-Uniform Inlet Temperature Generator for the QinetiQ Transient Turbine Research Facility," ASME Paper No. GT2003-38469.
[27] Miller, K. L., and Crawford, M. E., 1984, "Numerical Simulation of Single, Double and Multiple Row Film Cooling Effectiveness and Heat-Transfer," ASME Paper No. 84-GT-112.
[28] Tafti, D. K., and Yavuzkurt, S., 1987, "Prediction of Heat Transfer Characteristics for Discrete Hole Film Cooling for Turbine Blade Applications," ASME J. Turbomach., **109**, pp. 504–511.
[29] Neelakantan, S., and Crawford, M. E., 1995, "Prediction of Film Cooling Effectiveness and Heat Transfer Due to Streamwise and Compound Angle Injection on Flat Surfaces," ASME Paper No. 95-GT-151.
[30] Neelakantan, S., and Crawford, M. E., 1996. "Prediction of Effectiveness and Heat Transfer Using a New 2-D Injection and Dispersion Model of the Film Cooling Process," ASME Paper No. 96-GT-224.
[31] Weigland, B., Bonhoff, B., and Ferguson, J. R., 1997, "A Comparative Study Between 2D Boundary Layer Predictions and 3D Navier-Stokes Calculations for a Film Cooled Vane," presented at ASME National Heat Transfer Conference.
[32] Leylek, J. H., and Zerkel, R. D., 1994, "Discrete-Jet Film Cooling: A Comparison of Computational Results With Experiments," ASME J. Turbomach., **116**, pp. 358–368.
[33] Abhari, R. S., 1996, "Impact of Rotor-Stator Interaction on Turbine Blade Film Cooling," ASME J. Turbomach., **118**, pp. 123–133.
[34] Bernsdorf, S., Rose, M. G., and Abhari, R. S., 2005, "Modeling of Film Cooling—Part I: Experimental Study of Flow Structure," ASME Paper No. GT2005-68783.
[35] Burdet, A., Abhari, R. S., and Rose, M. G., 2005, "Modeling of Film Cooling—Part II: Model for Use in 3D CFD," ASME Paper No. GT2005-68780.
[36] Camci, C., 1989, "An Experimental And Numerical Investigation of Near Cooling Hole Heat Fluxes on a Film Cooled Turbine Blade," ASME J. Turbomach., **111**, pp. 63–70.
[37] Murphy, J. S., 2004, "Control of the "Heat-Island" Effect on the Measurement of Pyrex Thin-Film Button Gauges Through Gauge Design," M.S. thesis, Mechanical Engineering Department, Ohio State University.
[38] Eaton, J., 2000–2004, private communication about turbulence grid.
[39] Dunn, M. G., 1986, "Heat-Flux Measurements for the Rotor of a Full-Stage Turbine—Part 1: Time-Averaged Results," ASME J. Turbomach., **108**, pp. 90–97.
[40] Dunn, M. G., Martin, H. L., and Stanek, M. J., 1986, "Heat Flux and Pressure Measurements and Comparison With Prediction for a Low Aspect Ratio Turbine Stage," ASME J. Turbomach., **108**(1), 108–115.
[41] Dunn, M. G., Moller, J. C., and Steel, R. C., 1989, "Operating Point Verification for a Large Shock Tunnel Test Facility," WRDC-TR-2027, May.
[42] Haldeman, C. W., 2003, "An Experimental Investigation of Clocking Effects on Turbine Aerodynamics Using a Modern 3-D One and One-Half Stage High Pressure Turbine for Code Verification and Flow Model Development," Ph.D. thesis, Aeronautical and Astronautical Engineering Department, Ohio State University.
[43] Haldeman, C. W., Dunn, M. G., Barter, J. W., Green, B. R., and Bergholz, R. F., 2004, "Aerodynamic and Heat-flux Measurements With Predictions on a Modern One and 1/2 Stage High Pressure Turbine," ASME J. Turbomach., **127**, pp. 522–531.

Aerodynamic and Heat Flux Measurements in a Single-Stage Fully Cooled Turbine—Part II: Experimental Results

C. W. Haldeman
R. M. Mathison
M. G. Dunn
S. A. Southworth
J. W. Harral

Gas Turbine Laboratory,
The Ohio State University,
Columbus, OH 43235

G. Heltland
Honeywell Aerospace,
Phoenix, AZ 85034

*This paper presents measurements and the companion computational fluid dynamics (CFD) predictions for a fully cooled, high-work single-stage HP turbine operating in a short-duration blowdown rig. Part I of this paper (Haldeman, C. W., Mathison, R. M., Dunn, M. G., Southworth, S. A., Harral, J. W., and Heltland, G., 2008, ASME J. Turbomach., **130**(2), p. 021015) presented the experimental approach, and Part II focuses on the results of the measurements and demonstrates how these results compare to predictions made using the Numeca FINE/Turbo CFD package. The measurements are presented in both time-averaged and time-accurate formats. The results include the heat transfer at multiple spans on the vane, blade, and rotor shroud as well as flow path measurements of total temperature and total pressure. Surface pressure measurements are available on the vane at midspan, and on the blade at 50% and 90% spans as well as the rotor shroud. In addition, temperature and pressure measurements obtained inside the coolant cavities of both the vanes and blades are presented. Time-averaged values for the surface pressure on the vane and blade are compared to steady CFD predictions. Additional comparisons will be made between the heat transfer on cooled blades and uncooled blades with identical surface geometry. This, along with measurements of adiabatic wall temperature, will provide a basis for analyzing the effectiveness of the film cooling scheme at a number of locations.*
[DOI: 10.1115/1.2750678]

1 Introduction

Part I [1] provided the background to this experiment, including the past experimental work that showed the complexity of full rotating cooling experiments. The changes that have been made to The Ohio State University (OSU) Gas Turbine Laboratory Turbine Test Facility (TTF) to support the cooling experiments were described. In addition, Part I [1] reviewed some of the lineage of the computational aspects of turbine cooling analysis and the need for design code validation. Part I [1] also described the experimental goals of this effort and the relationship among film cooling measurements, combustor temperature profiles, and turbulence measurements through a five-phase experimental approach. As such, none of this discussion will be repeated here. This paper examines the details of an experiment performed at a low Reynolds number condition. Data provided include the internal cooling pressures and temperatures corresponding to the external surface pressure and heat flux throughout a single-stage fully cooled turbine operating at design corrected conditions. The data are useful to those interested in the interaction between the internal cooling flow and the external flow field in a realistic environment. In addition, those individuals who are currently developing advanced cooling models may also find these results of interest. Steady-state predictions using a commercial design code are provided as a reference. This data set represents the largest set of cooling data obtained for a rotating turbine stage to date available in the public literature.

1.1 Experimental Setup. The turbine used in these experiments is a modern high-pressure turbine stage manufactured by Honeywell Engines. It is a single-stage transonic machine with a moderate pressure ratio. The rig configuration in the area of the turbine stage is shown in Fig. 1.

In this experimental setup, there are three separate cooling streams (the rotor, vane inner, and vane outer), all of which can be controlled externally. The cooling streams share a common supply source with mass flow to each circuit limited by venturi chokes. Small changes occur in the supplied conditions at the vanes and blades due to different internal losses in the piping. It is also possible to control the relative temperature between the streams by changing the length of the connecting tubes. This system utilizes a set of bearings on each side of the rotor and two slip-ring units (500 wires total) to obtain the rotating measurements. More details of the rig and its operation are given in Part I [1].

1.2 Instrument Locations. The stage is heavily instrumented with an emphasis on the blades. The vane is instrumented at 50% span with both heat-flux gauges and pressure transducers and with film heaters so that the wall temperature can be set for individual experiments in order to obtain the adiabatic film-cooled wall temperatures.

Twenty-two of the thirty-eight rotor blades carry some type of instrumentation. A list of what is available is provided in Table 1. Several measurements were repeated on different blades to check for uniformity within the stage and also to provide some measure of redundancy.

The vane has 16 pressure transducers mounted at 50% span with 8 on the pressure surface, 7 on the suction surface and one repeat location. The internal pressures are mounted in the endwall areas of the vane ring. The internal temperatures are mounted in a similar location. The vane also has 16 heat flux gauges mounted at the 50% location in locations similar to the pressure transducers.

The blade has a much more complete instrumentation package, as shown in Table 1. Four internal thermocouples are mounted at the root of the blade measuring the gas temperature entering

Contributed by the International Gas Turbine Institute of ASME for publication in the JOURNAL OF TURBOMACHINERY. Manuscript received July 13, 2006; final manuscript received July 17, 2006; published online March 24, 2008. Review conducted by David Wisler. Paper presented at the ASME Turbo Expo 2006: Land, Sea and Air (GT2006), May 8–11, 2006, Barcelona, Spain.

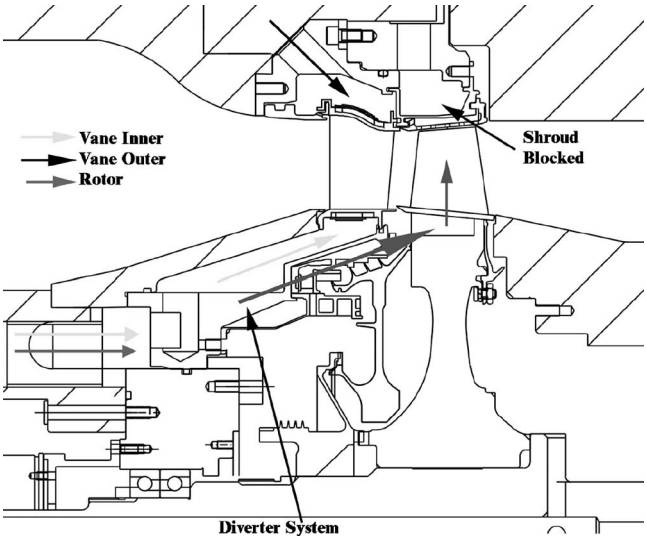

Fig. 1 Sketch of flow path in vicinity of stage

chamber 2 (see Fig. 2). Cartridge heaters are installed in the uncooled blades in order to obtain the uncooled adiabatic wall temperatures. Two of the film-cooled blades have HFGs located in the recessed tip. The stationary shroud (or blade outer air seal) is also instrumented with HFGs and pressure transducers.

A sketch of the blade cooling system is shown in Fig. 2 (not to scale). The main features of this configuration are that the cooling flow enters two main chambers (2 and 3). The flow in chamber 2 exits through chamber 1, where it feeds cooling rows B–F. The cooling flow enters chamber 3, moving hub to tip, then feeds chambers 4–7 before it exits out the trailing edge, feeding cooling rows A, G, and H along the way. In chamber 4, the flow moves from tip to hub, and in chamber 5, it moves from hub to tip, and the pattern repeats itself (see Fig. 2 for flow direction). Internal pressure transducers are mounted in each chamber with the exception of chamber 7 (due to size restrictions). The internal pressure measurement in chamber 1 is repeated on several blades to verify uniformity.

Table 1 Rotor instrumentation locations

Span (%)	External press (cooled)	Internal press. (cooled)	External HFGs (cooled)	External HFGs (uncooled)	Internal temps
0					4
15			14		
50	17	11	43	9	
90	14		20	12	

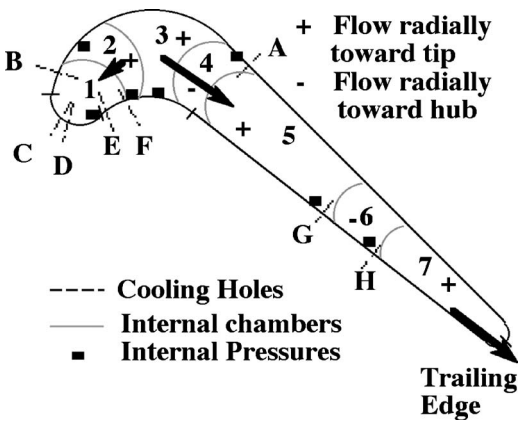

Fig. 2 Blade internal cooling passage sketch (not to scale, with internal pressures)

Table 2 Operating conditions

Property	Rig operating point	Rig set point
Total pressure ratio	3.672 ± 0.085	Not available
Corrected speed (rpm)	9719	9719
T_{core}/T_{metal}	1.39	1.40
$T_{cooling}/T_{metal}$	0.883	Rotor = 0.893 Vane inner and outer = 1
Mass flow ratio (vane inner to vane outer)	1.816	2.44
Mass flow ratio (vane inner to rotor)	1.057	1.03
OTDF max	2.9%	0% (uniform)
Reynolds No.	17.6×10^6	17.15×10^6

2 Experimental Conditions

2.1 Stage Conditions. The operating point for the reported measurements is a low Reynolds number case matching the proper design corrected speed and flow function. The coolant mass flows were set to the lowest cooling mass flow case of interest to verify the overall resolution of the system by looking at low heat transfer rates. The overall operational condition was provided and discussed in more detail in Part I [1] and is shown in Table 2 as a reference. Note that the experimental Reynolds number (which is provided using a reference length of 1 m and is based on the mass flow through the machine, is a little less than half the design Reynolds number, showing that this is a low Reynolds number case, as intended.

The overall mass flow rates were reduced from the nominal condition for this experiment, while maintaining the ratios of each coolant stream. The overall temperature ratios were reduced as well, which led to a reduction of the heat transfer loads. Most of the properties were maintained with the exception of the vane outer mass flow, which was lower than expected. Since this experimental condition was a verification point for the overall system resolution, the low vane outer mass flow is not an issue.

2.2 Data Reduction. The primary data reduction procedure is fairly standard. The high-frequency data are sampled at 100 KHz and is acquired using 45 KHz Butterworth anti-aliasing filters. The pressure transducers are calibrated through the entire data recording system against a Heise HPO 150 psia (0.05% accurate) pressure standard just prior to the experiment by pressurizing the dump tank containing the entire rig. Pressure transducers are checked for any large rotating effects by examining the initial pressures before the external flow reaches the sensors. The spanwise averaged inlet total pressure (five pressure sensors per rake) is generally used to normalize the local pressure measurements for presentation purposes. No other processing (such as external filtering or averaging) is performed.

The heat-flux data are primarily acquired using double-sided Kapton sensors. These use a different numerical technique to calculate the heat flux compared to the standard Cook-Felderman technique used to generate heat flux from semi-infinite heat transfer situations involving single-sided sensors. The numerical techniques are not new and have a long history, starting with Skinner in 1960 [2] and progressing to Oxford in 1980 [3]. In 1985, Epstein et al. [4] implemented this procedure numerically at MIT in support of the double-sided Kapton sensors that were being developed. This technique was modified and combined with the traditional Cook-Felderman techniques and calibrations used with the single-sided sensors used at Calspan in 1994 by Weaver et al. [5]. At OSU, these techniques have been refined and modified to sup-

port a wider variety of sensors and have been incorporated into standard LabView code as described by Cohen [6], where a more detailed explanation of how the algorithms work can be found.

Like the pressure data, the heat-flux data were all sampled at 100 KHz with anti-aliasing filters applied. The data were acquired using constant current power supplies, which have a 1% roll-off point in the several hundreds of kilohertz range. Heat-flux data are derived quantities that are based on the temperature time histories of the sensors and gauge material properties.

It is important to note that unlike single-sided gauges, double-sided gauges require that both the top and bottom gauges function properly to obtain heat-flux data. In addition, the end product of interest is the net heat-flux reduction as defined by Bogard's group at the University of Texas [7]

$$\Delta q_r = 1 - \frac{q_f''}{q_0''}$$

q_f'' = heat flux in presence of filmcooling

q_0'' = heat flux without cooling

Calculating this value requires four functioning sensors at the same location (top and bottom cooled, and top and bottom uncooled). Even more challenging is the local adiabatic surface temperature that must be determined for more detailed analysis of the cooling flows, such as derivation of the heat-transfer augmentation factor and adiabatic film effectiveness as proposed by Abhari [8]

$$\varepsilon = \frac{\mathrm{Nu}_{fc}/\mathrm{Nu}_0}{1 - \theta\eta_{ad}}$$

$$\varepsilon = \frac{\text{heat transfer coefficient (cooled)}}{\text{heat transfer coefficient (uncooled)}} = \frac{h_{fc}}{h_0}$$

$$\theta = \text{nondimensional coolant temp} = \frac{(T_r - T_c)}{(T_r - T_w)}$$

$$\eta_{ad} = \frac{(T_r - T_{ad})}{(T_r - T_w)}$$

T_r = adiabatic recovery temperature without film cooling

T_{ad} = film-cooled adiabatic surface temperature

T_c = temperature of coolant

Nu_x = Nusselt number based on blade axial chord

Inlet total temperature and thermal conductivity at wall

The local adiabatic surface temperature is usually derived via several independent experiments by changing the wall temperature, measuring the local heat flux, and extrapolating on the data to the wall temperature at zero heat flux. At a minimum, this usually requires three experiments to achieve. Thus, the same four gauges must function over three different experiments in order to produce one part of this data set. The challenge imposed by cooling experiments is not just understanding the flow, but also ensuring that all the instrumentation survive in a usable fashion to get the most from the data set.

2.3 Time-Averaged Versus Time-Accurate Data. Data presented in this paper will focus on both the time-averaged and time-accurate components. The procedure for processing the data has been described extensively by Haldeman [9] and will not be described in great detail here. The main implications are that all the data acquired are time-resolved data and that basic numerical processing is done over parts of the data (the data window) to obtain the information used for the analysis. Most of the definitions are straightforward, but one point that will be re-emphasized is that there are often many ways to characterize the time-resolved data. Power spectrums of the data are obtained, and the amplitudes of the signals at the fundamental frequency (blade or vane passing) are often used as indicators of the time-resolved data. However, as pointed out by Haldeman et al. [10,11], this can lead to an underprediction of the amplitude due to the fact that many of the higher-order harmonics contribute to the overall shape of the unsteadiness. Thus, the alternative of using the envelope magnitude (the average maximum minus the average minimum when the data are ensemble averaged) will also be used to provide an estimate of the unsteady effects.

The pressue envelopes are created by splitting a revolution (or multiple revolutions) of data up into the appropriate number of passages (if looking at blade data, then it would be the number of vanes), and then combining all the passages together to get an average value. For ease of viewing the passage is repeated so that one sees two passages together. More details on this method can be found in [9].

2.4 Uncertainty Analysis and Data Accuracy. Throughout this paper, the data will be presented with range bars, which may imply different connotations based on what information is trying to be presented. In each figure, though, there may also be a statement of the individual sensor accuracy based on error propagation, calibration accuracy, etc. The basic definitions for the data presented in the range bars will be shown below, as well as the derivation of the calibration accuracy for the different measurements. Each figure will describe which type of range bar is being used.

(a) Unsteady envelopes—having the range bars indicate the unsteady envelopes helps show the impact of unsteadiness on the data, as in the averaging procedure all the nonharmonic noise is canceled out and only the envelopes are left.

(b) Standard deviation of the average—when the range bars are used in this manner they describe the stability of the variable, but not its absolute accuracy. One has to be careful here in that often the unsteadiness will dominate these ranges. In some cases, what is plotted is the traditional 95% confidence limit of ± 2 standard deviations, which provides a much closer estimate for the real range of the data. Performing a pure maximum minus minimum range is subject to over estimation due to spurious nose in the signals.

(c) Accuracy range—this takes the propagated measurements and calculates the accuracy of the derived property using a standard method of root sum squares (rss). With lots of data, one can statistically do this, checking for Gaussian distribution and then creating a standard deviation of each property, which provides a confidence limit on the resultant (e.g., the resultant is $x \pm 2^* y$, to within 95% confidence limit). However, with smaller amounts of data, the accuracies are generally stated as limits and then propagated to provide a final answer, which is the method used here.

As multiple runs are developed over the course of the main experimental matrix, the uncertainties from individual runs, such as shown here, become the weighting factor as values are combined to derive a weighted average for the experimental condition. The range on this value is then checked against the propagated uncertainties of the individual components to assure there are no missing parts of the process (as shown by [9]). Thus, although the values shown in this paper are for a single run, they will form the basis of the uncertainty analysis in the future.

2.4.1 Pressure Accuracy. For the measurements presented in this work, the pressure sensors were calibrated before the experiment, in the facility against a Heise HPO 1034 KPa (150 psia)

0.05% accurate pressure sensor. In addition, prior to the experiment, the sensors had been calibrated many times looking for long-term stability. Overall pressure accuracy is ~1 KPa (±0.15 psia) over the calibrated range of the sensors of 0–310 KPa (0–45 psia). This accuracy is generally a worst case, with most of the sensors providing improved accuracy. Given the input total pressure, the overall calibration accuracy (including the stability of the A/D system and the power supplies, the overall accuracy in terms of inlet total pressure is about ±0.005, or ~0.5% of inlet total pressure. This value can be compared directly to the range bars on the pressure data given in the figures. For Fig. 5, which has the data presented in terms of the coolant supply pressure, the value is 0.004 (since the coolant supply pressure is higher).

2.4.2 Temperature Accuracy. For the Kapton heat-flux sensors, linear calibrations were used which generally result in a calibration accuracy of about ±0.3 K over a range of 300–380 K. The Kapton sensors are nickel-based and exhibit a relatively large quadratic behavior when compared to our more traditional Pyrex® sensors, which would be accurate to ±0.1 K over this same range. In the future, quadratic calibration may be employed to improve the overall accuracy if needed. However, as will be shown in Fig. 10, all the heat-flux sensors were within ±0.5 K of each other at the beginning of the experiment (when the rig was at a constant temperature), which supports the overall claim of the ±0.3 K accuracy of the calibrations when one accounts for small variations of initial temperature in the rig.

2.4.3 Heat-Flux Accuracy. Even with gauges perfectly calibrated for temperature, the conversion to heat flux requires several parameters that are a function only of the gauge material and the installation. In practice, these calibrations are difficult to characterize, having first been attempted by Epstein et al. at MIT [4]. More recently, Murphy [12] revisited this problem and proceeded with some alternative procedures to calibrate the current group of sensors at OSU. The values reported by Murphy are used for the reduction of the measurements reported.

Although Murphy found that overall calibration accuracy was about ± 5% of reading for the current set of gauges over the range of Reynolds number typically used in a turbine measurements, the main source of time-dependent variation (as shown later in Fig. 11) comes from numerical noise. Cohen [6] spent considerable effort investigating techniques that could be used to reduce the noise generated by the numerical schemes. Traditionally, multiple runs are used to quantify the variation in the time-averaged value of the heat flux. For previous experiments, the range bars, indicated by ± the standard deviation of the data, tended to overestimate the error in the repeatability of the sensor. For the data reported, this range will be plotted with the 5% accuracy value included in the plot as a reference value. Propagating this uncertainty into an uncertainty in the net heat flux reduction parameter results in an uncertainty of ~7.1% of reading

3 Computational Information

The goal of the computational study is to verify and calibrate the CFD code and associated modeling being used against the measurements. The CFD code, FINE/TURBO, is a Reynolds-averaged Navier-Stokes (RANS) based code capable of making steady or time-accurate calculations; in this paper only the steady results will be presented. More background information on the CFD code is provided in Sec. 3.1, as well as a discussion of the implementation procedure (as opposed to the computational modeling). The objective was to obtain pressure-loading predictions for the full stage HPT and compare to the experimental data as a means of providing confidence in the code's prediction capabilities before beginning the heat transfer predictions and comparisons. Subsequently, the goals of the computational study are provided and future plans for the CFD analysis are discussed.

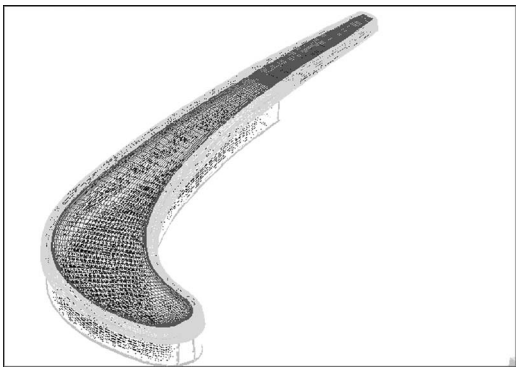

Fig. 3 Blade tip grid blocks (O-mesh)

3.1 FINE/TURBO Background. The CFD analyses used NUMECA's time-accurate and steady code, FINE/TURBO. As the name indicates, FINE/TURBO is a code configuration specialized for turbomachinery. The flow solver is a multipurpose code for 2D and 3D flows in complex geometries and utilizes the Reynolds-averaged Navier-Stokes equations. The preprocessor, solver, and post-processor are bundled into one software system, FINE, which is capable of completing the simulation from grid generation to visualization.

The CFD analyses used the steady, 3D, viscous code that solves the RANS equations in Cartesian coordinates. The flow solver is capable of treating flows that can be modeled as inviscid (Euler) or as viscous (laminar or turbulent Navier-Stokes), but only the turbulent Navier-Stokes model is used for this work. The turbulence model used is the k-ε extended wall function model. For this k-ε model, the y^+ value should be in the range of $15 < y^+ < 100$. The y^+ range used varies from 0 to 140 with the majority of the values within the desired range (15–100). The y^+ values tend to be higher within the tip region, which is where the values over 100 are all occurring. This should not raise concern as the tip clearance flow consists of thoroughly sheared vortical fluid that undergoes significant acceleration and is therefore quite different than a standard boundary layer. More details of the FINE/TURBO code can be found in Hakimi [13].

3.2 Computational Modeling. The meshing process for the set of multiblock grids is quite sophisticated. The inlet and vane blocks are made of HOH-mesh grids using the FINE/IGG AutoGrid automated meshing tool. The blade block is made of an H&I-mesh grid also made in AutoGrid. An external grid process was developed at Honeywell to automatically create tip cavity, tip cap, and plenum blocks. These blocks are all O-mesh grids and among these three blocks shown in Fig. 3, there are 165,039 cells in the blade tip alone. The vane consists of ~271,000 cells, and the blade, not including the tip region, contains over 269,000 cells, for a total of over 730,000 cells making up the entire model shown in Fig. 4. The cooling flows and rim leakage flows were introduced as source terms in the model. The model boundary conditions were obtained from the measured data set, which uses a uniform inlet total temperature and total temperature condition.

3.3 CFD Future Plans. The initial predictions and comparisons made were the pressure loading on the vane and blade. The steady data were extracted from the CFD, and solution results indicated that changes in the grid refinement and replacement of generic boundary conditions with the measured boundary conditions were required to match the experimental measured stage pressure ratio. Both adiabatic and isothermal cases have been run with cooling and without cooling, but the cooling cases are being examined further due to unexpected behavior with the blade suction-side predictions. A new release of FINE/TURBO has an update to the cooling injection model that may influence the solution

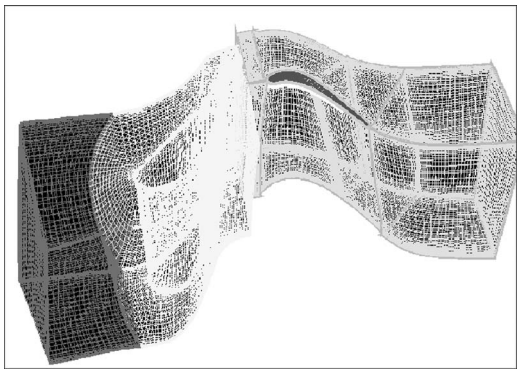

Fig. 4 Entire meshed model, including blocks for inlet, vane, blade, and tip grids

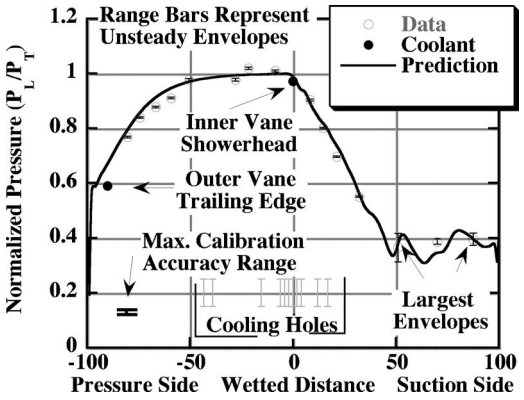

Fig. 6 Vane Time-average pressures 50% span

results. Upon completion of the steady model, the time-accurate model will be run using the same set of adiabatic, isothermal, cooled, and uncooled cases.

4 Data and Analysis

4.1 Internal Pressures and Temperature. The internal rotor pressures provide an interesting measure of the effect of rotation on the internal cavity pressures. Two conditions were compared, one with the rotor operating at design corrected speed, and a second with the rotor stationary. In both cases, the data were examined when the rotor was in a vacuum and there was no external flow (thus, the coolant flow was choked at the cooling holes, as well as at the mass-flow metering point). The blade internal cooling pressures were normalized by the source coolant supply pressure, accounting for variations in the temperature between the cases. The reduced data are shown in Fig. 5. The range bars represent ± 2 standard deviations of the data, which represent the realistic range of the data, and are small and difficult to see on this plot. As a comparison, the maximum range one would expect the pressure to deviate due to calibration is ± 0.004 (see Sec. 2.3) and is shown in the box in the figures. One can see that while the data seem stable enough from the range bars over the time averaged, the spread in data at location PI1 can be explained by calibration accuracy.

The internal pressure locations (see Fig. 2) have been indicated as a function of wetted distance. Toward the leading-edge area ($\pm 20\%$ WD), where the blade is thickest, the biggest effect of rotation is observed. For transducers mounted on the pressure side of the blade (PI8 and PI4), rotation causes the pressure to increase by $\sim 2\%$ of the supply pressure, which is on the order of ~ 7 KPa (or 1 psi) for the data presented in this paper. For the sensors mounted on the suction surface (PI1), the rotation decreases the pressure. As the blade thins out on both the suction side and pressure side, the rotation effects are not as measurable. In the stationary case (black), PI1 and PI8 are expected to be the same value and the maximum seen in the blade. In the sensor locations that show the largest shift due to rotation (PI4, PI1, and PI8), these shifts are larger than can be explained by the worst-case calibration accuracy range, indicating that this effect is real.

The internal temperatures were provided in Part I [1], and the discussion here will focus on the blowing ratios and mass flows for this experimental condition at one location on the blade as an example of the calculation. The blowing ratio is given as

$$\mathrm{BR}_x = \frac{\rho_x u_x}{\rho_\infty u_\infty} \Rightarrow \frac{P_x M_x}{P_\infty M_\infty} \sqrt{\frac{\gamma_x R_\infty T_\infty}{\gamma_\infty R_x T_x}}$$

This implies that one needs the Mach number distribution around the blade (which is not directly measured but that can be inferred from the external pressure distribution and/or obtained from a CFD calculation). For the rotor suction-side hole at $\sim 45\%$ wetted distance (the "Gill" row), the blowing ratio based on the current conditions for this run was ~ 1.07 with an uncertainty of $\sim \pm 10\%$ based on an error propagation of the basic variables. This uncertainty analysis includes the combined calibration accuracy, prediction stability (Mach number), and signal quality. As described earlier, the blowing ratio at this location was low compared to the design point value of 1.44.

4.2 Vane

4.2.1 Vane Pressure. The vane time-averaged internal and external pressures are shown in Fig. 6 along with the external predictions. An arbitrary reference pressure has been used to normalize the data in Figs. 6 and 7 only; other plots use the inlet total pressure for the normalization factor.

The range envelopes represent the unsteady envelopes taken

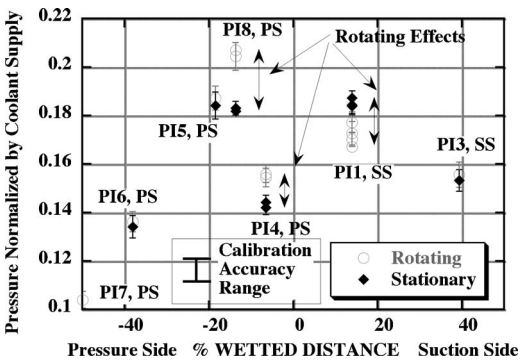

Fig. 5 Rotor internal pressures

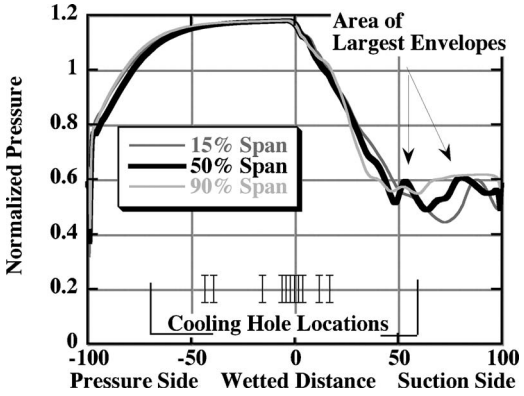

Fig. 7 Vane time-average predictions, various spans

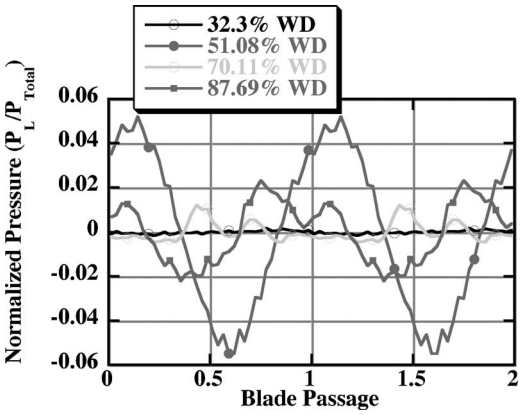

Fig. 8 Vane envelope shapes

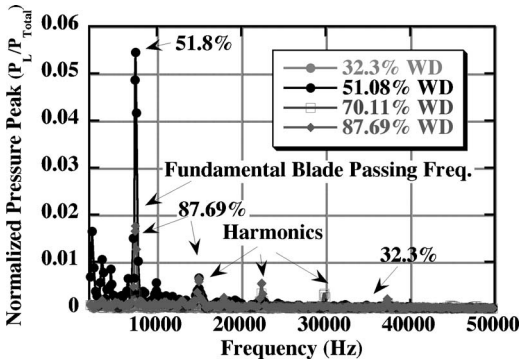

Fig. 9 Vane pressure frequency domain data

over one revolution of data as described earlier. In addition, the calibration accuracy is also shown on the plot. Figure 6 shows that most of the periodic blade effects are evident at the trailing-edge side of the suction surface from ~50% wetted distance back to the trailing edge. To provide a reference, the approximate cooling-hole locations are shown as well. The pressure measurements at the vane inner and outer plenum locations are shown on the plot in red (bold) at the main points of injection (the shower-head area, 0%WD, and at the trailing edge, −90%). The cooling pressures are given as point locations, but it is important to note that the injection occurs at multiple locations. The vane outer plenum injects at the trailing edge, which covers an area from −90% to −100% wetted distance on the pressure side. The vane inner plenum is shown at 0%, the showerhead forms an area about ±10% of wetted distance around the leading edge, and there are cooling holes that go from −40% to ~20%, all of which are fed by this plenum.

A close examination of Fig. 6 shows that on the pressure surface toward the leading edge, there is a small discrepancy between the prediction and the data, which is not typically seen on the vane. This is the area of the cooling holes, and since the current prediction is uncooled, it suggests that the cooling flow may have an influence on the external pressure distribution (~2.3% at −25%WD). At these pressure levels, this represents a difference of ~4.75 KPa (0.7 psia) and while measurable is small. Future experiments will investigate this deviation, since it is close to the maximum error expected due to calibration accuracy. Since pressure measurements were only collected at one vane span location, the behavior at different spans must be investigated through CFD predictions alone. Figure 7 shows that the pressure distribution undergoes some significant changes at different spans over the last half of the blade on the suction surface, which is also the area of the largest unsteady envelopes. It is important to note that, like their uncooled counterparts, the cooled transonic vanes have large periodic pressure fluctuations in this area, especially when compared to their local pressure values. At 50% wetted distance, the pressure fluctuation level is about ±25% of the time-averaged value.

The unsteady pressure envelopes on the trailing-edge suction side are shown in Fig. 8. At 32% wetted distance, there is no coherent signal, but the shape becomes very pronounced at 51%WD before it shrinks back and then becomes larger again at the trailing edge. This is not unusual for a choked vane, where one sees much diminished action upstream of the choke point somewhere between 51% and 32% wetted distance on the suction surface in this case. In addition, the amplitudes aft of the choke point often increase or decrease, depending on the specific geometry of the turbine stage, and this behavior does not seem to be a result of the addition of cooling to the system.

In Fig. 8, the uncertainty estimates of the envelopes have been omitted to aid in the visualization of the data. Some examples of typical uncertainties for this type of procedure are shown in Haldeman [9]. Although the envelopes provide an overall description of the time-dependent data in the time-domain, additional information is available when examining the frequency content as shown in Fig. 9 for the same four sensors.

Here, as in the envelope data, the transducer at 51%WD dominates the spectrum at the fundamental frequency. All the transducers, from 50% aft to the trailing edge, show similar magnitudes in the first and second harmonics. The frequency data for the 32%WD position are buried in the noise on this plot, showing no clear frequency as would be anticipated since this location is forward of the shock location.

The current CFD model predicts the time-averaged pressure well over the vane surface, but being a steady solution, it cannot pickup unsteady fluctuations, which are of interest for structural and cooling issues.

4.2.2 Vane Heat-Flux and Temperature Data. By use of the pre-experiment calibration, the individual heat-flux gauge temperature history can be deduced and used to calculate the heat flux based on a numerical algorithm outlined earlier. The gauge temperatures (both the upper sensor, which is a measure of the film temperature, and the lower sensor, which is close to the metal temperature) provide an indication of how uniform the metal temperature is at the design point (Fig. 10).

In Fig. 10, the range bars on the data represent the ±2 standard deviations of the data over four revolutions. The scale of this figure makes it difficult to see the range bars, which are buried inside the symbols. The bars combine all the time-dependent effects (unsteadiness, noise, etc.) Figure 10 shows that the variation in the lower (or metal) temperature becomes more pronounced with distance from a cooling hole. The small range bars shows that the temperatures are steady over this small time frame. Immediately prior to arrival of the test gas at the turbine location

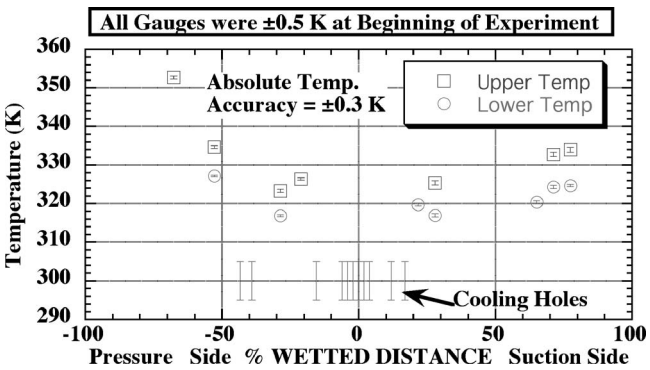

Fig. 10 Vane 50% upper and lower gauge temperatures

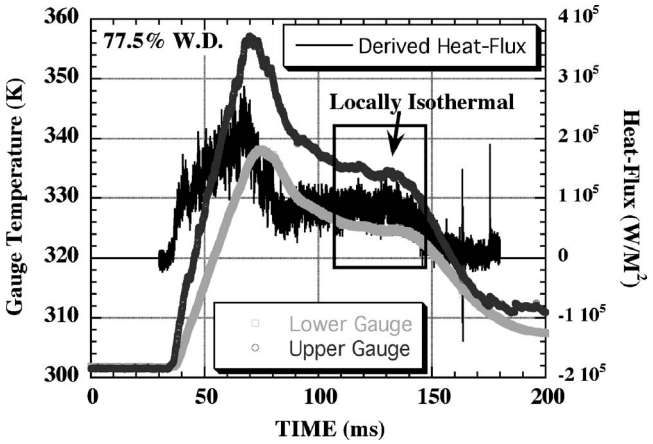

Fig. 11 Time-dependent vane temperature data for gauge located at 50% span and 77.5%WD

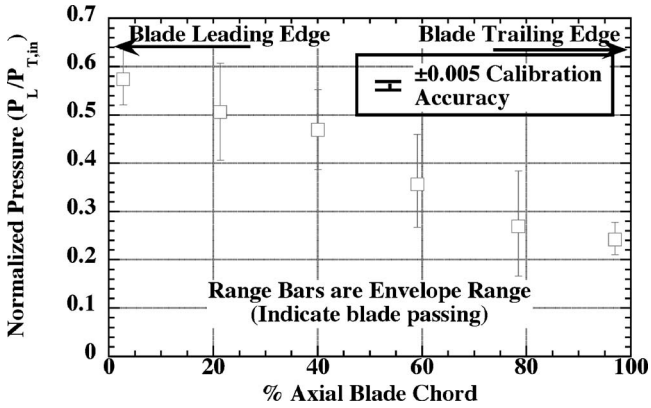

Fig. 13 Time-averaged rotor shroud pressures

(0–38 ms on Fig. 11) all of the heat-flux gauges were reading within ±0.5 K. Thus, the large temperature gradients shown in Fig. 10 did not develop during the ~1500 ms from when the coolant was started to when the data was acquired. Therefore, these gradients develop as a result of the film cooling. The overall calibration accuracy of ±0.5 K is stated on the plot, but it is difficult to see on this scale.

Although the time-averaged temperatures at each location on the vane are different at the design point (as expected since the vane is cooled), the time-dependent data over the entire course of the experiment show that the system remains isothermal during the main part of the experiment when the data are acquired.

Figure 11 illustrates the time history of both the upper and lower temperature sensors along with the derived heat flux for a location of 77.5% wetted distance on the vane. The initial compression heating is evident from 40 ms to ~70 ms after the initial start of data acquisition (which is ~1500 ms after the start of the coolant flow; see Part I [1]). After ~90 ms, the heat flux has stabilized and the temperatures are relatively stable after ~110 ms. This provides a locally isothermal condition over as many rotor revolutions as required for the analysis. The data reported in Fig. 11 are for a sensor far away from the cooling holes. However, a sensor sandwiched between two cooling-hole rows on the pressure side of the vane also showed the same characteristics (with the bottom and top sensor starting at the same temperature), and they are within 0.2 K of these values.

The vane heat flux for the 50% span is given in Fig. 12, which shows that the heat flux is lower on the pressure side where the gauges are more heavily influenced by the cooling holes. Note that the differences in heat flux between the suction and pressure surfaces are minimal at these low cooling rates. In addition, as stated earlier, the overall accuracy of the sensor (about ±5%) is significantly less than the variation generated from the standard deviation of the time-dependent data, and, thus, these range bars are capturing a wide range of effects. The unsteady effects determined by a fast Fourier transform (FFT) show many characteristic vane and blade passing frequencies in the data, but a detailed discussion of the time-dependent heat-transfer data is beyond the scope of this paper and will be addressed in the future.

4.3 Blade Shroud (Blade Outer Air Seal). The blade shroud is a region of high unsteady pressure loading. From about 20% to 80% of the blade axial chord, the magnitude of the unsteady pressure fluctuation is both large and reasonably constant. However, the time-averaged pressure decreases over the same axial chord region (because of work extraction), increasing the importance of the unsteadiness as shown in Figs. 13–15. The normalized shroud pressures are plotted as a function of the blade axial chord in

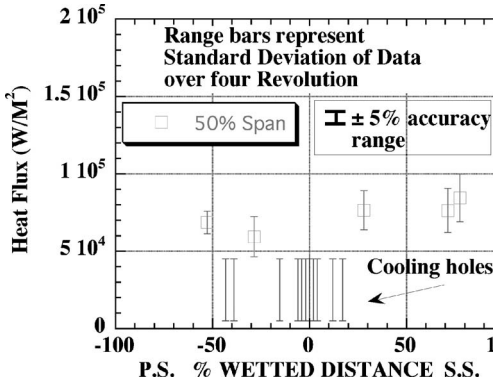

Fig. 12 Vane 50% heat flux

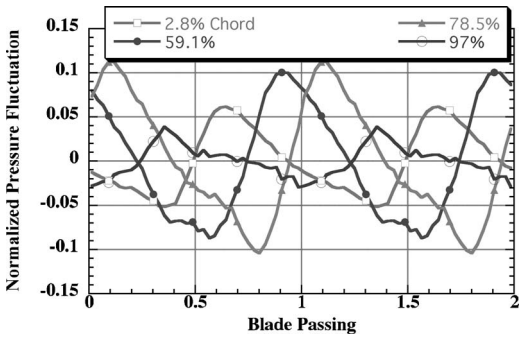

Fig. 14 Rotor shroud pressure envelopes

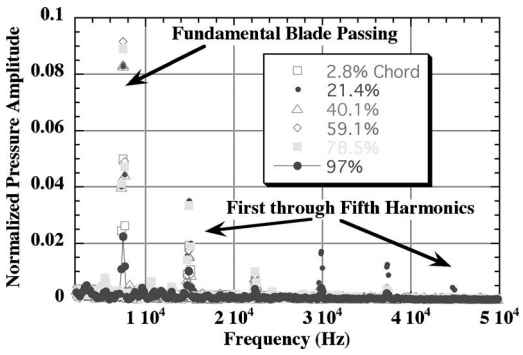

Fig. 15 Rotor shroud time-resolved data

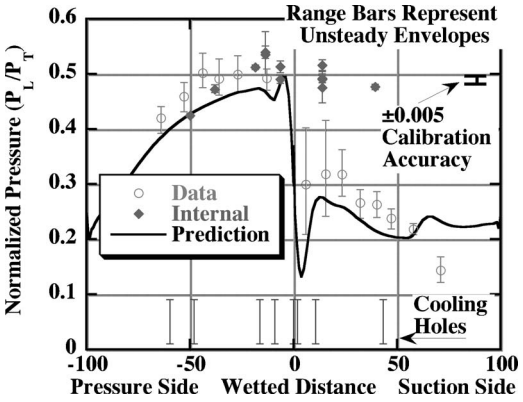

Fig. 16 Blade 50% pressures (internal and external)

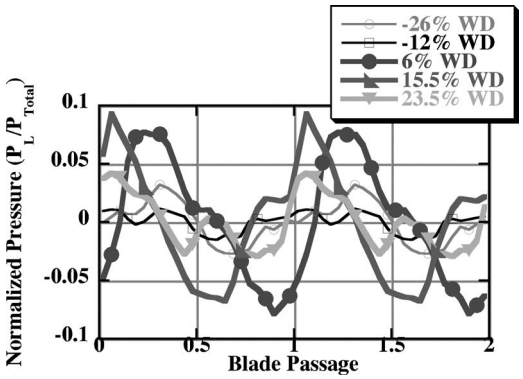

Fig. 17 Blade 50% time-resolved pressure data

Fig. 13.

The range bars represent the envelope size with the overall pressure sensor accuracy shown. At ~80% chord, the envelope size is ~20% of the vane inlet total pressure, and the time-averaged value is only ~27% of that pressure; thus, a variation of almost 100% of the time-averaged value is occurring at this location, illustrating the importance of the unsteady effects.

The unsteady fluctuations responsible for the range bars of Fig. 13 are shown in Fig. 14 for select locations. In this plot, only the periodic signal is shown (the time-averaged value is subtracted out), which provides a good indication of how little the unsteady signal changes over the main part of the shroud.

The leading-edge transducer (shown in red (bold)) is about one-half the amplitude of the transducers at 59.1% and 78.5% axial chord. The phase shift between the signals is due to the time delay that occurs from the blade passing over one sensor and then the other. Although the main amplitudes are similar for the different sensors, higher harmonics are indicated at 59% and 78% sensors, as shown in Fig. 15.

The higher harmonics are visible in the pressure data shown in Fig. 15. Care is needed in interpreting the absolute value of the fifth harmonic, since the anti-aliasing filters of the A/D system may cause some attenuation. Future work will use the new high-frequency spectral dynamics system to look for higher harmonics (see Part I [1]).

4.4 Blade

4.4.1 Blade Pressure. The flow over the blade at 50% span is much more complicated than for the vane. Figure 16 shows the internal and external pressures at this location. The cooling-hole locations are also marked. The range bars correspond to the unsteady envelopes, and as compared to the vane, the envelopes are large over most of the surface, with the largest being at ~10% wetted distance on the suction side. However, the magnitude of the unsteadiness is relatively uniform along the entire pressure surface, which is the region of minimum backflow margin. There are multiple internal cooling pressure measurements at one location, which is represented in some of the spread of the data at ~20% WD. The overall sensor calibration accuracy is also shown, which is comparable to the relatively low level of the spread of data for these sensors. These sensors calibrations are good, but at these low levels the calibration accuracy may be the limiting factor.

The current predictions capture the trend of the data but are lower than the data by ~3% of the inlet total pressure. The predictions and the data do separate at ~70% wetted distance, and unfortunately, the thin blades do not allow instrumentation further toward the trailing edge for further comparison. The largest dip in the prediction, just aft of the leading edge on the suction side, corresponds to the area of highest periodic behavior. It is also critical to remember that these predictions truly were "predictions," where the only data supplied to those doing the CFD were the stage pressure ratio and inlet pressures and temperatures. No refinement was done with the grid or modeling techniques to improve the overall agreement. As such, it represents a fairly good evaluation of how well a nontuned commercially available code (both steady and uncooled) does at predicting the external aerodynamics of a cooled turbine. This does not imply that the predictions cannot be improved, only that in the absence of any other external information, this is the level of agreement one would expect. The reader is left to evaluate whether this is good enough.

A cursory examination of the data reveals that the internal pressure was less than the external pressure on the pressure side and that main flow ingestion may have occurred at this operating condition. However, as shown later in Fig. 19, the pulsation parameters are all positive. This is because in Fig. 16 the actual internal pressures as measured by the sensors are plotted, and not the pressure extrapolated to the exit of the cooling holes. Specifically, the internal pressure at −50% (Fig. 16) corresponds to the location in chamber 6 (Fig. 2), which feeds the very last coolant hole row at about −60% WD. Thus, one has to be very careful about where the pressure measurements are located on these plots (physical sensor location versus injection location). This also shows the advantage of running these low mass flow rates initially since the data from those experiments often reveal issues with the experiment and computations, which are easily masked at higher flow rates.

Samples of the envelopes for the external pressures around the leading edge are provided in Fig. 17. Here, one can see the very large pressure fluctuations caused by the vane/blade interaction, especially on the suction surface. The waveforms are complicated, and frequency detail is given in Fig. 18.

A review of Figs. 17 and 18 shows that both the time and frequency domains can be helpful. The fundamental blade passing amplitudes for both the 6% and 15.5% WD locations are almost

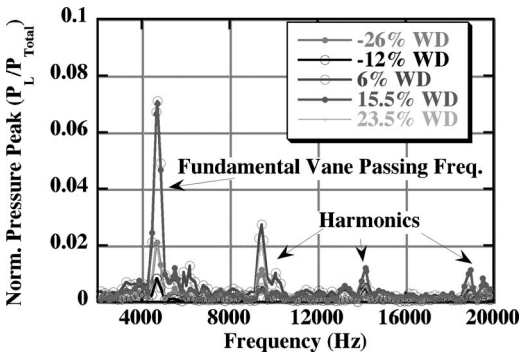

Fig. 18 Blade 50% leading-edge frequency content

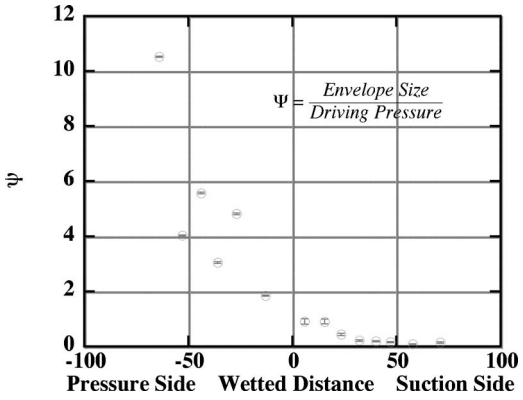

Fig. 19 Pulsation parameter on blade, 50% span

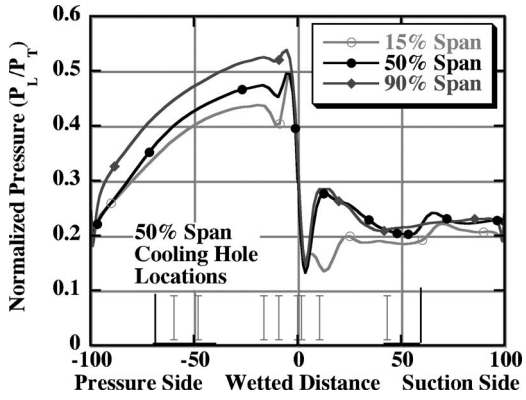

Fig. 20 Blade 15%, 50%, and 90% span steady pressure predictions

7% of total inlet pressure. The first fundamental frequency is missing at the 15.5%WD location, but is made up for in the higher harmonics. It is this component that changes the shape of the data in Fig. 17 and keeps the overall magnitude between the 6% and 15% wetted distances similar. The data at 23.5% show that almost all the energy is split between the fundamental and first harmonic. Higher harmonics are visible between 20 KHz and the 50 KHz Nyquist frequency, but they are much smaller and were not shown on this plot to bring out the resolution at the lower frequencies. However, the time-resolved plot of Fig. 17 is critical to designers who are looking for the integral effect over all the harmonics and are trying to decide on how much cooling margin is needed. Clearly, the values change, moving away from the leading edge, and having the ability to design for the lower margin toward the trailing edge of the blade is useful for higher overall engine efficiencies.

Abhari [8] suggested that one way to look at the unsteady effects on cooling is to examine a "pulsation parameter," which is a measure of how important the unsteady effects are for a given location. His definition of the pulsation parameter relied on using the amplitude of the fundamental blade passing frequency as a measure of the unsteadiness. As pointed out earlier, this can lead to underprediction of the true unsteadiness since the higher harmonics can contribute significantly to the overall envelope size. Thus, the definition has been modified here to take the envelope size as the measure of unsteadiness. The definition used is

$$\Psi_x = \frac{\text{envelope size}}{\text{driving pressure}} = \frac{\max - \min_{\text{envelope}}}{P_{\text{coolant}} - P_x}$$

In this equation, the coolant pressure is taken from the cavity driving the cooling hole immediately upstream of the sensor location (x). Figure 19 shows the change in pulsation parameter over the blade surface.

In Fig. 19, the unsteadiness on the pressure side is far more critical than on the suction side (as noted earlier). Note that the cutoff level for quasi-static behavior of 0.2 suggested by Abhari [8] occurs from the pressure side all the way to ~30% wetted distance on the suction side. Figure 16 shows that the overall unsteadiness remains essentially constant throughout the blade, but that the driving pressure margin on the pressure side is small for this current operating condition.

The predictions for the 15%, 50%, and 90% span locations are shown in Fig. 20, which shows that on the pressure side of the blade, the shape is similar between the different spans, but the absolute levels vary by ~10% of the vane inlet pressure. However, on the suction surface, the 15% pressure prediction is substantially different from the other two spans. Data from the pressure sensors mounted at the 90% location were not available for this data set due to a mechnical failure, but will be available in future papers.

4.4.2 Blade Heat-Flux. Film cooling has a significant influence on the blade, even at these low flow rates. Figure 21 presents the upper- and lower-gauge temperatures for the cooled and uncooled blades at 50% span. The two colors (shades) on the plot represent the different cases (cooled and uncooled) and the open round symbols are the metal temperature (or bottom sensor). Clearly, the largest change occurs on the suction side where the uncooled film temperature is dramatically higher from the leading edge to ~50% wetted distance. However, the cooling effect decays with increasing distance from the cooling holes. For Figs. 21–26, the range bars will not be plotted, since that tends to make the figures confusing. The absolute accuracy of the temperature measurements (such as for the vane sensors) is ±0.3 K, and the heat-flux accuracy is given as ±5% of reading, as shown for the vane (or ~7500 W/M^2 for the highest loading case on the blade).

The heat-flux levels for all three span locations are shown in

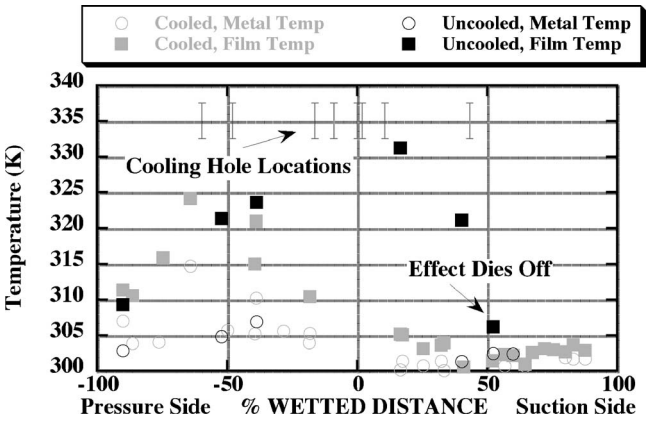

Fig. 21 Blade 50% gauge temperatures (cooled and uncooled)

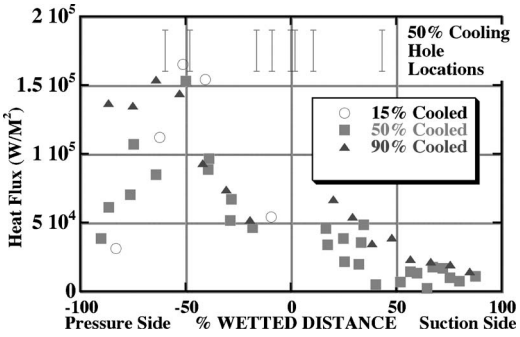

Fig. 22 Blade cooled heat flux (various spans)

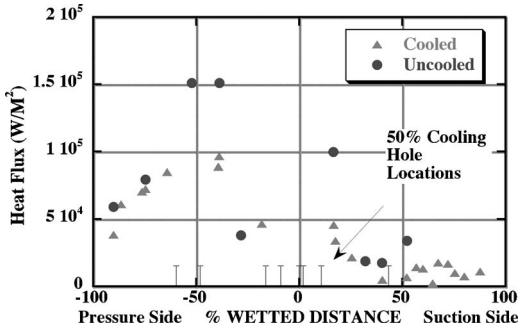

Fig. 23 50% span cooled and uncooled heat flux

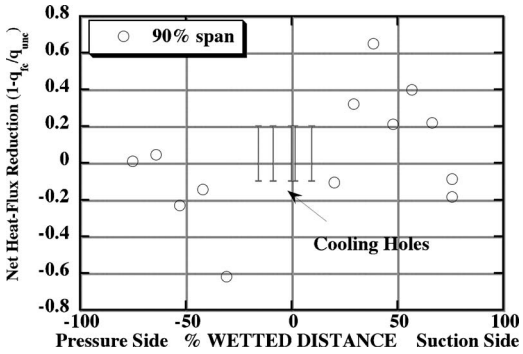

Fig. 27 Blade 90% net heat flux reduction

Fig. 22. The cooling-hole locations at 50% span are shown to make the plot more readable. The suction side does not exhibit much difference due to span. The 90% data ride slightly higher than the 50% data. However, on the pressure side, there are substantial differences in the span data with the 90% span data heading to high values by −50% wetted distance and basically stabilizing, while the 15% and 50% spans achieve the same peak level, then decrease.

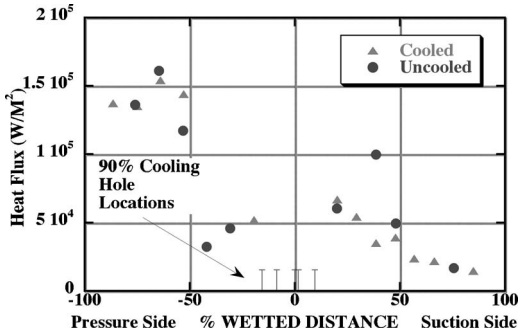

Fig. 24 Blade 90% cooled and uncooled heat flux

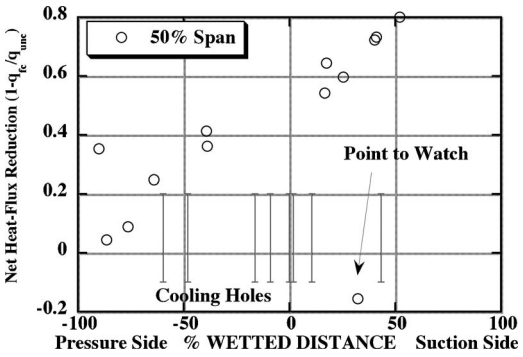

Fig. 25 Blade 50% net heat flux reduction

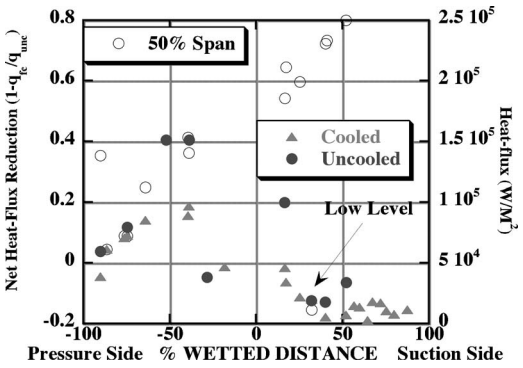

Fig. 26 50% net heat flux reduction with heat flux

This is due to the fact that the cooling hole locations at approximately −50% WD do not exist for the 90% gauges. The 50% sensors see two cooling-hole rows, while the 90% see one (see photographs in Part 1 [1]). Variations due to span are not uncommon in uncooled stages, but the effects here may be aggravated by the presence of cooling and gas migration. If that is the case, then these loadings will change as the cooling levels change.

The 50% span data (Fig. 23) and the 90% span data (Fig. 24) are examples of the effect of cooling on the heat-flux measurements. The 90% span data indicates the film cooling gas is detaching from the blade immediately after the cooling holes on the suction side and then reattaching at ~40% wetted distance. On the pressure side, there is no real difference at these levels after about −50% WD, but there is an interaction closer to the leading edge. This may also indicate some effects of tip leakage flows. The 50% span data show similar results, but note that the heat flux drops toward the trailing edge of the pressure surface for the 50% data, but stays high at the 90% span location.

4.4.3 Blade Effectiveness. The overall net heat-flux reduction can be plotted for both the 50% and 90% locations. The effectiveness for the 50% location is given in Fig. 25 along with the cooling hole locations. Figure 25 shows the effectiveness follows a very linear path from its maximum value at ~50% WD on the suction side to having almost no effect at the trailing edge on the pressure side. There is one outlier on this plot that occurs just forward of the 50% WD hole. As mentioned earlier, the propagated uncertainty for these values is ~7.1% of reading, or on this scale 0.056 for the maximum values that occur at 0.8.

To better understand this point, it is helpful to also examine the heat flux data, shown in Fig. 26. From this plot, it can be seen that the low effectiveness point in question comes from an extremely low heat-flux level in both the cooled and uncooled cases. Thus, the point may be an artifact of the particular test condition being examined. A review of the instrumentation showed this sensor to be functioning properly and thus no reason to discard the data point. The 90% effectiveness is given in Fig. 27. Since there are fewer cooling holes at this span location, the overall effect is lower on the pressure side. It is also worth noting that both the 90% and 50% spans tend to be most effective at about the 40% WD locations.

5 Conclusions

The focus in Part II has been directed at the experimental results for the fully cooled high-pressure turbine stage. The data presented are for a low Reynolds number, low coolant mass-flow case that represents one of the experimental conditions of interest

within a large experimental matrix. This condition was chosen because it represents one of the more difficult measurements to perform as a result of the low signal levels.

The effect of rotation on the inner static pressure distribution in the rotor is demonstrated. The importance of the unsteady flow on the cooling is evident in the pulsation parameter and the power spectrum of the pressure transducers located inside of the blade cooling passages. The net heat-flux reduction is presented for two span locations on the blade and shown to be significant. In addition, the techniques developed here are pointing to strong interactions that occur between the blade rows as the effectiveness diminishes, which will require further investigation as the cooling mass flows are changed in other experiments.

Although much has been learned experimentally, effort has also been devoted to utilization of available design codes for predictions in the presence of film cooling. The predicted and measured vane and blade surface pressure distributions are compared and shown to be better for the vane than for the blade, which is not surprising since the codes are steady and uncooled. However, the agreement is remarkably good in certain areas, and for some design cases, may be a viable solution.

In addition, the overall uncertainty in the measurements, while generally very good, indicates that to resolve the small difference that occur in the cooling passages, we may be at the limit of the sensor resolution using the current calibration techniques for this low mass-flow range. Increasing overall pressure levels is one path toward improving overall system accuracy, as well as developing improved calibration techniques. However, for the main experimental matrix that has been outlined in Part I [1], the current calibration techniques should be acceptable.

Acknowledgment

The research reported here is supported by the NASA/DoD URETI for Aeropropulsion and Power at The Ohio State University. The technical monitor for this effort is Kimlan T. Pham of the NASA Glenn Research Center. The authors want to acknowledge the dedicated staff of the OSU GTL for their efforts in preparing the instrumented turbine stage and for helping in completion of the measurements. The authors would also like to thank their friend, Reza Abhari, who was heavily involved in the conception and formulation of this experiment when they were all together at Calspan Corporation and at the OSU GTL.

Nomenclature

Experimental Parameters That are Set

PR = pressure ratio measured at rake locations, $P_{T,\mathrm{inlet}}/P_{T,\mathrm{outlet}}$

$\mathrm{TR}_{\mathrm{core}}$ = core to wall temperature ratio, $T_{T,\mathrm{inlet}}/T_{\mathrm{metal}}$

N_{corr} = corrected speed, $N_{\mathrm{phy}}\sqrt{T_{\mathrm{ref}}/T_{T,\mathrm{inlet}}}$ (rpm)

$T_{T,\mathrm{inlet}}$ = total temperature at inlet rake

T_{ref} = reference temperature, 288 K (519 R)

N_{phy} = physical speed of the turbine

FF = flow function, $\dot{m}(P_{\mathrm{ref}}/P_{T,\mathrm{inlet}})\sqrt{T_{T,\mathrm{inlet}}/T_{\mathrm{ref}}}$

P_{ref} = reference pressure, 101.356 KPa (14.7 psia)

TR_x = cooling to wall temperature ratio at location x, $T_{T,\mathrm{inlet}}/T_x$

Mr_x = mass flow fractions, $\dot{m}_x/\dot{m}_{\mathrm{core}}$

BR_x = blowing ratio, $(\rho_x/\rho_\infty)(u_x/u_\infty) \Rightarrow (P_x/P_\infty) \times (\mathrm{Ma}_x/\mathrm{Ma}_\infty)\sqrt{(\gamma_x/\gamma_\infty)(R_\infty/R_x)(T_\infty/T_x)}$

Ma = local Mach number

OTDF = temp profile, $T_{\mathrm{local}}-T_{\mathrm{mean}}/T_{\mathrm{mean}}-T_{\mathrm{wall}}$

RTDF = temp profile, $T_{\mathrm{radial}}-T_{\mathrm{mean}}/T_{\mathrm{mean}}-T_{\mathrm{wall}}$

T_{radial} = temperature at a given radial location averaged circumferentially

Re = Reynolds number, $(\dot{m}/A)(1/\mu)L$

A = choke area

L = characteristic length (1 m)

Experimental Parameters That are Measured

Net Heat-Flux Reduction

Δq_r = $1-(q_f/q_0)$, $\dot{q}_f/q_0$= (heat flux of film cooling/(heat flux without cooling)

Adiabatic Film Effectiveness

η_{ad} = $(T_r-T_{ad})/(T_r-T_c)$, T_c is temperature of coolant

T_r = adiabatic recovery temperature without film cooling

T_{ad} = film-cooled adiabatic surface temperature

References

[1] Haldeman, C. W., Mathison, R. M., Dunn, M. G., Southworth, S., Harral, J. W., and Heltland, G., 2008, "Aerodynamic and Heat Flux Measurements in a Single-Stage Fully Cooled Turbine—Part I: Experimental Approach," ASME J. Turbomach., **130**(2), p. 021015.

[2] Skinner, G. T., 1960, "Analog Network to Convert Surface Temperature to Heat-Flux," Cornell Aeronautical Laboratory.

[3] Oldfield, M. L. G., Burd, H. J., and Doe, N. G., 1982, "Design of Wide-Bandwidth Analogue Circuit for Heat-Transfer Instrumentation in Transient Tunnels," *Heat Transfer in Rotating Machines*, Hemisphere, Washington, DC.

[4] Epstein, A. H., Guenette, G. R., Norton, R. J. G., and Yuzhang, C., 1986, "High-Frequency Response Heat-Flux Gauge," Rev. Sci. Instrum., **57**(4), pp. 639–649.

[5] Weaver, M. M., Moselle, J. R., Dunn, M. G., and Guenette, G. R., 1994, "Reduction of Data From Heat-Flux Gauges—A Documentation of the MIT ACQ Code and an Adaptation to Single-Sided Gauges," Calspan Report No. 7733-4.

[6] Cohen, B., 2005, "Numerical and Experimental Investigation of Unsteady Heat-Transfer Data Reduction Algorithms," M.S. thesis, Mechanical Engineering Department, Ohio State University.

[7] Mouzon, B. D., Albert, J. E., Terrell, E. J., and Bogard, D. G., 2005, "Net Heat Flux Reduction and Overall Effectiveness for a Turbine Blade Leading Edge," ASME Paper No. GT2005-69002.

[8] Abhari, R. S., 1996, "Impact of Rotor-Stator Interaction on Turbine Blade Film Cooling," ASME J. Turbomach., **118**, pp. 123–133.

[9] Haldeman, C. W., 2003, "An Experimental Investigation of Clocking Effects on Turbine Aerodynamics Using a Modern 3-D One and One-Half Stage High Pressure Turbine for Code Verification and Flow Model Development," Ph.D. thesis, Aeronautical and Astronautical Engineering Department, Ohio State University.

[10] Haldeman, C. W., Dunn, M. G., Barter, J. W., Green, B. R., and Bergholz, R. F., 2004, "Aerodynamic and Heat-Flux Measurements With Predictions on a Modern One and 1/2 Stage High Pressure Turbine," ASME J. Turbomach., **127**, pp. 522–531.

[11] Haldeman, C. W., Dunn, M. G., Barter, J. W., Green, B. R., and Bergholz, R. F., 2004, "Experimental Investigation of Vane Clocking in a One and 1/2 Stage High Pressure Turbine," ASME J. Turbomach., **127**, pp. 512–521.

[12] Murphy, J. S., 2004, "Control of the "Heat-Island" Effect on the Measurement of Pyrex Thin-Film Button Gauges Through Gauge Design," M.S. thesis, Mechanical Engineering Department, Ohio State University.

[13] Hakimi, N., 1997, "Preconditioning Methods for Time-Dependent Navier-Stokes Equations," Ph.D. thesis, Vrije.

Experimental and Numerical Analysis of High Heat Transfer Phenomenon in Minichannel Gaseous Cooling

Kazuo Hara
Fluid Science Laboratory,
Division of Mechanical Science,
Kyushu University,
Fukuoka, Japan

Masato Furukawa
Fluid Science Laboratory,
Division of Mechanical Science,
Kyushu University,
Fukuoka, Japan

Naoki Akihiro
Riso Kagaku Corporation,
Ibaraki, Japan

The authors have reported that a minichannel flow system had a high heat transfer coefficient. We investigated the heat transfer and flow structure of single and array minichannels combined with an impingement flow system experimentally and numerically. The diameter D of the channel was 1.27 mm*, and length to diameter ratio L/D was 5. The minichannel array was so-called shower head, which was constructed by 19 minichannels located at the apex of equilateral triangle, the side length S of which was* 4 mm *a single stage block was used to investigate the heat transfer without impinging flow system. Two stage blocks were combined in series to compose an impingement heat transfer system with an impingement distance of H. H/D ranged from 1.97 to 7.87. The dimensionless temperature increased as the impingement distance became short. A comparison of heat transfer performance was made between minichannel flow and impingement jet by comparing the single- and two-stage heat transfer experiments. It was found that dimensionless temperature of the minichannel exceeded that of the impingement jet. The mechanism of high heat transfer was studied numerically by the Reynolds-averaged Navier-Stokes equation and k-ω turbulence model. The limiting streamline pattern was correlated well to the surface heat flux distribution. The high heat transfer was achieved by suppressing the development of boundary layer under strong pressure gradient near the channel inlet. This heat transfer mechanisms became dominant when the channel size fell into the region of the minichannel.* [DOI: 10.1115/1.2751146]

Introduction

It was found by Hara et al. [1] that the heat transfer coefficient was several times higher than fully developed pipe flow in the minichannel operating at high-pressure ratio. The heat transfer coefficient included the heat transferred from an inlet and an outlet plane of the minichannel, and had a meaning that total amount of heat was evaluated by the channel side surface area. It may be a practical thermal boundary condition that inlet and outlet planes are not thermally insulated. The result of the experiment also showed that Stanton number was almost inversely proportional to the minichannel length to diameter ratio L/D. This suggested the importance of heat transfer at the inlet or the outlet of the channel because the ratio of perimeter length to the cross-sectional area of the channel increases as the channel size becomes small.

Impingement jet is well known to be a flow field of high heat transfer. Lee et al. [2] showed, experimentally, that Nusselt number became large with increasing nozzle diameter. Zuckerman and Lior [3] listed the many experiments for impinging jet in which the nozzle diameters were generally from 6.35 mm to 12.7 mm and were larger than the regime of minichannel. A channel or a nozzle, however, is always necessary to form an impinging jet. There may be little meaning to only consider the impingement heat transfer in the case that channel temperature is equivalent to target wall temperature, if the minichannel heat transfer coefficient is sufficiently large.

A high-pressure ratio operation is not generally used for cooling purposes because the pumping of air consumes a large amount of energy. A gas turbine cooling system, however, is an important application in which impingement cooling and film cooling plays an important role with high-pressure ratio operation. Impinging jet cools inside of the blade and film cooling jet insulates the blade metal from high-temperature working gas. Minichannels are used as injectors for both cases. The standard channel size is ~1 mm, length to diameter ratio is ~5, and pressure ratio is <1.8. Heat transfer coefficient of the cooling hole was considered to be equivalent to fully developed turbulent pipe flow due to the work of Gillespie et al. [4]. Their work, however, was executed for the scale-up model under the condition of atmospheric pressure and small pressure difference between inlet and outlet. If the heat transfer at the inlet and the outlet of the channel becomes important, a new understanding of the phenomenon becomes necessary.

Impingement jet is well known as a flow system with high heat transfer coefficient. The application to gas turbine blade cooling was introduced in Zuckerman and Lior [3]. It is considered that the injected jet flows back as a "fountain" after impinged on the target wall.

The fluid supplied for cooling must be removed from the flow field. The jet interacts with a cross-flow to the exit port in some distance [5]. In the application of a gas turbine, new minichannels are bored in the target plate for the injection hole of film cooling and cooling air issues through the minichannels. A sink effect due to these minichannels is considered to affect the impinging jet flow and heat transfer. In an application of food freezing [6], the cross-flow may affect little on the impinging jet, although the pressure gradient exists locally around the stagnation point. This is because the jet is injected into semi-infinite space. In an application of gas turbine cooling, however, cross-flow seriously affects the impinging jet due to the narrow space between nozzle plate and blade outer skin. In this study, small impingement distances were utilized regarding the gas turbine application.

In our minichannel system, the dimensionless temperature achieved ~0.4, and it was 0.7 for combined system of minichan-

Contributed by the Turbomachinery Division of ASME for publication in the JOURNAL OF TURBOMACHINERY. Manuscript received August 23, 2006; final manuscript received October 10, 2006; published online March 24, 2008. Review conducted by David Wisler.

nel and impingement jet. This means that blade is more cooled from inside than expected, and then the temperature of the film cooling jet becomes much higher than expected. The cooling system of gas turbine blade was basically regarded as a heat exchanger [7]. Improvement of dimensionless temperature in the blade has a direct effect to reduce the metal temperature.

A characteristics of minichannel flow field operating at high-pressure ratio is a strong pressure gradient on the inlet surface. The velocity profile of the boundary layer is affected by pressure gradient and is not described by the law of the wall. Such a boundary layer is called nonequilibrium boundary layer [8]. A numerical turbulent flow analysis usually uses the wall function regardless of whether the pressure gradient is strong or weak. The outer layer velocity profile of boundary layer is modified by a RANS (Reynolds-averaged Navier-Stokes) equation according to the pressure gradient. In a region of $y^+ < 5$, however, assumption of linear velocity profile may neglect the effect of pressure gradient. It is recommended that the first grid point should be set at $y^+ < 1$ [8,9] to evaluate the pressure gradient effect.

The high heat transfer coefficient in the impinging jet is considered to be caused by strong turbulence in the main stream of wall jet because there is a strong correlation between Nusselt number and turbulence [10]. Zuckermann and Lior [3] commented on the turbulence model from this point of view. In this paper, however, we did not make special treatment for this point.

Experimental Method

Apparatus. As we discussed in the Introduction, the heat transfer of the impinging jet and that of the minichannel have opposite dependency on the channel size. It is interesting to know how these heat transfers take part in the combined cooling system in the minichannel regime, where the impinging jet must be created by a minichannel. We intended to extract the characteristics of minichannel heat transfer by varying the thermal or fluid dynamic boundary condition variously. Schematic of the experimental apparatus is shown in Fig. 1. The main part of heat transfer elements were made by oxygen-free copper and were composed of block 1, impingement chamber and block 2. They were stacked up with steel blocks and Teflon® plates and were tightened by steel bolts like a sandwich. Air flowed into upstream plenum, which was composed of Teflon plate and block 1 and was 29 mm dia. The end plate of block 1 was 6.35 mm thick, in which single or 19 minichannels were machined. The channel diameter was 1.27 mm and the length to diameter ratio L/D was 5 considering the heat flow through the copper metal to the minichannel. The jet impinged the block 2 crossing the impingement chamber of distance H, which were set 2.5 mm, 5 mm and 10 mm by replacing the Teflon plate. As with block 1, the end plate of block 2 was 6.35 mm thick, in which single or 19 minichannels were also machined. All the minichannels was not chamfered.

Air was supplied through an air compressor, dryer, pressure controller, and mass flowmeter. The inlet temperature T_1 was measured by the upstream thermocouple 1. The exit temperature T_2 was measured by thermocouple 2, downstream of mixing screen at the exit of plenum. The inner walls of the copper blocks were thermally insulated by silicon foam rubber, as shown in Fig. 1. Blocks 1 and 2 were electrically heated by ring heaters bound tightly by metal bands. Two temperature controllers controlled the block temperature independently by utilizing the thermocouple signal at the tip radius of 10 mm.

The arrangements of minichannels are shown in Fig. 2. Figure 2(a) shows the single minichannel, which were offset 2 mm each other from the center. A coaxial channel arrangement and staggered channel arrangement in $S=4$ mm were possible by turning each block 180 deg. Figure 2(b) shows the 19 minichannels configuration. The minichannels were located at the apex of equilateral triangles, the side length S of which was 4 mm. For staggered arrangement, minichannels of block 1 were located at the centroid

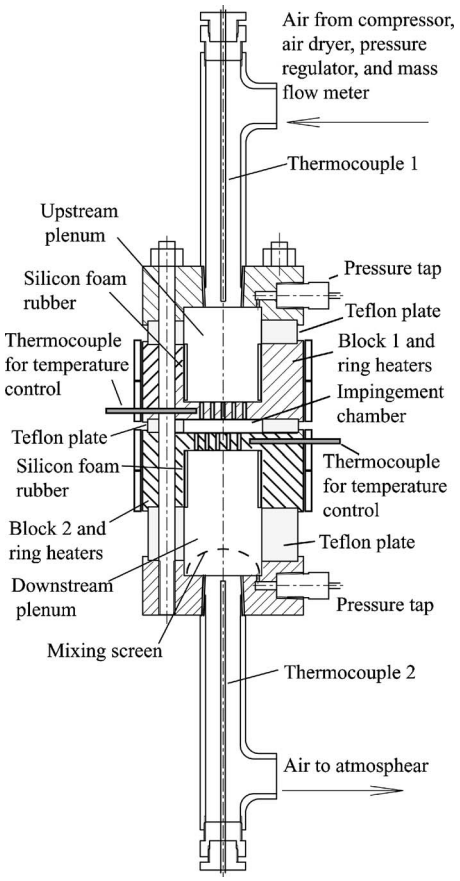

Fig. 1 Experimental setup for experiment 1, two stage, for the cases A to L in Table 1. The figure shows for $H=5$ mm and 19 minichannels.

of the equilateral triangles of block 2. The detail of impingement chambers is shown in Fig. 3 for $H=2.5$ mm. In Fig. 3, the names of the walls are defined for convenience.

Experimental Method. Inlet air was supplied by a compressor through air dryer at room temperature. Wall temperatures were kept 70°C for both blocks 1 and 2. The combinations of experimental configuration are given in Table 1, in which number of channels, impingement distance and stagger or coaxial arrangement are listed. Dimensionless temperature was defined by Eq. (1) for all experiments using the inlet temperature T_1, outlet temperature T_2, and wall temperature T_w.

$$\theta = \frac{T_2 - T_1}{T_w - T_1} \tag{1}$$

Test procedures were as follows:

Experiment 1. As shown in Fig. 1, we conduct the heat transfer experiment connecting block 1 and block 2 in series with back pressure valve fully opened for case A to case L in Table 1. The series of inlet pressure was controlled to get an almost constant mass flow rate increment. The dimensionless temperatures for these cases were described by θ without subscript, and the experiment was called "2 stage."

Experiment 2. Heat transfer experiments were conducted only using block 1 as shown in Fig. 4(a) for cases M and O in Table 1 to simulate the flow and thermal condition of block 1 of experiment 1. Downstream pressure was controlled by the back pressure valve to get the same flow rate and same inlet pressure with the

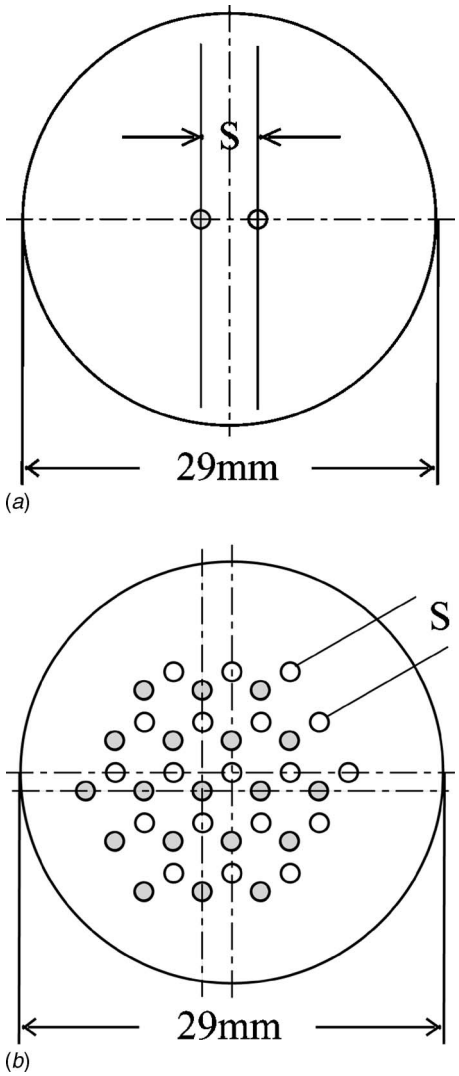

Fig. 2 Plane view of minichannel for staggered configuration. The channels of block 1 and block 2 are shown together: (*a*) single channel and (*b*) 19 channels.

test condition of cases A and G of experiment 1. The dimensionless temperature was described by θ_1 for this experiment and the experiment was called "single stage."

Experiment 3. Heat transfer experiment was conducted only using block 2, as shown in Fig. 4(*b*), for cases N and P in Table 1 to simulate the flow and thermal condition of block 2 of experiment 1. Inlet pressure was controlled to get the same flow rate with the test condition of cases A and G of experiment 1 with the

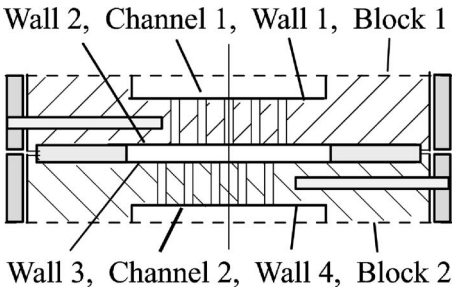

Fig. 3 Detail of the impingement chamber for *H*=2.5 mm and the definition of the name of the heat transfer surface

Table 1 List of configuration for experimental and numerical analysis

Case	Comment	N	H(mm)	Arrangement
A		1	2.5	stagger, 2 stages
B		1	5	stagger, 2 stages
C	Fig. 12	1	10	stagger, 2 stages
D		1	2.5	coaxial, 2 stages
E		1	5	coaxial, 2 stages
F		1	10	coaxial, 2 stage
G	Figs. 9 and 14, Table 3	19	2.5	stagger, 2 stages
H		19	5	stagger, 2 stages
I	Fig. 13	19	10	stagger, 2 stages
J		19	2.5	coaxial, 2 stages
K		19	5	coaxial, 2 stages
L		19	10	coaxial, 2 stages
M	See note[a]	1	-	block 1, 1 stage
N	Figs. 10 and 11 Table 2	1	-	block 2, 1 stage
O	See note [a]	19	-	block 1, 1 stage
P		19	–	block 2, 1 stage

[a]Increasing downstream pressure by a back pressure valve.

back pressure valve fully opened. The dimensionless temperature was described by θ_2 for this experiment and the experiment was also called single stage. The Reynolds number ranged from 1000 to 20,000 based on channel diameter and inlet temperature.

Experimental Results and Discussions

Figure 5 is the dimensionless temperature of the single channel. For cases A and B, θ was sufficiently high for staggered arrangement of H=2.5 mm and 5 mm. This meant that heat transfer was large for the case that potential core hit the target plate directly. H/D is 1.97 for this case. A dependency of heat transfer to pressure ratio was weak. Case N was operated at atmospheric exit pressure condition and had good reproducibility when compared to the same configuration and operation described in Hara et al. [1]. Case M was operated by increasing downstream pressure by means of the back pressure valve. The difference of dimensionless temperature between case M and case N is unresolved. The difference remained if θ was plotted on Reynolds number.

Figure 6 is a result of dimensionless temperature for 19 minichannels. As the impingement distance decreased, the dimensionless temperature increased for staggered arrangement, while it decreased for coaxial arrangement. They, however, almost coincided for H=10 mm. For H=2.5 m, the dimensionless temperature showed higher value than typical values of 0.5 of gas turbine blade cooling shown in Torbidori and Horlock [7]. One can see a discrepancy for single-stage test between the data of case O, the increasing downstream pressure by the back pressure valve, and case P, the atmospheric downstream pressure. The two plots, however, coincided with each other when they were plotted on the Reynolds number. This means that pressure ratio is not a principal variable for representing heat transfer phenomena.

Dimensionless temperature of the single minichannel was greater than that of 19 minichannels. The result of numerical calculation for a single channel, shown later, indicates that large and systematic recirculating flow was formed in the impingement chamber and downstream plenum. In the flow field of 19 minichannels, such a recirculating flow was not formed. This was the cause of difference of heat transfer result between single and 19 minichannels.

Comparison Between Impingement and Minichannel Heat Transfer. It is well known that impingement jet has high heat transfer enhancement effect. It may be interesting to know the roles minichannel and impingement heat transfer, respectively, play in the combined heat transfer processes. We considered a model to evaluate the thermal contributions by assuming that three heat transfer processes were connected in series as follows.

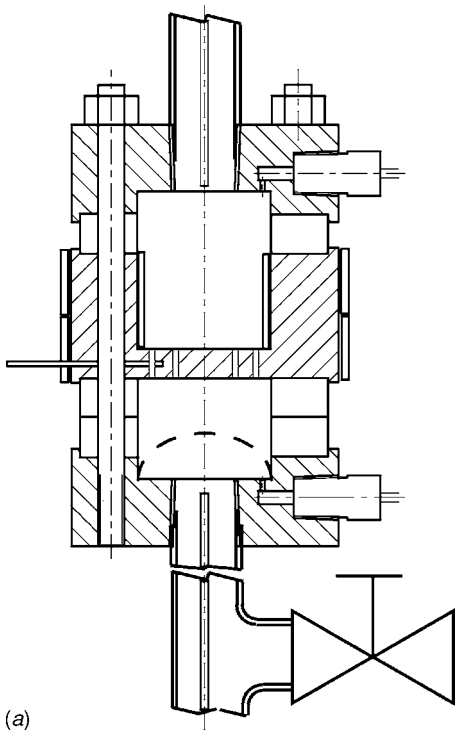

(*a*)

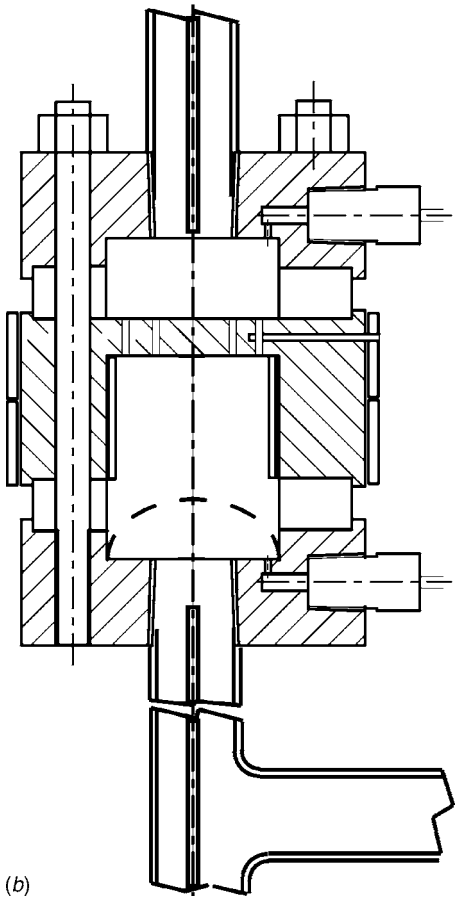

(*b*)

Fig. 4 Experimental setup for experiments 2 and 3: (*a*) experimental setup for experiment 2, using block 1 with the back pressure valve control for cases M and O in Table 1, and (*b*) experimental setup for experiment 3 using block 2 without the back pressure valve for the cases N and P in Table 1

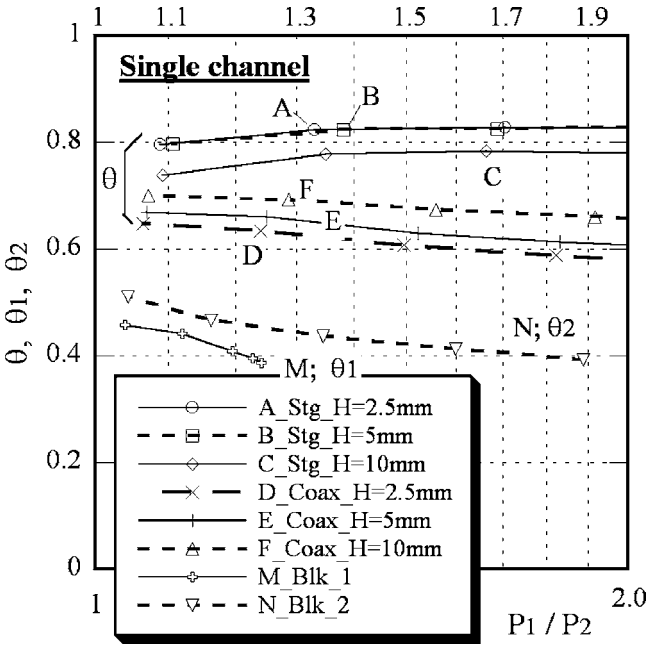

Fig. 5 Correlation of dimensionless temperature and pressure ratio

1. Temperature increases from T_1 to T_{1e} in the minichannel of block 1. The dimensionless temperature is assumed to be equal to θ_1 of experiment 2, described in the previous paragraph with increasing downstream pressure by the back pressure valve.
2. Temperature increases from T_{1e} to T_i by impinging on the target wall of wall 3. The dimensionless temperature of this process is denoted as θ_i.
3. Temperature increases from T_i to exit temperature T_2. The dimensionless temperature is assumed to be equal to θ_2 of experiment 3.

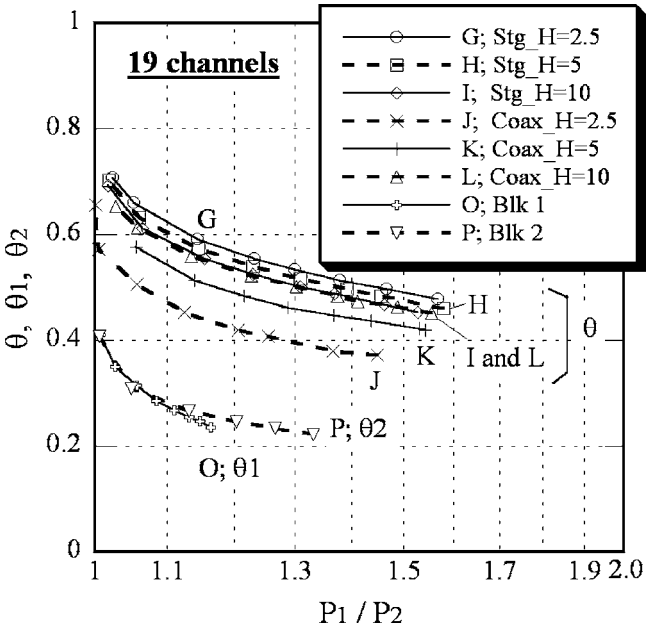

Fig. 6 Correlation of dimensionless temperature and pressure ratio

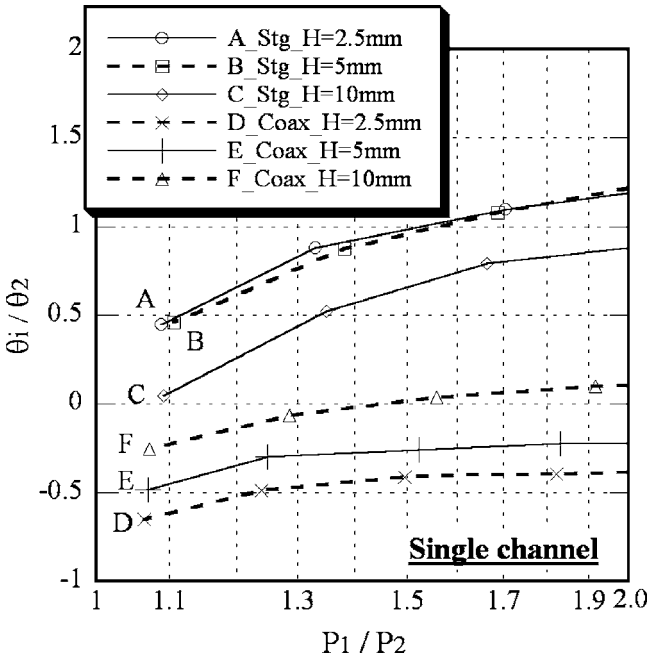

Fig. 7 Correlation of dimensionless temperature and pressure ratio

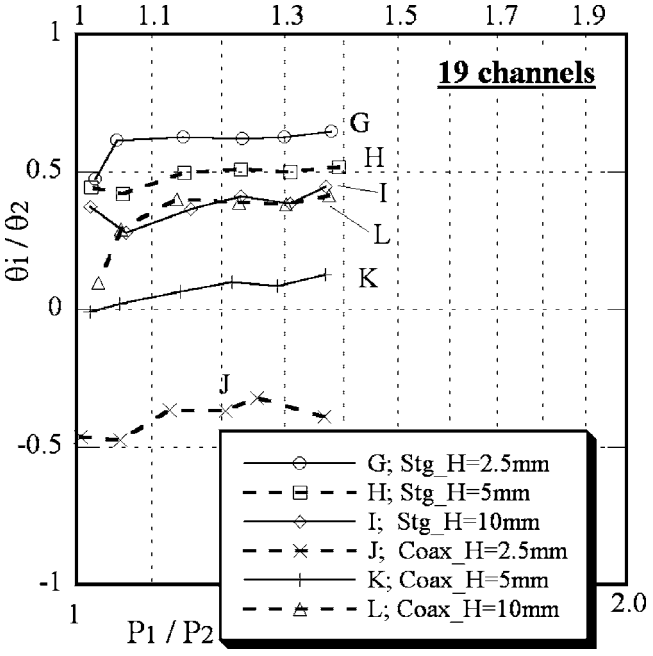

Fig. 8 Correlation of dimensionless temperature and pressure ratio

This assumption of dividing the heat transfer process into three series of elemental processes may be reasonable for staggered arrangement of small H from the result of flow structure by CFD.

The temperature increase from inlet temperature T_1 to exit temperature T_2 can be described by the following trivial equation:

$$\frac{T_2 - T_1}{T_w - T_1} = \frac{T_{1e} - T_1}{T_w - T_1} + \frac{T_i - T_{1e}}{T_w - T_1} + \frac{T_2 - T_i}{T_w - T_1} \tag{2}$$

We can modify Eq. (2) to Eq. (3), assuming that the temperature of blocks 1 and 2 are at the same value of T_w,

$$\theta = \theta_1 + (1 - \theta_1)\theta_1 + \{1 - \theta_1 - (1 - \theta_1)\theta_i\}\theta_2 \tag{3}$$

θ_i was calculated from the experimental value of θ, θ_1 and θ_2. θ_i was then normalized by θ_2 to compare the heat transfer performance of minichannel with impingement jet.

Figure 7 is a single channel result. Impingement heat transfer was large in the case of staggered arrangement and small H. The performance of impingement heat transfer exceeded minichannel heat transfer especially for the high pressure ratio. The pressure dependency implies that the influence area of impingement was extended widely for high pressure ratio.

Figure 8 shows the result for 19 minichannels. For coaxial channel arrangement of blocks 1 and 2, the effect of impingement heat transfer was small and retarded the heat transfer in the case of H=2.5 mm. The impingement heat transfer was evaluated to be smaller than the minichannel heat transfer, for all cases, and did not vary greatly with pressure ratio. This means that influence area of impingement jet did not increase for minichannel array by the mutual interference of the jets. Minichannel heat transfer exceeded the impingement heat transfer when the channel size fell into the regime of minichannel.

Numerical Analysis

Outline. A commercial software of CFX 10.0 (ANSYS) was used for CFD, based on a three-dimensional compressible Reynolds-averaged Navier-Stokes equation (RANS) in the steady calculation. A k-ω based shear stress transport (SST) model was used for turbulence model. The minichannel was 1.27 mm dia and 6.35 mm long. Upstream plenum, impingement chamber, and downstream plenum were equivalent to the configuration shown in Fig. 1. The total number of unstructured grid was 1.98 million and total number of grid point was 4.3 million. Fine grid resolution was provided on the heated wall to evaluate the heat transfer strictly. A ten-layer prism mesh was used on the inlet and outlet plane of the minichannel. The y^+ of grid point on the wall was 10 from the limitation of computational resource.

Static pressures were specified at the inlet and outlet tube in Fig. 1. A constant pressure ratio of 1.8 and atmospheric exit pressure was given. A constant wall temperature of 70°C was given from wall 1 to wall 4 and the channel surface except adiabatic condition for other walls. The inlet temperature was kept constant at 25°C.

Computational Results and Discussions

Comparison of CFD With Experiment. Figure 9 shows a comparison of experiment and CFD result for 19 minichannels and two stage. It seems that the agreement was slightly insufficient, but it might be sufficient to discuss about the relationship between flow structure with heat transfer.

Surface Heat Flux and Flow Structure. A local heat transfer coefficient was defined by a calculated wall heat flux and a temperature difference between wall temperature and inlet air temperature by

$$h = \frac{W}{T_w - T_1} \tag{4}$$

The equation was normalized by the convective heat flux, which was evaluated by the channel sectional mass flow of air per 1°C to get local Stanton number by

$$\mathrm{St} = \frac{h}{C_p(m/A)} \tag{5}$$

A pseudo-limiting streamline was drawn by connecting the velocity vector of the cells most close to the wall to discuss about the relationship between heat transfer and flow structure.

Figure 10(a) is a result of limiting streamline and local Stanton number for single channel, single stage and P_1/P_2=1.8. This is

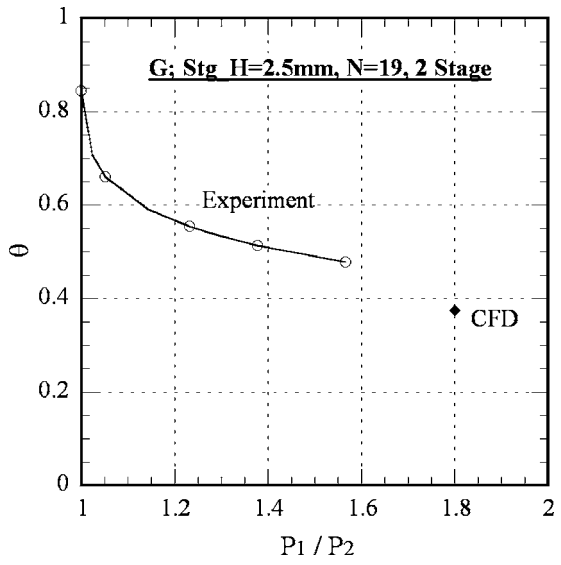

Fig. 9 Comparison of experiment and CFD result for 19 channel and two stage

equivalent to case N of Table 1. The white broken line is a projection of inlet tube inner diameter. The dynamic pressure of the air in the inlet tube affected on the flow pattern of the wall 1

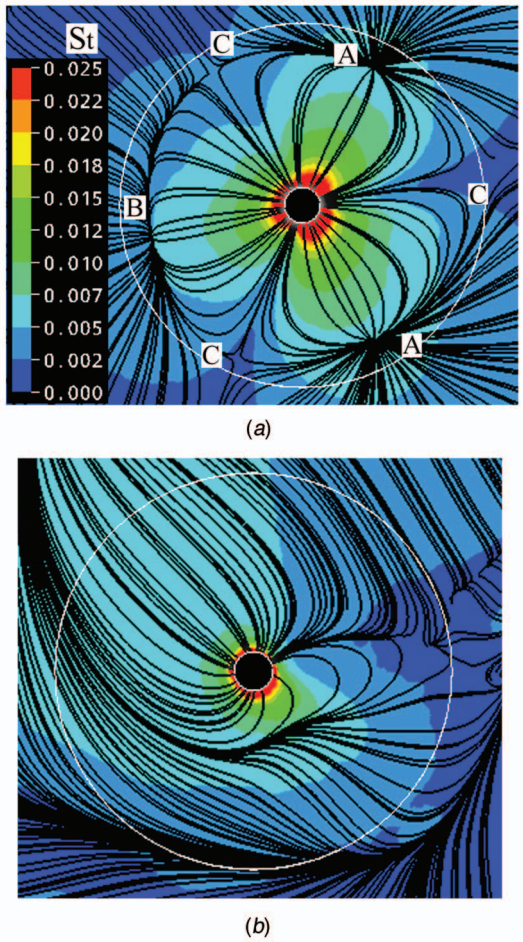

Fig. 10 Stanton number distribution and pseudo-limitting streamline for single channel and single stage, case N: (*a*) heat flux on wall 1 and (*b*) heat flux on wall 2

Table 2 Rate of heat transfered through each surface for single channel and single stage by the CFD

	Rate of heat transfer (W)	Percent (%)
Wall 1	1.51	34
Channel 1 (single channel)	0.98	22
Wall 1	1.98	44

because some singular points were set near the inner diameter of the inlet tube. A in Fig. 10(*a*) is a stagnation point. B is an attachment line. The local Stanton number became large at the stagnation point because the low-temperature air approached the wall. The Stanton number was not high near a saddle point of C. This is because the air was heated while the air was flowing along the stream line to the saddle point. A streamline departing from stagnation point flowed into the minichannel and local Stanton number became extremely large around the channel inlet. The distribution of the Stanton number was influenced by the flow structure and was not axisymmetric.

Figure 10(*b*) is a pseudo-limiting streamline and local Stanton number on the exit plane of wall 2. The flow structure was more complicated than the inlet plane; however, the local high Stanton number region was observed around the exit of the channel. Table 2 shows rates of heat transfer from each surface. The high heat flux region was small on the wall 2, but the total value of transferred heat was large compared to wall 1. The total heat transfer rate was 100/22=4.5 times greater than the channel heat transfer. This means that the effect of inlet and outlet surface heat transfer took a large part when the channel size reduced to the regime of minichannel.

Figure 11 shows a wall heat flux, pressure gradient, and static pressure distribution along the radial line on the inlet surface of the channel, where the strong pressure gradient suppressed the development of the boundary layer and enhanced the wall heat transfer. The result of CFD analysis may explain the high heat transfer coefficient in the experiment of Hara et al. [1].

Figure 12 is a bird's-eye view of the computational result for case C in Table 1, showing the Stanton number and velocity vector in the central cross section. Heat transfer was enhanced around the inlet of the minichannel on wall 1 and was extremely enhanced on wall 3, where very strong impingement effect was observed. There was a large recirculating flow system formed in the impingement chamber, and it rose as a fountain to bump against wall 2 in the periphery of it. These result corresponded to high dimensionless temperature shown in Fig. 5. Although the figures

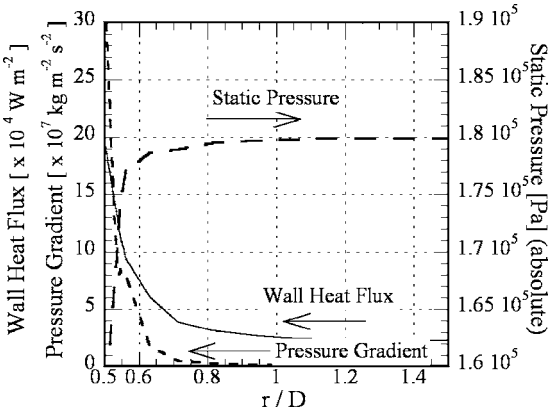

Fig. 11 Correlation of surface heat flux, pressure gradient and static pressure near the channel inlet surface for case N

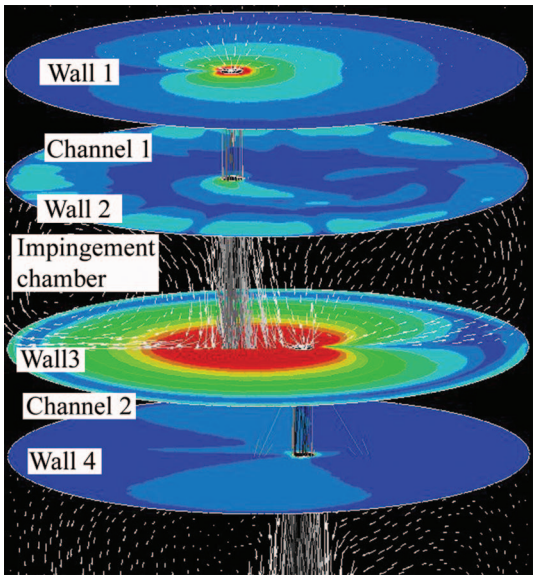

Fig. 12 Stanton number and velocity vector for case C, *H* =10 mm, Stagger arrangement (color scale given in Fig. 10)

are not shown in this paper, a very depressed but distinct recirculating flow region was formed for case A of $H=2.5$ mm and drove the fountain flow stronger than the case of $H=10$ mm.

Figure 13 is a numerical result of case I in Table 1 for 19 minichannels, $H=10$ mm and staggered arrangement, where scale of the Stanton number was reduced from 0.025 of Fig. 12 to 0.008 in Fig. 13. The maximum value of the Stanton number greatly reduced for the array of 19 minichannels. The enhancement of heat transfer was observed around the inlet of minichannels in walls 1 and 3.

A pseudo-limiting streamline was superimposed on Stanton number distribution in Fig. 14 for the 19 staggered minichannels, $H=2.5$ mm and case G in Table 1. The direction of viewing is from upstream to downstream for all figures. In Fig. 14(*a*) of wall 1, the cellular structure surrounded each channel inlet with an attachment line depicted by A from which stream lines departed and was drawn into the minichannel showing the higher heat transfer than the surrounding region depicted by B. The region of especially high heat transfer enhancement seemed to be limited to

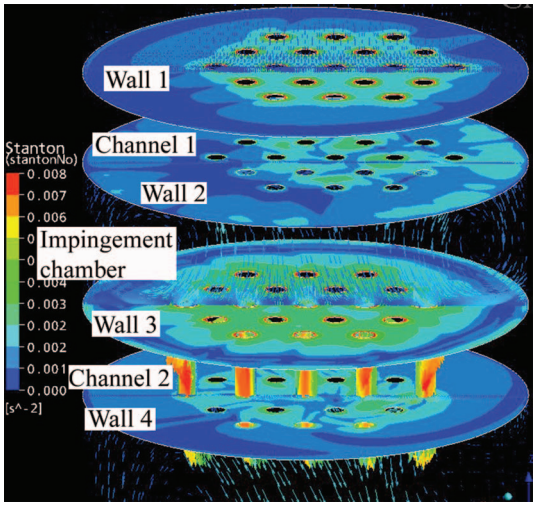

Fig. 13 Stanton number and velocity vector for case I, *H* =10 mm, stagger arrangement

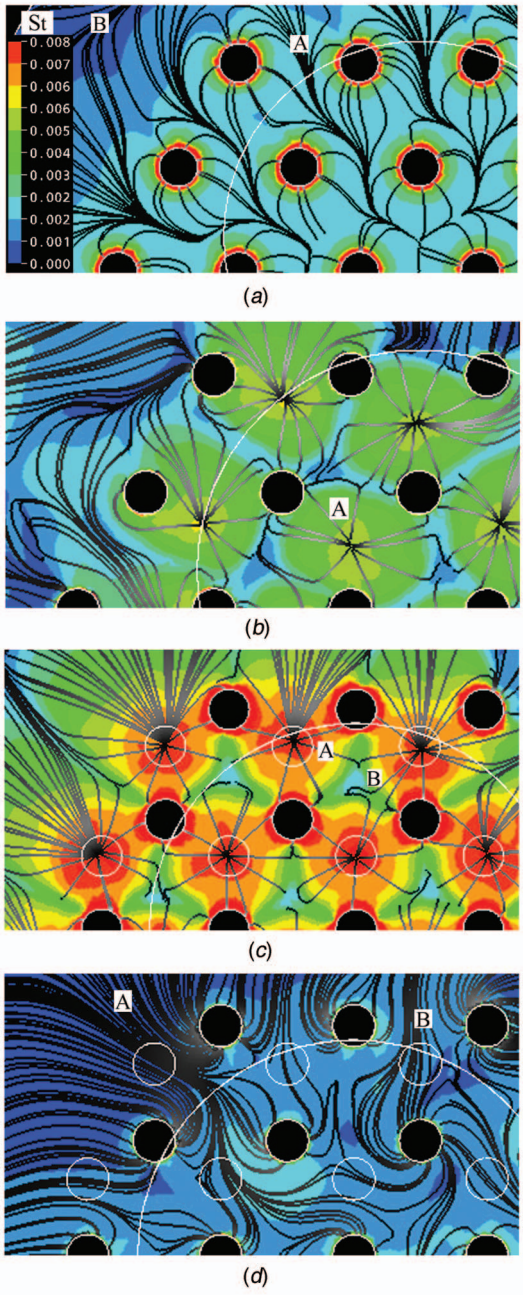

Fig. 14 Stanton number distribution and psuedo-limitting streamline case G, *H*=2.5 stagger arrangement, *N*=19: (*a*) wall 1, (*b*) wall 2, (*c*) wall 3, and (*d*) wall 4

narrow ringlike area around the channel inlet.

Figure 14(*b*) shows the same for wall 2, the exit plane of first minichannel. The sign A was a stagnation point of "fountain" flow from wall 3 and was involved by high heat transfer cellular region.

Figure 14(*c*) is a result of wall 3. Small white circles are a projection of minichannels in block 1. Sign A is a stagnation point of the minichannel jet from block 1. Parts of the streamlines were drawn directly into the minichannels; however, the other part of them gathered to point B and flowed back to block 1 as a fountain. The high Stanton number rings were again observed around the channel inlet, like that in Fig. 14(*a*) and seemed to be isolated from high heat transfer region of impinging jet. This proved partly the validity of assumption that we separated the minichannel heat

Table 3 Rate of heat transferred through each surface for 19 channels and for two stages by the CFD

	Rate of heat transfer (W)	Percent (%)
Wall 1	11.73	11
Channel 1 (19 channels)	20.51	20
Wall 2	14.23	14
Wall 3	28.43	27
Channel 2 (19 channels)	20.36	19
Wall 4	6.94	7

transfer from impingement heat transfer in Eq. (2).

Figure 14(*d*) shows a result of wall 4. Streamlines came from the periphery of minichannel array depicted by A or from the attachment line depicted by B. They showed entrainment effect of the jet. Heat transfer slightly increased around the channel exit.

Table 3 is a heat transfer rate from each surface by the CFD. The definitions of the surfaces are given in Fig. 3. The rate of heat transfer from upstream channel was 11+20=31%. That of walls 2 and 3, where the impingement effect was included, was 14+27 =41%. Roughly speaking, the impingement heat transfer contributed about 41–31=10% to the total heat transfer process. The result showed that the minichannel heat transfer was considerably large compared to the impingement heat transfer.

Concluding Remarks

The dependency of minichannel heat transfer on its size is opposite to that of impingement jet. The heat transfer of minichannel was compared to impingement jet experimentally, assuming that the heat transfer processes were isolated from each other. The heat transfer of minichannel was found to exceed that of impingement jet for the array of 19 minichannels.

Numerical result showed that high heat transfer region around the channel inlet existed separately on the target plate of the impinging jet. The streamline pattern agreed well with the local Stanton number distribution both for single and 19 minichannels. The minichannel heat transfer was considerably large compared to the impingement heat transfer.

The high heat transfer coefficient in the single minichannel was caused by the hear transferred through the inlet and outlet surface of the channel. A strong pressure gradient suppressed the development of boundary layer and enhanced the heat transfer around and channel inlet. A large recirculation structure was formed in the downstream plenum and also enhanced the heat transfer.

Nomenclature

A = cross-sectional area of a single channel
C_p = specific heat of air
D = diameter of the minichannel
H = impingement distance
h = local heat transfer coefficient
L = length of minichannel
m = mass flow rate per a minichannel
N = number of minichannels, 1 or 19
P = total pressure of the plenum
Re = Reynolds number
r = radial distance measured from minichannel center
S = spacing of the minichannel
St = Stanton number
T = total temperature
W = local convective heat flux from the metal surface

Greek

θ = dimensionless temperature of two stage blocks
θ_1 = dimensionless temperature of block 1
θ_2 = dimensionless temperature of block 2
θ_t = dimensionless temperature of impinging jet

Subscripts

w = wall
1 = upstream plenum
2 = downstream plenum

References

[1] Hara, K., Furukawa, M., and Akihiro, N., 2005, "Experimental Investigation of Heat Transfer in Square and Circular Minichannel Air Flow for Wide Range of Pressure Ratio," ASME Paper No. ICMM2005-75184.
[2] Lee, Dh., Song, J., and Jo, M. C., 2004, "The Effects of Nozzle Diameter on Impinging Jet Heat Transfer and Fluid Flow," ASME J. Heat Transfer, **126**(4), pp. 554–557.
[3] Zuckerman, N., and Lior, N., 2005, "Impingement Heat Transfer: Correlations and Numerical Modeling," ASME J. Heat Transfer, **127**, pp. 544–552.
[4] Gillespie, D. R. H., Byerley, A. R., Ireland, P. T., Wang, Z., Jones, T. V., Kohler, S. T., 1996, "Detailed Measurements of Local Heat Transfer Coefficient in the Entrance to Normal and Inclined Film Cooling Holes," ASME J. Turbomach., **118**, pp. 285–290.
[5] Goldstein, R. J., and Behbahani, A. I., 1982, "Impingement of a Circular Jet With and Without Cross Flow," Int. J. Heat Mass Transfer, **25**(9), 1377–13829.
[6] Olsson, E. F. M., Ahrne, L. M., Tragardh, A. C., 2004, "Heat Transfer From a Slot Air Jet Impinging on a Circular Cylinder," J. Food. Eng., **63**, pp. 393–401.
[7] Torbidoni, L., and Horlock, J. H., 2005, "A New Method to Calculate the Coolant Requirements of a High-Temperature Gas Turbine Blade," ASME J. Turbomach., **127**(1), pp. 191–199.
[8] Castillo, L., and Wang, X., 2004, "Similarity Analysis for Nonequilibrium Turbulent Boundary Layers," ASME J. Fluids Eng., **126**(5), pp. 827–834.
[9] De La Calzada, P., and Alonso, A., 2003, "Numerical Investigation of Heat Transfer in Turbine Cascades With Separated Flows," ASME J. Turbomach., **125**(2), pp. 260–266.
[10] Siba, F. A., Ganesa-Pillai, M., Harris, K., and Haji-Sheikh, A., 2003, "Heat Transfer in a High Turbulence Air Jet Impinging Over a Flat Circular Disk," ASME J. Heat Transfer, **125**(2), pp. 257–265.

Xinqian Zheng
Department of Automotive Engineering,
Tsinghua University,
Beijing, 100084, China
and
National Key Laboratory of Aircraft Engine,
Beihang University,
Beijing, 100083, China

Sheng Zhou

Yajun Lu

Anping Hou

Qiushi Li

National Key Laboratory of Aircraft Engine,
Beihang University,
Beijing, 100083, China

Flow Control of Annular Compressor Cascade by Synthetic Jets

An experimental investigation conducted in a stationary annular cascade wind tunnel demonstrated that unsteady flow control using synthetic jets (zero mass flux) could effectively reduce flow separation in the axial compressor cascade. The synthetic jets driven by speaker were introduced through the casing radially into the flow-field just adjacent to the leading edge of the compressor cascade. The experimental results revealed that the aerodynamic performance of the compressor cascade could be improved amazingly by synthetic jets and the maximum relative reduction of loss coefficient was up to 27.5%. The optimal analysis of the excitation frequency, excitation location was investigated at different incidences. In order to obtain detailed information on flow-field structure, the digital particle image velocimetry (DPIV) technique was adopted. The experimental results indicated that the intensity of wake vortices became much weaker and streamlines became smoother and more uniform with synthetic jets. [DOI: 10.1115/1.2751147]

1 Introduction

Flow separation is a major problem that constrains the design of most devices involving flow. Separation drastically reduces lift and increases drag of airfoils, reduces the efficiency of nozzles and turbomachinery, and leads to a local "hot spot" in heat transfer. Consequently, engineers have been preoccupied, for almost a century, with shifting the separation point downstream or eliminating separation entirely [1,2]. There has been a tremendous amount of research and development into the control of boundary layer separation. Except for choosing optimal airfoils (such as controlled diffusion airfoils) and nozzle geometries to delay separation, many effective control methods are developed, including surface-based actuators (e.g., leading-edge slats, slotted flaps, vortex generators, moving wall, etc.) and fluidic-based actuators (e.g., dynamic forcing) [3,4]. It is well known that strong adverse pressure gradient (sometimes due to the local curvature) and decreased momentum of the boundary layer are the two critical factors of boundary layer separation. Therefore, almost all the targets of separation control focus on accelerating the low momentum of fluid on adverse pressure gradient notwithstanding the methods are different.

Fluidic-based methods have been developed for a long time, including steady suction, blowing, and oscillating jets. Historically, suction is the first method ever proposed by Prandtl for the control of separation. The basic principle is to remove decelerated fluid near a surface and deflect the high-momentum free-stream fluid towards the surface. Seifert et al. [5] found that for a given level of mixing the injected mass flow could be reduced by an order of magnitude by using oscillating jets rather than steady jets. It is demonstrated that unsteady control methods are much more effective than steady ones and can be realized at very low level of power input.

Routing of bleed air (suction, blowing, pulse blowing, etc.) for flow control may present a prohibitive addition of complexity and weight. With a synthetic jet, this problem could be avoided [6,7]. Synthetic jets, with the characteristics of zero net mass flux and nonzero momentum flux, do not require a complex system of pumps and pipes [8]. This technique is very efficient because at the suction part of the cycle the low-momentum fluid is sucked into the device, whereas in the blowing part of the cycle a high-momentum wall jet is superimposed on the separating velocity profile. In both cases, the spanwise vorticity is enhanced [9].

In axial compressors, the adverse pressure gradient is generally stronger than that in any other fluid machines. Since the adverse pressure gradient associated with the diffusion become stronger at the high-loading levels in modern designs, unsteady separation is inevitable. This has a negative impact on stall margin, efficiency, and pressure rise capability and even leads to rotating stall or surge. But, only a few studies have been conducted to control separation of axial compressors using unsteady excitation. Culley et al. [10] used embedded injection to control separation of stator vanes in a low-speed axial multistage compressor. Zheng et al. [11,12] showed that the disordered unsteady separated flow could be effectively controlled by unsteady excitation in a wide range of incidence, resulting in enhancement of time-averaged aerodynamic performances of the axial compressor cascade.

Synthetic jets as a typical unsteady excitation method hold an advantage over continuous or pulsed jets in that they require no net mass flow [13]. However, to the authors' knowledge, little research has been performed on separation control by using synthetic jet actuators in axial flow compressors. In the present study, synthetic jets were used to control separation of axial compressor stator vanes in stationary annular cascade wind tunnel experiments. The synthetic jets were introduced through the casing radially into the cascade. There are many parameters that could be varied in a synthetic jet study, such as jet velocity, jet location, jet oscillating frequency, etc. The roles of these parameters were investigated and discussed primarily.

2 Apparatus and Procedures

2.1 Annular Cascade Wind Tunnel. The panorama of the low-speed stationary annular cascade wind tunnel is shown in Fig. 1, which consists of inlet section, testing section, joint section, and power section. The inlet section is a lemniscate-horn-shaped gas contractor to make the flow uniform at the guiding ring, and there are four static holes on the straight section for measuring flow rate. The testing section is made of Plexiglas® including inlet bulb, inlet guide vanes, compressor stator vanes, measurement

Contributed by the International Gas Turbine Institute of ASME for publication in JOURNAL OF TURBOMACHINERY. Manuscript received August 29, 2006; final manuscript received November 14, 2006; published online March 24, 2008. Review conducted by David Wisler. Paper presented at the ASME Turbo Expo 2006: Land, Sea and Air (GT2006), May 8–11, 2006, Barcelona, Spain.

Fig. 1 Photo of the annular cascade

passage, and exit bulb in the downstream direction. The joint section is between the testing section and power section. The airflow is provided by the axial blower of two stages at the end of the annular cascade (i.e., power section).

The guide vanes and compressor stator vanes are also made of Plexiglas. The incidence of five compressor stator vanes is design to be adjustable. The main design parameters of the annular cascade facility are listed in Table 1.

The synthetic jets applied to separation control are generated by a high-power loudspeaker. Inside the speaker, a piston is driven by electromagnetic force to move back and forward, sucking and blowing the air regularly, resulting in a synthetic jet. The speaker is driven by an audio amplifier (HuSan PB2500), which is driven by a function generator (GFG-813). For the present study, the function generator is set to output a sine wave. The loudspeaker is mounted on the casing between guide vanes and compressor stator vanes. The synthetic jet is introduced via a guiding cone through the casing radially into the cascade just adjacent to the leading edge on the suction side of compressor stator vane tested (Fig. 2). The velocity exit is level with the inner surface of casing. The passage of the guiding cone is of the shape of tapered cylinder with the diameter of 19 mm at the end connected to the speaker and the diameter of 3.6 mm at the jet nozzle. The tapered guiding cone can significantly enhance the jet velocity at the nozzle. Since different excitation location may bring about different results, slots are drilled on the shroud in order to shift the excitation location as shown in Fig. 3.

2.2 Performance Measurement. The benefit to dynamic performance due to the synthetic jets with no mass addition is quantified using a total pressure loss coefficient ϖ. The conventional definition of loss coefficient for a blade passage is

$$\varpi = \frac{p_1^* - p_2^*}{p_1^* - p_1} \tag{1}$$

Table 1 Design parameters

Parameters	Values
Outer diameter	450 mm
Stator vane span	56 mm
Number of guide vanes	23
Number of stator vanes	19
Stator vane pitch	65 mm
Stator vane chord length	56 mm
Stator vane inlet angle	30 deg
Stator vane exit angle	52 deg
Rotational speed of blower	2950 rev/min
Mass flow	5 kg/s
Inlet Mach number	0.07

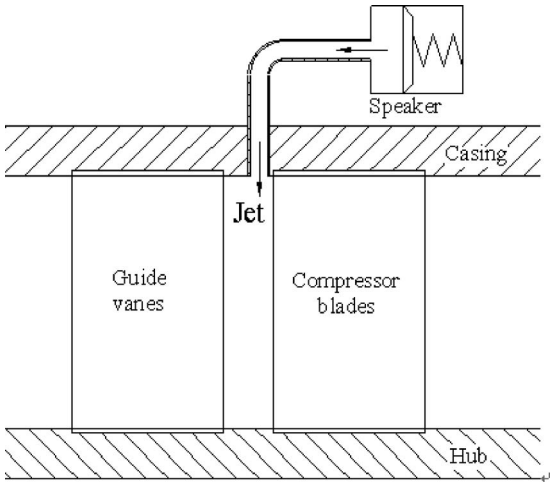

Fig. 2 Sketch of excitation location

At the location 3 mm behind the compressor cascade (i.e., 5% of the chord length) and 50% of the blade span, total pressures are measured at 13 points by a 13-hole total pressure rake along the circumferential direction and within just one pitch space, and their area-averaged value is taken as p_2^*. There are merely five measurement points in the wake region for the restricting of experiment conditions, but which is enough to testify the change of the wake region by synthetic jets. The error of pressure measurement is >10 Pa.

The velocity of synthetic jets is measured at the central line just outside of the speaker's conduit by a one-dimensional hot-wire anemometer (TSI probe mode 1210-T1.5) and data acquisition is implemented by the data acquisition system TSI-IFA300. The sensor diameter is 3.8 μm, and the active length is 1.27 mm. Data are acquired for 6.5536 s at a 40 kHz sampling rate (2^{18} samples). All raw data are saved. The high sampling rate provides an essentially continuous signal, and the long sampling time results in low uncertainty in statistical quantities. Inaccuracy in velocity measurement is estimated to be <0.5 m/s.

Part of experimental results had been presented by our groups in Ref. [14]. However, the control mechanism was explained as acoustic excitation (i.e., pressure wave). Based on the research and analysis of this paper, it could be affirmed that the key parameter of the excitation is jet velocity instead of pressure wave. Therefore, the measurement of jet velocity is very important.

2.3 DPIV Measurement. In order to obtain detail information on flow-field structure, A TSI 2D DPIV system is used which mainly consists of two pulsed laser generators, a CCD camera, and a synchronizer. Small particles are introduced into and carried

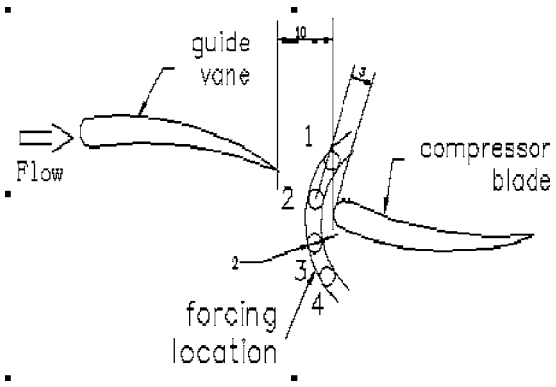

Fig. 3 Four stations for synthetic jets

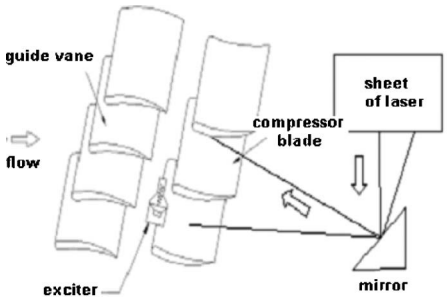

Fig. 4 Arrangement of optical path

by the flow. The displacement of particles in two or more time interval is measured and velocity is calculated accordingly, which are assumed to be the local velocity of the flow field.

The laser generator is an Nd:YAG pulsed laser generator, which provides laser pulses with a maximum energy of 200 mJ. The pulse duration is 8 ns. The operation frequency of the laser is 10 Hz. Appropriate lens are used to transform the laser beam emitted from the laser generator into a sheet of laser, which is introduced into the interior of compressor by a self-made planar mirror, as shown in Fig. 4.

A cross-correlation charge-coupled device with 1024×1280 pixels is adopted in photographic system. Since the entire experimental section is made of Plexiglas, there is no need to drill holes on the shroud for CCD photography and record. The CCD camera can shoot or take photos through the Plexiglas shroud.

Since the blades are made of Plexiglas, there appears severe optical reflection, which would not only damage the CCD camera, but also distort the images severely. Therefore, this becomes the key problem for successful application of DPIV. After several trials, it is finally decided that the blades are first painted with black alkyd paint, and then carbon powder is uniformly cast on its surface before it is dried, and finally redundant carbon powder is removed after the paint is dried. The finished blades are proved effective in preventing optical reflection and qualified for the experiments.

The solid particles as the tracer are glycol produced by LZL particle generator. The diameter of the particles is 0.6–1.2 μm, which has been proved to be a good tracer.

A sequence of 60 pairs of images is acquired at each operation condition. The images are acquired at a frequency of 3.75 Hz, and the time delay between two frames is 10 μs. The Insight 3.0 software is used to process the images. These sequences are used to compute time-averaged velocity and vorticity. It is estimated that the uncertainty of measured velocity is $\sim$3%.

3 Results and Analysis

3.1 Influence of Excitation Frequency and Amplitude. In order to indicate the improvement of aerodynamic performance by synthetic jets, the relative reduction of loss coefficient $\delta(\varpi)$ as a function of excitation frequency is shown in Fig. 5(*a*) for six incidences. The excitation location is fixed at station 3 (as shown in Fig. 3) since it appeared to provide better results than the other stations for most cases. First, focus on the curve of $i=15$ deg. When the excitation frequency is at the range of 700–850 Hz, the prominent positive effect is obtained and the maximum relative reduction of loss coefficient $\delta(\varpi)$ up to 27.5% at the frequency of 800 Hz. The positive effect decreases sharply when the excitation frequency is $<$700 Hz or $>$850 Hz. There is no positive effect obtained when the excitation frequency is $<$600 Hz or $>$1000 Hz. The relations of $\delta(\varpi)$ vs f_e exhibit similar well-regulated variations at other incidences.

Why does the prominent positive effect is obtained just when the excitation frequency is about at the range of 700–850 Hz?

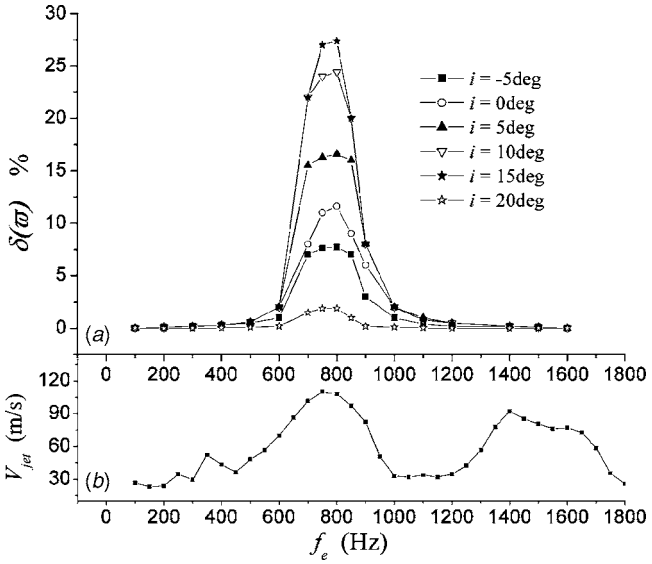

Fig. 5 (*a*) Relative reduction of loss coefficient and (*b*) jet velocity versus excitation frequency

Figure 5(*b*) shows the peak velocity of synthetic jet as a function of excitation frequency. The profile of curves in Figs. 5(*a*) and 5(*b*) is similar basically. The positive effect is directly correlated with the velocity of synthetic jet instead of excitation frequency itself. It could be also affirmed that the key parameter of the excitation is jet velocity instead of pressure wave. When the excitation frequency is about at the range of 700–850 Hz, the V_{jet} is more than 95 m/s ($\bar{A}=3.96$, the freesteam velocity is $\sim$24 m/s), and the prominent positive effect is obtained. When the excitation frequency is $<$600 Hz or $>$1000 Hz, the V_{jet} is reduced to 60–80 m/s ($\bar{A}=2.5-3.33$) and the positive effect is negligible. It is obvious that the jet velocity (or $\bar{A}$) plays a great role and must be sufficiently high exceeding the threshold value. In the present case, the threshold value is about $\bar{A}=3.0$.

This paper is a follow-up of the recent numerical paper of Ref. [12]. The threshold value is about $\bar{A}=0.1$ from the numerical results, which is very much lower than the threshold value with $\bar{A}=3.0$ from the experiment results. There are two reasons for difference between experimental and numerical result. One reason is different excitation mode. In numerical research, jet holes were drilled on suction side, directly. However, in present experiment, jet velocity is reduced severely when the jet flow arrived to the midspan of stator vane from casing for excitation located on casing and measuring points located on midspan of vane. Another reason is the choosing of other excitation parameters. The optimal values of other parameters (such as excitation frequency, excitation location, etc.) were chosen to analyze the function of excitation amplitude during the process of numerical research, which is difficult to do well in experiment.

Furthermore, it is noted that the high jet velocity with 92 m/s presented at frequency of 1400 Hz does not generate any reduction in loss coefficient as shown in Fig. 5. Two hypotheses maybe explain this phenomenon. One hypothesis is that the attenuation of jet velocity along the spanwise is stronger when the frequency is higher. For the jet located on casing and measuring points located on middle of stator vane, jet velocity may be reduced to below the threshold value. Accordingly, positive effect could not be achieved. The alternative hypothesis is that the coupling of excitation frequency and characteristic frequency of the flow field affects the result. The excitation frequency of 1400 Hz may be outside of the effective frequency range. Further research should be performed on this phenomenon.

In the present experiments, the jet velocity instead of frequency

itself affects the control effect. The role of frequency could not be visualized by the present experiments because the jet velocity is dependent on the resonance characteristic of the loudspeaker. In order to investigate the role of frequency, it is necessary to devise a fluidic actuator, the jet velocity of which is independent of the frequency. Of course, optimal analysis of individual parameters relying on reliable numerical simulation is also an economical and effective method.

The main difference of the steady method (such as suction or blowing) and unsteady method on separation flow control is that the excitation frequency plays a role by the unsteady method. Many researches show that the excitation frequency is correlated with the instability of the shear layer or wake. Zheng et al. [12] found that optimal excitation frequency is nearly equal to the characteristic frequency of vortex shedding, and the effective excitation frequency spans a wide spectrum by the synthetic jets in the axial compressor cascade. Wu et al. [15] showed that the largest lift increase is attained when excitation is half of the vortex shedding frequency over a post-stall airfoil. Amitay and Glezer [16] investigated the effect of the actuation frequency on the coupling between the synthetic jets and the cross-flow over a stalled airfoil in detail, and the experiment results showed that there are two distinct frequency bands in response of the separated flow to actuation. These researches have indicated that the excitation frequency plays an important role. In particular, the flow of the axial compressor is more complex than the flow over an airfoil and full of unsteady vortexes that move randomly with different scales and frequencies and constitute a highly nonlinear multifrequency system. There are more challenges and opportunities to investigate the essential role of excitation frequency using the synthetic jet in the axial compressor, which is the further object.

3.2 Influence of Incidence. The positive effect is different at different incidences with the flow rate kept unchanged as shown in Fig. 5(*a*). Figure 6 indicates the influence of incidence further. The excitation frequency is fixed at 800 Hz since the optimal effect is attained. When the $i=15$ deg, the maximum positive effect is obtained and the relative reduction of loss coefficient $\delta(\varpi)$ is up to 27.5%. The positive effect is decreased slightly along with the decreasing incidence. However, the positive effect is decreased sharply when the incidence is up to 20 deg.

The numerical study in Ref. [12] shows a gain over the entire incidence range covered from 0 deg to 25 deg, where the gain decreases with increasing incidence. The present paper shows a steady rise of the gain from −5 deg to 15 deg incidence until it drops very fast for a further rise in incidence. The optimal values of other parameters (such as excitation frequency, excitation amplitude, excitation location, etc.) were chose to analyze the function of incidence during the process of numerical research, which is difficult to do well in experiment.

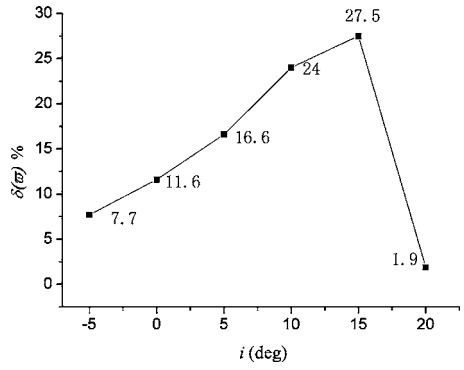

Fig. 6 Relative reduction of loss coefficient versus incidence

3.3 Influence of Excitation Location. In order to investigate the influence of excitation location, the frequency is fixed at 800 Hz. The distributions of total pressure loss along the pitch direction at the four stations (as shown in Fig. 3) with and without excitation are shown in Fig. 7, which is selected from the figures that indicate the effects of the forcing location on total pressure loss at the six incidences. The *y*-axis is total pressure loss *pl*. The effect of blade separation is a significant widening and deepening of the blade wake. At station 3, the total pressure loss in the wake region is reduced significantly for most incidences with the synthetic jet imposed, whereas the main flow has no change. At location 2, excitation does not reduce the total pressure loss but increases it for all incidences. This is because that station 3 is close to the separating point of suction side, and the excitation may enhance the mixing of the main flow and boundary layer flow to suppress separation flow. However, station 2 is near the stagnant point; thus, the jet here may become the perturbing energy to disarrange the flow. At station 1, excitation may reduce the pressure loss a little (such as $i=-5$ deg) or increase it a little, which depends on the incidence. At station 4, there is still a positive effect, especially at large incidence, but the positive effect is less than that of station 3.

3.4 Change of Space-Time Structure of the Flow Field. The positive results of improved aerodynamic performances have been presented, and now we turn to the corresponding change of the space-time structure of the flow field. Instantaneous vorticity field and streamlines measured by DPIV are shown in Fig. 8.

With the inlet flow rate unchanged, the instantaneous vorticity field and streamlines measured at different incidences without excitation are shown in Fig. 9, in which the existence of wake vortices is clearly displayed. As the incidence increases from 5 deg to 16 deg, streamlines become more and more twisted and chaotic and the separation area becomes larger and larger. Meanwhile, the intensity of wake vortices becomes stronger, the wake spreads wider, and the distribution of vorticity intensity becomes much more chaotic. This means, as the incidence increases, the flow field becomes more and more chaotic and the separation becomes more and more severe.

With the inlet flow rate unchanged, instantaneous vorticity field and streamlines measured at different incidences with excitation are shown in Fig. 10. It is obvious that the intensity of wake vortices becomes much weaker with excitation imposed and streamlines become smoother and more uniform from its comparison to Fig. 9. The comparison of time-averaged vorticity without and with excitation is also presented in Figs. 11 and 12, which shows that the time-averaged vorticity also became weaker by synthetic jet. The enhancement of overall performance of the flow field is the result of the improvement of the space-time structure of the flow field.

The space-time structure of unsteady separated flows can be divided into two types, one is to describe of the spatial structure of the flow field at any fixed time, and another is to describe the time variation of the flow field at any given point. Figures 11 and 12, obtained by DPIV technique, belong to the former, whereas the latter chiefly uses frequency spectrum. We will not go into detail here for brevity.

3.5 Efficiency of the Synthetic Jet Separation Control System. In this flow control scheme, electric energy is consumed to bring the total pressure recovery. Thus, to evaluate the efficiency of this control method objectively, a comparison between the total pressure recovery obtained and the electric energy consumed must be made. What is the ratio between the total pressure recovered due to the implementation of synthetic jets and the total pressure rise that would be achieved on the cascade throughflow if one used the power required to drive the loudspeakers to isentropically compress the air?

For the condition of $i=10$ deg and $f_e=800$ Hz, the total pres-

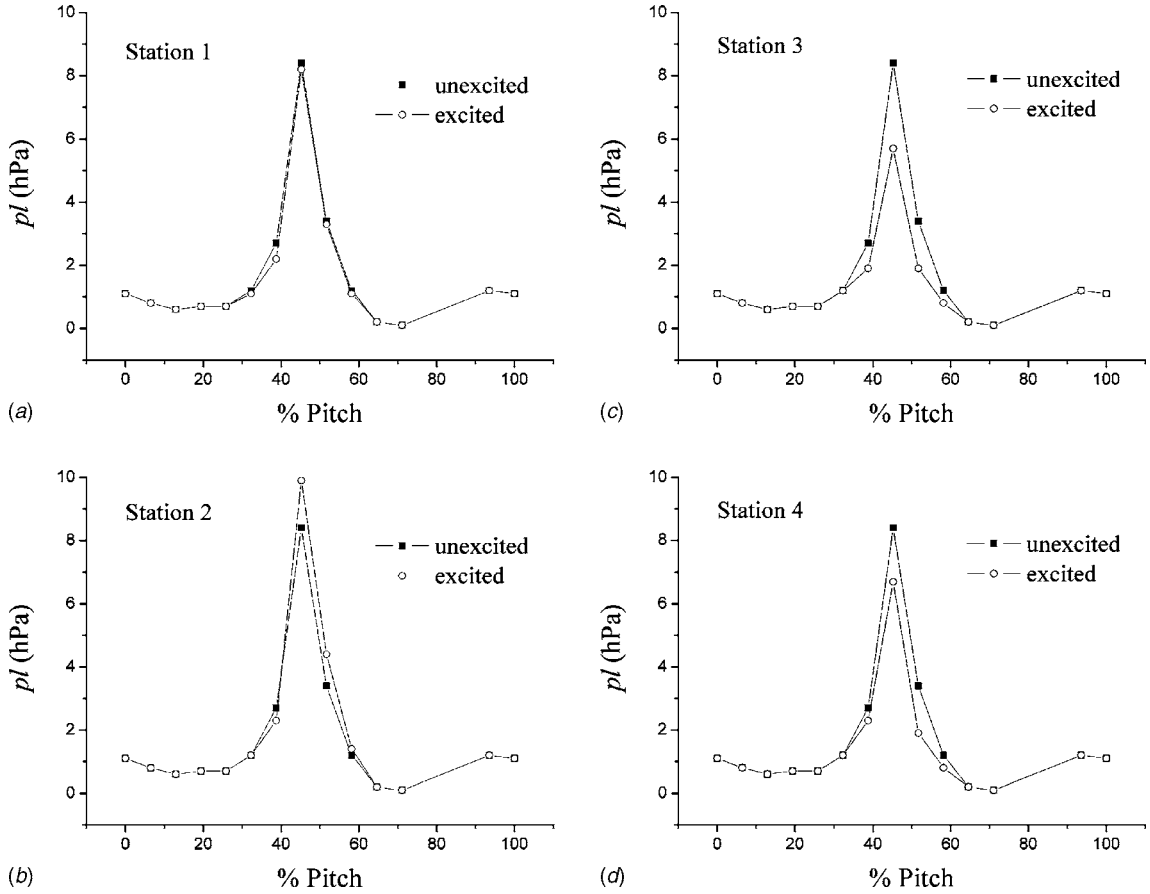

Fig. 7 Total pressure loss along pitch distance with and without synthetic jet for the four station, i=10 deg

sure recovery Δp_2^* is 60 Pa, the power of loudspeaker N is 30 W, and the air volume flow rate $\dot{Q}$ is 3.3 m^3/s. If all the electric energy can be converted to the total pressure rise isentropically, the total pressure rise produced by the actuator is $\Delta p_{iso}^* = N/\dot{Q}$. The ratio between Δp_2^* and Δp_{iso}^*, i.e., the "efficiency" of the synthetic jet separation control system, is $k = \Delta p^*/\Delta p_{iso}^* = \Delta p^* \dot{Q}/N = 60 \times 3.3/30 = 6.6$. In other words, 6.6 portions power could be obtained if one portion power is consumed.

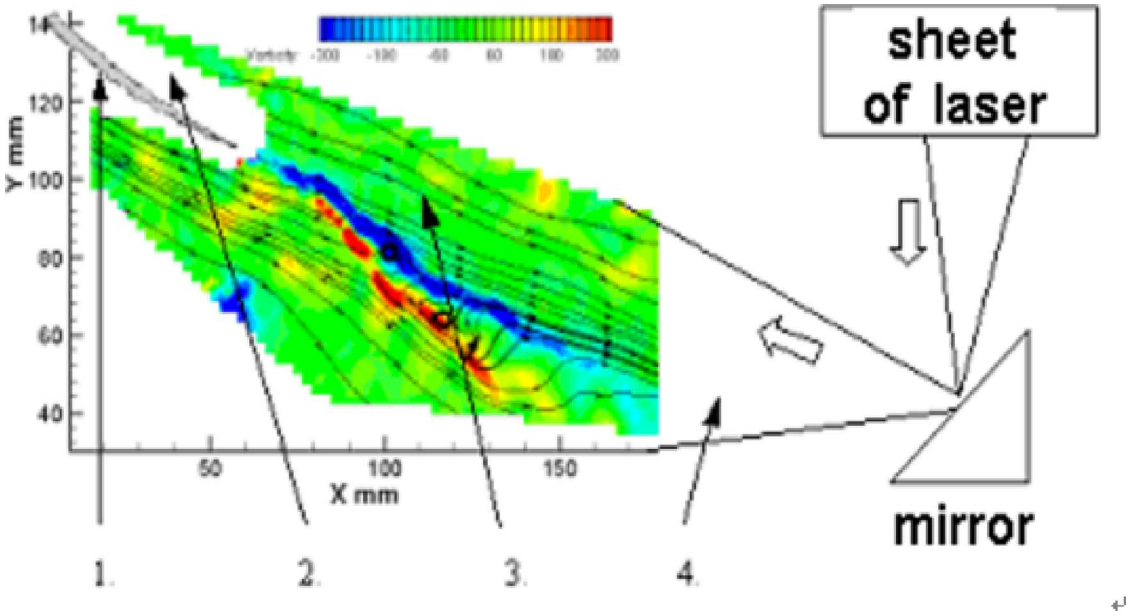

Fig. 8 Introduction of the picture by DPIV: 1, profile of compressor cascade; 2, inaccessible region; 3, streamlines; 4, laser sheet after reflecting from planar mirror: (*a*) i=5 deg, (*b*) i=10 deg, and (*c*) i=16 deg

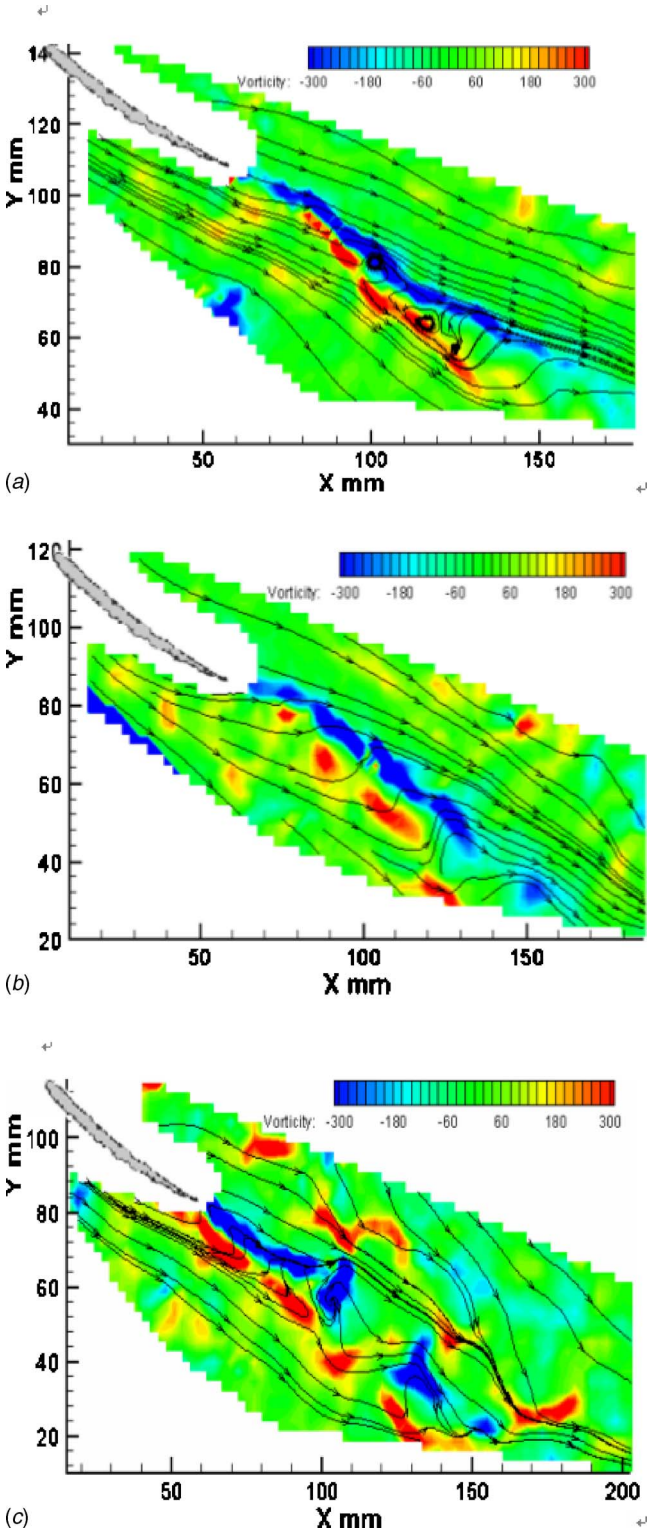

Fig. 9 Instantaneous vorticity field and streamline without synthetic jet: (*a*) *i*=5 deg, (*b*) *i*=10 deg, and (*c*) *i*=16 deg

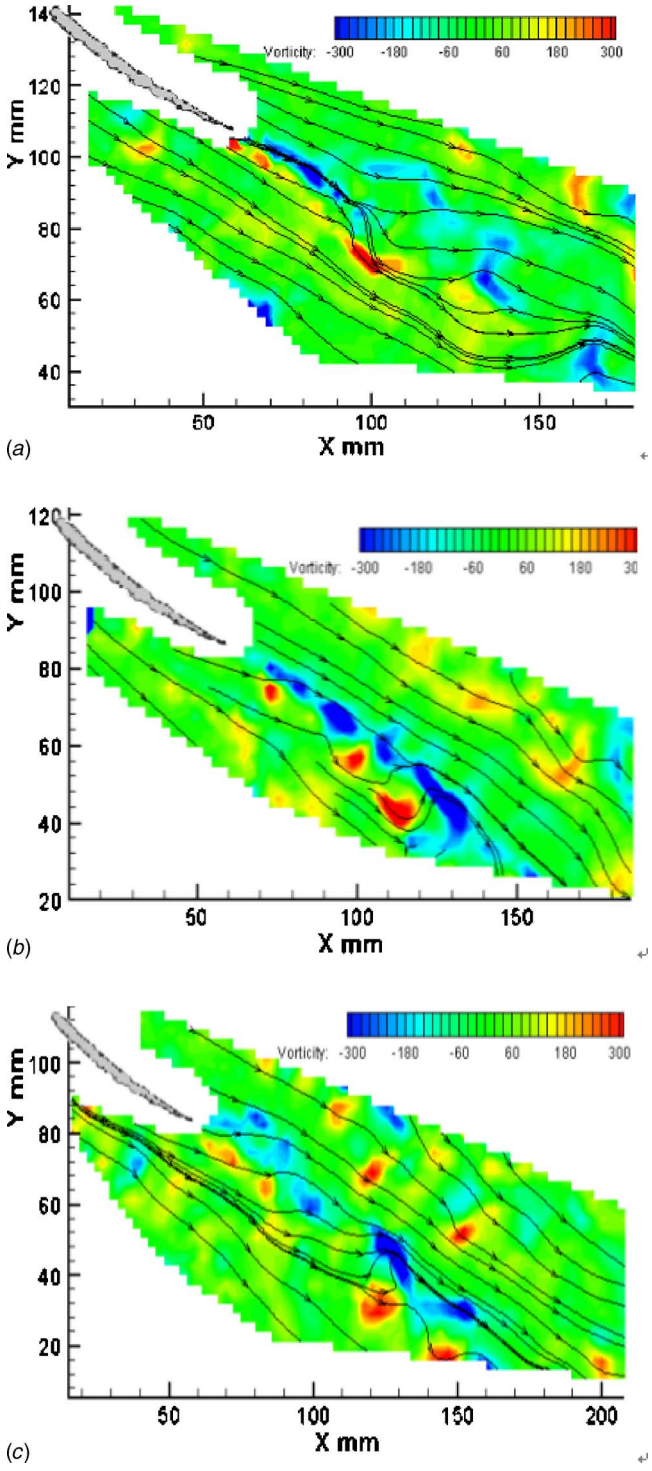

Fig. 10 Instantaneous vorticity field and streamline with synthetic jet

Conclusions

Active separation control had been successfully demonstrated on axial compressor stator vanes using synthetic jets. The experiments were performed in a stationary annular cascade wind tunnel at different incidences. The experiment results had shown that the aerodynamic performance could be a substantial increase and the maximum relative reduction of loss coefficient was up to 27.5%. The separation was basically eliminated, and the intensity of wake vortices was weakened by synthetic jets.

The roles of some parameters, such as excitation frequency, amplitude, incidence, and location, were researched. In order to investigate the role of frequency and take advantage of an instability mechanism, it is necessary to devise a new fluidic actuator, the jet velocity of which is independent of frequency. The results showed that the jet amplitude played an important role. The positive effect was obtained when the jet velocity exceeded the thresh-

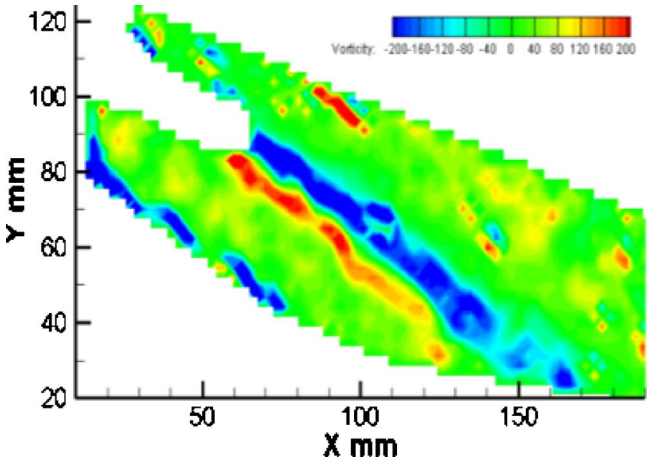

Fig. 11 Time-averaged vorticity field without synthetic jet, i =10 deg

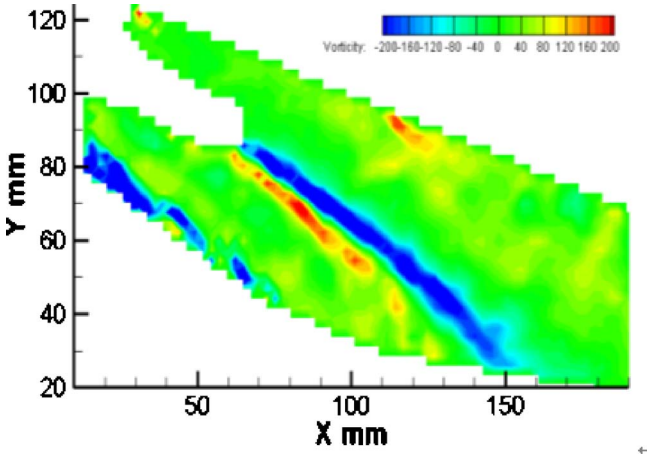

Fig. 12 Time-averaged vorticity field with synthetic jet, i =10 deg, f_e=750 Hz

old value. The positive effect was attained in a wide range of incidence, and the optimal positive effect was obtained at 15 deg. Four excitation stations were tested. For most cases, the optimal positive effect was obtained at station 3. These results led the authors to conclude that the application of synthetic jet for separation flow control on axial compressor stator vanes showed great promise. In addition, an evaluation on the efficiency of the synthetic jet separation control system was discussed. The ratio between the gain and the expense was up to 6.6.

Acknowledgment

This work was supported by China Postdoctoral Science Foundation (No. 20060400088) and by the foundation from National Key Laboratory of Diesel Engine Turbocharging Technology (Grant No. 9140C3301020601).

Nomenclature

$\bar{A}$ = relative excitation amplitude, $\bar{A}=V_{\text{jet}}/c_\infty$
c_∞ = freesteam velocity
f_e = excitation frequency
i = incidence
k = ratio, $k=\Delta p^*/\Delta p^*_{iso}$
N = power of loudspeaker
p_1 = static pressure at cascade inlet
p^*_1 = total pressure at cascade inlet
p^*_2 = total pressure at cascade exit
$(p^*_2)_{ex}$ = total pressure at cascade exit with excitation
$(p^*_2)_{un}$ = total pressure at cascade exit without excitation
Δp^*_2 = total pressure recovery, $\Delta p^*_2=(p^*_2)_{ex}-(p^*_2)_{un}$
Δp^*_{iso} = total pressure rise produced by the actuator, $\Delta p^*_{iso}=N/\dot{Q}$
pl = total pressure loss, $pl=p^*_1-p^*_2$
$\dot{Q}$ = air volume flow rate
V_{jet} = peak velocity of synthetic jets
ϖ = loss coefficient, $\varpi=(p^*_1-p^*_2)/(p^*_1-p_1)$
ϖ_{un} = loss coefficient without excitation
ϖ_{ex} = loss coefficient with excitation
$\delta(\varpi)$ = relative reduction of loss coefficient, $\delta(\varpi)=(\varpi_{un}-\varpi_{ex})/\varpi_{un}\times 100\%$

References

[1] Greenblatt, D., and Wygnanski, I. J., 2000, "The Control of Flow Separation by Periodic Excitation," Prog. Aerosp. Sci., **36**, pp. 487–545.
[2] Schaeffler, N. W., Hepner, T. E., Jones, G. S., and Kegerise, M. A., 2002, "Overview of Active Flow Control Actuator Development at NASA Langley Research Center," AIAA Paper No. 2002-3159.
[3] Smith, B. L., and Glezer, A., 1997, "Vectoring and Small-Scale Motions Effected in Free Shear Flows Using Synthetic Jet Actuators," AIAA Paper No. 97-0213.
[4] Compton, D. A., and Johnston, J. P., 1992, "Streamwise Vortex Production by Pitched and Skewed Jets in a Turbulent Boundary Layer," AIAA J., **30**(3), pp. 640–647.
[5] Seifert, A., Bachar, T., Koss, D., Shepshelovich, M., and Wygnanski, I. J., 1993, "Oscillatory Blowing: A Tool to Delay Boundary-Layer Separation," AIAA J., **31**(11), pp. 2052–2060.
[6] Gilarranz, J. L., Traub, L. W., and Rediniotis, O. K., 2005, "A New Class of Synthetic Jet Actuators—Part I: Design, Fabrication and Bench Top Characterization," ASME J. Fluids Eng., **127**, 367–376.
[7] Gilarranz, J. L., Traub, L. W., and Rediniotis, O. K., 2005, "A New Class of Synthetic Jet Actuators—Part II: Application to Flow Separation Control," ASME J. Fluids Eng., **127**, 377–387.
[8] Smith, D. R., 2002, "Interaction of a Synthetic Jet with a Crossflow Boundary Layer," AIAA J., **40**(11), pp. 2277–2288.
[9] Seifert, A., and Pack, L. G., 1999, "Oscillating Control of Separation at High Reynolds Number," AIAA J., **37**(9), pp. 1062–1071.
[10] Culley, D. E., Bright, M. M., Prahst, P. S., and Strazisar, A. J., 2004, "Active Flow Separation Control of a Stator Vane Using Embedded Injection in a Multistage Compressor Experiment," ASME J. Turbomach., **126**, pp. 24–34.
[11] Zheng, X. Q., Zhou, S., Hou, A. P., and Xiong, J. S., 2005, "Unsteady Cooperative Flow Type in the Axial Compressor," Prog. Nat. Sci., **15**(10), pp. 930–936.
[12] Zheng, X. Q., Zhou, X. B., and Zhou, S., 2005, "Investigation on a Type of Flow Control to Weaken Unsteady Separated Flows by Unsteady Excitation in Axial Flow Compressors," ASME J. Turbomach., **127**, pp. 489–496.
[13] Volino, R. J., 2003, "Separation Control on Low-Pressure Turbine Airfoils Using Synthetic Vortex Generator Jets," ASME J. Turbomach., **125**, pp. 765–777.
[14] Qiu, Y. X., Ge, J. D., Lu, Y. J., Zhou, S., and Li, Q. S., 2003, "Research on Sound-Vortex Resonance in Enhancing Performance of an Annular Cascade," ASME Paper No. GT2003-38022.
[15] Wu, J. Z., Lu, X. Y., Denny, A. G., Fan, M., and Wu, J. M., 1998, "Post-Stall Flow Control on an Airfoil by Local Unsteady Forcing," J. Fluid Mech., **371**, pp. 21–58.
[16] Amitay, M., and Glezer, A., 2002, "Role of Actuation Frequency in Controlled Flow Reattachment Over a Stalled Airfoil," AIAA J., **40**(2), pp. 209–216.

Heat Transfer at High Rotation Numbers in a Two-Pass 4:1 Aspect Ratio Rectangular Channel With 45 deg Skewed Ribs

Fuguo Zhou

Sumanta Acharya

Turbine Innovation and Energy Research (TIER) Center, College of Engineering, Louisiana State University, Baton Rouge, LA 70803

Heat transfer measurements are reported for a rotating 4:1 aspect ratio (AR) coolant passage with ribs skewed 45 deg to the flow. The study covers Reynolds number (Re) in the range of 10,000–70,000, rotation number (Ro) in the range of 0–0.6, and density ratios (DR) between 0.1 and 0.2. These measurements are done in a rotating heat transfer rig utilizing segmented copper pieces that are individually heated, and thermocouples with slip rings providing the interface between the stationary and rotating frames. The results are compared with the published data obtained in a square channel with similar dimensionless rib-geometry parameters, and with the results obtained for a 4:1 AR smooth channel. As in a 1:1 AR channel, rotation enhances the heat transfer on the destabilized walls (inlet-trailing wall and outlet-leading wall), and decreases the heat transfer ratio on the stabilized walls (inlet-leading wall and outlet-trailing wall). However, the rotation-induced enhancement/degradation for the 4:1 rectangular channel is much weaker than that in the square ribbed channel, especially in the inlet (the first passage). The results on the inlet-leading wall are in contrast to that in the smooth channel with the same AR, where rotation causes heat transfer to increase along the inlet-leading wall at lower Reynolds number (Re = 10,000 and 20,000). Higher DR is observed to enhance the heat transfer on both ribbed walls in the inlet (the first passage) and the outlet (the second passage), but the DR effects are considerably weaker than those in a ribbed square channel. Measurements have also been parameterized with respect to the buoyancy parameter and results show the same general trends as those with respect to the rotation number. In addition, pressure drop measurements have been made and the thermal performance factor results are presented.
[DOI: 10.1115/1.2752185]

Introduction

One approach for increasing the efficiency of gas turbines is to raise the turbine inlet temperature, which typically exceeds the allowable material limits for the blade. A common technique for blade cooling is to circulate coolant air through internal cooling passages within the turbine blades. A key goal of the turbine heat transfer community is to maximize the cooling efficiency of internal cooling passages and to accurately quantify the performance of the coolant passages for parameters relevant to engine operating conditions. As a result, many studies have focused attention on different cross-sectional geometries, different turbulator configurations, and different flow parameters for both stationary and rotating internal coolant passages. These studies have provided valuable insights on the effect of Coriolis and centrifugal forces on the flow and heat transfer characteristics for specific geometries, and have provided guidelines for implementing improved internal-cooling strategies.

The early research in the field focused attention mainly on straight, smooth, tubes with a circular cross section [1–3]. This was extended to square smooth cross-section ducts [4,5] and detailed measurements were reported in a straight and a serpentine, rotating channel. Their study investigated the effects of rotation, density ratio, and centrifugal force-driven buoyancy. Wagner et al. [6] and Johnson et al. [7] further studied serpentine, square cross-section rotating channels with turbulators (ribs) on the trailing and leading walls. Both normal (90 deg) ribs or skewed (45 deg) ribs, with rib pitch-to-height ratio P/e of 10, and the rib height-to channel diameter ratio e/D_h of 0.1, were studied. Their results, for the smooth and the two ribbed models, showed that in the radially outward (inlet) leg of the coolant passage the heat transfer ratio on the trailing walls steadily increased with increasing rotation number. However, on the inlet leading wall, the heat transfer ratio initially decreased as the rotation number increased, but beyond a critical rotation number (depending on the wall conditions, the density ratio and streamwise location) the heat transfer ratio increased with rotation number. In the radially inward (outlet) passages, the heat transfer ratio demonstrated more complex behavior due to bend effects. In these studies [4–7], uniform wall temperature conditions were maintained.

The cross section in the coolant passages of the first stage turbine blade airfoil ranges typically from tall passages (low aspect ratio) in the thickest portion of the turbine blade airfoil, to wide rectangular passages (high aspect ratio) in the trailing edge. In the later blade stages, where the cooling flow requirements are lower, typically the second pass has a higher aspect ratio, and therefore higher aspect ratio passages are encountered across the entire airfoil. Most of the early reported studies have focused attention on square passages. However, several studies have reported measure-

Contributed by the International Gas Turbine Institute of ASME for publication in the JOURNAL OF TURBOMACHINERY. Manuscript received October 8, 2006; final manuscript received January 10, 2007; published online March 24, 2008. Review conducted by David Wisler. Paper presented at the ASME Turbo Expo 2006: Land, Sea and Air (GT2006), Barcelona, Spain, May 8–11, 2006, Paper No. GT2006-90391.

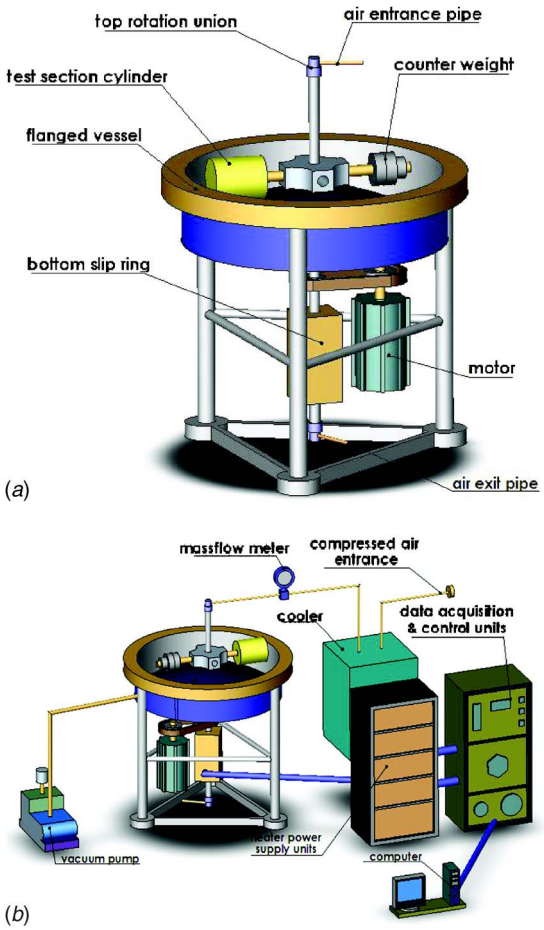

Fig. 1 Experimental setup: (*a*) rotation rig; (*b*) experimental apparatus

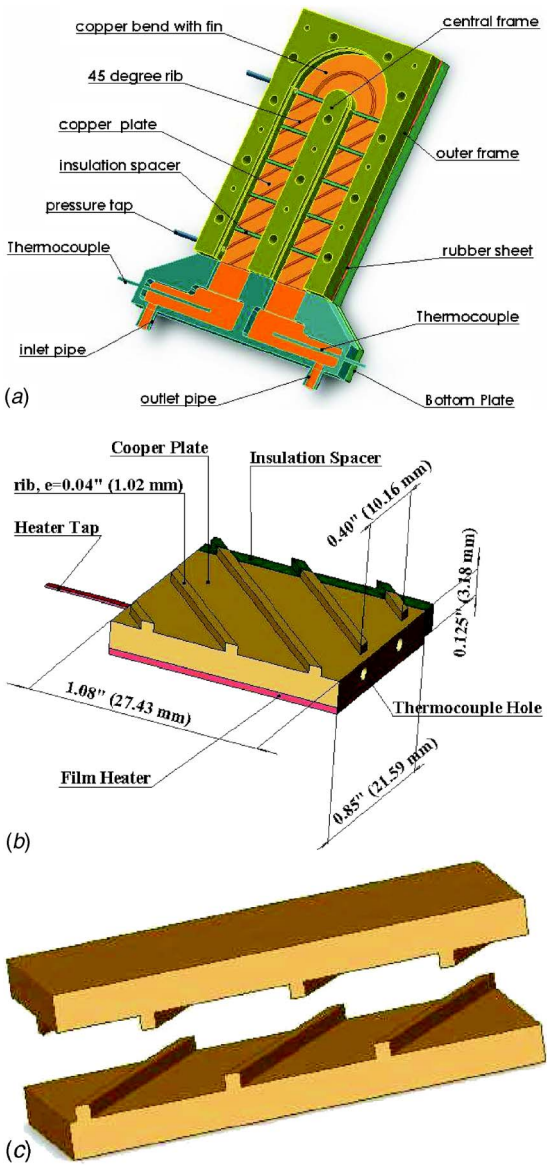

Fig. 2 Heat transfer model and the ribbed copper elements: (*a*) lower portion of the 45 deg ribbed model; (*b*) 45 deg ribbed copper element with heater and spacer; (*c*) ribs configuration on the leading and trailing walls

ments in rectangular cross-section internal passages. Guidez [8] first studied a radial straight smooth channel of aspect ratio (AR)=2:1 for Reynolds numbers from 17,000 to 41,000 and rotation numbers up to about 0.2, and found the same trends as described in Wagner et al. [4]. Morris et al. [9] also studied a straight rectangular channel with AR=2:1, covering Re from 10,000 to 25,000 and Ro from 0 to 0.2, but noted weaker rotation effects than those reported by Wagner et al. [4]. Iacovides et al. [10] performed a numerical study on an AR=2:1 straight rectangular channel with rotation. Their results revealed that at low rotation numbers Coriolis forces induced a pair of symmetric streamwise vortices. The vortex pair could be transitioned to a more complex four-vortex structure at high rotation numbers due to the flow instability on the pressure wall. Soong et al. [11] conducted a series of tests on square and rectangular channels with different aspect ratios, but mainly focused attention on the laminar flow regime, and rotation numbers less than 0.05 for the turbulent flow cases. Han et al. [12] conducted a series of stationary measurements of heat transfer and pressure drop in straight channels with AR=1:1, 2:1, and 4:1. Two opposite walls were roughened with square cross-sectional ribs. The experiments covered Reynolds number in the range of 10,000–60,000, e/D_h of 0.047 and 0.078, P/e of 10 and 20, and rib angles of α=90 deg, 60 deg, 45 deg, and 30 deg. Their results showed that the heat transfer and friction decreased with decreasing AR. In square channels, the heat transfer was 30% higher at α=30–45 deg than at α=90 deg. However, in a 4:1 rectangular channel the heat transfer was almost the same for α=30–90 deg. Griffith et al. [13] experimentally studied straight, smooth, and 45 deg ribbed, rectangular models of AR=4:1 over a parameter range that extended from a Ro=0.305 at Re=5,000 to Ro=0.038 at Re=40,000. Their results indicated that the heat transfer ratio on both leading and trailing walls increased with rotation number. This observation was different from that reported for square channels [4–7]. Zhou et al. [14] reported a study on a smooth, two-pass, rectangular channel of AR=4:1 with Reynolds number from 10,000 to 150,000, rotation number from 0 to 0.6, and density ratio from 0.10 to 0.20. The results indicated that, for low Reynolds number (Re=10,000 and 20,000), rotation enhanced the heat transfer in inlet passage on both leading and trailing walls as Griffith et al. [13] reported for the smooth and ribbed walls. However, for high Reynolds numbers, the inlet-leading surface heat transfer decreased as rotation number increased. The study also found that increasing density ratio enhances the heat transfer on all walls.

The configuration of interest in the present study is that of a two-pass, rectangular coolant channel of AR=4:1, with ribs oriented at 45 deg to the flow direction. This configuration has received limited attention, and only for limited parameter ranges.

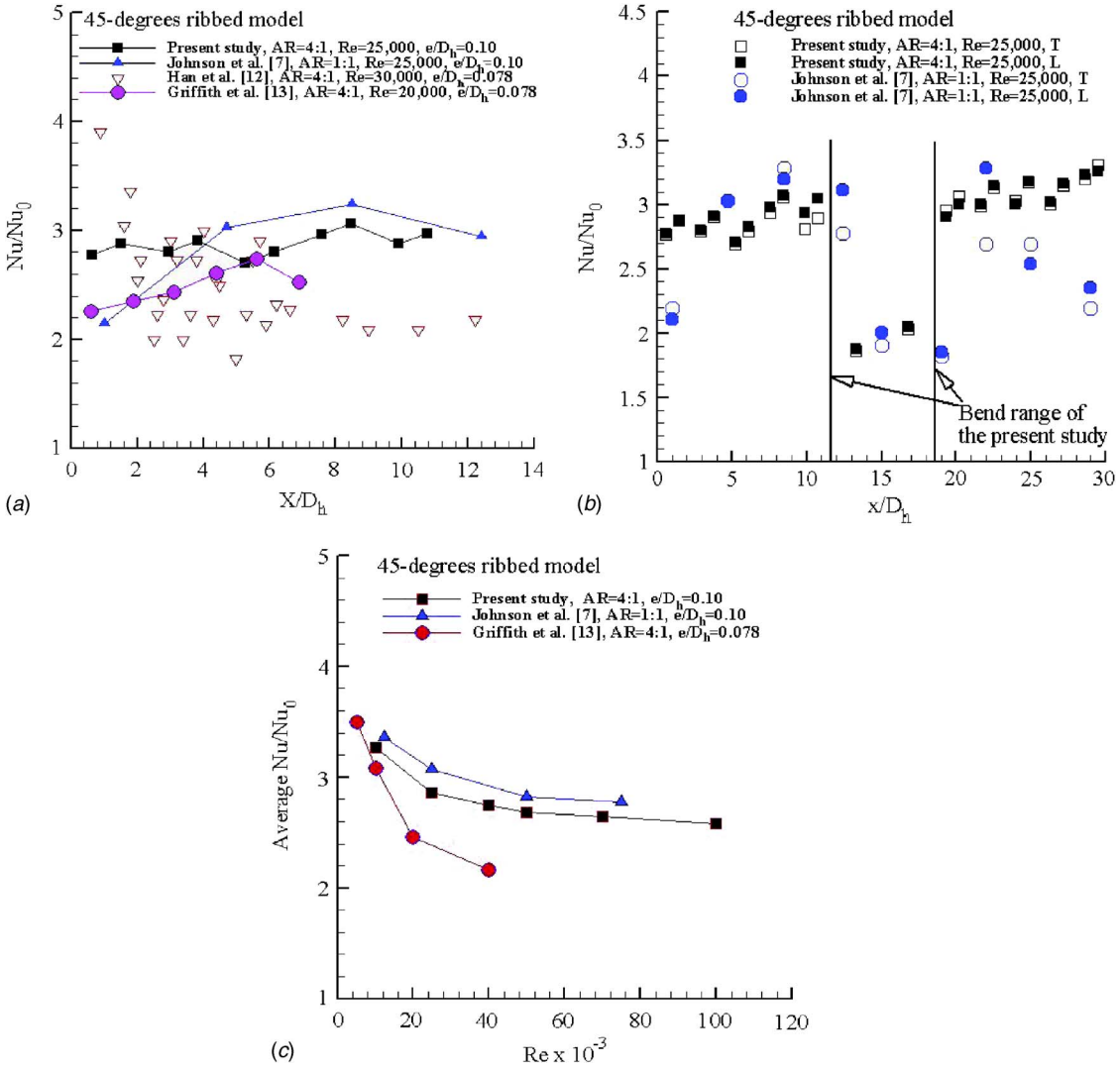

Fig. 3 Comparisons with previous studies at stationary conditions, P/e=10, *T* refers to trailing wall; and *L* refers to leading wall: (*a*) Nu/Nu_0 distributions in the inlet; (*b*) Nu/Nu_0 distributions in the inlet, bend, and outlet; and (*c*) Reynolds number effects in the inlet

For example, at a Re=20,000 a maximum Ro of 0.075, and at a Re=40,000 a maximum Ro of 0.038 has been reported by Griffith et al. [13]. Realistic parameter ranges of interest include a typical Reynolds number of 25,000, and a rotation number in the range of 0.2–0.4. Higher parameter ranges are possible in closed-loop steam cooled blades. Moreover, density ratio effects and buoyancy effects on the heat transfer need to be quantified for this geometry; however, no such data are available. The objectives of the present study are to investigate the effects of rotation number, density ratio or buoyancy parameter, and Reynolds number on the heat transfer and pressure drop characteristics in a 4:1 AR rectangular channel with skewed 45 deg ribs. The parameter ranges of interest include: Reynolds number Re from 10,000 to 70,000, rotation number Ro from 0 to 0.6, density ratio (DR) from 0.1 to 0.2, and buoyancy parameter Bo from 0 to 3.0. The highest Ro (0.6) and Bo (3.0) are achieved only at the lowest Re (10,000). At Re =25,000, the highest Ro and Bo achieved are 0.25 and 0.58, respectively. Results for these parameter ranges, and particularly the higher Ro, Re, and Bo are not available in the literature, and serve as the main motivation for the present study.

In analyzing the present measurements for a 4:1 AR, results will be directly compared with published results for a 1:1 AR geometry [7] with skewed 45 deg ribs. This comparison will help define the role of AR on parametric effects.

Experimental Details

Experimental Setup. The rotating rig shown in the Fig. 1(*a*), and originally used by Wagner et al. [4–6], and Johnson et al. [7], has been utilized in the present study. The facility has two major components: the containment vessel and the rotating arm assembly. The containment vessel is 1.83 m (6 feet) in diameter and consists of two symmetrical flanged sections. The upper section (not shown in Fig. 1(*a*)) of the vessel is removable to allow access to the rotating arm, and the lower section is anchored and supported by a steel support frame shown in Fig. 1(*a*) The vessel is designed for operation at 5 mm Hg absolute pressure to reduce the viscous heating and the power requirement of the rotating arm.

The arm assembly consists of the vertical shaft and the horizontal arm, which are driven by a 15 horsepower dc motor. The rotational speed of the shaft can be varied from 0 to a maximum of 1500 rpm by a feedback electronic controller. The vertical shaft

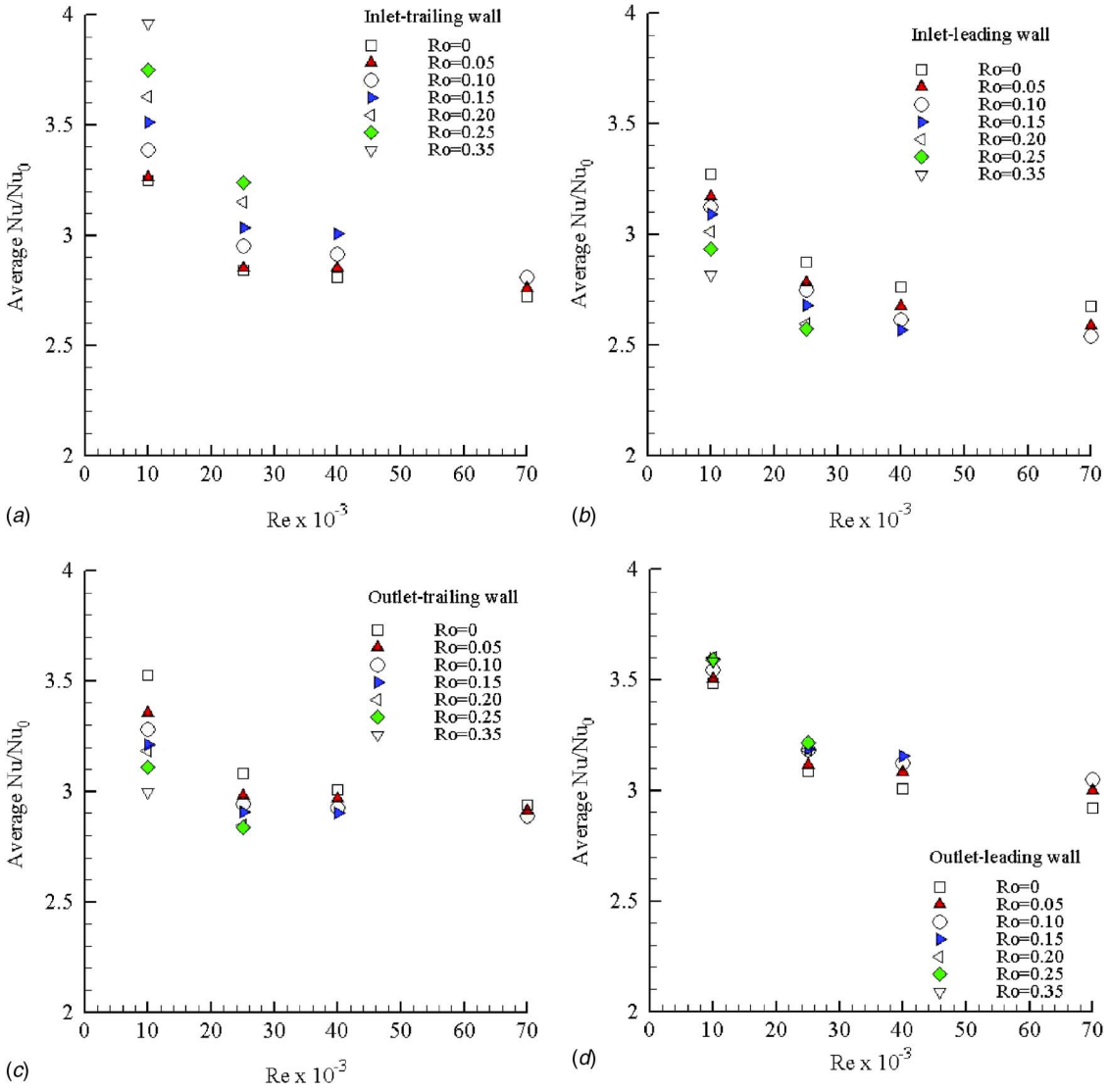

Fig. 4 Re number effects with variation of rotation number at DR=0.13 (*a*) inlet-trailing wall; (*b*) inlet-leading wall; (*c*) outlet-trailing wall; and (*d*) outlet-leading wall

consists of the main outer shaft and an inner concentric shaft. Together the shafts provide dual fluid paths for the rotary unions mounted on each end of the main shaft. In the present experiments, only the inner shaft is used as the air path. The rotary unions and the paths in the shafts were designed to sustain 1034 kPa (about 10 atm).

On the exterior surface of the main shaft, recessed grooves allow signal and power leads to run from the rotating arm assembly to two slip rings, one located on the upper end of the main shaft (not shown in the figure) and the other on the lower end. The two slip rings provide a total of 240 channels for power and instrumentation wires between the stationary and rotating frames.

A cylindrical pressure vessel containing the test section is mounted on one end to the horizontal arm. On the other end, a counter weight, with variable mass and positioning capabilities, is mounted to allow for static and dynamic balancing of different test sections. Stainless-steel tubing along the arm provides an air passage from the test section to the shaft. A Kulite and a Scanivalve pressure transducer are mounted on the arm to measure the absolute pressure and differential pressure inside the test section, respectively.

Air entering the test section is circulated through a refrigerant cooling loop to alter and maintain the temperature of the inlet airflow in order to achieve the desired density ratio, as shown in Fig. 1(*b*). The air is provided by a compressor-dryer-reservoir system, with a maximum mass flow rate and pressure of 0.5 kg/s and 20 atm (300 psia), respectively. The power supply unit has 72 independent channels for providing the 0–45 V of dc power for the heaters inside the test section. The data are acquired through Hewlett-Packard data acquisition systems (HP 3497A and HP 3498A Extender), which are connected to a Dell computer through a GPIB port and controlled by a custom-written C program. The pressure signals, shaft speed, thermocouple readings, and heater power readings are all recorded by this system. The mass flow rate of the airflow is read separately through a Rosemount mass flow metering unit.

Heat Transfer Models. Figure 2(*a*) shows a section view of the lower portion of the 45 deg ribbed model. The lower portion of the test section consists of a 6.35 mm (0.25 in.) thick G-10 Garolite (continuous-woven laminated glass fabric with a thermal conductivity of 0.1 W/(m K)) bottom plate; a 0.794 mm (0.031 in.) thick silicon rubber sheet sandwiched between the bottom plate and the frames; a 12.7 mm (0.5 in.) thick G-10 Garolite central and outer frame; and 11 copper elements (ten rectangular plates

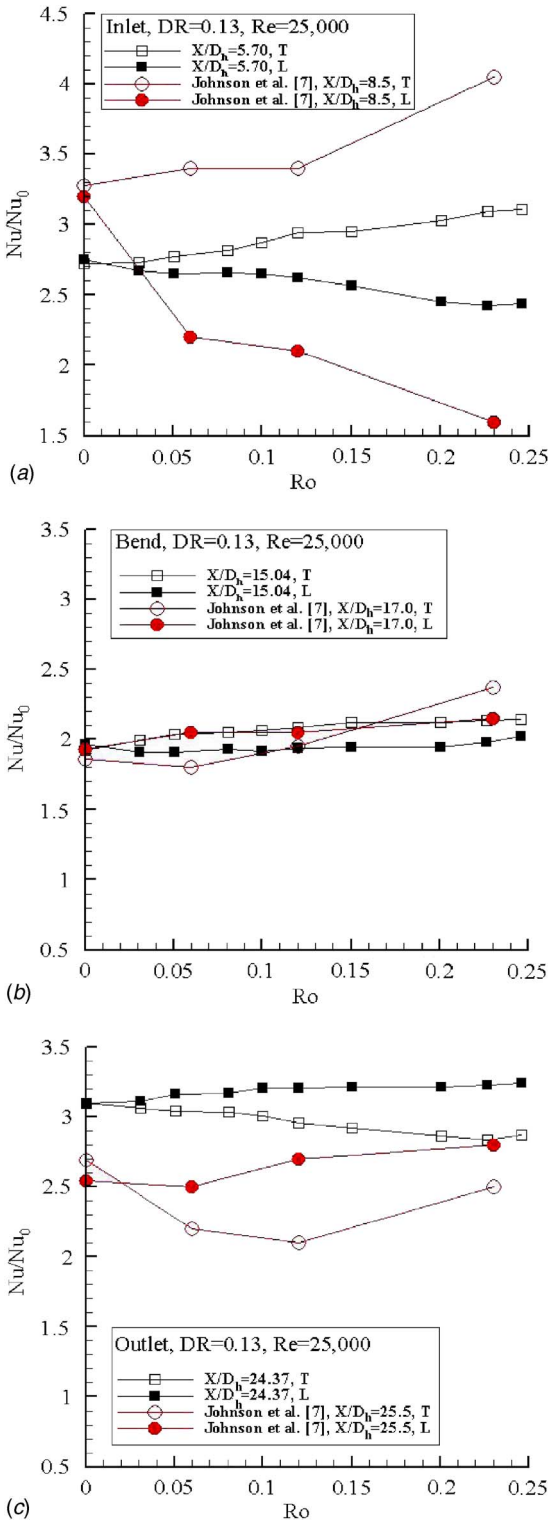

Fig. 5 Rotation effects in comparisons with Johnson et al. [7] at Re=25,000 and DR=0.13: (*a*) inlet (the first passage); (*b*) bend; and (*c*) outlet (the second passage)

plus a bend) 3.175 mm (0.125 in.) thick. The assembled copper elements rest on the shoulders of both the central and outer frames, and are flush with the bottom surface of the frame. The assembled copper elements that make up the top of the test section (not shown in Fig. 2(*a*)) are flush with the top of the frame. Together they form a U-shaped channel with a cross-section width of 25.4 mm (1 in.) wide by 6.35 mm (0.25 in.) tall (aspect ratio of 4:1 and hydraulic diameter of 10.16 mm (0.4 in.)). An additional silicon rubber sheet and a G-10 Garolite top plate, identical to the those at the bottom, rests on the top of the frame, and the whole unit is held together by screws through the smaller holes in the frames.

The straight inlet and outlet sections of the test channel are 117.475 mm (4.625 in.) long, and the outer diameter of the bend is 69.85 mm (2.75 in.). The smooth inner and outer sidewalls, which are not heated during the tests, are formed by the G-10 frame surfaces. In the inlet channel, two pressure taps are installed to measure the inlet static pressure and pressure drop across the length of the first straight leg of the channel.

A steel two-channel transition section is inserted between the top and bottom G-10 plates and aligned with the inlet and exit planes of the test section. This section provides the transition between the test channel and the air-feeds on the rotation rig. The transition section is also equipped with screens to stabilize the flow, and two *K*-type thermocouples to measure the inlet and outlet flow temperatures.

The whole unit is bolted between two steel support plates, and the assembly is mounted inside a cylindrical pressure vessel. The thermocouple leads, power wires, and the pressure transducer tubes are routed out of the vessel through sealed plugs on one of the cylinder's planar faces.

The typical copper element configuration with 45 deg ribs is shown in Fig. 2(*b*). Each copper plate has the dimensions of 27.432 mm (1.08 in.) by 21.59 mm (0.85 in.) by 3.175 mm (0.125 in.). On the back of each copper plate, a Minco Kapton-backed foil heater is installed using thermally conductive adhesive film. Two *K*-type thermocouples are installed into two blind holes inside each copper plate using thermally conductive glue. Each copper plate is isolated by a G-10 Garolite spacer with dimensions of 1.905 mm (0.075 in.) by 27.432 mm (1.08 in.) by 3.175 mm (0.125 in.) to impede heat conduction between different copper plates. The inner surfaces of the spacers are carefully flush mounted with the surfaces of the copper elements in the channel. A total of 20 copper plates separated by spacers collectively form the top and bottom of inlet and outlet straight channels.

The ribs are machined directly on the copper plates. Skewed ribs are also machined through the G-10 insulation spacers, and the copper plates and G-10 spacers are carefully aligned so that the ribs are continuous as shown in Fig. 2(*b*). The rib pitch $P=10.16$ mm (0.4 in.), resulting in $e/D_h=0.1$ and $P/e=10$. The upper and lower ribs are both oriented at 45 deg to the flow direction, and their radial locations are staggered relative to each other, as shown in Fig. 2(*c*).

In addition, a continuous copper element is used to form each bend. Each bend plate (top and bottom) is equipped with a foil heater with the same surface area as the bend and two *K*-type thermocouples.

Data Reduction. During each run of the experiments, the wall temperature, T_w, of each copper plate is maintained at a constant value. In order to achieve the uniform wall temperature condition, the electric current to each individual heater is adjusted so that all copper elements are at the same wall temperature T_w. By varying T_w and inlet flow temperature, T_{in}, different density ratios are obtained. The local heat transfer coefficient h_i at the ith copper plate is calculated from the net heat flux, $q''_{\text{net},i}$ from the heated plate to the coolant air, the surface temperature of the plate, T_w, and the local bulk mean air temperature, $T_{b,i}$ at the midpoint of the plate. The following equation is used

$$h_i = q''_{\text{net},i}/(T_w - T_{b,i})$$

where

$$q''_{\text{net},i} = (q_i - q_{\text{loss},i})/A_i \text{ and } q_i = I_i^2 \cdot R_i \quad (1)$$

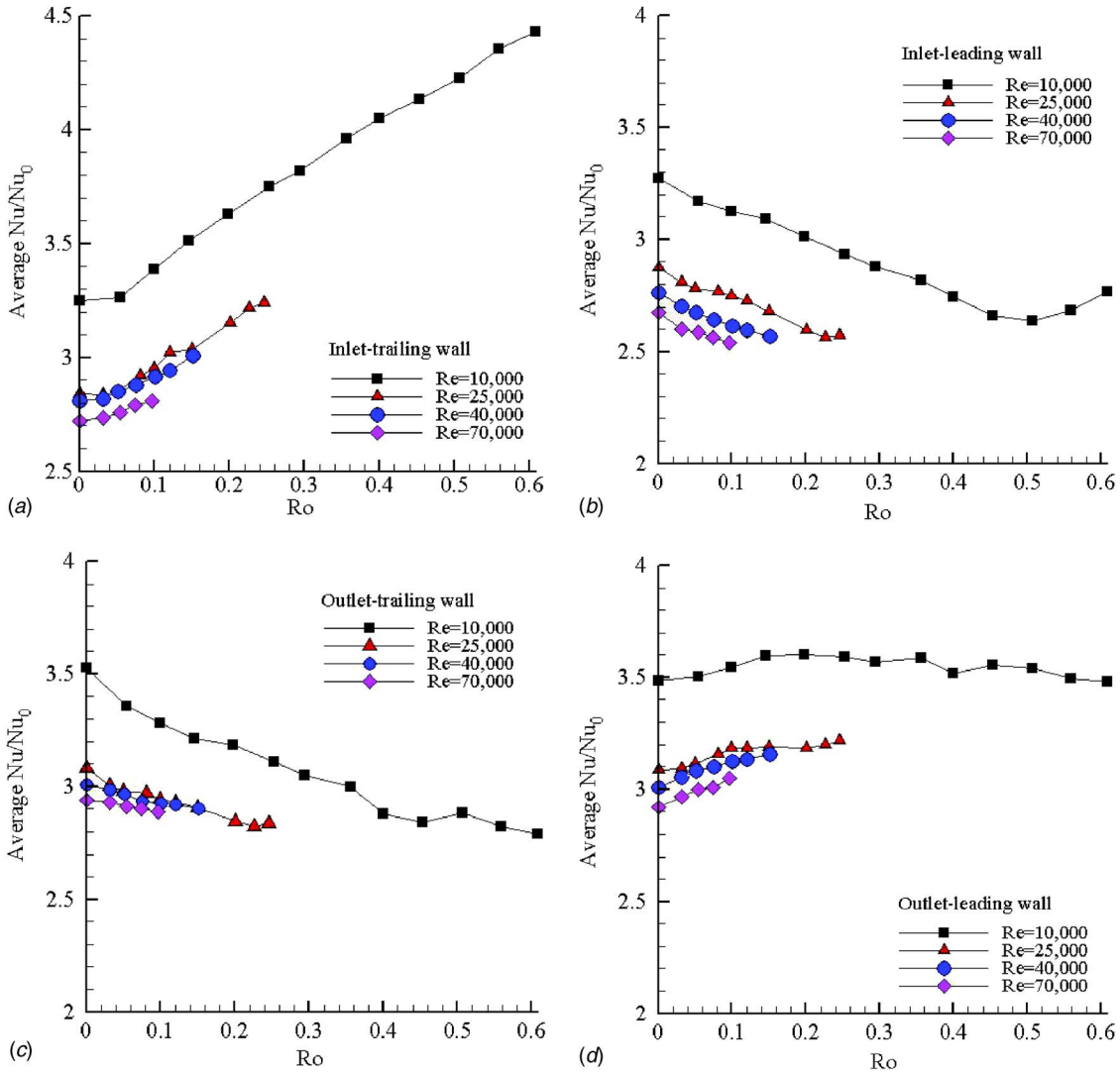

Fig. 6 Rotation effects with variable Re numbers at DR=0.13 (DR=0.10 for Re=70,000): (*a*) inlet-trailing wall; (*b*) inlet-leading wall; (*c*) outlet-trailing wall; and (*d*) outlet-leading wall

In the above equation, I_i and R_i are the current and the resistance of the ith copper plate, respectively; $q'_{\text{loss},i}$ is the heat loss from the ith plate; and A is the projected area of the copper plate. The maximum temperature reached by the plates over the range of test conditions is 386 K, and the resistance of the heaters are constant in this temperature range as per data sheets provided by Minco Inc.

The heat loss for each copper plate is determined by a series of stationary tests, without flow. Under equilibrium conditions, the heat input is balanced by the heat loss, and the heat loss can be calibrated to the wall temperature. The total heat loss is verified by an energy balance between the inlet and exit utilizing the measured inlet and outlet temperature and the measured mass flow rate $\dot{m}$. It is found that the total heat losses calculated by the overall energy balance and the stationary heat loss tests, are very close to each other. For example, at Re=25,000 and DR=0.15, the ratio of the total heat loss to the total heat power is about 7%, and the ratio of the maximum difference of the total heat losses calculated by the two methods to the total heat power is only 1.15%.

The local bulk mean air temperature, $T_{b,i}$, is given by:

$$T_{b,i} = T_{\text{in}} + \left(\sum_{j=1}^{i-1} (q_j - q_{\text{loss},j})_{\text{leading}} + \frac{1}{2}(q_i - q_{\text{loss},i})_{\text{leading}} \right) \Big/ (\dot{m} \cdot C_p) + \left(\sum_{j=1}^{i-1} (q_j - q_{\text{loss},j})_{\text{trailing}} + \frac{1}{2}(q_i - q_{\text{loss},i})_{\text{trailing}} \right) \Big/ (\dot{m} \cdot C_p) \tag{2}$$

where $\dot{m}$ is the mass-flow rate; and C_p is the specific heat. The Nusselt number, Nu, is then obtained from (k is based on the film temperature $(T_w+T_b)/2$)

$$\text{Nu}_i = h_i \cdot D_h / k \tag{3}$$

where D_h is the hydraulic diameter of the test channel (0.4 in.); and k is the air conductivity. Then Nu_i is normalized by the Dittus-Boelter correlation

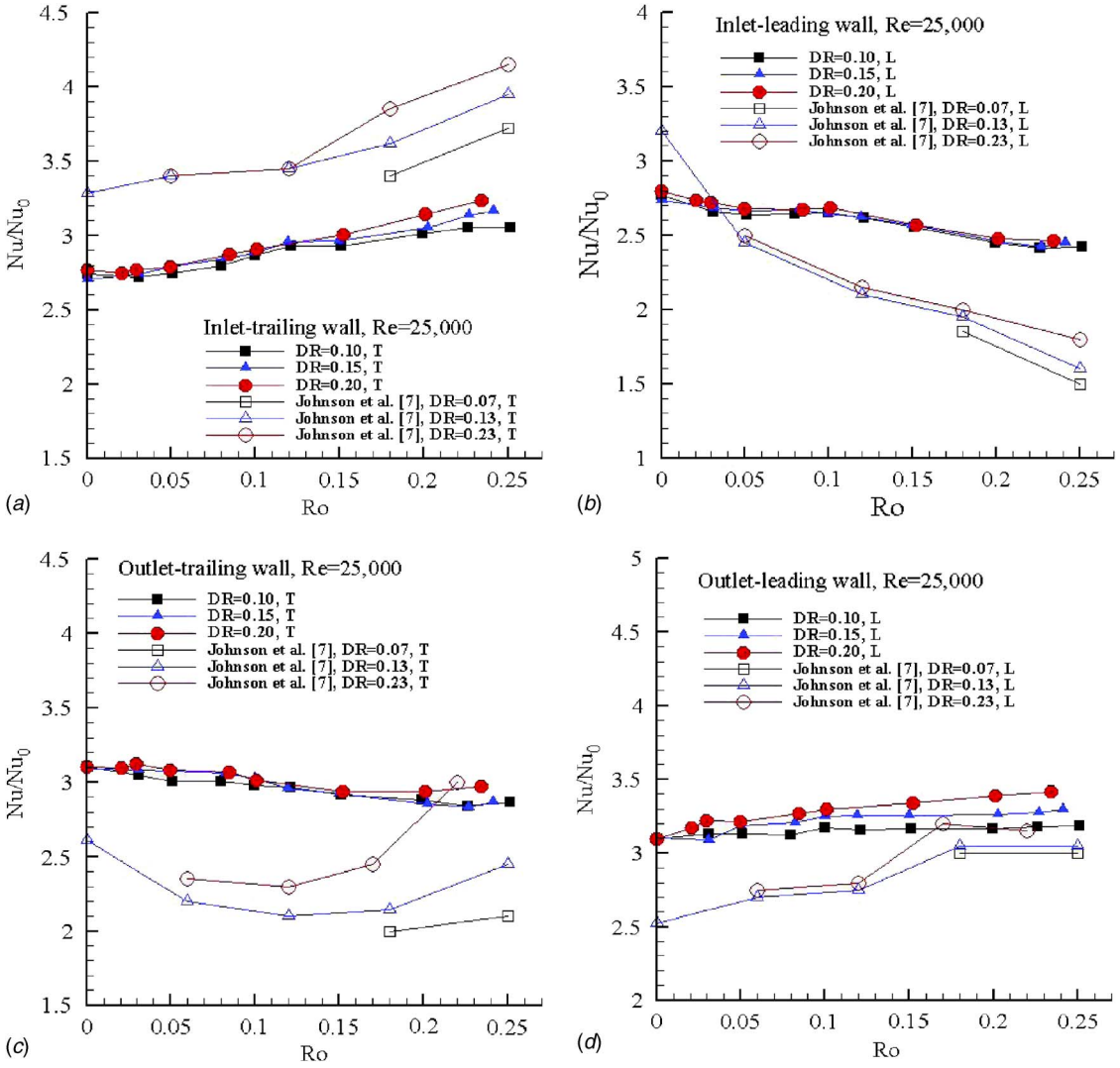

Fig. 7 DR effects in comparisons with Johnson et al. [7] on the middle copper plates at Re=25,000: (*a*) present: X/D_h=5.70; Johnson et al. [7]: X/D_h=8.50; (*b*) present: X/D_h=5.70; Johnson et al. [7]: X/D_h=8.50; (*c*) present: X/D_h=24.37; Johnson et al. [7]: X/D_h=25.50; and (*d*) present: X/D_h=24.37; Johnson et al. [7]: X/D_h=25.50

$$\mathrm{Nu}_{\mathrm{ref}} = 0.023 \cdot \mathrm{Re}^{0.8} \cdot \mathrm{Pr}^{0.4}$$

Thus

$$\mathrm{Nu}_i/\mathrm{Nu}_{\mathrm{ref}} = h_i \cdot D_h/(k \cdot 0.023 \cdot \mathrm{Re}^{0.8} \cdot \mathrm{Pr}^{0.4}) \quad (4)$$

To enable direct comparison with the square channel, Nu is normalized by Nu_0, where Nu_0 is the Nusselt number in the fully developed region of the corresponding stationary smooth channel with the same aspect ratio AR. The friction factor, f, is calculated by

$$f = (\Delta P \cdot D_h)/(4L \cdot 1/2 \cdot \rho \cdot V^2) \quad (5)$$

where L is the distance between the two pressure taps; ΔP is the pressure drop; ρ is the flow density; and V is the mean velocity of the flow. Then f is normalized by the Karman-Nikuradse equation [15], $f_0 = 0.046 \cdot \mathrm{Re}^{-0.2}$

$$f/f_0 = (\Delta P \cdot D_h)/(4L \cdot 1/2 \cdot \rho \cdot V^2 \cdot 0.046\,\mathrm{Re}^{-0.2}) \quad (6)$$

Finally, the thermal performance factor (TPF) is defined as is standard by

$$\mathrm{TPF} = (\mathrm{Nu}/\mathrm{Nu}_{\mathrm{ref}})/(f/f_0)^{1/3} \quad (7)$$

Uncertainty. Using the Kline and McClintock [16] method, the typical uncertainty in the calculated heat transfer coefficient in the inlet is estimated to be approximately 9% for current test conditions based on a maximum potential error of thermocouple readings of 0.5°C. Repeatability tests with different runs indicated that the thermocouple readings were repeatable to within 0.2°C.

Results and Discussions

During the experiments, the pressure in the test section was maintained at 1034 kPa (150 psia). The inlet air temperature varied from 22°C for stationary tests to 35°C for tests at the highest rotational speeds. During individual test runs, the wall temperature on each copper plate was maintained at the same value. To achieve the density ratio DR values from 0.10 to 0.20, the wall temperature was varied between 55°C and 113°C. The rotation speed was varied from 0 rpm to 1100 rpm to achieve Ro values from 0 to 0.6.

In the present study, the sidewalls are not heated and not instrumented, so the discussion below will focus on the leading walls and trailing walls in the inlet and outlet channels. It should also be

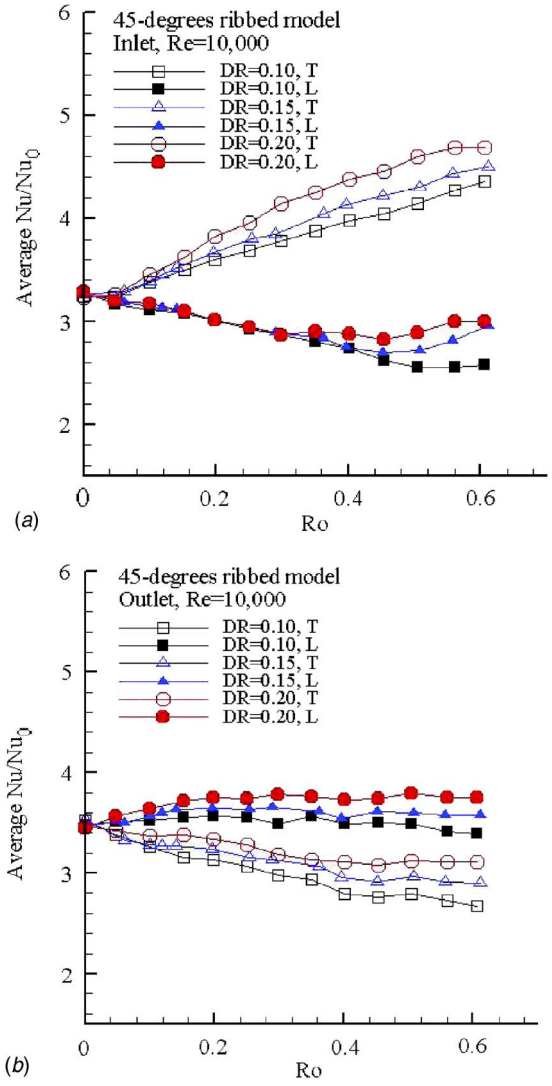

Fig. 8 Average DR effects at Re=10,000: (*a*) inlet; and (*b*) outlet

noted that the flow coming into the test section is not fully developed as is the case for most real turbine inflow conditions.

Comparisons With Previous Studies Under Stationary Conditions. To validate the experimental procedure, a series of tests under stationary conditions are carried out, and the results are compared with those from previous studies. Figure 3(*a*) shows the Nu/Nu_0 streamwise distributions in the first passage. The results of Johnson et al. [7], Han et al. [12], and Griffith et al. [13] are also shown for comparison. Note that the ratio of pitch to rib height (P/e) is 10 for all of the three cases; e/D_h is 0.10 for the current study and Johnson et al. [7]; and 0.078 for Han et al. [12]. Also note that the sidewalls in Ref. [7,12] are heated, but the sidewalls in the present model are not heated. To minimize any effects caused by the differences of channel aspect ratio, entrance conditions, and thermal boundary conditions, the Nusselt number Nu is normalized by Nu_0, the value in the fully developed region of the corresponding smooth model under stationary conditions. The Nu_0 value for the 4:1 AR case in the present study is obtained from measurements [14]. The Nu/Nu_0 in the present study shows a relatively flat distribution along the streamwise direction unlike that of a smooth model where Nu/Nu_0 decreases with increasing X/D_h [14]. Beyond X/D_h of 4, similar behavior is observed by Johnson et al. [7] and Han et al. [12]. For $X/D_h < 4$, the observed differences are likely a consequence of differing entrance effects. While there is intrinsic scatter in the data from the different sources, by taking the streamwiseaverage for the three cases shown in Fig. 3(*a*), it is found that the present study has an average Nu/Nu_0 of 2.87, while it is 3.07 for Johnson et al. [7], 2.47 (at Re=30,000) for Han et al. [12], and 2.53 (at Re=20,000) for Griffith et al. [13]. The maximum difference between the present study and the three previous studies is 13%.

Figure 3(*b*) shows the Nu/Nu_0 distributions along the streamwise direction at Re=25,000 in the inlet ($X/D_h \leqslant 11.5$), in the bend region ($11.5 < X/D_h < 18.4$), and in the outlet ($X/D_h \geqslant 18.4$), and comparisons are made with Johnson et al. [7]. As in Fig. 3(*a*), Nu_0 represents the smooth fully developed value for the corresponding AR case, and is different for the 1:1 and 4:1 AR cases. The key difference in trend between the two AR cases is the entrance effect in the inlet, and in the region downstream of the bend, where the 1:1 AR case shows a bend effect with a high Nu/Nu_0 on the leading wall immediately downstream of the bend. The 4:1 AR case shows no noticeable bend effect, and further, the Nu/Nu_0 values remain relatively flat in the outlet duct unlike the 1:1 AR case where there is a decrease in Nu/Nu_0 with X/D_h.

Figure 3(*c*) presents the variation of Nu/Nu_0 with Re in the inlet duct at Ro=0 for the present case and those reported in Ref. [7,13] For all three models, the average Nu/Nu_0 decreases with increasing Re. For the present model, there is a 23% variation in Nu/Nu_0 in the range of Re=10,000–100,000; however beyond a Re=25,000 Nu/Nu_0 values asymptote to around 2.6 with a subsequent decrease of less than 8.6% in the Nusselt number ratio. Johnson et al. [7] show the same trend as observed in the present study with the differences in Nu/Nu_0 between the present study and Johnson et al. [7] being around 5%. In Griffith et al. [13], significant Re effects are however observed. Nu/Nu_0 drops from 3.5 to 2.2, as Reynolds numbers change from 5,000 to 40,000. The maximum difference between Nu/Nu_0 in the present study and Griffith et al. [13] is 25%.

Reynolds Number Effects. In Fig. 3(*c*), Re number effects are shown for Ro=0. Figure 4 shows the Reynolds number effects for the rotational cases along both the inlet and outlet ducts. It is clear from Fig. 4 that there is a consistent Reynolds number effect for all cases with rotation, and that this effect is comparable in magnitude for the various Ro. As for the stationary case, there is an asymptotic behavior for Re $\geqslant$ 25,000 beyond which the Re effects are weak.

Rotation Effects. Figure 5 shows the rotation effects on the heat transfer ratio in the inlet (Fig. 5(*a*)), in the bend (Fig. 5(*b*)), and in the outlet (Fig. 5(*c*)) for Re=25,000 and DR=0.13. The results for square channels from Johnson et al. [7] are also shown for comparison. Note that for both cases, the data presented are at the midpoint in the inlet and in the outlet. Rotation number is varied from 0 to 0.25. As seen earlier in Fig. 3, under stationary conditions the Nu/Nu_0 value is higher in the inlet passage for the 4:1 AR channel. It should be noted, however, that the effects of centrifugal buoyancy cannot be separated from the effects of the Coriolis force by simply keeping density ratio DR as constant.

Destabilized Surfaces. For the 4:1 AR channel, it can be seen that Nu/Nu_0 increases steadily with rotation number along the trailing wall (denoted by T in the figure) in the inlet passage and the bend and along the leading wall (denoted by L) in the outlet passage. These surfaces that see enhancement, called destabilized surfaces, have Coriolis-induced secondary flows (proportional to the rotation number) directed toward them.

These secondary flows that impinge on the destabilized surface enhance mixing and turbulence along the surface, and therefore also increase heat transfer. This behavior has been extensively documented and quantified for the 1:1 AR geometry [4–7]. In the inlet passage Nu/Nu_0 along the trailing surface increases by 14% or $\Delta(Nu/Nu_0)=0.38$ at Ro=0.25 ($Nu/Nu_0=3.11$) from its station-

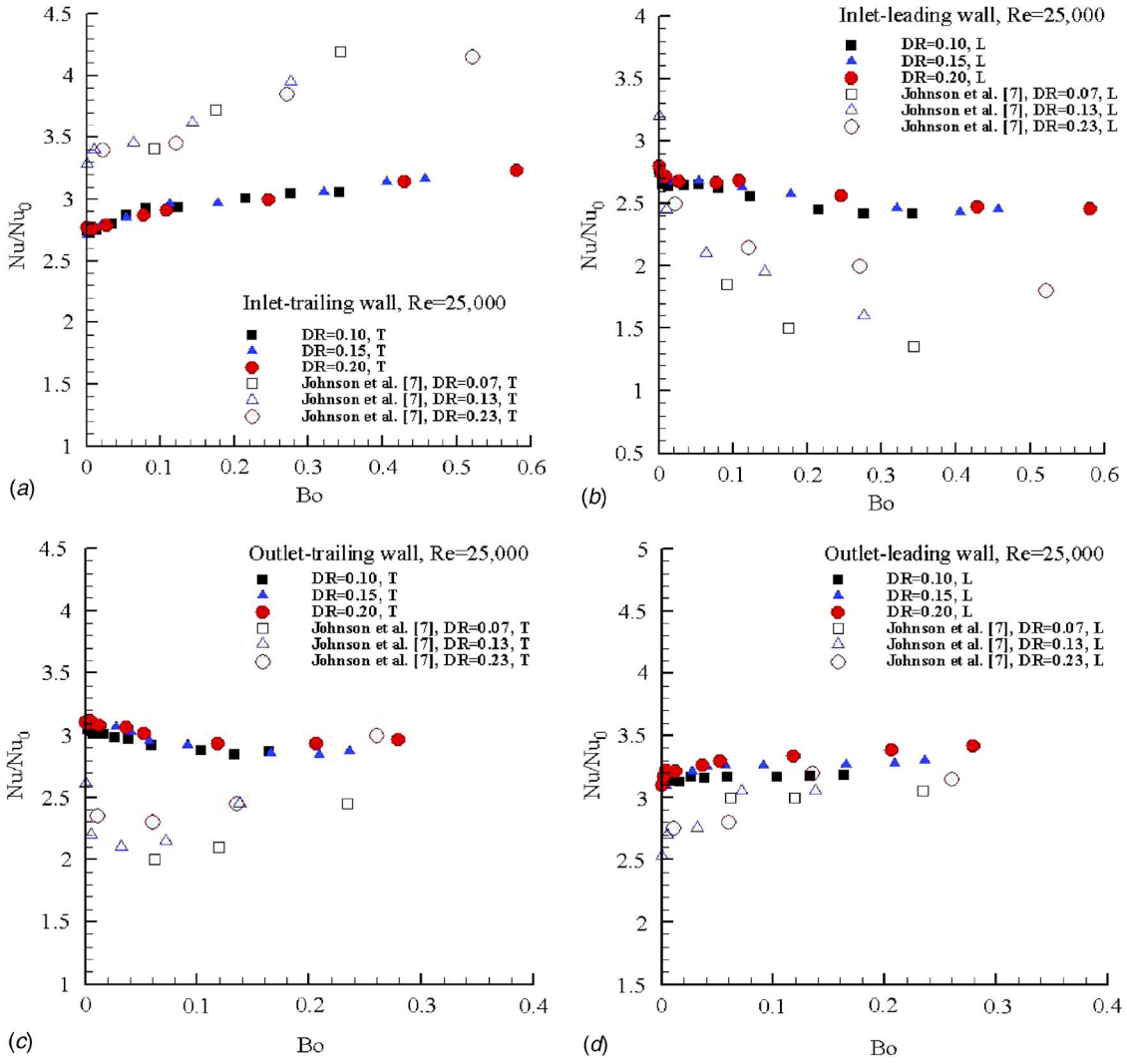

Fig. 9 Buoyancy effects in comparisons with Johnson et al. [7] on the middle copper plates at Re=25,000: (*a*) present: X/D_h=5.70; Johnson et al. [7]: X/D_h=8.50; (*b*) present: X/D_h=5.70; Johnson et al. [7]: X/D_h=8.50; (*c*) present: X/D_h=24.37; Johnson et al. [7]: X/D_h=25.50; and (*d*) present: X/D_h=24.37; Johnson et al. [7]: X/D_h=25.50

ary value (Nu/Nu_0=2.73). In the outlet passage and along the bend, the corresponding increase in Nu/Nu_0 with rotation is only about 5% at a Ro=0.25. The comparison with square channel data [7] indicates that there is an increase of 22% in Nu/Nu_0 or $\Delta(Nu/Nu_0)$=0.75 along the inlet trailing wall as Ro is increased to 0.23 (Nu/Nu_0=4.03) from the stationary condition (Nu/Nu_0=3.28). On the trailing wall in the bend, Nu/Nu_0 shows only a slight increase as in the 4:1 rectangular channel. On the leading wall in the second passage, the increase in Nu/Nu_0 is only 9% at Ro=0.23.

It is clear that the rotation effects in the square and rectangular channels show similar behavior on the destabilized walls in the range of Ro numbers covered by the current study. The key difference appears to be that rotation-induced enhancements on the destabilized surface appear to be substantially smaller (by as much as 49%) for the 4:1 AR with $\Delta(Nu/Nu_0)$=0.38 relative to the 1:1 AR geometry with $\Delta(Nu/Nu_0)$=0.75. The smaller rotation effects in the current rectangular channels relative to the square channels are attributed to the Coriolis force-induced secondary flow cells being weaker as the AR increases and the leading wall and the trailing wall being closer to each other.

The larger increase in Nu/Nu_0 on the trailing wall in the first passage relative to the second passage (observed for both 4:1AR and 1:1AR) is caused by the extra generation of near-wall turbulence due to the buoyancy-driven flow close to the wall, as discussed by Johnson et al. [7]. In the inlet, the near-wall centrifugal buoyancy-driven flow moves inward toward the axis of rotation, and the mean coolant flow is radially outward. This counterflow pattern generates additional near-wall turbulence due to the strong shear or velocity gradient. In the second passage, the direction of the mean coolant flow and the near-wall buoyancy-driven flow are coincident, and the generation of the near-wall turbulence is likely to be weaker.

Stabilized Surfaces. In Fig. 5(*a*), the behavior on the stabilized surface in the inlet-leading wall for the 4:1 AR is generally consistent with those of the 1:1 AR. In both cases, the heat transfer ratio decreases with Ro. A similar behavior is seen for the outlet-trailing wall except that for the 1:1 AR there is an initial decrease until Ro=0.12 followed by a small increase at Ro=0.23. For the 4:1 AR the largest reduction in Nu/Nu_0 with Ro is almost the same on both walls (10% decrease on the inlet-leading wall and 8% on the outlet-trailing wall at Ro=0.25 relative to the stationary value). In square channels, along the leading-inlet wall there is a decrease in Nu/Nu_0 of 51% at Ro=0.23 from the stationary value

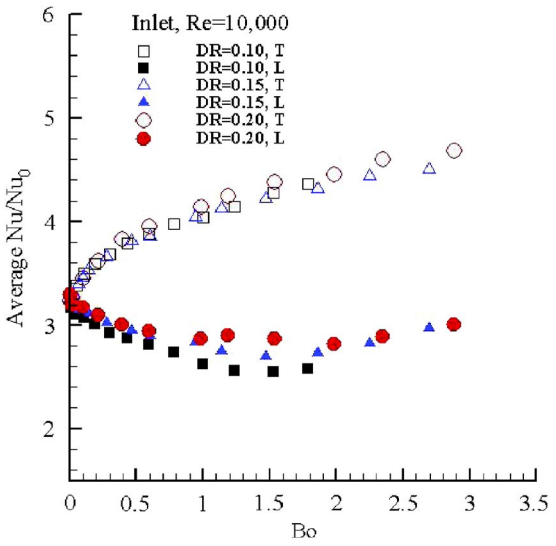

Fig. 10 Average buoyancy effects at Re=10,000, inlet

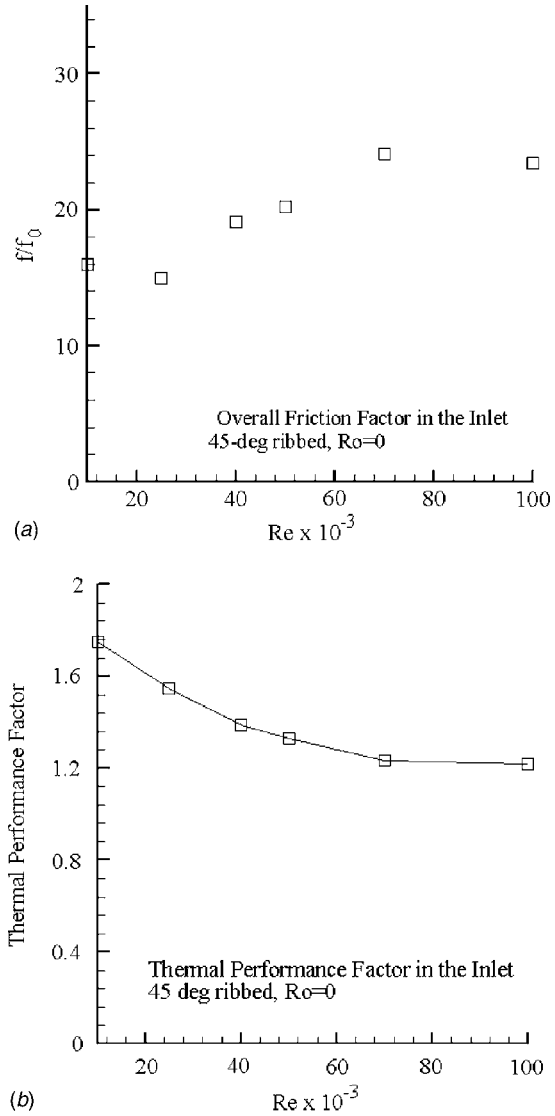

Fig. 11 Friction factor and thermal performance factor versus Re number in the inlet at Ro=0: (*a*) Friction factor in the inlet; and (*b*) TPF in the inlet

(Fig. 5(*a*)). On the trailing wall in the second passage (Fig. 5(*c*)), Nu/Nu_0 initially decreases with Ro by 21% at Ro=0.12 beyond which there is a modest increase.

It is evident that the rotation effects are much greater in the 1:1 square channel than in the 4:1 rectangular channel. In the inletchannel the reduction on the stabilized surface is nearly fivefold greater for the 4:1 AR, while in the outlet channel the reductions in Nu/Nu_0 are twofold greater for the square channel. It should be noted that the present results are in contrast to that of Griffith et al. [13] who, for a 4:1 AR 45 deg ribbed channel, reported a monotonic increase in heat transfer rate on the leading wall with radiallyoutward flow in the range of Re=5,000–40,000. However, in their study at Re=40,000, the maximum rotation number was only Ro=0.038. In the present study, Ro numbers up to 0.25 at Re =25,000 have been studied, and a monotonic decrease is observed over this range. It should be noted that Zhou et al. [14], for a 4:1 smooth channel, also observed an increase in the inlet-leading heat transfer with Ro. This behavior was rationalized through companion computational results which showed that for the 4:1 smooth channel, a multiroll secondary flow pattern was observed, and that both the leading and trailing surfaces experienced downwash of the secondary flow resulting in enhanced heat transfer on both surfaces with rotation. However, with inclined ribs on the wall, the secondary flow pattern is likely to be different, and the present measurements support this expectation.

It is apparent that the rotational effects are stronger in the inlet than in the outlet by comparing Figs. 5(*a*) and 5(*c*). That is, the gap of Nu/Nu_0 between the leading and the trailing walls is larger in the inlet than in the outlet. This is caused partially by the different effects of rotational buoyancy force on the destabilized surfaces. In the first pass with radially outward flow, both rotational buoyancy and Coriolis force enhance the heat transfer on the trailing wall. In the second pass with radially inward flow, the rotational buoyancy weakens the heat transfer on the leading wall, reducing the heat transfer enhancement induced by the Coriolis force. Therefore, the heat transfer enhancement on the destabilized wall is stronger in the inlet than that in the outlet.

Figure 5(*b*) shows the rotation effects in the bend region. For the present 4:1 model, rotation effects in the bend are rather small as for the square channel. This is to be expected since the flow over a significant portion of the bend is oriented in the direction of rotation leading to reduced Coriolis forces.

To provide a better perspective of the rotational effects at all Reynolds number studied (10,000–70,000), the 4:1 AR data in the form of streamwise-averaged Nu/Nu_0 is plotted separately for each wall, and each Re, as a function of the Ro (Fig. 6). At each Re, the rotational effects are consistent with that shown in Fig. 5. Rotation causes a monotonic increase in the heat transfer on the destabilized walls, and this effect is clearly greater in the inlet channel. In the outlet channel, the enhancement appears to decrease somewhat with decreasing Re. In fact, at Re=10,000, Nu/Nu_0 along the outlet-leading wall almost remains constant over the full range of Ro values from 0 to 0.6. On the other hand, rotation results in a monotonic decrease in heat transfer on the stabilized walls. The only exception occurs again at Re=10,000 with Ro higher than 0.4, where the Nu/Nu_0 on the inlet-leading wall increases as Ro increases, implying that at these conditions the buoyancy-driven effects override the Coriolis-force effects on this wall.

Density Ratio Effects. The local density ratio is defined as $DR=(\rho_b-\rho_w)/\rho_b=(T_w-T_w)/T_w$. In the present study, the inlet bulk density is used as the nominal density ratio, but local DR actually decreases as X/D_h increases, since T_w is constant, while T_b increases as X/D_h increases. The density ratio, caused by the temperature gradient normal to the wall, induces the centrifugal buoyancy force on the flow under rotational conditions. This

buoyancy force is expected to become more significant as either DR or Ro number increases. By holding Ro constant, the influence of DR can be examined.

Figure 7 presents the Nu/Nu_0 ratio for different DR at the midpoint of the channels: $X/D_h=5.7$ for the inlet, and $X/D_h=24.4$ for the outlet. At this midpoint location, R/D_h is 65.7, where R is defined as the local radius of the midpoint of the channel. Also shown are the results of Johnson et al. [7] for the ribbed square channel at the midpoint of the inlet and outlet channels. These results are presented at Re=25,000.

In general, increasing DR increases Nu/Nu_0 for both the 1:1 AR and 4:1 AR ribbed channels, but the DR effects for the 4:1 AR channels are relatively small and on the order of the measurement uncertainty. However, these measurements are repeatable and repeated runs produced the same behavior. For the 4:1 AR, the effects of DR on the stabilized surfaces are marginal (~2–4%), while on the destabilized surfaces the Nu/Nu_0 increases by 6–7% at Ro=0.23 when DR is doubled from 0.1 to 0.2. For the square channel, the effects of DR are more evident. At Ro=0.24 as DR increases from 0.07 to 0.23, Nu/Nu_0 increases 15% on the inlet-trailing wall, 5% on the inlet-leading wall, 43% on the outlet-trailing wall, and 20% on the outlet-leading wall. From these differences, it is clear that the DR effects are stronger in the second passage with radially inward flow than in the first passage with radially outward flow.

The density ratio effects are more clearly shown in Fig. 8 for Re=10,000 with Ro up to 0.6. Again the heat transfer enhancement due to higher DR is observed. In Fig. 8(*a*), the increase in Nu/Nu_0 on the inlet-leading wall is observed for each of the three DR values only after Ro passes a critical point and approaches higher values. Note that the critical Ro becomes smaller as DR increases. This fact clearly indicates that it is the centrifugal buoyancy force that causes this phenomenon.

Buoyancy Effects. The combination of rotation effects and density ratio effects can be represented by a buoyancy parameter, which is defined as

$$\mathrm{Bo} = [(\rho_w - \rho_b)/\rho_w][\Omega R/V][\Omega D_h/V]$$

where R is the rotation radius. Expressed in another form, the buoyancy parameter can be written as

$$\mathrm{Bo} = (\mathrm{DR})\mathrm{Ro}^2 R/D_h$$

The buoyancy parameter Bo correlates the buoyancy effects for both rectangular (4:1) and square (1:1) channels at Re=25,000 (Fig. 9) reasonably well on the destabilized surfaces (inlet trailing and outlet leading). Nu/Nu_0 for the destabilized surface increases monotonically with increasing Bo. On the stabilized surfaces (inlet leading and outlet trailing), Nu/Nu_0 for the 4:1 AR initially decreases with increasing Bo, but at higher Bo values, Nu/Nu_0 plateaus (Fig. 9(*b*)) or increases slightly (Fig. 9(*c*)) with Bo. For the 1:1 AR a similar behavior is observed, but the correlation with respect to the Bo is better for the rectangular channel than for the square channel. It was shown earlier that the effects of both the Ro and DR are weaker for the 4:1 AR channel, and the better correlation with Bo for the 4:1 AR may be a consequence of this fact.

Figure 10 shows the buoyancy effects for Re=10,000 in the inlet duct with Bo parameters as high as 3. Once again, Bo appears to be a good correlating parameter.

Thermal Performance Factors. Figure 11 shows friction factor ratio and the TPF at Ro=0 based on the pressure drops measured with a Scanivalve ZOC-14 transducer. These pressure drops were normalized to yield friction factors (Eq. (6)) that are then combined with the Nu/Nu_{ref} to yield thermal performance factors (Eq. (7)). The friction factor ratios show an increase with Re beyond 25,000 and up to 70,000 beyond which the values remain relatively constant. The TPF values show an initial decrease with Re, but beyond a Re of 70,000, the TPF remains fairly flat at around 1.2.

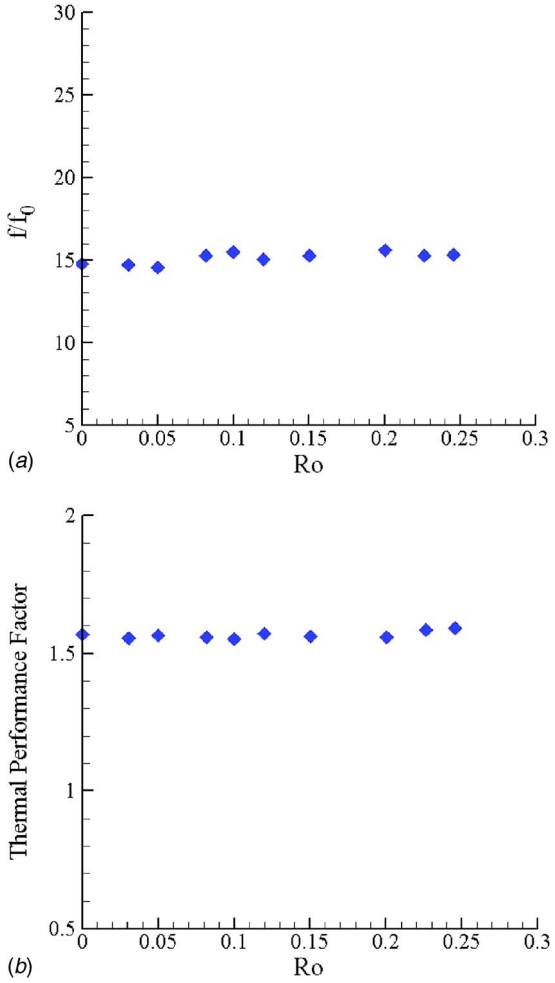

Fig. 12 Friction factor and thermal performance factor versus Ro number in the inlet with DR=0.15 and Re=25,000 (*a*) friction factor in the inlet; and (*b*) TPF in the inlet

Figure 12 shows the effect of rotation on the friction factor ratio and TPF at Re=25,000. It is evident that rotation has no significant influence on the friction factor and the thermal performance factor. Note that the Nu/Nu_{ref} employed to calculate TPF is the average values for all the copper plates (leading plus trailing) in the inlet passage. This average Nu/Nu_{ref} does not change significantly with rotation [17–20].

Concluding Remarks

Heat transfer measurements are reported in a rotating rig to examine the effects of rotation number, density ratio, and the buoyancy parameter on the heat transfer characteristics in a two-pass 4:1 AR internal coolant passage with ribs skewed at 45 deg to the main flow. The results are compared to the data obtained in a 1:1 AR square rotating channel with the same dimensionless rib geometry and reported by Johnson et al. [7]. The following major conclusions are drawn:

1. Rotation effects enhance the heat transfer on the destabilized surfaces of the 4:1 AR channel. This enhancement is stronger on the inlet-trailing wall than on the outlet-leading wall. Rotation effects degrade heat transfer on the stabilized walls, and cause a decrease in Nu/Nu_0 on the inlet-leading and outlet-trailing walls. However, for the lower Re (Re=10,000), there is an increase in Nu/Nu_0 on the stabilized inlet-leading wall at higher Ro numbers (>0.4);

2. In the range of Ro number covered in the present study (at Re=25,000), the 4:1 AR rectangular channels exhibit similar but weaker rotation effects compared to the results reported by Johnson et al. [7] for a 1:1 AR channel;
3. Higher density ratio enhances heat transfer on all of the four walls in the inlet and in the outlet of the 4:1 AR. However the DR effect is considerably weaker compared to that observed for the 1:1 AR channel;
4. Buoyancy parameter (Bo) is observed to correlate the Nu/Nu_0 data reasonably well. This corrlelation is stronger for the 4:1 AR. The data suggest that the buoyancy effects in the present study are dominated by the centrifugal acceleration due to rotation; and
5. The present data for the 45 deg 4:1 AR geometry show a trend along the inlet leading wall that is in contrast with the 4:1 AR smooth channel where the leading wall heat transfer increased with Ro.

Nomenclature

A = area
Bo = buoyancy parameter, $DR^{*}Ro^{2*}R/D_h$, where DR is the local density ratio
C_p = specific heat
D = diameter
DR = coolant to wall density ratio at the inlet, DR $=(\rho_b-\rho_w)/\rho_b=(T_w-T_b)/T_w$
TPF = thermal performance factor, $(Nu/Nu_{ref})/(f/f_0)^{1/3}$
f = average friction factor
H = the height of the sidewalls, which are smooth and unheated
h = heat transfer coefficient
I = current applied to heater
k = heat conductivity of air, or 1000 in representing Re values
L = channel length
$\dot{m}$ = mass flow rate
Nu = Nusselt number
P = pressure, or streamwise rib pitch
Pr = Prandtl number
ΔP = pressure drop
q = heat transferred through copper element
q'' = heat flux per unit area
R = resistance of heater, or rotating radius
Re = Reynolds number, $\rho VD/\mu$
Ro = rotation number, $\Omega D_h/V$
T = temperature
V = average velocity
W = the width of the leading and trailing walls, where ribs are located
X = distance from the entrance of the inlet, along the streamwise direction
Ω = rotational speed
ρ = density of air

Subscripts

0 = value in the fully developed region in the smooth channel with the same aspect ratio at Ro=0
b = bulk value
h = hydraulic
i = ith copper plate
w = wall

References

[1] Mori, Y., Fukada, T., and Nakayama, W., 1971, "Convective Heat Transfer in a Rotating Circular Pipe (2nd Report)," Int. J. Heat Mass Transfer, **14**, pp. 1807–1824.
[2] Metzger, D. E., and Stan, R. L., 1977, "Entry Region Heat Transfer in Rotating Radial Tubes," AAIA Paper No. 77-189.
[3] Morris, W. D., and Ayhan, T., 1979, "Observations on the Influence of Rotation On Heat Transfer in the Cooling Channels of Gas Turbine Rotor Blades," Proc. Inst. Mech. Eng., **193**, pp. 303–311.
[4] Wagner, J. H., Johnson, B. V., and Hajek, T. J., 1991, "Heat Transfer in Rotating Passages with Smooth Walls and Radial Outward Flow," J. Turbomach., **113**, pp. 42–51.
[5] Wagner, J. H., Johnson, B. V., and Kopper, F. C., 1991, "Heat Transfer in Rotating Serpentine Passages With Smooth Walls," J. Turbomach., **113**, pp. 321–330.
[6] Wagner, J. H., Johnson, B. V., Graziani, R. A., and Yeh, F. C., 1992, "Heat Transfer in Rotating Serpentine Passages With Trips Normal to the Flow," J. Turbomach., **114**, pp. 847–857.
[7] Johnson, B. V., Wagner, J. H., Steuber, G. D., and Yeh, F. C., 1994, "Heat Transfer in Rotating Serpentine Passages With Trips Skewed to the Flow," J. Turbomach., **116**, pp. 113–123.
[8] Guidez, J., 1989, "Study of the Convective Heat Transfer in a Rotating Coolant Channel," J. Turbomach., **111**, pp. 43–51.
[9] Morris, W. D, and Ghavami-Nasr, G., 1991, "Heat Transfer Measurements in Rectangular Channel With Orthogonal Mode Rotation," J. Turbomach., **113**, pp. 339–345.
[10] Iacovides, H., and Launder, B. E., 1991, "Parametric and Numerical Study of Fully Developed Flow and Heat Transfer in Rotating Rectangular Ducts," J. Turbomach., **113**, pp. 331–338.
[11] Soong, C. Y., Lin, S. T., and Hwang, G., J., 1991, "An Experimental Study of Convective Heat Transfer in Radially Rotating Rectangular Ducts," J. Heat Transfer, **113**, pp. 604–611.
[12] Han, J. C., Park, J. S., and Ibrahim, M. Y., 1986, "Measurement of Heat Transfer and Pressure Drop in Rectangular Channels With Turbulence Promoters," Paper No. NASA CR 4015.
[13] Griffith, T. S., Al-Hadhrami, L., and Han, J. C., 2002, "Heat Transfer in Rotating Rectangular Cooling Channels (AR=4) with Angled Ribs," J. Heat Transfer, **124**, pp. 1–9.
[14] Zhou, F., Lagrone, J., and Acharya, S., 2004, "Internal Cooling in 4:1 AR Passage at High Rotation Numbers," ASME Paper No. GT2004-53501.
[15] Kays, W. M., and Crawford, M. E., 1993, *Convective Heat and Mass Transfer*, 3rd ed., McGraw-Hill, New York.
[16] Kline, S. J., and McClintock, F. A., 1953, "Describing Uncertainties in Single-sample Experiments," Mech. Eng. (Am. Soc. Mech. Eng.), **75**, No. 1, pp. 3–8.
[17] Johnson, B. V., Wagner, J. H., and Steuber, G. D., 1993, "Effects of Rotation on Coolant Passage Heat Transfer, Volume II—Coolant Passages With Trips Normal and Skewed to the Flow," Paper No. NASA CR 4396.
[18] Han, J. C., and Zhang, P., 1991, "Effects of Rib-Angle Orientation on Local Mass Transfer Distributions in a Three-Pass Rib-Roughened Channel," J. Turbomach., **113**, pp. 123–130.
[19] Rache, P. H., and Johnston, J. P., 1979, "Free Shear Layer Behaviors in Rotating System," ASME J. Fluids Eng., **101**, pp. 117–120.
[20] Gebhart, B., Jaluria, Y., Mahajan, R. L., and Sammakia, B., 1988, *Buoyancy-induced Flows and Transport*, Hemisphere, Washington, DC, ISBN 0–89116–728–5, pp. 517–520.

Evolution of Surface Deposits on a High-Pressure Turbine Blade—Part I: Physical Characteristics

James E. Wammack
Jared Crosby
Daniel Fletcher
Jeffrey P. Bons

Department of Mechanical Engineering,
Brigham Young University,
Provo, UT 84602

Thomas H. Fletcher

Department of Chemical Engineering,
Brigham Young University,
Provo, UT 84602

Turbine blade coupons with three different surface treatments were exposed to deposition conditions in an accelerated deposition facility. The facility simulates the flow conditions at the inlet to a first stage high-pressure turbine (T=1150°C, M=0.31). The combustor exit flow is seeded with dust particulate that would typically be ingested by a large utility power plant. The three coupon surface treatments included: (1) bare polished metal; (2) polished thermal barrier coating with bondcoat; and (3) unpolished oxidation resistant bondcoat. Each coupon was subjected to four successive 2 h *deposition tests. The particulate loading was scaled to simulate 0.02 parts per million weight (ppmw) of particulate over* 3 months *of continuous gas turbine operation for each* 2 h *laboratory simulation (for a cumulative* 1 year *of operation). Three-dimensional maps of the deposit-roughened surfaces were created between each test, representing a total of four measurements evenly spaced through the lifecycle of a turbine blade surface. From these measurements the surface topology and roughness statistics were determined. Despite the different surface treatments, all three surfaces exhibited similar nonmonotonic changes in roughness with repeated exposure. In each case, an initial buildup of isolated roughness peaks was followed by a period when valleys between peaks were filled with subsequent deposition. This trend is well documented using the average forward facing roughness angle in combination with the average roughness height as characteristic roughness metrics. Deposition-related mechanisms leading to spallation of the thermal barrier coated coupons are identified and documented.* [DOI: 10.1115/1.2752182]

Keywords: deposition, roughness, turbines

Introduction

Land-based and aircraft gas turbines ingest large quantities of air during operation. In land-based gas turbines, filters are used to remove contaminants found in the atmosphere. These contaminants are composed of a variety of substances such as dust or airborne pollutants produced by the combustion of fossil fuels. Even with the best filtration, some of these particles pass through the combustor where they are heated by the exhaust gases. As they continue through the engine's turbine section, the particles tend to erode the turbine blades if they are below the softening temperature, or to adhere to the turbine blades if they are above the softening temperature. This latter case creates deposits on the blade surfaces. Once beyond the temperature where the particulate changes phase, the rate of particulate agglomeration increases while the rate of blade erosion decreases [1]. Studies involving aircraft engines indicate that this threshold occurs between 980°C and 1150°C [1–3]. In one study involving volcanic ash ingestion by an aircraft engine, deposits did not occur at temperatures lower than 1121°C [4]. Once formed, deposits roughen the blade surfaces resulting in an increase in skin friction and in the convective heat transfer rate between the exhaust gases and the turbine blades. Deposits can also clog vital coolant passages, thus further aggravating the thermal load of the turbine components.

Unfortunately, because this deposition process requires thousands of hours (for a land-based turbine), little is known about the evolution of deposition on turbine blade surfaces. Even if a study was commissioned to monitor turbine deposition as a function of service time, it would be prohibitively expensive to shut down an operating land-based turbine facility at frequent enough intervals for a detailed study. Consequently, turbine surface degradation studies to date have involved numerous turbine components taken from different engines operating under a wide range of conditions. For example, Fig. 1 contains centerline-averaged surface roughness (Ra) data for a collection of aero-engine (from Tarada and Suzuki [5]) and land-based engine components (from Bons [6]) plotted versus service hours. The measurements were taken from a variety of gas turbines, each operating under different conditions and in different environments. The scatter in the data indicates that service time is not the only parameter influencing turbine surface condition. Unless a study is conducted with the same turbine operating at the same conditions over an extended period of time, it will be impossible to understand the evolution of deposits under a given set of conditions.

The difficulty of obtaining deposits for study under controlled conditions has been addressed recently with the creation of a facility that rapidly reproduces the sort of deposition found on in-service turbine blade surfaces [7]. The Turbine Accelerated Deposition Facility (TADF) consists of a specialized combustor capable of creating deposits on circular turbine blade coupons at a vastly accelerated rate and under controllable conditions. The principle behind the production of accelerated deposition is that of matching the product of the particle concentration in the air flow (measured in parts per million weight (ppmw)) and the number of hours of operation. Thus, to simulate a particle flow rate of 0.02 ppmw through a gas turbine over 10,000 h of operation, the

Contributed by the International Gas Turbine Institute of ASME for publication in the JOURNAL OF TURBOMACHINERY. Manuscript received September 8, 2006; final manuscript received November 14, 2006; published online March 25, 2008. Review conducted by David Wisler. Paper presented at the ASME Turbo Expo 2006: Land, Sea and Air (GT2006), Barcelona, Spain, May 8–11, 2006. Paper No. GT2006-91246.

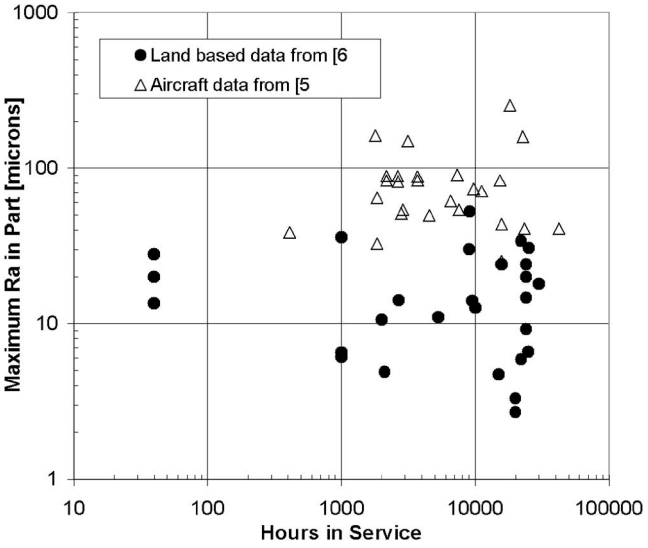

Fig. 1 Distribution of *Ra* (μm) for multiple aero and land-based turbine blades (from Refs. [5,6])

TADF could be operated at 20 ppmw of particle flow for only 10 h. The validation of this testing methodology was the subject of a previous paper by Jensen et al. [7]. In that study, deposits generated in the accelerated deposition facility were compared with deposits on in-service hardware. It was found that for all of the critical features affecting convective heat transfer (i.e., deposit surface roughness) and conduction heat transfer (i.e., deposit thickness, structure, and elemental constituents), the accelerated test produced comparable results to longer duration exposure. The TADF was subsequently employed for a study of deposition from various synfuels with considerable success [8]. The objective of the present study is to document the evolution of turbine deposition with successive exposure in the accelerated deposition facility. Testing was performed at constant operating conditions for the three most common material systems found on modern gas turbine airfoils: uncoated superalloy, thermal barrier coating (TBC), and oxidation resistant coating. Due to the prevalence of TBC coatings in modern gas turbines, three of the TBC coupons were tested (one without particulate in the combustor).

Experimental Facility

A detailed description of the Turbine Accelerated Deposition Facility is provided by Jensen et al. [7]; only a brief summary of the essential features is given here. During operation, a horizontal stream of air is introduced into the base of the TADF (Fig. 2). This stream is diffused within a region filled with 1.3-cm-diameter marbles to ensure that the flow is evenly distributed across the entire 30.5-cm-diameter base of the combustor. The diffused flow, now following a vertical path, is straightened by an aluminum honeycomb and enters the combustion region. Within this region, four upward curving tubes introduce partially premixed natural gas, which is immediately ignited.

Particulate is introduced into the combustor through a line that is bypassed from the primary air line. This secondary stream passes through a glass bulb into which particulate is slowly injected with a motor-driven syringe. The particulate used in this study is identical to that used by Jensen et al. [7], and is primarily composed of silicon and aluminum oxides (80%) with smaller concentrations of Na, K, Mg, Ca, and Fe. The mass mean diameter is 15 μm. The particulate is entrained into the flow and is sent into the combustor through a tube that enters the combustion region (Fig. 2). The particulate laden flow, now mixed with the hot exhaust gases, passes through a cone directly above the combustion region which accelerates the flow. Immediately beyond the

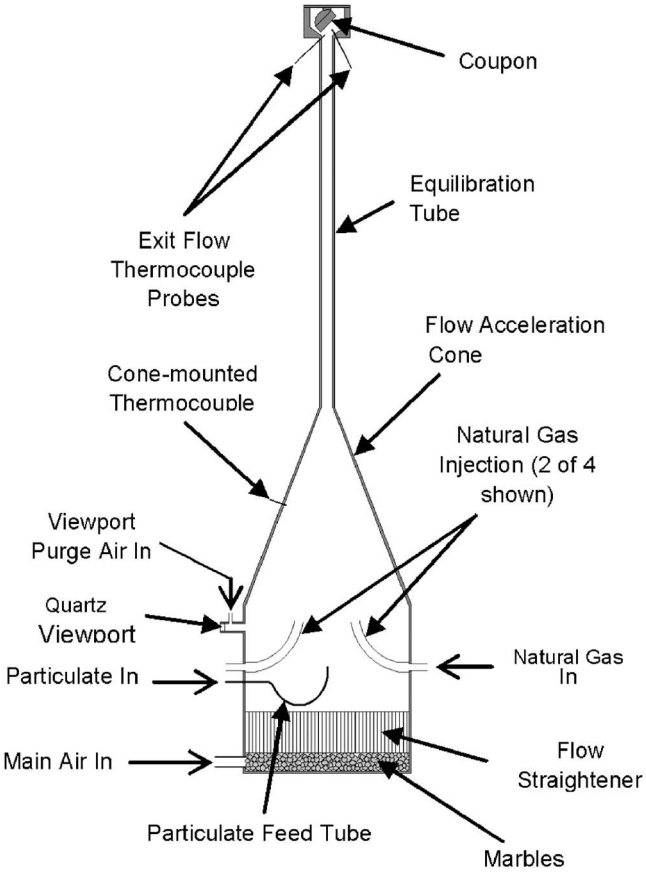

Fig. 2 Turbine Accelerated Deposition Facility

cone, the flow passes through a 1 m long equilibration tube with a 1.58 cm inner diameter. The tube length is sufficient to bring a 40-μm-diameter particle up to the freestream temperature and velocity of the exit flow under test conditions [7]. At the exit, the flow velocity is approximately 220 m/s (M=0.31). This value is typical of the inlet flow Mach number experienced by first stage high-pressure (HP) turbine blades and vanes during operation. The uncertainty in the mass flow was $\pm 4\%$ for the nominal flow rate (0.011 kg/s).

The equilibration tube terminates into a cup-shaped region where the turbine blade coupon is held (Fig. 3). The coupon holder is located 2–3 jet diameters above the exit of the equilibration tube. At this point, the average jet temperature of 1150°C matches that found in the first stage of a G-class gas turbine. The coupon holder can be positioned at angles of 45 deg, 60 deg, or 90 deg to the jet. For the current study, an angle of 45 deg was selected due to the observation by Jensen et al. [7] that the statistical roughness factors *Ra* and *Rt* peaked when the coupon was held at an angle 45 deg to the flow. Additionally, of the three available angles, 45 deg ensures that the greatest possible coupon area is exposed to parallel flow rather than impinging flow. No cooling was applied to the coupons, so the system operates approximately isothermally at the gas temperature. Temperature gradients through the coupon thickness that exist in the engine are therefore not simulated. Overall error in temperature measurements is less than 15°C at the operating temperature of 1150°C.

The mass flow rate of air into the TADF is determined through the use of a choked flow orifice plate in the main air line. The natural gas flow rate is measured with a rotometer with an attached pressure gauge. This flow rate is adjusted throughout the course of an experiment in order to maintain the desired exit temperature, although it is generally 4% of the air mass flow rate. The

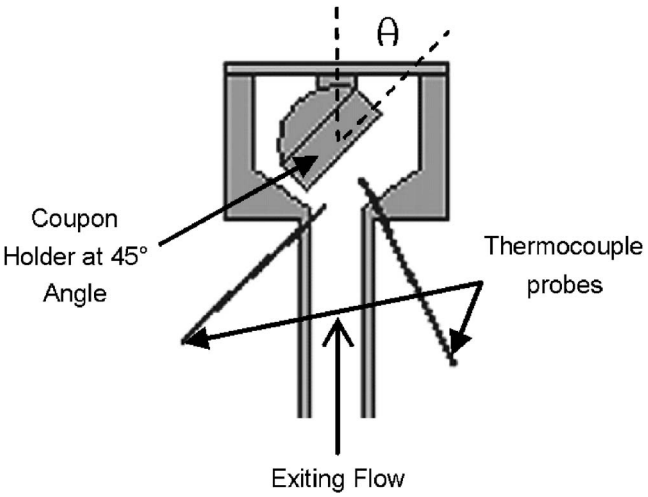

Fig. 3 Schematic of TADF turbine coupon holder

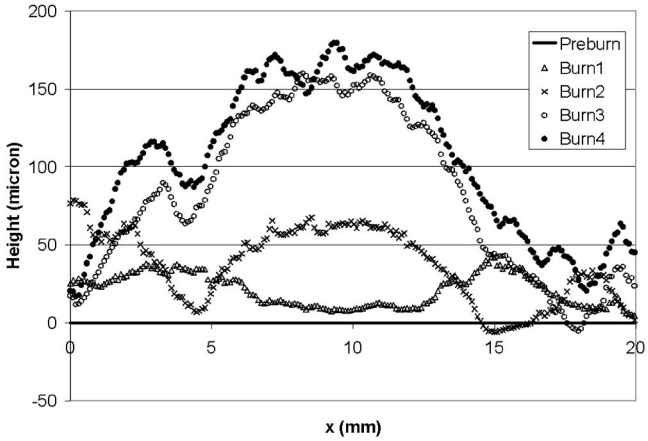

Fig. 4 Streamwise-averaged surface traces of the bare metal coupon deposit at five different points in its evolution

TADF exit temperature is measured by two 0.8-mm-diameter Super OMEGACLAD *K*-type thermocouple probes protruding into the flow (Fig. 3). The mass flow rate, the data from the thermocouple probes, and the cross-sectional area of the TADF exit nozzle are used to calculate the flow Mach number using the ideal gas law relation for the speed of sound.

The turbine blade coupons donated from the gas turbine industry for this study were flat, circular disks with a diameter of approximately 2.54 cm. Like actual turbine blades, the coupons consisted of a nickel–cobalt superalloy substrate with various surface treatments. Three types of surface treatment were studied: (1) bare polished metal; (2) polished thermal barrier coating with bondcoat; and (3) unpolished, 310-μm-thick oxidation resistant bondcoat. The TBC was approximately 1-mm-thick air plasma-sprayed (APS), yttria stabilized zirconia (YSZ). The polished bare metal and TBC coupons both had initial roughness levels (Ra) less than 0.6 μm, while the "as-applied" oxidation resistant bondcoat had a roughness level of 16 μm. This initial level of surface roughness had a significant effect on deposition evolution as will be shown.

Each of the coupons used in this study underwent four consecutive experiments (hereafter referred to as "Burns") in the TADF. Each burn was intended to simulate approximately one-quarter of an operational cycle between maintenance periods. During a burn, each coupon experienced approximately 45 min of warmup time, during which the TADF was brought to an operational freestream temperature of 1150°C and a flow Mach number of approximately 0.31. Once steady state had been reached, particulate was introduced into the facility. This particulate flow was maintained for a period of 2 h. During each 2 h burn, an average of 25 ppmw of particulate was introduced into the TADF for a total of 50 ppmw h. This is intended to simulate approximately 2500 h of operation with a particulate concentration of 0.02 ppmw, for a total of 10,000 simulated h during a standard series of four experiments per coupon. Uncertainty in the particle concentration measurement was <6 ppmw for typical flow conditions.

Following an experiment, the coupon was allowed to cool for several hours, after which it was removed from its fixture. Upon removal, the coupon was placed in a profilometer fixture while topological measurements were taken. Following this process, the coupon was stored until the subsequent burn.

Experimental Measurements

The surface topology was measured before and after each burn using a Hommel Inc. T8000 profilometer equipped with a TKU600 stylus. The stylus tip was conical in shape and had a 5 μm tip radius. Three-dimensional surface representations were constructed from a series of two-dimensional traces separated by 10 μm. Data points within each trace were also separated by 10 μm, resulting in a square surface data grid. Three-dimensional surface representations and roughness statistics were produced after form removal using a fourth-order polynomial fit. The statistics of most interest for this study were the centerline averaged roughness, Ra, the average roughness height, Rz, and the average forward-facing surface angle, $\bar{\alpha}_f$. The centerline averaged roughness was calculated using the following

$$Ra = \frac{1}{IJ}\sum_{i=0}^{I-1}\sum_{j=0}^{J-1}|z_{i,j}| \tag{1}$$

Rz was calculated as the mean of the vertical distance between the highest peak and deepest valley every 2.5 mm of a 2D surface trace. The average forward-facing angle was calculated using the methodology proposed by Bons [9] in which the surface is traversed in the flow direction and forward-facing angles are averaged with all leeward-facing angles set equal to zero (Eq. (2))

$$\bar{\alpha}_f = \frac{1}{I}\sum_{i=0}^{I-1}\alpha_i \tag{2}$$

where, if $(z_{i+1}-z_i)>0$

$$\alpha_i = \tan^{-1}\left(\frac{z_{i+1}-z_i}{y_{i+1}-y_i}\right) \quad \text{else}\ , \alpha_i = 0$$

Typically, Rz and $\bar{\alpha}_f$ are calculated as the average of multiple 2D surface traces. In addition to surface measurements, once the final burn was completed, each coupon was prepared for analysis in the FEIXL30 environmental scanning electron microscope (ESEM). The coupons were potted in epoxy, cut, and polished in order to image the cross section of the final deposit. X-ray spectroscopy was used to distinguish regions of deposit from TBC and bondcoat.

Results and Discussion

Bare Metal Coupon. The virgin uncoated coupon had a highly polished surface (Ra=0.1 μm) and experienced significant deposit flaking. Large regions of bare substrate were exposed when the overlying deposits flaked off after removing the coupon from the TADF. This flaking is believed to be caused by differing thermal coefficients of expansion. As the coupon cools and contracts, the deposits are put under stress and respond by cracking off. This flaking was most pronounced after Burn 1, when the surface prior to deposition was in its highly polished (virgin) state. Figure 4 shows the streamwise (y direction) averaged surface traces after

each burn. The uncertainty in absolute vertical position is ± 8 μm, due to errors in relocating the coupon in the measurement fixture after each burn. Following the first burn, the center of the deposit ($5 < x < 15$) flaked off, producing the crater-like surface trace. The next burn produced durable deposit growth in the center of the coupon while the edges experienced flaking. The final two burns produced continuous (though nonlinear) deposit growth.

Though not evident from Fig. 4, the deposit structure also changes substantially from Burn 2 to Burn 4. Figure 5 contains a series of 3D topologies showing the deposit evolution on a 3 mm $\times$ 5 mm area near the coupon center. The most dramatic changes occur during Burn 2, after the residue beneath the flaked off deposit from Burn 1 has altered the virgin surface by roughening it slightly ($Ra = 0.5$ μm after Burn 1). The deposit structures become noticeably less peaked after Burn 3, as the subsequent deposit fills in valleys in the irregular surface. Finally, Burn 4 again shows the reemergence of new deposit peaks.

This evolution can be summarized quantitatively by plotting the trend of roughness height (as represented by *Ra* and *Rz*) and the roughness shape (as represented by $\bar{\alpha}_f$). These data are plotted in Fig. 6 for the same 3 mm $\times$ 5 mm region of the coupon shown in Fig. 5.

If the surface left behind after Burn 1—in which nearly all deposits had flaked off—was taken as a starting point for deposit evolution, then an interesting trend is revealed. Roughness height (*Ra* and *Rz*) initially increases substantially (Burn 1–Burn 2). This is followed by a phase in which the rate of increase slows (Burn 2–Burn 3). Finally, the roughness increases again (Burn 3–Burn 4). At the same time, the peakedness of the deposit structures varies also, as shown both by a visual examination of the three-dimensional surface representations (Fig. 5) as well as by the average forward facing angle (Fig. 6). After Burn 1 and the subsequent flaking of the local deposits, the zoomed surface showed a relatively low value of $\bar{\alpha}_f$. This value increased dramatically after Burn 2, resulting in the peak-dominated surface seen in Fig. 5(*c*). With Burn 3, a "wavier" surface was produced with an attendant 40% drop in average forward facing angle. Finally, Burn 4's surface returned to a more peaked state. It is noteworthy that the levels of *Ra*, *Rz*, and $\bar{\alpha}_f$ shown in Fig. 6 (and subsequent Figs. 9 and 11) are comparable to those reported for measurements on actual turbine hardware [5,6]. Specifically, the *Ra* values measured after Burn 1 on the bare metal coupon (Fig. 6) are consistent with those shown in Fig. 1. Thus, the accelerated deposition process adequately simulates the actual deposition environment in the engine as far as surface roughness condition is concerned. This is consistent with the findings of Jensen et al. [7].

TBC Coupons. Unlike the bare metal coupon, the deposits formed on the TBC coupons were relatively uniform with little noticeable deposit flaking. This may be due to several factors: first, the TBC coupon's preburn surface was rougher ($Ra = 0.6$ μm) than the polished bare metal surface. Second, unlike the polished metal substrate, the TBC surface is a relatively porous ceramic material. The porosity of the TBC would likely allow deposits to become better anchored during formation. Finally, the lower coefficient of thermal expansion inherent in a ceramic coating such as the TBC would produce less strain on any attached deposits during cooldown. Consequently, the average deposit thickness was 68 μm after the first burn on the TBC1 coupon (Fig. 7). Following Burn 1, the spanwise-average height of the deposit grew only slightly before exhibiting substantial reductions with Burns 3 and 4. This phenomenon is due to TBC spallation which occurred near the coupon edges, thus skewing the streamwise average of the deposit height. In reality, the deposit thickness continued to grow in the unspalled regions near the center of the coupon. Spallation was particularly severe in the region shown on the left side of Fig. 7 ($x < 8$ mm) where repeated thermal cycling caused portions of the TBC to crack and lift away from the rest of the surface, creating a 100 μm vertical step. Further damage oc-

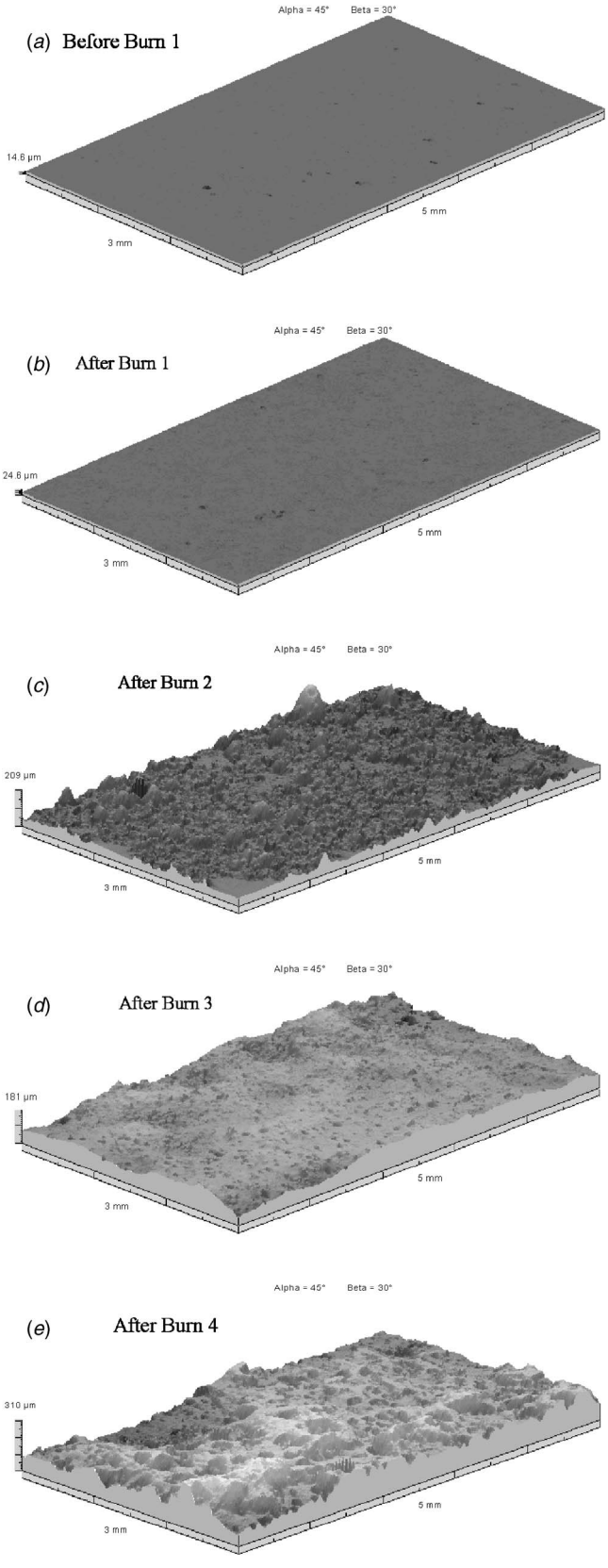

Fig. 5 Surface topologies of 3 mm $\times$ 5 mm section of deposit on bare metal coupon after each burn. Vertical scale shows peak roughness height: (*a*) before Burn 1, (*b*) after Burn 1; (*c*) after Burn 2; (*d*) after Burn 3; and (*e*) after Burn 4.

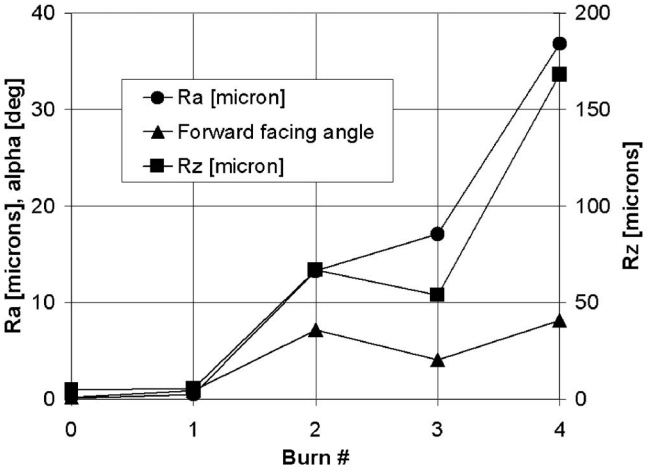

Fig. 6 Roughness statistics for the bare metal coupon deposit

curred when these raised portions of the TBC were mechanically removed prior to the Burn 3 measurement to avoid damage to the Hommel profilometer stylus.

Figure 8 contains a series of 3D topologies showing the deposit evolution on a 5.7 mm×9.5 mm region of the TBC1 coupon away from the spallation at the coupon edges. Once again, Burns 2–4 appear to fill the valleys between the initial deposit peaks created during the first period of exposure. This trend is even more evident when reviewing the evolution of roughness statistics for the TBC coupons (Fig. 9). Data for two TBC coupons are shown in Fig. 9 to explore the repeatability of the testing procedure. The second coupon (TBC2) was subjected to a similar four burn testing sequence though with roughly 30% lower net particulate loading. It also began to show signs of spallation after the second burn, however the spallation was more pronounced than for the TBC1 coupon (~60% of the surface for TBC2 versus ~20% for TBC1).

As was the case with the bare metal coupon after the flaking subsided, the roughness height (i.e., *Ra* and *Rz*) on the TBC coupons increased markedly during the first burn. This was then followed by a gradual increase over the next Two burns. Finally, the roughness height again increased more rapidly with Burn 4. The average forward facing angle also followed a trend similar to that shown in Fig. 6 for the bare metal coupon. After the first burn, $\bar{\alpha}_f$ for TBC1 climbed to 7 deg. Following this there was a slight decline with Burn 2 and a leveling off with Burn 3. Finally, the average forward facing angle climbed back above 7 deg with

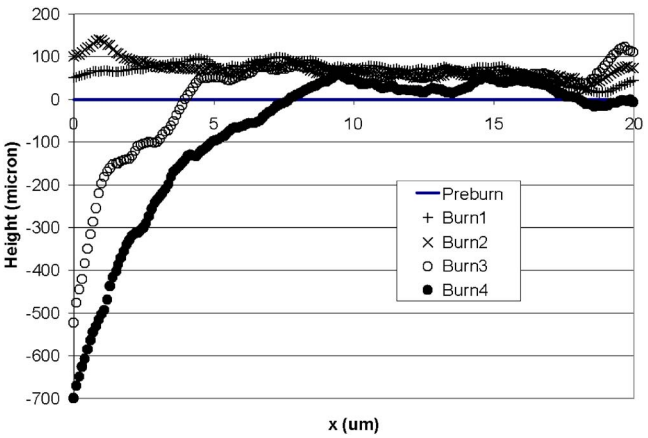

Fig. 7 Streamwise-averaged surface traces of the TBC1 coupon deposit at five different points in its evolution

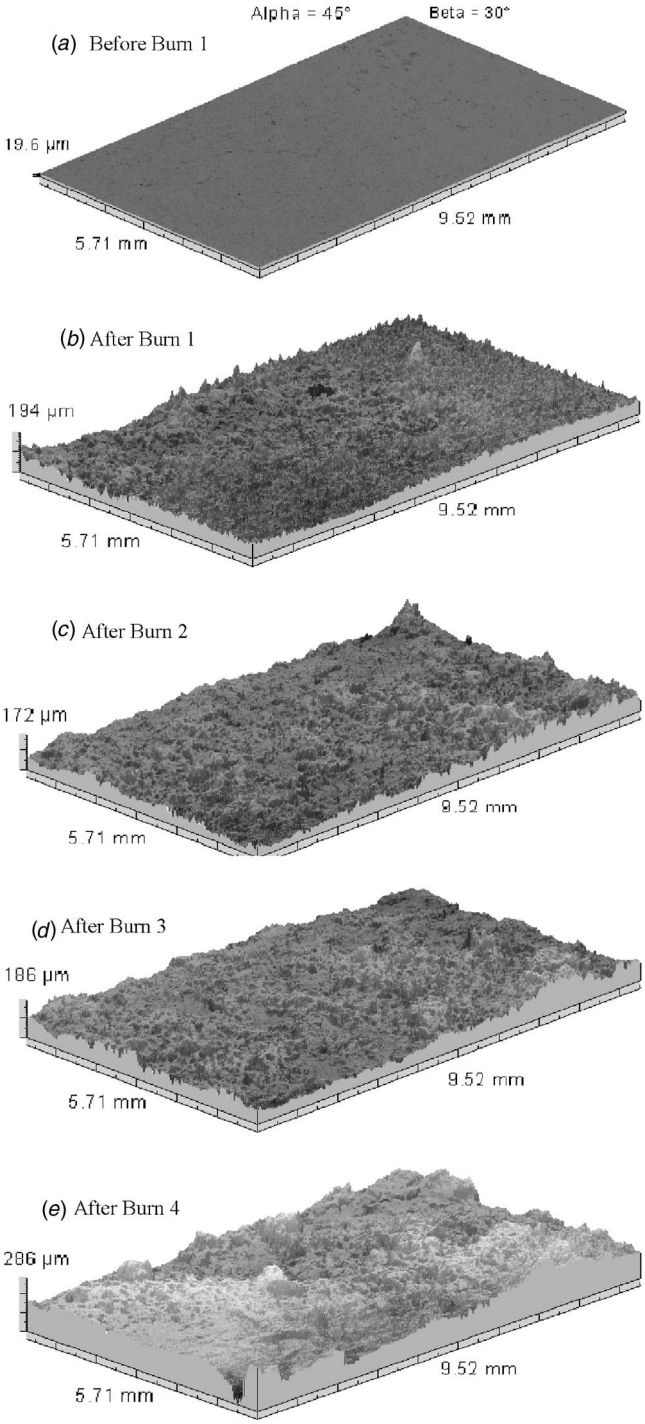

Fig. 8 Surface topologies of 5.7 mm×9.5 mm section of deposit on the TBC1 coupon after each burn. Vertical scale shows peak roughness height: (*a*) before Burn 1; (*b*) after Burn 1; (*c*) after Burn 2; (*d*) after Burn 3; and (*e*) after Burn 4.

Burn 4. The trend for TBC2 is similar.

The data from the bare metal and TBC coupons suggest that for the conditions studied, deposition begins with isolated fragments of molten particulate that attach to the surface due to inertial impaction. The initial distribution of these isolated peaks is such that subsequent deposition fills in the valleys between the peaks. Thus, the actual deposit roughness height and shape exhibit a nonmonotonic trend with service time. This trend has direct implications for skin friction (and thus aerodynamic efficiency) and heat trans-

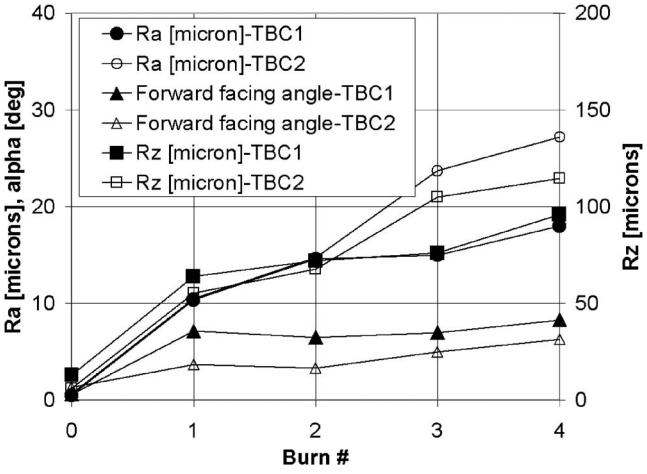

Fig. 9 Roughness statistics for the TBC1 and TBC2 coupon deposits

fer on turbine blade surfaces since both parameters are functions of roughness size and shape. Data accumulated by Bons [8] using roughness characterizations obtained from serviced turbine components indicate that the effect of roughness on c_f and St is reduced as the average forward facing angle decreases for the same mean roughness height (Rz). Bons proposed a correlation for the dependency of ks/k on $\bar{\alpha}_f$

$$\frac{k_s}{k} = 0.0191\bar{\alpha}_f^2 + 0.0736\bar{\alpha}_f \tag{3}$$

In Eq. (3), k is the average roughness height which can be approximated by Rz; and k_s is the equivalent sandgrain roughness that appears in most correlations used for estimating the effect of roughness on c_f and St (e.g., Ref. [10]). Bons [9] showed that the $\bar{\alpha}_f$ parameter was approximately equivalent to another roughness shape parameter, Λ_s, proposed originally by Sigal and Danberg [11]. The primary difference between the two parameters is that $\bar{\alpha}_f$ can be calculated from a handful of 2D surface traces, whereas Λ_s requires a full 3D surface topology. This makes $\bar{\alpha}_f$ more suitable for rapid field measurements of gas turbine components.

The observation that Rz and $\bar{\alpha}_f$ experience a temporary lull in growth during deposit evolution suggests that a turbine blade may actually experience periods of heat load reduction as deposits fill the isolated peaks created during initial operation. It is possible that this trend may be repeated numerous times with continued exposure (i.e., beyond Burn 4).

Unpolished Oxidation Resistant Coating Coupon. To further explore this finding that turbine deposits can form in such a way as to produce a nonmonotonic change in roughness size and shape, one final coupon was subjected to four successive burns in the TADF. This coupon had an "as-applied" oxidation resistant bondcoat (310 μm thick) without polishing of any kind. This resulted in an initial surface roughness level of $Ra=16$ μm, a value much larger than the typical turbine surface before operation.

A sequence of 3D topological maps is shown in Fig. 10 for an 18 mm$\times$7.99 mm measurement region. The deposits showed little or no evidence of flaking after the coupon was removed from the TADF. Although the topological maps show deposition occurring during each burn, the surface does not become increasingly rougher with each experiment. In fact, the value of Ra decreased from one test to the next in all but one case (Fig. 11). It is believed that this behavior was caused primarily by the initially high level of roughness of the coupon surface. Given the large number of peaks on the preburn surface, there were few locations where new peaks could be formed but a large number of regions where valleys could be filled in. Additionally, the average forward facing

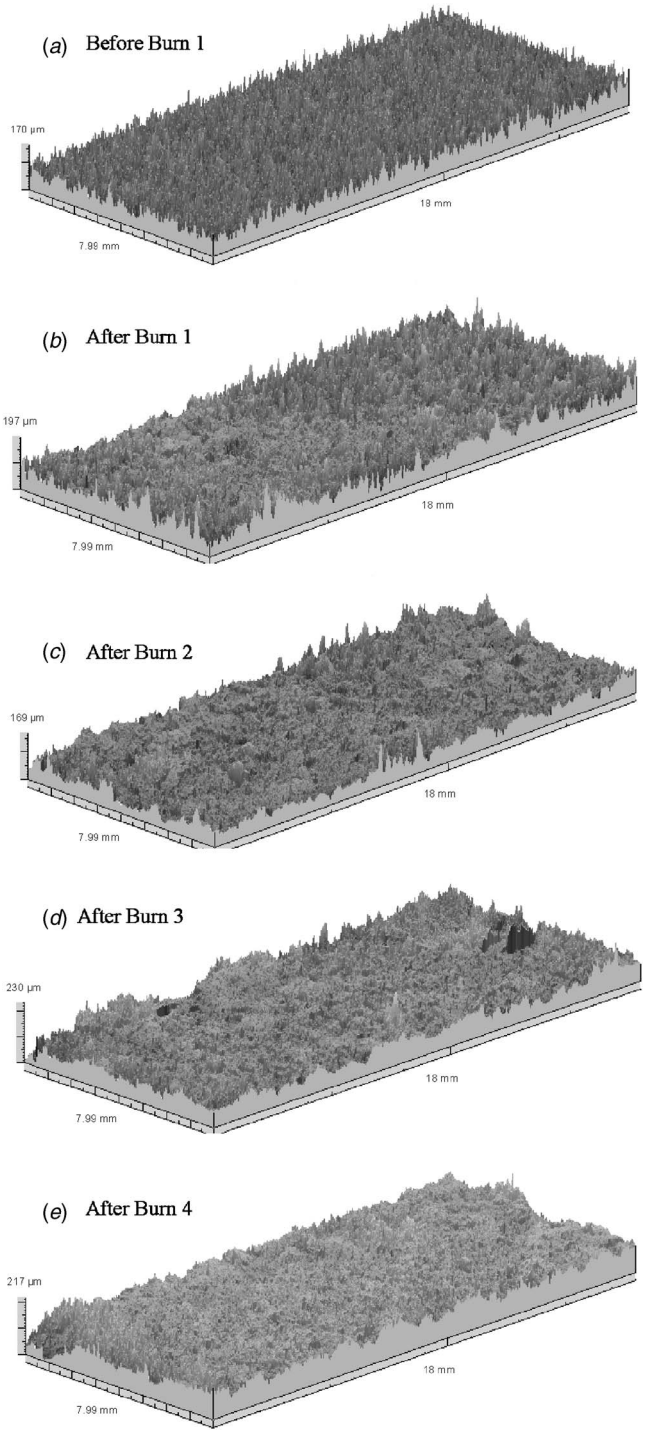

Fig. 10 Surface topologies of 8 mm$\times$18 mm section of deposit on unpolished coupon after each burn. Vertical scale shows peak roughness height: (*a*) before Burn 1; (*b*) after Burn 1; (*c*) after Burn 2; (*d*) after Burn 3; and (*e*) After Burn 4.

angle experiences only a single slight rise between Burns 2 and 3. Otherwise, the angle decreases steadily. If the coupon were subjected to more testing, it is possible that the surface roughness could eventually rise again as it did with Burn 4 for the two previous coupons. Without further testing, it is unknown at which point a trend of increasing roughness would occur. In the testing conducted by Jensen et al. [7], using coupons with the same surface treatment and the same particle-laden flow conditions, surface roughness levels of up to $Ra=40$ μm were recorded in some

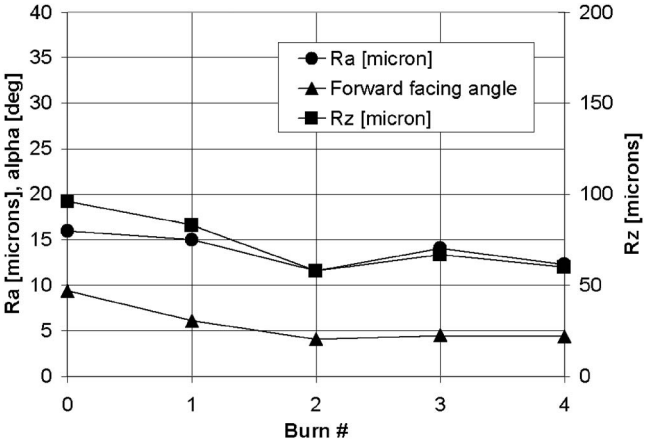

Fig. 11 Roughness statistics for the unpolished coupon deposit

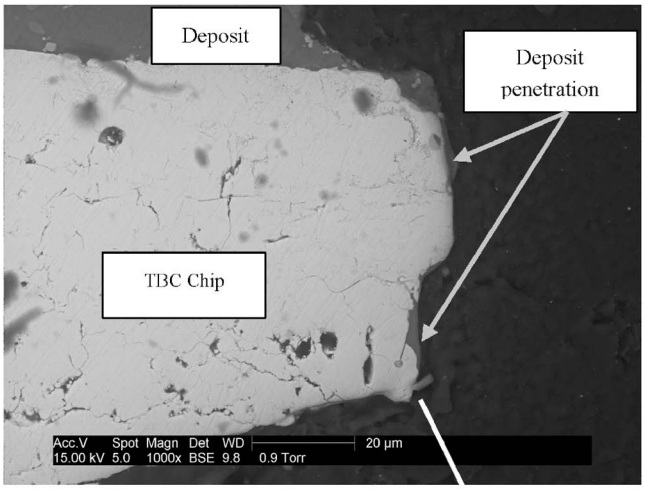

(*a*) Edge of spalled TBC chip removed after Burn 3. (Image enlarged for clarity– see scale)

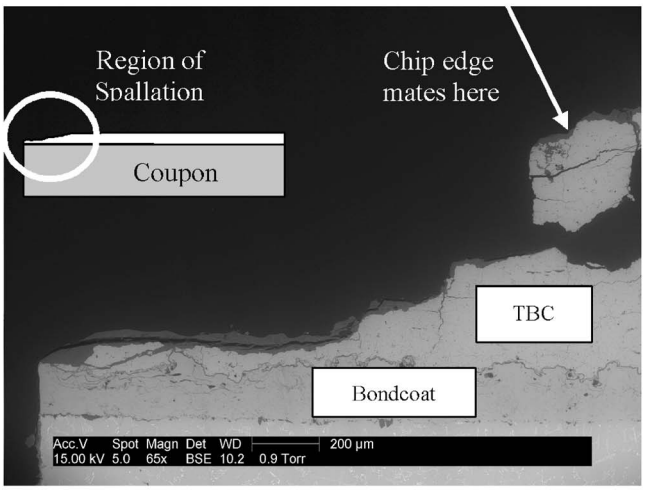

(*b*) Spalled region of TBC1 coupon after Burn 4

Fig. 12 ESEM cross section of spalled region of the TBC1 coupon and spalled chip: (*a*) edge of spalled TBC chip removed after Burn 3 (image enlarged for clarity—see scale); and (*b*) spalled region of TBC1 coupon after Burn 4

cases. This is most likely due to the fact that Jensen et al. used a much higher particulate loading (200–900 ppmw h) than was used in this study (50 ppmw h). Thus, the current findings may be specific to the testing procedure employed.

TBC Spallation. As indicated above, both TBC coupons began to show signs of spallation after the second burn. For the TBC1 coupon, this initially consisted of shallow 1–2 mm patches of TBC that became dislocated from the surface leaving small 50–100 μm deep valleys in the TBC layer. This process came to a head after Burn 3 when a 6-mm-long crack formed near the left edge of the coupon. The TBC on the side of the crack nearest the coupon edge was raised up 100 μm from the central portion of the coupon. This prevented the contact stylus of the Hommel profilometer from traversing this section of the coupon. Accordingly, the crack was manually enlarged until the entire edge of TBC spalled away from the coupon. The spalled piece of TBC was retained for later evaluation. This explains the 700 μm surface height deficit in the region $x<8$ mm in Fig. 7. The remaining coupon was then exposed to deposition in Burn 4. For the TBC2 coupon, the spallation process was much more rapid. Nearly 30% of the coupon surface showed TBC loss after Burn 2, increasing to over 60% after Burn 4. Some of the coupon edges experienced TBC loss down to the metal substrate.

To better understand the role of deposition in TBC spallation and crack development, the broken off piece from TBC1 as well as the entire coupon were prepared for cross-section analysis with the ESEM. Figures 12(*a*) and 12(*b*) show the cracked region and the spalled chip of TBC. Regions where deposit compounds were identified using X-ray spectroscopy are indicated in the figure. The top right corner of the chip shows significant penetration of deposit through cracks in the TBC. This is the portion of the chip nearest the exposed coupon surface that lifted away from the surface during Burn 3. The lower portions of the TBC chip show no signs of deposition penetration, which is understandable since this is the region where the crack was manually forced to propogate after Burn 3. The exposed TBC surface in the spalled crater does show signs of significant deposit, due to the subsequent burn (Burn 4) after the chip was removed. Thus, it seems likely that spallation was initiated by the penetration of deposits into the upper corner of the TBC chip. Whether the crack would have naturally propogated to the coupon edge during the ensuing burn is difficult to speculate. It is clear, however, that deposition played a role in the development of the spalled region. To ascertain if the spallation was merely a result of thermal cycling, a third TBC coupon (TBC3) was subjected to the identical 4×2 h testing sequence in the TADF, but without injecting particulate into the combustor. The surface showed no signs of spallation during the testing cycle, though the mean *Rz* roughness increased by a factor of three.

Conclusions

Successive deposits were generated on gas turbine blade coupons in an accelerated test facility at a gas temperature and velocity representative of first stage high-pressure turbines. Three coupon surface treatments were investigated including: (1) bare polished metal; (2) polished thermal barrier coating with bondcoat; and (3) unpolished oxidation resistant bondcoat. Each coupon was subjected to four successive 2 h deposition tests. The particulate loading was scaled to simulate 0.02 ppmw of particulate over 3 months of continuous gas turbine operation for each 2 h laboratory simulation (for a cumulative 1 year of operation). Based on the results presented in this study, the following conclusions are offered:

(1) For the conditions studied, deposit roughness size (*Rz*) and shape ($\bar{\alpha}_f$) experience a temporary lull in growth during the deposit evolution. This suggests that a turbine blade may experience periods of heat load reduction as deposits fill the

isolated peaks created during initial operation, particularly since the deposit provides additional insulation to the blade;
(2) The initial surface preparation has a significant effect on deposit growth. Highly polished bare metal prevented durable deposits within the first 2 h (equivalent to 3 months) of operation when the coupon experienced thermal cycling; and
(3) Thermal cycling combined with particle deposition caused extensive TBC spallation while thermal cycling alone caused none. Deposit penetration into the TBC is a significant contributor to spallation.

Acknowledgment

Various individuals provided invaluable support to this research effort. The authors would particularly like to thank Dr. Tom Taylor of Praxair Surface Technologies and Gerry McQuiggan from Siemens who generously donated coupon specimens for this study. Thanks also go to Ken Forster, Kevin Cole, and John Pettit for performing a myriad of helpful tasks. Michael Standing's expert assistance with the ESEM and X-ray spectrometer measurements was invaluable. This work was sponsored by a generous grant from the BYU Mechanical Engineering Department and by the US Department of Energy—National Energy Technology Laboratory through a cooperative agreement with the South Carolina Institute for Energy Studies at Clemson University. The views expressed in this paper are those of the authors and do not reflect the official policy or position of the Department of Energy or U.S. Government.

Nomenclature

i = summation index in y direction
I = number of surface data points in the y direction
j = summation index in y direction
J = number of surface data points in the x direction
k_s = equivalent sandgrain roughness
M = Mach number
Ra = centerline averaged roughness (μm) (Eq. (1))
Rt = maximum peak-to-valley roughness (μm)
$Rz=k$ = mean peak-to-valley roughness (μm)
T = flow temperature (°C)
x = surface dimension perpendicular to the gas stream
y = surface dimension parallel to the gas stream
z = height of an individual roughness element
$\bar{\alpha}_f$ = average forward-facing angle (Eq. (2))
Λ_s = roughness shape/density parameter [11]
θ = flow impingement angle

References

[1] Wenglarz, R. A., and Wright, I. G., 2002, "Alternate Fuels for Land-Based Turbines," *Proceedings of the Workshop on Materials and Practices to Improve Resistance to Fuel Derived Environmental Damage in Land-and Sea-Based Turbines*, Colorado School of Mines, Golden, CO, October 22–24.
[2] Smialek, J. L., Archer, F. A., and Garlick, R. G., 1992, *The Chemistry of Saudi Arabian Sand: A Deposition Problem on Helicopter Turbine Airfoils, Advances in Synthesis and Processes*, F. H. Froes, eds., SAMPE, Vol. 3, pp. M92M101.
[3] Toriz, F. C., Thakker, A. B., and Gupta, S. K., 1988, "Thermal Barrier Coatings for Jet Engines," ASME Paper No. 88-GT 279.
[4] Kim, J., Dunn, M. G., and Baran, A. J. et al., 1993, "Deposition of Volcanic Materials in the Hot Sections of Two Gas Turbine Engines," J. Eng. Gas Turbines Power, **115**, pp. 641–651.
[5] Tarada, F., and Suzuki, M., 1993, "External Heat Transfer Enhancement to Turbine Blading due to Surface Roughness," ASME Paper No. 93-GT-74.
[6] Bons, J. P., Taylor, R., McClain, S., and Rivir, R. B., 2001, "The Many Faces of Turbine Surface Roughness," ASME J. Turbomach., **123**(4), pp. 739–748.
[7] Jensen, J. W., Squire, S. W., and Bons, J. P., 2005, "Simulated Land-Based Turbine Deposits Generated in an Accelerated Deposition Facility," ASME J. Turbomach., **127**, pp. 462–470.
[8] Bons, J. P., Crosby, J., Wammack, J. E., Bentley, B. I., and Fletcher, T. H., "High Pressure Turbine Deposition in Land-Based Gas Turbines With Various Synfuels," ASME Paper No. GT2005-68479.
[9] Bons, J. P., 2005, "A Critical Assessment of Reynolds Analogy for Turbine Flows," ASME J. Heat Transfer, **127**, pp. 472–485.
[10] Schlichting, H., 1979, *Boundary Layer Theory*, 7th ed., McGraw-Hill, New York.
[11] Sigal, A., and Danberg, J. E., 1990, "New Correlation of Roughness Density Effects on the Turbulent Boundary Layer," AIAA J., **28**, pp. 554–556.

Evolution of Surface Deposits on a High-Pressure Turbine Blade—Part II: Convective Heat Transfer

Jeffrey P. Bons
James E. Wammack
Jared Crosby
Daniel Fletcher

Department of Mechanical Engineering,
Brigham Young University,
Provo, UT 84602

Thomas H. Fletcher
Department of Chemical Engineering,
Brigham Young University,
Provo, UT 84602

A thermal barrier coating (TBC)-coated turbine blade coupon was exposed to successive deposition in an accelerated deposition facility simulating flow conditions at the inlet to a first stage high pressure turbine ($T=1150°C$, $M=0.31$). The combustor exit flow was seeded with dust particulate that would typically be ingested by a large utility power plant. The turbine coupon was subjected to four successive 2 h deposition tests. The particulate loading was scaled to simulate 0.02 parts per million weight (ppmw) of particulate over 3 months of continuous gas turbine operation for each 2 h laboratory simulation (for a cumulative 1 year of operation). Three-dimensional maps of the deposit-roughened surfaces were created between each test, representing a total of four measurements evenly spaced through the lifecycle of a turbine blade surface. From these measurements, scaled models were produced for testing in a low-speed wind tunnel with a turbulent, zero pressure gradient boundary layer at $Re=750{,}000$. The average surface heat transfer coefficient was measured using a transient surface temperature measurement technique. Stanton number increases initially with deposition but then levels off as the surface becomes less peaked. Subsequent deposition exposure then produces a second increase in St. Surface maps of St highlight the local influence of deposit peaks with regard to heat transfer. [DOI: 10.1115/1.2752183]

Keywords: deposition, roughness, turbines

Introduction

Land-based and aircraft gas turbines ingest large quantities of air during operation. Contaminants found in the atmosphere or in the fuel are known to generate deposits on the blade surfaces [1,2]. Once formed, these deposits roughen the blade surfaces resulting in an increase in skin friction and in the convective heat transfer rate between the exhaust gases and the turbine blades [3,4]. Deposits can also clog vital coolant passages, thus further aggravating the thermal load of the turbine components [5]. The effects of elevated levels of surface roughness on turbomachinery performance have been studied for over 25 years. These studies include fundamental flat-plate wind tunnel research [6], multiblade cascade facilities [7], and full system level tests [8] in addition to numerous computational studies [9]. These studies all support the expected result that roughness increases surface drag and heat transfer (though to varying degrees). For turbomachinery, this translates to higher heat loads, accelerated part degradation, and lower stage efficiencies.

Unfortunately, because this deposition process takes place over thousands of hours (for a land-based turbine), little is known about the evolution of deposition on turbine blade surfaces. A companion paper [10] reports on a combustor simulator that was used to evolve deposits on a turbine coupon with thermal barrier coating (TBC). This was done in the Turbine Accelerated Deposition Facility (TADF) which is a specialized combustor capable of creating deposits at a vastly accelerated rate and under controllable conditions. The facility is described in detail in Ref. 11, but the essential principle is that of matching the product of the particle concentration in the air flow (measured in parts per million weight, ppmw) and the number of hours of operation. Deposits were generated at constant operating conditions over four successive 2 h tests, simulating 3 months of gas turbine operation for each test. The companion paper Part I [10] reviewed the evolution of surface roughness character with successive deposition for the three most common material systems found on modern gas turbine airfoils: uncoated superalloy, thermal barrier coating (TBC), and oxidation resistant coating. A significant observation from this study was that deposit roughness size (Rz) and shape ($\overline{\alpha_f}$) experienced a temporary lull in growth during deposit evolution for the conditions studied. This occurred as deposits filled the isolated peaks created during initial operation. Because of the well-documented link between roughness size and surface heat transfer, the objective of this study is to explore the implications of this surface evolution on the heat load to the turbine.

Roughness Models

Of the three surface treatments included in the Part I study, the TBC1 coupon was selected for this convective heat transfer study due to its relevance to modern gas turbines. After each 2 hour deposition test (denoted as "burns" in what follows), the surface topology of the coupon deposit was measured using a Hommel Inc. T8000 profilometer equipped with a TKU600 stylus. The stylus tip was conical in shape and had a 5 μm tip radius. Three-dimensional surface representations were constructed from a series of two-dimensional traces separated by 10 μm. Data points within each trace were also separated by 10 μm, yielding a square data grid. Three-dimensional surface representations and roughness statistics were produced with the Hommelwerke Hommel Map software. The statistics of most interest for this study were the centerline averaged roughness, Ra, the average roughness

Contributed by the International Gas Turbine Institute of ASME for publication in the JOURNAL OF TURBOMACHINERY. Manuscript received September 8, 2006; final manuscript received November 15, 2006; published online March 25, 2008. Review conducted by David Wisler. Paper presented at the ASME Turbo Expo 2006: Land, Sea and Air (GT2006), Barcelona, Spain, May 8–11, 2006, Paper No. GT2006-91257.

height, Rz, and the average forward-facing surface angle, $\overline{\alpha_f}$. The centerline averaged roughness was calculated using the following

$$Ra = \frac{1}{IJ}\sum_{i=0}^{I-1}\sum_{j=0}^{J-1}|z_{i,j}| \tag{1}$$

Rz was calculated as the mean of the vertical distance between the highest peak and deepest valley every 10 mm of a 2D surface trace. Based on the scaled roughness model images shown in Fig. 1, this appeared to be a representative roughness dimension for the deposits in this study. The average forward-facing angle was calculated using the methodology proposed by Bons [12] in which the surface is traversed in the flow direction and forward-facing angles are averaged with all leeward-facing angles set equal to zero (Eq. (2))

$$\bar{\alpha}_f = \frac{1}{I}\sum_{i=0}^{I-1}\alpha_i \tag{2}$$

where, if $(z_{i+1}-z_i)>0$

$$\alpha_i = \tan^{-1}\left(\frac{z_{i+1}-z_i}{y_{i+1}-y_i}\right) \quad \text{else,}\ \alpha_i = 0$$

Typically, Rz and $\overline{\alpha_f}$ are calculated as the average of multiple 2D surface traces.

The TBC1 coupon experienced continuous deposit growth over the entire four-burn sequence in the TADF. In addition, during the third and fourth burns, significant TBC spallation occurred near the coupon edges. Since spallation roughness was not the focus of this study, scaled roughness models were made from a region at the coupon center, where spallation was minimal. Figure 1 contains a series of 3D topologies showing the deposit evolution on a 3.3 mm × 4.2 mm region away from the spallation at the coupon edges. Burns 2–4 appear to fill the valleys between the initial deposit peaks created during the first period of exposure. This trend is even more evident when reviewing the evolution of roughness statistics for the scaled models of the TBC1 coupon (Fig. 2). As outlined previously, the roughness height (i.e., Ra and Rz) on the TBC1 coupon increased markedly during the first burn. This was then followed by a gradual increase over the next two burns. Finally, the roughness height again increased rapidly with Burn 4. The average forward facing angle followed a similar trend. The initial rise in $\overline{\alpha_f}$ with Burn 1 was followed by a slight decline with Burn 2 and a leveling off with Burn 3. Finally, the average forward facing angle climbed back above 7 deg with Burn 4. It is noteworthy that the levels of Ra, Rz, and $\overline{\alpha_f}$ shown in Fig. 2 are comparable to those reported for measurements on actual turbine hardware [3,4], as discussed in Part I.

The topological measurements from the Hommel profilometer shown in Fig. 1 were used to create the CNC-compatible code and produce the scaled models. Model scaling was guided by the ratio of roughness height to boundary layer momentum thickness, Rz/θ. This ratio was maintained near a value of 0.5 [4,13,14]. With this as guidance, a scaling factor of 20 was determined to be appropriate. Because of this scaling factor, and due to the limited size of the largest usable rectangular region of roughness, the original data formed 25% of the total model surface. The remaining 75% of the 22 cm × 38 cm wind tunnel space provided for the model was filled by mirroring this section of data.

With the CNC code, the roughness models were cut out of 2.54-cm-thick Plexiglas acrylic sheets using a modified countersink. The countersink was chosen because it most closely approximated the tip of the profilometer stylus that scanned the surface originally. Both are conical in shape with a 90 deg included angle. This was to ensure that the model contours would be as close as possible to the original surface measurements. A comparison of the scaled model surfaces to the original coupon roughness indicated that while the roughness height was well matched (within 10%), the angle was not. The countersink tool that was used, with a 0.5 mm tip radius, flattened out the transitions in the surface producing a 25% drop in mean forward facing angle. These adjustments are reflected in the roughness statistics for the scaled model shown in Fig. 2.

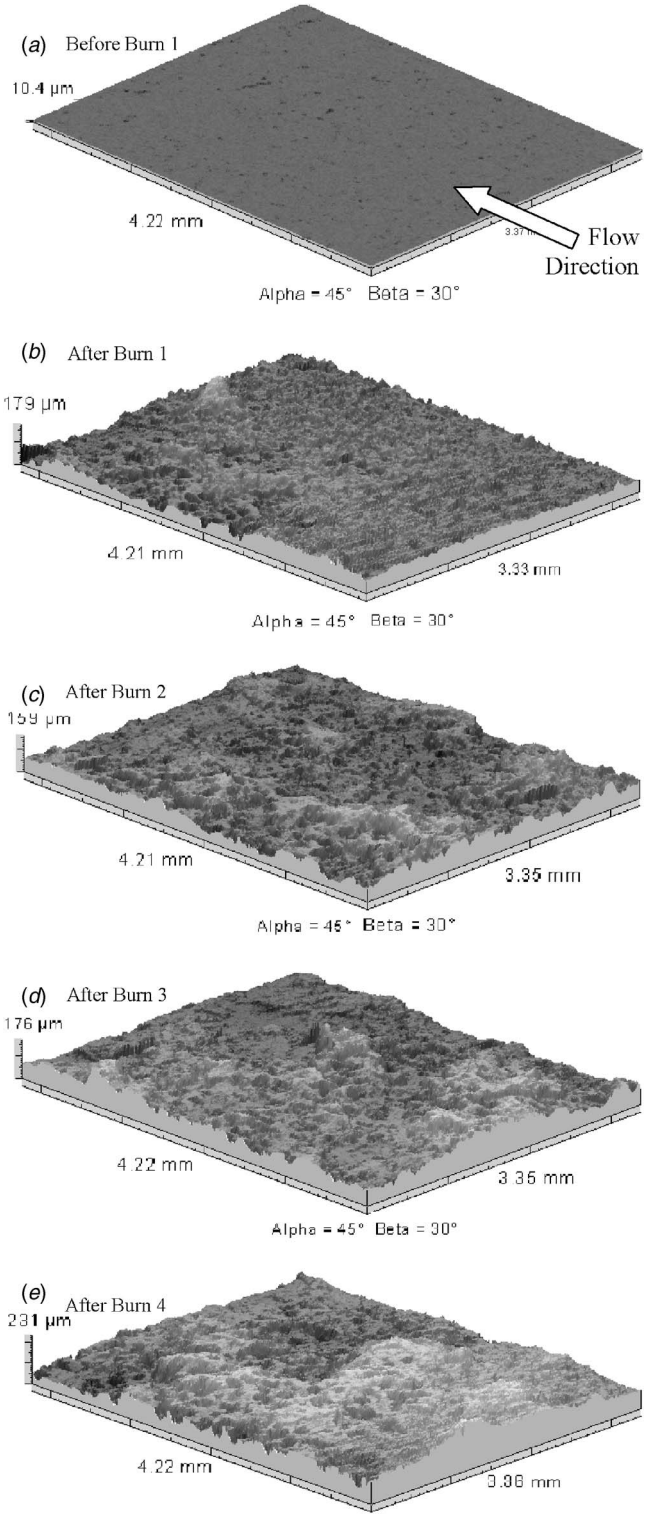

Fig. 1 Surface topologies of 3.3 mm × 4.2 mm from surface deposit on TBC1 coupon after each burn. Vertical scale shows peak roughness height.

Experimental Facility

A schematic of the research facility used for the experiments is shown in Fig. 3. The open loop wind tunnel uses a main flow

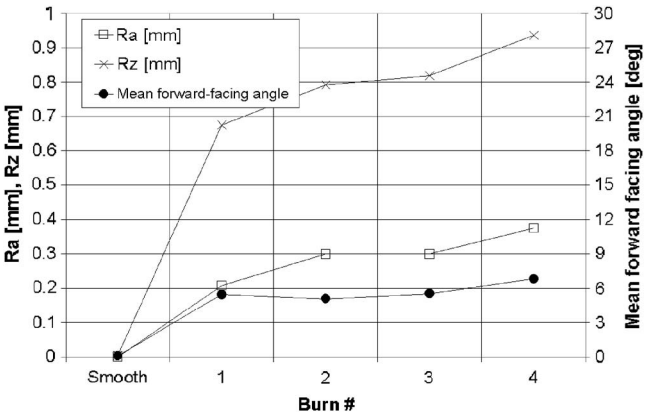

Fig. 2 Roughness statistics for the scaled model surface

blower to provide a nominal mass flow of 1.8 kg/s to the test section. A heat exchanger at the main flow blower discharge can be used to vary the flow temperature from 20°C to 50°C. The main flow enters a 0.6-m-diameter conditioning plenum before reaching the square test section. This conditioning plenum has one layer of perforated aluminum plate followed by 7.6 cm of honeycomb straightener, and five layers of fine screen. A circular-to-square foam nozzle conducts the flow from the plenum cross section to the 0.38 m by 0.38 m acrylic test section. With this conditioning, 2D flow uniformity of ±0.4% in velocity and ±1°C is obtained over the center 0.18 m of the test section span. The freestream turbulence level in the wind tunnel is 0.5%.

At 1.52 m from the plenum exit a knife-edge boundary layer bleed with suction removes the bottom 2.7 cm of the growing boundary layer. The top wall of this final section pivots about its forward end in order to adjust the pressure gradient in the tunnel. For the tests presented here, the wall was adjusted to produce zero freestream acceleration over the roughness test panels. At 2.5 cm from the boundary layer suction point, a 2-mm-diameter cylinder spans the test section to trip the boundary layer to turbulent. The leading edge of the roughness panel is located 1.04 m from the boundary layer suction point. The roughness panels are installed in a 0.22 m streamwise gap in the lower wall as shown in Fig. 1. The tunnel then continues 0.3 m beyond the trailing edge of the roughness panels. In this configuration, the flow in the tunnel experiences a transition from a smooth to rough wall condition at the leading edge of the roughness panels. This experimental setup departs from traditional roughness experiments in which the entire development length of the boundary layer is roughened. Studies by Antonia and Luxton [15] and more recently by Taylor and Chakroun [16] show that this smooth to rough transition results in an initial overshoot in c_f and St followed by a fairly rapid adjustment to the appropriate rough-wall values. Both researchers report an adjustment length equivalent to 3–4 boundary layer thicknesses

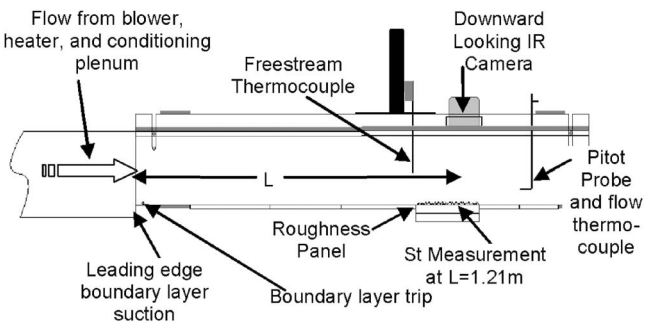

Fig. 3 Wind Tunnel Facility

with up to 20% initial overshoot. To mitigate the effect of this transition region, the heat transfer data were taken on the downstream half of the roughness section (beyond the expected adjustment length of approximately 9 cm).

As additional verification of this testing procedure, heat transfer data were also acquired with multiple upstream roughness panels extending to 1 m upstream of the measurement point, and the data showed no perceptible effect beyond the uncertainty of the measurement. Thus, all data were acquired with the smooth to rough transition at 1.04 m from the tunnel boundary layer bleed. The mean elevation of the roughness panel was aligned vertically with the upstream smooth panel to prevent acceleration or deceleration of the bulk flow (U_∞).

Flow velocity was measured using a pitot-static probe with a co-located flow thermocouple with 0.13 mm bead diameter for flow temperature measurement. The two instruments are positioned at midspan just outside the boundary layer and downstream of the roughness panel during the transient testing. A second thermocouple was located upstream of the test panel and further away from the wall in the freestream, as shown in Fig. 3. Uncertainty in the velocity measurement was within ±1.5% at flow rates of interest.

A boundary layer pitot probe with a co-located 0.13 mm bead diameter flow thermocouple was used to determine the boundary layer velocity and thermal profiles at the St measurement location. With the smooth test panel installed at the test section, the velocity boundary layer thickness was approximately 22 mm, with momentum and displacement thicknesses of 2.7 mm and 3.6 mm, respectively (shape factor=1.36). The thermal boundary layer shape varies during the St measurement due to the transient testing procedure and nonconstant wall temperature. However, the thermal layer thickness remains roughly equivalent to the velocity boundary layer thickness (approximately 2 cm).

St Measurement. For the heat transfer measurements, a FLIR Thermacam SC 3000 infrared (IR) camera system is mounted with the lens fit into a hole in the acrylic ceiling of the tunnel. The camera has a sensitivity of 0.03°C (at 30°C) and allows framing rates of approximately 1 Hz. The IR camera was focused on a 67 mm (crossstream) × 83 mm (streamwise) field of view. This limited field of view was centered at a distance of $L=1.21$ m from the leading edge of the tunnel floor. This puts the streamwise position of the heat transfer measurement roughly 6 cm downstream of the center of the roughness panel. The 240 × 320 pixels of the FLIR camera allowed excellent resolution of the roughness features during the transient experiments.

The Stanton number was determined from this surface temperature history using a three-dimensional unsteady conduction finite-volume algorithm with time-varying boundary conditions. The time-varying surface heat flux is calculated from the surface normal temperature gradient in the solid. This technique assumes the panels are a semi-infinite solid at constant temperature at time $t=0$. To accomplish this, the entire test section was soaked at room temperature for several hours before testing. Using the main flow heat exchanger, a hot-gas air flow (50°C) was then initiated instantaneously while monitoring the freestream velocity and temperature, as well as the average surface temperature (with the IR camera).

Radiative heat flux from the test plate to the surrounding tunnel walls was always less than 1% of the calculated convective heat flux. The thermophysical properties, thermal conductivity (κ) and thermal diffusivity ($\alpha=\kappa/\rho c_p$), for the plastic panels were determined experimentally by Thermal Properties Research Laboratory. The measurements yielded the following values: $\kappa=0.196$ W/m K ± 6% and $c_p=1330$ J/kg K ± 3%. The plastic density is 1188 kg/m^3 ± 2%.

During testing the 25-mm-thick acrylic roughness panel was mounted on a second 25-mm-thick smooth acrylic panel with the same material properties. A thermocouple sandwiched between

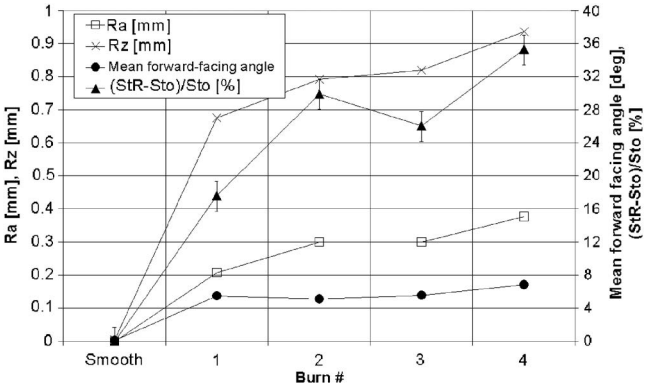

Fig. 4 Stanton number augmentation and roughness statistics for the scaled roughness models

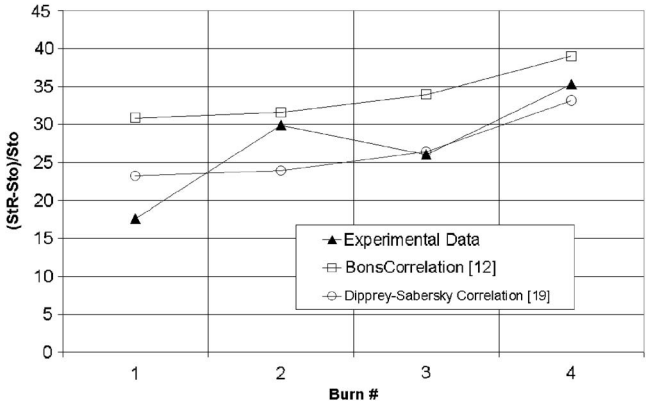

Fig. 5 Comparison of experimental St augmentation with empirical prediction

the two panels indicated no change in temperature during the first 5 min for the typical test case. Due to the low thermal diffusivity of the acrylic plates, test times shorter than 5 min yield a Fourrier number ($\mathrm{Fo}=\alpha t/b^2$) less than 1/16, which is the semi-infinite limit. This confirmed the use of the semi-infinite conduction assumption in the data processing. Also, it was discovered that the infrared measurement is sensitive to the temperature of the surfaces surrounding the roughness panels. This occurs because some of the radiation that is incident on the camera originates from the wind tunnel enclosure and is reflected off the roughness panel. The magnitude of this component of radiation changes as a function of the tunnel wall temperature. The FLIR software accounts for this by allowing the user to specify the ambient enclosure temperature. Since the heat transfer test was transient, this input was adjusted in post-processing to track the tunnel wall temperature as a function of time. Six 50 μm bead diameter thermocouples were flush mounted to each of the acrylic test panels to verify the IR surface temperature measurement. This allowed calibration of the camera to within $\pm 0.3^\circ$C of the initial surface temperature and corroborated the St calculation procedure for the rough panels relative to the smooth panel. The area-average St numbers presented in this paper were calculated by averaging the initial 250 s of the plate's transient response over the full 67 mm $\times$ 83 mm camera viewfield. The smooth plate St value was found to be within 1% of a standard correlation. Repeatability was within $\pm 3\%$ and bias uncertainty was estimated at ± 0.00015 for the smooth plate measurement of $\mathrm{St}_0=0.00228$ at $\mathrm{Re}_L=750{,}000$.

Results and Discussion

Heat transfer measurements were made at constant flow velocity ($\mathrm{Re}_L=750{,}000$) for each of the four deposit models and a smooth baseline panel. Figure 4 shows the Stanton number computed using the area-averaged surface temperature as obtained from the IR camera measurement described above. Each data point in Fig. 4 represents the average of at least three separate transient tests, usually conducted on different days. Error bars show the range of measurements for each data point. The Stanton number values are presented as a percent difference between the rough surface value (St_R) and the smooth surface reference value (St_0). The smooth reference panel used in the wind tunnel study had a centerline average roughness of $Ra=0.5$ μm. This is significantly lower than the roughness level of $Ra=12$ μm that would have been obtained if the preburn polished TBC surface had been scaled by the same factor of 20 used for the roughness panels. However, the roughness Reynolds number (Re_{ks}) for both cases is well below the aerodynamically smooth limit for these wind tunnel conditions. Thus, the percent change in St would be similar with either reference. Also shown in the figure are the model roughness statistics from Fig. 2 for comparison. These statistics are computed for the portion of the roughness model surface in the direct field of view of the IR camera and may differ somewhat from those presented in Part I.

The trend in Stanton number follows closely the trend in roughness statistics. The St augmentation levels off between Burns 2 and 3 followed by a marked rise with Burn 4 as the roughness height and mean angle experience a resurgence. Data accumulated by Bons [12] using roughness characterizations obtained from serviced turbine components indicate that the effect of roughness on c_f and St is reduced as the average forward facing angle decreases for the same mean roughness height ($\overline{Rz}$). Bons proposed a correlation for the dependency of k_s/k on $\bar{\alpha}_f$.

$$\frac{k_s}{k} = 0.0191\bar{\alpha}_f^2 + 0.0736\bar{\alpha}_f \tag{3}$$

Though the skin friction coefficient was not measured for the roughness models, an empirical correlation proposed by Schlichting was used to estimate its value [17]

$$c_f = [2.87 + 1.58\log(L/k_s)]^{-2.5} \tag{4}$$

This was combined with a correlation for Reynolds analogy (RA) factor ($\mathrm{RA}=2\mathrm{St}/c_f$) proposed by Bons for a turbulent boundary layer over rough surfaces [12] to obtain an empirical estimate for St

$$\frac{\mathrm{RA}}{\mathrm{RA}_0} = 0.5\left(1 + \exp\left(-0.9\frac{k_s}{\theta}\right)\right) \tag{5}$$

The value for RA_0, the smooth wall value of Reynolds analogy, for a turbulent boundary layer was 1.2.

The results of this empirically based St correlation (Eqs. (3)–(5)) are shown with the experimental data in Fig. 5. The predictions are higher than the experiment in all cases. A different correlation based on the roughness Reynolds number (Re_{ks}) by Dipprey and Sabersky [18] is also shown for comparison

$$\mathrm{St} = \frac{0.5c_f}{1 + \sqrt{0.5c_f}(5.19\,\mathrm{Re}_{ks}^{0.2}\,\mathrm{Pr}^{0.44} - 8.5)} \tag{6}$$

Both models capture the general trend of increasing roughness with repeated exposure, although Eq. (6) shows better overall agreement.

The spatial resolution of the infrared camera combined with the 3D finite-volume analysis technique allows a detailed evaluation of the heat transfer around specific roughness features in addition to the area-averaged St measurements presented above. The unsteady conduction algorithm properly accounts for lateral conduction within the three-dimensional roughness features on the scaled model. Table 1 contains the minimum, average, maximum, and standard deviation of St for each of the roughness surfaces. The

Table 1 Spatial statistics for heat transfer coefficient

Burn	Min St	Avg St	Max St	Std dev St (%)
1	0.00078	0.00273	0.00794	20.1
2	0.00138	0.00294	0.00637	19.4
3	0.00105	0.00292	0.00675	23.1
4	0.00001	0.00309	0.00797	27.7

values in the table represent only a 20 s time average from 80 to 100 s after flow initiation, whereas the area-averaged data in Figs. 4 and 5 are averaged over the full 250 s test time.

In all four cases, there is a substantial variation in heat transfer over the rough surfaces. In general, roughness peaks can experience 2–3 times higher heat transfer than the area average. These results are consistent with measurements from Henry et al. [19] who reported up to a factor of 2.5 heat transfer augmentation at the leading edge of spherical protuberances in a turbulent boundary layer. This effect is partially due to the energetic interaction between the flow and the roughness peak as the flow accelerates to navigate around the obstruction. In addition, roughness peaks reach further from the wall into the thermal boundary layer where higher temperature fluid (on average) is present; thus, the elevated measurements in these regions. This is actually welcome news for turbine thermal load management. Since a substantial portion of the heat transfer augmentation occurs at these elevated peaks of the deposit, the path to the metal substrate (through the deposit peak) is longer, resulting in a greater thermal resistance. Thus, the increase in local metal temperature beneath the deposit (and TBC) will be less severe. Unfortunately, flow separation behind the deposit roughness peaks generates highly turbulent flow in the wake of the protuberances. This is shown in Fig. 6 which contains side-by-side surface height and St contour plots for the region near roughness peaks on the Burn 1 and 2 models. Though not as high as the heat transfer at the roughness peak, the wake regions (indicated by circles in Figs. 6(*a*) and 6(*d*)) still experience heat transfer augmentation that is 75% higher than the surrounding surface when compared to the smooth surface heat transfer. And if the deposit is thinner in this wake-affected region, the lack of added insulation from the deposit could result in a local hot spot penetrating deep into the TBC layer. Finally, the standard deviation data in Table 1 show a trend similar to that exhibited by the mean forward-facing angle in Fig. 4. As might be expected, the heat transfer variations become more pronounced as the deposit surface becomes more peaked.

Conclusions

Successive deposits were generated on a TBC coupon in an accelerated test facility at a gas temperature and velocity representative of first stage high-pressure turbines. The coupon was subjected to four successive 2 h deposition tests. The particulate loading was scaled to simulate 0.02 ppmw of particulate over 3 months of continuous gas turbine operation for each 2 h laboratory simulation (for a cumulative 1 year of operation). Convective heat transfer measurements were made using scaled models of the deposit roughness after each exposure period. Based on the results presented in this study, the following conclusions are offered:

(1) For the conditions studied, deposit roughness size (Rz) and shape ($\overline{\alpha_f}$) experienced a temporary lull in growth during the deposit evolution. This produced a comparable plateau in measured heat transfer coefficient (St) as deposits filled the valleys between isolated peaks created during initial operation. The implication is that heat load management may be most severe during the initial phase of deposition, when the deposit peaks are distributed over the relatively smooth surface. The subsequent valley filling reduces the roughness signature as well as provides additional insulation to the blade. Existing Stanton number correlations based on various roughness statistics captured the trend in the experimental data; and

(2) Surface roughness features can create local St variations of up to a factor of three from the area average. Isolated peaks result in substantially elevated levels of convective heat transfer in the wake directly downstream of the protuberance.

Acknowledgment

Various individuals provided invaluable support to this research effort. The authors would particularly like to thank Dr. Tom Taylor of Praxair Surface Technologies and Gerry McQuiggan from Siemens who generously donated coupon specimens for this study. Thanks also to Ken Forster, Kevin Cole, and Spencer Grange for performing a myriad of helpful tasks. This work was sponsored by a generous grant from the BYU Mechanical Engineering Department and by the US Department of Energy—National Energy Technology Laboratory through a cooperative agreement with the South Carolina Institute for Energy Studies at Clemson University. The views expressed in this paper are those of the authors and do not reflect the official policy or position of the Department of Energy or U.S. Government.

Nomenclature

I = total number of y direction surface measurements
J = total number of x direction surface measurements
L = wind tunnel length from bleed to measurement location (1.21 m)
M = Mach number
Pr = Prandtl number
RA = Reynolds analogy factor ($2\mathrm{St}/c_f$)
Ra = centerline averaged roughness (mm) (Eq. (1))
Re_L = flow Reynolds number $U_\infty L/\nu$
Re_{ks} = roughness Reynolds number $u_\tau k_s/\nu$
Rt = maximum peak-to-valley roughness (mm)
Rz = k=mean peak-to-valley roughness (mm)
St = Stanton number ($h/\rho c_p U_e$)
T = flow temperature (°C)
U_∞ = wind tunnel velocity (13 m/s)
b = plate thickness (25 mm)
c_f = skin friction coefficient
c_p = specific heat
i = y direction indexing variable
j = x direction indexing variable
k = average roughness height ($\approx Rz$)
k_s = equivalent sandgrain roughness
t = time
x = surface dimension perpendicular to the gas stream
y = surface dimension parallel to the gas stream
z = height of an individual roughness element
α = thermal diffusivity
$\overline{\alpha_f}$ = average forward-facing angle (Eq. (2))
κ = thermal conductivity
ν = kinematic viscosity
θ = boundary layer momentum thickness
ρ = density

Subscripts

0 = flat plate baseline
R = roughness
s = surface

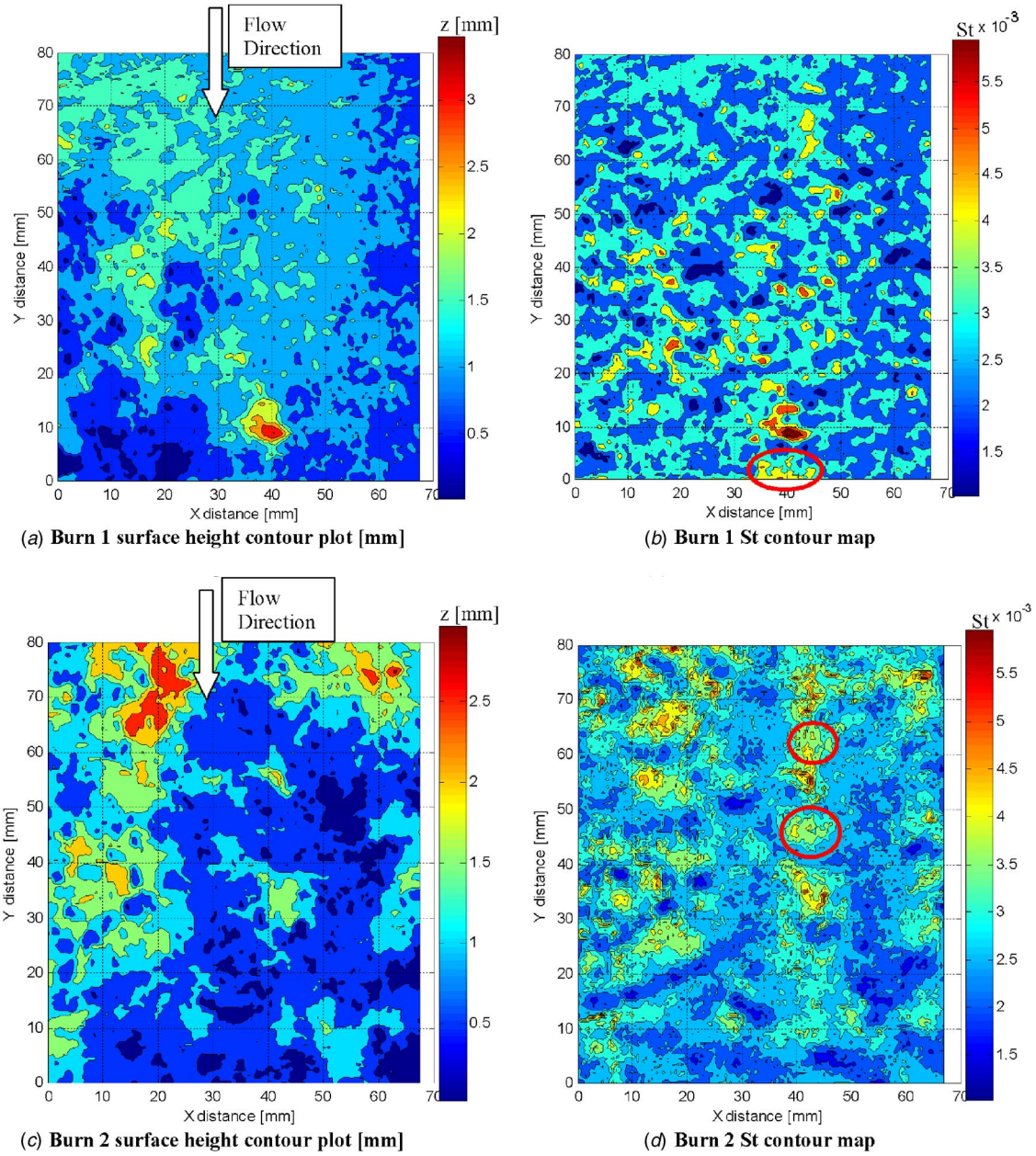

Fig. 6 Heat transfer coefficient and surface height plots for a 67 mm×83 mm region on the Burn 1 and 2 roughness models. (Flow direction is from top to bottom as indicated.) Wake regions with elevated St values are circled: (*a*) Burn 1 surface height contour plot (mm); (*b*) Burn 1 St contour map; (*c*) Burn 2 surface height contour plot (mm); and (*d*) Burn 2 St contour map.

∞ = freestream

References

[1] Borom, M. P., Johnson, C. A., and Peluso, L. A., 1996, "Role of Environmental Deposits and Operating Surface Temperature in Spallation of Air Plasma Sprayed Thermal Barrier Coatings," Surf. Coat. Technol., **86–87**, pp. 116–126.

[2] Wenglarz, R. A., and Fox, R. G., Jr., 1990, "Physical Aspects of Deposition From Coal-Water Fuels Under Gas Turbine Conditions," J. Eng. Gas Turbines Power, **120**, pp. 9–14.

[3] Tarada, F., and Suzuki, M., 1993, "External Heat Transfer Enhancement to Turbine Blading due to Surface Roughness," ASME Paper No. 93-GT-74.

[4] Bons, J. P., 2002, "St and C_f Augmentation for Real Turbine Roughness with Elevated Freestream Turbulence," ASME J. Turbomach., **124**, pp. 632–644.

[5] Kim, J., Dunn, M. G., and Baran, A. J., et al., 1993, "Deposition of Volcanic Materials in the Hot Sections of Two Gas Turbine Engines," J. Eng. Gas Turbines Power, **115**, pp. 641–651.

[6] Acharya, M., Bornstein, J., and Escudier, M., 1986, "Turbulent Boundary Layers on Rough Surfaces," Exp. Fluids, **4**, pp. 33–47.

[7] Hoffs, A., Drost, U., and Bolcs, A., 1996, "Heat Transfer Measurements on a Turbine Airfoil at Various Reynolds Numbers and Turbulence Intensities Including Effects of Surface Roughness," ASME Paper No. 96-GT-169.

[8] Blair, M. F., 1994, "An Experimental Study of Heat Transfer in a Large-Scale Turbine Rotor Passage," J. Turbomach., **116**(1), pp. 1–13.

[9] Guo, S. M., Jones, T. V., Lock, G. D., and Dancer, S. N., 1998, "Computational Prediction of Heat Transfer to Gas Turbine Nozzle Guide Vanes With Roughened Surfaces," J. Turbomach., **120**(2), pp. 343–350.

[10] Wammack, J. E., Crosby, J., Fletcher, D., Bons, J. P., and Fletcher, T. H., 2008, "Evolution of Surface Deposits on a High-Pressure Turbine Blade—Part I: Physical Characteristics," ASME J. Turbomach., **130**(2), p. 021020.

[11] Jensen, J. W., Squire, S. W., and Bons, J. P., 2005, "Simulated Land-Based Turbine Deposits Generated in an Accelerated Deposition Facility," ASME J. Turbomach., **127**, pp. 462–470.

[12] Bons, J. P., 2005, "A Critical Assessment of Reynolds Analogy for Turbine Flows," ASME J. Heat Transfer, **127**, pp. 472–485.

[13] Bogard, D. G., Schmidt, D. L., and Tabbita, M., 1998, "Characterization and Laboratory Simulation of Turbine Airfoil Surface Roughness and Associated

Heat Transfer," J. Turbomach., **120**(2), pp. 337–342.
[14] Barlow, D. N., and Kim, Y. W., 1995, "Effect of Surface Roughness on Local Heat Transfer and Film Cooling Effectiveness," ASME Paper No. 95-GT-14.
[15] Antonia, R. A., and Luxton, R. E., 1971, "The Response of a Turbulent Boundary Layer to a Step Change in Surface Roughness. Part 1: Smooth to Rough," J. Fluid Mech., **48**, pp. 721–726.
[16] Taylor, R. P., and Chakroun, W. M., 1992, "Heat Transfer in the Turbulent Boundary Layer with a Short Strip of Surface Roughness," AIAA Paper No. 92-0249.
[17] Schlichting, H., 1979, *Boundary Layer Theory*, 7th ed., McGraw-Hill, New York.
[18] Dipprey, D. F., and Sabersky, R. H., 1962, "Heat and Momentum Transfer in Smooth and Rough Tubes at Various Prandtl Numbers," Int. J. Heat Mass Transfer, **6**, pp. 329–353.
[19] Henry, R. C., Hansman, R. J., and Breuer, K. S., 1995, "Heat Transfer Variation on Protuberances and Surface Roughness Elements," J. Thermophys. Heat Transfer, **9**(1), pp. 175–180.

Filippo Rubechini
e-mail: filippo.rubechini@arnone.de.unifi.it

Michele Marconcini

Andrea Arnone

"Sergio Stecco" Department of Energy Engineering,
University of Florence,
via di Santa Marta 3,
50139 Firenze, Italy

Massimiliano Maritano
e-mail: massimiliano.maritano@aen.ansaldo.it

Stefano Cecchi

Ansaldo Energia,
via Lorenzi 8,
16152 Genova, Italy

The Impact of Gas Modeling in the Numerical Analysis of a Multistage Gas Turbine

In this work a numerical investigation of a four stage heavy-duty gas turbine is presented. Fully three-dimensional, multistage, Navier-Stokes analyses are carried out to predict the overall turbine performance. Coolant injections, cavity purge flows, and leakage flows are included in the turbine modeling by means of suitable wall boundary conditions. The main objective is the evaluation of the impact of gas modeling on the prediction of the stage and turbine performance parameters. To this end, four different gas models were used: three models are based on the perfect gas assumption with different values of constant c_p, and the fourth is a real gas model which accounts for thermodynamic gas properties variations with temperature and mean fuel/air ratio distribution in the through-flow direction. For the real gas computations, a numerical model is used which is based on the use of gas property tables, and exploits a local fitting of gas data to compute thermodynamic properties. Experimental measurements are available for comparison purposes in terms of static pressure values at the inlet/outlet of each row and total temperature at the turbine exit. [DOI: 10.1115/1.2752187]

Introduction

A realistic numerical analysis of a turbomachine cannot leave the issue of working fluid modeling out of consideration. The choice of the model to adopt is not unique, but depends on the specific application considered, and has to be intended as a good compromise between two opposite needs: accuracy and limited computational cost. In fact it is mandatory for the turbomachinery industry to reduce the time and cost of developing components, while improving the accuracy and reliability of the design tools. In the design of industrial turbines and compressors, different evolving fluids are encountered, working over a wide range of thermodynamic conditions. In this paper attention is focused on gas turbines, and hence the working fluid is intended to be either air or a mixture of combustion gases. As suggested by [1], the behavior of gases can be classified, in order of increasing complexity, as calorically perfect, thermally perfect, chemically reacting mixtures of thermally perfect gases, and real gases. A gas is thermally perfect if it obeys the thermal equation of state. For a thermally perfect gas, here referred to as an ideal gas, the specific internal energy and the enthalpy are functions of the temperature only. A special case is the calorically perfect gas, for which the specific heats are constant. A gas that is both thermally and calorically perfect here is referred to as perfect gas. The ideal gas equation of state is an accurate representation for gases and gas mixtures except for conditions of high pressure and/or low temperature, with respect to their critical values, and in the absence of chemical reactions. There is a number of turbomachinery applications dealing with working fluids whose behavior at typical operating conditions is far from ideal (e.g., Ref. [2]), for example the wet steam in LP steam turbines or the hydrocarbon mixtures in some cryogenic compressors. As far as gas turbines are concerned, processes undergone by the working fluid occur well above its critical temperature and below its critical pressure, within a thermodynamic range where effects of intermolecular forces are negligible, and hence small deviations from ideal behavior are observed. This statement is no longer valid when dissociation of combustion gases is taken into account, since pressure has a significant effect on the amount of dissociation and hence c_p and gamma become a function of pressure as well as of temperature. Dissociation, as reported by Banes et al. [3], may start to have a significant impact on c_p at temperatures above about 1500 K. In fact at 1800 K, both for air and combustion products corresponding to low values of fuel/air ratio, an increase of pressure from 1 bar to 100 bar decreases c_p by only about 1%, the corresponding change in gamma being even smaller. It is therefore the proper choice, for the analysis of the flow path downstream of the combustion chamber of a gas turbine, to leave any effect of pressure out of consideration, and assume the specific heat to be a function of temperature only. Under the above hypotheses, the behavior of the combustion products evolving in a gas turbine is well represented by the ideal gas equation of state.

A clarification is necessary about the water vapor in the gas mixture. The presence of water impacts on the gas properties by significantly raising both c_p and γ. There are several reasons why water vapor may be present in the gas evolving in a gas turbine: ambient humidity, water/ice ingestion, or water/steam injection. The above are additional to the water vapor produced by combustion. The amount of the latter depends on fuel properties and fuel/air ratio, and for most gas turbines the water mass fraction is sufficiently low (about 5% or lower) that the gas mixture behaves essentially as an ideal gas. When the water concentration is higher than around 10%, due, for example, to water or steam injection, this assumption is no longer valid, and the actual nonideal behavior of steam needs to be considered. Water injection has been employed for both aeronautical and industrial gas turbines to improve performance, using one of the two following strategies: injection at first compressor entry, to boost power or thrust, or injection into the combustor, primarily to reduce emissions for industrial gas turbines. It must be pointed out that both practices are now largely superseded by other technologies, like increased temperature capabilities and higher bypass ratios for aero-engines, or dry low-emission combustion technology for industrial engines.

Some additional considerations are required to account for the variation of the gas composition related to the turbine cooling. In a typical gas turbine, a large amount of cooling air is added to the

Contributed by the International Gas Turbine Institute of ASME for publication in the JOURNAL OF TURBOMACHINERY. Manuscript received November 2, 2006; final manuscript received November 9, 2006; published online March 25, 2008. Review conducted by David Wisler. Paper presented at the ASME Turbo Expo 2006: Land, Sea and Air (GT2006), Barcelona, Spain, May 8–11, 2006, Paper No. GT2006-90129.

mainstream inlet flow, a value near 30% being common. As a consequence, the evolving fluid undergoes significant variation of its properties not only because of the large temperature variations, but also because the gas composition varies with the fuel/air ratio as coolant is added. It is worth considering that the mean molecular weight of the combustion products from typical hydrocarbon fuels is little different from that of cooling air, and therefore the variation of the gas constant R of the mixture related to the change in the composition is in general negligible. This fact is of particular relevance, as it translates into the possibility of accurately modeling the evolving fluid as an ideal gas with a fixed gas constant, and of relegating its nonideal behavior to a proper modeling of its specific heat. In light of the above considerations it is inferred, following Young and Wilcock [4], that the ideal gas assumption of fixed R and varying c_p gives good accuracy for gas turbine computations, and introducing more complex equations of state or pressure dependence for the specific heats is an unnecessary complication that does little to improve accuracy.

In the open literature, few investigations are available concerning the impact of gas modeling in the numerical analysis of gas turbines. Yao and Amos [5] considered the effect of varying c_p with temperature in a three stage industrial turbine with a temperature drop of about 600 K, using polynomial curve fits to get the gas data. External cooling flows and tip leakage flows were not included in the computations.

Recently Northall [6] followed a similar approach for the analysis of a gas turbine composed of a single high pressure (HP) stage followed by a single intermediate pressure (IP) stage, with a temperature drop of about 700 K. Approximately 25% of the turbine inlet mass flow was added as cooling air flows, and the fuel/air ratio convection through the flowpath was considered by solving an extra transport equation for the fuel fraction. This allowed him to model the actual c_p as a function of both temperature and local fuel/air ratio. In addition he considered three simpler models, based on constant c_p for all the turbines, with constant c_p differing for each blade row, and c_p as the variable with temperature and prescribed through-flow distribution of fuel/air ratio. Comparisons between results obtained using the more physical model and the simpler models showed small effects on turbine performance prediction.

In this work, a numerical investigation was carried out on a four stage heavy-duty gas turbine, designed in a joint development project between Siemens and Ansaldo Energia. The main goal was to analyze the impact of gas modeling on the prediction of the turbine performance parameters. Four different gas models were used: three models are based on the perfect gas assumption with different values of constant c_p, and the fourth is a real gas model which accounts for thermodynamic gas properties variation with temperature and mean fuel/air ratio distribution in the through-flow direction. The numerical model to account for real gas behavior is based on the use of gas property tables, and exploits a local fitting of gas data to compute thermodynamic properties [2].

Four Stage Turbine Description

The numerical/experimental comparison described in this paper is based on the results of the Ansaldo Energia/Siemens joint test campaign run in the test bed in Berlin on the V64.3A gas turbine. This engine is of the 70 MW size, fitted with a gearbox making it suitable for operation in both 50 Hz and 60 Hz applications [7]. The turbine is composed of four stages with unshrouded rotor blades. The first two vanes are cooled by means of impingement, film cooling, and trailing edge ejection; and vane 3 is cooled by trailing edge ejection. The first two blades are cooled with multipass channels feeding film cooling and trailing edge ejection. The turbine meridional channel is shown in Fig. 1.

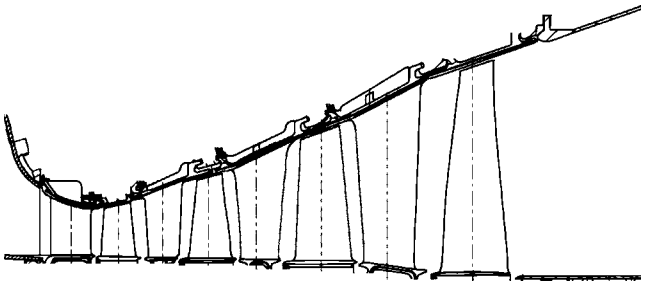

Fig. 1 V64.3A gas turbine meridional view

Computational Procedure

The multirow, multiblock release of the TRAF code [8] was used in the present work. The unsteady, three-dimensional, Reynolds averaged Navier-Stokes equations are written in conservative form in a curvilinear, body-fitted coordinate system and solved for density, absolute momentum components, and total energy.

The space discretization is based on a cell-centered finite volume scheme. Both scalar and matrix artificial dissipation models introduced by Jameson et al. [9] and Swanson and Turkel [10] are available in the code. In order to minimize the amount of artificial diffusion inside the shear layers, an eigenvalue scaling was implemented to weigh these terms. The system of governing equations is advanced in time using an explicit four stage Runge-Kutta scheme. Residual smoothing, local time stepping, and multigridding are employed to speed up convergence to the steady-state solution. The time step is locally computed on the basis of the maximum allowable Courant number, typically 5.0, and accounts for both convective and diffusive limitations [11].

The code features several turbulence closures, namely the algebraic Baldwin-Lomax model [12], the one-equation Spalart-Allmaras model [13], the two-equation Wilcox's $k-\omega$ model [14], and the shear stress transport (SST) model of Menter [15]. In the present work, the Baldwin-Lomax model was employed. The computational time was about 10 h per run on a Intel® Xeon CPU 3.20 GHz.

Boundary Conditions. Spanwise distributions of total pressure, total temperature, and flow angles are imposed at the subsonic first row inlet, while the outgoing Riemann invariant is taken from the interior. At the subsonic last row outlet, the static pressure profile is prescribed, while density and momentum components are extrapolated. The linking between consecutive rows can be carried out on the common interface plane either by a characteristic one-dimensional approach or by a nonreflecting treatment [16,17]. In the first approach the match is provided through appropriate calculation of phantom cell values, keeping the spanwise distribution while averaging in the blade-to-blade direction. In the second approach, the variation of each incoming characteristic variable at the inlet and outlet boundaries is decomposed into the sum of a uniform, pitch-averaged part, and a circumferential varying fluctuation. The average variations of incoming characteristics are set in order to match pitch-averaged flow variables at the interface of two rows. The local variations are treated according to nonreflecting conditions derived from a Fourier analysis of linearized, quasi-3D Euler equations. The outgoing characteristic changes are extrapolated from the interior of the domain. Since the turbine studied works in a transonic regime, and stator and rotor rows are stacked very close to each other, the nonreflecting approach was selected for all the computations.

The clearance region is handled by imposing periodicity conditions across the airfoil without any modelization of the blade cross section.

Flow injection and extraction modeling features, including a blade/flowpath film cooling model and the capability of modeling annulus wall flows, are available. Flow injections are handled by

Table 1 Turbine mesh size

	Turbine			
	First stage	Second stage	Third stage	Fourth stage
Vane	112×68×80	108×68×80	104×68×80	108×68×80
Blade	108×68×80	104×68×80	112×68×80	120×68×80

imposing mass flow rate, flow angles, and stagnation temperature, and the static pressure is extrapolated from the interior. Flow extractions can be imposed either by prescribing the mass flow rate or by imposing the static pressure on the extraction surface area. In the latter case the extracted mass flow is a result of the computation. The real geometry of the injection/extraction area is not gridded in any case. The injection/extraction region can be prescribed as group of mesh cells representative of a slot, or by assigning a hole-equivalent area to a mesh cell face. The latter approach allows a correct imposition of the jet momentum components when dealing with hole areas smaller than the mesh cells. More detailed models are used for film cooling in heat transfer analyses [18] and for resolving the flow in labyrinth seal cavities [19]. The injection/extraction model adopted in this study has the main advantage of simplicity and ease of implementation, and can represent an acceptable level of approximation when focusing on overall aerodynamic performance.

In the turbine studied, more than 30% of the inlet mass flow is added as cooling air, of which about 14% is added in the first stage, 10% in the second, 5% in the third, and 3% in the last one, while no flow extractions are present along the flowpath. The impact of the cooling air is noticeable both in terms of mass flow increase and thermodynamic effects. For this reason the uncooled case, which may lead to a completely incorrect aerodynamic behavior of the flow, was not considered in the present analysis.

All computations were carried out using the measured temperature profile exiting the combustion chamber as the inlet condition.

Computational Grids. Stator and rotor blade rows were discretized using single block grids obtained by stacking two-dimensional elliptically generated meshes on blade-to-blade surfaces at constant radii. In order to minimize the grid skewness, on blade-to-blade surfaces, a nonperiodic H-type grid structure was

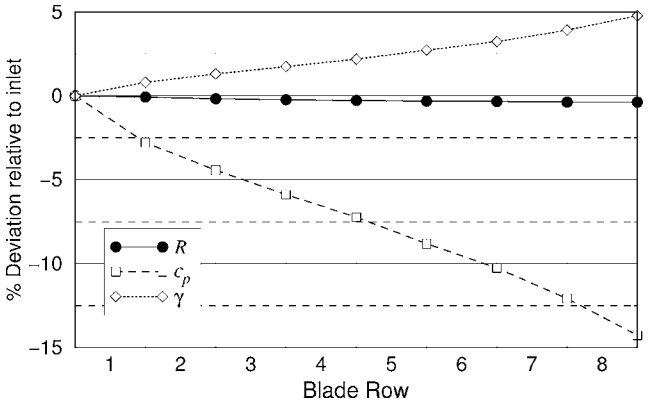

Fig. 3 Variation of R, c_p, and γ with temperature and fuel/air ratio through the four stage turbine

adopted. Table 1 summarizes grid dimensions, where the average grid size for each blade row is about 615,000 cells. The rotors' tip clearance gap was discretized with 16 mesh cells. A view of the turbine's meridional channel grid is shown in Fig. 2 where one-half of grid lines are omitted in the spanwise direction for the sake of clarity. In the same figure, a schematic of cooling and secondary air flows is presented.

Gas Models. As previously remarked, the evolving gas mixture undergoes significant variations in its properties not only because of the large temperature variations, but also because the gas composition varies with the fuel/air ratio as cooling air is added. In the present case about 30% of pure cooling air is added to the inlet mass flow, the consequent reduction of the fuel/air ratio from inlet to outlet being near 25%.

The variation of the gas properties along the turbine flowpath, which accounts for the combined effects of temperature drop (around 900 K) and change in gas composition, is shown in Fig. 3. A negligible variation of the gas constant R is observed, which allows us to model the gas mixture as an ideal gas with the equation of state given by $pv=RT$. The specific heat c_p and the specific heats ratio γ undergo significant variations, of about 15% and 5%, respectively.

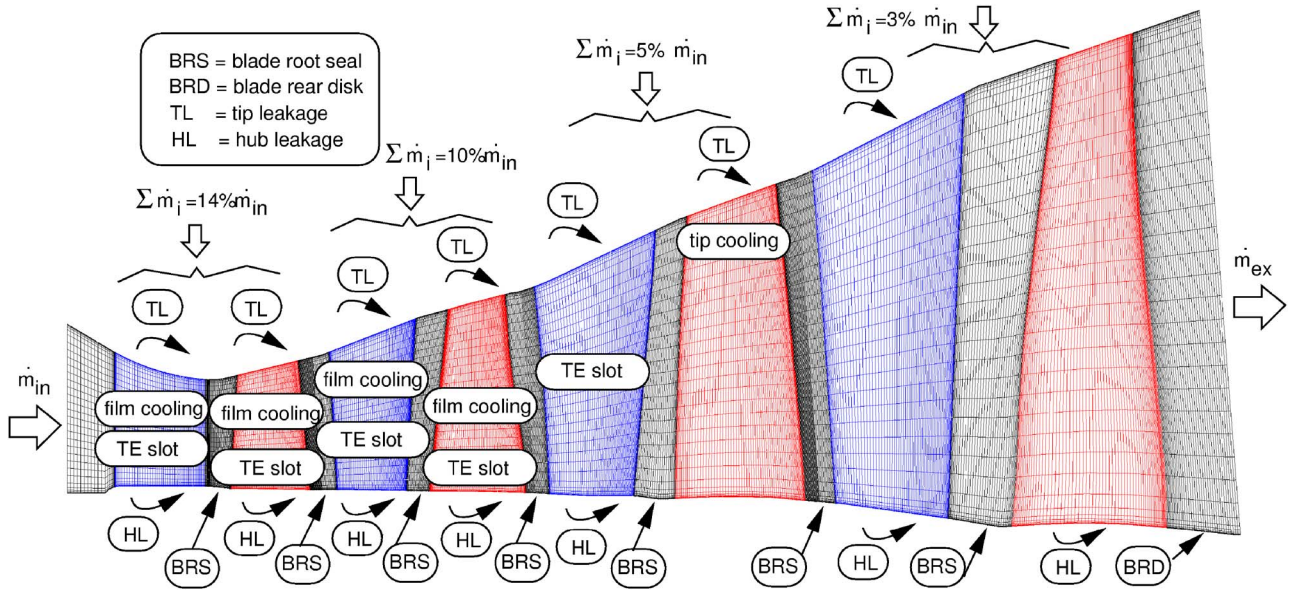

Fig. 2 Turbine cooling and secondary air flows

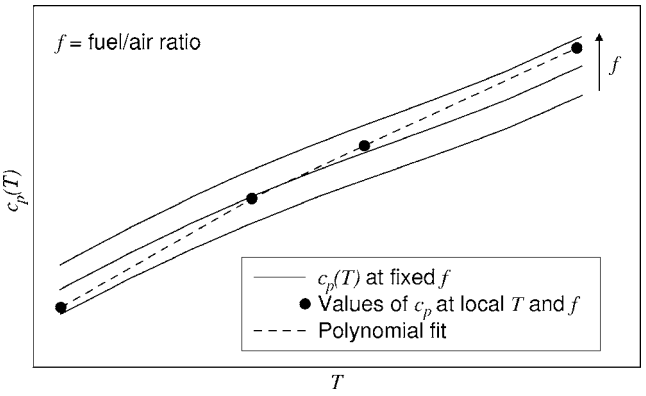

Fig. 4 Variation of c_p with temperature and fuel/air ratio

To investigate the impact of the calorically imperfect behavior of the gas mixture, the following gas models were considered:

1. Perfect gas model (PG) with constant c_p:
   - c_p at inlet conditions (PG_{in});
   - c_p average (PG_{av}); and
   - c_p at exit conditions (PG_{ex}).
2. Real Gas Model (RG) with variable c_p: c_p is a function of local temperature and fuel/air ratio; where the latter varies only in the through-flow direction. In this case the real gas model is used to model the gas as ideal, with varying c_p and constant R.

The use of an average value of c_p is a common practice in gas turbine computations based on a perfect gas model. Values of c_p based on inlet and exit conditions were chosen as opposite values to emphasize the impact of these extreme choices on the gas thermodynamic transformation. The former is sometimes used since it should give the best estimate of the mass flow being closer to the first vane throat value, especially if the first row operates near choking conditions. The average value of c_p is computed in order to ensure the same enthalpy drop as the variable one between the same temperatures

$$c_{p,\mathrm{av}} = \frac{1}{T_{\mathrm{ex}} - T_{\mathrm{in}}} \int_{T_{\mathrm{in}}}^{T_{\mathrm{ex}}} c_p(T)\,dT \tag{1}$$

In the present work, the following procedure is used to model the variation of c_p with temperature while also accounting for the variation of gas composition in the turbine. Knowing the gas composition at inlet and the amount of cooling air supplied at each injection, the actual average value of the fuel/air ratio is computed in various locations along the machine. Providing an estimate of the average temperature at the same locations by means of a preliminary analysis tool (typically through flow), the corresponding values of c_p are computed as functions of local temperature and fuel/air ratio (see Fig. 4). Finally, a fourth-order polynomial law is used to express the functional dependence of c_p from temperature.

An intrinsic error is present in the computation of the c_p of the cooling air, since the single-fluid model adopted does not allow one to treat the injected air with its actual c_p, which should be that of pure air (null fuel/air ratio) at the cooling temperature. Although this limitation is recognized, it should be noted that the error in the computation of the coolant specific heat is reduced when c_p is computed as described above. The reason for this is that c_p varies in the same sense with temperature and fuel/air ratio. Since c_p was determined as a function of temperature as well as of the fuel/air ratio corresponding to that temperature in the actual turbine, when cooling air is supplied at a low temperature its c_p is implicitly assumed to correspond to low values of the fuel/air ratio (see Fig. 4).

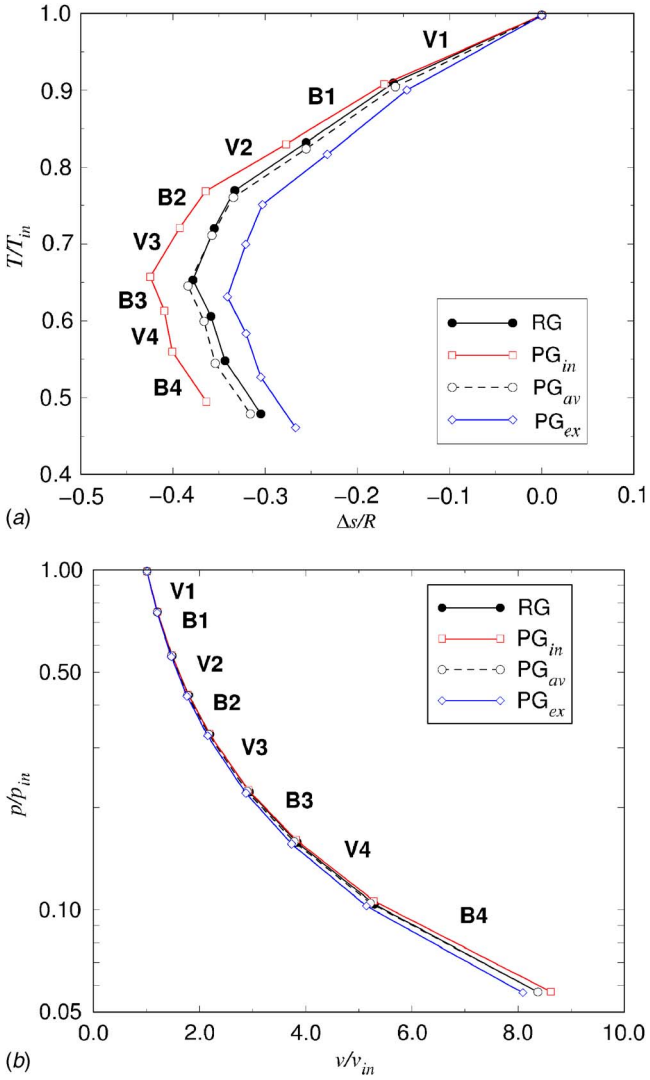

Fig. 5 Gas expansion for the four stage turbine computed with perfect gas (PG) and real gas (RG) models: (*a*) *T*–*s* plane; and (*b*) *p*–*v* plane

Results

The mean expansion undergone by the gas at the inlet and outlet of each blade row through the turbine is reported in Fig. 5. Four transformations are compared in the $T-s$ plane (Fig. 5(*a*)) and in the $p-v$ plane (Fig. 5(*b*)), which were obtained using the real gas model and the perfect gas model with different values of c_p. The relative position of the transformations in the $T-s$ plane is mainly determined by the value of c_p of the mainstream. This thermodynamic effect can be explained by considering a reversible process of a perfect gas in absence of cooling, for which the global entropy change is given by

$$\frac{\Delta s}{R} = \ln\left(\frac{p_{\mathrm{in}}}{p_{\mathrm{ex}}}\right) - \frac{c_p}{R}\ln\left(\frac{T_{\mathrm{in}}}{T_{\mathrm{ex}}}\right) \tag{2}$$

Since the inlet conditions are fixed and the same back pressure is imposed, the first term of the right hand side is the same for all gas models, and the differences in the entropy change are due to the second term, which is associated with an entropy drop. This term has a bigger magnitude for the PG_{in} model because of the

higher c_p (in spite of its higher exit temperature), and consequently the final exit entropy is lower for the PG_{in} model than for the PG_{ex} one, the one predicted by the PG_{av} model obviously being the intermediate one.

Considering now the effect of the cooling air, the heat removal from the mainstream due to coolant injection produces an entropy reduction causing all the expansions to move to the left in the $T-s$ diagram, as observed in Fig. 5(*a*). This effect is more pronounced in the first two stages where a larger amount of cooling air is supplied and tends to vanish downstream of the third vane.

The dominant effect in determining the final temperature is again associated with the value of c_p of the mainstream. For the fixed c_p models, higher values of c_p lead to higher exit temperatures, as observed in Fig. 5(*a*) going from PG_{ex} to PG_{in}.

In the PG models the cooling air is injected using the same c_p as for the mainstream. For all three models this c_p value will be generally higher than the one that should correspond to pure air at the typical injection temperatures, the difference being lower for the PG_{ex} model. In the absence of refrigeration, the difference in the thermodynamic properties at the expansion end between the PG_{av} and the RG models would be negligible, due to the suitable averaging process used to define the value of $c_{p,av}$. Therefore the differences found at the expansion end between these two models can be attributed to the different modelization of the cooling air. The heat removal effect of the cooling air is overestimated by the PG_{av} model since in this model the coolant is injected with a c_p higher than it should be. As a result the final exit entropy and temperature predicted by this model are slightly lower. Despite the small deviation of the exit properties between the PG_{av} and RG models, it is worth considering that, even in absence of cooling, greater differences are found through the turbine, since the actual properties at various points are not accurately predicted by the PG_{av} model.

The comparison of the four transformations in the $p-v$ plane is shown in Fig. 5(*b*). At the first vane inlet, the same conditions are imposed for all models. As the expansion goes on, the PG models with extreme c_p values progressively deviate from the values of the specific volume predicted by the RG model. At the fourth blade outlet, where back pressure is imposed, the PG_{in} model gives an overestimate of about 3%, whereas the PG_{ex} model underestimates the specific volume by about 3.5%. Once again, differences at the expansion end are negligible between the PG_{av} and the RG model.

The results obtained with the different gas models were compared in terms of stages and turbine overall performance, and a summary of the percent change of the main parameters with respect to the real gas model results is given in Table 2 and in Fig. 6. The parameters considered are efficiency, inlet mass flow, specific work, total enthalpy, and total temperature drops. The work done on the rotor can be evaluated either by integrating pressure and shear forces on all the rotating surfaces to compute the torque, or with an enthalpy balance on a control volume including the blade row. Here the specific work is computed from an enthalpy balance, and defined with respect to the inlet mass flow

$$w \equiv \left(\dot{m}_{in} h_{0in} + \sum_{i=1}^{Ni} (\dot{m} h_0)_i - \sum_{i=1}^{Ne} (\dot{m} h_0)_i - \dot{m}_{ex} h_{0ex} \right) \Big/ \dot{m}_{in} \quad (3)$$

where *Ni* and *Ne* are the number of injections and extractions. The total-to-total efficiency is defined as

$$\eta \equiv \frac{\dot{m}_{in} h_{0in} + \sum_{i=1}^{Ni} (\dot{m} h_0)_i - \sum_{i=1}^{Ne} (\dot{m} h_0)_i - \dot{m}_{ex} h_{0ex}}{\dot{m}_{in} h_{0in} + \sum_{i=1}^{Ni} (\dot{m} h_0)_i - \sum_{i=1}^{Ne} (\dot{m} h_0)_i - \dot{m}_{ex} \bar{h}_{0ex,s}} \quad (4)$$

where $\bar{h}_{0ex,s}$ is a mass averaged isentropic total enthalpy defined as

Table 2 Calculated turbine performance versus gas model

% Error relative to RG model	Gas model PG_{in}	Gas model PG_{av}	Gas model PG_{ex}
Stage 1			
Efficiency η	−0.01	−0.33	−0.65
Inlet mass flow $\dot{m}_{in}$	−0.04	0.48	1.10
Specific work w	−0.66	−0.51	−0.31
Total enthalpy drop Δh_0	2.37	−0.33	−3.12
Total temperature drop ΔT_0	1.76	5.10	9.08
Stage 2			
Efficiency η	0.02	−0.14	−0.28
Inlet mass flow $\dot{m}_{in}$	−0.03	0.43	0.99
Specific work w	−1.43	−1.58	−1.76
Total enthalpy drop Δh_0	1.42	−0.87	−3.28
Total temperature drop ΔT_0	−2.48	1.13	5.37
Stage 3			
Efficiency η	0.05	−0.00	−0.04
Inlet mass flow $\dot{m}_{in}$	−0.04	0.40	0.93
Specific work w	−0.66	−1.69	−2.91
Total enthalpy drop Δh_0	0.94	−1.16	−3.46
Total temperature drop ΔT_0	−5.65	−2.02	2.16
Stage 4			
Efficiency η	−0.09	−0.03	0.07
Inlet mass flow $\dot{m}_{in}$	−0.03	0.39	0.90
Specific work w	1.85	−0.79	−3.90
Total enthalpy drop Δh_0	2.81	−0.39	−4.06
Total temperature drop ΔT_0	−7.35	−4.74	−1.97
Turbine			
Efficiency η	−0.60	−0.57	−0.49
Inlet mass flow $\dot{m}_{in}$	−0.03	0.44	1.01
Specific work w	0.08	−1.11	−2.50
Total enthalpy drop Δh_0	2.05	−0.58	−3.42
Total temperature drop ΔT_0	−2.90	0.34	4.07

$$\bar{h}_{0ex,s} = \frac{\dot{m}_{in} h_{0ex,s} + \sum_{i=1}^{Ni} (\dot{m} h_{0ex,s})_i}{\dot{m}_{in} + \sum_{i=1}^{Ni} \dot{m}_i} \quad (5)$$

and $h_{0ex,s}$ is the total enthalpy of each of the inlets expanded isentropically to the mainstream mass average total pressure at exit.

As far as the inlet mass flow is concerned it is confirmed that with the PG_{in} model, which uses a constant c_p computed at the first stator row inlet conditions, the value predicted by the RG model with variable c_p is nearly matched. A relative error of about 0.4% is found with the PG_{av} model and the maximum error of about 1% with the PG_{ex} model, which adopts a value of c_p much lower than that corresponding to the first stator throat.

Considering now the total temperature drops for the whole turbine, as previously observed, the choice of a constant c_p corresponding to the turbine inlet conditions leads to a higher level of exit total temperature, while an opposite behavior is found if the exit conditions are chosen. As expected, the PG_{in} model gives a better estimate of the temperature drop in the first stage, while tending to a progressive underestimation towards the turbine exit. The opposite behavior is exhibited by the PG_{ex} model, whereas the PG_{av} model gives intermediate results for each stage, overestimating the temperature drop in the first two stages and underestimating it in the last two.

The total enthalpy drops are closely related to those of the total temperature, but smaller deviations from the RG model are in general observed. The reason for this better accuracy in computing the enthalpy drop rather than that of the temperature is that c_p

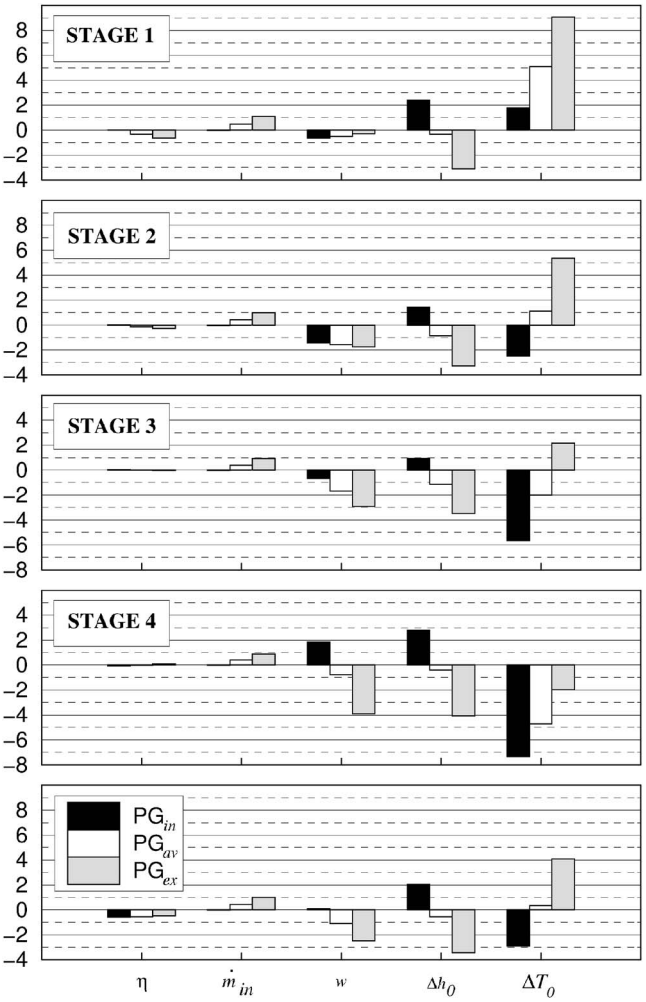

Fig. 6 Calculated turbine performance versus gas model (% error relative to RG model)

and γ vary in the opposite direction with temperature. If, for a given expansion, the value of γ is overestimated, so will the temperature drop, but this error will be compensated for in the computation of the enthalpy drop by the fact that c_p will be lower than it should be.

The specific work of each stage is generally underestimated by all the PG models, with the exception of the PG_{in} model prediction in the fourth stage. Concerning the whole turbine, the specific work predicted by the PG_{av} model is affected by an error of near 1% with respect to the RG model. Without coolant injection the specific work of each component would be equal to the corresponding total enthalpy drop. When cooling is considered, the specific work is given by Eq. (3), which can be rewritten as follows (with $Ne=0$)

$$w = \Delta h_0 + \alpha(h_{0\text{inj}} - h_{0\text{ex}}) \tag{6}$$

where

$$\alpha = \sum_{i=1}^{Ni} \dot{m}_i/\dot{m}_{\text{in}}; \quad h_{0\text{inj}} = \sum_{i=1}^{Ni} (\dot{m}h_0)_i \Big/ \sum_{i=1}^{Ni} \dot{m}_i$$

Since, in general, $h_{0\text{inj}} < h_{0\text{ex}}$, the second term of the right hand side in Eq. (6) will be negative, and hence the specific work will be lower than the corresponding total enthalpy drop. As a result of compensating errors in the computation of $h_{0\text{inj}}$ and $h_{0\text{ex}}$, the PG_{in} model predicts the best estimate of the overall specific work.

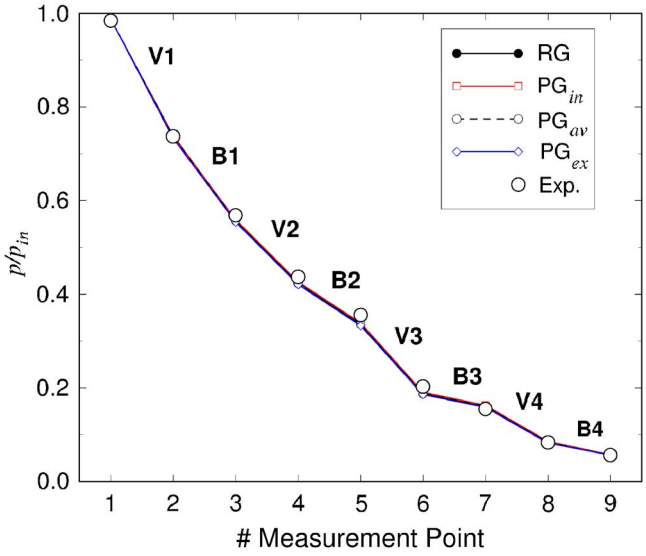

Fig. 7 Comparison between measured and computed static pressure between rows (hub values)

All the PG models give similar results in terms of turbine efficiency, predicting an underestimate of about 0.5%. Differences in stage efficiencies are negligible for the last two stages, where the amount of cooling is lower. A similar trend was found by Northall [6] who adopted the same efficiency definition as in the present study.

Experimental measurements are available for comparison purposes in terms of static pressure values at the inlet/outlet of each row and total temperature at the turbine exit. In Fig. 7 computed and measured values of static pressure at the hub are compared. No major impact of the gas model is appreciable, and a good agreement between measured and computed values can be noticed in each measurement station.

Figure 8 shows a comparison between the normalized total temperature distributions along the spanwise direction at the turbine exit, computed using the four gas models. The mixed out average value of measured total temperature is indicated as a constant level in the figure. The shape of the distributions obtained with the perfect gas models is the same as the one obtained with the RG

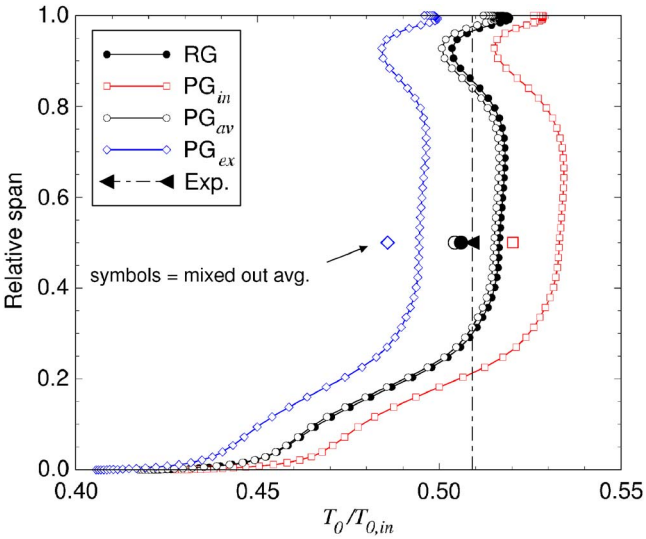

Fig. 8 Computed and measured total temperature at turbine exit

model. As previously remarked, the PG_{in} model predicts a higher level of exit total temperature, while an opposite behavior is found with the PG_{ex} model. As far as the average value of c_p is concerned, the predicted exit temperature distribution is in good agreement with the one computed with the real gas model. Moreover, the mixed out average values of total temperature obtained by the two models are closer to the measured value, the difference being about −0.9% and −0.6%, respectively. Large errors are obtained using both the PG_{in} and the PG_{ex} models, of about 2.2% and −4.6%, respectively.

Conclusions

A numerical investigation of a four stage heavy-duty gas turbine was carried out. Cooling air injection, cavity purge flows, and leakage flows were included in the computations. The impact of gas modeling on the prediction of the stage and overall turbine performance was assessed by comparing the results obtained using different gas models based on the perfect gas assumption to those obtained with a real gas model. In the present case, where the gas properties behavior deviates from that of a perfect gas basically from a caloric point of view, the real gas model accounts for the variation of the specific heat c_p with temperature. Changes in gas mixture composition in the through-flow direction due to coolant addition are accounted for by using a suitable polynomial fit of c_p.

Due to the large variation of the actual gas properties, associated with the high levels of both the temperature drop and the coolant injection, significant impact of the gas model used for computation was found. As far as the mass flow is concerned, the choice of the c_p value corresponding to the inlet conditions proved to give the best estimate. This is because this value is closer to that experienced at the first vane throat. However, the error found using the PG_{av} model is lower than 0.5%.

All the PG models predicted similar results in terms of turbine efficiency, with an underestimation of about 0.5% with respect to the RG model.

The major impact of gas modeling was detected in the prediction of temperature and enthalpy drops. With a suitable choice of an average c_p the error on these parameters can be reduced to negligible values at the turbine exit, and the small deviation between PG_{av} and RG models is attributed to the different treatment of the cooling air. Comparison between measured and computed values of mixed out total temperature at the turbine exit showed that this parameter is well predicted by both the RG and the PG_{av} models, whereas important deviations were obtained using the other models. In light of the present findings it can be concluded that the PG_{av} model represents a good compromise for a perfect gas computation. However, even by using such a model, the actual temperatures along the gas path are not accurately predicted, and for a detailed component design it is necessary to reproduce the correct thermodynamic behavior of the working fluid.

Acknowledgment

The authors would like to express their gratitude to Dr. Franco Rocca of Ansaldo Energia for the numerous and helpful discussions.

Nomenclature

$\dot{m}$ = mass flow rate
c_p = specific heat at constant pressure
h = specific enthalpy
p = pressure
R = gas constant
s = specific entropy
T = temperature
v = specific volume
w = specific work
PG = perfect gas
RG = real gas

Greek

η = total-to-total efficiency
γ = ratio of specific heats

Subscripts

0 = total quantity
av = average quantity
ex = exit conditions
in = inlet conditions
s = isentropic quantity

References

[1] Anderson, J. D., 1989, *Hypersonic and High Temperature Gas Dynamics*, McGraw-Hill, New York.
[2] Boncinelli, P., Rubechini, F., Arnone, A., Cecconi, M., and Cortese, C., 2004, "Real Gas Effects in Turbomachinery Flows: a CFD Model for Fast Computations," ASME J. Turbomach., **126**(2), pp. 268–276.
[3] Banes, B., McIntyre, R. W., and Sims, J. A., 1967, "Properties of Air and Combustion Products With Kerosene and Hydrogen Fuels," AGARD Conference, Technical Report, Derby, UK.
[4] Young, J. B., and Wilcock, R. C., 2002, "Modeling the Air-Cooled Gas Turbine: Part 1—General Thermodynamics," ASME J. Turbomach., **124**(2), pp. 207–213.
[5] Yao, Y., and Amos, I., 2004, "Numerical Study of Axial Turbine Flow With Variable Gas Property," ASME Paper No. GT2004–53748.
[6] Northall, J. D., 2006, "The Influence of Variable Gas Properties on Turbomachinery CFD," ASME J. Turbomach., **128**(4), pp. 632–638.
[7] Granser, D., and Rocca, F., 1996, "New High-Efficiency 70 MW Heavy-Duty Gas Turbine," *Proceedings Power-Gen Europe 96*, Budapest, Hungary, PGE June 26–28.
[8] Arnone, A., 1994, "Viscous Analysis of Three-Dimensional Rotor Flow Using a Multigrid Method," ASME J. Turbomach., **116**(3), pp. 435–445.
[9] Jameson, A., Schmidt, W., and Turkel, E., 1981, "Numerical Solutions of the Euler Equations by Finite Volume Methods Using Runge-Kutta Time-Stepping Schemes," AIAA Paper No. 81–1259.
[10] Swanson, R. C., and Turkel, E., 1992, "On Central-Difference and Upwind Schemes," J. Comput. Phys., **101**, pp. 292–306.
[11] Arnone, A., and Swanson, R. C., 1993, "A Navier-Stokes Solver for Turbomachinery Applications," ASME J. Turbomach., **115**(2), pp. 305–313.
[12] Baldwin, B. S., and Lomax, H., 1978, "Thin Layer Approximation and Algebraic Model for Separated Turbulent Flows," AIAA Paper No. 78–257.
[13] Spalart, P. R., and Allmaras, S. R., 1994, "A One-Equation Turbulence Model for Aerodynamic Flows," La Rech. Aerosp., **1**, pp. 5–21.
[14] Wilcox, D. C., 1998, *Turbulence Modeling for CFD*, 2nd ed., DCW Industries Inc., La Cañada, CA.
[15] Menter, F. R., 1994, "Two-Equations Eddy Viscosity Turbulence Models for Engineering Applications," AIAA J., **32**(8), pp. 1598–1605.
[16] Giles, M. B., 1988, "UNSFLO: A Numerical Method For Unsteady Inviscid Flow in Turbomachinery," Department of Aerospace and Astronomy, MIT, Technical Report No. GTL 195.
[17] Saxer, A. P., and Giles, M. B., 1993, "Quasi-Three-Dimensional Nonreflecting Boundary Conditions for Euler Equations Calculations," J. Propul. Power, **9**(2), pp. 263–271.
[18] Garg, V. K., 2002, "Heat Transfer Research on Gas Turbine Airfoils at NASA GRC," Int. J. Heat Fluid Flow, **23**(2), pp. 109–136.
[19] Cherry, D., Wadia, A., Beacock, R., Subramanian, M., and Vitt, P., 2005, "Analytical Investigation of a Low Pressure Turbine With and Without Flowpath Endwall Gaps, Seals and Clearance Features," ASME Paper No. GT2005–68492.

Impulse Response Processing of Transient Heat Transfer Gauge Signals

M. L. G. Oldfield
Department of Engineering Science,
University of Oxford,
Oxford OX1 3PJ, UK

A new, computationally efficient method is presented for processing transient thin-film heat transfer gauge signals. These gauges are widely used in gas turbine heat transfer research, where, historically, the desired experimental heat transfer flux signals, q, are derived from transient measured surface-temperature signals, T, using numerical approximations to the solutions of the linear differential equations relating the two. The new method uses known pairs of exact solutions, such as the T response due to a step in q, to derive a sampled approximation of the impulse response of the gauge system. This impulse response is then used as a finite impulse response digital filter to process the sampled T signal to derive the required sampled q signal. This is computationally efficient because the impulse response need only be derived once for each gauge for a given sample rate, but can be reused repeatedly, using optimized MATLAB filter routines and is highly accurate. The impulse response method can be used for most types of heat flux gauge. In fact, the method is universal for any linear measurement systems which can be described by linear differential equations where theoretical solution pairs exist between input and output. Examples using the new method to process turbomachinery heat flux signals are given. [DOI: 10.1115/1.2752188]

Introduction

The new impulse response processing techniques of thin-film gauge heat transfer gauge signals described in this paper were initially described in an internal user guide [1] and were first used by Guo et al. [2] and Anthony et al. [3,4]. This paper is the first time the new techniques have been fully described.

Thin-film gauges were initially used in hypersonic wind tunnels [5] and were subsequently used in turbomachinery research from the 1970s [6,7]. Initially gauges consisted of arrays of platinum thin-film resistance thermometers fired onto the surface of shaped quartz or Pyrex inserts mounted in turbine blade cascade models, but this was superseded by films fired onto blades machined in Corning Macor, a machinable glass ceramic [6] as shown in Fig. 1.

In the short (<1 s) running time of the transient tunnels used, the heat conduction under the thin films can be considered as semi-infinite, one-dimensional heat conduction, and these are known as semi-infinite heat transfer gauges. In an age where computing power was rare and expensive, the surface temperature signals were processed into surface heat transfer fluxes by the use of analogue electronic circuits which simulated the heat conduction process with a resistance-capacitance ladder circuit [5,8]. The surface temperature was recovered by a computational procedure which approximated the recorded heat flux signal be a series of steps or ramps [6].

In the 1980s, transient turbine facilities made it possible to make high-frequency heat transfer measurements on rotating turbine blades provided robust heat transfer gauges could be manufactured [9]. While sufficient strength could be obtained by inserting small Pyrex or quartz "button" gauges into a rotating blade surface [10], new two layer thin-film gauges sufficiently robust to stand the stresses of rotating turbines were developed and these required new data processing techniques. At Oxford a vitreous enamel insulating layer was fired onto the surface of metal blades, and the thin-film thermometers were painted and fired on top [11]. The signals from the gauges were first passed through an analog and then processed digitally using an analysis of the unsteady two layer heat conduction problem [12], a computationally long processing process. At MIT [13], a double sided gauge was developed on a flexible insulator which could be wrapped round a strong metal turbine blade and secured by an adhesive. By measuring the top and bottom temperature, low-frequency heat transfer measurements could be made by a steady-state conduction assumption, but an unsteady analysis was necessary to extract high frequency, blade passing, and events.

Since then, many successful variants of the two sided gauge have been developed, including the "direct heat transfer gauge" [14] and Fig. 2 and layered thermocouple gauges [15].

Recently, high density arrays of thin-film gauges which share a common current source, along with low noise current sources and high-frequency boosting preamplifiers have been developed [3] and used to image bypass transition [4]. Another approach for fabricating miniature thin-film gauges by using a laser to etch the gauges and connecting track patterns is given in Ref. [16]

Since the 1980s, various computer based signal processing techniques have been developed to extract the time-varying heat flux from temperature measurements. Fourier transform methods [17] are attractive, but require zero padding and other careful techniques to avoid the consequences of the inherent periodicity of discrete Fourier transforms of finite length sampled data sets. Some researchers [e.g., Ref. [18]] use a numerical solution of the unsteady conduction equations using a Crank-Nicholson scheme or a finite element process that can deal with multiple substrate thermal properties. Such techniques are powerful, in that they can deal with highly three-dimensional multilayered substrates, with temperature dependent thermal properties, under the thin-film gauges, but have a high computational cost and may have difficulties in encompassing short and long time-scale phenomena in the same calculation.

For most heat transfer gauge systems the new impulse response method presented below is more computationally efficient, simpler and more accurate than the methods described above.

Contributed by the International Gas Turbine Institute of ASME for publication in the JOURNAL OF TURBOMACHINERY. Manuscript received November 6, 2006; final manuscript received December 23, 2006; published online March 25, 2008. Review conducted by David Wisler. Paper presented at the ASME Turbo Expo 2006: Land, Sea and Air (GT2006), Barcelona, Spain, May 8–11, 2006, Paper No. GT2006-90949.

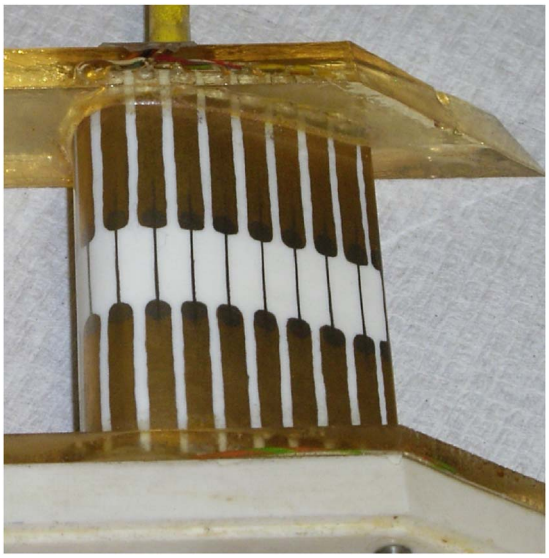

Fig. 1 Early Macor blade showing fired platinum thin-film gauges on surface with gold leads

Basis of the Impulse Response Method

The impulse response method uses discrete deconvolution to derive filter impulse responses of the same length as the data being processed from analytically derived response functions, and is accurate up to this length, with none of the zero padding etc. needed to use frequency based methods [17]! Useful books on the digital signal processing, Fourier, and z transforms used here are described in Ref. [19] (which uses MATLAB [20]), and Ref. [21].

It is applicable to any linear time invariant (LTI) system where the readings to be processed are steady at the start of the recorded data.

The response of any LTI system such as a thin-film gauge (surface temperature $T(t)$, surface heat transfer rate $q(t)$) can be calculated from the impulse response $h(t)$ of that system by the convolution integral

$$q(t) = h(t) * T(t) = \int_{-\infty}^{\infty} h(\tau)T(t-\tau)d\tau$$

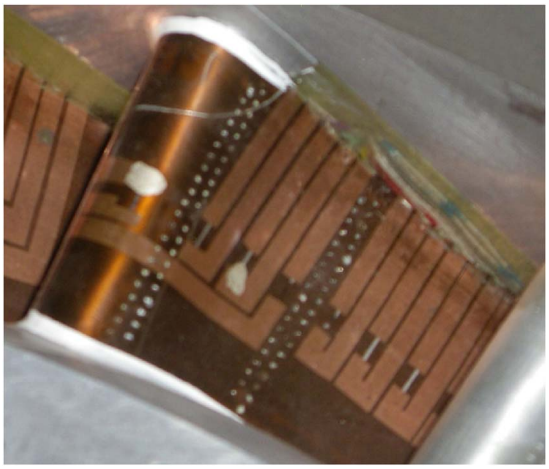

Fig. 2 Kapton (polyimide) sheet with sputtered heat flux gauges wrapped round a metal nozzle guide vane with film cooling holes

Unfortunately, in the continuous-time domain, this integral can be difficult to evaluate [5] and $h(t)$ often has singularities at the origin.

However, in the discrete-time domain, where the continuous signals $T(t)$ and $q(t)$ are sampled at sampling period T_s, or sampling frequency $f_s = 1/T_s$ to give discrete sequences

$$T[n] = T(nT_s) \quad \text{for } n = \cdots -3,-2,-1,0,1,2,3,\cdots$$

The convolution integral is replaced by the discrete convolution sum

$$q[n] = h[n] * T[n] = \sum_{k=-\infty}^{\infty} h[k]T[n-k] = \sum_{k=-\infty}^{\infty} h[n-k]T[k]$$

As will be shown, this convolution sum can be manipulated to avoid the difficulties at the singularities and the convolution can be successfully used.

The challenge is then that of deriving suitable discrete time impulse functions $h[n]$ which are sampled approximations to the continuous impulse function $h(t)$.

In the processing considered here, all signals and impulse responses are assumed to be 0 for $n<0$ and the signals are all of a finite length N (i.e., they have been sampled for a time NT_s seconds). We are not interested in results of the convolution for $n>N$, and only need the first N terms of $h[n]$. So the discrete convolution becomes

$$q[n] = h[n] * T[n] = \sum_{k=0}^{N-1} h[k]T[n-k] = \sum_{k=0}^{N-1} h[n-k]T[k]$$

$$\text{for } k = 0,1,2,\ldots,N-1$$

This discrete convolution can be carried out by the MATLAB filter function, or, much more efficiently, by the MATLAB signal processing toolbox function fftfilt. Users should note that MATLAB arrays start with index 1, not 0 as above, and this may require some care, as the above sums will be from 1 to N.

How can the required discrete impulse response function sequence $h[n]$ be obtained? If we know a pair of nonsingular analytical solutions $q_1(t)$ and $T_1(t)$ (the basis functions) for the underlying heat transfer equations in the gauge substrate (e.g., a step function in q and the corresponding "parabolic" function in T for a semi-infinite substrate), these can be sampled and are then related to the required impulse response by the convolution

$$q_1[n] = h[n] * T_1[n]$$

$h[n]$ can then be found by deconvolution, which is most efficiently carried out by the MATLAB function filter, using the discrete impulse function $\delta[n]=1,0,0,0,\ldots$. Taking z transforms (described in e.g., Ref. [19]), the convolution operator $*$ is replaced by multiplication

$$Q_1(z) = H(z)T_1(z) \quad \text{or} \quad H(z) = \frac{Q_1(z)}{T_1(z)}$$

Now, convoluting the impulse response with an impulse function will, by definition, simply reproduce the impulse response, so that in the z transform domain

$$H(z) = H(z)\Delta(z) = \frac{Q_1(z)}{T_1(z)}\Delta(z)$$

where $\Delta(z)$ is the z transform of $\delta[n]$.

Thus the required impulse response can be obtained by digitally filtering the impulse function $\delta[n]$ by the infinite impulse response (IIR) filter whose coefficients are given by $Q_1(z)/T_1(z)$ using the MATLAB function

```
h = filter(q1,T1,impulse)
```

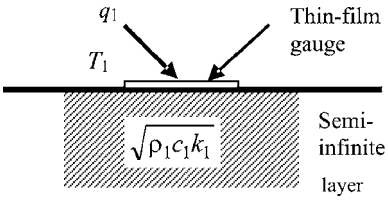

Fig. 3 Semi-infinite heat transfer gauge

This $h[n]$, evaluated once for each set of heat transfer gauge parameters, can then be stored and then subsequently used repeatedly to process sampled data, say $T[n]$ into $q[n]$ by using the very fast function fftfilt in the MATLAB signal processing toolbox

$$q = \text{fftfilt}(h, T)$$

The impulse response method obviously depends on the choice of suitable basis functions $q_1(t)$ and $T_1(t)$. Also it should be realized that an implicit assumption of the method is that, between samples, the functions $q(t)$ and $T(t)$ follow the form (e.g., step and parabola) of the basis functions $q_1(t)$ and $T_1(t)$.

Note that the impulse response method is a more sophisticated generalization of the superposition method first used by Ref. [6] in 1978.

Design of Discrete Impulse Responses for Particular Heat Transfer Gauge Systems

The theoretical responses of commonly used forms of heat transfer gauges to known input temperature signals are now analyzed and these are used to derive suitable basis functions $q_1(t)$ and $T_1(t)$. MATLAB is then used to design the required discrete impulse functions $h[n]$. These $h[n]$ functions are then tested with known solutions to check for any numerical problems. The function filter used in the design process will not work if the first term of $q_1[n]$ is zero. In that case, the $q_1[n]$ sequence is moved one place to the left and a flag shift is set in the software to indicate the shift necessary to correct the output when using the filters.

Semi-infinite Substrate Heat Transfer Gauges. A cross section through a semi-infinite thin-film gauge is shown in Fig. 3 and the theory of such gauges is given in Ref. [12].

The most convenient (but not only) basis functions for transforming T to q and the reverse process of q to T used to generate $h[n]$ are the response $T_1(t)$ for a step in $q_1(t)$. In Laplace transformed form, the solution of the heat conduction equations for a semi-infinite substrate gives

$$\bar{T}_1(s) = \frac{1}{\sqrt{\rho_1 c_1 k_1}} \frac{1}{\sqrt{s}} \bar{q}_1(s)$$

For a step in $q_1(t) = u(t)$, $\bar{q}_1(s) = 1/s$, and so

$$\bar{T}_1(s) = \frac{1}{\sqrt{\rho_1 c_1 k_1}} s^{-(3/2)}$$

Taking the inverse Laplace transform

$$T_1(t) = \frac{2}{\sqrt{\rho_1 c_1 k_1}} \sqrt{\frac{t}{\pi}}$$

Sampling $q_1(t)$ and $T_1(t)$ and applying the impulse response theory above gives the required impulse functions $h[n]$.

As an example, the impulse filter to change a surface temperature trace T to q for a 10,000 point sample at 10,000 samples/s and for a substrate with the thermal product $\sqrt{\rho_1 c_1 k_1} = 2000 \text{ J m}^{-1} \text{ K}^{-1}$ (similar to Corning Macor) is shown in Fig. 4.

The corresponding impulse filter to perform the reverse transformation from q to T is shown in Fig. 5.

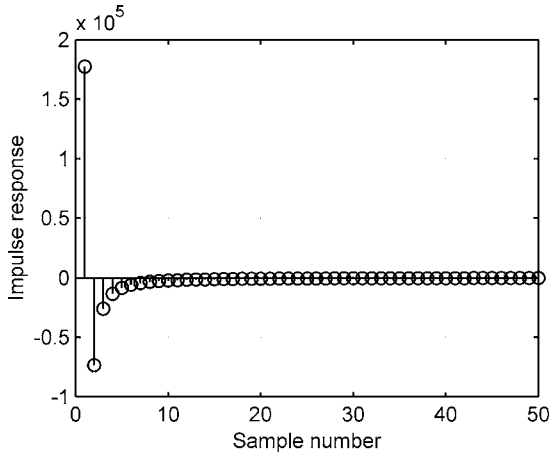

Fig. 4 First 50 points of Impulse response $h[n]$ of impulse filter to convert T to q for semi-infinite heat transfer gauge

It should be noted that the continuous impulse response is infinite at $t=0$: For an impulse in $q_1(t) = \delta(t)$, $\bar{q}_1(s) = 1$, and so

$$\bar{T}_1(s) = \frac{1}{\sqrt{\rho_1 c_1 k_1}} s^{-1/2}$$

Taking the inverse Laplace transform

$$T_1(t) = \frac{1}{\sqrt{\rho_1 c_1 k_1}} \sqrt{\frac{1}{\pi t}}$$

The early points of the sampled versions in Figs. 4 and 5 are, clearly, finite, and the high 15 figure accuracy of MATLAB enables them to be used accurately, as will be shown.

The designed impulse functions were tested by using the sampled version of $T_1(t) = 2/\sqrt{\rho_1 c_1 k_1}\sqrt{t/\pi}$ as a test signal, and seeing how close the resulting q signal was to a unit step. The result is shown in Fig. 6. This tests the numerical errors, which are $< 6 \times 10^{-14}$, which is negligible.

Two Layer Substrate Heat Transfer Gauges. A cross section through a two layer thin-film gauge is shown in Fig. 7, and the

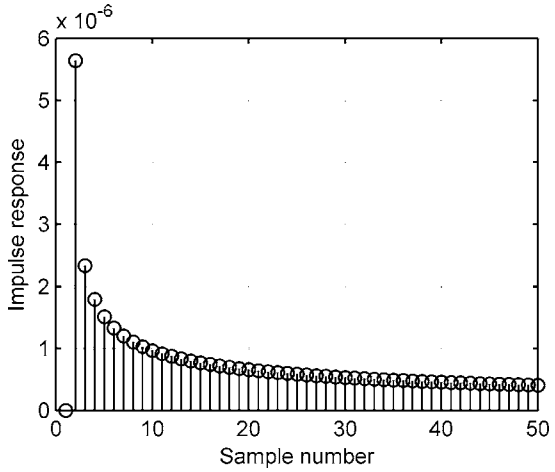

Fig. 5 First 50 points of Impulse response $h[n]$ of impulse filter to convert q to T for semi-infinite heat transfer gauge

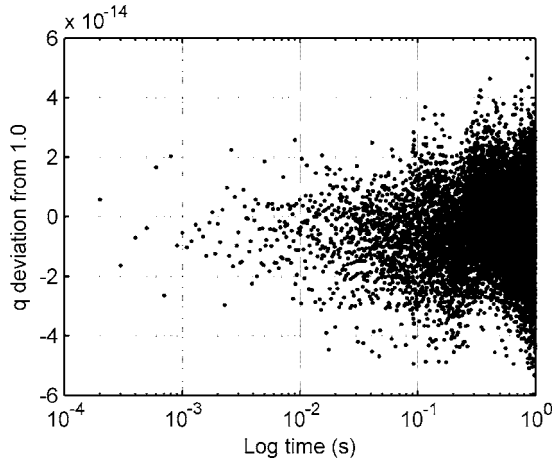

Fig. 6 Test result showing that the deviation from the ideal unit step in q when processing a parabola in T is less than $\pm 6 \times 10^{-14}$ over 10,000 points

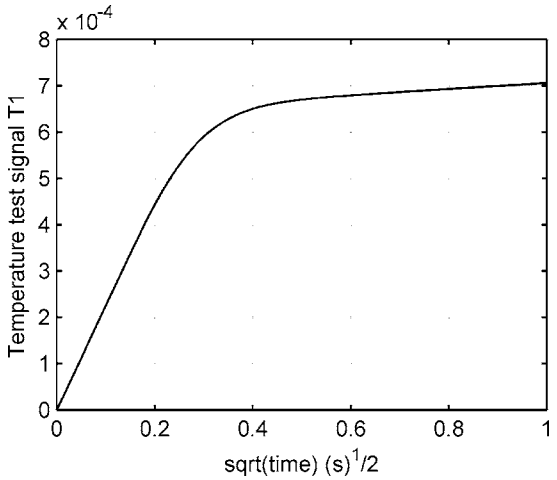

Fig. 8 Two layer gauge test signal to ideally give step q output

theory of such gauges was first given in Ref. [12].

The basis functions are those for a step in $q_1(t)$. In Laplace transformed form, the solution of the heat conduction equations for two layer substrate , gives

$$\bar{T}_1(s) = \frac{1}{\sqrt{\rho_1 c_1 k_1}} \frac{1}{\sqrt{s}} \bar{q}_1(s) \frac{\left[1 + A \exp\left(-2a\sqrt{\frac{s}{\alpha_1}}\right)\right]}{\left[1 - A \exp\left(-2a\sqrt{\frac{s}{\alpha_1}}\right)\right]}$$

where

$$A = \frac{\sqrt{\rho_1 c_1 k_1} - \sqrt{\rho_2 c_2 k_2}}{\sqrt{\rho_1 c_1 k_1} + \sqrt{\rho_2 c_2 k_2}}$$

and the thermal diffusivity $\alpha_1 = k_1/\rho_1 c_1$.

For a step in $q_1(t) = u(t)$, $\bar{q}_1(s) = 1/s$, and so

$$\bar{T}_1(s) = \frac{1}{\sqrt{\rho_1 c_1 k_1}} s^{-(3/2)} \frac{\left[1 + A \exp\left(-2a\sqrt{\frac{s}{\alpha_1}}\right)\right]}{\left[1 - A \exp\left(-2a\sqrt{\frac{s}{\alpha_1}}\right)\right]}$$

Expanding the denominator as a power series, and taking the inverse Laplace transform

$$T_1(t) = \frac{2}{\sqrt{\rho_1 c_1 k_1}} \left[\sqrt{\frac{t}{\pi}} + \sum_{n=1}^{\infty} 2A^n \left\{ \sqrt{\frac{t}{\pi}} \exp\left(-\frac{k_s^2}{4t}\right) - \frac{k_s}{2} \operatorname{erfc}\left(\frac{k_s}{2\sqrt{t}}\right) \right\} \right]$$

where

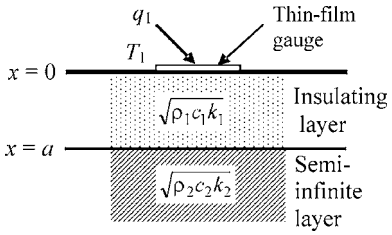

Fig. 7 Two layer heat transfer gauge

$$k_s = \frac{2an}{\sqrt{\alpha_1}} = 2n\sqrt{\rho_1 c_1 k_1}\left(\frac{a}{k_1}\right)$$

Thus the surface temperature response $T_1(t)$ to a unit step in surface heat transfer $q_1(t) = u(t)$ can be calculated if the thermal products $\sqrt{\rho_1 c_1 k_1}$ and $\sqrt{\rho_2 c_2 k_2}$, along with the effective thickness a/k_1, are known for a particular gauge.

Sampling $q_1(t)$ and $T_1(t)$ and applying the impulse response theory above gives the required impulse functions, which are similar in appearance to those shown for the semi-infinite gauge in Figs. 4 and 5.

The designed impulse functions are tested by sampling the $T_1(t)$ above to get a step in q.

Typical values for a 100-μm-thick polyimide top layer on an aluminum semi-infinite substrate are

$$\sqrt{\rho_1 c_1 k_1} = 500 \text{ J m}^{-1} \text{ K}^{-1}, \quad \sqrt{\rho_2 c_2 k_2} = 19{,}000 \text{ J m}^{-1} \text{ K}^{-1},$$
$$\text{and } a/k_1 = 6.5 \times 10^{-4} \text{ m}^2 \text{ K W}^{-1}$$

With these gauge properties for 10^4 samples at 10^4 samples/s for typical values, the numerical errors are again small, less than $\pm 1 \times 10^{-13}$ over 10,000 points. The test $T_1(t)$ plotted against $\sqrt{t}$ shown in Fig. 8 is interesting in that it shows the change of slope due to the metal semi-infinite layer predicted by Ref. [12].

Double Sided Heat Transfer Gauges—Method 1. Double sided gauges, such as used by Ref. [13], direct heat transfer gauges [14], and double thermocouple gauges [15], all measure the temperatures on the top T_1 and bottom T_2 of the insulating layer on the model surface under test. This has the advantage that the heat transfer rate can be obtained without having to know the thermal properties of the underlying material, but at the cost of having to measure two temperatures rather than one.

At low frequencies, the heat transfer rate is given simply by

$$q_1 = \frac{k}{a}(T_1 - T_2)$$

but at higher frequencies a full transient analysis is necessary.

A double sided thin-film gauge, as shown in Fig. 9, with top and bottom measured temperatures T_1 and T_2, respectively, can be considered to be the superposition of a differential gauge with temperatures $(T_1 - T_2)/2$ and $-(T_1 - T_2)/2$ top and bottom, together with a common mode gauge with temperatures $(T_1 + T_2)/2$ both top and bottom. Both of these can be modeled by the solution given previously for the two-layer substrate gauge:

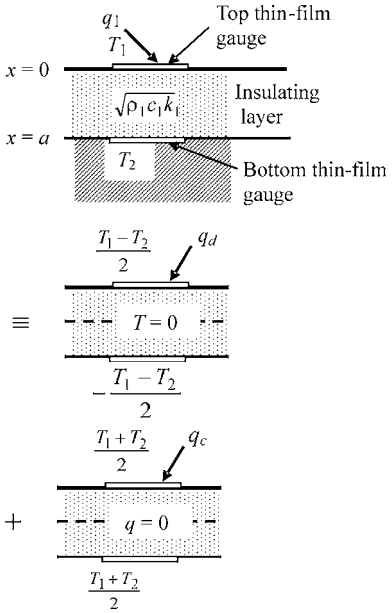

Fig. 9 Double-sided thin-film heat transfer gauge seen as a sum of differential and common mode gauges

1. The differential gauge has $T=0$ at the mid-depth $x=a/2$, and corresponds to an infinitely conducting lower substrate giving $A=-1$; and
2. The common mode gauge has $q=0$ at the mid-depth $x=a/2$, and corresponds to an insulating lower substrate giving $A=+1$.

These solutions are used to with q_d and q_c unit steps, to give differential and common mode impulse responses $h_d[n]$ and $h_c[n]$. The impulse responses of the top surface q_1 to T_1 and T_2 are then derived by superimposing the solutions

$$q_1 = q_d + q_c = h_d * \frac{T_1 - T_2}{2} + h_c * \frac{T_1 + T_2}{2} = \frac{h_d + h_c}{2} * T_1 + \frac{h_c - h_d}{2} * T_2 = h_1 * T_1 + h_2 * T_2$$

from which

$$h_1 = \frac{h_d + h_c}{2} \quad \text{and} \quad h_2 = \frac{h_c - h_d}{2}$$

To test the functions given for the double sided gauge the previously used two-layer gauge model is used with the additional calculation of the interface temperature T_2, as shown in the top of Fig. 9. Following the analysis in Ref. [12]

$$T_2(s) = T(a,s) = \frac{1}{\sqrt{\rho_1 c_1 k_1}} \frac{1}{\sqrt{s}} \bar{q}_1(s) \frac{[1+A]\exp\left(-a\sqrt{\frac{s}{\alpha_1}}\right)}{\left[1 - A\exp\left(-2a\sqrt{\frac{s}{\alpha_1}}\right)\right]}$$

where

$$A = \frac{\sqrt{\rho_1 c_1 k_1} - \sqrt{\rho_2 c_2 k_2}}{\sqrt{\rho_1 c_1 k_1} + \sqrt{\rho_2 c_2 k_2}}$$

and the thermal diffusivity $\alpha_1 = k_1/\rho_1 c_1$.

For a step in $q_1(t)=u(t)$, $\bar{q}_1(s)=1/s$, and so

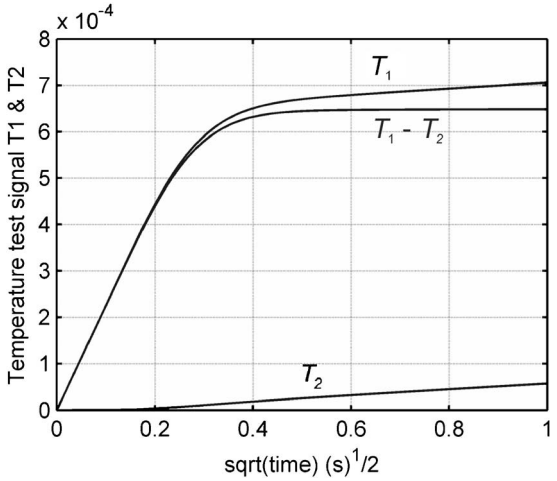

Fig. 10 Test signals for double sided gauge processing functions

$$T_2(s) = \frac{1}{\sqrt{\rho_1 c_1 k_1}} s^{-(3/2)} \frac{[1+A]\exp\left(-a\sqrt{\frac{s}{\alpha_1}}\right)}{\left[1 - A\exp\left(-2a\sqrt{\frac{s}{\alpha_1}}\right)\right]}$$

Expanding the denominator as a power series, and taking the inverse Laplace transform

$$T_2(t) = \frac{2[1+A]}{\sqrt{\rho_1 c_1 k_1}} \left[\sum_{n=0}^{\infty} A^n \left\{ \sqrt{\frac{t}{\pi}} \exp\left(-\frac{k_a^2}{4t}\right) - \frac{k_a}{2} \operatorname{erfc}\left(\frac{k_a}{2\sqrt{t}}\right) \right\} \right]$$

where

$$k_a = \frac{(2n+1)a}{\sqrt{\alpha_1}} = (2n+1)\sqrt{\rho_1 c_1 k_1}\left(\frac{a}{k_1}\right)$$

Figure 10 shows test signals T_1, T_2, and (T_1-T_2) for a unit step output in the predicted q_1 for 10^4 samples at 10^4 samples/s for the same typical values of

$$\sqrt{\rho_1 c_1 k_1} = 500 \text{ J m}^{-1} \text{ K}^{-1}, \quad \sqrt{\rho_2 c_2 k_2} = 19{,}000 \text{ J m}^{-1} \text{ K}^{-1},$$
$$\text{and } a/k_1 = 6.5 \times 10^{-4} \text{ m}^2 \text{ K W}^{-1}$$

Note how slowly the back wall temperature rises and how the difference (T_1-T_2) tends toward the expected steady value.

Figure 11 shows that the maximum error of the impulse method

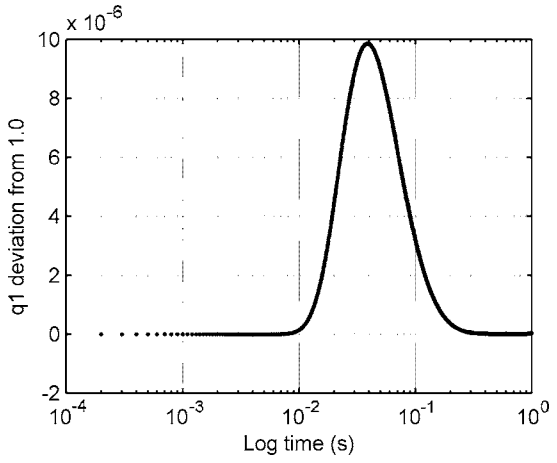

Fig. 11 Error of double sided method is less than 0.014%

for this test case is $<0.001\%$, and is greatest at the time when the presence of the back wall is first significant.

Double Sided Heat Transfer Gauges—Method 2. Jones and Guo [22] have shown that, for double sided gauges, there is a solution for the surface heat transfer q_1 for the case where top and bottom gauge temperatures are of the form $T_1=\sqrt{t}$ and $T_2=0$, or $T_1=0$ and $T_2=\sqrt{t}$. In Laplace transformed form

$$\bar{q}_1(s)=\sqrt{\rho_1 c_1 k_1}\sqrt{s}\left\{\frac{\left[1+\exp\left(-2a\sqrt{\frac{s}{\alpha_1}}\right)\right]}{\left[1-\exp\left(-2a\sqrt{\frac{s}{\alpha_1}}\right)\right]}\bar{T}_1(s)-2\frac{\exp\left(-a\sqrt{\frac{s}{\alpha_1}}\right)}{\left[1-\exp\left(-2a\sqrt{\frac{s}{\alpha_1}}\right)\right]}\bar{T}_2(s)\right\}$$

Putting $\bar{T}_1(s)=\sqrt{\pi}/2s^{-3/2}$ and $\bar{T}_2(s)=0$, or $\bar{T}_1(s)=0$ and $\bar{T}_2(s)=\sqrt{\pi}/2s^{-3/2}$ and expanding the denominators as a power series gives:

Heat transfer response to $T_1=\sqrt{t}$

$$q_{11}(t)=\Gamma(1.5)\sqrt{\rho_1 c_1 k_1}\left[1+2\sum_{n=1}^{\infty}\left\{\mathrm{erfc}\left(\frac{k_s}{2\sqrt{t}}\right)\right\}\right]$$

where

$$k_s=\frac{2an}{\sqrt{\alpha_1}}=2n\sqrt{\rho_1 c_1 k_1}\left(\frac{a}{k_1}\right)$$

Heat transfer response to $T_2=\sqrt{t}$

$$q_{12}(t)=-\Gamma(1.5)\sqrt{\rho_1 c_1 k_1}\left[2\sum_{n=0}^{\infty}\left\{\mathrm{erfc}\left(\frac{k_a}{2\sqrt{t}}\right)\right\}\right]$$

where

$$k_a=\frac{(2n+1)a}{\sqrt{\alpha_1}}=(2n+1)\sqrt{\rho_1 c_1 k_1}\left(\frac{a}{k_1}\right)$$

The desired impulse responses h_1 and h_2 are then obtained in the usual way by deconvolution using (q_{11} and T_1) and (q_{12} and T_2) as pairs of basis functions.

In the two layer gauge test cases above, these impulse functions work, but the error corresponding to Fig. 11 is larger, about 0.5%. Therefore it is recommended that Method 1 is used in preference to Method 2. This difference in accuracy probably comes about because Method 2 implicitly assumes that the bottom temperature $T_2\approx\sqrt{t}$ which Fig. 10 shows is not generally so.

De-Emphasizing or De-Boosting Thin-Film Gauge Signals

In the frequency domain, thin-film gauge signals have a response $T(\omega)/q(\omega)$ which decreases with rising frequency. Since the voltage change measured across the thin-film gauge at constant current is proportional to T, this signal is very small at high frequencies, and can be corrupted by electrical noise.

As well as using low noise amplifiers and constant current supplies [3] thin-film voltage signals are often passed through an analog filter which preamplifies (otherwise known as "boosting" or "pre-emphasis") the higher frequency signals to counter digitization errors in the smaller high-frequency signals and to reduce the affects of electrical noise after the initial amplifier. Oldfield et al. [6] used an electrical analog with the inverse frequency response of the semi-infinite thin-film gauge. Ainsworth et al. [17] used a four break point filter. Neal et al. [23] and Anthony et al. [3] used simpler, two break-point filters.

As the 15 figure accuracy of MATLAB does not suffer from this problem, it is desirable to correct this pre-emphasized, or boosted signal back to the thin-film voltage signal.

The MATLAB signal processing toolbox has been used to develop multipole IIR digital filters which have the inverse frequency response of the preamplifiers, and these filters can be used to recover the measured temperatures from the recorded signals.

Compensating for Analogue Response. Often the logarithmically spaced ten section electrical analogue described by Ref. [8] has been used to boost the high-frequency thin-film gauge signals. Since the inverse of the analogue response is given approximately, in Laplace transformed form by

$$\frac{\bar{V}_{\mathrm{in}}}{\bar{V}_{\mathrm{out}}}=\sqrt{\frac{r}{c}}\frac{1}{R_F}\frac{1}{\sqrt{s}}$$

(see Ref. [8] for symbols used here), the input thin-film voltage can be recovered using the MATLAB functions already developed for the semi-infinite substrate by replacing $\sqrt{\rho_1 c_1 k_1}$ by $R_F\sqrt{c/r}$.

IIR Filter Processing for Semi-infinite Substrate Heat Transfer Gauges. An IIR filter alternative to the impulse response technique applicable to semi-infinite substrate heat transfer gauges is described by Ref. [3] and is not repeated here.

Generally the previously described impulse response method is more accurate than this IIR filter method, and so is preferred. The IIR method is, however, slightly faster for processing very long data sequences, and so has a place.

Accuracy of Impulse Response Theory

The inherent mathematical accuracy of the impulse response method depends mainly on the rounding errors of the processing tools used. MATLAB has proven to be excellent in this regard and, as shown by Figs. 6 and 11, the errors due to the processing are negligible with suitably chosen sample rates and numbers. Of course, before using the filters, checks should be made and these have been incorporated in the MATLAB software.

Obviously, the overall accuracy of the impulse response sequence $h[n]$ derived for a particular heat transfer gauge depends on the accuracy of the input thermal products $\sqrt{\rho_1 c_1 k_1}$ and $\sqrt{\rho_2 c_2 k_2}$, and the effective thickness a/k_1, for that gauge, along with the measurement accuracy of the input (e.g., $T_1(t)$) signal. Much effort (see Refs. [6,7,11,12,14,18]) has been expended in measuring these parameters, which aren't always the same as those quoted by the manufacturers. In the author's experience, heat transfer measurements to accuracy of 10% are easily made, and an accuracy of 1% is difficult to obtain. Users of the impulse response method should conduct numerical experiments, varying the parameters, to determine the sensitivity of their measurements to the accuracy of their parameters. For example, they will find that, for semi-infinite gauges, the errors are proportional to those in the single parameter $\sqrt{\rho_1 c_1 k_1}$, whereas two layer gauges are insensitive to $\sqrt{\rho_2 c_2 k_2}$ for short times (e.g., $t<40$ ms in Fig. 8).

Fortunately, the numerical processing by the impulse response method does not add significantly to the errors arising from these parameters.

Application of Impulse Response Theory

MATLAB software, which designs the impulse response Fourier infrared (FIR) filters described above and processes thin-film gauge data, has been written and tested and is described in Ref. [1] and can be obtained from the author.

The processing sequence is as follows:

1. Calibrate all the gauges used in a particular experiment;

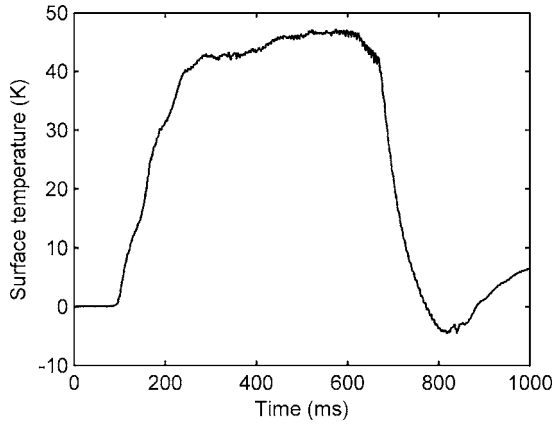

Fig. 12 Surface temperature trace from rotor tip direct heat transfer gauge for a complete run of the QinetiQ ILPF rotating turbine as described in Ref. [24]

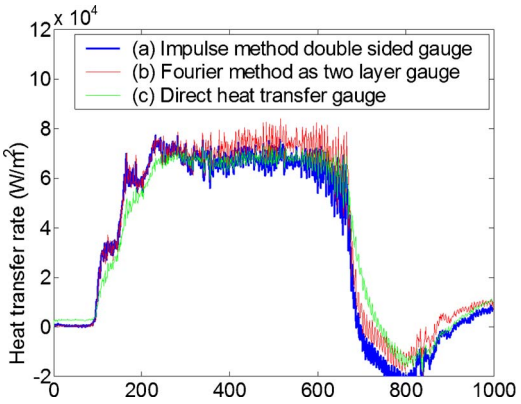

Fig. 13 Heat transfer rate traces processed from the data shown in by three different methods: (*a*) new impulse response method as a double sided gauge; (*b*) Fourier transform method [16] as a two layer gauge; and (*c*) from temperature difference as a direct heat transfer gauge

2. Decide on the data sampling rate and the number of samples for each gauge for each experimental run;
3. Use the MATLAB software to design impulse response filters for each gauge and deboosting filters for the preamplifiers used;
4. Run the experiment and digitally record the heat flux gauge signals; and
5. Process these signals with the designed filters to obtain surface temperature and heat flux, using the MATLAB function filter function or, much more rapidly, the MATLAB signal processing toolbox function fftfilt.

The computational efficiency of the impulse filter method comes about because step 3 need only be done once for a set of experiments and the data processing in step 5 is simply a digital filtering process and is fast and efficient.

Examples of Use of Method

QinetiQ ILPF Rotor Facility. Kam Chana of QinetiQ has used the impulse response method to process examples of his heat transfer data. In a typical example, a rotor tip thin-film heat flux gauge signal from a rotating blade mounted heat sensor in the QinetiQ ILPF transient turbine facility [24] is shown in Fig. 12 for a complete tunnel run. This gauge used a thin-film thermometer on a thin *Upilex* (polyimide) insulating layer [14] on a metal rotor blade whose temperature was measured by a thermocouple. Since the gauge measured both the surface temperature and the metal temperature underneath, the data could be processed in three ways as shown in Fig. 13.

The results are similar in that the traces overlay each other, but there are interesting differences. In the initial rise, the impulse method curve (*a*) and the Fourier method curve (*b*) are identical, but (*b*) drifts away during the run, possibly due to three-dimensional conduction in the metal lower substrate. The direct heat transfer calculation (*c*), with a lower frequency response, cannot match the other two curves in the rapidly changing rise and fall regions at the beginning and end of the run. However, (*a*) tracks (*c*) in the flat central portion, where the direct heat transfer trace (*c*) is known to be accurate. The conclusion is that the Impulse method is superior to both, having a better long-time response than the Fourier method (*b*) and a higher frequency response than the direct heat transfer gauge (*c*).

Oxford Rotor Facility Overtip Measurements. Thorpe et al. [25,26] have recently published unsteady time resolved heat transfer measurements on the shroud surface over a rotating turbine, using a laser-cut, semi-infinite heat transfer gauge array shown in Fig. 14, in the Oxford light isentropic piston tunnel rotor facility and have made one of the temperature traces available to the author.

The temperature trace in Fig. 15 shows part of a tunnel run in which 200,000 readings were taken at 500,000 readings/ s. The gauge substrate had a thermal product $\sqrt{\rho_1 c_1 k_1} = 1728$ J m^{-1} K^{-1}.

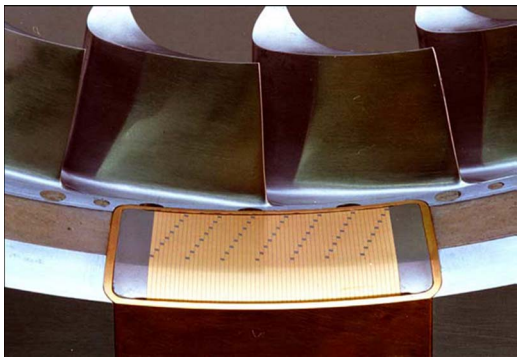

Fig. 14 Laser-cut semi-infinite thin-film gauge array to measure overtip time-resolved heat transfer signals. The rotor (not shown here) passes over the gauges (from Ref. [25]).

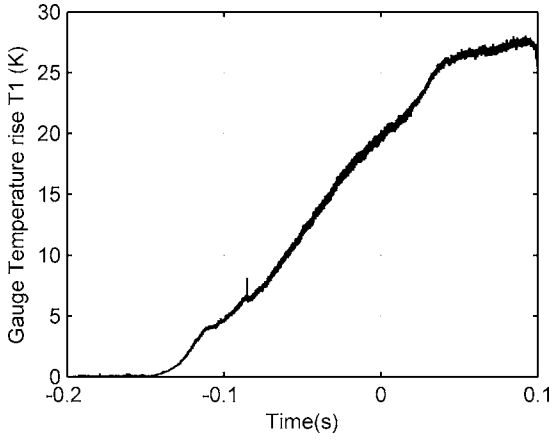

Fig. 15 Raw temperature trace with 200,000 points at 500,000 samples/s

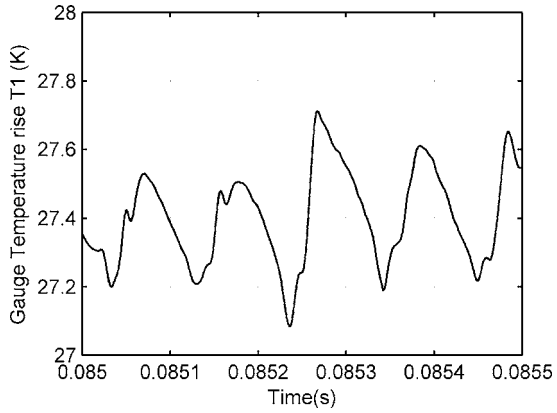

Fig. 16 Magnified section of temperature trace showing blade passing events

In Fig. 16 a magnified segment of Fig. 15 it can be seen that the temperature trace contains small periodic fluctuations associated with the rotor blade tips passing the gauge on the shroud.

The new impulse response method was then used to process the 200,000 temperature readings. On a 1.7 GHz laptop with 1 Gbyte of RAM, generation of the 200,000 point impulse response sequence took 20 min, but this, of course, need only be calculated once for each gauge at each sample rate. The processing of the temperature signal with this impulse response filter took a mere 2 s. This demonstrates the computational efficiency of the new method

At first sight, the processed heat flux signal in Fig. 17 looks very noisy, until it is realized that the spread is due to the large heat flux variations due to the rotor blade passing noted in Ref. [26]. Low pass filtering of the heat flux trace (Fig. 18) shows the mean levels in accordance with those reported in Ref. [25] and the magnified section of Fig. 17 shown in Fig. 18 confirms the large heat transfer flux fluctuations reported in Ref. [26]. Interestingly, Fig. 19 shows both the heat flux calculated by the new impulse method and that calculated by the authors of Ref. [26] using a refined method [27] derived from the earlier methods in Refs. [5,6,12]. The agreement is excellent, confirming the accuracy of the new method, which is much quicker and simpler to implement.

These two examples clearly demonstrate the effectiveness of the new method even with signals containing large numbers of samples.

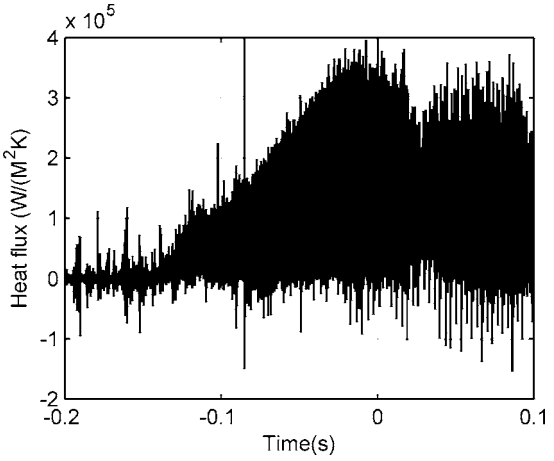

Fig. 17 Heat flux signal processed by impulse method

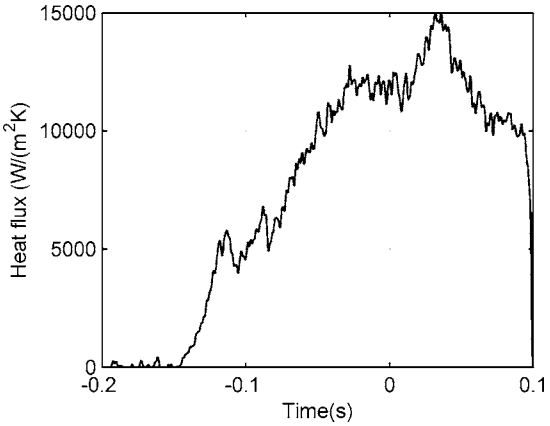

Fig. 18 Low pass filtered heat flux signal

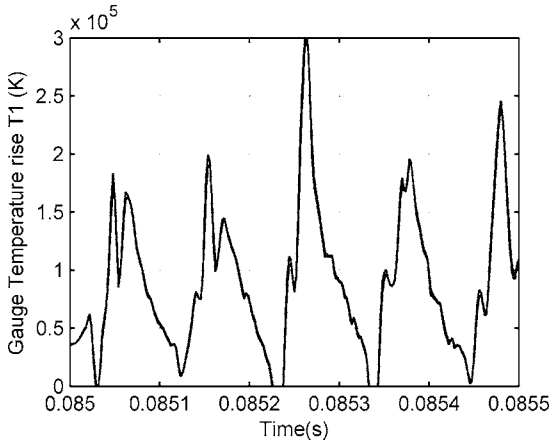

Fig. 19 Magnified section of heat flux traces showing blade passing events. New and old [27] processing agree excellently.

Conclusions

An efficient signal processing system for thin-film heat flux gauges based on impulse response filters has been developed and tested. It is applicable to any linear (i.e., constant property) measurement system where a known solution exists for the equations which describe the relationship between the measured signals and the physical parameters to be measured. It is limited to measurements where the readings are steady at the start of the recorded data, which is the usual situation in short duration facilities.

The impulse response filter method has proved, in practice, to be more accurate and faster than previous methods for processing heat flux gauge signals. This system offers significant advantages to the users of heat transfer instrumentation in turbomachinery research and in other fields.

Acknowledgment

Thanks are due to Professor T. V. Jones, for many years of fruitful discussions on heat flux measurement techniques, without which the impulse method would not have evolved. Thanks also go to Dr. S. M. Guo and Dr. R. J. Anthony for their faith in being the first to use these methods. Many thanks to Kam Chana, Steve Thorpe, Roger Ainsworth, and Nick Atkins for generously providing examples of heat transfer signals processed by the new method.

Nomenclature

a = thickness of insulating layer
c = specific heat capacity
$f_s = 1/T_s$ = sampling frequency
h = impulse response function
k = thermal conductivity
k = summation variable
n = sample number
N = number of points in sampled signal
q = heat transfer rate
$q_1(t)$ = basis function for heat transfer
$Q(z)$ = z transform of $q[n]$
s = Laplace transform variable
t = time
T = temperature
$T(z)$ = z transform of $T[n]$
$T_1(t)$ = basis function for temperature
T_s = sampling interval
$u(t)$ = unit step function
z = z transform variable
$\delta[n] = 1,0,0,0,\ldots$ = discrete impulse function
$\Delta(z)$ = z transform of $\delta[n]$
$\alpha = k/(\rho c)$ = thermal diffusivity
ρ = density
τ = dummy time variable in convolution integral

References

[1] Oldfield, M. L. G., 2000, "Guide to Impulse Response Heat Transfer Signal Processing Version 2," OUEL Report No. 2233/2000, Department of Engineering Science, University of Oxford.

[2] Guo, S. M., Lai, C. C., Jones, T. V., Oldfield, M. L. G., Lock, G. D., and Rawlinson, A. J., 2000, "Influence of Surface Roughness on Heat Transfer and Effectiveness for a Fully Film Cooled Nozzle Guide Vane Measured by Wide Band Liquid Crystals and Direct Heat Flux Gauges," ASME J. Turbomach., **122**, pp. 709–716.

[3] Anthony, R. J., Oldfield, M. L. G., Jones, T. V., and LaGraff, J. E., 1999, "Development of High-Density Arrays of Thin Film Heat Transfer Gauges," *Proceedings 5th ASME/JSME Thermal Engineering Joint Conference*, San Diego, CA, March 15–19.

[4] Anthony, R. J., Jones, T. V., and LaGraff, J. E., 2005, "High Frequency Surface Heat Flux Imaging of Bypass Transition," J. Turbomach., **127**, pp. 241–250.

[5] Schultz, D. L., and Jones, T. V., 1973, "Heat Transfer Measurements in Short Duration Hypersonic Facilities," Paper No. AGARD AG-165.

[6] Oldfield, M. L. G., Jones, T. V., and Schultz, D. L., 1978, "On-Line Computer for Transient Turbine Cascade Instrumentation," IEEE Trans. Aerosp. Electron. Syst., **14**(5), pp. 738–749.

[7] Jones, T. V., 1995 "The Thin Film Heat Transfer Gauges—A History and New Developments," *Proceedings 4th National UK Heat Transfer Conference*, Manchester, UK, pp. 1–12.

[8] Oldfield, M. L. G., Burd, H. J., and Doe, N. G., 1984, "Design of Wide-Bandwidth Analogue Circuits for Heat Transfer Instrumentation in Transient Tunnels," *Heat & Mass Transfer in Rotating Machinery, Proceedings 16th Symposium of the International Centre for Heat and Mass Transfer*, Dubrovnik, September 1982, D. E. Metzger and N. H. Afga, eds., Hemisphere, Washington, DC.

[9] Jones, T. V., Oldfield, M. L. G., Ainsworth, R. W., and Arts, T., 1993, "Transient Cascade Testing," *Advanced Methods for Cascade Testing* (AGARDograph AGARD-AG-328), C. Hirsch, ed., NATO AGARD, pp. 103–152.

[10] Dunn, M. G., 1985, "Measurement of Heat flux and Pressure in a Turbine Stage," ASME J. Eng. Gas Turbines Power, **107**, pp. 76–83.

[11] Doorly, J. E., and Oldfield, M. L. G., 1986, "New Heat Transfer Gauges for Use on Multi-layered Substrates," ASME J. Turbomach., **108**, pp. 153–160.

[12] Doorly, J. E., and Oldfield, M. L. G., 1987, "The Theory of Advanced Multilayer Thin Film Heat Transfer Gauges," Int. J. Heat Mass Transfer, **30**(6), pp. 1159–1168.

[13] Epstein, A. H., Guenette, G. R, Norton, R. J. G., and Yuzhang, G., 1986, "High Frequency Response Heat Flux Gauges," Rev. Sci. Instrum., **54**(4), pp 639–649.

[14] Piccini, E., Guo, S. M., and Jones, T. V., 2000, "The Development of a New Direct Heat Flux Gauge for Heat Transfer Facilities," Meas. Sci. Technol., **11**(4), pp. 342–349.

[15] Diller, T. E., 1993, "Advances in Heat Flux Measurements," *Advances in Heat Transfer*, Vol. 23, Academic, New York, NY, Vol. 23, pp. 279–368.

[16] Thorpe, S. J., Yoshino, S., Ainsworth, R. W., and Harvey, W., 2004, "Improved Fast-Response Heat Transfer Instrumentation for Short-Duration Wind Tunnels," Meas. Sci. Technol., **15**, pp. 1897–1909.

[17] Ainsworth, R. W., Allen, J. L., Davies, M. R. D., Doorly, J. E., Forth, C. J. P., Hilditch, M. A., Oldfield, M. L. G., and Sheard, A. G., 1989, "Developments in Instrumentation and Processing for Transient Heat Transfer Measurements in a Full Stage Model Turbine," ASME J. Turbomach., **111**, pp. 20–27.

[18] Iliopoulou, V., Denos, R., Billiard, N., and Arts, T., 2004, "Time-Averaged and Time-Resolved Heat Flux Measurements on a Turbine Stator Blade Using Two-Layered Thin-Film Gauges," ASME J. Turbomach., **126**, pp. 570–577.

[19] Denbigh, P., 1998, *System Analysis and Signal Processing*, Addison-Wesley, Reading, MA.

[20] Matlab, "The Mathworks," 2007, ⟨http://www.mathworks.com⟩

[21] Proakis, J. G., and Manolakis, D. M., 1992, *Digital Signal Processing: Principles, Algorithms and Applications*, 2nd ed., Macmillan, New York.

[22] Jones, T. V., and Guo, S. M., 1999, "Double Sided Heat Transfer data Analysis," private communication.

[23] Neal, P. M., Oldfield, M. L. G., and Cameron, S. A., 1992, "A Modular, High Speed Transputer Based Data Acquisition System," *Transputer/Occam Japan*, S. Noguchi, ed., *Proceeding 4th Transputer/Occam International Conference*, Tokyo, Japan, June 2–5, IOS Press, Vol. 4, pp. 242–264.

[24] Chana, K. S, and Jones, T. V., 2003, "An Investigation on Turbine Tip and Shroud Heat Transfer," ASME J. Turbomach., **125**, pp. 513–520.

[25] Thorpe, S. J., Yoshino, S., Ainsworth, R. W., and Harvey, N. W., 2004, "An Investigation of the Heat Transfer and Static Pressure Field on the Over-Tip Casing of a Shroudless Transonic Turbine Rotor at Engine Representative Flow Conditions. (I). Time-Mean Results," Int. J. Heat Fluid Flow, **25**, pp. 933–944.

[26] Thorpe, S. J., Yoshino, S., Ainsworth, R. W., and Harvey, N. W., 2004, "An Investigation of the Heat Transfer and Static Pressure Field on the Over-tip Casing of a Shroudless Transonic Turbine Rotor at Engine Representative Flow Conditions. (II). Time-Resolved Results," Int. J. Heat Fluid Flow, **25**, pp. 945–960.

[27] Yoshino, S., 2002, "Heat Transfer in Rotating Experiments," D.Philosopy thesis, University of Oxford, Oxford, UK.

A Comparison of Approximate Versus Exact Geometrical Representations of Roughness for CFD Calculations of c_f and St

J. P. Bons
Department of Mechanical Engineering,
Brigham Young University,
Provo, UT 84602-4201
e-mail: jbons@byu.edu

S. T. McClain
Department of Mechanical Engineering,
University of Alabama-Birmingham,
Birmingham, AL 35294-4461
e-mail: smcclain@eng.uab.edu

Z. J. Wang
e-mail: zjw@iastate.edu

X. Chi
e-mail: chixingk@egr.msu.edu

T. I. Shih
e-mail: tomshih@iastate.edu

Department of Aerospace Engineering,
Iowa State University,
Ames, IA 50011-2271

Skin friction (c_f) and heat transfer (St) predictions were made for a turbulent boundary layer over randomly rough surfaces at Reynolds number of 1×10^6. The rough surfaces are scaled models of actual gas turbine blade surfaces that have experienced degradation after service. Two different approximations are used to characterize the roughness in the computational model: the discrete element model and full 3D discretization of the surface. The discrete element method considers the total aerodynamic drag on a rough surface to be the sum of shear drag on the flat part of the surface and the form drag on the individual roughness elements. The total heat transfer from a rough surface is the sum of convection on the flat part of the surface and the convection from each of the roughness elements. Correlations are used to model the roughness element drag and heat transfer, thus avoiding the complexity of gridding the irregular rough surface. The discrete element roughness representation was incorporated into a two-dimensional, finite difference boundary layer code with a mixing length turbulence model. The second prediction method employs a viscous adaptive Cartesian grid approach to fully resolve the three-dimensional roughness geometry. This significantly reduces the grid requirement compared to a structured grid. The flow prediction is made using a finite-volume Navier-Stokes solver capable of handling arbitrary grids with the Spalart-Allmaras (S-A) turbulence model. Comparisons are made to experimentally measured values of c_f and St for two unique roughness characterizations. The two methods predict c_f to within $\pm8\%$ and St within $\pm17\%$, the RANS code yielding slightly better agreement. In both cases, agreement with the experimental data is less favorable for the surface with larger roughness features. The RANS simulation requires a two to three order of magnitude increase in computational time compared to the DEM method and is not as readily adapted to a wide variety of roughness characterizations. The RANS simulation is capable of analyzing surfaces composed primarily of roughness valleys (rather than peaks), a feature that DEM does not have in its present formulation. Several basic assumptions employed by the discrete element model are evaluated using the 3D RANS flow predictions, namely: establishment of the midheight for application of the smooth wall boundary condition; c_D and Nu relations employed for roughness elements; and flow three dimensionality over and around roughness elements. [DOI: 10.1115/1.2752190]

Introduction

Surface roughness is an important parameter in the design and operation of fluid machinery. Common examples of surface roughness include fouling of compressors or pumps, ice accretion on airfoil surfaces, deposits and corrosion in industrial piping, and thermal barrier coating erosion in turbines. Typically, roughness levels increase dramatically during operation. For example, gas turbine blade surface measurements indicate an order of magnitude or greater increase in rms roughness between maintenance cycles for a first stage high-pressure turbine [1–3].

Understanding the influence of increased surface roughness on fluid flow and heat transfer is critical to insuring the efficient operation of fluid machinery. Since roughness is known to increase both surface drag and heat transfer, it can lead to undesirable consequences: higher heat load in turbines, accelerated part degradation in industrial piping, increased airfoil drag, and/or lower pump efficiencies. For example, Blair [4] reported a roughness-related St increase of nearly 100% on a rotating turbine facility due to premature boundary layer transition and other roughness-induced effects. Guo et al. [5] also reported a twofold increase in heat transfer for a factor of 25 increase in roughness height on a fully scaled nozzle guide vane facility. Likewise, several studies with roughened blades in compressors and pumps observed losses in efficiency of 3–5 points [6,7].

Historically, the two principle methods for evaluating the effects of surface roughness on drag and heat transfer have been the equivalent sand-grain roughness (k_s) model and the discrete element model (DEM). The equivalent sand-grain roughness model, first proposed by Schlichting [8], is an empirical model in which rough surfaces with various features are compared to data from Nikuradse [9] concerning flow in pipes with varying sizes of sieved sand glued to the wetted surface. Rough surfaces are assigned a value of equivalent sand-grain roughness height based on comparisons with Nikuradse's data. This involves the use of empirical correlations derived from experiments. Typically, the same value of k_s is used to characterize rough-wall skin friction and heat transfer. Because of its relative simplicity and generality, the sand-grain roughness model continues to be the most widely used roughness model.

Submitted to ASME for publication in the JOURNAL OF TURBOMACHINERY. Manuscript received November 30, 2005; final manuscript received March 16, 2006; published online March 25, 2008. Review conducted by David Wisler. Paper presented at the 2005 ASME International Mechanical Engineering Congress (IMECE 2005), Orlando, FL, USA, November 5–11, 2005.

Table 1 Surface statistics for scaled roughness models

Type	Ra (mm)	$k=Rz$ (mm)	Rt (mm)	Λ_s [14]	k^+ (Re_k)	kf_α [23] (mm)	S_w/S
Fuel deposit	1.17	4.04	7.3	35.1	322	7.86	1.22
Erosion	0.52	2.68	4.23	22.1	481	8.23	1.20

With the advent of computational fluid dynamics, the equivalent sand-grain roughness characterization has been routinely employed to apply rough-wall boundary conditions for nonsmooth surfaces. One common implementation is to adjust the near-wall van Driest damping constant when calculating the Prandtl mixing length in a turbulence closure model [5,10,11]. An alternative formulation employed in the Spalart-Allmaras one-equation turbulence model assumes a nonzero eddy viscosity at the wall and adjusts the distance from the wall where the wall boundary conditions are imposed [12]. Both of these implementations use empirical k_s correlations to characterize the roughness height. Thus, despite progress in the prediction of roughness effects using these models, their accuracy still hinges on the k_s value employed.

Numerous researchers have proposed alternatives to Schlichting's original tabulated k_s values using more general correlations based on roughness height, shape, and/or density [13–15]. Nonetheless, several critical shortcomings of the equivalent sand-grain method continue to plague its use [16]. First, since k_s correlations have been universally developed using ordered arrays of discrete roughness elements (e.g., cones, hemispheres), they are not always appropriate for use with randomly rough (i.e., "real") surfaces [15]. In addition, the common practice of using the same k_s value to predict both skin friction and heat transfer is at times problematic [12,15]. There is no physical reason that two surfaces with the same skin friction coefficient (which implies that they would have the same k_s value from a friction standpoint) should have the same Stanton numbers [16].

Unlike the equivalent sand-grain model, the DEM evaluates the effects of roughness by considering the physical characteristics of the roughness elements in the solution of the boundary layer equations. The discrete element model is semi-empirical in the sense that the closure relationships used to determine the drag and heat transfer from the individual roughness elements are based on empirical data. The basis for the discrete element model was also described by Schlichting in his 1937 paper [8]. In attempting to explain the effect of roughness element density on the effective sand-grain height, Schlichting suggested that the total drag on a rough surface is the sum of skin friction on the flat part of the surface and the form drag on the individual roughness elements. Methods to solve the boundary layer equations for flow over rough surfaces [17–19] have incorporated momentum sink terms into the boundary layer equations based on Schlichting's suggestion. The form of the discrete element roughness model presented in this work originated with Finson [17] and was rigorously derived by Taylor [16]. It was recently adapted to accommodate irregular roughness representations typical of degraded turbine blade surfaces [20].

Though recent progress with DEM is promising, more extensive validation is required before the technique can be broadly applied to complex three-dimensional, unsteady flowfields. This will require flow and surface data with high spatial density for a variety of flow conditions (e.g., elevated freestream turbulence, nonzero pressure gradient, surface curvature, etc…). While data for this purpose have traditionally been supplied from experiments, recent advances in computational power and grid-generation algorithms have opened up the possibility of using computational data from fully 3D roughness simulations to perform model validation for DEM. One recent noteworthy advance in computational capability is the viscous Cartesian grid generation method which was developed for use with complex geometries such as irregular surface roughness. When employed over a rough surface, this gridding strategy reduces the cell count by over an order of magnitude compared to standard structured grid architectures. This novel grid generation scheme was employed with a RANS Spalart-Allmaras turbulence model to provide rough-wall c_f and St predictions for comparison with DEM predictions. The modified DEM model and 3D RANS model were both applied to two roughness geometries that have also been characterized experimentally. The objective of this study is to compare the results of the two methods and provide a comprehensive assessment of the modeling assumptions intrinsic to the DEM method. At the same time, the 3D RANS model results provide some indication as to how soon practicing engineers might be able to dispense with the need for roughness modeling altogether.

Roughness Panels

This study employed the same roughness characterizations used in previous studies by the authors [1,15]. Surface measurements were made on over 100 turbine components assembled from various manufacturers. The components were selected by each manufacturer to be representative of surface conditions generally found in the gas turbine inventory. In order to respect proprietary concerns of the manufacturers, strict source anonymity has been maintained for all data in this publication.

3D surface measurements were made on the assembled hardware using a Taylor-Hobson Form Talysurf Series 2 contact stylus measurement system. The complete results are reported in Ref. [1]. Of the surfaces available, two different configurations were selected for this study. These include one fuel deposit surface and one erosion/deposit surface. The fuel deposit surface contains large, widely spaced roughness peaks elongated in the flow direction while the erosion surface has smaller roughness elements that are more evenly distributed. The surfaces were scaled to match the roughness height to boundary layer momentum thickness ratios typical of other turbine studies (i.e., $0.5<k/\theta<3$, where $\theta=2.2$ mm in the experimental facility) [21,22]. Table 1 contains roughness statistics for the two surfaces. Both surfaces would be considered "fully rough" according to the established criterion, $k^+>70$. The scaled models were fabricated into 280 mm (streamwise) $\times$ 360 mm (cross-stream) $\times$ 6 mm (average thickness) test panels using a StrataSys Inc. GeniSys Xi 3D plastic printer. The same 3D surface data used by the printer were also used for the CFD models. The surface data spatial resolution was 0.3 mm in all but the y direction, which matched the minimum resolution of the printer.

Experimental Facility and Database

The research facility used for the experiments is described in detail in Ref. [15] and only a brief summary will be given here. The open loop wind tunnel located at Wright-Patterson AFB uses a centrifugal blower to provide a nominal mass flow of 1.2 kg/s to the test section (Fig. 1), yielding approximately $\mathrm{Re}_x \cong 900{,}000$ at the roughness panels. A heat exchanger was used to vary the flow temperature from 18°C to 54°C for heat transfer measurements. The flow from the blower enters a conditioning plenum of 0.6 m diameter before reaching the final rectangular wind tunnel section. The freestream turbulence level at the measurement location is 1%. At 1.22 m from the plenum exit a knife-edge boundary layer bleed with suction restarts the boundary layer, making the

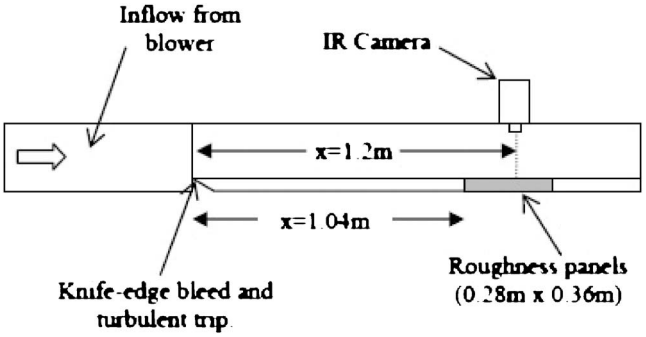

Fig. 1 Schematic of flat plate wind tunnel at the Air Force Research Laboratory (shown for St measurement)

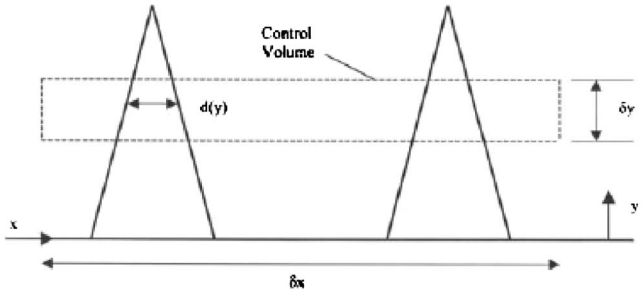

Fig. 2 The discrete-element roughness model control volume schematic

aspect ratio (span/height) of the final wind tunnel section approximately 1.7. The top wall of this final section was adjusted for (nominally) zero pressure gradient. A trip located 2.5 cm from the leading edge insures turbulent boundary layer development.

The roughness panels are preceded by 1.04 m of smooth Plexiglas wall (of comparable thermal properties to the plastic panels). Accordingly, the flow experiences a transition from a smooth to rough wall condition at the leading edge of the roughness panels. To reduce the influence of the abrupt change in surface roughness, the first 20 mm of roughness was scaled to transition linearly from the smooth upstream wall to the full roughness height.

The skin friction measurement was made using a hanging element balance [15]. Essentially, the balance consists of a free-floating test section suspended from an apparatus atop the tunnel using thin Nichrome wires. The wires are positioned outside the wind tunnel and are affixed to the four corners of a metal support plate upon which the plastic test panels are mounted. The test panels are positioned flush with the bottom of the wind tunnel. When air is flowing in the tunnel, the plate moves downstream under the applied shear force. This motion was a maximum of approximately 2.5 mm for the highest drag case tested. For such small plate translations, the restoring force of the suspended apparatus is approximately linear with streamwise plate deflection. Using a string-pulley calibrator with fractional gram weights, this restoring force was calibrated over the full range of deflections observed in practice. The plate deflection was measured using a Capacitec Model No. 4100-S capacitance meter mounted to the side of the test plate, outside the tunnel walls.

The test plate is suspended with a 0.5 mm gap at the leading edge and a trailing edge gap which is set to 0.5 mm greater than the maximum expected excursion. These gaps allow unrestrained motion of the plate under the applied shear force. The gaps also permit differential pressure forces to affect the net displacement of the test plate. To mitigate these pressure forces, the leading edge gap was covered with a 0.05-mm-thick stainless-steel sheet with 7 mm overlap with the roughness panels. The initial 10 mm of each panel was smooth to accommodate this overlap without interference. Despite this precaution, differential pressures still contributed to the net plate motion. To calculate this component of the force, pressure taps were installed at midplate thickness on the adjoining stationary plexiglass pieces, both upstream and downstream of the suspended aluminum support plate with the roughness panels. This differential pressure (upstream to downstream) was measured and deducted from the total displacement (force) measured by the Capacitec meter. With these precautionary measures, baseline smooth plate c_f values were found to be within 5% of a correlation from Mills [24]. Repeatability was within $\pm 2\%$ and bias uncertainty was estimated at ± 0.0002 for the baseline measurement of $c_f = 0.0035$ at $\mathrm{Re}_x \cong 900{,}000$.

For the heat transfer measurements, a FLIR Thermacam SC 3000 infrared camera was mounted over a hole in the Plexiglas ceiling of the tunnel. The camera setup and data reduction procedure are documented in Ref. [15]. The camera field of view was roughly 70×90 mm, centered at $x = 1.2$ m. The surface temperatures recorded by the camera were area averaged to obtain the surface temperature history from which the Stanton number was determined using the method of Schultz and Jones [25]. This transient technique uses Duhamel's superposition method to calculate the surface heat flux given the surface temperature history. It assumes the panels are a semi-infinite solid at constant temperature at the start of the transient. To accomplish this, the plastic panels were mounted on a 12-mm-thick acrylic sheet rather than an aluminum plate for this measurement. This acrylic has approximately the same thermophysical properties as the plastic panels to avoid thermal wave reflections at the contact surface, thus confirming the use of the semi-infinite conduction assumption in the data processing.

Prior to heat transfer testing, the entire test section was maintained at room temperature for several hours. Using the flow heat exchanger, hot air flow was then initiated instantaneously while monitoring the freestream velocity and temperature above the measurement site as well as the average surface temperature (with the infrared (IR) camera). The spatially averaged heat transfer coefficient (h) at each time step was then calculated using the expression in Ref. [15]. With this procedure, baseline smooth plate St values were found to be within 3% of a correlation from Mills [24]. Repeatability was within $\pm 5\%$ and bias uncertainty was estimated at ± 0.00015 for the baseline measurement of St $= 0.00215$ at $\mathrm{Re}_x \cong 900{,}000$.

Discrete Element Model

The discrete-element model is formulated for roughness elements with three-dimensional shapes for which the element cross section can be defined at every height, y. Basic to this approach is the idea that the two-dimensional, time-averaged turbulent boundary-layer equations can be applied in the flow region below the crests of the roughness elements. The differential, boundary-layer equations including roughness effects are derived by applying the basic conservation statements for mass, momentum, and energy to a control volume such as that shown in Fig. 2.

The flow variables are spatially averaged over the transverse (z) direction and the streamwise (x) direction. The physical effects of the roughness elements on the fluid in the control volume are modeled by considering the flow blockage (α), the local element heat transfer, and the local element form drag. The total form drag force on the control volume is due to all of the roughness elements penetrating the control volume and is expressed using a local drag coefficient as

$$F_D = \frac{1}{2}\rho u^2 \delta y \sum_{i=1}^{N_r} C_{D,i} d_i(y) \tag{1}$$

For roughness elements with noncircular cross sections, the following expression was used to determine the local element drag coefficient

$$C_{D,i} = \begin{cases} \left(\frac{\mathrm{Re}_{d,i}}{1000}\right)^{-0.125} \varepsilon_i^{0.73456} & \mathrm{Re}_{d,i} < 60{,}000 \\ 0.6\varepsilon_i^{0.73456} & \mathrm{Re}_{d,i} > 60{,}000 \end{cases} \quad (2)$$

where the local roughness element Reynolds number is

$$\mathrm{Re}_{d,i} = \frac{\rho u d_i}{\mu} \quad (3)$$

and the eccentricity, ε_i, is determined as the maximum (cross-stream) width of blockage divided by the maximum (streamwise) length of the blockage at the given elevation (y).

Likewise, the rate of heat transfer between the elements penetrating the control volume and the fluid is expressed using a local Nusselt number as

$$Q = (T_R - T)\delta y \sum_{i=1}^{N_r} P_{w,i} \frac{k_f \mathrm{Nu}_{d,i}}{d_i} \quad (4)$$

For roughness elements with noncircular shapes, the wetted perimeter, P_w, is difficult to determine with certainty even when the surface is completely characterized using three-dimensional profilometry. For this study, the blockage element perimeter is determined using an elliptical-element analogy such that the total heat transfer into the control volume is evaluated as

$$Q = \pi k_f (T_R - T)\delta y \sum_{i=1}^{N_r} K_{\varepsilon,i} \mathrm{Nu}_{d,i} \quad (5)$$

where K_ε is a wetted perimeter correction factor based on the eccentricity of the blockage element

$$K_{\varepsilon,i} = \left[\frac{1}{2}\left(1 + \frac{1}{\varepsilon_i^2}\right) - \frac{1}{8.8}\left(1 - \frac{1}{\varepsilon_i}\right)^2\right]^{1/2} \quad (6)$$

and the local Nusselt number is found from the relationship

$$\mathrm{Nu}_{d,i} = \begin{cases} 1.7\mathrm{Re}_{d,i}^{0.49}\mathrm{Pr}^{0.4} & \text{for } \mathrm{Re}_{d,i} \leqslant 13{,}776 \\ 0.0605\mathrm{Re}_{d,i}^{0.84}\mathrm{Pr}^{0.4} & \text{for } \mathrm{Re}_{d,i} > 13{,}776 \end{cases} \quad (7)$$

Using the above ideas, the continuity, momentum, and energy equations for a steady, Reynolds averaged, two-dimensional turbulent boundary layer with roughness become

$$\frac{\partial}{\partial x}(\rho\beta u) + \frac{\partial}{\partial y}(\rho\beta v) = 0 \quad (8)$$

$$\beta\rho u\frac{\partial u}{\partial x} + \beta\rho v\frac{\partial u}{\partial y} = -\frac{\partial}{\partial x}(\beta P) + \frac{\partial}{\partial y}\left[\beta\left(\mu\frac{\partial u}{\partial y} - \overline{\rho u' v'}\right)\right] - \frac{1}{2}\rho\frac{u^2}{L_p L_t}\sum_{i=1}^{N_r} C_{D,i} d_i \quad (9)$$

$$\beta\rho u\frac{\partial H}{\partial x} + \beta\rho v\frac{\partial H}{\partial y} = \frac{\partial}{\partial y}\left[\beta\left(\frac{k_f}{c_p}\frac{\partial H}{\partial y} - \overline{\rho v' h'}\right)\right] + u\frac{\partial}{\partial x}(\beta P) + \beta\frac{\partial u}{\partial y}\left(\mu\frac{\partial u}{\partial y} - \overline{\rho u' v'}\right) + \frac{1}{2}\rho\frac{u^3}{L_p L_t}\sum_{i=1}^{N_r} C_{D,i} d_i + \frac{\pi k_f}{L_p L_t}(T_R - T)\sum_{i=1}^{N_r} K_{\varepsilon,i}\mathrm{Nu}_{d,i} \quad (10)$$

The void fraction, β, is defined as the fraction of the area open to flow at a given elevation (y) and equals $(1-\alpha)$, where α is the blockage fraction. The discrete element model was originally developed for ordered arrays of uniform roughness elements (e.g., hemispheres or cones, Fig. 2) mounted to a smooth, base surface. In this case, c_D and Nu are the same for all the roughness elements and L_p and L_t are the streamwise and transverse spacing parameters respectively. DEM was recently adapted by McClain et al. [20] for use with nonuniform roughness, in which case the c_D and Nu of each element are calculated separately before being summed. L_p and L_t are, respectively, the streamwise length and transverse width of the control volume.

One additional modification necessary for nonuniform roughness is the location of the application of the wall boundary condition. For the irregular surface, this is placed at the mean elevation (y_{me}) since there is no flat base surface at the minimum elevation ($y=0$). The boundary conditions for the discrete-element boundary-layer equations with roughness are then

Uniform roughness (e.g., Fig. 2)	Nonuniform roughness
$y=0$: $u=v=0$, $H=H_w$	$y=y_{me}$: $u=v=0$, $H=H_w$
$y\to\infty$: $u=U_e$, $H=H_e$	$y\to\infty$: $u=U_e$, $H=H_e$

The turbulence model is not modified to include roughness effects since the physical effects of the roughness on the flow are explicitly included in the differential equations. The Prandtl mixing length with van Driest damping is used for turbulence closure, with a turbulent Prandtl number, Pr_t, of 0.9 for the energy equation.

Once the boundary-layer equations have been solved, the skin friction coefficient is evaluated as

$$C_f = \frac{(1-\alpha)\mu\left.\frac{du}{dy}\right|_{y=y_{me}} + \frac{1}{2}\frac{1}{L_t L_p}\int_{y_{me}}^{\infty}\left(\rho u^2\sum_{i=1}^{N_r} C_{D,i} d_i\right)dy}{\frac{1}{2}\rho U_e^2} \quad (11)$$

The Stanton number is determined using the expression

$$\mathrm{St} = \frac{-(1-\alpha)k_f\left.\frac{dT}{dy}\right|_{y=y_{me}} + \frac{1}{L_t L_p}\int_{y_{me}}^{\infty}\pi k_f (T_R - T)\sum_{i=1}^{N_r} K_{\varepsilon,i}\mathrm{Nu}_{d,i} dy}{\rho U_e c_p (T_w - T_e)} \quad (12)$$

The discrete-element roughness model was implemented in the finite difference code boundary layer computation (BLACOMP), which was used in this study to predict the skin friction and heat transfer results for the rough surfaces. To solve the boundary-layer equations in BLACOMP, the boundary equations were transformed using the modified-Illingsworth coordinate transformations. An implicit finite difference scheme is used to solve the transformed boundary layer equations. An expanding grid in the computational y direction is used in BLACOMP. Because an expanding grid is used, Lagrangian interpolation polynomials are used to evaluate second-order accuracy derivatives in the y direction. Derivatives in the x direction are determined using the first-order backward-difference technique. Detailed information on the solution method can be found in Ref. [16].

For the predictions, the flow was modeled with variable properties as a function of temperature. The ideal gas law was used for density and Sutherland's law was used for viscosity. Changes in thermal conductivity were determined by allowing the Prandtl number to vary with temperature using an empirical quadratic curvefit [26].

Before executing BLACOMP, the surface data matrix for each rough surface was evaluated to determine all of the necessary geometric parameters: y_{me}, $\beta(y)$, as well as $d(y)$ and $\varepsilon(y)$ for each roughness element above y_{me}. This process required approximately 2 h on a standard PC, although it was not optimized for speed. The computational grid was then developed in BLACOMP with a streamwise (x) spacing of 0.0025 m. This x spacing was used to apply 105 x stations in the roughness region of the wind tunnel. For the entire computational space from the leading knife edge to the downstream edge of the roughness panels ($0 \leqslant x \leqslant 1.32$ m), 529 x stations were used. The initial y spacing was

0.005 (equivalent $y^+=0.19$ at midplate). One hundred y points were used. This provided 41 points with values of y less than one and a maximum y value of 57.9 mm. The total grid node count for all three test cases (smooth, fuel deposit, and erosion) was then 52,900. Finer grid spacing yielded no appreciable improvement in the solution. BLACOMP is suitable for use on a standard PC, with typical run times requiring 2–3 min.

3D RANS Model With Viscous Cartesian Grid Generation

The viscous Cartesian grid generation method is a recently developed automatic grid generation approach for very complex, and possibly "dirty" geometries [27]. The three major steps in the method are described as follows.

Adaptive Cartesian Grid Generation. The grid generation method is initiated by specifying the minimum and maximum sizes of Cartesian grid cells to be generated. The adaptive Cartesian grid is generated by recursively subdividing a single coarse root Cartesian cell. Since the root grid cell must cover the entire computational domain, the surface geometry is contained in the root cell. The size of the Cartesian cells intersecting the geometry is controlled by constraining the cell size in the geometry normal and tangential directions. The recursive subdivision process stops when all the Cartesian cells intersecting the geometry satisfy the length scale requirements. To ensure solution accuracy, the maximum cell aspect ratio and grid smoothness were also monitored. In the present study, the sizes of any two neighboring cells in any coordinate direction cannot differ by a factor exceeding two.

Cartesian Grid Front Generation and Smoothing. In order to "insert" a viscous layer grid between the Cartesian grid and the body surface, Cartesian cells intersected by the geometry must be removed, leaving an empty space between the Cartesian grid and the body surface. All the Cartesian cells intersected by the geometry are determined using a tree-based search algorithm. Once the Cartesian cells intersected by the geometry, and cells outside the computational domain are removed, a Cartesian grid "volume" remains. The boundary faces of this volume form the Cartesian front. Before this front is "projected" to the geometry, it is smoothed with a Laplacian smoother.

Projection of the Cartesian Front to the Body Surface. After the smoothed Cartesian front is obtained, each node in the front needs to be connected to the body surface to form the viscous grid needed to resolve the turbulent boundary layer. After the front is projected to the boundary geometric entities, a "water-tight" surface grid is generated on the boundary. The "foot prints" of the layer grids on the body surface have the same topology (or connectivity) as the Cartesian front. By connecting each point on the Cartesian front with the corresponding projected point on the boundary, a single layer of prism grids is obtained. This single layer can be subdivided into multiple layers with proper grid clustering near the geometry to resolve a viscous boundary layer.

Examples of viscous adaptive Cartesian grids for both the fuel deposit and the erosion surface geometries are displayed in Fig. 3. The surface grid generated from the Cartesian front projection is displayed in Fig. 4 (for the erosion surface only). The grid cells near the roughness panels are adaptively refined to resolve the roughness elements.

Numerical Method. A flow solver capable of handling arbitrary polyhedrons has been developed to uniformly handle the adaptive Cartesian and the viscous layer grids [27]. The Reynolds-averaged Navier-Stokes equations can be written in the following integral form

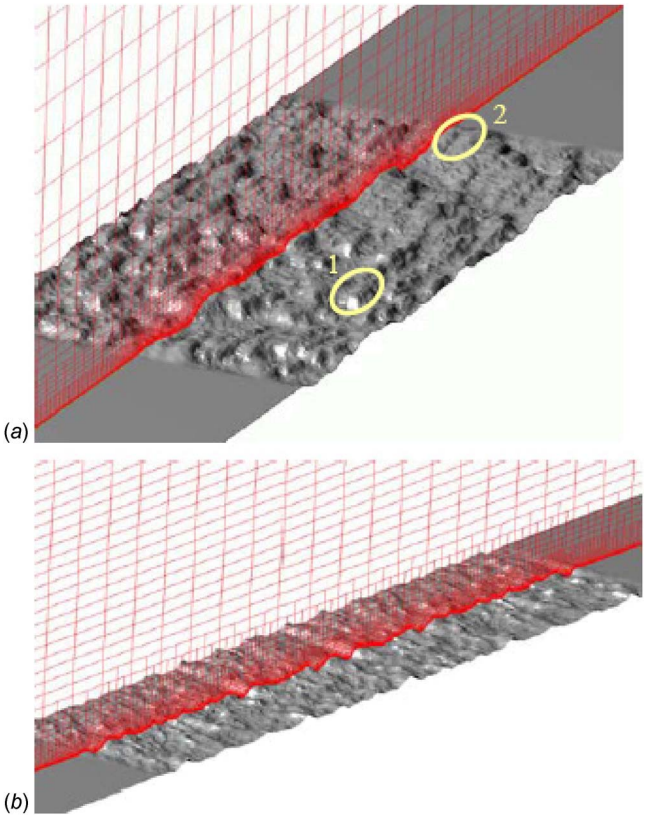

Fig. 3 Cutting planes showing the viscous adaptive Cartesian grids for the: (*a*) fuel deposit; and (*b*) erosion surfaces. Roughness regions are 240 mm×120 mm and 240 mm×60 mm, respectively. The two circles in (*a*) denote roughness peaks referred to in subsequent discussion.

$$\int_V \frac{\partial Q}{\partial t} dV + \oint_S (F - F_v) dS = 0 \tag{13}$$

where Q is the vector of conserved variables; and F and F_v are inviscid and viscous flux vectors, respectively. The integration of Eq. (13) in an arbitrary control volume, V_i, gives

$$\frac{d\bar{Q}_i}{dt} V_i + \sum_f F_f S_f = \sum_f F_{v,f} S_f \tag{14}$$

where $\bar{Q}_i$ is the vector of cell-averaged conserved variables; F_f and $F_{v,f}$ are the numerical inviscid and viscous flux vectors through face f; and S_f is the face area. To compute the inviscid and viscous fluxes through any given face, the standard Godunov-

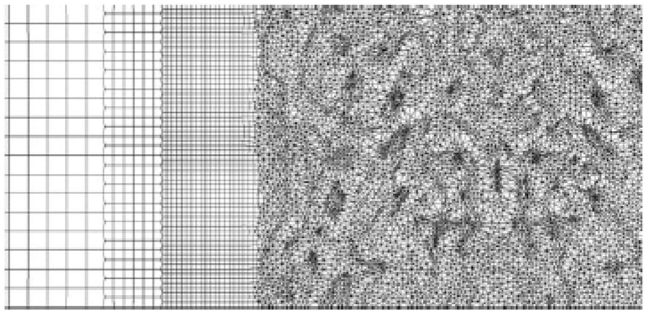

Fig. 4 Surface grid on the erosion surface showing grid refinement near leading edge

Table 2 Grid sizes for 3D RANS model

	Number of cells	Average y^+
Smooth wall—coarse	37,888	0.8
Smooth wall—fine	58,368	0.3
Fuel deposit surface—coarse	364,005	~1
Fuel deposit surface—fine	1,260,051	~1
Erosion surface—coarse	873,221	~1
Erosion surface—fine	1,601,430	~1

type finite volume approach is employed. Using a linear least-squares reconstruction algorithm, a cell-wise linear distribution can be built for each solution variable (in the present study the primitive variables). To compute the inviscid flux, an approximate Riemann solver such as Roe flux difference splitting [28] is used given the reconstructed solutions at both sides of a face. To handle steep gradients or discontinuities, a limiter due to Venkatakrishna [29] is used. The viscous flux is computed using a simple and robust approach presented by Wang [30] without a separate viscous reconstruction.

Although explicit schemes are easy to implement, and are often useful for steady-state, inviscid flow problems, implicit schemes are found to be much more effective for viscous flow problems with highly clustered computational grids. An efficient block (LU-SGS) lower-upper symmetric Gauss-Seidel (LU-SGS) implicit scheme [31] has been developed for time integration on arbitrary grids. This block LU-SGS (BLU-SGS) scheme takes much less memory than a fully (linearized) implicit scheme, while having essentially the same or better convergence rate. The BLU-SGS scheme can be used to integrate Eq. (13) with first- or second-order accuracy. For steady flow computations, the backward Euler approach is employed, i.e.

$$\frac{Q_i^{n+1} - Q_i^n}{\Delta t} V_i + \sum_f F_f^{n+1} S_f = \sum_f F_{v,f}^{n+1} S_f \tag{15}$$

To simulate flow turbulence, a RANS Spalart-Allmaras (*S-A*) model was employed without modifications as described in Refs. [32,33] The computational domain extends from $x=0$ m to 2.04 m in the wind tunnel shown in Fig. 1. To further reduce the computational cost, only 1/3 of the 0.36 m transverse span of the tunnel is included in the computational domain for the fuel deposit surface, while only 1/6 is included for the erosion surface. Symmetry or slip wall boundary conditions are used on the two end walls in the spanwise direction.

Two viscous adaptive Cartesian meshes were generated for each of three cases: smooth wall, fuel deposit surface, and erosion surface. The cell count and average $y+$ for the first layer grid next to the wall are shown in Table 2.

For the rough surfaces, the fine grid essentially doubles the grid resolution near the roughness panels while maintaining an average $y+$ of 1 in the wall normal direction. The coarse mesh has a spanwise direction grid resolution of about 1 mm, while the fine mesh has a spanwise grid resolution of about 0.5 mm. The fine grids have about 50–80 layers in the tunnel height direction. If structured grids were used for this configuration, the fine grid would have about 10–25 million cells. Thus, by using the viscous adaptive Cartesian grid approach, the number of grid cells is reduced by over an order of magnitude.

To further speed convergence, local time steps are used in Eq. (15). The flow convergence is monitored by the history of the average c_f and St over the roughness panels, with the solution typically converging after a few thousands of iterations. Grid generation was executed on a Pentium 4 Linux workstation (2.8 GHz), requiring 2–4 h/rough surface. Due to the size and complexity of the surfaces, even the finer computational grids required that the surface data matrix be sampled by every fourth data point in the streamwise (x) and spanwise (z) directions. The surface resolution was thereby reduced from the printed experimental model, with approximately 14% less wetted surface area. The RANS solver required 24 h to reach a converged solution on a Linux cluster with eight processors.

To simulate the transient method used for the experimental St measurement, both models start the thermal and velocity boundary layers simultaneously at $x=0$ (without an unheated starting length). Also, since the thermal boundary condition at the wall is neither constant wall temperature nor constant wall heat flux, the models employed an exponential $T_w(x)$ boundary condition derived empirically by Ref. [34], i.e., $[T_e - T_w(x)]/\Delta T_{TS} = (x/x_{TS})^{0.1}$. This distribution accounts for the increased thermal resistance of the thermal boundary layer from the leading edge to the measurement location. The experimental freestream velocity and temperature were used as inflow conditions.

Results and Discussion

Table 3 contains the predicted and experimental values of area-averaged c_f and St for the smooth and rough panels. The 3D RANS data are for the fine and coarse grid models. Also shown in the table are smooth and rough-wall correlation values which are provided as a reference [24,35–39]. The various rough wall correlations were all derived using a sand-grain roughness height (k_s) based on the experimentally measured Sigal-Danberg (Λ_s) parameter from Table 1. The smooth wall empirical correlations for c_f and St were taken from Ref. [24].

The skin friction predictions for both the DEM and 3D RANS fine-grid models are within ±8% of the experimental values in all three cases. This is a marked improvement over the k_s-based empirical correlations for c_f which ranged from 16% below to 20%

Table 3 Comparison of c_f and St data from experiment, computation, and correlations

	Smooth	Fuel deposit	Erosion surface
Skin friction, c_f			
Experimental	0.00349	0.00937	0.0103
Discrete element model (DEM)	0.00375	0.00940	0.0111
3D RANS model—fine	0.00345	0.00971	0.0100
3D RANS model—coarse	0.00333	0.0128	0.0113
Empirical correlations [24,35–37]	0.00367	0.0083–0.0112	0.0087–0.0119
Stanton number, St			
Experimental	0.00215	0.00308	0.00308
Discrete element model (DEM)	0.00225	0.00360	0.00345
3D RANS model—fine	0.00204	0.00268	0.00288
3D RANS model—coarse	0.00199	0.00255	0.00259
Empirical correlations [24,36,38,39]	0.00219	0.0034–0.0037	0.00345–0.0038

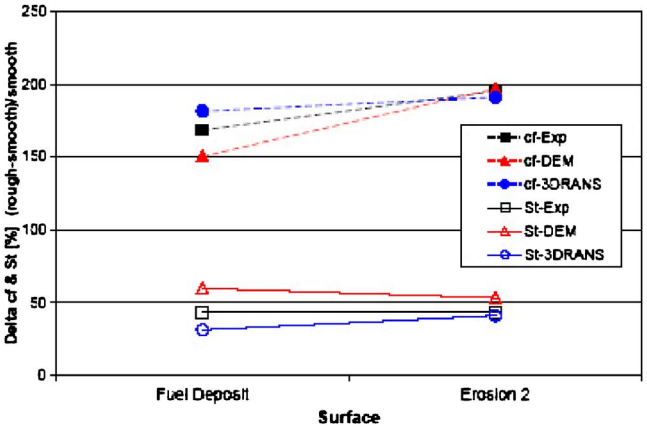

Fig. 5 Comparison of % change in c_f and St from experiment and computation: (3D RANS data from fine grid only)

above the measured values. The agreement in St is not as good, with the two model predictions falling within ±17% of the experimental data (compared to ±23% for the empirical correlations).

An alternative comparison can be made by calculating the percent change in c_f (or St) from the smooth baseline value in each data set. Since the smooth-wall values were not equivalent, this comparison focuses exclusively on the changes in skin friction or heat transfer due to roughness alone (Fig. 5). From this perspective it is clear that both models are in closer agreement with the experimental data for the erosion surface compared to the fuel deposit surface. The surface maps in Fig. 3 and the roughness data in Table 1 show that the largest roughness elements (Rt) on the fuel deposit surface are 70% larger than for the erosion surface. The discrete element model is based on the premise that roughness effects can be modeled as bulk momentum deficit (and heat transfer) source terms in the turbulent boundary layer equations. Boundary layer development in the "nonblocked" portion of the control volume is modeled as a two-dimensional equilibrium boundary layer. These assumptions become less accurate as large roughness elements protrude to nearly 25% of the boundary layer thickness. Consequently, it is not surprising that the DEM underestimates the pressure drag component of c_f on the largest elements for the fuel deposit panel. At the same time, DEM overestimates the augmented heat transfer (Nu) associated with heightened mixing in the wake of these large elements. Since the roughness element Nu correlations (Eq. (7)) are based on local Re_d, they do not account for the mutual influence of randomly clustered roughness elements which tend to alter coherent wake structures. This disconnect becomes more pronounced as the roughness peaks become larger and less evenly distributed (Fig. 3). This could explain why the DEM ΔSt prediction is 10% higher than the experimental ΔSt for the erosion surface and 17% higher for the fuel deposit panel.

The RANS fine-grid simulation also yields closer agreement to the experiment in the case of the smaller roughness (erosion) surface compared to the fuel deposit surface. However, the trends in the 3D RANS prediction for the fuel deposit surface are opposite that of the DEM. The Δc_f prediction is 15% above the experimental value while the ΔSt prediction is 14% below. This is due at least in part to the resolution of the viscous layer grid adjacent to the body surface. The data in Table 3 show that a doubling of the near wall grid resolution (from coarse grid to fine grid) produced a much closer agreement with the experimental data for both c_f and St. As indicated earlier, even the fine-grid model required a sparser sampling of the roughness data (i.e., every fourth point) for a tractable 3D simulation. The corresponding decrease in wetted surface area could explain the lower predicted heat transfer.

Table 4 Comparison of c_f and St contributions above and below mean elevation

	Deposit surface 3D RANS	Deposit surface DEM	Erosion surface 3D RANS	Erosion surface DEM
c_f above y_{me} (%)	58	83.4	62	89.5
c_f below y_{me} (%)	42	16.6	38	10.5
St above y_{me} (%)	59.3	68.6	55.9	62.8
St below y_{me} (%)	40.7	31.4	44.1	37.2

Also, the decreased definition of the larger roughness elements on the fuel deposit surface creates smoother peaks protruding into the boundary layer and may overestimate their pressure drag component. Thus, it is likely that increased grid definition may produce even closer agreement with experimental data for surfaces with large roughness elements.

In summary, despite the enormous increase in required analysis time (2–3 min for 2D DEM versus 24 h for 3D RANS on a fine grid) the results show nearly equivalent accuracy but with opposing trends when compared to the experimental data. Nevertheless, the spatial resolution in the three-dimensional RANS simulation provides a unique opportunity to evaluate the various assumptions made in the discrete element model. One of these assumptions is the location of the reference height at which the smooth wall shear and heat transfer is evaluated. For this study, the mean elevation of the roughness surface (y_{me}) was used since it is the average height of the "no-slip" location along the surface. This is consistent with the observations of Schlichting and Taylor [8,16] that yielded most meaningful results when the "melt down" surface was used as the reference height. The "melt down" surface is the resulting surface if all the material were melted down and allowed to solidify with a constant height in the same planform area. The "melt down" surface height is thus equivalent to the mean elevation height.

To evaluate the use of the mean elevation as the reference plane, the 3D RANS c_f and St data were divided into contributions from above and below the midplane. These data are shown in Table 4 as percentages of the c_f (or St) for the entire roughness panel. Also shown in Table 4 are the DEM data which have been split into contributions from the roughness elements (above y_{me}) and from the smooth reference surface (at y_{me}).

In all cases, it appears that the discrete element model overemphasizes the relative contribution of the roughness peaks above the mean elevation when compared to the 3D RANS simulation. This disparity is more pronounced in the case of skin friction due to the large contribution of pressure drag that is only attributed to that portion of the roughness peaks above the mean elevation in the DEM simulation. The discrete element model used in this study was originally developed from experimental data with ordered roughness element arrays (e.g., cones or hemispheres) mounted to a smooth, flat subsurface. In that case, the mean elevation plane is located a fixed distance above the flat subsurface, which is a solid surface with no flow below it. The air volume between the subsurface and y_{me} is in the lower portion of the boundary layer, thus drag forces due to velocity gradients (τ_w) are likely to be more significant than drag forces proportional to velocity magnitude (pressure drag). Also, the horizontal surface area of the mean elevation plane is approximately equal to that of the flat subsurface. Thus, neglecting the flow below the mean elevation and accounting for all of the contributions to drag (and heat transfer) associated with the valleys at the smooth mean elevation surface are reasonable approximations.

When DEM was adapted to real rough surfaces, the same assumptions were employed. By approximating the roughness below the mean elevation in this way, DEM underestimates both the wetted surface area and the integrated pressure force on the rough-

ness elements. Table 1 indicates that the wetted surface area for the two roughness models (S_w) is approximately 20% greater than the equivalent smooth planform surface area (S). Assuming that half of this increased wetted area (i.e., 10%) is below the mean elevation, this is roughly equivalent to the 7–9% underestimate of the fraction of St below y_{me} made by the DEM (compared to 3D RANS). For the net drag force, both the wall shear and pressure drag components are affected. Thus, the wetted surface area reduction would affect skin friction drag by the same 7–9% and pressure drag would be responsible for the rest of the disparity in total drag (19–22%). This of course assumes that the 3D RANS data accurately represent the flow over the rough surface. Since the agreement between the RANS simulation and the experimental data is hardly better than that for the DEM (Fig. 5), it is premature to suggest modifications to the DEM approximations that were borrowed from ordered roughness element experiments.

In fact, the beauty of the discrete element model is that it produces such good agreement with the experimental data without special treatment for random versus ordered roughness and without the need for complicated three-dimensional surface grids. This agreement is made possible through careful treatment of the roughness peaks above the mean elevation, which compensates for the underestimate of the roughness valleys. To illustrate this point, the drag and heat transfer distributions for two isolated peaks on the fuel deposit surface were evaluated using both 3D RANS and DEM. The peak locations are indicated with circles in Fig. 3(*a*). Both peaks are elliptical in shape with maximum streamwise extents at y_{me} of 40 mm and 36 mm, respectively (for Peaks 1 and 2) and maximum spanwise extents at y_{me} of 16 mm and 12 mm. The maximum elevations are approximately 3 mm above the mean panel height of 6 mm (i.e., 9 mm) for both peaks.

For this comparison, the isolated peaks were first evaluated using the 2D discrete element model. The mean velocity profiles at the streamwise locations corresponding to the peaks centers were evaluated to determine the $\mathrm{Re}_d(y)$ distributions which were then used in Eqs. (2) and (7). This yielded the drag deficit and heat transfer source terms (as functions of elevation, y) that were then incorporated into the two-dimensional turbulent boundary layer equations (Eqs. (8)–(10)). These drag and heat transfer distributions are presented in Fig. 6. This figure shows the percentage of total drag (and heat transfer) at 12 equal intervals through the roughness elements' maximum peak-to-valley height. The contributions from the surface region below y_{me} are shown at a constant value to represent the fraction of c_f and St accounted for at the mean elevation in the DEM model. Thus, the total area to the left of each plot sums to 100%. Also, the area represented in the regions above and below y_{me} (6 mm) match those indicated for the fuel deposit surface DEM results in Table 4 (i.e., 83.4% of c_f and 68.6% of St above y_{me}.)

The same data were also extracted from the 3D RANS fine-grid simulation and are included in Fig. 6 as well. It should be noted that since the elevation intervals considered in Fig. 6 (0.5 mm) are comparable in size to the fine-grid surface resolution, the pressure drag component of c_f integrated over the roughness elements is extremely sensitive to the cutoff elevation intervals being considered. Thus, when considering a single peak, the $c_f(y)$ distribution fluctuates dramatically making a direct comparison of c_f between DEM and 3D RANS for an isolated peak impossible. These fluctuations are attenuated considerably when the entire roughness surface is evaluated and a polynomial curve fit to the $c_f(y)$ distribution is used. This global measurement curve is shown in Figs. 6(*a*) and 6(*b*). Thus the 3D RANS $c_f(y)$ distributions are identical for both peaks. The St distributions are not sensitive in this way and the figure shows the individual data for each peak.

The primary observation from Fig. 6 is that nearly 50% of the total drag in the 3D RANS prediction occurs below $y=6$ mm. To compensate for this large drag component, the discrete element model necessarily exaggerates the drag for the part of the roughness peak above the mean elevation relative to the 3D RANS prediction. As indicated earlier, the empirical relations used by the DEM to calculate the drag coefficient (Eq. (2)) were determined by extensive calibrations using a number of deterministic surface roughness data sets [40]. These data sets were all taken using smooth subsurfaces to which roughness elements were added. When the smooth subsurface is not present, as is the case with the real roughness surfaces evaluated here, some of the flow momentum necessarily enters the valleys below the mean elevation, creating increased drag in this region. This three-dimensional flow shift also decreases the effective Reynolds number on the upper half of the roughness peak, reducing the drag component in this region. Figure 7 highlights this three-dimensional flow behavior using flow streamlines around roughness Peak 2 from the 3D RANS fine-grid simulation. All of the streamlines start at $x=1.23$ m and various y and z locations between 4 mm and 6 mm elevation in front of the roughness peak.

For roughness with modest peak elevations (such as the erosion surface) the redistribution of momentum assumed by the discrete element method maintains an appropriate level of total drag for the surface. Apparently, as the roughness peaks become large relative to the boundary layer thickness (such as for the deposit surface), the redistribution undercompensates for the pressure drag

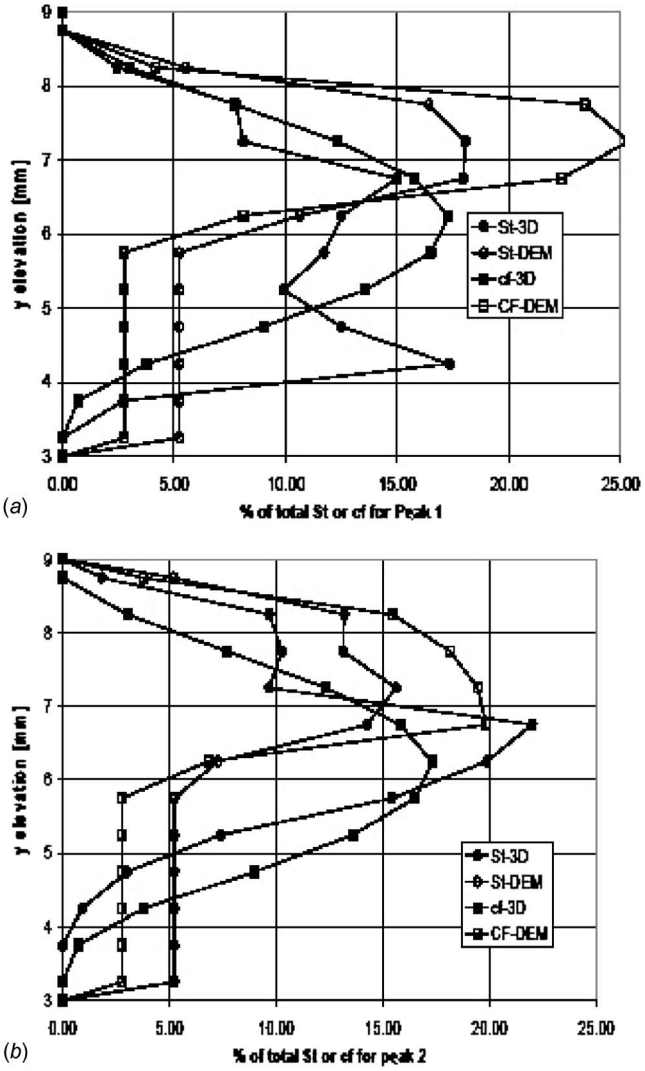

Fig. 6 Drag and heat flux distributions with elevation for isolated peaks on deposit surface. Both DEM and 3D RANS results shown: (*a*) Peak 1 and (*b*) Peak 2.

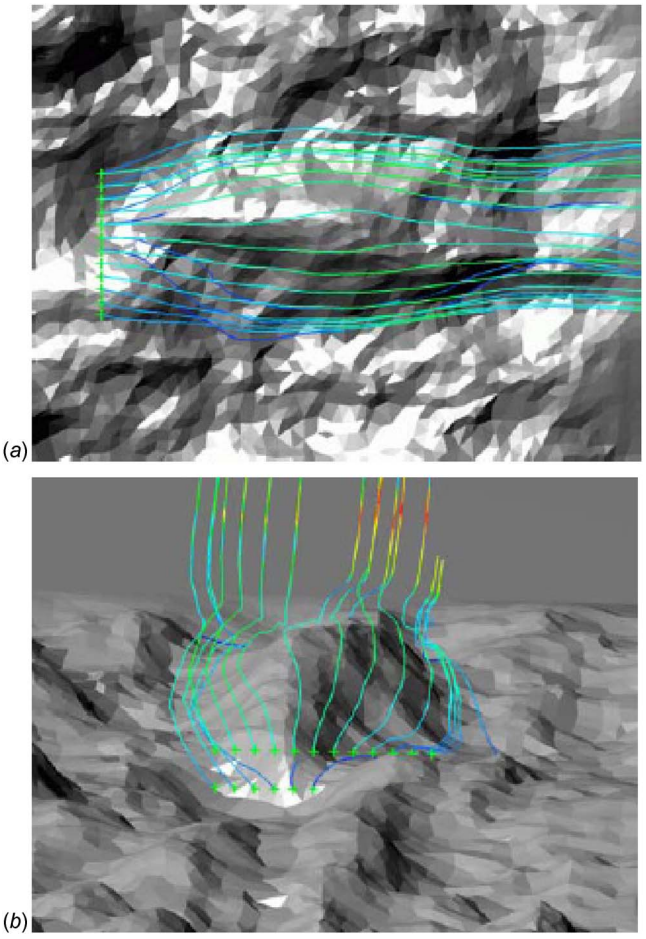

Fig. 7 Flow streamlines around Peak 2 on deposit surface (from 3D RANS simulation): (*a*) top view—flow is left to right; and (*b*) view from upstream

component and thus DEM underpredicts the total drag force. The opposite occurs for heat transfer where the DEM redistribution of boundary layer momentum overcompensates for the heat transfer below the mean elevation, thus producing an overestimate for St as roughness elements become large.

The observation that the discrete element model underestimates the contributions to c_f and St from the roughness elements below the mean reference surface raises a limitation in the application of this model. DEM accounts for roughness elements that protrude into the boundary layer from the smooth reference surface, but in its present formulation it does not account for the influence of roughness valleys (below the reference level). Thus a dimpled surface would be evaluated as essentially smooth, though dimples are known to generate vortical structures that enhance heat transfer and (to a lesser extent) increase skin friction [41]. Bons et al. [1] found that for turbines, surface pitting and thermal barrier coating (TBC) spallation are both roughness characterizations with a strong negative skewness (large valleys below the mean). It is expected that the DEM model would underestimate the c_f and St for these surfaces. The 3D RANS model, however, fully discretizes the roughness valleys as well as the roughness peaks and does not experience this deficiency. To demonstrate this capability, a third roughness surface scaled from TBC spallation on a first stage turbine blade was simulated with the RANS model using a fine grid. The predicted Δc_f due to roughness was 134% (compared to 121% from experiment) and the predicted ΔSt was 24% (compared to 30% from experiment). These predictions show closer agreement to the experimental values than for the fuel deposit surface, although the trend is the same as that noted in Fig. 5 (overestimate for c_f and underestimate for St). This TBC spallation surface also has large peak-to-valley roughness features (Rt =6.4 nm) though the skewness is −0.7 compared to 0.1 for the fuel deposit surface.

Conclusions

Skin friction (c_f) and heat transfer (St) predictions were made for a turbulent boundary layer over randomly rough surfaces at a Reynolds number of 900,000. Two different approximations are used to characterize the roughness in the computational model: the discrete element model and full 3D discretization of the surface. Comparisons were made to experimentally measured values of c_f and St for two unique roughness characterizations. The following conclusions are offered based on the results:

(1) Both methods predict c_f to within $\pm 8\%$ and St within $\pm 17\%$, the RANS code yielding slightly better agreement. This is a significant improvement over the standard empirical roughness correlations;
(2) In both cases, agreement with the experimental data is less favorable for the surface with large roughness features (deposit surface);
(3) The improved accuracy of the 3D RANS simulation comes with a 2–3 order of magnitude increase in computational time (2–3 min for DEM versus 24 h for 3D RANS). Indications are that even finer grid resolution may be necessary to improve the 3D RANS model predictions;
(4) The 3D RANS simulation is also capable of analyzing surfaces composed primarily of roughness valleys (rather than peaks), a feature that DEM does not have in its present formulation;
(5) The versatility of the discrete element model is evidenced by the successful application of correlations developed using ordered roughness elements to random roughness characterizations without modification or adaptation; and
(6) The DEM underestimates the drag and heat transfer contributions from the roughness below the mean elevation. This is compensated for by exaggerated roughness contributions above the mean elevation. This adjustment appears to work well for deterministic roughness and for real roughness as long as the peak elevations are small relative to the boundary layer thickness. The compensation breaks down with larger roughness peaks, yielding an overestimate for St and underestimate for c_f.

Acknowledgment

The authors are indebted to industrial partners for providing the turbine hardware; primary among these are: Dr. Boris Glezer formerly of Solar Turbines; Dr. Ron Bunker and Mr. Paul Suttmann at General Electric; Mr. Mohan Hebbar at Siemens-Westinghouse, and Dr. William Troha and Mr. Shawn Pollock of Honeywell Corporation. In addition, collaborations with Dr. Keith Hodge at Mississippi State University and Dr. Richard Rivir and Dr. Rolf Sondergaard of the Air Force Research Lab are appreciated. This work was sponsored by the US Department of Energy—National Energy Technology Laboratory through a cooperative agreement with the South Carolina Institute for Energy Studies at Clemson University. The views expressed in this article are those of the authors and do not reflect the official policy or position of the Department of Energy.

Nomenclature

c_D = local element drag coefficient
c_f = skin friction coefficient, $\tau_w/(0.5\rho U_e^2)$
c_p = specific heat at constant pressure
d = roughness element mean diameter
h = convective heat transfer coefficient
H = specific enthalpy

k = average roughness height ($\approx Rz$)
k_f = fluid conductivity
k_s = equivalent sand-grain roughness
k^+ = $k_s u_\tau / \nu \equiv \mathrm{Re}_k$
kf_α = roughness height adjusted for mean angle [23]
K_ϵ = elliptical element area correction factor
N_r = number of roughness elements
Nu_d = local element Nusselt number (hd/k_f)
P = pressure
P_w = roughness element wetted perimeter
Pr = Prandtl number (ν/α)(=0.71)
Pr_t = turbulent Prandtl number ($\cong 0.9$)
Q = local element heat transfer
Ra = centerline average roughness
Re_x = Reynolds number ($U_e x/\nu$)
Rt = maximum peak to valley roughness
Rz = average peak to valley roughness
s = flat model (planform) surface area
Sk = skewness of height distribution
St = Stanton number, $h/(\rho c_p U_e)$
S_w = roughness model wetted surface area
T = temperature
t = time
U_∞ = freestream velocity
u = local streamwise velocity
u_τ = friction or shear velocity $\sqrt{\tau_w/\rho}$
v = local velocity normal to wall
x = streamwise distance from tunnel floor leading edge
y = surface normal coordinate
z = spanwise coordinate
α = thermal diffusivity ($k_f/\rho c_p$), blockage fraction
β = void fraction ($1-\alpha$)
δ = boundary layer thickness
ε = ellipse eccentricity
Λ_s = Sigal-Danberg roughness parameter [14]
μ = dynamic viscosity
ν = kinematic viscosity
θ = boundary layer momentum thickness
ρ = density
τ_w = wall shear

Subscripts

e = freestream
i = individual roughness element
me = mean elevation
R = roughness element
TS = test section measurement location
w = surface or wall

References

[1] Bons, J. P., Taylor, R., McClain, S., and Rivir, R. B., 2001, "The Many Faces of Turbine Surface Roughness," ASME J. Turbomach., **123**(4), pp. 739–748.
[2] Taylor, R. P., 1990, "Surface Roughness Measurements on Gas Turbine Blades," ASME J. Turbomach., **112**(1), pp. 175–180.
[3] Tarada, F., and Suzuki, M., 1993, "External Heat Transfer Enhancement to Turbine Blading due to Surface Roughness," ASME Paper No. 93-GT-74.
[4] Blair, M. F., 1994, "An Experimental Study of Heat Transfer in a Large-Scale Turbine Rotor Passage," ASME J. Turbomach., **116**(1), pp. 1–13.
[5] Guo, S. M., Jones, T. V., Lock, G. D., and Dancer, S. N., 1998, "Computational Prediction of Heat Transfer to Gas Turbine Nozzle Guide Vanes With Roughened Surfaces," ASME J. Turbomach., **120**(2), pp. 343–350.
[6] Suder, K. L., Chima, R. V., Strazisar, A. J., and Roberts, W. B., 1995, "The Effect of Adding Roughness and Thickness to a Transonic Axial Compressor Rotor," ASME J. Turbomach., **117**, pp. 491–505.
[7] Ghenaiet, A., Elder, R. L., and Tan, S. C., "Particles Trajectories through an Axial Fan and Performance Degradation due to Sand Ingestion," ASME Paper No. 2001-GT-497.
[8] Schlichting, H., 1936, "Experimental Investigation of the Problem of Surface Roughness," Ing.-Arch., VII(1).
[9] Nikuradse, J., 1933, "Laws for Flows in Rough Pipes," VDI-Forschungsh., **361**.
[10] Cebeci, T., and Chang, K. C., 1978, "Calculation of Incompressible Rough-Wall Boundary Layer Flows," AIAA J., **16**(7), pp. 730–735.
[11] Boyle, R. J., 1994, "Prediction of Surface Roughness and Incidence Effects on Turbine Performance," ASME J. Turbomach., **116**, pp. 745–751.
[12] Aupoix, B., and Spalart, P. R., 2002, "Extensions of the Spalart-Allmaras Turbulence Model to Account for Wall Roughness," ONERA Technical Report No. TP 2002-173.
[13] Simpson, R. L., 1973, "A Generalized Correlation of Roughness Density Effects on the Turbulent Boundary Layer," AIAA J., **11**, pp. 242–244.
[14] Sigal, A., and Danberg, J., 1990, "New Correlation of Roughness Density Effect on the Turbulent Boundary Layer," AIAA J., **28**(3), pp. 554–556.
[15] Bons, J. P., 2002, "St and Cf Augmentation for Real Turbine Roughness With Elevated Freestream Turbulence," ASME J. Turbomach., **124**(4), pp. 632–644.
[16] Taylor, R. P., 1983, "A Discrete Element Prediction Approach for Turbulent Flow Over Rough Surfaces," Ph.D. dissertation, Mississippi State University, Mississippi State, MS.
[17] Finson, M. L., 1982, "A Model for Rough Wall Turbulent Heating and Skin Friction," AIAA Paper No. 82-0199.
[18] Adams, J. C., and Hodge, B. K., 1971, "The Calculation of Compressible Transitional Turbulent and Relaminarizational Boundary Layers over Smooth and Rough Surfaces Using an Extended Mixing-Length Hypothesis," AIAA Paper No. 77-682, (1977).
[19] Lin, T. C., and Bywater, R. J., 1980, "The Evaluation of Selected Turbulence Models for High-Speed Rough-Wall Boundary Layer Calculations," AIAA Paper No. 80-0132.
[20] McClain, S. T., Hodge, B. K., and Bons, J. P., 2004, "Predicting Skin Friction and Heat Transfer for Turbulent Flow over Real Gas-Turbine Surface Roughness Using the Discrete-Element Method," ASME J. Turbomach., **126**, pp. 259–267.
[21] Bogard, D. G., Schmidt, D. L., and Tabbita, M., 1998, "Characterization and Laboratory Simulation of Turbine Airfoil Surface Roughness and Associated Heat Transfer," ASME J. Turbomach., **120**(2), pp. 337–342.
[22] Barlow, D. N., and Kim, Y. W., 1995, "Effect of Surface Roughness on Local Heat Transfer and Film Cooling Effectiveness," ASME Paper No. 95-GT-14.
[23] Bons, J. P., 2005, "A Critical Assessment of Reynolds Analogy for Turbine Flows," ASME J. Heat Transfer, **127**, pp. 472–485.
[24] Mills, A. F., 1992, *Heat Transfer*, 1st ed., Irwin, IL.
[25] Schultz, D. L., and Jones, T. V., 1973, "Heat-transfer Measurements in Short-duration Hypersonic Facilities," Advisory Group for Aerospace Research and Development, Report No. 165, NATO, Belgium.
[26] Gatlin, B., and Hodge, B. K., 1990 *An Instructional Computer Program for Computing the Steady, Compressible Turbulent Flow of an Arbitrary Fluid Near a Smooth Wall*, 2nd printing, Mississippi State University Press, Mississippi State, MS.
[27] Wang, Z. J., and Chen, R. F., 2002, "Anisotropic Solution-Adaptive Viscous Cartesian Grid Method for Turbulent Flow Simulation," AIAA J., **40**, pp. 1969–1978.
[28] Roe, P. L., 1983, "Approximate Reimann Solvers, Parameter Vectors, and Difference Schemes," J. Comput. Phys., **43**, p. 357.
[29] Venkatakrishnan, V., 1995, "Convergence to Steady State Solutions of the Euler Equations on Unstructured Grids with Limiters," J. Comput. Phys., **118**, pp. 120–130.
[30] Wang, Z. J., 1998, "A Quadtree-Based Adaptive Cartesian/Quad Grid Flow Solver for Navier-Stokers Equations," Comput. Fluids, **27**(4), pp. 529–549.
[31] Chen, R. F., and Wang, Z. J., 2000, "Fast, Block Lower-Upper Symmetric Gauss-Seidel Scheme for Arbitrary Grids," AIAA J., **38**(12), pp. 2238–2245.
[32] Spalart, P. R., and Allmaras, S. R., 1992, "A One-Equation Turbulence Model for Aerodynamic Flows," Paper No. AIAA-92-0439.
[33] Spalart, P. R., and Allmaras, S. R., 1994, "A One-Equation Turbulence Model for Aerodynamic Flows," Rech. Aerosp., **1**, pp. 5–21.
[34] Bons, J. P., and McClain, S. T., 2004, "The Effect of Real Turbine Roughness and Pressure Gradient on Heat Transfer," ASME J. Turbomach., **126**, pp. 385–394.
[35] White, F. M., 1991, *Viscous Fluid Flow*, 2nd ed., McGraw-Hill, New York.
[36] Kays, W. M., and Crawford, M. E., 1993, *Convective Heat and Mass Transfer*, 3rd ed., McGraw-Hill, New York.
[37] Schlichting, H., 1979, *Boundary Layer Theory*, 7th ed., McGraw-Hill, New York.
[38] Dipprey, D. F., and Sabersky, R. H., 1962, "Heat and Momentum Transfer in Smooth and Rough Tubes at Various Prandtl Numbers," Int. J. Heat Mass Transfer, **6**, pp. 329–353.
[39] Wassel, A. T., and Mills, A. F., 1979, "Calculation of Variable Property Turbulent Friction and Heat Transfer in Rough Pipes," ASME J. Heat Transfer, **101**, pp. 469–474.
[40] Taylor, R. P., and Hodge, B. K., 1993, "A Validated Procedure for the Prediction of Fully-Developed Nusselt Numbers and Friction Factors in Pipes with 3-Dimensional Roughness," J. Enhanced Heat Transfer, **1**, pp. 23–35.
[41] Kithcart, M. E., and Klett, D. E., 1997, "Heat Transfer and Skin Friction Comparison of Dimpled Versus Protrusion Roughness," NASA Report No. N97-27444, pp. 328–336.